DISSERTATION ZUR ERLANGUNG DES DOKTORGRADES
DER FAKULTÄT FÜR CHEMIE UND PHARMAZIE
DER LUDWIG-MAXIMILIANS-UNIVERSITÄT MÜNCHEN

Pushing for Alternatives – Lead-free Primary Explosives under the Concept of Energetic Coordination Compounds

Simon Maximilian Josef Endraß
aus
Augsburg, Deutschland
2025

Erklärung

Diese Dissertation wurde im Sinne von § 7 der Promotionsordnung vom 28. November 2011 von Herrn Prof. Dr. Dr. h. c. Thomas M. Klapötke betreut.

Eidesstattliche Versicherung

Diese Dissertation wurde eigenständig und ohne unerlaubte Hilfe erarbeitet.

München, 15.10.2025

_____

(Simon Endraß)

Dissertation eingereicht am 15.10.2025

1. Gutachter: Prof. Dr. Dr. h. c. Thomas M. Klapötke

2. Gutachter: Prof. Dr. Konstantin Karaghiosoff

Mündliche Prüfung am 27.11.2025

„Die Freiheit der Wissenschaft hat der Menschheit ein immenses Maß an Erkenntnissen über sich selbst und die Welt, in der wir leben, beschert. Man könnte meinen, die Wissenschaft sei unangreifbar, aber das ist sie nicht. Sie bedarf des andauernden, bewussten und entschiedenen Rückhalts in der Gesellschaft."

Ulrich Woelk in „Das Grundgesetz – Ein literarischer Kommentar"

DANKSAGUNG

Als Naturwissenschaftler neigt man dazu sachlich und emotionslos zu schreiben. Über Jahre trainiert man diese Kunst und schiebt deshalb einen unverzichtbaren Teil der Arbeit immer wieder vor sich her: die Danksagung. Nachdem der lange Weg von Schule und Studium aber auf sich allein gestellt nicht möglich wäre, ist sie selbstverständlich unverzichtbar. Dieser Abschnitt gilt deshalb allen Menschen ohne die diese Arbeit nie zustande gekommen wäre.

Fangen wir mit dem Offensichtlichen an. Eine Doktorarbeit ohne Doktorvater ist in etwa so logisch wie ein Butterbrot ohne Brot. Mein Dank gilt deshalb Prof. Dr. Dr. h. c. Thomas M. Klapötke dafür, dass er mich in seinem Arbeitskreis aufgenommen, unterstützt und gefördert hat. Am meisten geschätzt habe ich immer, wie hoch er die Wissenschaftsfreiheit hält. Nicht nur lässt er sich selbst nicht verbiegen, sondern auch die Art und Weise wie man als Doktorand seinen Interessen und Vorstellungen folgen kann, hat die Zusammenarbeit stets bereichert.

Ebenfalls danken möchte ich Prof. Dr. Konstantin Karaghiosoff. Conny ist nicht einfach nur der Zweitkorrektor dieser Arbeit, sondern hat auch durch die Messung der aufwändigeren NMRs zu den Ergebnissen beigetragen. Außerdem denke ich kann ich getrost behaupten, dass er der Kapitän unseres X-Ray-Teams ist und wie jeder weiß, ist ein Team ohne Kapitän ziemlich planlos.

An dieser Stelle möchte ich mich zudem bei der Prüfungskommission, bestehend aus Herrn Prof. Dr. Wolfgang Weigand, Frau Prof. Dr. Silvija Markic, Herrn Prof. Dr. George Cutsail und Herrn Prof. Dr. Oliver Trapp bedanken. Es heißt ja immer scherzhaft der schwierigste Teil einer Dissertation ist es ausreichend viele Professoren für die Prüfung zur selben Zeit in einen Raum zu bekommen. Danke, dass Sie sich an diesem Gerücht offensichtlich nicht beteiligen wollen.

Thematisch aufgeschmissen wäre ich außerdem ohne den großen Beitrag von Dr. habil. Jörg Stierstorfer. Seien es gute Ideen, Korrekturen der Publikationen, Unterstützung bei der Stellensuche oder auch einfach nur ein direktes, ehrliches Feedback, Jörg findet dafür immer eine Minute, wenn man zu ihm kommt. Der Einstieg in eine Doktorarbeit ist nicht immer leicht, aber Deine Unterstützung und Erfahrung war für mich von unschätzbarem Wert und hat es mir so einfach wie nur irgendwie möglich gemacht! Dass Du mich schon früh in die EMTO GmbH aufgenommen hast und mir somit den Einblick in die Industrie ermöglicht hast, hat die Zeit an der LMU für mich enorm bereichert.

Komplett alleine wäre diese Arbeit natürlich auch langweilig geworden und eines kann man im AK Klapötke definitiv behaupten: Langweilig ist es hier definitiv nicht! Deshalb vielen Dank an meine Kolleginnen und Kollegen: Markus Rösch, Lukaš Likas Josh Bauer, Lukas Eberhardt, Jenny Heidrich, Dr. Andreas Neuer, Alex Gisnapp, Alex Schweiger, Dr. Jonathan Gutenthaler-Tietze, Dr. Maxi Benz, Dr. Jasmin Lechner, Dr. Christian Riedelsheimer, Dr. Tobi Lenz, Dr. Moritz Kofen, Dr. Alex Harter, Dr. Michael Voggenreiter, Michi Gruhne, Marcus Lommel, Dr. Maximilian Wurzenberger, Dr. Anne Friedrichs, Jelly Reinhardt, Willy Cremers, Andreas Bartonek und Stefan Huber dafür, dass ich nie das Gefühl hatte zu arbeiten, sondern mit Freunden an lustigen Projekten zu basteln! Insbesondere die gemeinsamen Fahrten auf die NTREM, den Trip nach Frankreich mit Jörg und Marcus und die Reise nach Zagreb mit Jasmin und Lukaš werde ich immer in Erinnerung behalten, inklusive Flugtrauma. Besonders erwähnen möchte ich noch einmal Andreas Neuer, der mich am ersten Tag des Studiums sozusagen adoptiert hat und mich seitdem nicht wieder losgeworden ist. Selbst auf seinem BAföG-Schein bin ich plötzlich aufgetaucht – wenn das mal kein Zeichen ist!

Bedanken möchte ich mich auch bei meinen Praktikantinnen und Praktikanten, die diese Arbeit durch ihren Beitrag mitermöglicht haben. Sadiq Strey, Filip Topic, Melanie Werner, Daniel Eichmeier, Leo Brajkovic und Patrycja Jasinska zu betreuen war für mich eine spannende Aufgabe, durch die ich viel gelernt habe. Insbesondere die Bachelorarbeit von Melanie und der F-Bericht von Sadiq haben hervorragende Grundlagen für die jeweiligen Publikationen geliefert und mir das Leben somit sehr erleichtert.

Dankbar bin ich zudem meinen Chemie- und Biologielehrkräften des Justus-von-Liebig Gymnasium Neusäß. Dass der Mathematisch-Naturwissenschaftliche Zweig sich als die richtige Wahl herausgestellt hat, kann man wohl mittlerweile sagen, ohne die Begeisterung, die mir an dieser Schule vermittelt wurde, hätte es allerdings auch anders laufen können.

Meiner Erfahrung nach zweifelt im Laufe des Studiums so gut wie jeder irgendwann daran ob es die richtige Fachrichtung war und ob man überhaupt gut genug ist. In solchen Momenten kann man nur hoffen, dass man das richtige Umfeld und gute Freunde hat, die einen unterstützen und antreiben. Für diese Unterstützung möchte ich meinem gesamten Freundeskreis danken, insbesondere drei Menschen, die mich immer wieder gepusht haben: David Hohenegger, Tobias Farger und Saskia Wieczorek.

Zum Schluss bleiben mir jetzt noch die wichtigsten Menschen: meine Familie. Dass ich mich immer auf eure Unterstützung verlassen konnte, ist so unglaublich wichtig für mich und hat mir

überhaupt erst diesen gesamten Weg ermöglicht. Ich könnte mir keine besseren Eltern als meine Mutter Bea und meinen Vater Günter vorstellen. Ihr habt mir immer gezeigt, dass ihr voll hinter mir steht und dass ich für mich und meine Entscheidungen einstehen muss. Dazu hatte ich als Vorbilder meine großen Brüder Manu und Flo, die unsere Familie durch Gabi, Elias, Lenia und Julius, sowie Steffi und Matthias bereichert haben. Durch euch wurden unsere Treffen ein bisschen wilder, aber dafür noch einmal deutlich unterhaltsamer! Zuletzt möchte ich mich noch bei Vroni bedanken. Vielen Dank, dass du mich jetzt schon seit acht Jahren aushältst und das obwohl unsere Urlaube immer im Chaos enden. Ich kann es kaum erwarten herauszufinden, wie das Chaos weiter geht.

Table of Content

1 Introduction

1.1 Coordination Chemistry

While the benefits of coordination chemistry have followed humanity for quite some time, the scientific field itself is a relatively modern appearance. [1] One example of such benefits is the use of coordination compounds in dyes, which allows a wide range of substances and colors. [2] Historically, the use of such substances reaches back to ancient times in India, Persia and Egypt, where alizarin was obtained from the madder plant and combined with clay to form the bright red alizarin dye due to coordination to the Al^{3+}-metal center. [3-4] As time passed, more coordination compounds, such as Prussian Blue [5], Vauquelin's Salt [6] and Zeise's Salt [7] (Figure 1) were discovered. Despite all discoveries, the breakthrough of the structural theory behind coordination chemistry was only achieved in the late 19th. century by Alfred Werner, who introduced the concept of the coordination number, which he described by the german name *Nebenvalenz*. [3, 8]

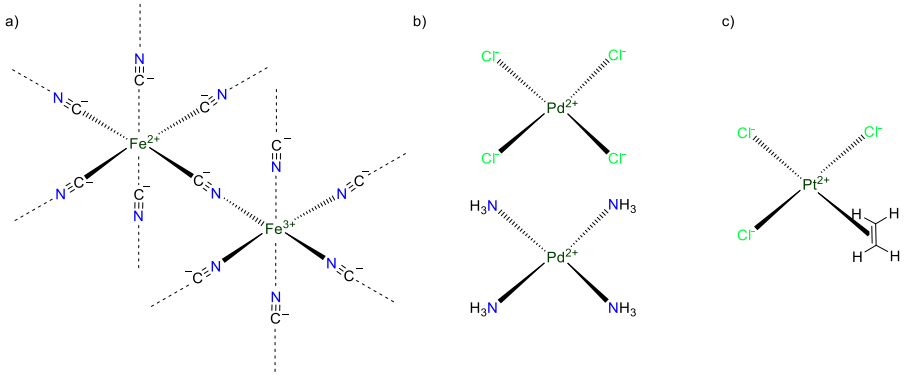

Figure 1. Structural elements of the coordination within **a)** Prussian Blue**, b)** Vauquelin's Salt and **c)** Zeise's Salt.

As a result of the understanding of the structural theory and modern methods for structural elucidation, such as single crystal X-ray diffraction, different coordination numbers and their associated coordination polyhedrons have been observed. The typical polyhedrons, that can be observed for the coordination numbers 2–6 are displayed in Figure 2. For reasons of simplification, the metal center is generalized as M, ligands are shown as green circles and planes are represented in gray. The coordination number and polyhedron can be correlated with the nature of the central metal and the steric demand of the ligand. In addition, it should be noted, that ligand fields with different ligands can show isomerism.

Interestingly, the coordination number 6 always results in an octahedron despite the fact that other polyhedrons such as the trigonal prism, the trigonal antiprism and the planar hexagon are possible alternatives. [9]

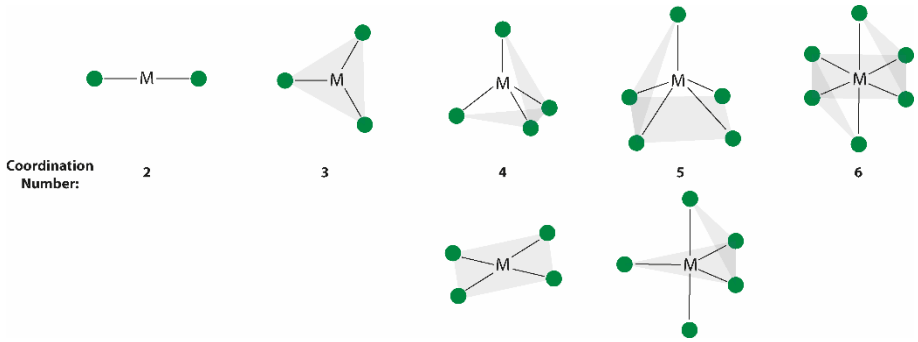

Figure 2. Observable coordination polyhedrons for the coordination numbers 2–6.

Through this new concept Werner laid the groundwork of the modern coordination chemistry, which was essential for the design of multiple metal-based drugs. [10-12] Apart from the use in modern medicine, coordination compounds found their use in material science. Materials like organic light-emitting diodes (OLEDs) often contain metal-organic coordination compounds and have revolutionized many fields of daily life. [13-14] In similar ways, the field of organic chemistry has profited from catalysts such as the Grubbs catalysts and the understanding of cross-coupling agents (Figure 3). [15-20]

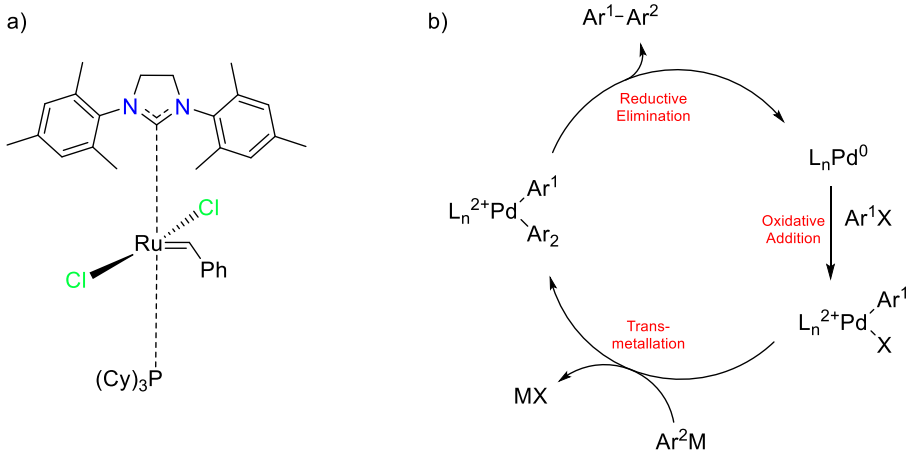

Figure 3. Examples of coordination chemistry with application in organic synthesis. **a)** Grubbs II catalyst, **b)** Systematic description of cross-coupling reactions.

These examples show not only how coordination chemistry changed different fields of research, but also how the complexity of ligands evolved. While early coordination compounds contained mostly simple ligands, with their focus on the basic understanding

of the nature of the coordination bond, modern chemical approaches draw attention to an application. Another such application, which has gained interest in the scientific community are the so-called energetic coordination compounds (ECCs). These compounds can often be described as relatively simple combinations of oxidizer and fuel within the coordination sphere. This allows for the release of energy ranging from simple burning, often accompanied by visible color, depending on the central metal, up to violent detonation. The range of the output hereby can be explained by the combination of the ligand, which is mostly considered as the fuel and the anion, which is in many cases of oxidizing nature. Some of these compounds already reached the verge of industrial application as primary explosives, like for example cobalt(II) pentaamine 5-cyanotetrazolato perchlorate (CP) [21], cobalt(III) tetramine bis-(5-nitrotetrazolato) perchlorate (BNCP) [22] and nickel(II) trihydrazine nitrate (NHN) [23-25] (Figure 4).

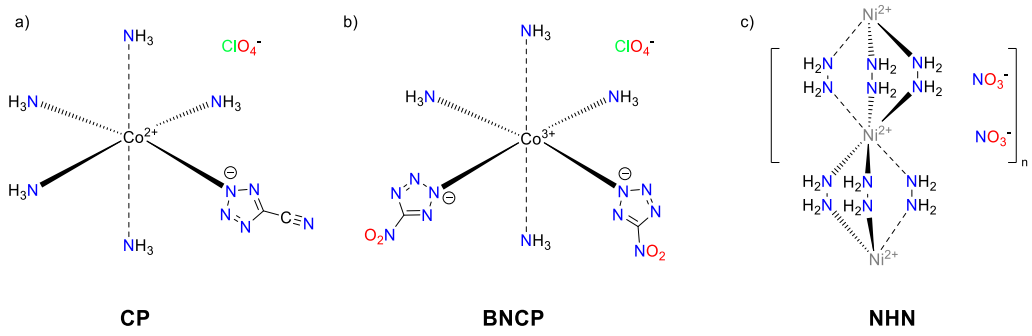

Figure 4. Illustration of the commercially interesting ECCs **a)** CP, **b)** BNCP and **c)** NHN.

1.2 Energetic Materials and their Application

As energetic materials cover a whole range of applications in the civil sector (*e.g.* mining and blasting) and military (*e.g.* ammunition, protective systems and optical signaling), there are multiple ways of categorization. One simple way is to differentiate between molecular energetic materials and mixtures of substances, which by themselves, might not be an explosion hazard. This allows for an insight into the reaction mechanism, which, in the case of Figure 5a) is driven by the contact surface and therefore is highly dependent on the mixing process and in the case of Figure 5b) mostly relies on the intramolecular reaction.

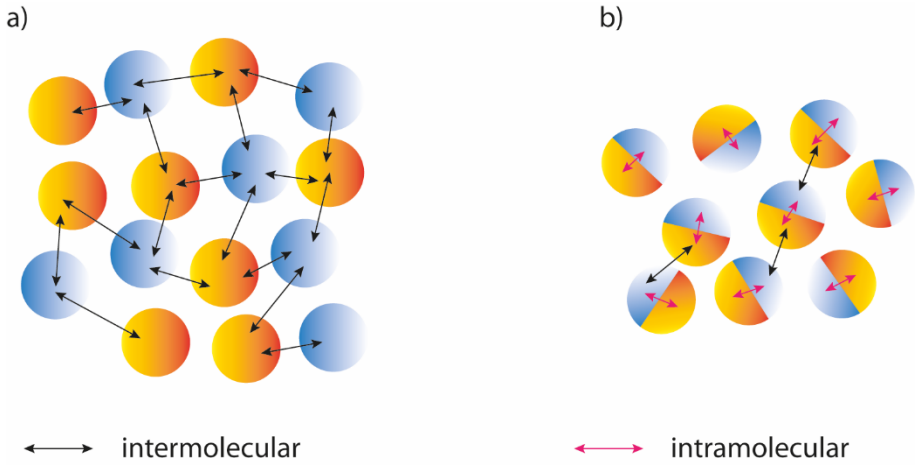

Figure 5. Intermolecular versus intramolecular reaction in **a)** energetic mixtures and **b)** molecular energetic materials.

While the understanding of the reaction mechanism might be a beneficial approach in early stages of teaching the principles of the behavior of energetic materials, it does not provide any information about the potential use of the material. For this reason, other categorization methods have been developed, in which the focus is on the use case. While this method does not provide information about the chemical composition or predominant reaction pathway, it focuses on the industrial application, and therefore, in many ways, the properties of the respective class. This leads to a tree diagram (Figure 6) which first divides the field into pyrotechnics, propellants and explosives, which themselves can be subdivided. Despite the fact, that further subdivision of each class is possible, this chapter focusses on this simple way of classification to give a broad overview over some specific applications.

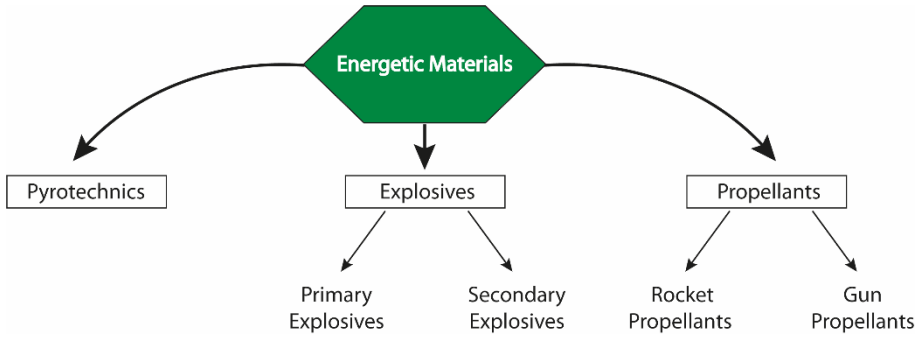

Figure 6. Classification of energetic materials depending on their application.

Pyrotechnical devices and mixtures are most likely the group of energetic materials, which are the best known to the general public. [26-27] They are usually energetic mixtures, which upon burning create a sort of acoustic or optical emission, as in fireworks and emergency

flares, or produce a dense smoke, which can be colored by the addition of dye for the use of signal smokes. [28] The properties of the individual pyrotechnical mixtures depend strongly on their composition. While a detonation of such mixture is in most cases not desirable, it may still be a possible outcome, especially under confinement. [29-30] Typically, physical mixtures of oxidizer and fuel are combined with metal salts as colorants for light-emitting pyrotechnics. [31] The optical impression therefore can be described as a result of the excitation and relaxation of electrons within the color-giving metal cation. Common illuminators hereby rely on Sr(II) for red, Na(I) for yellow, Ba(II) for green and Cu(I) for blue impression. [32] In more recent research, special focus has been drawn toward lithium-based replacements for red-light-emitting pyrotechnics, due to the concern about incorporation of strontium in the human skeleton. [33]

Similar to pyrotechnics, the desired reaction of propellants is below the level of a detonation. [34] Depending on the application the propellant is supposed to burn off evenly, producing constant thrust as in rocket propellants or burn fast enough to produce a breech pressure in gun propellants. [35] The differentiation between gun and rocket propellants from a chemical point of view can also be seen as an issue of technical complexity of the propulsion system itself, as rocket engines are of much higher complexity and vary drastically depending on their specific use. Since the invention of the so-called smokeless powder, which is a single-base propellant based on nitrocellulose, only small adjustments in the field of gun propellants have been made. After the addition of nitroglycerine to nitrocellulose (double-base propellant) to improve the performance, further changes focused mostly on increasing the longevity of the gun barrel, as often seen in triple-base propellants. [36] As mentioned before, rocket propellants are more diverse compared to gun propellants. They can in general be divided into solid and liquid propellants, which again can themselves be split into different categories. The choice of which propellant shape and system is ideal, depends strongly on the specific application, as storage requirements, fast usability and thrust profile may vary. [37]

Unlike in the fields of pyrotechnics and propellants, a controlled detonation is a desirable outcome for the class of explosives. The emphasis hereby lies on the term “controlled”. Safety aspects for manufacturing, storage and handling therefore rely on the strict separation of primary and secondary explosives. Secondary explosives are powerful substances which can be brought to detonation under the right circumstances, should however require a strong stimulus to do so. This requirement allows for safe handling, as the majority of the net quantity of an explosive device, which consists of secondary

explosives or mixtures thereof, shows an acceptable range in terms of friction sensitivity (FS), impact sensitivity (IS) and resistance toward electrostatic discharge (ESD). In addition, the thermal stability of secondary explosives typically exceeds that of primary explosives. Figure 7 shows several examples of commercially used secondary explosives, as well as three modern representatives of the class, which have received high interest in the energetic community.

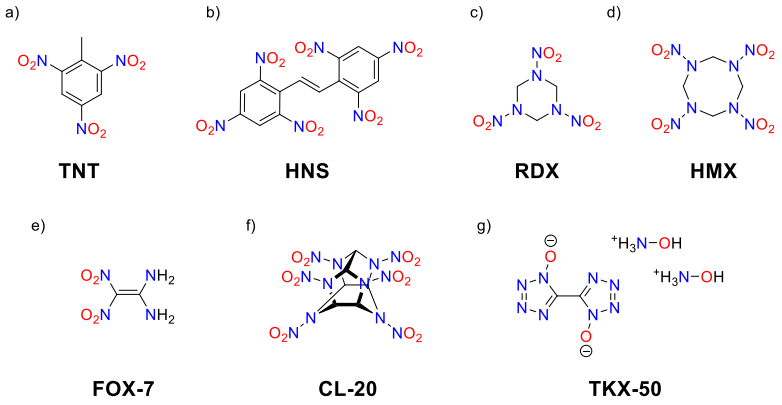

Figure 7. Classical examples of commercially used secondary explosives **a)** 2,4,6-trinitrotoluene (TNT), **b)** hexanitrostilbene (HNS), **c)** 1,3,5-trinitro-1,3,5-triazinan (RDX) **d)** octahydro-1,3,5,7-tetranitro-1,3,5,7-tetrazocin (HMX), as well as the three modern examples **g)** 1,1-diamino-2,2-dinitroethen (FOX-7), **f)** 2,4,6,8,10,12-hexanitrohexaazaisowurtzitan (CL-20) and **g)** dihydroxylammonium-5,5′-bistetrazolyl-1,1′-diolat (TKX-50).

As mentioned, the initiation of a secondary explosive requires a strong stimulus, which is typically generated by a primary explosive. Primary explosives are usually more sensitive toward friction, impact and ESD. Their purpose is to undergo a rapid deflagration-to-detonation-transition (DDT) and pass on the resulting shockwave to the secondary explosive or flame front to a propellant. Early developments of primary explosives were mercury fulminate, which was replaced in detonators by lead azide (LA), as well as lead styphnate (LS), and potassium 4,6-dinitrobenzofuroxanate (KDNBF). Nowadays, lead azide and lead styphnate dominate the market for primary explosives, leading to massive lead contamination of shooting grounds and surrounding areas. [38-39]

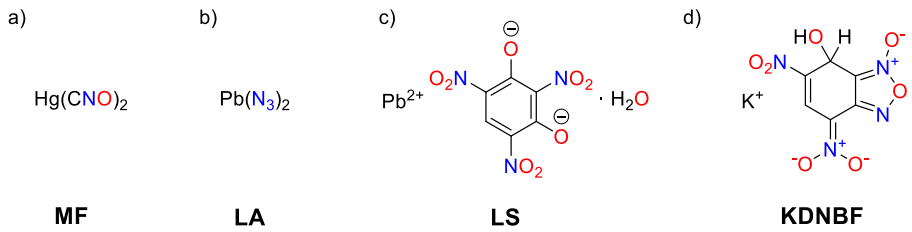

Figure 8. Classical examples of primary explosives. **a)** Mercury fulminate (MF), **b)** lead azide (LA), **c)** lead styphnate (LS), and **d)** potassium 4,6-dinitrobenzofuroxan (KDNBF).

This persistent contamination leads to one of the main problems of lead azide and lead styphnate – their toxicity. [40] Exposure to lead is known to cause severe damage to brain and kidney, and result in behavioral problems and lowered intelligence in children. [41] To reduce the distribution of lead in the environment, researchers around the world have taken serious efforts [42-44], producers have started to focus on alternatives [45-46], and governmental organizations have started banning such compounds of high concern for special applications. [47-48] Both LA and LS have furthermore been added to the REACH "Candidate list of Substances of Very High Concern for Authorisation" in December 2011. [49]

Modern attempts to replace lead-based primary explosives include, copper(I) nitrotetrazolate (DBX-1) [50], potassium 1,1'-dinitramino-5,5'bistetrazolate (K_2DNABT) [51] and other highly energetic potassium salts [52], various ECCs based on copper(II) azide [53-56], transition metal perchlorates [57-60] and energetic perovskites. [61-62] In application, these substances can either be used directly or in mixtures within different devices such as primer caps, cutting devices, or detonators. In any case of application, the primary explosive is used in relatively small quantities and relies on a simple impulse, such as flame, electrical current, mechanical stress or optical excitation. The respective devices are then built in accordance with the stimulus to which they should respond, while ideally being relatively resistant toward the other possible impulses. The two types of detonators, for which the EU directive aims to ban lead azide, are of electric and electronic nature. [47-48] A systematic overview of these two types is shown in Figure 9. In the case of the electric detonator, an example of the modern NME-type (non-mass-explosive) was chosen. This detonator type is known for its improved safety due to the NME body, which shields the primary explosive from external shockwaves. This reduces the likelihood of a mass explosion of multiple detonators, which are stored together, thereby limiting the damage to one unit.

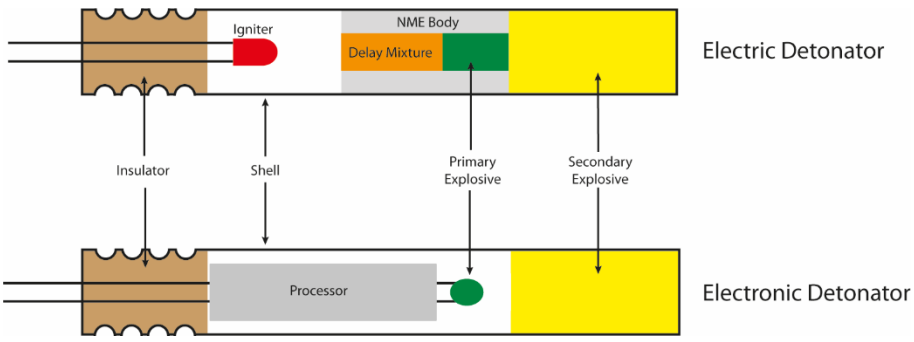

Figure 9. Schematic depiction of electric and electronic detonators.

1.3 Motivation and Objectives

There are multiple reasons to replace lead styphnate and lead azide, especially in civil use cases, where the EU already laid the groundwork for scientifically supported prohibition. The reason why no broad range of lead-free detonators have entered the market, is that the existing alternatives might be options for a specific use case but not for the overall market. The high bulk density, exceptional thermal stability and acceptable mechanical stability of LA (*e.g.* RD-1333) combined with its low price point are a challenge for the "green" alternatives. [63-64] As general requirements for a compound to be considered a possible replacement candidate, it needs to undergo a rapid DDT and successfully transfer the detonation to a secondary explosive. To be considered a drop-in candidate it should furthermore do so with a similar volume of substance, and therefore not influence the geometry or processing of the device. [65] The replacement candidate should possess suitable no-fire limits to allow safe processing and must be compatible with all materials it is brought to contact with. Long-term stability, absence of toxicity, ideally in the overall process, good processability, including high yield and flowability, and a low price can be considered mandatory for industrialization. While the necessary thermal stability of the compound may vary depending on the specific application, the lower acceptance limit is generally considered 150 °C. [35, 66] As mentioned, one concept for the preparation of "green" primary explosives is the formation of energetic coordination compounds. This concept relies on the combination of cation, ligand and anion (Figure 10) for the overall performance and physico-chemical properties, as proven by complexation of copper(II) azide, which results in stabilized ECCs. [54-55] Hereby, the energy content can be controlled by parameters such as the quantity and endothermicity of the ligand and its ratio to the anion, which can in many cases be described as the ratio of fuel to oxidizer. The solubility

of the ECCs can be influenced by using bridging and chelating ligands. While each component of the ECC does influence the toxicity, special focus lies on the exclusion of high-toxicity heavy metals such as lead, cadmium and mercury.

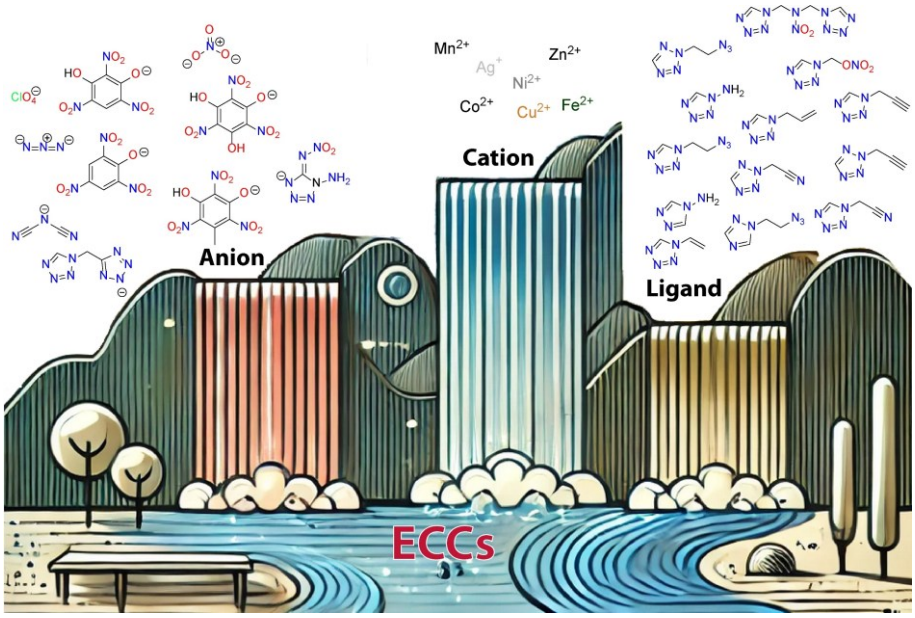

Figure 10. Illustration of the concept of energetic coordination compounds. [67]

In the recent years, publications in the field of ECCs often focused on the increase of the enthalpy of formation of the ligand, ultimately increasing the N+O content of the compounds, while using oxidizing anions, such as perchlorate, chlorate, bromate and nitrate. [57-59, 68-71] The result was an increase of sensitivity for ECCs with comparable stoichiometry. As an alternative method of increasing the enthalpy of formation, this work relies on the introduction of tetrazoles with unsaturated side-chains. In an alternative approach, the authors showed the value of chelating ligands, which by definition coordinate to at least two sites of the central metal, resulting not only in a desirable decrease of solubility, but also as a method to improve the ratio of ligand to oxidizing anion or the amount of azide, in copper(II) azides. [60, 72-75] In a similar manner, this work acknowledges the value of different coordination modes, by studying the structural motifs, observed in single-crystal XRD, and evaluating the resulting trends. Therefore, the main goals of the underlying publications are to emphasize the mechanical and thermal stability in order to ensure safe production and handling, while maintaining certain performance parameters such as a fast and reliable DDT. The analysis of the sensitivities is performed by BAM (Bundesanstalt für Materialforschung und -prüfung) standard protocols on the BAM friction tester and the BAM drophammer. ESD sensitivity is evaluated on an OZM

XSpark10 machine. Thermal stabilities of the compounds are measured by DTA or DSC and combined with TGA measurements. The performance of the respective substance is in first instance tested by hot plate and hot needle tests, and furthermore evaluated in self-assembled detonator set-ups for their potential to initiate PETN, as well as their potential to function in laser-ignitable primer caps.

1.4 References

[1] E. Constable, *Chemistry* **2019**, *1*, 126–163.

[2] J. N. Chakraborty, in *Handbook of Textile and Industrial Dyeing, Vol. 1* (Ed.: M. Clark), Woodhead Publishing, **2011**, pp. 446–465.

[3] G. B. Kauffman, in *Encyclopedia of Inorganic and Bioinorganic Chemistry*, **2011**.

[4] M. C. Whiting, *Chem. Unserer Zeit* **1981**, *15*, 179–189.

[5] A. Kraft, *Bull. Hist. Chem.* **2008**, *33*, 61–67.

[6] N. L. Vauquelsin, *Ann. Chim.* **1813**, *88*, 167–186.

[7] W. C. Zeise, *Ann. Phys.* **1831**, *97*, 497–541.

[8] N. P. E. Barry, P. J. Sadler, **2014**, *86*, 1897–1910.

[9] B. Weber, *Koordinationschemie*, 2nd. ed., Springer Spektrum Berlin, Heidelberg, **2021**.

[10] V. Kumar Singh, V. Kumar Singh, A. Mishra, Varsha, A. Abha Singh, G. Prasad, A. Kumar Singh, *Polyhedron* **2023**, *241*, 116485.

[11] S. Jurisson, D. Berning, W. Jia, D. Ma, *Chem. Rev.* **1993**, *93*, 1137–1156.

[12] L. Ronconi, P. J. Sadler, *Coord. Chem. Rev.* **2007**, *251*, 1633–1648.

[13] J. Kalinowski, V. Fattori, M. Cocchi, J. A. G. Williams, *Coord. Chem. Rev.* **2011**, *255*, 2401–2425.

[14] Q.-C. Zhang, H. Xiao, X. Zhang, L.-J. Xu, Z.-N. Chen, *Coord. Chem. Rev.* **2019**, *378*, 121–133.

[15] T. M. Trnka, R. H. Grubbs, *Acc. Chem. Res.* **2001**, *34*, 18–29.

[16] R. H. Grubbs, T. M. Trnka, in *Ruthenium in Organic Synthesis*, **2004**, pp. 153–177.

[17] A. O. King, N. Okukado, E.-I. Negishi, *J. Chem. Soc., Chem. Commun.* **1977**, 683.

[18] K. Sonogashira, *J. Organomet. Chem.* **2002**, *653*, 46–49.

[19] K. Tamao, K. Sumitani, M. Kumada, *J. Am. Chem. Soc.* **1972**, *94*, 4374–4376.

[20] R. F. Heck, in *Organic Reactions*, **2005**, pp. 345–390.

[21] M. B. Talawar, A. P. Agrawal, S. N. Asthana, *J. Hazard. Mat.* **2005**, *120*, 25–35.

[22] S. Daoud, T. R. Berger, M. J. Vileburn, Insensitive munition-type BNCP explosive material and methods for forming the same, **2009**, US8444784B2.

[23] B. Hariharanath, K. S. Chandrabhanu, A. G. Rajendran, M. Ravindran, C. B. Kartha, *Def. Sci. J.* **2006**, *56*, 383–389.

[24] M. Cartwright, *Propellants, Explos. Pyrotech.* **2018**, *43*, 1270–1276.

[25] O. S. Bushuyev, P. Brown, A. Maiti, R. H. Gee, G. R. Peterson, B. L. Weeks, L. J. Hope-Weeks, *J. Am. Chem. Soc.* **2012**, *134*, 1422–1425.

[26] G. Steinhauser, T. M. Klapötke, *Angew. Chem. Int. Ed.* **2008**, *47*, 3330–3347.

[27] M. Scheid, M. Rusan, T. M. Klapötke, S. Schwarzer, *Chem. Teach. Int.* **2021**, *3*, 285–294.

[28] O. Zeman, V. Pelikan, J. Pachman, *ACS Sustain. Chem. Eng.* **2022**, *10*, 4788–4791.

[29] J.-Q. Zhao, Y.-C. Cheng, H.-Y. Hou, W.-C. Chen, *J. Loss Prev. Process Ind.* **2021**, *69*, 104381.

[30] A. Basco, F. Cammarota, E. Salzano, *Chem. Eng. Trans.* **2010**, *19*, 231–236.

[31] T.-w. Wang, Z.-x. Yi, L. Zhang, Y.-k. Wang, Y. Li, J.-g. Zhang, *Cryst. Growth Des.* **2022**.

[32] J. J. Sabatini, *Propellants, Explos. Pyrotech.* **2018**, *43*, 28–37.

[33] A. M. W. Dufter, T. M. Klapötke, M. Rusan, A. Schweiger, J. Stierstorfer, *ChemPlusChem* **2020**, *85*, 2044–2050.

[34] Y. R. Alexander, N. Rathi, P. A. Ramakrishna, *FirePhysChem* **2024**, *4*, 107–113.

[35] T. M. Klapötke, *Chemistry of High-Energy Materials*, 6th ed., De Gruyter, Berlin, Boston, **2022**.

[36] E. Rozumov, in *Energetic Materials: From Cradle to Grave* (Eds.: M. K. Shukla, V. M. Boddu, J. A. Steevens, R. Damavarapu, J. Leszczynski), Springer International Publishing, Cham, **2017**, pp. 23-65.

[37] C. Tola, M. Nikbay, in *52nd AIAA/SAE/ASEE Joint Propulsion Conference*, American Institute of Aeronautics and Astronautics, **2016**.

[38] H. Stucki, *CHIMIA* **2004**, *58*, 409–413.

[39] D. R. S. Lima, M. L. S. Bezerra, E. B. Neves, F. R. Moreira, *Rev. Environ. Health* **2011**, *26*, 101–110.

[40] S. Aliyu Haruna, A. Musa, *GSC Biol. Pharm. Sci.* **2021**, *15*, 055–062.

[41] D. A. Gidlow, *Occup. Med.* **2015**, *65*, 348–356.

[42] M. H. V. Huynh, M. A. Hiskey, T. J. Meyer, M. Wetzler, *Proc. Natl. Acad. Sci. U.S.A.* **2006**, *103*, 5409–5412.

[43] M. A. Ilyushin, I. V. Tselinsky, I. V. Shugalei, *Cent. Eur. J. Energ. Mater.* **2012**, *9*, 293–327.

[44] K. D. Oyler, in *Green Energetic Materials*, **2014**, pp. 103–132.

[45] H. Zöllner, M. Joas, R. Schirra, K. Kaplan, Lead-free initiating agents or initiating agent mixtures, **2017**, WO2018011134A1.

[46] J. W. Fronabarger, J. G. Bragg, M. D. Williams, Method for preparation of silver azide, **2015**, US9969623B2.

[47] DIRECTIVE 2011/65/EU OF THE EUROPEAN PARLIAMENT AND OF THE COUNCIL of 8 June 2011 on the restriction of the use of certain hazardous substances in electrical and electronic equipment, European Union, **2011**.

[48] COMMISSION DELEGATED DIRECTIVE (EU) 2021/647 of 15 January 2021 amending, for the purposes of adapting to scientific and technical progress, Annex III to Directive 2011/65/EU of the European Parliament and of the Council as regards an exemption for the use of certain lead and hexavalent chromium compounds in electric and electronic initiators of explosives for civil (professional) use, European Union, **2021**.

[49] https://echa.europa.eu/de/candidate-list-table/, accessed November 2024.

[50] J. W. Fronabarger, M. D. Williams, W. B. Sanborn, J. G. Bragg, D. A. Parrish, M. Bichay, *Propellants, Explos. Pyrotech.* **2011**, *36*, 541–550.

[51] D. Fischer, T. M. Klapötke, J. Stierstorfer, *Angew. Chem. Int. Ed.* **2014**, *53*, 8172–8175.

[52] B. Guo, X. Zhang, X. Lin, H. Huang, J. Yang, *New J. Chem.* **2021**, *45*, 20426–20431.

[53] M. M. Puszynski, N. Mehta, G. Cheng, K. D. Oyler, D. Fischer, T. M. Klapötke, J. Stierstorfer, *J. J. Inorg. Chem.* **2016**, *1*, 003.

[54] M. H. H. Wurzenberger, M. Lommel, M. S. Gruhne, N. Szimhardt, J. Stierstorfer, *Angew. Chem. Int. Ed.* **2020**, *59*, 12367–12370.

[55] M. H. H. Wurzenberger, M. S. Gruhne, M. Lommel, N. Szimhardt, J. Stierstorfer, *Mater. Adv.* **2022**, *3*, 579–591.

[56] H. Li, Y. Wang, Z. Wei, X. Yang, L. Liang, L. Xia, M. Long, Z. Li, T. Zhang, *Chem. Eng. J.* **2022**, *430*, 132739.

[57] M. H. H. Wurzenberger, V. Braun, M. Lommel, T. M. Klapötke, J. Stierstorfer, *Inorg. Chem.* **2020**, *59*, 10938–10952.

[58] N. Szimhardt, M. H. H. Wurzenberger, T. M. Klapötke, J. T. Lechner, H. Reichherzer, C. C. Unger, J. Stierstorfer, *J. Mater. Chem. A* **2018**, *6*, 6565–6577.

[59] M. H. H. Wurzenberger, M. S. Gruhne, M. Lommel, N. Szimhardt, T. M. Klapötke, J. Stierstorfer, *Chem. Asian J.* **2019**, *14*, 2018–2028.

[60] T. Wang, Z. Lu, S. Bu, B. Kuang, L. Zhang, Z. Yi, K. Wang, S. Zhu, J. Zhang, *Def. Technol.* **2024**, *31*, 271–277.

[61] S. Chen, Z. Yi, C. Jia, Y. Li, H. Chen, S. Zhu, L. Zhang, *Small* **2023**, 2302631

[62] Y. Feng, J. Zhang, W. Cao, J. Zhang, J. N. M. Shreeve, *Nat. Commun.* **2023**, *14*, 7765.

[63] M. S. Gruhne, M. Lommel, M. H. H. Wurzenberger, N. Szimhardt, T. M. Klapötke, J. Stierstorfer, *Propellants, Explos. Pyrotech.* **2020**, *45*, 147–153.

[64] T. M. Klapötke, *Energetic Materials Encyclopedia, Vol. 1–3*, 2nd ed., DeGruyter, Berlin/Boston, **2021**.

[65] T. M. Klapötke, D. G. Piercey, N. Mehta, K. D. Oyler, J. J. Sabatini, **2014**, *69*, 125–127.

[66] N. Mehta, K. Oyler, G. Cheng, A. Shah, J. Marin, K. Yee, *Z. Anorg. Allg. Chem.* **2014**, *640*, 1309–1313.

[67] Parts of this illustration were created using *ChatGPT* 3.5, OpenAI, **2022**, accessed: 29.10.2024.

[68] M. H. H. Wurzenberger, S. M. J. Endraß, M. Lommel, T. M. Klapötke, J. Stierstorfer, *ACS Appl. Energy Mater.* **2020**, *3*, 3798–3806.

[69] M. Kofen, M. Lommel, M. H. H. Wurzenberger, T. M. Klapötke, J. Stierstorfer, *Chem. Eur. J.* **2022**, e202200492.

[70] M. Joas, T. M. Klapötke, N. Szimhardt, *Eur. J. Inorg. Chem.* **2014**, *2014*, 493–498.

[71] M. H. H. Wurzenberger, N. Szimhardt, J. Stierstorfer, *Inorg. Chem.* **2018**, *57*, 7940–7949.

[72] T. Wang, S. Bu, Z. Lu, B. Kuang, Z. Yi, Z. Xie, C. Zhang, Y. Li, J. Zhang, *Chem. Eng. J.* **2023**, *457*, 141267.

[73] T. Wang, S. Bu, K. Wang, L. Zhang, Z. Yi, C. Zhang, W. Cao, S. Zhu, J. Zhang, *Chem. Eng. J.* **2023**, *452*, 139472.

[74] Y.-F. Yan, J.-G. Xu, F. Wen, Y. Zhang, H.-Y. Bian, B.-Y. Li, N.-N. Zhang, F.-K. Zheng, G.-C. Guo, *Inorg. Chem. Front.* **2022**, *9*, 5884–5892.

[75] Y.-F. Yan, Q.-Y. Wang, M. Cui, H.-Y. Bian, Y.-F. Han, J.-G. Xu, F.-K. Zheng, G.-C. Guo, *Chem. Eng. J.* **2023**, *472*, 144982.

2 Trinitro-orcinolate and Trinitro-resorcinate – Sensitivity Trends in Nitroaromatic Energetic Materials

Simon M. J. Endraß, Andreas Neuer, Thomas M. Klapötke, Jörg Stierstorfer

published in *ChemistrySelect,* **2022**

DOI: 10.1002/slct.202203140

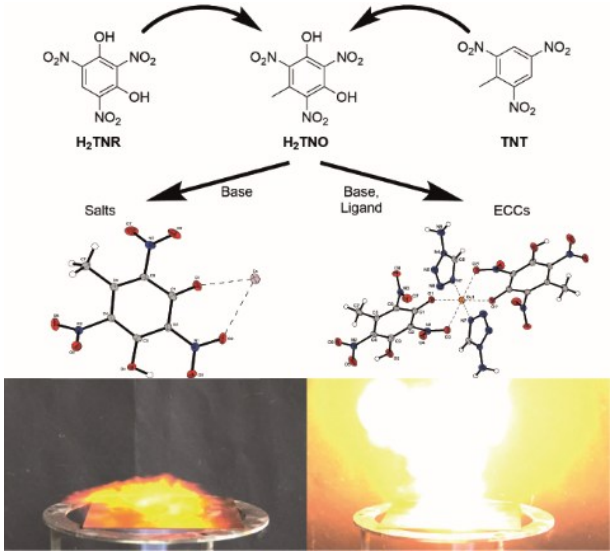

Abstract: 5-Methyl-2,4,6-trinitrobenzene-1,3-diol (trinitro-orcinol, H_2TNO) as a close structural relative to the well-known energetic materials trinitroresorcinol (styphnic acid) and trinitrotoluene (TNT) is prepared in high purity and analyzed concerning its vapor pressure using the transpiration method. Several energetic coordination compounds (ECCs) of its respective anion were produced and compared with structurally close styphnate complexes to give an insight in physiochemical trends of the ECC. The synthesized compounds were further analyzed by elemental analysis, IR spectroscopy, differential thermal analysis and low temperature X-ray diffraction analysis. To classify the reported compounds among the energetic materials, they were tested for their sensitivities towards mechanical stimuli such as impact, friction and electrostatic discharge as well as their behavior towards flame.

2.1 Introduction

Nitroaromatic compounds can be found in multiple industries and applications for example as drugs, dyes, pesticides and energetic materials. [1, 2] Therefore, these compounds are distributed throughout the whole ecosystem and by various sources despite their well-known structure-toxicity relationship. [3-5] This is problematic as many compounds of this kind have been proven to be persistent in soil and are degraded within long time spans by different species. [6-8] Within the field of energetic materials, various nitroaromatic compounds have been studied and commonly found application as the oxidation of the carbon backbone can create interesting physiochemical properties. [9-11] By variation of the structural motifs and formation of salts and coordination compounds (Figure 1), different fields of application of the energetic materials have been achieved depending on the performance and sensitivities of the compounds. [12-14] However, this structural variety also leads to the necessity of methods for detection in order to provide safety precautions to civilians and military. [15, 16]

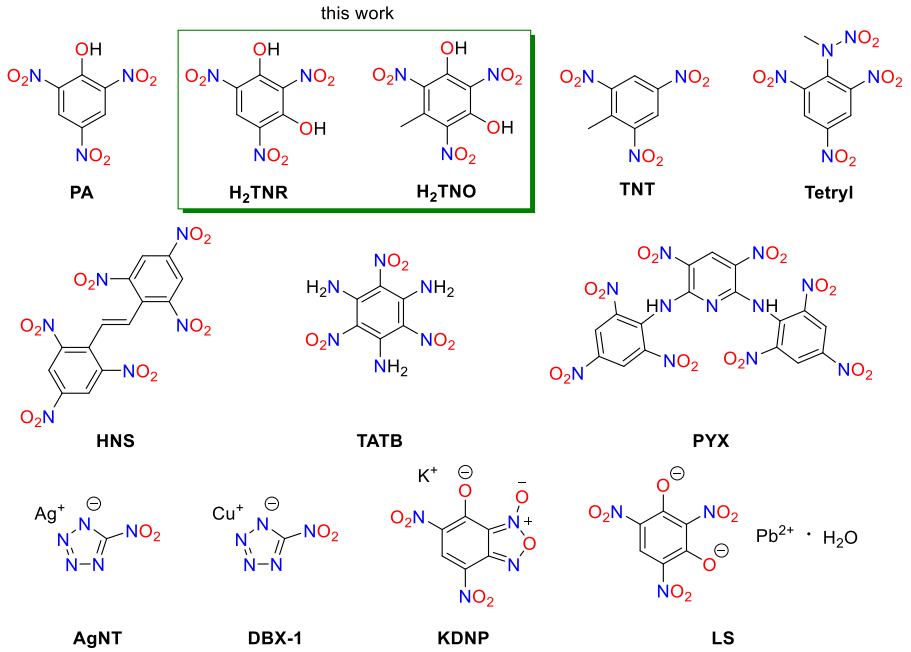

Figure 1. Overview of few examples of nitroaromatic energetic materials for different fields of application:[17, 18] PA: picric acid, H_2TNR: styphnic acid, TNT: trinitrotoluene, HNS: hexanitrostilbene, TATB: 1,3,5-triamino-2,4,6-trinitrobenzene, PYX: 2,6-Bis(picrylamino)-3,5-dinitropyridine, AgNT: silver(I) 5-nitrotetrazolate, DBX-1: copper(I) 5-nitrotetrazolate, KDNP: potassium 5,7-dinitro-[2,1,3]-benzoxadiazol-4-olate 3-oxide, LS: lead styphnate.

Often, the detection and possibilities for sample processing are limited by the type of design and exact way of application of the ordnance which might only allow measurement of the vapor pressure. [19, 20] Trinitro-orcinol (H_2TNO) has been known since the 1870s but despite its structural similarities with styphnic acid (H_2TNR) and trinitro-toluene (TNT) it was not considered a potential energetic material. [21, 22] This changed when in 2016 this group published first results of H_2TNO and the formation of its energetic salt Cs_2TNO. [23, 24] Preliminary flame tests and the information that H_2TNO could serve as a potential starting material for primary explosives was described. However, no information on the initiation performance and potential application were given. In order to provide possible trends of energetic salts and coordination compounds the goal of this work was to synthesize and characterize several compounds and compare them with literature known styphnate compounds. Furthermore, neat trinitro-orcinol was evaluated concerning its vapor pressure to deliver an additional safety aspect of detection.

2.2 Results and Discussion

2.2.1 Synthesis

Trinitro-orcinol (**1**) was prepared by nitration of commercially available orcinol (5-methylbenzene-1,3-diol) as described in the literature (Scheme 1). [25] The nitration can be performed under relatively mild conditions leading to high yields due to the activating effect of the hydroxy groups. [26]

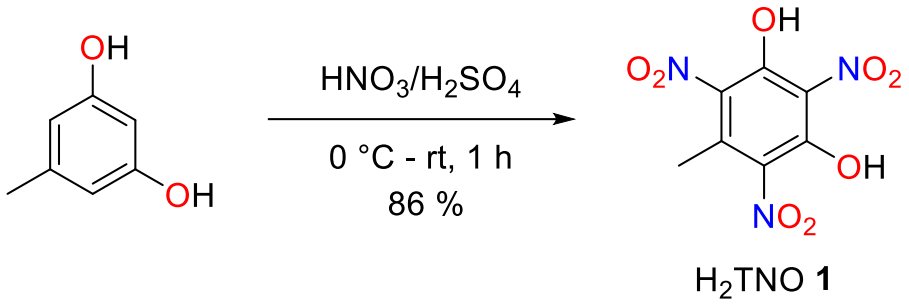

Scheme 1. Preparation of trinitro-orcinol (H_2TNO).

The obtained H_2TNO was further reacted in acid-base reactions (Scheme 2) which led to aqueous solutions of the respective salts (basic copper carbonate, zinc carbonate, cesium carbonate or magnesium oxide). These solutions were left to crystallize at room temperature to obtain the salts or used for complexation. Apart from compounds **4**, **9**, **10**, **12** and **14** single crystals suitable for X-ray diffraction analysis were obtained from the mother liquor. Compounds **9** and **12** were recrystallized from EtOH at room temperature to isolate single crystals of the compounds. In the case of PbTNO, the synthetic approach of the commonly used β-lead styphnate was applied. [27] For this matter, MgO was added to a suspension of H_2TNO in water at 55 °C. The resulting solution was filtered off and lead(II) nitrate was added, which led to precipitation of the product.

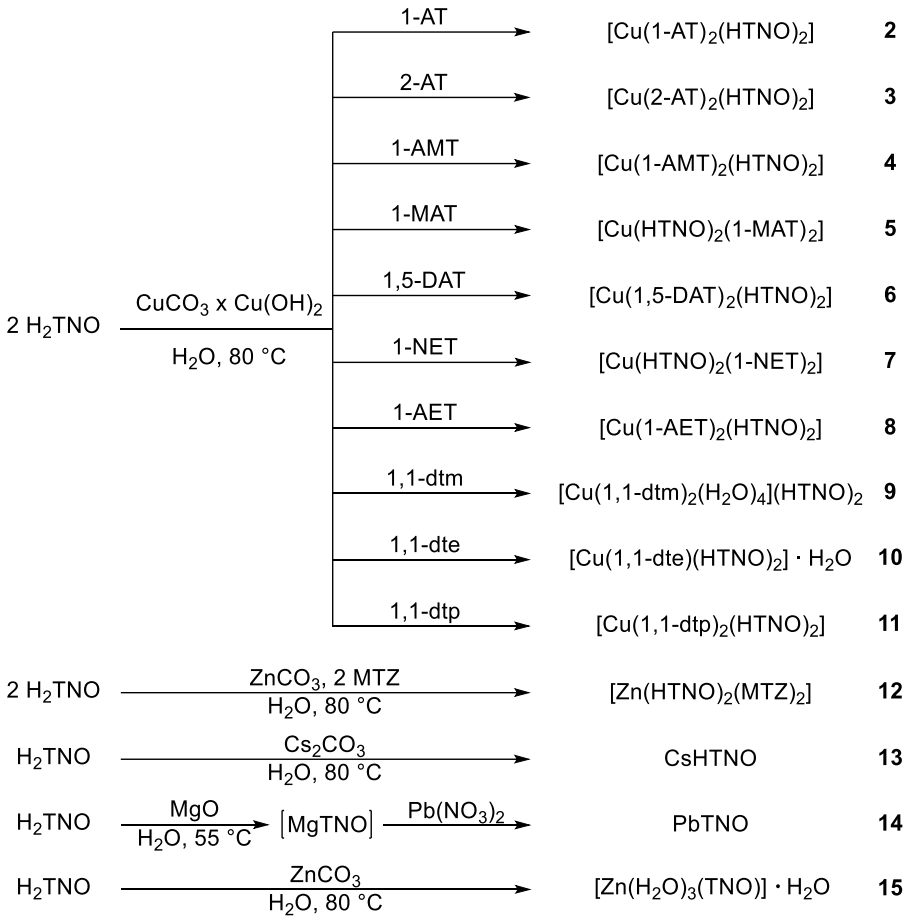

Scheme 2. Complexation and formation of salts of H_2TNO.

In addition, three previously unknown styphnate complexes were prepared to compare them with trinitro-orcinolate complexes that carry the same ligand. In the case of the 1,5-diaminotetrazole (1,5-DAT) ligand, a styphnate complex was described in the literature, however the sensitivity determination was carried according to a different standard which is not comparable. [28] Instead of the literature-known $[Cu(1,5\text{-}DAT)_2(HTNR)_2]$, the double deprotonated styphnate species $[Cu(1,5\text{-}DAT)_2(TNR)]$ was obtained in all attempts of preparation. An overview over the prepared styphnate complexes is given in Scheme 3.

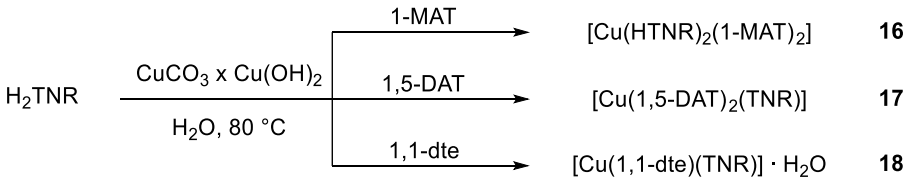

Scheme 3. Preparation of styphnate complexes **16–18**.

2.2.2 Vapor Pressure

The experimental vapor pressures p_{sat} as well as the thermochemical properties such as molar enthalpies of sublimation $\Delta_{cr}^{g}H_{m}^{\circ}(T)$ and molar entropies of sublimation $\Delta_{cr}^{g}S_{m}^{\circ}(T)$ of H_2TNO was determined using the transpiration method with coupled quantification via high pressure liquid chromatography assisted by an UV-diode array detector (HPLC-DAD) and was categorized in the existing literature of related nitroaromatics (H_2TNR, TNT). [29, 30] Here, the data acquisition was obtained from a complete *p-T* dataset with an elaborate calculation based on the *Clausius-Clapeyron* equation. [31] The extrapolation to the standard temperature T_{ref} was carried out by the application of the modified *Clarke-Glew* fit function (see Supporting Information).

This technique allowed the determination of the sublimation behavior of H_2TNO in the temperature range of 332.4–380.7 K (for further information see Supporting Information). The absolute vapor pressures p_{sat} and thermodynamic properties of sublimation including the *Clark-Glew* fit function were presented in Table S8 of the ESI. From these results, the molar enthalpy of sublimation was found to be 122.7 ± 1.7 kJ·mol^{-1} and the extrapolated vapor pressure at reference temperature of 298.15 K was derived to be 7.27 µPa.

Since this work determined the appointed thermochemical properties for the first time, the substance H_2TNO was contextualized to the related compounds H_2TNR and TNT. To enable a suitable comparison, the existing literature data were processed in the same manner as described in this paper. For this purpose, the revised properties were presented in Table 1 and Figure 2.

The vaporization behavior of H_2TNR was measured by *Cundall* in the temperature range of 330.2–440.9 K. [30] The molar enthalpy of sublimation was found to be 124.5 kJ mol^{-1} and from these findings the vapor pressure at reference temperature of 298.15 K (6.66×10^{-4} µPa) was extrapolated based on a calculated *p-T* data set via the published *Clausius-Clapeyron* equation and the application of the *Clark-Glew* fit function together with the calculated molar heat capacity (see Table S7).

In addition, the vaporization behavior of TNT was measured by *Cundall* and revised by *Östmark*. [29, 30] The reported *Antoine* equation was determined in the temperature range of 285.1–353.4 K and converted into the *Clarke-Glew* fit function considering the molar heat capacity (see Table S7). The molar enthalpy of sublimation was found to be 114.1 kJ mol^{-1} and from these findings the vapor pressure at reference temperature of 298.15 K (714 µPa) were extrapolated.

Table 1. Comparison of thermodynamic properties of the compounds H_2TNR, H_2TNO and TNT: Vapor pressure p_{sat} and molar enthalpies of sublimation $\Delta_{cr}^{g}\boldsymbol{H}_{\mathbf{m}}^{\circ}$ at 298.15 K.

Experiment	T-Range	$\Delta_{cr}^{g}H_m^{\circ}$(298.15 K)[a]	p_{sat}[b]
	K	kJ·mol^{-1}	µPa
H_2TNO	332.4–380.7	122.7 ± 1.7 [c]	7.27
H_2TNR [30]	330.2–440.9	124.5	6.66×10^{-4}
TNT [29]	285.1–353.4	114.1	714

[a] Molar enthalpies of sublimation were adjusted according to Chickos et al. [32] with values of $\Delta_{cr}^{g}C_{p,m}^{\circ}$, $C_{p,m}^{\circ}$(cr) stated in Table S7. [b] Vapor pressure at 298.15 K extrapolated from the p-T-data. [c] Uncertainties for molar enthalpies of sublimation at reference temperatures are expressed as expanded uncertainties with confidence level of 0.95 (k = 2).

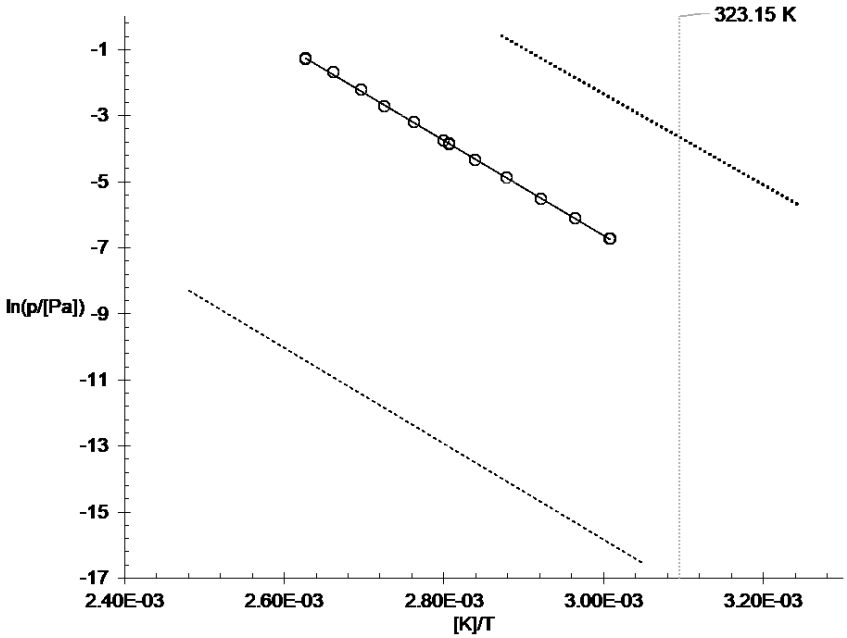

Figure 2. Comparison of the experimental vapor pressure values with the *Clausius-Clapeyron* fit function of the investigated H_2TNO with the corresponding published fit function of H_2TNR and TNT. Here ○ and solid line is H_2TNO; dashed line is H_2TNR; dotted line is TNT. The vertical dotted line serves merely as a guide.

By contrasting H_2TNO, the volatility was found to settle in between the two comparative substances H_2TNR and TNT. Thus, H_2TNO has a volatility four orders of magnitude higher than H_2TNR and a volatility two orders of magnitude lower than TNT. In addition, the sublimation enthalpy changes marginally compared to H_2TNR and by around 10 kJ mol^{-1} compared to TNT. Also, the illustrated fit function (see Figure 2) indicates that the slope of the fit functions approximates and the offset decreases from TNT over H_2TNO to H_2TNR. This classification corroborates our research results, since in an analogous way as the volatility, polarity can also be lined up: H_2TNR has the highest polarity in comparison and TNT the

lowest. Since a higher polarity has a direct demeaning effect on the volatility, it can be argued that the particular volatility of H_2TNO is plausible. Moreover, it can be observed that a similar fit function slope can be expected for related substances. Based on these considerations and the assured reproducibility of the measured values (procedure described in previous publications), we have a high degree of confidence in the determined values and have gained access to the thermochemical properties for the first time.

2.2.3 Detonation Properties

The energetic properties of compound **1** are calculated with EXPLO5 program code and are displayed in Table 2. [33] Therefore, the enthalpy of formation was determined by applying the atomization method using room temperature CBS-4M enthalpy and the experimentally determined molar enthalpy of sublimation. For better comparability, the properties of styphnic acid and TNT were recalculated using the same version of EXPLO5. Additionally, CBS-4M results of all three substances are given in the Supplementary Information. Especially the detonation pressure at the *Chapman-Jouguet* point and the detonation velocity correspond very well to the structural similarities of the compounds.

Table 2. Energetic properties of H_2TNO compared to H_2TNR and TNT.

	H_2TNO (1)	**H_2TNR** [34]	**TNT** [34]
Formula	$C_7H_5N_3O_8$	$C_6H_3N_3O_8$	$C_7H_5N_3O_6$
M [g mol^{-1}]	259.13	245.10	227.13
ρ [g cm^{-3}]	1.71[a]	1.83	1.65
N [%][b]	16.22	17.14	18.50
Ω_{CO} [%][c]	−9.3	3.3	−24.7
$\Delta_f H°$ [kJ mol^{-1}][d]	−436.7[j,k]	−374.3[j]	−59.3
Explo5 V6.05.04			
$-\Delta_{Ex}U$ [kJ kg^{-1}][e]	4024	4509	4406
$T_{det.}$ [K][f]	3026	3391	3177
V_0 [L kg^{-1}][g]	637	626	640
P_{CJ} [kbar][h]	198	252	183
$V_{det.}$ [m s^{-1}][i]	6987	7668	6798

[a] From X-Ray diffraction analysis recalculated to 298 K. [b] Nitrogen content. [c] Oxygen balance with respect to CO. [d] Enthalpy of formation. [e] Energy of explosion. [f] Detonation temperature. [g] Volume of detonation products (assuming only gaseous products). [h] Detonation pressure at the *Chapman−Jouguet* point. [i] Detonation velocity. [j] calculated by CBS-4M and atomization method; [k] corrected by gas-phase measurement.

2.2.4 Crystal Structures

Compounds **2**, **3**, **5**–**9**, **11**–**13** and **15** were further examined by low-temperature X-ray diffraction analysis. The data and parameters of the measurements as well as the refinements are given in the supporting information Tables S1–4. Deposition Numbers 2191773 (for **2**),

2191776 (for **3**), 2191775 (for **5**), 2191782 (for **6**), 2191777 (for **7**), 2191778 (for **8**), 2191779 (for **9**), 2191774 (for **11**), 2191783 (for **12**), 2191781 (for **13**) and 2191780 (for **15**) contain the supplementary crystallographic data for this paper. These data are provided free of charge by the joint Cambridge Crystallographic Data Center and Fachinformationszentrum Karlsruhe Access Structures service www.ccdc.cam.ac.uk/structures.

$[Cu(1\text{-}AT)_2(HTNO)_2]$ crystallizes in the monoclinic space group $P2_1/c$ with a calculated density of 1.90 g cm^{-3} at 101 K and two formula units per unit cell. The compound shows the typical *Jahn-Teller*-like distortion (Figure 3) of a d^9-metal center in octahedral coordination as expected for Cu^{2+}. The distorted axis is formed by the coordinating nitro groups of the trinitro-orcinolate anions, while the coordination bonds, that are formed by the deprotonated hydroxy group as well as the 1-aminotetrazole ligand are significantly shorter.

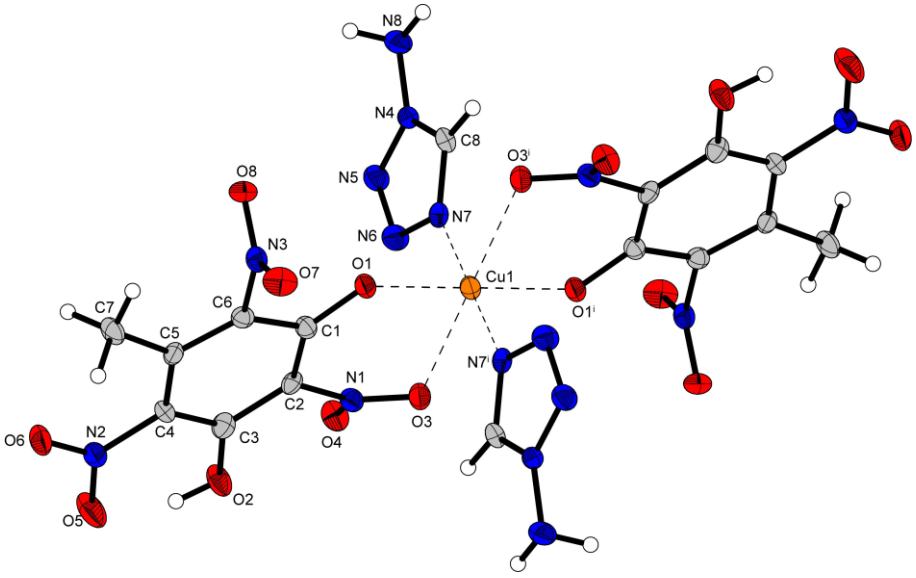

Figure 3. Crystal Structure of $[Cu(1\text{-}AT)_2(HTNO)_2]$ with typical structural motif. Selected bond lengths (Å): Cu1–O1 1.959(3), Cu1–O3 2.355(3), Cu1–N7 2.002(4); selected bond angles (°): O1–Cu1–O3 79.61(12), O1–Cu1–N7 88.98(15), O3–Cu1–N7 94.64(14); symmetry codes: (i) 1−x, 1−y, 1−z.

The comparison of this coordination pattern, however, reveals a significant difference compared to the styphnate anions that is displayed in Figure 4. While the styphnate anions are known to coordinate via the nitro groups in *ortho*-position to the remaining proton of the carbon backbone, nitro group that is involved in the coordination of trinitro-orcinolate, is in *para*-position to the methyl group. This coordination pattern is also observed for the ECCs **3**, **5**, **6**, **7**, **8** and **12**. The crystal structures of compounds **3** and **5**–**8** can be found in the Supplementary Information.

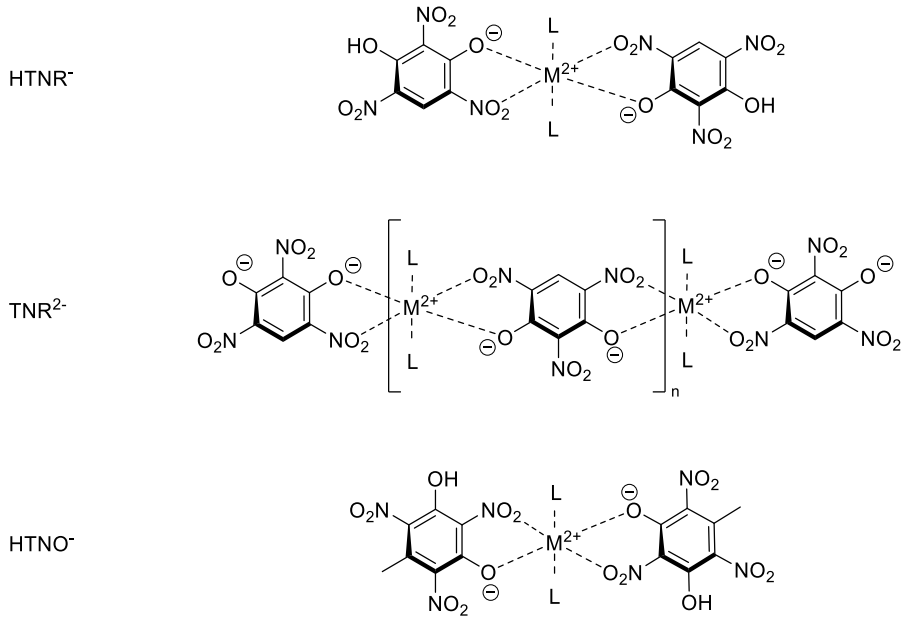

Figure 4. Typical coordination pattern of the styphnate anions $HTNR^-$ and TNR^{2-} in ECCs compared to $HTNO^-$.[35]

$[Cu(1,1\text{-dtm})_2(H_2O)_4](HTNO)_2$ crystallizes in the triclinic space group $P\bar{1}$ with a density of 1.78 g cm^{-3} at 173 K. Unlike in the literature known styphnate complex [Cu(1,1-dtm)(TNR)] · H_2O neither the anion nor the 1,1-dtm ligand showed bridging behavior in the case of compound **9**.[36] Instead a composition close to that of the respective picrate complex was observed as displayed in Figure 5. The $HTNO^-$ anion is pushed out of the coordination sphere of the copper(II) center and replaced by four molecules of water. Therefore, the metal center is still coordinated octahedrally, but unlike expected without the more common *Jahn-Teller*-like elongation distortion of the coordination sphere. Instead, the four molecules of water are close to evenly distributed with coordination bond lengths of 2.15–2.17 Å and a compressed axis with a Cu^{2+}–ligand distance of 2.01 Å resulting in a *Jahn-Teller*-like compression distortion.

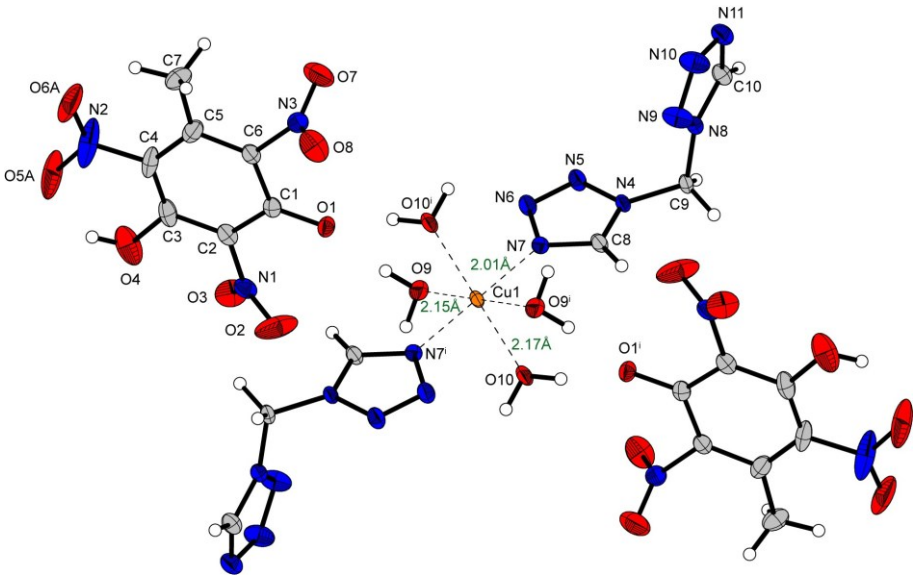

Figure 5. Crystal Structure of $[Cu(1,1\text{-dtm})_2(H_2O)_4](HTNO)_2$. Selected bond lengths (Å): Cu1–O9 2.153(3), Cu1–O10 2.177(3), Cu1–N7 2.007(3); selected bond angles (°): O9–Cu1–O10 90.60(11), O9–Cu1–N7 91.08(13), O10–Cu1–N7 86.76(13); symmetry codes: (i) 1−x, 1−y, 1−z.

The X-ray diffraction analysis of compound **11** (Figure 6) reveals the distorted octahedral coordination of the copper(II) center by two molecules of ligand and anion each. The elongated axis is taken up by the deprotonated hydroxide of the trinitro-orcinolate, while the xy-level of the octahedra is occupied by the lateral nitrogen atoms of both tetrazole rings. Therefore, no coordination by the nitro group is possible. The compound crystallizes in the monoclinic space group $P2_1/c$ with a density of 1.77 g cm^{-3} at 173 K and two formula units per unit cell.

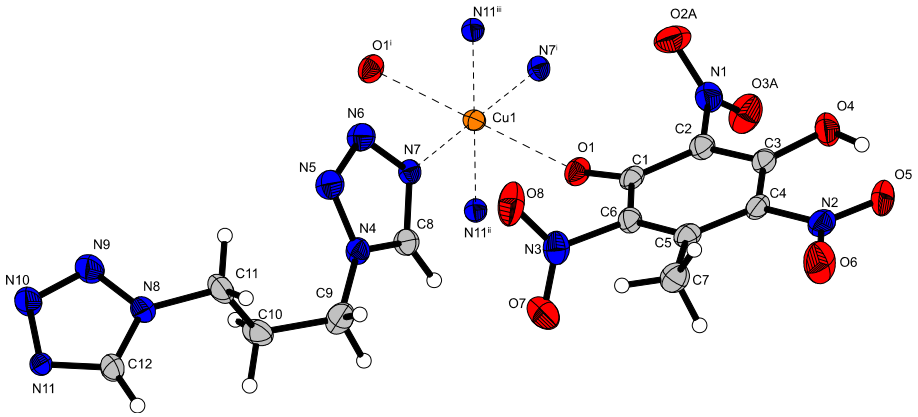

Figure 6. Asymmetric unit of $[Cu(1,1\text{-dtp})_2(HTNO)_2]$. Selected bond lengths (Å) O1–Cu1 2.3426(17) ,N7–Cu1 1.9956(15), N11–Cu1 2.0232(15); selected bond angles (°): N7–Cu1–N11^{ii} 90.54(6), N7–Cu1–O1 86.65(6), O1–Cu1–N11^{ii} 85.72(6); symmetry codes: (i) 2−x, 1−y, 1−z; (ii) 1+x, 1/2−y, 1/2+z; (iii) 1−x, 1/2+y, 1/2−z.

As displayed in Figure 7 $[Zn(HTNO)_2(MTZ)_2]$ shows the typical coordination pattern of the trinitro-orcinolate anion that was shown earlier. The compound crystallizes in the triclinic space group *P*-1 with a density of 1.83 g cm^{-3} at 98 K.

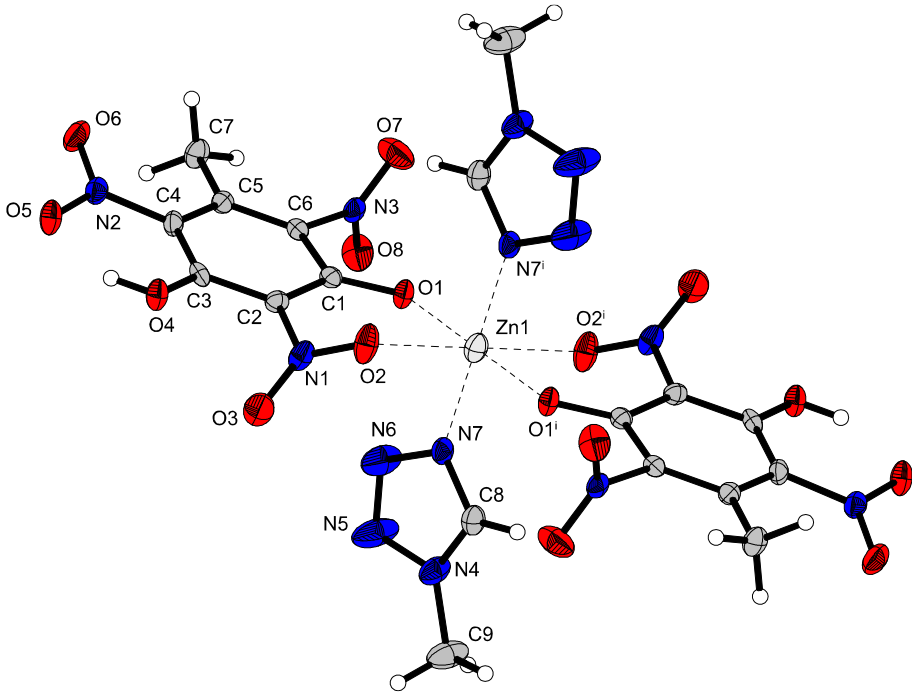

Figure 7. Crystal structure of $[Zn(HTNO)_2(MTZ)_2]$. Selected bond lengths (Å) Zn1–O1 1.940 (2), Zn1–O2 2.371(3), Zn1–N7 1.995(3); selected bond angles (°): O1–Zn1–O2 81.31(9), O1–Zn1–N7 89.32(11), O2–Zn1–N7 88.66(11); symmetry codes: (i) 1−x, 1−y, 2−z.

Figure 8 shows a representative of the double deprotonated anion TNO^{2-} in form of the coordination compound $[Zn(H_2O)_3(TNO)] \cdot H_2O$. The crystal structure indicates, that unlike the styphnate anion TNR^{2-}, no 1D-polymeric chains are formed by TNO^{2-}. Instead of a symmetric coordination by both hydroxides, the torsion angles of the nitro groups lead to a low symmetry coordination pattern. While the coordinating nitro group in *ortho*-position to methyl group shows a torsion angle of −28.4(4)° (O5–N2–C4–C3), the noncoordinating nitro group in *ortho*-position is twisted further to an angle of 67.2(4)° (O8–N3–C6–C1).

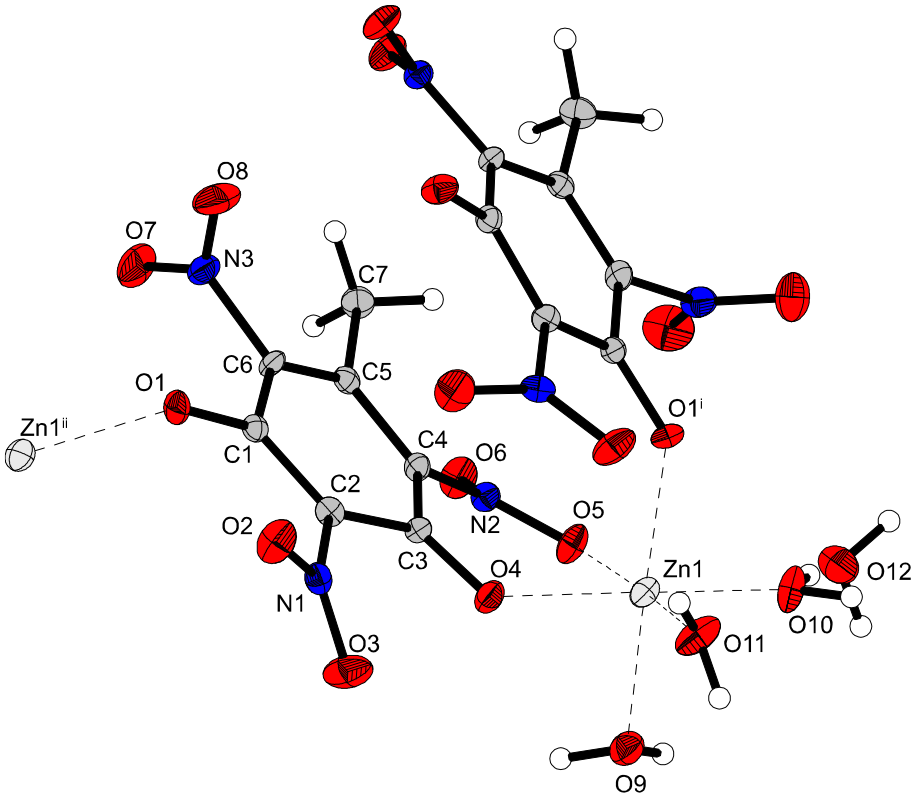

Figure 8. Crystal structure of compound **15**. Selected bond lengths (Å): Zn1–O1^{i} 2.073(2), Zn1–O4 2.028(2), Zn1–O5 2.123(3), Zn1–O9 2.123(2), Zn1–O10 2.039(3), Zn1–O11 2.062(3); selected bond angles (°): O1^{i}–Zn1–O9 175.07(12), O1^{i}–Zn1–O4 94.55(9), O1^{i}–Zn1–O5 92.13(11), O1^{i}–Zn1–O10 89.09(10), O1^{i}–Zn1–O11 86.57(11), O9–Zn1–O488.45(9), O9–Zn1–O5 84.50(11), O9–Zn1–O10 87.36(10), O9–Zn1–O11 97.19(12), O4–Zn1–O5 80.32(9), O4–Zn1–O11 93.09(10), O5–Zn1–O12 90.8(1), O11–Zn1–O12 95.89(11), O4–Zn1–O10 170.5(1), O5–Zn1–O11 173.17(10); symmetry codes: (i) 1/2+x, 1/2−y, z, (ii) −1/2+x, 1/2−y, z.

2.2.5 Physicochemical Properties

The thermal behavior of all compounds was investigated via differential thermal analysis (DTA) in a range of 25–400 °C with a heating rate of 5 °C min^{-1}. The observed events were given as onset temperatures. Endothermic events (e.g. melting point, loss of water or ligand, phase transition) were further investigated by thermogravimetric analysis (TGA) at a similar heating rate in the range 30–400 °C. Plots of every DTA measurement as well as TGA can be found in the supporting information. Detail on the cause of the endothermic events as well as the exothermic decomposition temperatures are briefly given in Table 3. The reported sensitivities classify all compounds except of **10** (insensitive) and **18** (sensitive) as very sensitive towards impact according to the "UN Recommendations on the Transport of Dangerous Goods". [37] Furthermore, compounds **5**, **8**, **13** are considered insensitive towards friction, while **6**, **9**, **18** are less sensitive. Compounds **2**, **7**, **10**, **11** and **12** have been tested to be

sensitive, **3**, **4**, **17** are very sensitive and only compound **14** is characterized as extremely sensitive towards friction. The general trend seems to be an increased impact sensitivity as well as lowered friction sensitivity and thermal stability of the trinitro-orcinolate complexes compared to the respective styphnates.

Table 3. Thermal Stability[a] and sensitivities to mechanical and electrical stimuli of compounds **2**–**14**, compared to literature known styphnates.

Compound	T_{endo}[b] [°C]	T_{exo}[c] [°C]	*IS*[d] [J]	*FS*[e] [N]	*ESD*[f] [mJ]	*HP*[g]	*HN*[h]
$[Cu(1\text{-}AT)_2(HTNO)_2]$ **2**	-	185	<1	96	50	def.	dec.
$[Cu(1\text{-}AT)_2(HTNR)_2]$ [35]	-	186	1.5	48	16	def.	def.
$[Cu(2\text{-}AT)_2(HTNO)_2]$ **3**	-	182	<1	80	50	def.	def.
$[Cu(2\text{-}AT)_2(HTNR)_2]$ [35]	-	206	3	48	20	def.	def.
$[Cu(1\text{-}AMT)_2(HTNO)_2]$ **4**	-	192	<1	60	250	def.	dec.
[Cu (1-AMT)$_2$(TNR)] [35]	-	212	2	16	6.3	def.	def.
$[Cu(HTNO)_2(1\text{-}MAT)_2]$ **5**	-	220	2	>360	90	def.	dec.
$[Cu(HTNR)_2(1\text{-}MAT)_2]$ **16**	-	249	2	>360	160	def.	dec.
$[Cu(1,5\text{-}DAT)_2(HTNO)_2]$ **6**	-	220	<1	360	200	def.	dec.
$[Cu(1,5\text{-}DAT)_2(HTNR)_2]$ [28]	-	242	1.5[i]	-[i]	n.d.	n.d.	n.d.
[Cu(1,5-DAT)$_2$(TNR)] **17**	-	229	<1	45	160	def.	dec.
$[Cu(HTNO)_2(1\text{-}NET)_2]$ **7**	-	159	<1	192	90	def.	dec.
[Cu(1-NET)$_2$(TNR)] [38]	-	195	2	96	480	def.	def.
$[Cu(1\text{-}AET)_2(HTNO)_2]$ **8**	-	191	<1	>360	90	def.	dec.
[Cu(1-AET)$_2$(TNR)] [39]	-	177	<1	240	123	def.	def.
$[Cu(1,1\text{-}dtm)_2(H_2O)_4](HTNO)_2$ **9**	100[j]	197	<1	360	160	dec.	dec.
[Cu(TNR)(1,1-dtm)] · H_2O [36]	-	236	2	192	188	def.	dec.
[Cu(1,1-dte)(HTNO)$_2$] · H_2O **10**	-	252	>40	192	200	def.	dec.
[Cu(1,1-dte)(TNR)] · H_2O **18**	-	264	20	360	200	def.	def.
$[Cu(1,1\text{-}dtp)_2(HTNO)_2]$ **11**	-	184	<1	240	200	def.	dec.
[Cu(1,1-dtp)(TNR)]·H_2O [40]	88 (− H_2O)	248	10	>360	500	n.d.	n.d.
$[Zn(HTNO)_2(MTZ)_2]$ **12**	-	229	2	168	33	def.	dec.
$[Zn(HTNR)_2(MTZ)_2]$ [41]	-	214	4	240	800	n.d.	n.d.
CsHTNO **13**	-	233	<1	>360	50	def.	det.
$[Cs_2(H_2O)(HTNR)(OH)]_n$ [42]	74 (− 2 H_2O)	292	-	-	-	n.d.	n.d.
PbTNO **14**	-	240	<1	<0.1	0.54	det.	det.
LS [34, 43]	-	282	8	0.45	0.9	det.	det.

[a] DTA onset temperatures at a heating rate of 5 °C min^{-1}. [b] Onset temperature of endothermic event in the DTA, indicating a melting point of the compound. [c] Onset of exothermic event in the DTA. [d] Impact sensitivity (BAM drophammer (1 of 6)). [e] Friction sensitivity (BAM friction tester (1 of 6)). [f] Electrostatic discharge devise (OZM XSpark10). [g] Hot plate test (det.: detonation, def.: deflagration, dec.: decomposition, n.d.: not determined). [h] Hot needle test (det.: detonation, def.: deflagration, dec.: decomposition, n.d.: not determined). [i] according to China National Military Standard.[28] [j] gradual loss of mass.

2.3 Conclusion

This work has provided 17 new compounds, among which 11 were characterized by low-temperature X-ray diffraction analysis. This analysis gave an interesting insight in the coordination behavior of trinitro-orcinolate compared to the anions of styphnic acid. Surprisingly, the investigation of the physiochemical properties showed, that despite the lower

enthalpy of formation, trends towards an increased impact sensitivity and lower thermal stability of the trinitro-orcinolates can be observed. The sensitivities towards friction, in contrast, seem followed to be lower compared to the respective styphnates. In addition, the experimental vapor pressure of H_2TNO was determined, using the transpiration method. This crucial parameter for explosives' detection was put in context by comparison with literature values of the close structural relatives trinitroresorcinol and trinitrotoluene. The observed similarities of the fit function slopes as well as the overall placement of the volatility in between the literature values plausibly represent the shared structural similarities. While the high sensitivities towards impact, that were observed for most trinitro-orcinolates, excludes them from application as a primary explosive, utilization as a replacement of lead styphnate or as a sensitizer in priming mixtures might be considered.

2.4 Acknowledgement

For financial support of this work by Ludwig-Maximilian University (LMU), the Office of Naval Research (ONR) under grant no. ONR N00014-19-1-2078 and the Strategic Environmental Research and Development Program (SERDP) under contract no. W912HQ19C0033 and the DAAD (German Academic Exchange Service) [grant no. 57299294] are gratefully acknowledged. The authors would like to thank Dr. Burkhard Krumm for NMR measurements and Kay Chen for proofreading.

2.5 Notes

Parts of this work were published on the NTREM 2022 conference. [44, 45]

2.6 References

[1] K.-S. Ju, E. Parales Rebecca, *Microbiol. Mol. Biol. Rev.* **2010**, *74*, 250–272.

[2] C. Kannigadu, D. D. N'Da, *Curr. Pharm. Des.* **2020**, *26*, 4658–4674.

[3] O. Isayev, B. Rasulev, L. Gorb, J. Leszczynski, *Mol. Divers.* **2006**, *10*, 233–245.

[4] H. Stucki, *Chimia* **2004**, *58*, 409–413.

[5] P. Kovacic, R. Somanathan, *J. Appl. Toxicol.* **2014**, *34*, 810–824.

[6] M. Megharaj, B. Ramakrishnan, K. Venkateswarlu, N. Sethunathan, R. Naidu, *Environ. Int.* **2011**, *37*, 1362–1375.

[7] J. C. Spain, *Annu. Rev. Microbiol.* **1995**, *49*, 523–555.

[8] J. S. Strehse, M. Brenner, M. Kisiela, E. Maser, *Arch. Toxicol.* **2020**, *94*, 4043–4054.

[9] M. H. H. Wurzenberger, J. T. Lechner, M. Lommel, T. M. Klapötke, J. Stierstorfer, *Propellants Explos. Pyrotech.* **2020**, *45*, 898–907.

[10] J. W. Fronabarger, M. D. Williams, W. B. Sanborn, D. A. Parrish, M. Bichay, *Propellants Explos. Pyrotech.* **2011**, *36*, 459–470.

[11] T. M. Klapötke, J. T. Lechner, J. Stierstorfer, *Propellants Explos. Pyrotech.* **2022**, *47*, e202100205.

[12] T. M. Klapötke, J. Stierstorfer, M. Weyrauther, T. G. Witkowski, *Chem. Eur. J.* **2016**, *22*, 8619–8626.

[13] J. W. Fronabarger, M. D. Williams, W. B. Sanborn, J. G. Bragg, D. A. Parrish, M. Bichay, *Propellants Explos. Pyrotech.* **2011**, *36*, 541–550.

[14] T. M. Klapötke, P. Mayer, C. Miró Sabaté, J. M. Welch, N. Wiegand, *Inorg. Chem.* **2008**, *47*, 6014–6027.

[15] A. W. Czarnik, *Nature* **1998**, *394*, 417–418.

[16] M. E. Germain, M. J. Knapp, *J. Am. Chem. Soc.* **2008**, *130*, 5422–5423.

[17] T. M. Klapötke, *Chemistry of High-Energy Materials*, 5th ed., De Gruyter, Berlin, Boston, **2019**.

[18] K. D. Oyler, in *Green Energetic Materials*, **2014**, pp. 103–132.

[19] S. J. Toal, W. C. Trogler, *J. Mater. Chem.* **2006**, *16*, 2871–2883.

[20] D. S. Moore, *Rev. Sci. Instrum.* **2004**, *75*, 2499–2512.

[21] V. Merz, G. Zetter, *Ber. Dtsch. Chem. Ges.* **1879**, *12*, 2035–2049.

[22] J. Stenhouse, C. E. Groves, *Ber. Dtsch. Chem. Ges.* **1880**, *13*, 1305–1308.

[23] A. Drechsel, T. M. Klapoetke, T. G. Witkowski, *J. J. Inorg. Chem.* **2016**, *1*, 1–8.

[24] T. G. Witkowski, Dissertation thesis, LMU Munich **2017**.

[25] A. J. Birch, R. A. Massy-Westropp, R. W. Rickards, H. Smith, *J. Chem. Soc.* **1958**, 360–365.

[26] A. P. Marchand, G. M. Reddy, *Synthesis* **1992**, *1992*, 261–262.

[27] M. A. Pierce-Butler, *Acta Crystallogr. B* **1982**, *38*, 3100–3104.

[28] Y.-G. Bi, Y.-A. Feng, Y. Li, B.-D. Wu, T.-L. Zhang, *J. Coord. Chem.* **2015**, *68*, 181–194.

[29] H. Östmark, S. Wallin, H. G. Ang, *Propellants Explos. Pyrotech.* **2012**, *37*, 12–23.

[30] R. B. Cundall, T. Frank Palmer, C. E. C. Wood, *J. Chem. Soc., Faraday Trans. 1* **1978**, *74*, 1339–1345.

[31] M. Härtel, Dissertation thesis, LMU München **2017**.

[32] W. Acree, J. S. Chickos, *J. Phys. Chem. Ref. Data* **2010**, *39*, 043101.

[33] M. Suceska, *EXPLO5 version V6.05 User's guide*, Zagreb, **2018**.

[34] T. M. Klapötke, *Energetic Materials Encyclopedia, Vol. 1–3*, 2nd ed., DeGruyter, Berlin/Boston, **2021**.

[35] M. H. H. Wurzenberger, B. R. G. Bissinger, M. Lommel, M. S. Gruhne, N. Szimhardt, J. Stierstorfer, *New J. Chem.* **2019**, *43*, 18193–18202.

[36] M. H. H. Wurzenberger, V. Braun, M. Lommel, T. M. Klapötke, J. Stierstorfer, *Inorg. Chem.* **2020**, *59*, 10938–10952.

[37] Impact: insensitive > 40 J, less sensitive ≥ 35 J, sensitive ≥ 4 J, very sensitive ≤ 3 J; Friction: insensitive > 360 N, less sensitive = 360 N, sensitive < 360 N and > 80 N, very sensitive ≤ 80 N, extremely sensitive ≤ 10 N, According to: *Recommendations on the Transport of Dangerous Goods, Manual of Tests and Criteria*, 4th. ed., United Nations, New York-Geneva, **1999**.

[38] M. S. Gruhne, T. Lenz, M. Rösch, M. Lommel, M. H. H. Wurzenberger, T. M. Klapötke, J. Stierstorfer, *Dalton Trans.* **2021**, *50*, 10811–10825.

[39] M. H. H. Wurzenberger, M. S. Gruhne, M. Lommel, N. Szimhardt, T. M. Klapötke, J. Stierstorfer, *Chem. Asian J.* **2019**, *14*, 2018–2028.

[40] N. Szimhardt, M. H. H. Wurzenberger, T. M. Klapötke, J. T. Lechner, H. Reichherzer, C. C. Unger, J. Stierstorfer, *J. Mater. Chem. A* **2018**, *6*, 6565–6577.

[41] N. Szimhardt, M. H. H. Wurzenberger, A. Beringer, L. J. Daumann, J. Stierstorfer, *J. Mater. Chem. A* **2017**, *5*, 23753–23765.

[42] J.-G. Zhang, K. Wang, Z.-M. Li, H. Zheng, T.-L. Zhang, L. Yang, *Main Group Chem.* **2011**, *10*, 205–213.

[43] M. S. Gruhne, M. Lommel, M. H. H. Wurzenberger, N. Szimhardt, T. M. Klapötke, J. Stierstorfer, *Propellants Explos. Pyrotech.* **2020**, *45*, 147–153.

[44] S. M. J. Endraß, T. M. Klapötke, J. Stierstorfer, *New Trends in Research of Energetic Materials* Pardubice, Czech Republic, 06–08 April, **2022**, 311–317.

[45] A. Neuer, G. Bikelyté, S. M. J. Endraß, T. M. Klapötke, J. Stierstorfer, *New Trends in Research of Energetic Materials* Pardubice, Czech Republic, 06–08 April, **2022**, 440–448.

2.7 Supporting Information

2.7.1 Compound Overview

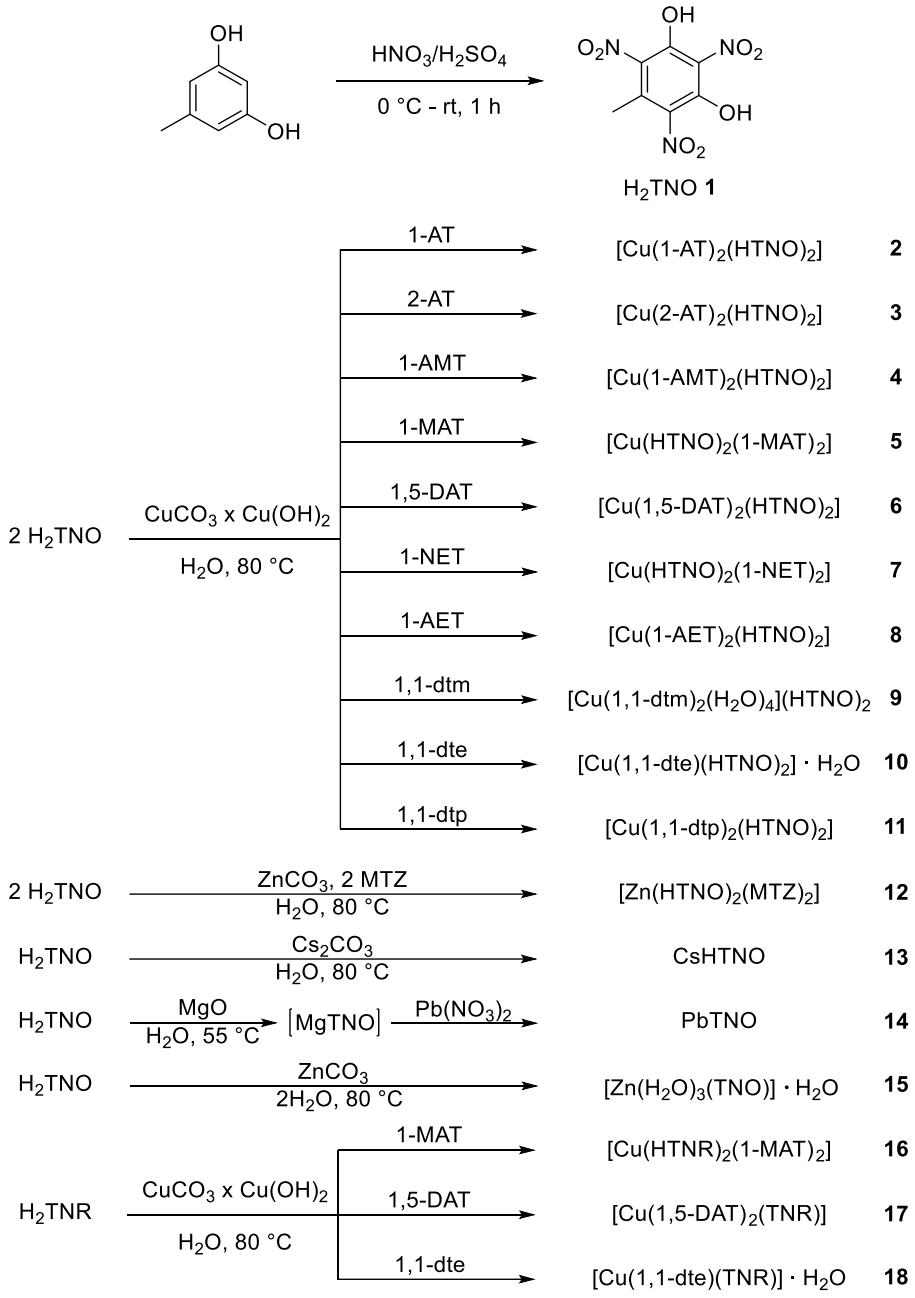

2.7.2 Single Crystal X-Ray Diffraction

For all crystalline compounds an Oxford Xcalibur3 diffractometer with a CCD area detector or Bruker D8 Venture TXS diffractometer equipped with a multilayer monochromator, a Photon 2 detector, and a rotating-anode generator were employed for data collection using Mo-Kα radiation (λ = 0.7107 Å). On the Oxford device, data collection and reduction were carried out using the CrysAlisPRO software. [S1] On the Bruker diffractometer, the data were collected with the Bruker Instrument Service v3.0.21, the data reduction was performed using the SAINT V8.18C software (Bruker AXS Inc., 2011). The structures were solved by direct methods (SIR-92, [S2] SIR-97, [S3,S4] SHELXS-97[S5,S6] or SHELXT[S7]), refined by full-matrix least-squares on *F2* (SHELXL[S5,S6]) and finally checked using the PLATON software[S8] integrated in the WinGX[S7,S9] or Olex2[S8] software suite. The non-hydrogen atoms were refined anisotropically and the hydrogen atoms were located and freely refined. The absorptions were corrected by a SCALE3 ABSPACK or SADABS Bruker APEX3 multi-scan method. [S11,S12] All DIAMOND2 plots are shown with thermal ellipsoids at the 50% probability level and hydrogen atoms are shown as small spheres of arbitrary radius.

Table S1. Crystallographic data and crystal structure refinement details of compounds **2**, **3** and **5**.

	[Cu(1-AT)$_2$(HTNO)$_2$] **(2)**	**[Cu(2-AT)$_2$(HTNO)$_2$]** **(3)**	**[Cu(HTNO)$_2$(1-MAT)$_2$]** **(5)**
Formula	$C_{18}H_{14}CuN_{16}O_{16}$	$C_{18}H_{14}CuN_{16}O_{16}$	$C_{18}H_{18}CuN_{16}O_{16}$
FW [g mol^{-1}]	749.97	749.97	778.02
Crystal system	monoclinic	triclinic	monoclinic
Space Group	$P2_1/c$	$P\bar{1}$	$P2_1/c$
Color / Habit	yellow platelet	green block	brown block
Size [mm]	0.10 × 0.25 × 0.50	0.35 × 0.50 × 0.50	0.05 x 0.08 x 0.10
a [Å]	5.9922(6)	6.1305(4)	9.5392(3)
b [Å]	20.417(3)	9.5436(6)	6.9389(3)
c [Å]	10.7258(12)	12.3575(10)	22.0638(9)
α [°]	90	71.952(7)	90
β [°]	94.481(10)	88.828(6)	100.916(1)
γ [°]	90	88.809(6)	90
V [Å^3]	1308.2(3)	687.20(9)	1434.01(10)
Z	2	1	2
$\rho_{calc.}$ [g cm^{-3}]	1.904	1.812	1.802
μ [mm^{-1}]	0.949	0.903	0.869
F(000)	758	379	790
$\lambda_{MoK\alpha}$ [Å]	0.71073	0.71073	0.71073
T [K]	101	102	173
θ Min–Max [°]	2.2, 25.3	2.2, 26.4	3.1, 26.4
Dataset	−6: 7; −24: 24; −12: 12	−7: 7; −11: 11; −15: 14	−11: 11; −8: 8; −27: 27
Reflections collected	11375	5325	23392
Independent refl.	2394	2806	2923
Rint	0.079	0.019	0.067
Observed reflections	1637	2553	2402
Parameters	226	226	246
R_1 (obs)[a]	0.0584	0.0304	0.0394
wR_2 (all data)[b]	0.1438	0.0803	0.0828
GooF[c]	1.09	1.09	1.10
Resd. Dens. [e Å^{-3}]	−0.55, 0.67	−0.31, 0.41	−0.39, 0.33
Absorption correction	multi-scan	multi-scan	multi-scan
CCDC	2191773	2191776	2191775

[a] $R_1 = \Sigma||F_0|-|F_c||/\Sigma|F_0|$; [b] $wR_2 = [\Sigma[w(F_0^2-F_c^2)^2]/\Sigma[w(F_0)^2]]^{1/2}$; $w = [\sigma c^2(F_0^2)+(xP)^2+yP]^{-1}$ and $P=(F_0^2+2F_c^2)/3$; [c] $S = \{\Sigma[w(F_o^2-F_c^2)^2]/(n-p)\}^{1/2}$ (n = number of reflections; p = total number of parameters).

Table S2. Crystallographic data and crystal structure refinement details of compounds **6**, **7** and **8**.

	[Cu(1,5-DAT)$_2$(HTNO)$_2$] **(6)**	**[Cu(HTNO)$_2$(1-NET)$_2$]** **(7)**	**[Cu(1-AET)$_2$(HTNO)$_2$]** **(8)**
Formula	$C_{16}H_{16}CuN_{18}O_{16}$	$C_{20}H_{18}CuN_{16}O_{22}$	$C_{20}H_{18}CuN_{20}O_{16}$
FW [g mol^{-1}]	780.01	898.04	858.08
Crystal system	monoclinic	triclinic	triclinic
Space Group	$P2_1/c$	$P\bar{1}$	$P\bar{1}$
Color / Habit	brown plate	blue rod	brown needle
Size [mm]	0.02 x 0.09 x 0.13	0.10 x 0.25 x 0.65	0.02 x 0.02 x 0.18
a [Å]	9.4135(4)	6.3401(7)	6.5701(3)
b [Å]	6.9680(3)	11.3649(10)	10.9956(5)
c [Å]	21.7172(8)	11.7504(11)	11.0329(6)
α [°]	90	84.287(7)	85.562(2)
β [°]	100.180(1)	77.034(9)	82.251(2)
γ [°]	90	87.473(8)	89.218(2)
V [Å^3]	1402.08(10)	820.78(14)	787.39(7)
Z	2	1	1
$\rho_{calc.}$ [g cm^{-3}]	1.848	1.817	1.810
μ [mm^{-1}]	0.891	0.786	0.804
F(000)	790	455	435
$\lambda_{MoK\alpha}$ [Å]	0.71073	0.71073	0.71073
T [K]	173	100	173
θ Min–Max [°]	3.1, 26.4	2.4, 26.4	2.5, 26.4
Dataset	−11: 11; −8: 8; −27: 27	−7: 7; −14: 14; −14: 14	−8: 7; −13: 13; −13: 13
Reflections collected	14989	12317	12758
Independent refl.	2865	3341	3185
Rint	0.029	0.047	0.051
Observed reflections	2631	2782	2729
Parameters	235	273	261
R_1 (obs)[a]	0.0326	0.0392	0.0468
wR_2 (all data)[b]	0.0802	0.1029	0.0987
GooF[c]	1.14	1.05	1.15
Resd. Dens. [e Å^{-3}]	−0.35, 0.35	−0.31, 0.53	−0.62, 0.49
Absorption correction	multi-scan	multi-scan	multi-scan
CCDC	2191782	2191777	2191778

[a] $R_1 = \Sigma||F_0|-|F_c||/\Sigma|F_0|$; [b] $wR_2 = [\Sigma[w(F_0^2-F_c^2)^2]/\Sigma[w(F_0)^2]]^{1/2}$; $w = [\sigma c^2(F_0^2)+(xP)^2+yP]^{-1}$ and $P=(F_0^2+2F_c^2)/3$; [c] $S = \{\Sigma[w(F_o^2-F_c^2)^2]/(n-p)\}^{1/2}$ (n = number of reflections; p = total number of parameters).

Table S3. Crystallographic data and crystal structure refinement details of compounds **9**, **11** and **12**.

	$[Cu(1,1\text{-dtm})_2(H_2O)_4](HTNO)_2$	**$[Cu(1,1\text{-dtp})_2(HTNO)_2]$**	**$[Zn(HTNO)_2(MTZ)_2]$**
	(9)	**(11)**	**(12)**
Formula	$C_{20}H_{24}CuN_{22}O_{20}$	$C_{24}H_{24}CuN_{22}O_{16}$	$C_{18}H_{16}N_{14}O_{16}Zn$
FW [g mol^{-1}]	956.15	940.19	749.82
Crystal system	triclinic	monoclinic	triclinic
Space Group	$P\bar{1}$	$P2_1/c$	$P\bar{1}$
Color / Habit	orange rod	green needle	colorless rod
Size [mm]	0.02 x 0.03 x 0.11	0.03 x 0.04 x 0.12	0.05 x 0.10 x 0.25
a [Å]	5.2974(3)	9.3675(3)	7.7858(7)
b [Å]	11.3737(7)	15.8281(5)	7.9349(6)
c [Å]	15.6337(10)	12.6632(4)	11.9254(9)
α [°]	107.674(2)	90	74.181(7)
β [°]	91.241(2)	109.793(1)	73.695(7)
γ [°]	95.972(2)	90	83.328(7)
V [Å^3]	891.21(9)	1766.65(10)	679.71(10)
Z	1	2	1
$\rho_{calc.}$ [g cm^{-3}]	1.782	1.768	1.832
μ [mm^{-1}]	0.730	0.727	1.011
F(000)	487	958	380
$\lambda_{MoK\alpha}$ [Å]	0.71073	0.71073	0.71073
T [K]	173	173	98
θ Min–Max [°]	2.7, 25.4	2.6, 26.4	2.7, 26.4
Dataset	−6: 6; −13: 13; −18: 18	−11: 11; −19: 19; −15: 15	−9: 9; −9: 9; −14: 14
Reflections collected	7736	28625	5951
Independent refl.	3233	3616	2773
Rint	0.035	0.033	0.037
Observed reflections	2730	3337	2184
Parameters	298	307	229
R_1 (obs)[a]	0.0558	0.0343	0.0547
wR_2 (all data)[b]	0.1231	0.0831	0.1153
GooF[c]	1.11	1.15	1.08
Resd. Dens. [e Å^{-3}]	−0.57, 0.64	−0.27, 0.36	−0.51, 0.55
Absorption correction	multi-scan	multi-scan	multi-scan
CCDC	2191779	2191774	2191783

[a]$R_1 = \Sigma||F_0|-|F_c||/\Sigma|F_0|$; [b]$wR_2 = [\Sigma[w(F_0^2-F_c^2)^2]/\Sigma[w(F_0)^2]]^{1/2}$; $w = [\sigma c^2(F_0^2)+(xP)^2+yP]^{-1}$ and $P=(F_0^2+2F_c^2)/3$; [c]$S = \{\Sigma[w(F_o^2-F_c^2)^2]/(n-p)\}^{1/2}$ (n = number of reflections; p = total number of parameters).

Table S4. Crystallographic data and crystal structure refinement details of compounds **13** and **15**.

	CsHTNO **(13)**	**$[Zn(H_2O)_3(TNO)] \cdot H_2O$** **(15)**
Formula	$C_7H_4CsN_3O_8$	$C_7H_{11}N_3O_{12}Zn$
FW [g mol^{-1}]	391.04	394.56
Crystal system	monoclinic	orthorhombic
Space Group	$P2_1/n$	$Pna2_1$
Color / Habit	brown platelet	yellow platelet
Size [mm]	0.02 × 0.10 × 0.20	0.02 x 0.10 x 0.12
a [Å]	11.3109(5)	7.3323(3)
b [Å]	5.2139(2)	20.1647(7)
c [Å]	18.9297(7)	8.8270(3)
α [°]	90	90
β [°]	106.019(1)	90
γ [°]	90	90
V [Å^3]	1073.01(7)	1305.10(8)
Z	4	4
$\rho_{calc.}$ [g cm^{-3}]	2.421	2.008
μ [mm^{-1}]	3.497	1.960
F(000)	744	800
$\lambda_{MoK\alpha}$ [Å]	0.71073	0.71073
T [K]	173	173
θ Min–Max [°]	3.4, 26.4	3.0, 27.1
Dataset	−14: 14; −6: 6; −23: 23	−9: 9; −25: 25; −11: 11
Reflections collected	25388	21641
Independent refl.	2195	2877
Rint	0.106	0.039
Observed reflections	2066	2772
Parameters	177	227
R_1 (obs)[a]	0.0240	0.0203
wR_2 (all data)[b]	0.0644	0.0499
GooF[c]	1.17	1.08
Resd. Dens. [e Å^{-3}]	−0.60, 1.20	−0.27, 0.28
Absorption correction	multi-scan	multi-scan
CCDC	2191781	2191780

[a] $R_1 = \Sigma||F_0|-|F_c||/\Sigma|F_0|$; [b] $wR_2 = [\Sigma[w(F_0^2-F_c^2)^2]/\Sigma[w(F_0)^2]]^{1/2}$; $w = [\sigma c^2(F_0^2)+(xP)^2+yP]^{-1}$ and $P=(F_0^2+2F_c^2)/3$; [c] $S = \{\Sigma[w(F_o^2-F_c^2)^2]/(n-p)\}^{1/2}$ (n = number of reflections; p = total number of parameters).

For $[Cu(2\text{-}AT)_2(HTNO)_2]$ (**3**) crystallization in the triclinic space group *P*−1 with a calculated density of 1.81 g cm^{-3} at 102 K was observed with one formula unit per unit cell. Coordination follows the typical pattern of the Trinitro-orcinolate complexes with a *Jahn-Teller*-like elongation distortion of the z^2-axis, which is occupied by the coordinating nitro groups.

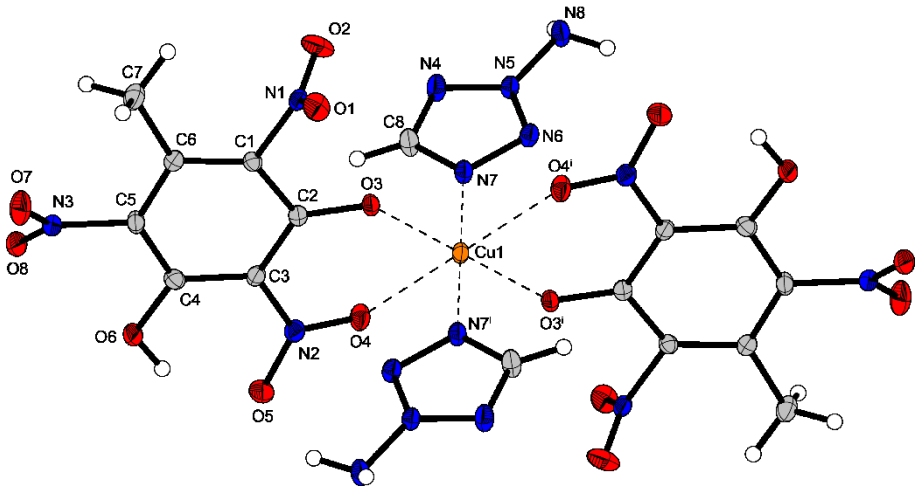

Figure S1. Crystal structure of compound **3**. Selected bond lengths (Å): Cu1–O3 1.9153(13), Cu1–O4 2.3892(13), Cu1–N7 1.9934(17); selected bond angles (°): O3–Cu1–O4 78.08(5), O3–Cu1–N7 88.66(6), O3–Cu1–O4^{i} 101.92(5), O3–Cu1–N7^{i} 91.34(6), O4–Cu1–N7 90.58(6), O4–Cu1–N7^{i} 89.43(6); symmetry codes: (i) 1−x, 1−y, 2−z.

[Cu(HTNO)$_2$(1-MAT)$_2$] (**5**) crystallizes in the monoclinic space group $P2_1/c$ with a calculated density of 1.80 g cm^{-3} at 173 K and two formula units per unit cell. Again, the typical coordination pattern of the Trinitro-orcinolate is observed, where the nitro group in *para*-position to the methyl group takes up the distorted axis with a bond length of 2.44 Å.

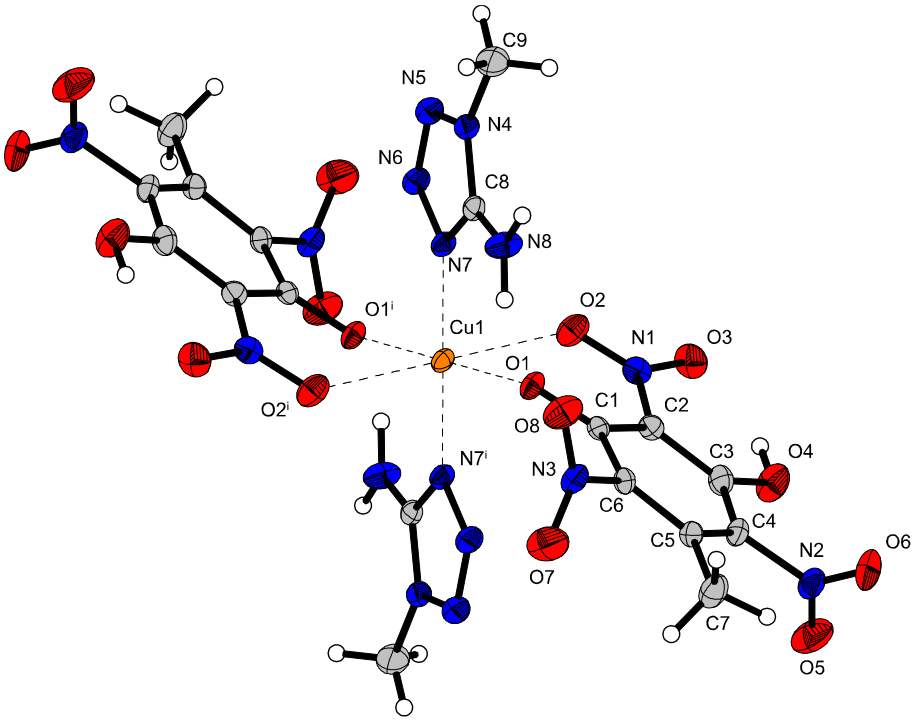

Figure S2. Crystal structure of **3**. Selected bond lengths (Å): Cu1–O1 1.9732(16), Cu1–O2 2.4411(19), Cu1–N7 1.981(2); selected bond angles (°): O1–Cu1–N7 89.84(8), O1–Cu1–O2 72.84(7), O2–Cu1–N7 86.89(7); symmetry codes: (i) 2−x, 1−y, 1−z.

Compared to compound **3**, the changes that result from the 1-amino group of 1,5-DAT instead of the 1-methyl of 1-MAT, are small. $[Cu(1,5\text{-}DAT)_2(HTNO)_2]$ (**6**) crystallizes in the monoclinic space group $P2_1/c$ with two formula units per unit cell and a slightly higher density of 1.85 g cm^{-3} compared to **5**.

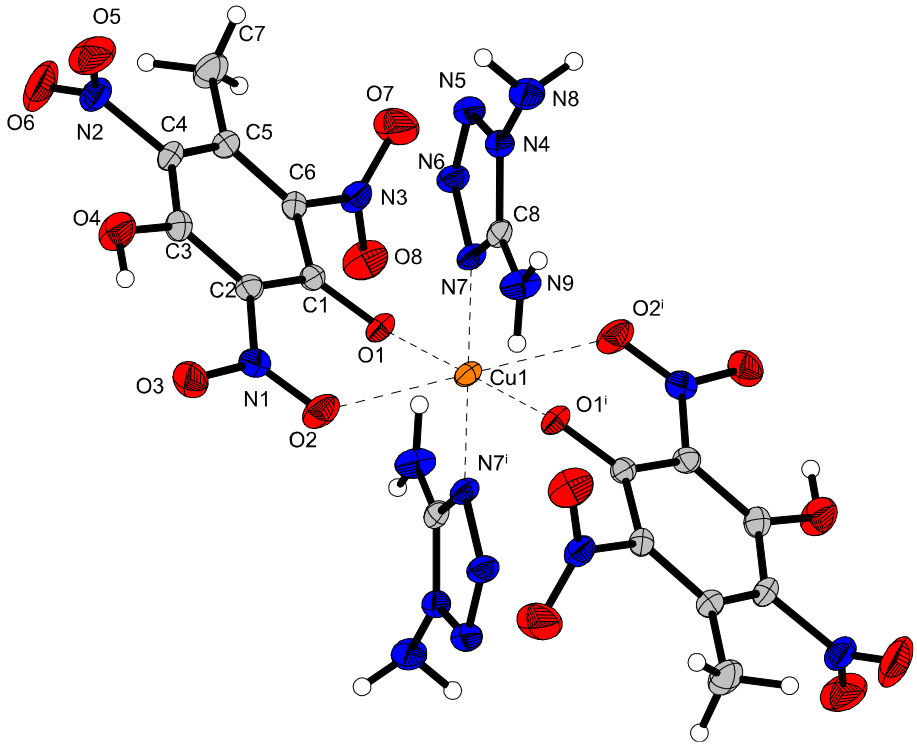

Figure S3. Crystal structure of **6**. Selected bond lengths (Å): Cu1–O1 1.9649(14), Cu1–O2 2.4331(17), Cu1–N7 1.9799(17); selected bond angles (°): O1–Cu1–N7 90.59(6), O1–Cu1–O2 73.25(6), O2–Cu1–N7 93.45(7); symmetry codes: (i) 2−x, 1−y, 1−z.

While the coordination pattern does not change for $[Cu(HTNO)_2(1\text{-}NET)_2]$ (**7**) and $[Cu(1\text{-}AET)_2(HTNO)_2]$ (**8**), , crystallization is observed in the triclinic space group *P*−1 with one formula unit per unit cell and a calculated density of 1.82 g cm^{-3} at a temperature of 100 K, respectively 1.81 g cm^{-3} at 173 K.

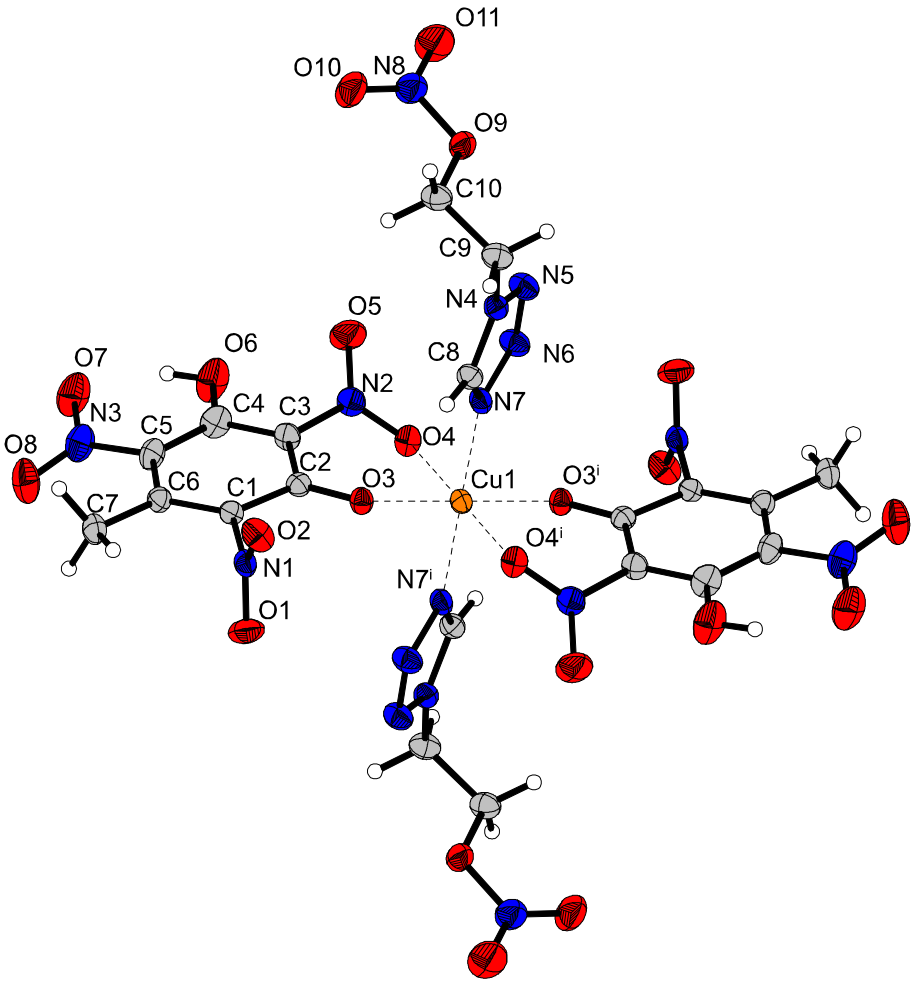

Figure S4. Crystal structure of **7**. Selected bond lengths (Å): Cu1–O3 1.9260 (16), Cu1–O4 2.3141(17), Cu1–N7 2.006(2); selected bond angles (°): O3–Cu1–N7 89.99(8), O3–Cu1–O4 85.35(6), O4–Cu1–N7 91.14(7); symmetry codes: (i) 1−x, 2−y, 1−z.

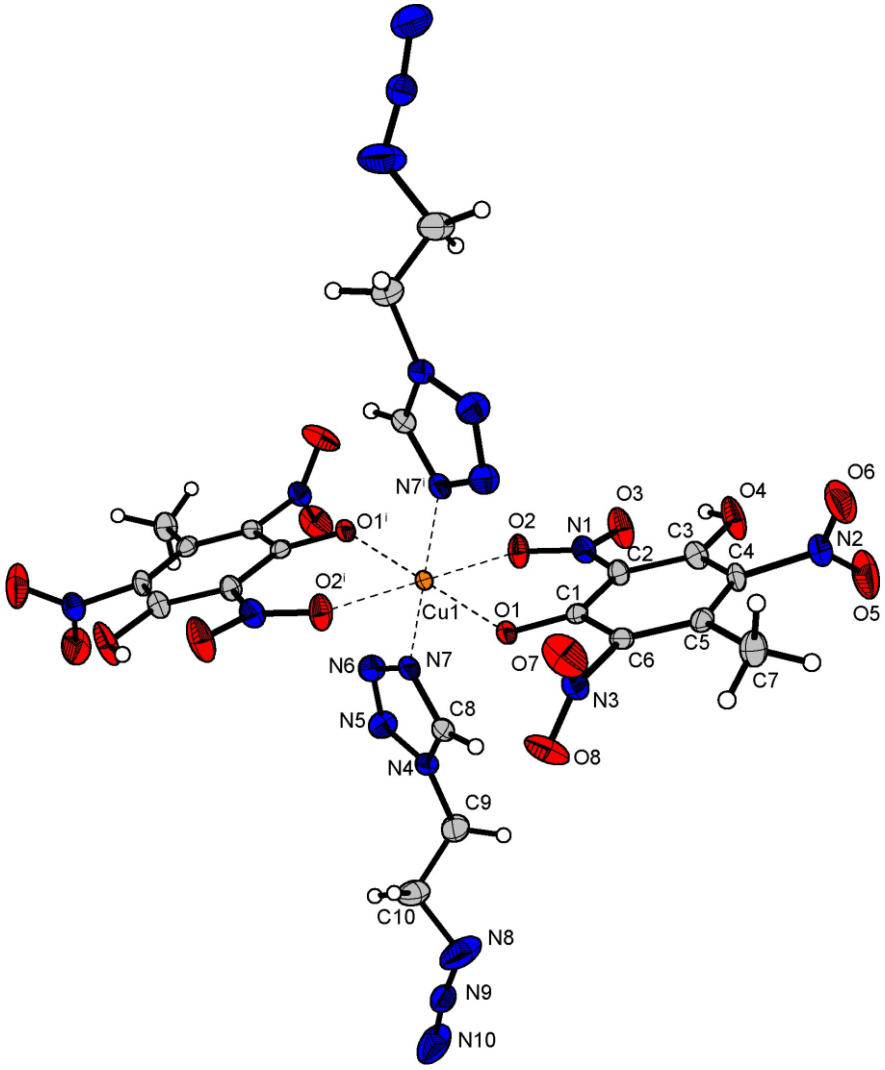

Figure S5. Crystal structure of **8**. Selected bond lengths (Å): Cu1–O1 1.929(2), Cu1–O2 2.324(2), Cu1–N7 1.998(3); selected bond angles (°): O1–Cu1–N7 87.77(9), O1–Cu1–O2 78.45(8), O2–Cu1–N7 88.66(9); symmetry codes: (i) −x, 2−y, 1−z.

CsHTNO (**13**) crystallizes in the monoclinic space group $P2_1/c$ with a density of 2.42 g cm^{-3} at 173 K. The Trinitro-orcinolate anion shows multiple interactions with the Cs^+ cation which results in a polymeric structure.

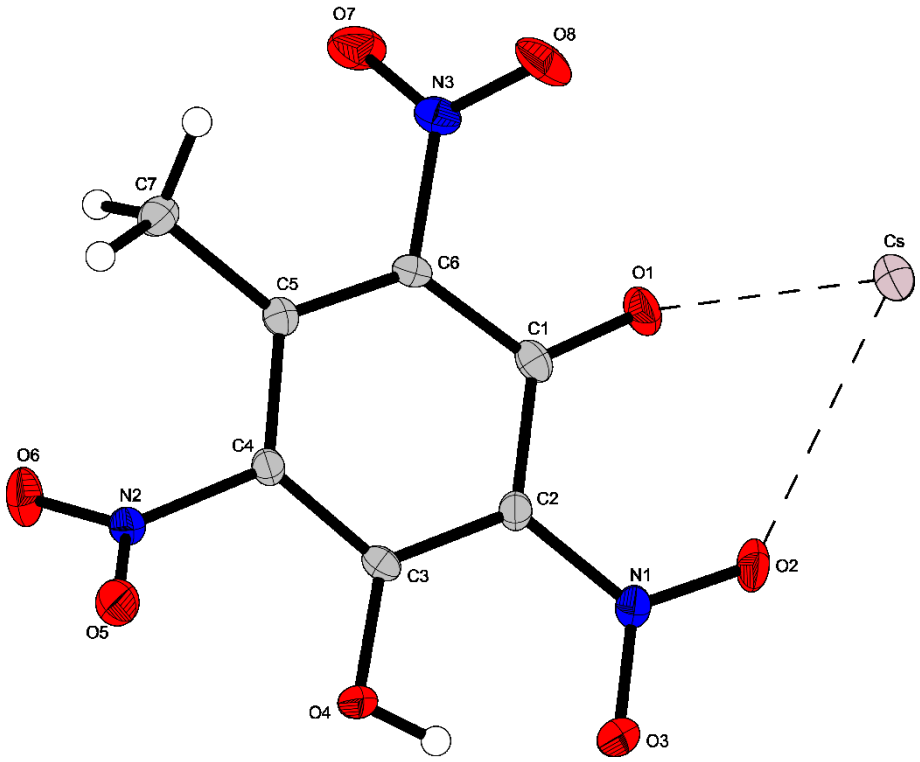

Figure S6. Crystal structure of **13**. Selected bond lengths (Å): Cs–O1 3.086(2), Cs–O2 3.322(2), Cs–O8^{i} 3.380(2), Cs–O1^{iii} 3.116(2), Cs–O2^{iii} 3.170(2), Cs–O2^{iv} 3.208(2), Cs–O4^{vi} 3.356(2), Cs–O5^{vi} 3.198(2), Cs–O6^{vii} 3.136(2); selected bond angles (°): O1–Cs–O2 48.05(5), O1–Cs–O8^{i} 105.82(6), O1–Cs–O1^{iii} 88.86(6), O1–Cs–O2^{iii} 130.49(6), O1–Cs–O2^{iv} 60.33(6), O1–Cs–O4^{vi} 144.76(5), O1–Cs–O5^{vi} 147.87(6), O1–Cs–O6^{vii} 96.89(6), O2–Cs–O8^{i} 90.57(5), O1^{iii}–Cs–O2 58.79(6), O2–Cs–O2^{iii} 84.11(6), O2–Cs–O2^{iv} 83.52(6), O2–Cs–O4^{vi} 137.58(6), O2–Cs–O5^{vi} 154.49(5), O2–Cs–O6^{vii} 144.56(5); symmetry codes: (i) x, −1+y, z; (iii) 1/2-x, −1/2+y, 1/2−z; (iv) 1/2−x, 1/2+y, 1/2−z; (vi) −1/2+x, 1/2−y, −1/2+z; (vii) −1/2+x, 3/2−y, −1/2+z.

2.7.3 Computations

All calculations were carried out using the Gaussian G09 program package. [S13] The enthalpies (H) and free energies (G) were calculated using the complete basis set (CBS) method of Petersson and coworkers in order to obtain very accurate energies. The CBS models use the known asymptotic convergence of pair natural orbital expressions to extrapolate from calculations using a finite basis set to the estimated complete basis set limit. CBS-4 begins with a HF/3-21G(d) geometry optimization; the zero point energy is computed at the same level. It then uses a large basis set SCF calculation as a base energy, and a MP2/6-31+G calculation with a CBS extrapolation to correct the energy through second order. A MP4(SDQ)/6-31+(d,p) calculation is used to approximate higher order contributions. In this study we applied the modified CBS-4M method (M referring to the use of minimal population localization) which is a re-parametrized version of the original CBS-4 method and also includes some additional empirical corrections. The enthalpies of the gas-phase species M were computed according to the atomization energy method (E1) (Table S5 & Table S6). [S13–S18]

$$\Delta_f \mathrm{H}^\circ_{(g,M,298)} = H_{(Molecule,298)} - \sum H^\circ_{(Atoms,298)} + \sum \Delta_f H^\circ_{(Atoms,298)} \qquad \text{(E1)}$$

Table S5. Literature values for atomic $\Delta \boldsymbol{H^\circ_f}^{\mathbf{298}}$ / kcal mol^{-1}

	$-H^{298}$ [a.u.]	NIST[S19]
H	0.50091	52.1
C	37.786156	171.3
N	54.522462	113.0
O	74.991202	59.6

The gas-phase heat of formations were converted to the solid/liquid state ones for neutrals: by subtracting the vaporization/sublimation enthalpies (calculated using the Trouton rule). [S20,S21] The calculation results are summarized in Table S6.

$$\Delta U_m = \Delta H_m - \Delta n\, R\, T \qquad \text{(E2)}$$

Table S6. CBS-4M results

Compound	$-H^{298}$[a] [a.u.]	$\Delta_f H^\circ(g,M)$[b] [kJ mol^{-1}]	$\Delta_f H^\circ(s)$[c] [kJ mol^{-1}]	Δn[d]	$\Delta_f U(s)$[e] [kJ mol^{-1}]
H_2TNO	1034.254647	−326.3	−410.0	−8.0	−390.2
H_2TNR	995.013296	−289.1	−374.3	−7.0	−356.9
TNT	883.954491	−9.6	−56.8	−7.0	−173.8

[a] CBS-4M electronic enthalpy; [b] gas phase enthalpy of formation; [c] standard solid state enthalpy of formation; [d] Δn being the change of moles of gaseous components when formed; [e] solid state energy of formation.

2.7.4 Vapor Pressure

After the isolation of H_2TNO, purity was tested via elemental analysis and complemented by ^{1}H-qNMR techniques ((99.37 ± 2.05) %; procedure described in previous publications [S22,23]). Since sufficient purity was found, the *p-T* data set were obtained based on the transpiration method using the following modified *Clarke-Glew* fit function:

$$\ln\frac{p_{\mathrm{sat,T}}}{p^\circ}=\frac{A}{R}+\frac{B}{RT}+\frac{\Delta_{\mathrm{cr}}^{\mathrm{g}}C_{\mathrm{p,m}}^\circ}{R}\,ln\frac{T}{T_{\mathrm{ref}}} \qquad \text{(E3)}$$

where p° is the reference pressure 1.0, in Pa; $\Delta_{\mathrm{cr}}^{\mathrm{g}}C_{\mathrm{p,m}}^\circ$ is the molar heat capacity difference between the crystalline (cr) and gaseous state (g) at constant pressure, in J·mol^{-1} K^{-1}; T_{ref} is the reference temperature 298.15, in K and A/B are specific fit coefficients (A: unitless; B: in K).

The exact method description can be found in previous publication and the HPLC-DAD parameters can be found in Table S9 and Table S10. [S22,23] The molar heat capacity at constant pressure $C_{\mathrm{p,m}}^\circ$ – required for the extrapolation via the *Clark-Glew* fit function – for H_2TNO and H_2TNR were not retrievable in the literature. Instead the values were obtained with the group additivity approach by *Chickos et al.*. [S24] The molar heat capacity differences between solid and gas state were calculated – including TNT – by a procedure described by *Chickos et al.*. [S25] The values are given in detail in Table S7.

Table S7. Estimated molar heat capacities and their differences for H_2TNO, H_2TNR and TNT (T = 298.15 K).

Compound	$C_{\mathrm{p,m}}^\circ(cr)$		$-\Delta_{\mathrm{cr}}^{\mathrm{g}}C_{\mathrm{p,m}}^\circ$
	Calc. [a]	Exp.	Calc. [b]
	J·mol^{-1}·K^{-1}	J·mol^{-1}·K^{-1}	J·mol^{-1}·K^{-1}
H_2TNO	302.9	n.a,	46.2
H_2TNR [S25]	283.8	n.a.	43.3
TNT [S26]	–	209.7 [8]	32.2

[a] Calculated according to the group additivity approach by *Chickos et al.*.[S24]
[b] Calculated by $-\Delta_{\mathrm{cr}}^{\mathrm{g}}C_{\mathrm{p,m}}^\circ = 0.75 + C_{\mathrm{p,m}}^\circ(cr) \times 0.15$.[S27]

The experimental vapor pressures as well as the thermochemical properties such as molar enthalpies of vaporization $\Delta_{\mathrm{l}}^{\mathrm{g}}H_{\mathrm{m}}^\circ(T)$ and molar entropies of vaporization $\Delta_{\mathrm{l}}^{\mathrm{g}}S_{\mathrm{m}}^\circ(T)$ were reported in Table S8 for H_2TNO.

Table S8. Experimental conditions and *Clark-Glew* fit function resulting in absolute vapor pressures $\boldsymbol{p_{sat}}$ and thermochemical properties of sublimation (molar enthalpy of sublimation $\Delta^{g}_{cr}\boldsymbol{H^{\circ}_{m}}$ and molar entropy of sublimation $\Delta^{g}_{cr}\boldsymbol{S^{\circ}_{m}}$). Obtained from the measurements of H_2TNO by the Transpiration Method[a].

H_2TNO: $\Delta^{g}_{cr}H^{\circ}_{m}$ (298.15 K) = (122.7 ± 1.7) kJ·mol^{-1}

$$\ln p_{sat}/p^{0} = \frac{359.4}{R} - \frac{136481.6}{RT} - \frac{46.2}{R} ln \frac{T}{298.15\ \mathrm{K}}$$

T[b]	m[c]	V_{N2}[d]	T_{amb}[e]	Flow	p_{sat}[f]	$u(p_{sat})$[g]	$\Delta^{g}_{l}H^{\circ}_{m}(T)$	$\Delta^{g}_{l}S^{\circ}_{m}(T)$
K	mg	dm^3	K	dm^3·h^{-1}	Pa	Pa	kJ·mol^{-1}	J·mol^{-1}·K^{-1}
332.4	0.016	128	297.1	5.4	1.17	0.07	121.13	212.6
332.4	0.012	98.8	298.3	4.2	1.20	0.07	121.13	212.7
332.6	0.010	80.4	296.8	4.8	1.20	0.07	121.12	212.6
337.4	0.021	89.6	297.0	4.8	2.21	0.13	120.90	211.8
342.3	0.010	25.0	297.2	4.8	3.99	0.23	120.67	210.9
347.4	0.007	8.72	297.4	4.8	7.65	0.45	120.44	210.5
352.3	0.021	15.8	296.7	4.8	12.9	0.76	120.21	209.3
356.3	0.021	9.36	296.4	4.8	21.6	1.27	120.03	209.3
356.3	0.118	52.7	296.5	3.0	21.2	1.24	120.02	209.1
357.2	0.016	6.64	297.1	4.7	23.6	1.39	119.98	209.0
362.0	0.010	2.38	297.1	4.8	41.0	2.41	119.76	208.6
366.9	0.013	1.83	297.3	4.8	65.5	3.84	119.54	207.4
370.9	0.014	1.19	296.4	4.8	110	6.47	119.35	207.7
375.8	0.024	1.19	296.4	4.8	192	11.3	119.13	207.6
380.7	0.038	1.27	296.3	4.8	287	16.8	118.90	206.2
380.7	0.034	1.19	296.5	4.8	275	16.1	118.90	205.9
380.7	0.036	1.19	296.4	4.8	286	16.8	118.90	206.2

[a] Experimental conditions: T is saturation temperature; m is mass of the transferred sample quantified via HPLC-DAD experiments; V_{N2} is volume of the carrier gas and T_{amb} is ambient temperature. The uncertainties for T, V, and m are standard uncertainties. The uncertainty of the molar enthalpy of sublimation is the standard uncertainty with a confidence level of 0.95 (k = 2), calculated including uncertainties of vapor pressure, uncertainties from the fitting equation, and the uncertainty of temperature adjustment to T = 298.15 K. Detailed information on the methods of calculations was published previously.[S22,29] [b] Saturation temperature ($u(T)$ = 0.1 K). [c] Mass of transferred sample condensed at 243 K. [d] Volume of nitrogen ($u(V)$ = 0.005 dm^3) used to transfer m ($u(m)/m$ = 1.5 %) of the sample. [e] T_{amb} is the temperature of the soap film flowmeter used for measurement of the gas flow. [f] Vapor pressure at temperature T, calculated from the m and the residual vapor pressure at the condensation temperature, calculated by an iteration procedure; p° = 1 Pa. [g] Relative standard uncertainty with confidence level 0.95 (k = 2) for p_{sat} was calculated to be $u(p)/p$ = 5.86 %, see previous publications[S22,29]

Compilation of the HPLC-DAD setup is presented in Table S9 and the parameters which were used in the experiments are compiled in Table S10.

Table S9. HPLC-Setup used for the mass quantification.

HPLC	*Shimadzu Prominence*® with LC-20AD pump module and SPDM20A Diode Array Detector; software *LabSolutions* v5.86
Analytical column	*Phenomenex Kinetex*® (2.6 µm Biphenyl, 100 Å, 150 × 4.6 mm)
Oven temperature	40 °C

Table S10. Compilation of HPLC parameters used for transpiration experiment of H_2TNO.

Substance	H_2TNO
Standard	DNAN
Mobile Phase	50 % MeCN, 50 % H_2O
Flow	0.65 mL/min
Injection Volume	1 µL
Analyte wavelength (1)	206 nm
Retention time 1	1.783 min
Standard wavelength (2)	295 nm
Retention time 2	5.660 min

2.7.5 NMR Spectroscopy of 1, 13 and 14

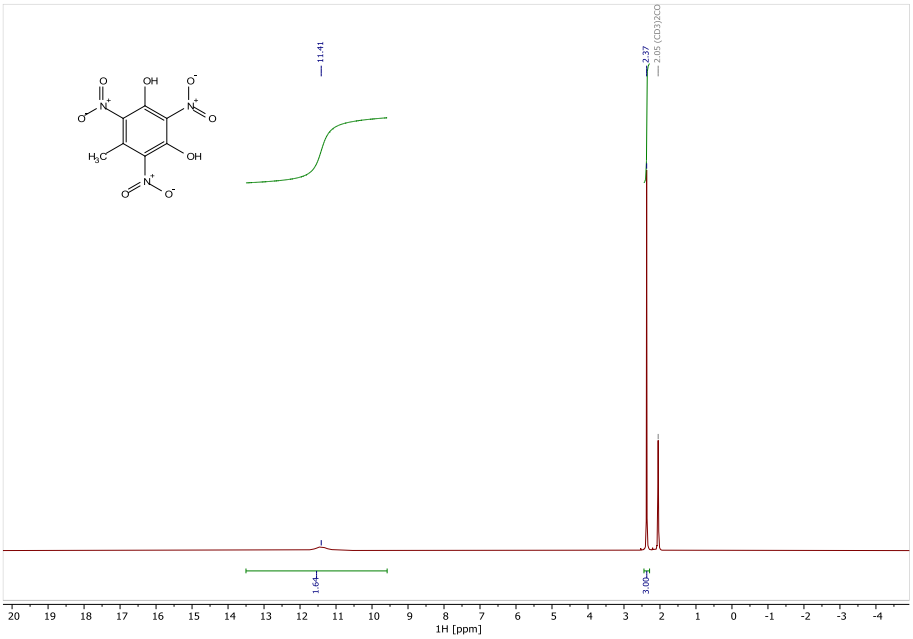

Figure S7. ^{1}H NMR spectrum (400 MHz, Acetone-d_6) of H_2TNO.

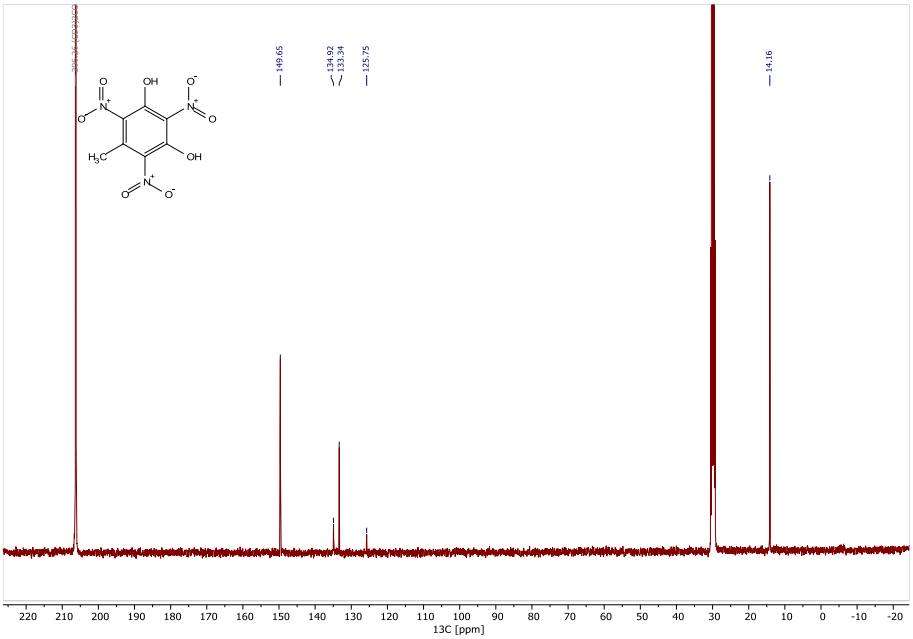

Figure S8. ^{13}C NMR spectrum (100 MHz, Acetone-d_6) of H_2TNO.

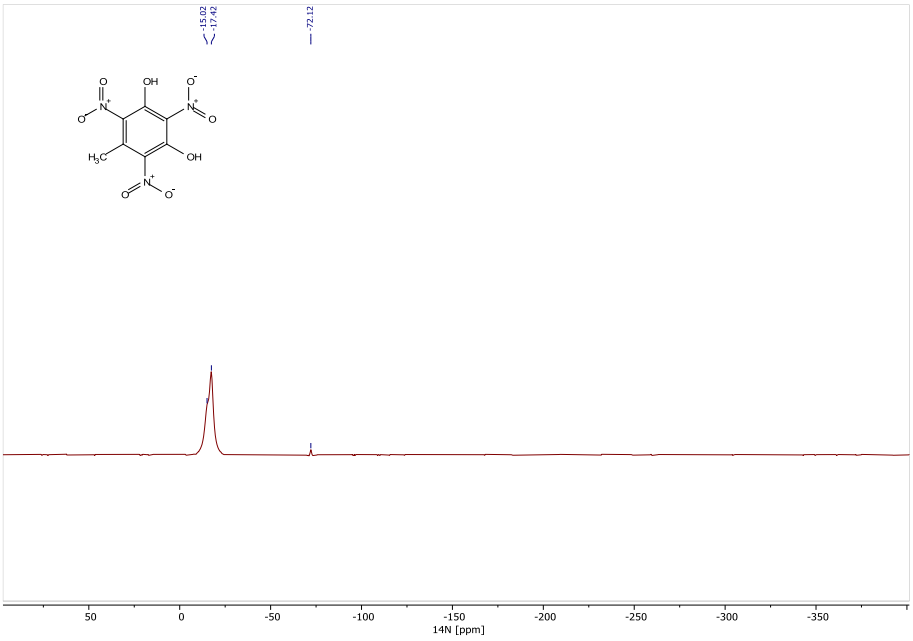

Figure S9. ^{14}N NMR spectrum (29 MHz, Acetone-d_6) of H_2TNO.

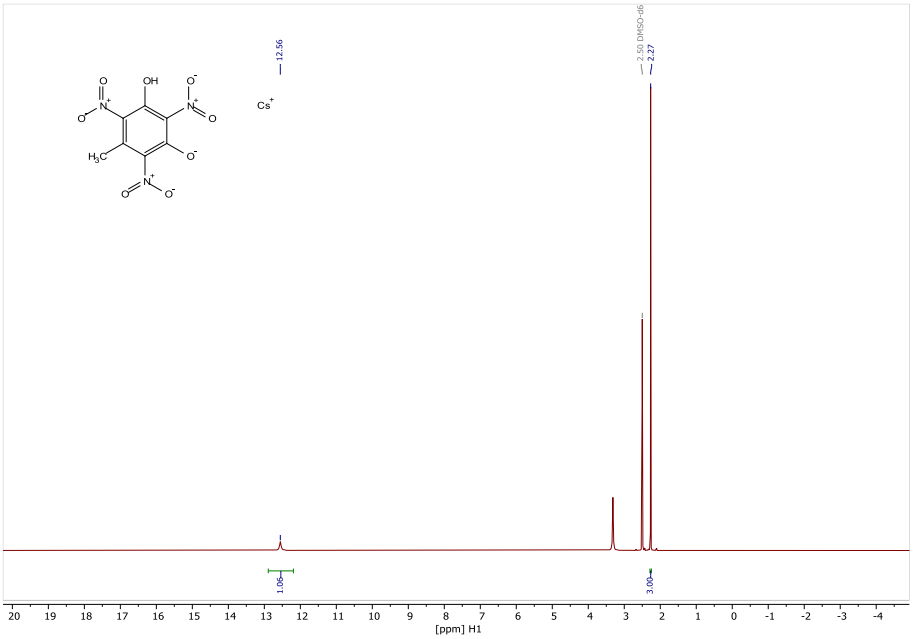

Figure S10. ^{1}H NMR spectrum (400 MHz, DMSO-d_6) of CsHTNO.

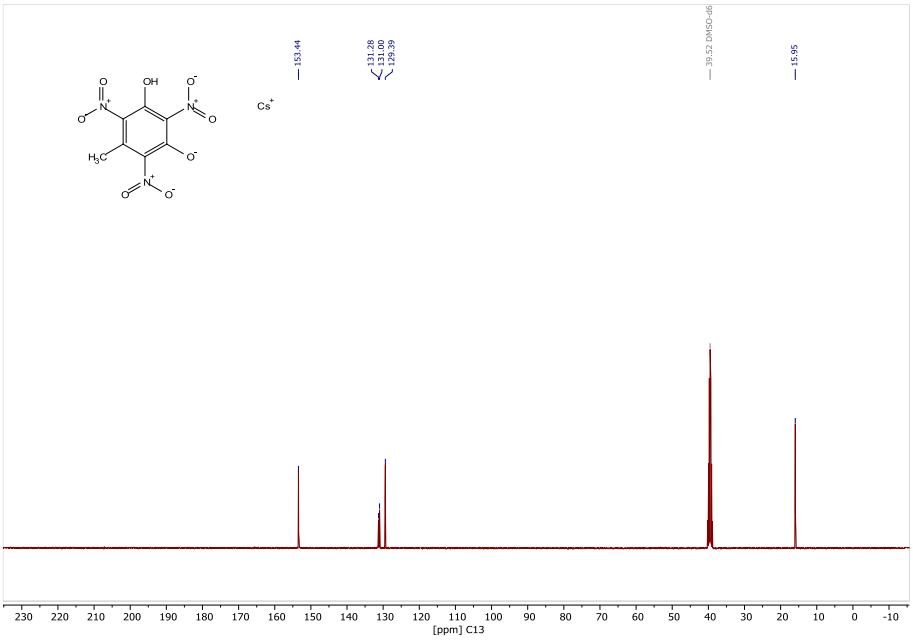

Figure S11. ^{13}C NMR spectrum (100 MHz, DMSO-d_6) of CsHTNO.

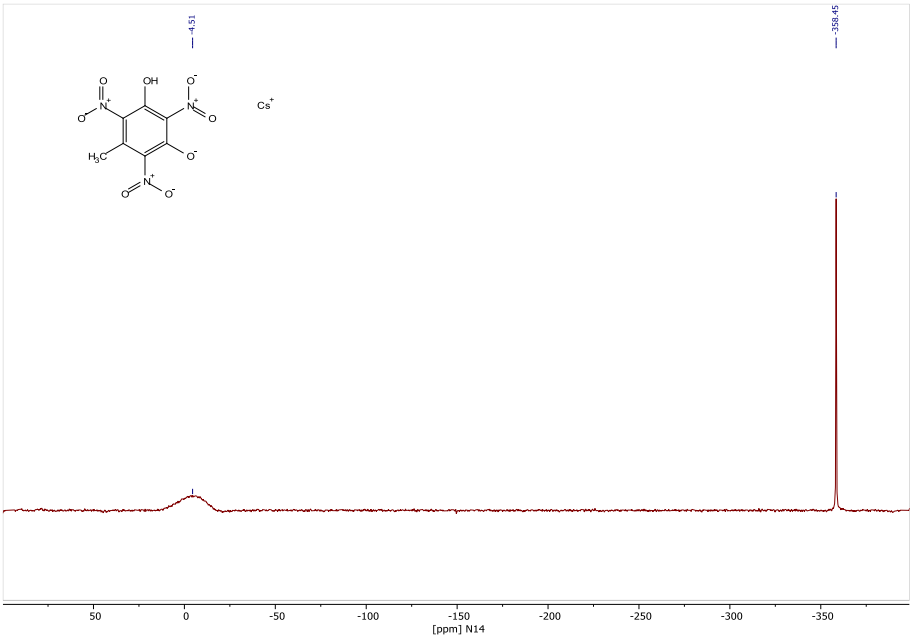

Figure S12. ^{14}N NMR spectrum (29 MHz, DMSO-d_6) of CsHTNO.

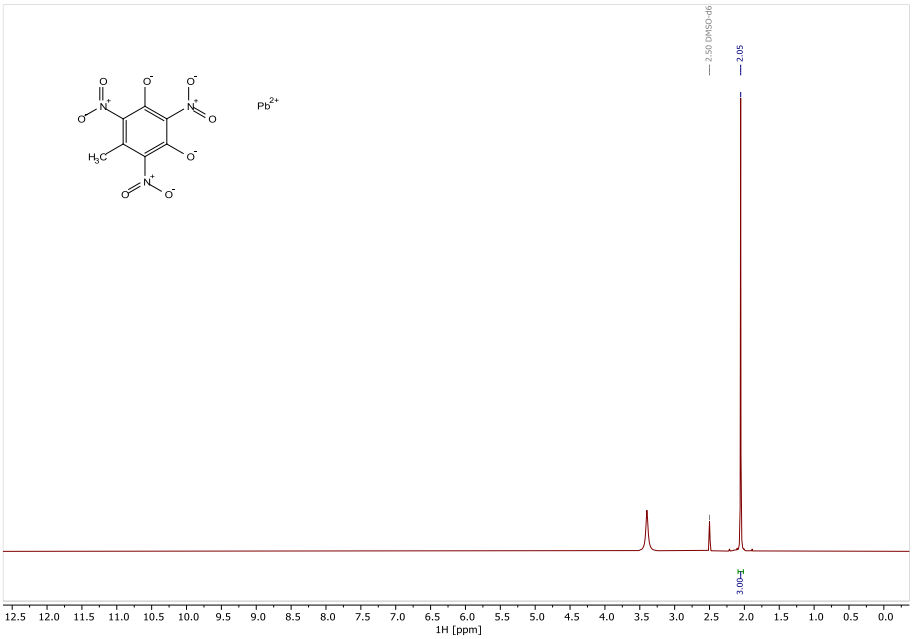

Figure S13. ^{1}H NMR spectrum (400 MHz, DMSO-d_6) of PbTNO.

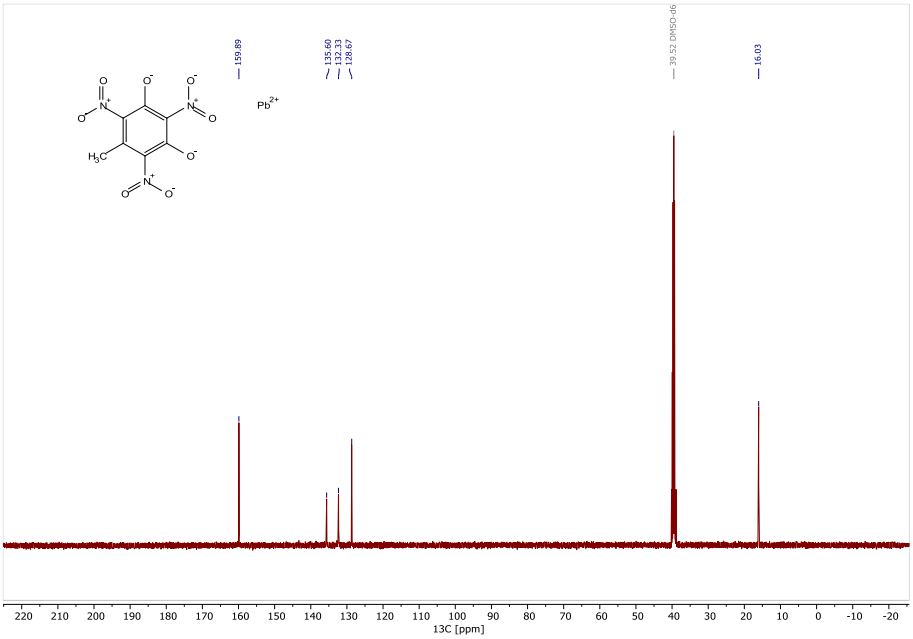

Figure S14. ^{13}C NMR spectrum (100 MHz, DMSO-d_6) of PbTNO.

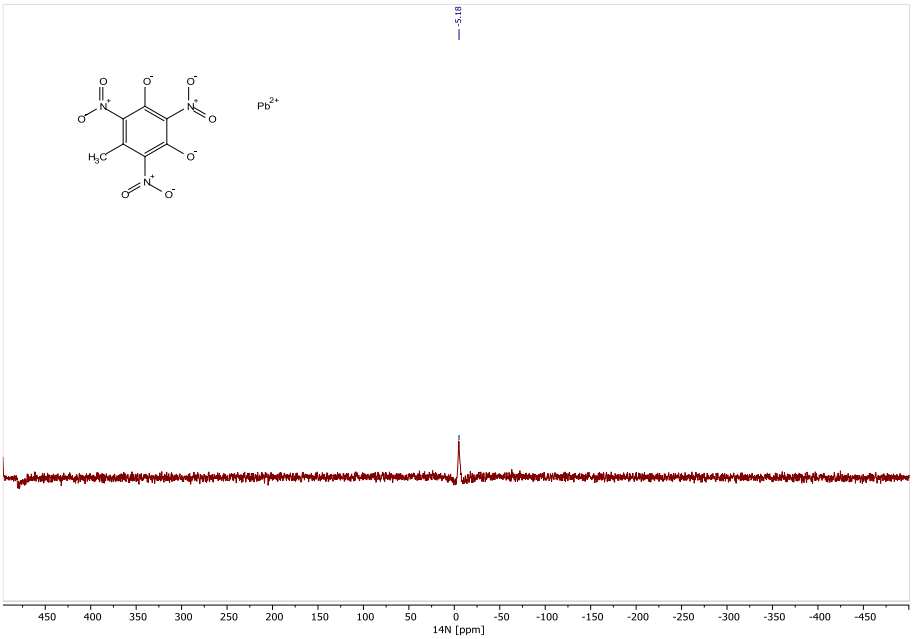

Figure S15. ^{14}N NMR spectrum (29 MHz, DMSO-d_6) of PbTNO.

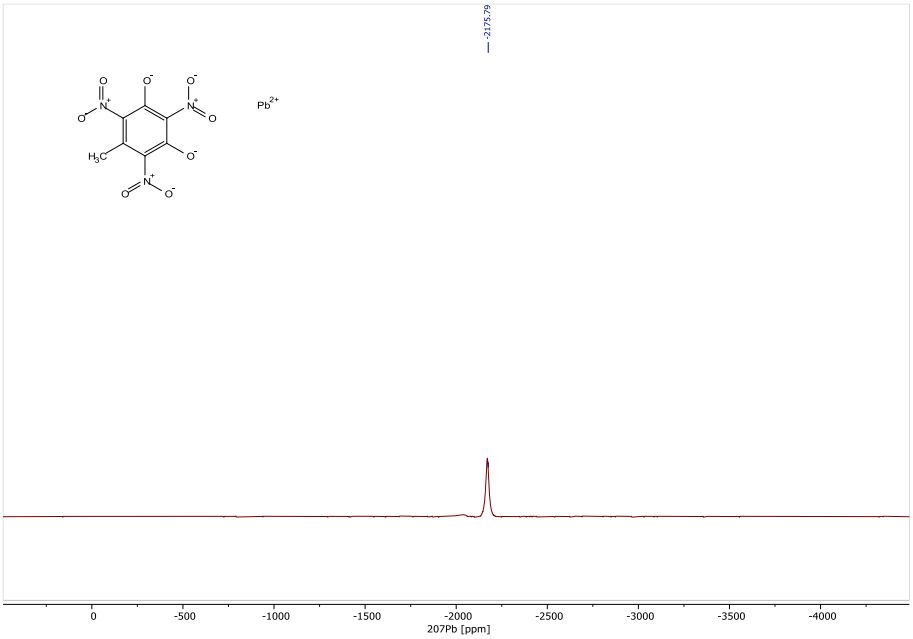

Figure S16. ^{207}Pb NMR spectrum (84 MHz, DMSO-d_6) of PbTNO.

2.7.6 IR Spectroscopy of 1–18

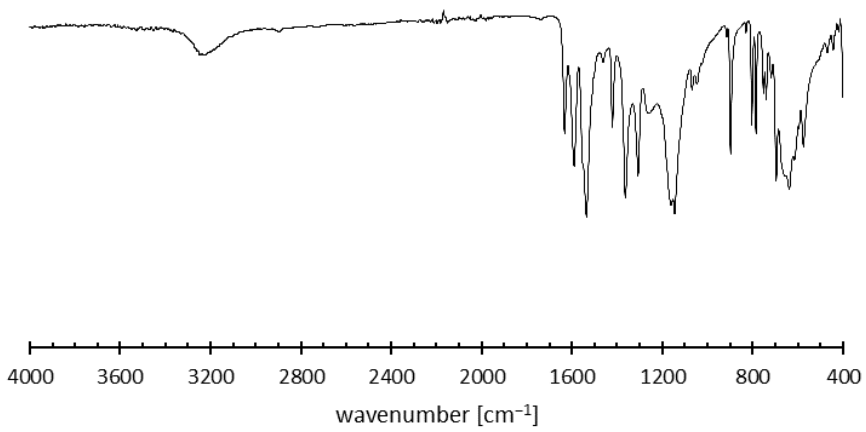

Figure S17. IR spectrum of H_2TNO

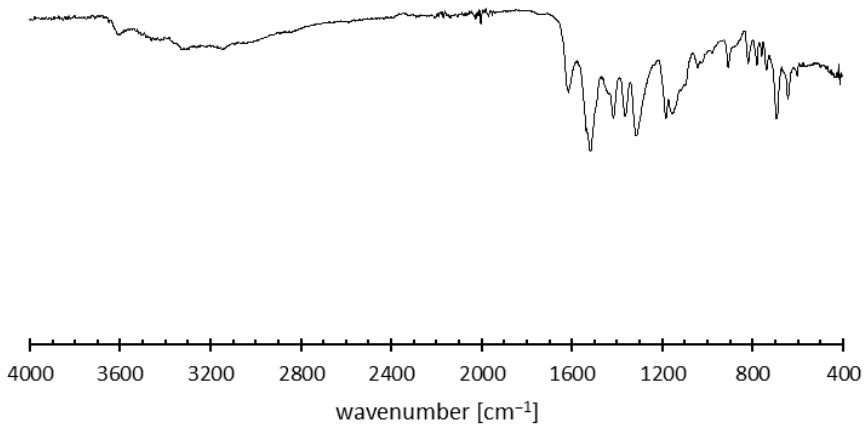

Figure S18. IR spectrum of $[Cu(1\text{-}AT)_2(HTNO)_2]$.

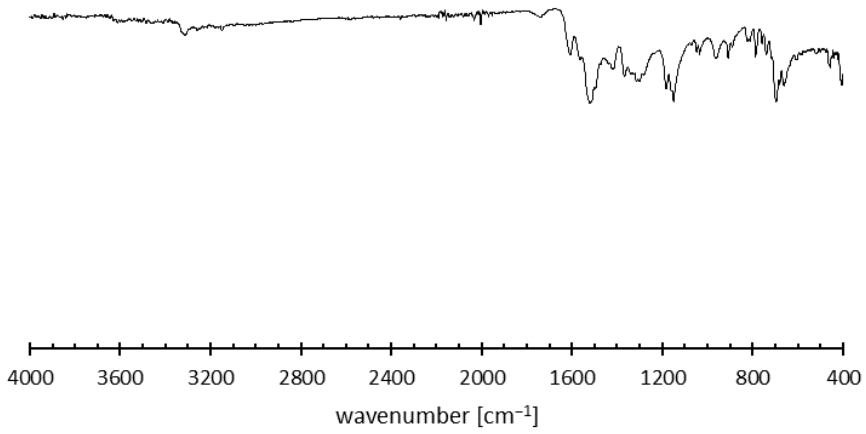

Figure S19. IR spectrum of $[Cu(2\text{-}AT)_2(HTNO)_2]$.

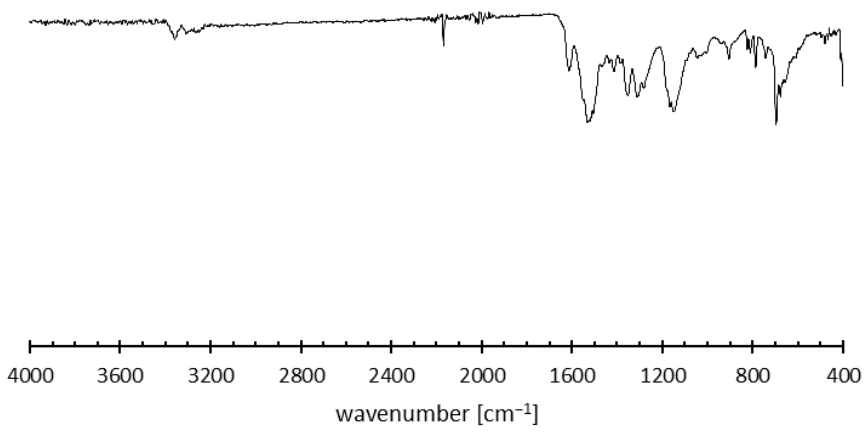

Figure S20. IR spectrum of $[Cu(1\text{-}AMT)_2(HTNO)_2]$.

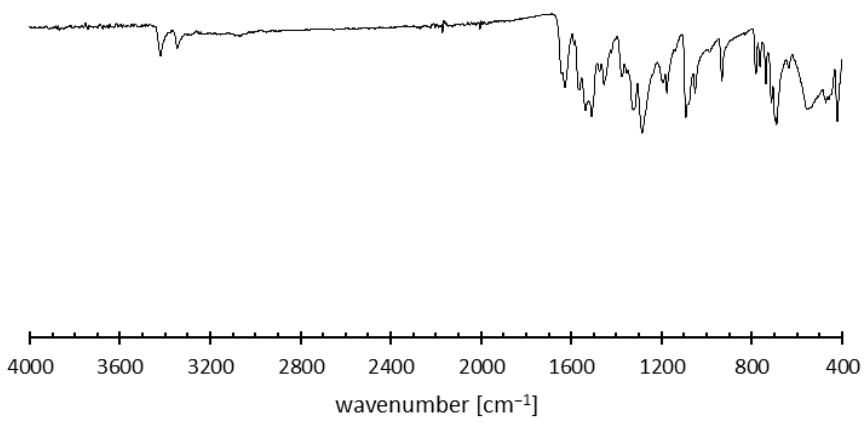

Figure S21. IR spectrum of $[Cu(HTNO)_2(1\text{-}MAT)_2]$.

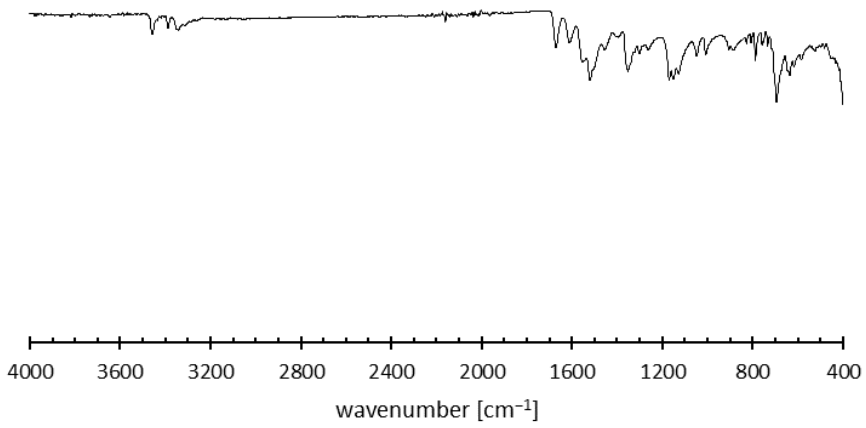

Figure S22. IR spectrum of $[Cu(1,5\text{-}DAT)_2(HTNO)_2]$.

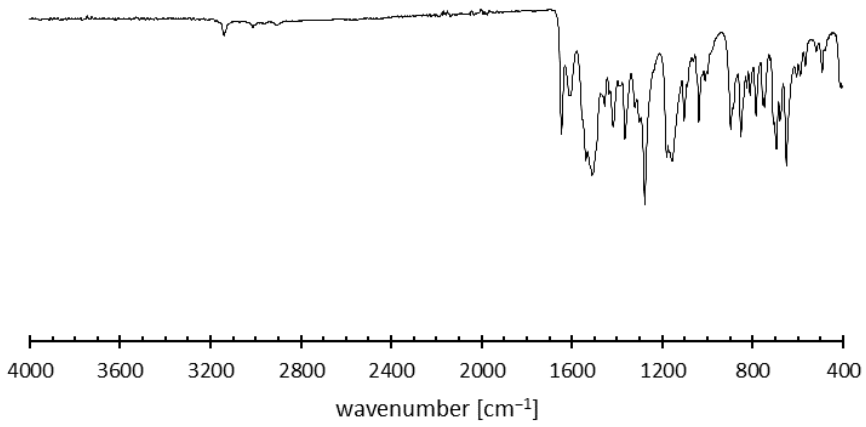

Figure S23. IR spectrum of $[Cu(HTNO)_2(1\text{-}NET)_2]$.

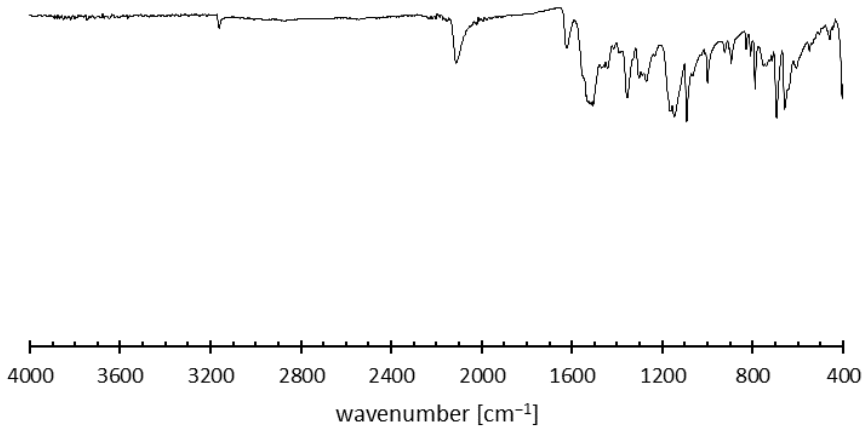

Figure S24. IR spectrum of $[Cu(1\text{-}AET)_2(HTNO)_2]$.

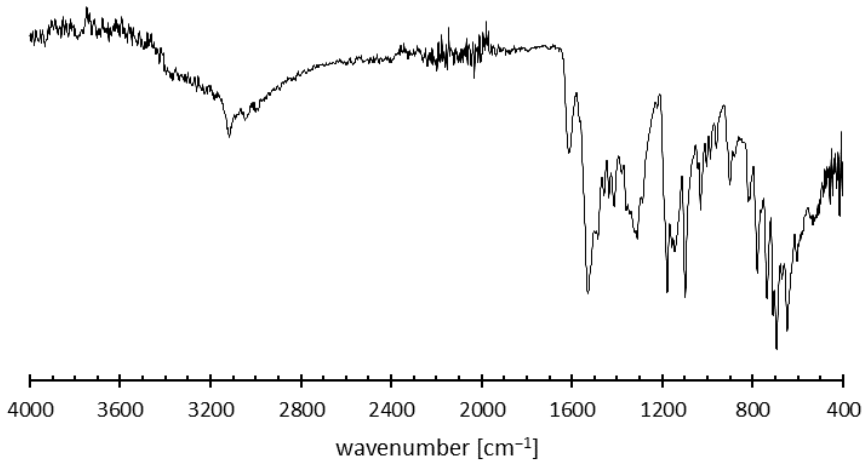

Figure S25. IR spectrum of $[Cu(1,1\text{-dtm})_2(H_2O)_4](HTNO)_2$.

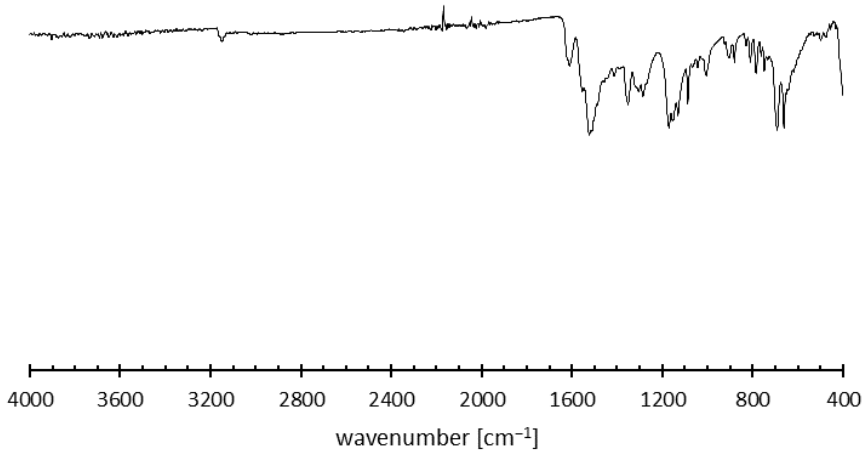

Figure S26. IR spectrum of $[Cu(1,1\text{-dte})_2(HTNO)_2] \cdot H_2O$.

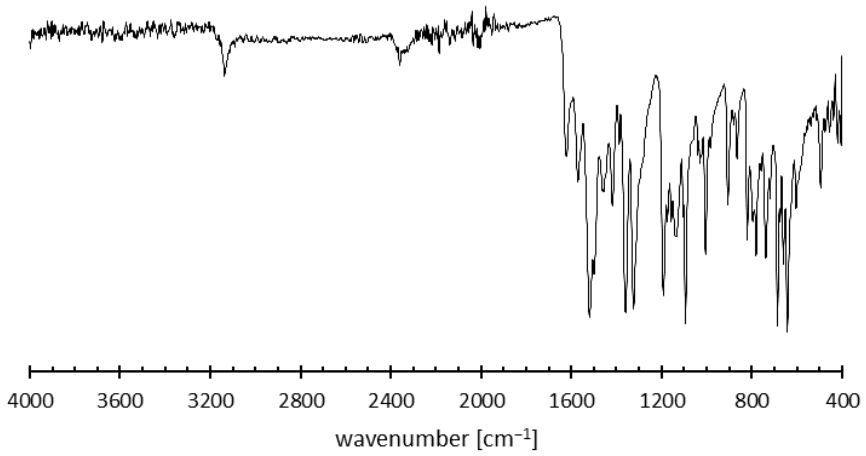

Figure S27. IR spectrum of $[Cu(1,1\text{-dtp})_2(HTNO)_2]$.

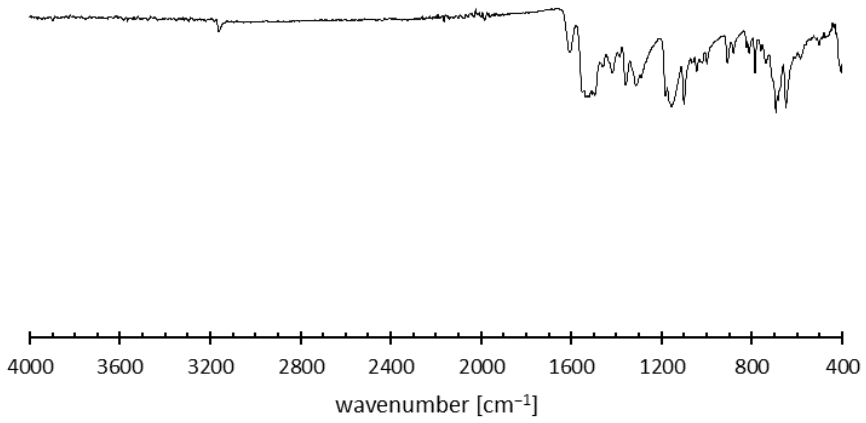

Figure S28. IR spectrum of $[Zn(HTNO)_2(1\text{-}MTZ)_2]$.

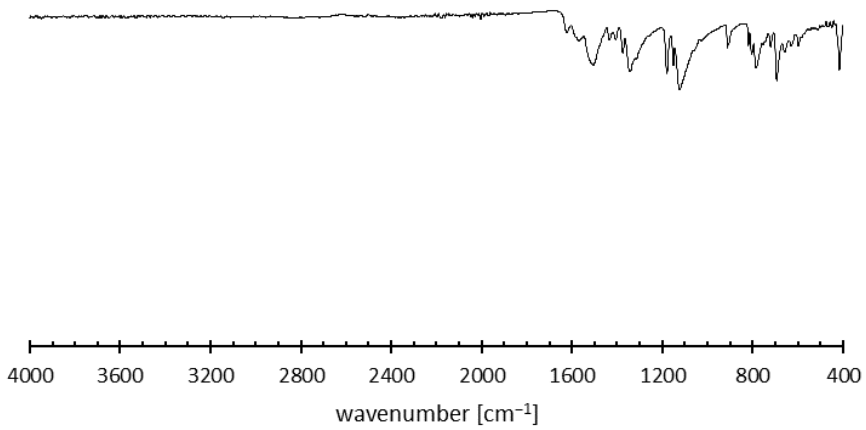

Figure S29. IR spectrum of CsHTNO.

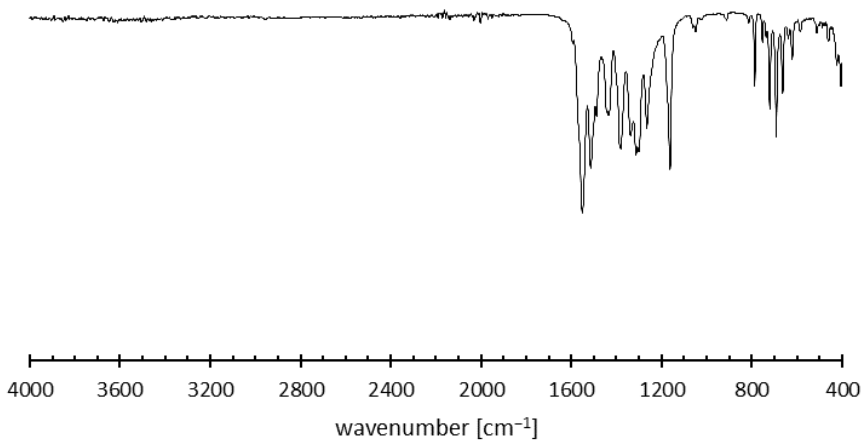

Figure S30. IR spectrum of PbTNO.

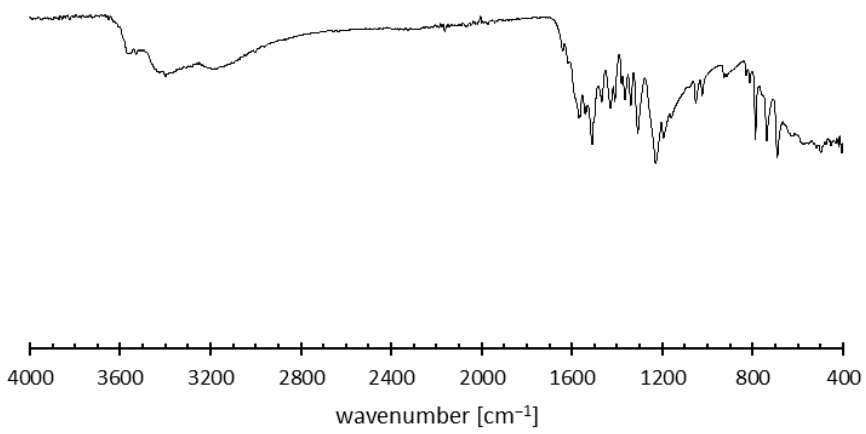

Figure S31. IR spectrum of $[Zn(H_2O)_3(TNO)] \cdot H_2O$.

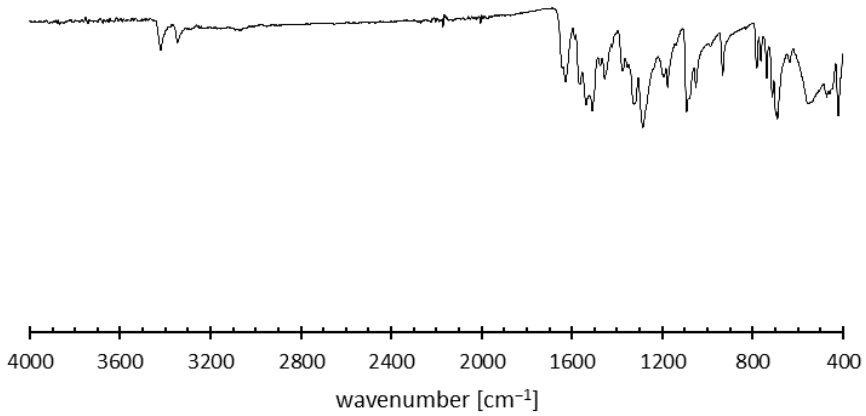

Figure S32. IR spectrum of $[Cu(HTNR)_2(1\text{-}MAT)_2]$.

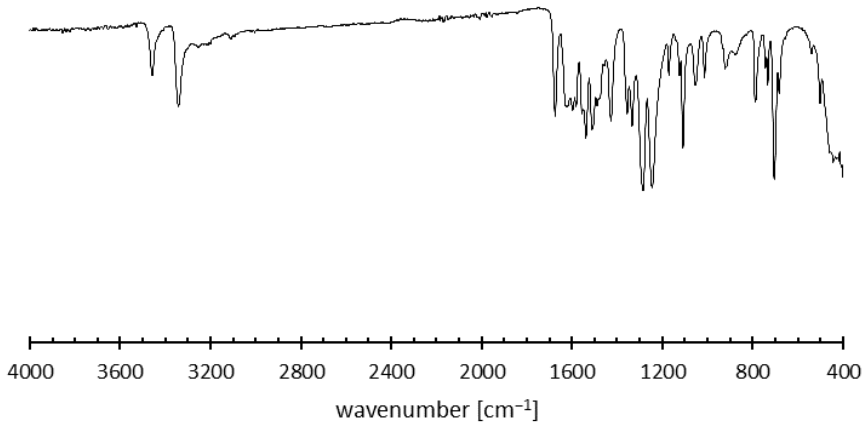

Figure S33. IR spectrum of $[Cu(1,5\text{-}DAT)_2(TNR)]$.

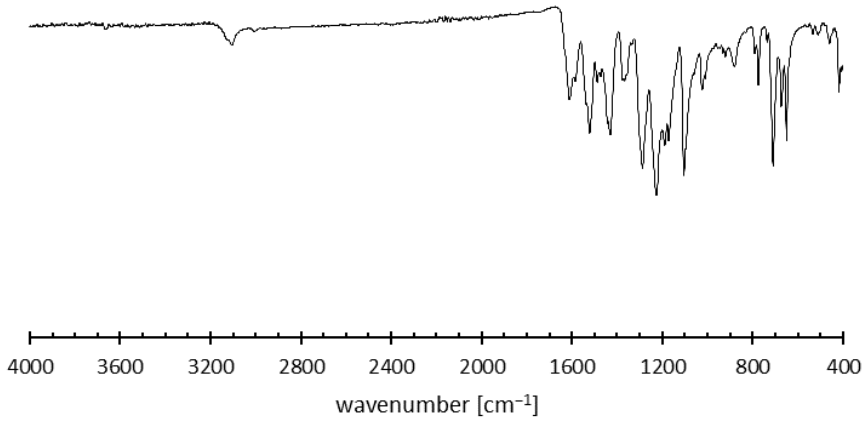

Figure S34. IR spectrum of [Cu(1,1-dte)(TNR)] · H_2O.

2.7.7 Thermal Analysis

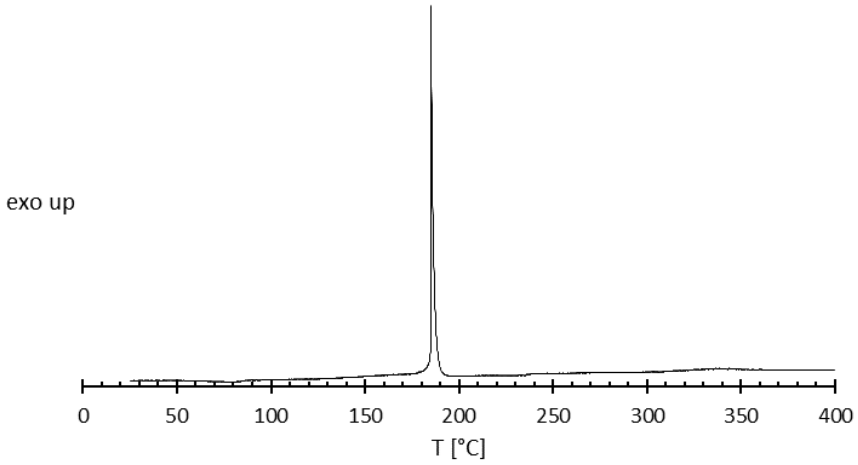

Figure S35. DTA plot of $[Cu(1\text{-}AT)_2(HTNO)_2]$ in the range of 25–400 °C.

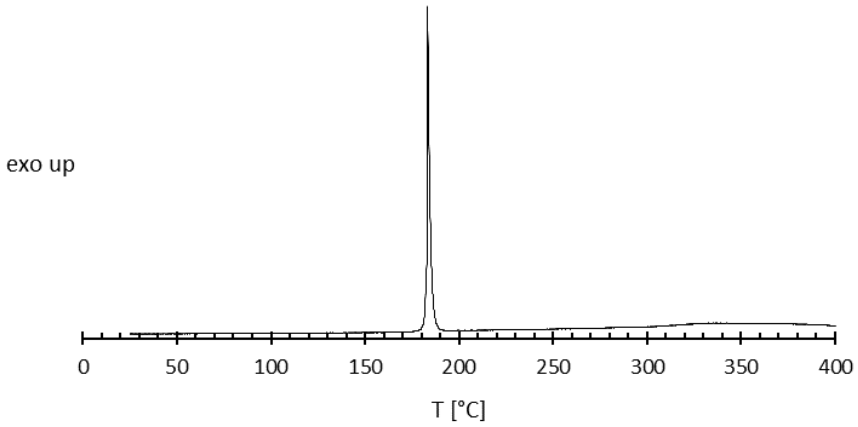

Figure S36. DTA plot of $[Cu(2\text{-}AT)_2(HTNO)_2]$ in the range of 25–400 °C.

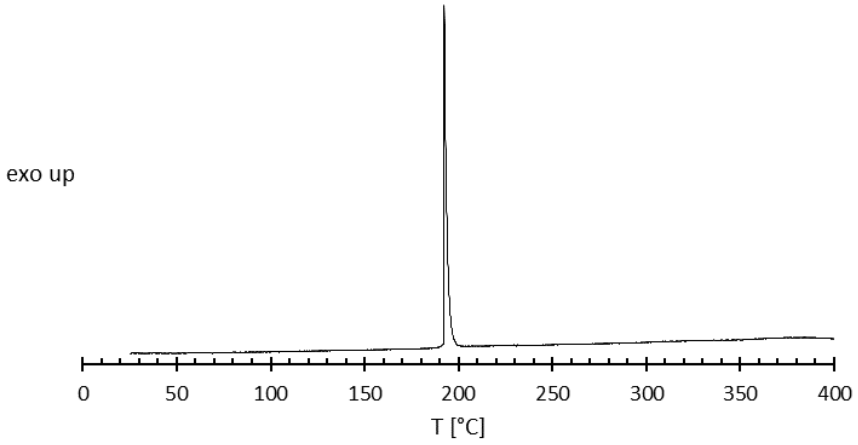

Figure S37. DTA plot of $[Cu(1\text{-}AMT)_2(HTNO)_2]$ in the range of 25–400 °C.

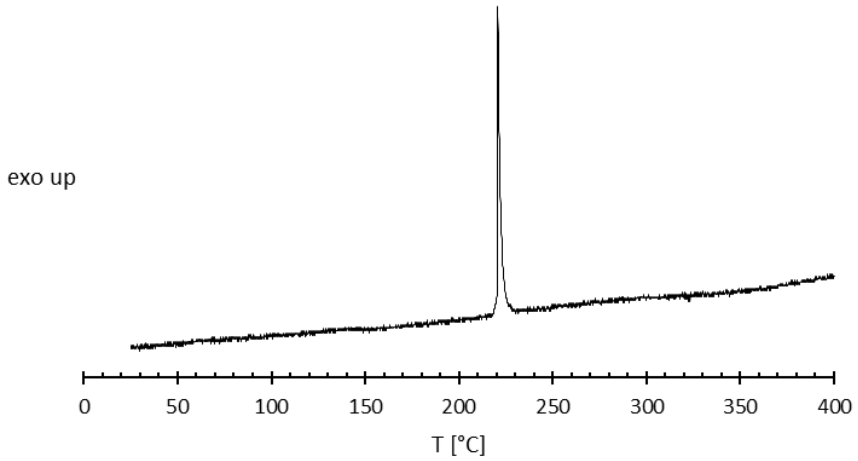

Figure S38. DTA plot of $[Cu(HTNO)_2(1\text{-}MAT)_2]$ in the range of 25–400 °C.

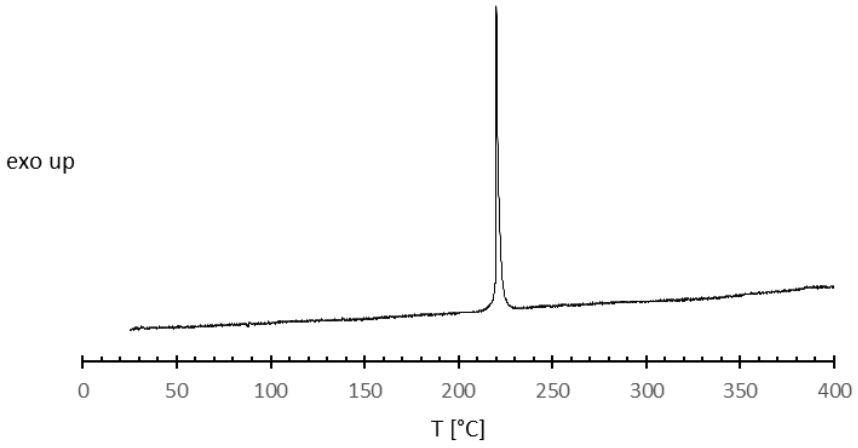

Figure S39. DTA plot of $[Cu(1,5\text{-}DAT)_2(HTNO)_2]$ in the range of 25–400 °C.

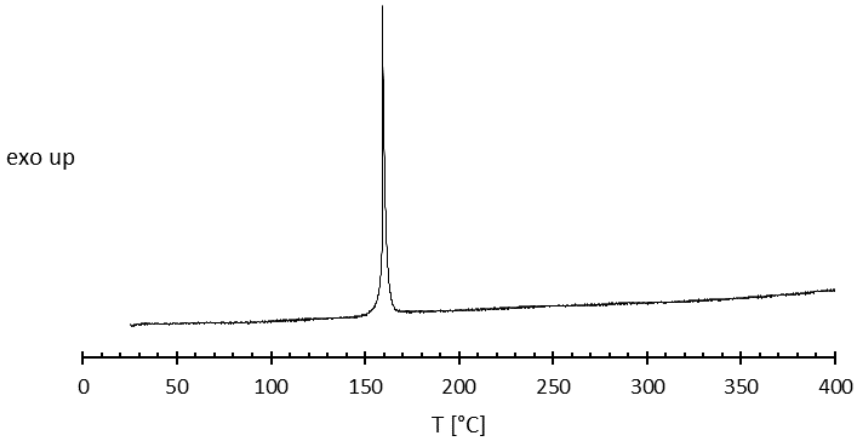

Figure S40. DTA plot of $[Cu(HTNO)_2(1\text{-}NET)_2]$ in the range of 25–400 °C.

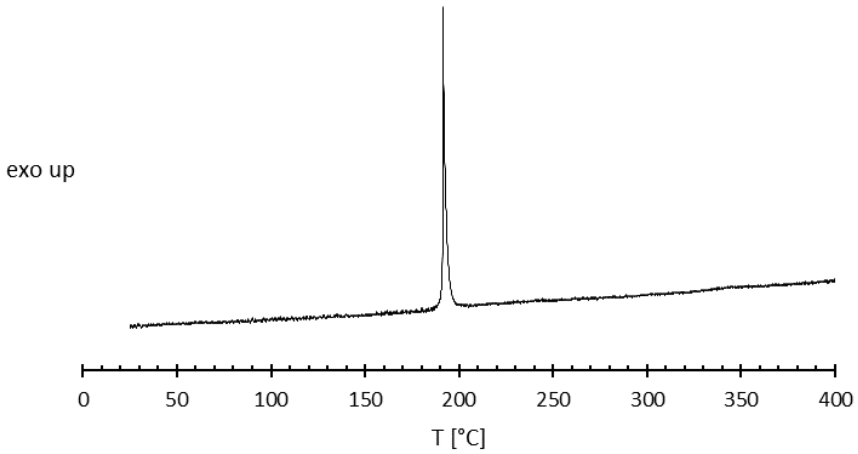

Figure S41. DTA plot of $[Cu(1\text{-}AET)_2(HTNO)_2]$ in the range of 25–400 °C.

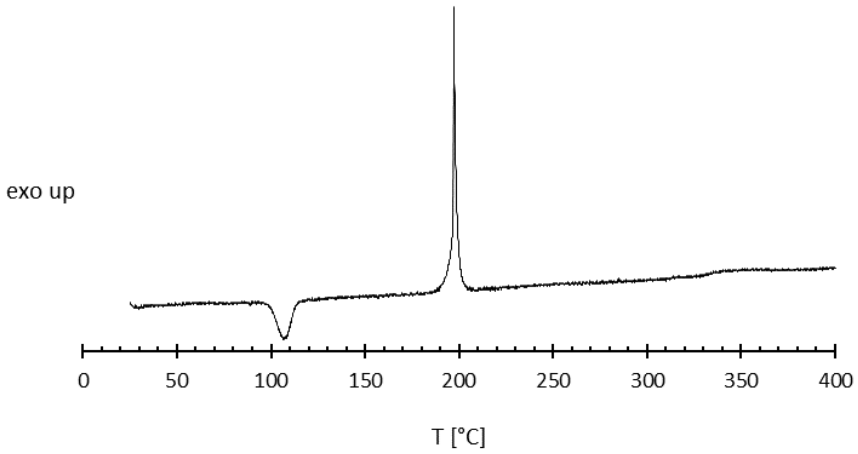

Figure S42. DTA plot of $[Cu(1,1\text{-}dtm)_2(H_2O)_4](HTNO)_2$ in the range of 25–400 °C.

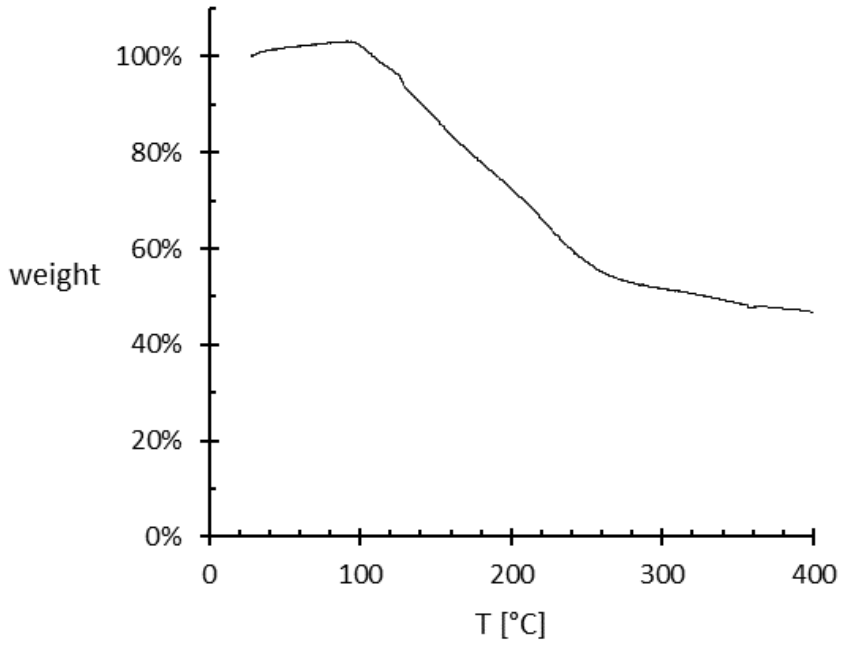

Figure S43. TGA plot of compound **9** in the range of 30–400 °C.

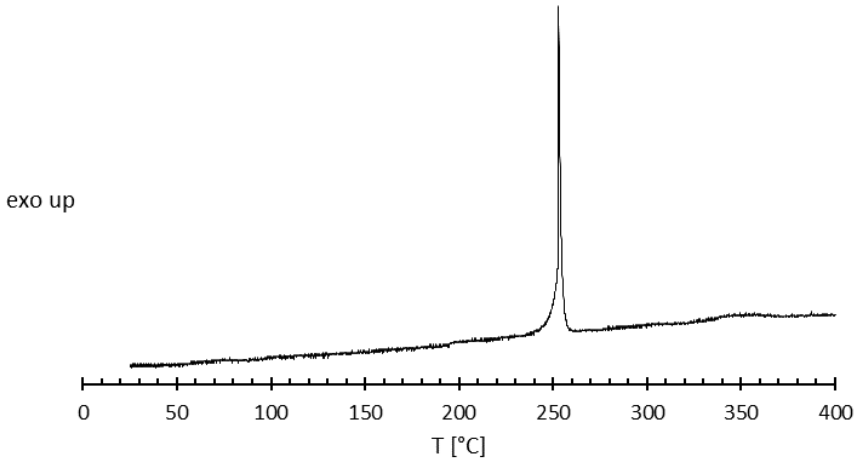

Figure S44. DTA plot of $[Cu(1,1\text{-dte})_2(HTNO)_2] \cdot H_2O$ in the range of 25–400 °C.

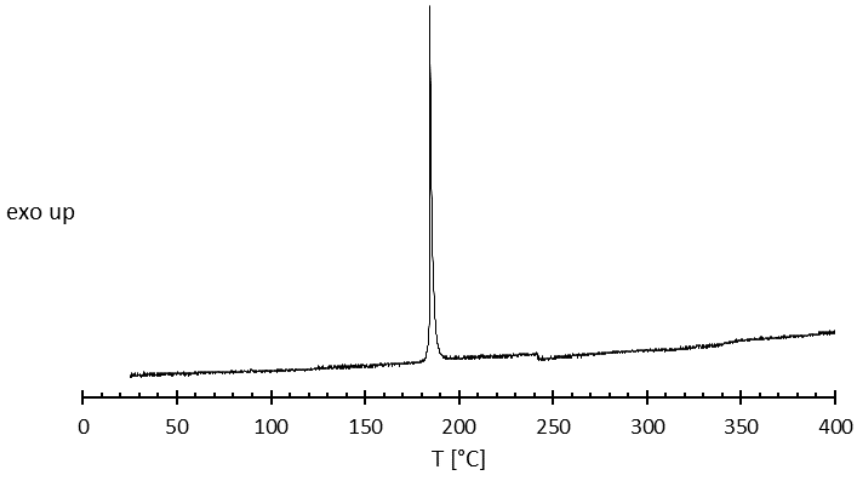

Figure S45. DTA plot of $[Cu(1,1\text{-dtp})_2(HTNO)_2]$ in the range of 25–400 °C.

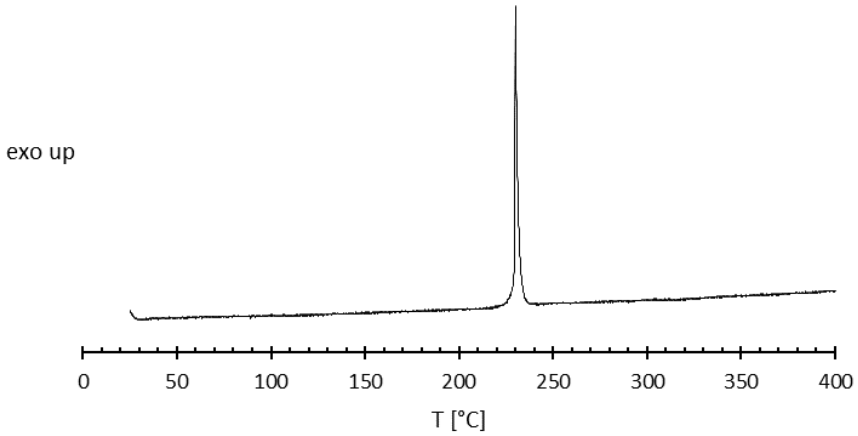

Figure S46. DTA plot of $[Zn(HTNO)_2(1\text{-MTZ})_2]$ in the range of 25–400 °C.

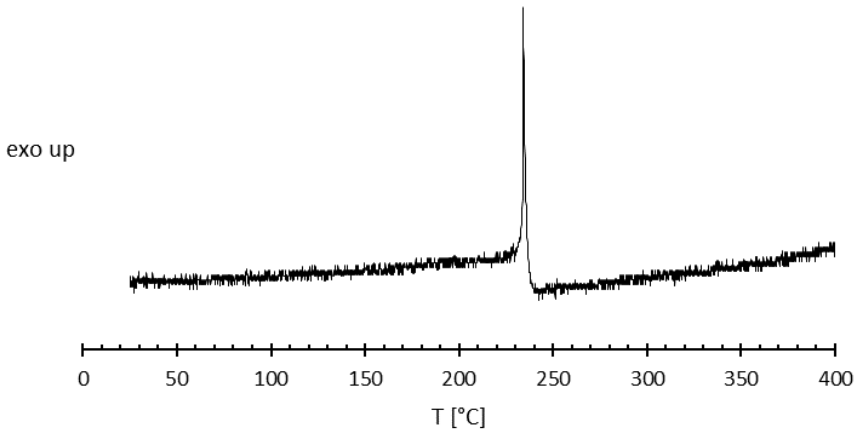

Figure S47. DTA plot of CsHTNO in the range of 25–400 °C.

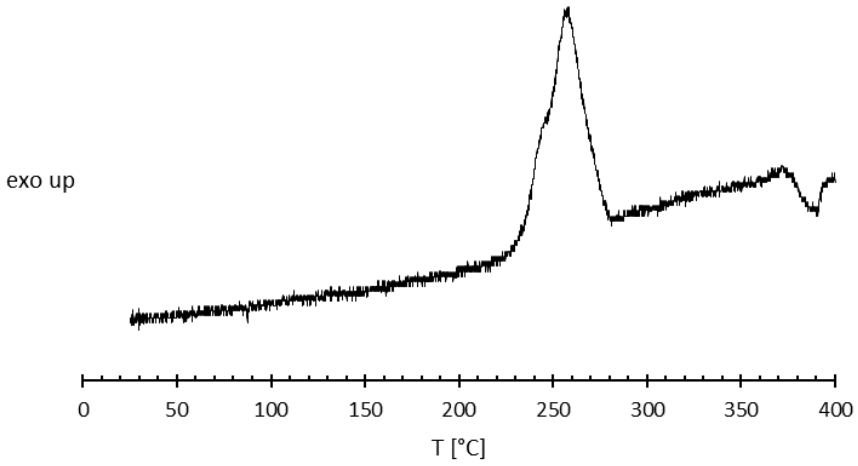

Figure S48. DTA plot of PbTNO in the range of 25–400 °C.

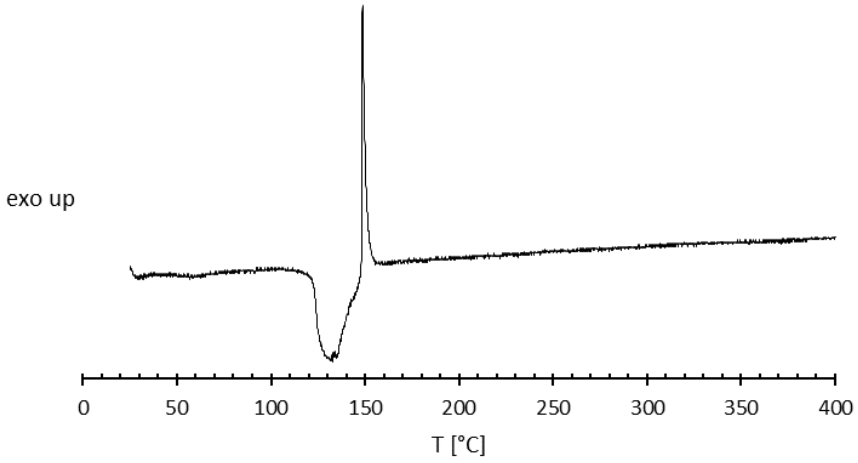

Figure S49. DTA plot of $[Zn(H_2O)_3(TNO)] \cdot H_2O$ in the range of 25–400 °C.

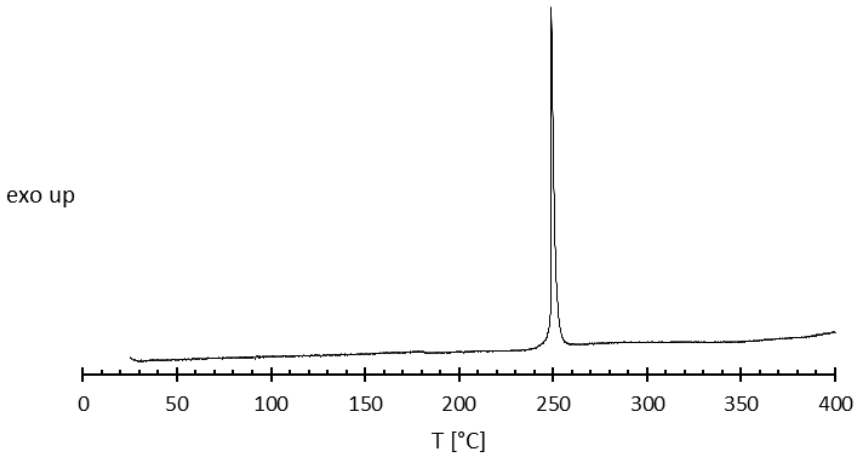

Figure S50. DTA plot of $[Cu(HTNR)_2(1\text{-}MAT)_2]$ in the range of 25–400 °C.

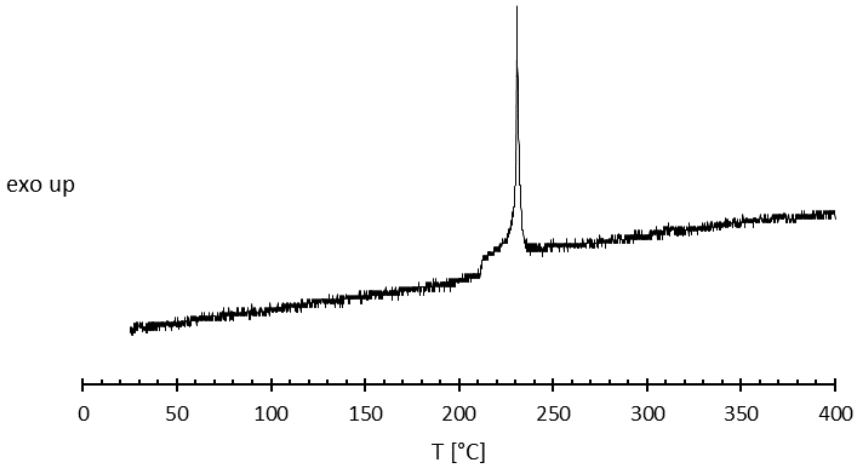

Figure S51. DTA plot of [Cu(1,5-DAT)$_2$(TNR)] in the range of 25–400 °C.

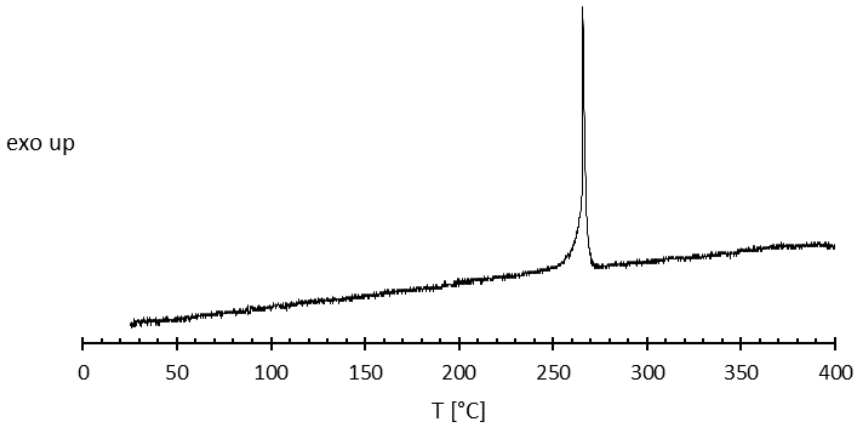

Figure S52. DTA plot of [Cu(1,1-dte)(TNR)] · H_2O in the range of 25–400 °C.

2.7.8 Hot Plate and Hot Needle Testing

Figure S53. Reaction of $[Cu(1\text{-}AT)_2(HTNO)_2]$ during hot plate (left) and hot needle test (right).

Figure S54. Deflagration of $[Cu(2\text{-}AT)_2(HTNO)_2]$ during hot plate (left) and hot needle test (right).

Figure S55. Reaction of $[Cu(1\text{-}AMT)_2(HTNO)_2]$ during hot plate (left) and hot needle test (right).

Figure S56. Reaction of $[Cu(HTNO)_2(1\text{-}MAT)_2]$ during hot plate (left) and hot needle test (right).

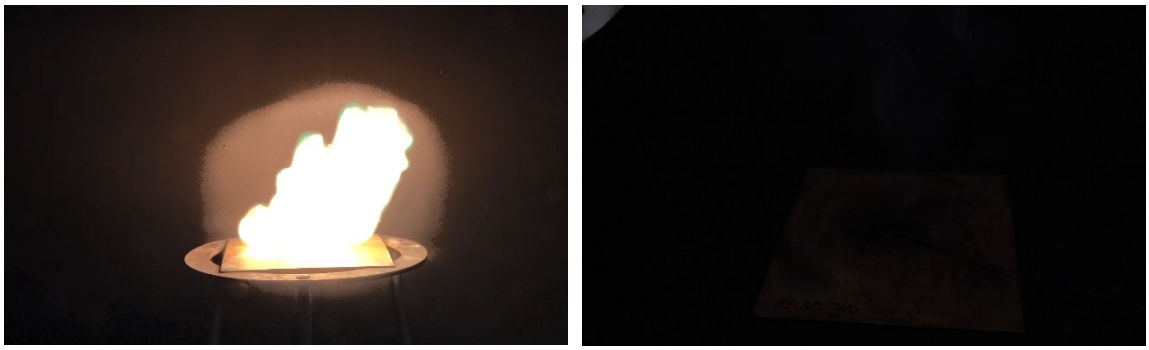

Figure S57. Reaction of $[Cu(1,5\text{-}DAT)_2(HTNO)_2]$ during hot plate (left) and hot needle test (right).

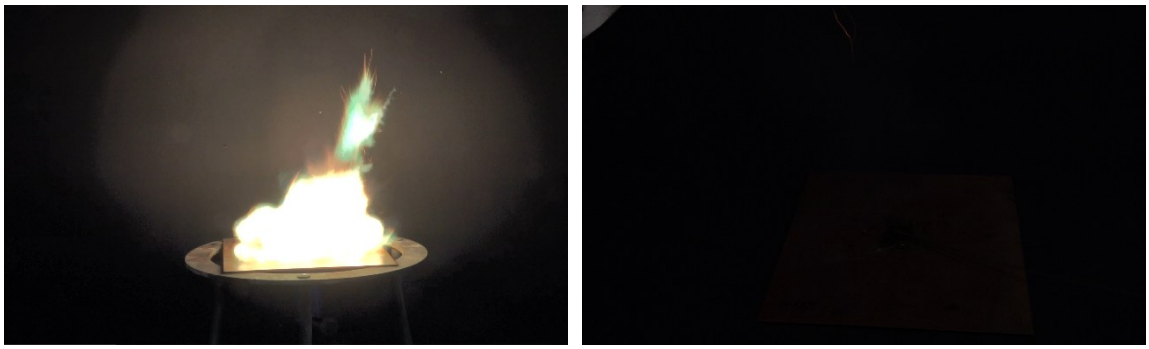

Figure S58. Reaction of $[Cu(HTNO)_2(1\text{-}NET)_2]$ during hot plate (left) and hot needle test (right).

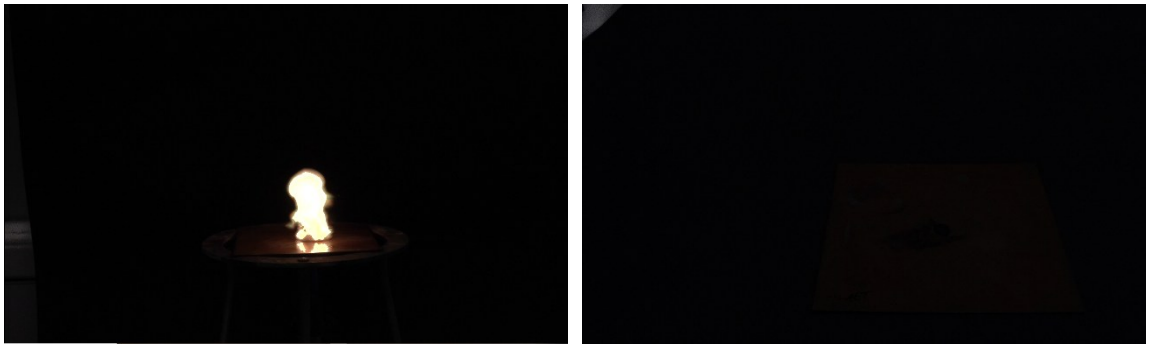

Figure S59. Reaction of $[Cu(1\text{-}AET)_2(HTNO)_2]$ during hot plate (left) and hot needle test (right).

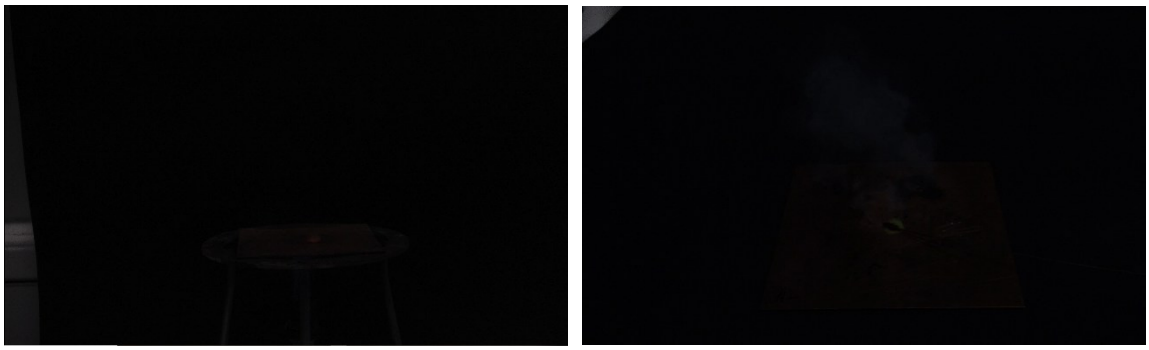

Figure S60. Decomposition of $[Cu(1,1\text{-}dtm)_2(H_2O)_4](HTNO)_2$ during hot plate (left) and hot needle test (right).

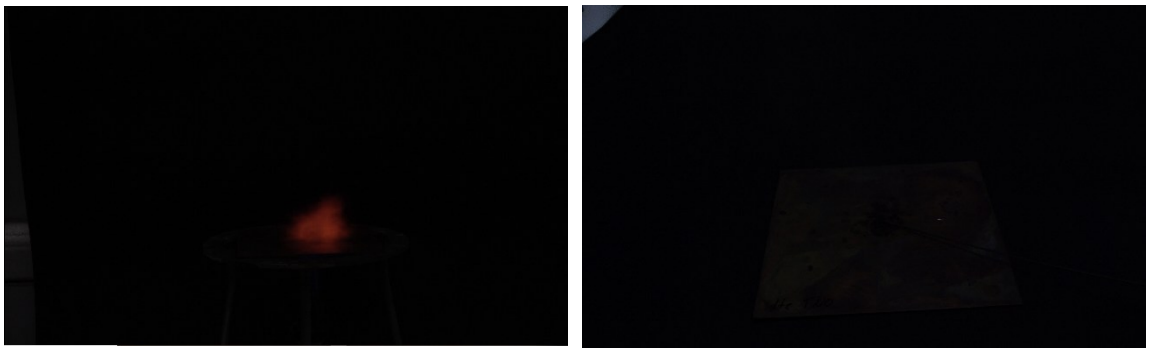

Figure S61. Reaction of $[Cu(1,1\text{-}dte)_2(HTNO)_2] \cdot H_2O$ during hot plate (left) and hot needle test (right).

Figure S62. Reaction of $[Cu(1,1\text{-dtp})_2(HTNO)_2]$ during hot plate (left) and hot needle test (right).

Figure S63. Reaction of $[Zn(HTNO)_2(1\text{-MTZ})_2]$ during hot plate (left) and hot needle test (right).

Figure S64. Reaction of CsHTNO during hot plate (left) and hot needle test (right).

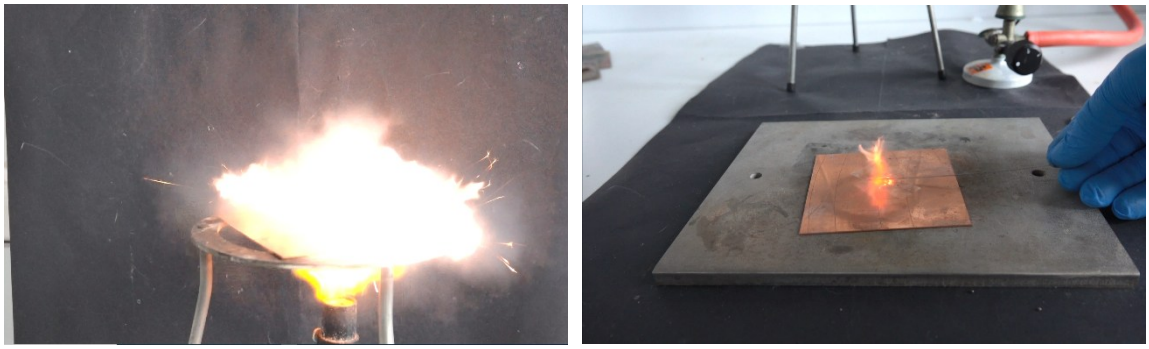

Figure S65. Detonation of PbTNO during hot plate (left) and hot needle test (right).

Figure S66. Deflagration of [Cu(HTNR)$_2$(1-MAT)$_2$] during hot plate (left) and hot needle test (right).

Figure S67. Reaction of [Cu(1,5-DAT)$_2$(TNR)] during hot plate (left) and hot needle test (right).

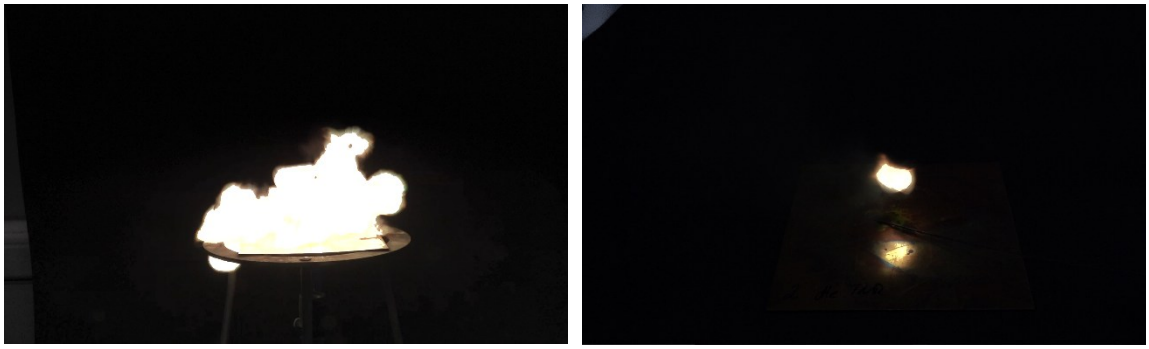

Figure S68. Deflagration of [Cu(1,1-dte)(TNR)] · H_2O during hot plate (left) and hot needle test (right).

2.7.9 General Methods

All chemicals and solvents were employed as received (Sigma-Aldrich, Fluka, Acros, ABCR). ^{1}H, $^{13}C\{^{1}H\}$, ^{14}N, ^{209}Pb spectra were recorded at ambient temperature using a JEOL Bruker 27400, Eclipse 270, JEOL EX 400 or a JEOL Eclipse 400 instrument. The chemical shifts quoted in ppm in the text refer to typical standards such as tetramethylsilane (^{1}H, ^{13}C) nitromethane (^{14}N,^{15}N) in DMSO-d_6 or acetone-d_6 as the solvent. Endothermic and exothermic events of the described compounds, which indicate melting, loss of crystal water or decomposition, are given as the extrapolated onset temperatures. The samples were measured in a range of 25–400 °C at a heating rate of 5 °C min^{-1} through differential thermal analysis (DTA) with an OZM Research DTA 552-Ex instrument. Infrared spectra were measured with pure samples on a Perkin-Elmer BXII FT-IR system with a Smith DuraSampler IR II diamond ATR. Determination of the carbon, hydrogen, and nitrogen contents was carried out by combustion analysis using an Elementar Vario El (nitrogen values determined are often lower than the calculated ones' due to their explosive behavior). Impact sensitivity tests were carried out according to STANAG 4489[S30] with a modified instruction[S31] using a BAM (Bundesanstalt für Materialforschung) drophammer.[S32] Friction sensitivity tests were carried out according to STANAG 4487[S35] with a modified instruction[S36] using the BAM friction tester. [S32,S33] The classification of the tested compounds results from the "UN Recommendations on the Transport of Dangerous Goods". [S37,S38] Additionally, all compounds were tested upon the sensitivity toward electrical discharge using the OZM Electric Spark XSpark10 device. [S33] Energetic properties have been calculated with the EXPLO5 6.05.04 computer code[S39] using the, to RT converted, X-ray density and calculated solid state heats of formation. These were computed by the atomization method as described in recently published papers. Electronic

enthalpies were calculated with the Gaussian09 software[S13] suite using the CBS-4M method.

2.7.10 Experimental Section

Caution! All investigated compounds are energetic materials and some of them show sensitivities towards various stimuli (e.g. elevated temperatures, impact, friction or electronic discharge). Although no hazards occurred, proper security precautions (safety glasses, face shield, earthed equipment and shoes, leather jacket, Kevlar sleeves, and earplugs) have to be worn while synthesizing and handling the described compounds.

Trinitro-orcinol (1)

Trinitro-orcinol (H_2TNO) was produced according to a modified literature procedure. [S40] Orcinol (1.24 g, 10.0 mmol) was added to conc. sulfuric acid (75 mL) at 0 °C. A precooled mixture of conc. sulfuric acid (8 mL) and conc. nitric acid (4 mL) was dropwise added. Another 3 mL of conc. nitric acid was cooled to 0 °C and added dropwise. After the addition was completed, the mixture was allowed to reach room temperature within 1 h. The resulting orange suspension was quenched on ice water (200 mL), filtered off and washed with water. A yellow solid was obtained which was dried at 120 °C to yield H_2TNO (2.23 g, 8.62 mmol, 86 %) in a purity of 99.3 % according to ^{1}H qNMR.

^{1}H NMR (d_6-Acetone, 25 °C) δ 11.41 (br, 2H, OH), 2.37 (s, CH_3) ppm. **^{13}C NMR** (d_6-Acetone, 25 °C) δ 149.7, 134.9, 133.3, 125.8, 14.2 ppm. **^{14}N NMR** (d_6-Acetone, 25 °C) δ −15, −17, −72 ppm. **DTA** (5 °C min^{-1}) onset: 172 °C (endothermic). **IR** (ATR, cm^{-1}): $\tilde{\upsilon}$ = 3231 (w), 1632 (m), 1590 (s), 1535 (vs), 1460 (w), 1420 (m), 1363 (vs), 1307 (s), 1260 (m), 1161 (vs), 1145 (vs), 1068 (m), 1047 (m), 1024 (w), 915 (w), 898 (s), 829 (w), 803 (m), 785 (m), 752 (m), 740 (m), 718 (m), 696 (s), 638 (s), 615 (s), 595 (m), 575 (s), 469 (w), 443 (w). **EA** ($C_7H_5N_3O_8$, 259.13 g mol^{-1}) calc.: C 32.45 H 1.94 N 16.22 %, found: C 32.30 H 2.03 N 16.04 %. **HRMS** (EI): m/z calc. for $C_7H_5N_3O_8^+$ $[M]^+$: 259.0077; found: 259.0076. **BAM drop hammer**: >40 J. **Friction tester**: 324 N (at grain size: 100–500 µm) **ESD**: 0.54 J.

General Procedure for complexes 2–11

A suspension of $CuCO_3 \times Cu(OH)_2$ (27.6 mg, 0.125 mmol, 0.50 eq.) and H_2TNO (129.6 mg, 0.50 mmol, 2.00 eq.) in 5 mL of water was heated to 80 °C until a clear solution was obtained. To this solution, the ligand L (0.50 mmol, 2.00 eq.) was added. The solution was kept at 80 °C for 5 min. and then left at room temperature to crystallize for 3 weeks. The resulting suspension was filtered off and washed with little cold water, ethanol and diethyl ether.

$[Cu(1\text{-}AT)_2(HTNO)_2]$ (2)

$[Cu(1\text{-}AT)_2(HTNO)_2]$ was prepared according to the general procedure using 1-AT (42.5 mg, 0.50 mmol, 2.00 eq.). The compound was obtained as a green solid (139.8 mg, 0.19 mmol, 73 %). **DTA** (5 °C min^{-1}) onset: 185 °C (exothermic). **IR** (ATR, cm^{-1}): $\tilde{\upsilon}$ = 3606 (w), 3326 (w), 3143 (w), 1615 (m), 1538 (s), 1520 (vs), 1516 (vs), 1440 (m), 1435 (s), 1416 (s), 1363 (s), 1315 (s), 1183 (s), 1154 (s), 1117 (m), 1098 (m), 1044 (m), 1025 (m), 979 (m), 908 (m), 884 (w), 819 (m), 781 (m), 760 (m), 739 (m), 694 (s), 643 (s), 603 (m), 413 (m). **EA** ($C_{16}H_{14}CuN_{16}O_{16}$, 749.93 g mol^{-1}) calc.: C 25.63 H 1.88 N 29.88 %, found C 25.56 H 2.08 N 28.79 %. **BAM drop hammer**: <1 J. **Friction tester**: 96 N (at grain size: 100–500 µm). **ESD**: 50 mJ.

$[Cu(2\text{-}AT)_2(HTNO)_2]$ (3)

$[Cu(2\text{-}AT)_2(HTNO)_2]$ was prepared according to the general procedure using 2-AT (42.5 mg, 0.50 mmol, 2.00 eq.). The compound was obtained as a green solid (109.3 mg, 0.15 mmol, 60 %). **DTA** (5 °C min^{-1}) onset: 182 °C (exothermic). **IR** (ATR, cm^{-1}): $\tilde{\upsilon}$ = 3313 (w), 2004 (w), 1738 (vw), 1608 (m), 1563 (m), 1519 (vs), 1495 (s), 1472 (m), 1438 (m), 1420 (s), 1416 (s), 1367 (s), 1339 (s), 1327 (s), 1314 (s), 1301 (s), 1283 (s), 1183 (s), 1159 (s), 1149 (vs), 1071 (m), 1048 (m), 1035 (m), 962 (m), 908 (m), 890 (m), 826 (m), 814 (m), 811 (m), 787 (m), 758 (m), 740 (m), 696 (vs), 680 (s), 661 (s), 604 (m), 519 (m), 462 (m), 456 (s), 411 (s), 406 (s), 661 (s), 604 (m), 519 (m), 462 (m), 456 (s), 411 (s), 406 (s). **EA** ($C_{16}H_{14}CuN_{16}O_{16}$, 749.93 g mol^{-1}) calc.: C 25.63 H 1.88 N 29.88 %, found C 25.51 H 1.86 N 29.74 %. **BAM drop hammer**: <1 J. **Friction tester**: 80 N (at grain size: 100–500 µm). **ESD**: 50 mJ.

[Cu(1-AMT)$_2$(HTNO)$_2$] (4)

[Cu(1-AMT)$_2$(HTNR)$_2$] was obtained by applying the general procedure to 1-amino-5-methyltetrazole (49.6 mg, 0.50 mmol, 2.00 eq.). The compound was obtained as a brown solid (130.5 mg, 0.17 mmol, 67 %). **DTA** (5 °C min^{-1}) onset: 192 °C (exothermic). **IR** (ATR, cm^{-1}): $\tilde{\upsilon}$ = 3375 (w), 3359 (w), 3309 (w), 2168 (w), 1614 (m), 1549 (s), 1531 (vs), 1526 (vs), 1521 (vs), 1506 (vs), 1471 (m), 1464 (m), 1435 (m), 1414 (m), 1385 (m), 1352 (s), 1310 (s), 1282 (s), 1166 (s), 1148 (s), 1093 (m), 1080 (m), 1042 (m), 1007 (m), 940 (w), 905 (m), 824 (m), 810 (m), 787 (m), 742 (m), 723 (m), 696 (vs), 677 (s), 667 (s), 656 (s), 631 (m), 616 (m), 608 (m), 592 (m), 479 (w), 409 (m). **EA** ($C_{18}H_{18}CuN_{16}O_{16}$, 777.98 g mol^{-1}) calc.: C 27.79 H 2.33 N 28.81 %, found C 27.81 H 2.18 N 28.90 %. **BAM drop hammer**: <1 J. **Friction tester**: 60 N (at grain size: 100–500 µm). **ESD**: 250 mJ.

[Cu(HTNO)$_2$(1-MAT)$_2$] (5)

By using 1-methyl-5-aminotetrazole (49.6 mg, 0.50 mmol, 2.00 eq.) as described in the general procedure, compound **5** was obtained in form of brown platelets (81.0 mg, 0.10 mmol, 42 %). **DTA** (5 °C min^{-1}) onset: 220 °C (exothermic). **IR** (ATR, cm^{-1}): $\tilde{\upsilon}$ = 3463 (w), 3337 (w), 3297 (w), 1651 (m), 1614 (m), 1584 (w), 1550 (s), 1525 (s), 1521 (s), 1516 (s), 1506 (s), 1454 (m), 1416 (m), 1394 (m), 1351 (s), 1301 (m), 1262 (m), 1166 (s), 1152 (s), 1133 (s), 1062 (m), 1043 (m), 980 (m), 918 (w), 905 (m), 826 (w), 808 (w), 787 (m), 757 (m), 750 (w), 734 (w), 693 (vs), 647 (m), 631 (m), 619 (m), 585 (m), 563 (w), 529 (w), 514 (w), 502 (w), 484 (m), 468 (w), 455 (m), 619 (m), 585 (m), 563 (w), 529 (w), 514 (w), 502 (w), 484 (m), 468 (w), 455 (m), 439 (w), 425 (w). **EA** ($C_{18}H_{18}CuN_{16}O_{16}$, 777.98 g mol^{-1}) calc.: C 27.79 H 2.33 N 28.81 %, found C 27.81 H 2.42 N 29.04 %. **BAM drop hammer**: 2 J. **Friction tester**: >360 N (at grain size: 100–500 µm). **ESD**: 90 mJ.

[Cu(1,5-DAT)$_2$(HTNO)$_2$] (6)

[Cu(1,5-DAT)$_2$(HTNO)$_2$] was prepared according to the general procedure with 1,5-DAT (50.0 mg, 0.50 mmol, 2.00 eq.). While cooling down to rt, the formation of yellow platelets was observed. After 5 days filtration and washing according to the general procedure yielded compound **6** (0.14 g, 0.18 mmol, 72 %). **DTA** (5 °C min^{-1}) onset: 220 °C (exothermic). **IR** (ATR, cm^{-1}): $\tilde{\upsilon}$ = 3458 (w), 3388 (w), 3349 (w), 3341 (w), 3313 (w), 1671 (m), 1612 (m), 1555 (m), 1520 (s), 1504 (s), 1455 (m), 1406 (w), 1394 (w), 1352 (s), 1324 (m), 1302 (m), 1263 (m), 1169 (s), 1151 (s), 1127 (s), 1048 (m), 1007 (m), 905 (m),

886 (m), 827 (m), 807 (m), 788 (m), 758 (m), 751 (m), 733 (m), 694 (vs), 645 (s), 636 (s), 617 (m), 584 (m), 556 (m), 543 (m), 522 (m), 498 (m), 481 (m), 454 (m), 446 (m), 439 (m), 584 (m), 556 (m), 543 (m), 522 (m), 498 (m), 481 (m), 454 (m), 446 (m), 439 (m), 431 (m), 425 (m), 419 (s).**EA** ($C_{16}H_{16}CuN_{18}O_{16}$, 779.96 g mol^{-1}) calc.: C 24.64 H 2.07 N 32.33 %, found C 24.62 H 2.34 N 31.92 %. **BAM drop hammer**: <1 J. **Friction tester**: 360 N (at grain size: 100–500 µm). **ESD**: 200 mJ.

[Cu(HTNO)$_2$(1-NET)$_2$] (7)

Compound **7** was prepared by applying 1-NET (79.6 mg, 0.50 mmol, 2.00 eq.) to the general procedure. [Cu(HTNO)$_2$(1-NET)$_2$] was obtained in form of green crystals (0.15 mg, 0.16 mmol, 64 %) **DTA** (5 °C min^{-1}) onset: 159 °C (exothermic). **IR** (ATR, cm^{-1}): $\tilde{\upsilon}$ = 3140 (w), 3013 (vw), 2906 (vw), 1646 (s), 1607 (m), 1539 (s), 1506 (s), 1455 (m), 1435 (m), 1417 (s), 1391 (m), 1365 (s), 1321 (m), 1301 (m), 1277 (vs), 1180 (s), 1157 (s), 1104 (m), 1088 (m), 1063 (w), 1038 (m), 1009 (m), 1003 (m), 897 (s), 886 (m), 852 (s), 826 (m), 811 (m), 785 (m), 755 (m), 746 (m), 707 (m), 695 (s), 680 (m), 650 (s), 606 (m), 589 (m), 567 (w), 519 (w), 492 (m), 480 (w), 413 (m), 402 (m), 650 (s), 606 (m), 589 (m), 567 (w), 519 (w), 492 (m), 480 (w), 413 (m), 402 (m), 526 (m), 511 (m), 494 (m), 475 (m), 457 (m), 438 (m), 419 (m), 404 (m). **EA** ($C_{20}H_{18}CuN_{16}O_{22}$, 898.00 g mol^{-1}) calc.: C 26.75 H 2.02 N 24.96 %, found C 26.76 H 1.92 N 25.24 %. **BAM drop hammer**: <1 J. **Friction tester**: 192 N (at grain size: 100–500 µm). **ESD**: 90 mJ.

[Cu(1-AET)$_2$(HTNO)$_2$] (8)

[Cu(1-AET)$_2$(HTNO)$_2$] (90.0 mg, 0.10 mmol, 42 %) was obtained in form of red-brown needles by using 1-azidoethyltetrazole (69.6 mg, 0.50 mmol, 2.00 eq.) according to the general procedure. **DTA** (5 °C min^{-1}) onset: 191 °C (exothermic). **IR** (ATR, cm^{-1}): $\tilde{\upsilon}$ = 3162 (w), 2113 (m), 1622 (m), 1548 (s), 1538 (s), 1531 (s), 1525 (s), 1520 (s), 1515 (s), 1506 (s), 1471 (m), 1464 (m), 1456 (m), 1442 (m), 1415 (m), 1392 (m), 1386 (m), 1355 (s), 1302 (s), 1288 (m), 1271 (s), 1234 (m), 1163 (vs), 1147 (vs), 1092 (vs), 1066 (s), 1027 (m), 1011 (m), 1000 (s), 923 (m), 904 (m), 895 (m), 828 (m), 809 (m), 789 (s), 752 (m), 740 (m), 723 (m), 713 (m), 694 (vs), 659 (s), 643 (s), 606 (m), 789 (s), 752 (m), 740 (m), 723 (m), 713 (m), 694 (vs), 659 (s), 643 (s), 606 (m), 564 (m), 548 (m), 539 (m), 505 (w), 459 (w), 443 (w), 403 (s). **EA** ($C_{20}H_{18}CuN_{20}O_{16}$, 858.03 g mol^{-1}) calc.: C 28.00 H 2.11 N 32.65 %, found C 28.29 H 2.28 N 32.95 %. **BAM drop hammer**: <1 J. **Friction tester**: >360 N (at grain size: 100–500 µm). **ESD**: 90 mJ.

[Cu(1,1-dtm)$_2$(H$_2$O)$_4$](HTNO)$_2$ (9)

Using 1,1-dtm (76.1 mg, 0.50 mmol, 2.00 eq.) as a ligand in the general procedure led to immediate precipitation of a yellow-green solid, which was filtered off and washed with water. After drying on air, the substance proved to be [Cu(1,1-dtm)$_2$(H$_2$O)$_4$](HTNO)$_2$ (0.17 g, 0.18 mmol, 71 %). Suitable single crystals for X-ray diffraction analysis were obtained by dissolving the compound in 5 mL of EtOH at 80 °C and letting the solvent evaporate at rt. **DTA** (5 °C min^{-1}) onset: 100 °C (endothermic), 197 °C (exothermic). **IR** (ATR, cm^{-1}): $\tilde{\nu}$ = 3117 (m), 1614 (m), 1564 (m), 1529 (s), 1485 (s), 1458 (m), 1436 (m), 1413 (m), 1379 (m), 1359 (m), 1344 (s), 1321 (s), 1310 (s), 1287 (m), 1222 (w), 1178 (s), 1158 (s), 1144 (s), 1098 (s), 1042 (m), 1031 (m), 1004 (m), 987 (m), 961 (m), 901 (m), 880 (m), 821 (m), 814 (m), 779 (s), 760 (m), 737 (s), 710 (vs), 694 (vs), 669 (s), 647 (vs), 603 (s), 529 (s), 522 (m), 498 (m), 481 (m), 454 (m), 446 (m), 439 (m), 647 (vs), 603 (s), 529 (s), 522 (m), 498 (m), 481 (m), 454 (m), 446 (m), 439 (m), 431 (m), 425 (m), 419 (s). **EA** (C$_{20}$H$_{24}$CuN$_{22}$O$_{20}$, 956.09 g mol^{-1}) calc.: C 25.13 H 2.53 N 32.23 %, found C 24.94 H 2.49 N 32.34 %. **BAM drop hammer**: <1 J. **Friction tester**: 360 N (at grain size: 100–500 µm). **ESD**: 160 mJ.

[Cu(1,1-dte)(HTNO)$_2$] · H$_2$O (10)

1,1-dte (83.1 mg, 0.50 mmol, 2.00 eq.) was applied according to the general procedure. A brown solid immediately started to precipitate. The suspension was filtered off and washed with hot water, rt EtOH and rt Et$_2$O. The compound was identified to be [Cu(1,1-dte)(HTNO)$_2$] · H$_2$O (0.16 g, 0.21 mmol, 85 %). **DTA** (5 °C min^{-1}) onset: 252 °C (exothermic). **IR** (ATR, cm^{-1}): $\tilde{\nu}$ = 3149 (w), 1610 (m), 1553 (s), 1523 (vs), 1513 (vs), 1486 (s), 1458 (m), 1445 (m), 1413 (m), 1377 (m), 1351 (s), 1319 (s), 1305 (s), 1285 (s), 1170 (vs), 1153 (s), 1130 (s), 1087 (s), 1067 (m), 1044 (m), 1004 (m), 923 (w), 905 (m), 881 (m), 829 (m), 810 (m), 783 (m), 761 (m), 748 (m), 734 (m), 717 (m), 691 (vs), 662 (vs), 650 (s), 643 (s), 619 (m), 583 (m), 528 (w), 514 (w), 499 (w), 475 (w), 455 (w), 431 (w), 643 (s), 619 (m), 583 (m), 528 (w), 514 (w), 499 (w), 475 (w), 455 (w), 431 (w), 439 (w), 425 (w). **EA** (C$_{18}$H$_{16}$CuN$_{14}$O$_{17}$, 763.95 g mol^{-1}) calc.: C 28.30 H 2.11 N 25.67 %, found C 28.53 H 2.07 N 25.96 %. **BAM drop hammer**: >40 J. **Friction tester**: 192 N (at grain size: 100–500 µm). **ESD**: 200 mJ.

[Cu(1,1-dtp)$_2$(HTNO)$_2$] (11)

The utilization of 1,1-dtp (99.1 mg, 0.50 mmol, 0.50 eq.) in the general procedure led to the formation of the desired product (0.18 g, 0.19 mmol, 77 %) in form of green blocks suitable for X-ray diffraction analysis. **DTA** (5 °C min^{-1}) onset: 184 °C (exothermic). **IR** (ATR, cm^{-1}): $\tilde{\upsilon}$ = 3138 (w), 1621 (m), 1570 (m), 1519 (vs), 1499 (s), 1461 (m), 1455 (m), 1417 (s), 1387 (m), 1359 (vs), 1324 (vs), 1191 (s), 1174 (s), 1157 (s), 1138 (s), 1134 (s), 1104 (s), 1094 (vs), 1061 (m), 1039 (m), 1029 (m), 1023 (m), 1005 (s), 983 (m), 906 (s), 880 (m), 865 (m), 821 (s), 795 (s), 781 (s), 758 (m), 738 (s), 719 (m), 686 (vs), 674 (s), 660 (s), 642 (vs), 604 (s), 582 (m), 563 (m), 553 (m), 547 (m), 538 (m), 674 (s), 660 (s), 642 (vs), 604 (s), 582 (m), 563 (m), 553 (m), 547 (m), 538 (m), 526 (m), 511 (m), 494 (m), 475 (m), 457 (m), 438 (m), 419 (m), 404 (m). **EA** ($C_{24}H_{24}CuN_{22}O_{16}$, 940.14 g mol^{-1}) calc.: C 30.66 H 2.57 N 32.78 %, found C 30.48 H 2.65 N 32.77 %. **BAM drop hammer**: <1 J. **Friction tester**: 240 N (at grain size: 100–500 µm). **ESD**: 200 mJ.

[Zn(HTNO)$_2$(MTZ)$_2$] (12)

[Zn(HTNO)$_2$(MTZ)$_2$] was prepared by dissolving $ZnCO_3$ (62.7 mg, 0.50 mmol, 1.00 eq.) and H_2TNO (259 mg, 1.00 mmol, 2.00 eq.) in 10 mL of water at 80 °C. MTZ (84.1 mg, 1.00 mmol, 2.00 eq.) was added and the solution was stirred for 5 min. After four weeks of crystallization at room temperature, the resulting solid was filtered off and washed with water. The compound was obtained as a green powder (293.0 mg, 0.39 mmol, 78 %). **DTA** (5 °C min^{-1}) onset: 229 °C (exothermic). **IR** (ATR, cm^{-1}): $\tilde{\upsilon}$ = 3162 (w), 1606 (m), 1549 (s), 1538 (s), 1532 (s), 1525 (s), 1521 (s), 1505 (s), 1495 (s), 1471 (m), 1462 (m), 1457 (m), 1417 (s), 1385 (m), 1359 (s), 1314 (s), 1291 (s), 1182 (s), 1155 (vs), 1100 (vs), 1065 (m), 1058 (m), 1045 (s), 1026 (m), 1019 (m), 998 (m), 907 (m), 881 (m), 824 (m), 812 (m), 786 (s), 760 (m), 738 (m), 707 (s), 693 (vs), 683 (s), 675 (s), 649 (vs), 607 (m), 584 (m), 562 (m), 500 (m), 475 (w), 693 (vs), 683 (s), 675 (s), 649 (vs), 607 (m), 584 (m), 562 (m), 500 (m), 475 (w), 407 (s). **EA** ($C_{18}H_{16}N_{14}O_{16}Zn$, 749.79 g mol^{-1}) calc.: C 28.83 H 2.15 N 26.15 %, found C 28.88 H 2.13 N 26.12 %. **BAM drop hammer**: 2 J. **Friction tester**: 168 N (at grain size: 100–500 µm). **ESD**: 33 mJ.

CsHTNO (13)

Cs_2CO_3 (0.49 g, 1.50 mmol, 0.50 eq.) was dissolved water (5 mL). After heating to 80 °C, H_2TNO (0.78 g, 3.00 mmol, 1.00 eq) was added and the suspension was kept at 80 °C until everything dissolved. The resulting red solution was left at rt to crystallize. The obtained

red solid was filtered off and washed with cold water to yield CsHTNO (0.95 g, 2.44 mmol, 81 %). **^{1}H NMR** (d_6-DMSO, 25 °C) δ 12.56 (s, 1H, O*H*) 2.24 (s, 3H, CH_3) ppm. **^{13}C NMR** (d_6-DMSO, 25 °C) δ 153.4, 131.3, 131.0, 129.4, 16.0 ppm. **^{14}N NMR** (d_6-DMSO, 25 °C) δ −5, −358 ppm. **DTA** (5 °C min^{-1}) onset: 233 °C (exothermic). **IR** (ATR, cm^{-1}): $\tilde{\upsilon}$ = 1622 (w), 1568 (m), 1511 (s), 1506 (s), 1434 (m), 1405 (m), 1375 (m), 1343 (s), 1315 (s), 1258 (m), 1180 (s), 1151 (s), 1122 (vs), 1058 (m), 1025 (m), 999 (m), 911 (m), 819 (m), 804 (m), 784 (s), 753 (m), 744 (m), 720 (m), 693 (s), 658 (m), 629 (m), 610 (m), 597 (m), 417 (s). **EA** ($C_7H_4CsN_3O_8$, 391.03 g mol^{-1}) calc.: C 21.50 H 1.03 N 10.75 %, found C 21.54 H 1.29 N 10.66 %. **BAM drop hammer**: <1 J. **Friction tester**: >360 N (at grain size: 100–500 µm). **ESD**: 50 mJ.

PbTNO (14)

MgO (0.23 g, 5.60 mmol, 1.14 eq.) was added to a suspension of H_2TNO (1.27 g, 4.90 mmol, 1.00 eq.) in water (20 mL) which was heated to 55 °C until a clear solution was formed. The solution was filtered off and lead nitrate (1.99 g, 6.00 mmol, 1.22 eq.) was slowly added under light stirring which led to precipitation of a yellow solid. The suspension was stirred for 30 min. The yellow solid was washed with water and acetone and dried at 100 °C to yield PbTNO (2.13 g, 4.59 mmol, 94 %). **^{1}H NMR** (d_6-DMSO, 25 °C) δ 2.05 (s, 3H, CH_3) ppm. **^{13}C NMR** (d_6-DMSO, 25 °C) δ 159.9, 135.6, 132.3, 128.7, 16.0 ppm. **^{14}N NMR** (d_6-DMSO, 25 °C) δ −5 ppm. **^{207}Pb NMR** (400 MHz, d_6-DMSO, 25 °C) δ −2176 ppm. **DTA** (5 °C min^{-1}) onset: 240 °C (exothermic). **IR** (ATR, cm^{-1}): $\tilde{\upsilon}$ = 1593 (w), 1551 (vs), 1514 (s), 1488 (m), 1443 (m), 1433 (m), 1380 (s), 1337 (s), 1313 (s), 1301 (s), 1265 (m), 1162 (s), 1061 (vw), 1048 (w), 911 (vw), 813 (vw), 787 (m), 753 (w), 737 (w), 720 (m), 691 (s), 663 (m), 638 (w), 621 (w), 585 (w), 511 (w), 461 (w), 423 (w), 404 (m). **EA** ($C_7H_3N_3O_8Pb$, 464.31 g mol^{-1}) calc.: C 18.11 H 0.65 N 9.05 %, found C 17.96 H 0.88 N 8.78 %. **BAM drop hammer**: <1 J. **Friction tester**: >0.1 N (at grain size: 100–500 µm). **ESD**: 0.54 mJ.

[Zn(H$_2$O)$_3$(TNO)] · H$_2$O (15)

$ZnCO_3$ (62.7 mg, 0.5 mmol, 1.00 eq.) and H_2TNO (0.13 g, 0.50 mmol, 1.00 eq.) were dissolved in water (5 mL) at 80 °C. After stirring for 5 min. the solution was allowed to cool to room temperature and left for crystallization. After complete evaporation of the solvent, the residual solid was washed with little cold EtOH to obtain compound **15** (12.6 mg, 0.03 mmol, 6 %) as an orange solid. **DTA** (5 °C min^{-1}) onset: 122 °C

(endothermic → exothermic). **IR** (ATR, cm^{-1}): $\tilde{\upsilon}$ =3569 (w), 3530 (w), 3432 (m), 3399 (m), 3181 (m), 1639 (w), 1618 (m), 1570 (s), 1542 (s), 1535 (s), 1509 (s), 1503 (s), 1468 (m), 1430 (s), 1410 (m), 1381 (m), 1364 (m), 1339 (s), 1308 (s), 1229 (vs), 1195 (s), 1160 (s), 1085 (m), 1051 (m), 1023 (m), 926 (m), 914 (m), 829 (m), 812 (m), 787 (s), 737 (s), 691 (vs), 626 (s), 577 (s), 552 (s), 517 (s), 499 (vs), 474 (s), 454 (s), 433 (s), 404 (vs), 468 (w), 455 (m), 552 (s), 517 (s), 499 (vs), 474 (s), 454 (s), 433 (s), 404 (vs), 468 (w), 455 (m), 439 (w), 425 (w). **EA** ($C_7H_{11}N_3O_{12}Zn$, 394.55 g mol^{-1}) calc.: C 21.31 H 2.81 N 10.65 %, found C 21.17 H 2.69 N 10.66 %.

[Cu(HTNR)$_2$(1-MAT)$_2$] (16)

A suspension of $CuCO_3 \times Cu(OH)_2$ (27.6 mg, 0.125 mmol, 0.50 eq.) and styphnic acid (122.6 mg, 0.50 mmol, 2.00 eq.) in 5 mL of water was heated to 80 °C until a clear solution was obtained. To this solution, 1-methyl-5-aminotetrazole (49.6 mg, 0.50 mmol, 2.00 eq.) was added in small portions. Upon stirring at 80 °C, a green solid started to precipitate, which was filtered off and washed with little cold water, ethanol and diethyl ether. The solid was identified to be [Cu(HTNR)$_2$(1-MAT)$_2$] (124.5 mg, 0.17 mmol, 68 %). **DTA** (5 °C min^{-1}) onset: 249 °C (exothermic). **IR** (ATR, cm^{-1}): $\tilde{\upsilon}$ = 3420 (m), 3346 (w), 1643 (m), 1627 (s), 1588 (w), 1566 (s), 1537 (s), 1520 (s), 1509 (s), 1474 (m), 1455 (m), 1421 (m), 1374 (m), 1353 (m), 1326 (s), 1319 (s), 1286 (vs), 1193 (m), 1176 (s), 1139 (m), 1092 (s), 1079 (s), 1051 (s), 986 (m), 933 (m), 829 (w), 782 (m), 763 (m), 737 (m), 713 (s), 697 (vs), 690 (vs), 636 (m), 557 (s), 551 (s), 547 (s), 539 (s), 523 (s), 489 (s), 471 (s), 459 (s), 447 (s), 420 (vs), 551 (s), 547 (s), 539 (s), 523 (s), 489 (s), 471 (s), 459 (s), 447 (s), 420 (vs), 439 (w), 425 (w). **EA** ($C_{16}H_{14}CuN_{16}O_{16}$, 749.93 g mol^{-1}) calc.: C 25.63 H 1.88 N 29.88 %, found C 25.34 H 1.89 N 29.97 %. **BAM drop hammer**: 2 J. **Friction tester**: >360 N (at grain size: 100–500 µm). **ESD**: 160 mJ.

[Cu(1,5-DAT)$_2$(TNR)] (17)

A suspension of $CuCO_3 \times Cu(OH)_2$ (27.6 mg, 0.125 mmol, 0.50 eq.) and styphnic acid (122.6 mg, 0.50 mmol, 2.00 eq.) in 5 mL of water was heated to 80 °C until a clear solution was obtained. To this solution, 1,5-diaminotetrazole (50.0 mg, 0.50 mmol, 2.00 eq.) was added. After stirring at 80 °C for 5 min. the solution was allowed to cool to rt and left to crystallize. During cooling down, precipitation of a green solid started and was completed after two days. The suspension was filtered off and washed with cold water, ethanol and diethyl ether. The solid was identified as [Cu(1,5-DAT)$_2$(TNR)] (54.2 mg, 0.17 mmol,

68 %). **DTA** (5 °C min^{-1}) onset: 229 °C (exothermic). **IR** (ATR, cm^{-1}): $\tilde{\nu}$ = 3458 (m), 3341 (m), 3254 (w), 3205 (w), 3109 (w), 1674 (m), 1624 (m), 1597 (m), 1581 (m), 1556 (m), 1538 (s), 1510 (s), 1488 (m), 1476 (m), 1457 (m), 1427 (s), 1355 (m), 1333 (s), 1285 (vs), 1244 (vs), 1170 (m), 1123 (m), 1108 (s), 1053 (m), 1013 (m), 922 (m), 916 (m), 876 (w), 789 (m), 743 (m), 733 (m), 703 (vs), 683 (m), 539 (w), 502 (m), 459 (s), 443 (s), 438 (s), 428 (s), 419 (s), 406 (s), 455 (m), 539 (w), 502 (m), 459 (s), 443 (s), 438 (s), 428 (s), 419 (s), 406 (s), 455 (m), 439 (w), 425 (w).**EA** ($C_8H_9CuN_{15}O_8$, 506.80 g mol^{-1}) calc.: C 18.96 H 1.79 N 41.46 %, found C 19.04 H 2.02 N 40.03 %. **BAM drop hammer**: <1 J. **Friction tester**: 45 N (at grain size: 100–500 µm). **ESD**: 160 mJ.

[Cu(1,1-dte)(TNR)] · H_2O (18)

A suspension of $CuCO_3 \times Cu(OH)_2$ (27.6 mg, 0.125 mmol, 0.50 eq.) and styphnic acid (61.3 mg, 0.25 mmol, 1.00 eq.) in 5 mL of water was heated to 80 °C until a clear solution was obtained. Addition of 1,2-di(1*H*-tetrazol-1-yl)-ethane (41.5 mg, 0.25 mmol, 1.00 eq.) led to immediate precipitation compound **18** (117.8 mg, 0.24 mg, 96 %) as a green powder. **DTA** (5 °C min^{-1}) onset: 264 °C (exothermic). **IR** (ATR, cm^{-1}): $\tilde{\nu}$ = 3106 (w), 3004 (w), 1610 (m), 1585 (m), 1538 (m), 1521 (s), 1488 (m), 1473 (m), 1442 (s), 1430 (s), 1374 (m), 1367 (m), 1335 (w), 1287 (s), 1226 (vs), 1189 (s), 1171 (s), 1104 (s), 1058 (m), 1023 (m), 1009 (m), 954 (w), 944 (w), 931 (w), 921 (w), 880 (m), 831 (w), 790 (w), 775 (m), 736 (w), 709 (s), 673 (m), 649 (s), 534 (w), 506 (w), 459 (w), 418 (m), 405 (m), 438 (s), 428 (s), 419 (s), 406 (s), 455 (m), 506 (w), 459 (w), 418 (m), 405 (m), 438 (s), 428 (s), 419 (s), 406 (s), 455 (m), 439 (w), 425 (w). **EA** ($C_{10}H_9CuN_{11}O_9$, 490.80 g mol^{-1}) calc.: C 24.47 H 1.85 N 31.39 %, found C 24.30 H 1.67 N 30.91 %. **BAM drop hammer**: 20 J. **Friction tester**: 360 N (at grain size: 100–500 µm). **ESD**: 200 mJ.

2.7.11 References

[S1] CrysAlisPRO (Version 171.33.41), Oxford Diffraction Ltd., **2009**.

[S2] A. Altomare, G. Cascarano, C. Giacovazzo, and A. Guagliardi, *J. Appl. Crystallogr.*, **1992**, *26*, 343.

[S3] A. Altomare, G. Cascarano, C. Giacovazzo, A. Guagliardi, A. G. G. Moliterni, M. C. Burla, G. Polidori, M. Camalli and R. Spagna, SIR97, **2003**.

[S4] A. Altomare, M. C. Burla, M. Camalli, G. L. Cascarano, C. Giacovazzo, A. Guagliardi, A. G. G. Moliterni, G. Polidori and R. Spagna, *J. Appl. Crystallogr.*, **1999**, *32*, 115.

[S5] G. M. Sheldrick, SHELXL-97, University of Göttingen, Germany, **1997**.

[S6] G. M. Sheldrick, *Acta Crystallogr. Sect. A*, **2008**, *64*, 112.

[S7] G. M. Sheldrick, *Acta Crystallogr. Sect. A*, **2015**, *71*, 3–8.

[S8] A. L. Spek, PLATON, Utrecht University, The Netherlands, **1999**.

[S9] L.J. Farrugia, *J. Appl. Cryst.*, **2012**, *45*, 849.

[S10] O. V. Dolomanov, L. J. Bourhis, R. J. Gildea, J. A. K. Howard and H. Puschmann, J. *Appl. Cryst.*, **2009**, *42*, 339–341.

[S11] Empirical absorption correction using spherical harmonics, implemented in SCALE3 ABSPACK scaling algorithm (CrysAlisPro Oxford Diffraction Ltd., Version 171.33.41, **2009**).

[S12] APEX3, Bruker AXS Inc., Madison, Wisconsin, USA.

[S13] M. J. Frisch, G. W. Trucks, H. B. Schlegel, G. E. Scuseria, M. A. Robb, J. R. Cheeseman, G. Scalmani, V.Barone, B. Mennucci, G. A. Petersson, H. Nakatsuji, M. Caricato, X. Li, H.P. Hratchian, A. F. Izmaylov, J. Bloino, G. Zheng, J. L. Sonnenberg, M. Hada, M. Ehara, K. Toyota, R. Fukuda, J. Hasegawa, M. Ishida, T. Nakajima, Y. Honda, O. Kitao, H. Nakai, T. Vreven, J. A. Montgomery, Jr., J. E. Peralta, F. Ogliaro, M. Bearpark, J. J. Heyd, E. Brothers, K. N. Kudin, V. N. Staroverov, R. Kobayashi, J. Normand, K. Raghavachari, A. Rendell, J. C. Burant, S. S. Iyengar, J. Tomasi, M. Cossi, N. Rega, J. M. Millam, M.Klene, J. E. Knox, J. B. Cross, V. Bakken, C. Adamo, J. Jaramillo, R. Gomperts, R. E. Stratmann, O. Yazyev, A. J. Austin, R. Cammi, C. Pomelli, J. W. Ochterski, R. L. Martin,

K. Morokuma, V. G. Zakrzewski, G. A. Voth, P. Salvador, J. J. Dannenberg, S. Dapprich, A. D. Daniels, O. Farkas, J.B. Foresman, J. V. Ortiz, J. Cioslowski and D. J. Fox, Gaussian 09 A.02, Gaussian, Inc., Wallingford, CT, USA, **2009**.

[S14] J. W. Ochterski, G. A. Petersson and J. A. Montgomery Jr., *J. Chem. Phys.*, **1996**, *104*, 2598–2619.

[S15] J. A. Montgomery Jr., M. J. Frisch, J. W. Ochterski and G. A. Petersson, *J. Chem. Phys.*, **2000**, *112*, 6532–6542.

[S16] L. A. Curtiss, K. Raghavachari, P. C. Redfern and J. A. Pople, *J. Chem. Phys.*, **1997**, *106*, 1063–1079.

[S17] E. F. C. Byrd and B. M. Rice, *J. Phys. Chem. A*, **2006**, *110*, 1005–1013.

[S18] B. M. Rice, S. V. Pai and J. Hare, *Comb. Flame*, **1999**, *118*, 445–458.

[S19] P. J. Lindstrom and W. G. Mallard, NIST Standard Reference Database Number 69, http://webbook.nist.gov/chemistry/, (accessed Mai 2022).

[S20] M. S. Westwell, M. S. Searle, D. J. Wales and D. H. Williams, *J. Am. Chem. Soc*. **1995**, *117*, 5013–5015.

[S21] F. Trouton, *Philos. Mag.* **1884**, *18*, 54–57.

[S22] Bikelytė, G.; Härtel, M. A. C.; Holler, M.; Neuer, A.; Klapötke, T. M., *J. Chem. Eng. Data* **2021**, *66* (4), 1709–1716.

[S23] M. A.Härtel, T. M. Klapötke, J. Stierstorfer, L. Zehetner, *Propellants Explos. Pyrotech.* **2019**, *44* (4), 484–492.

[S24] J. S. Chickos, D. G. Hesse, J. F. Liebman, *Struct. Chem.* **1993**, *4* (4), 261–269.

[S25] R. B. Cundall, T. Frank Palmer, C. E. C. Wood, *J. Chem. Soc., Faraday Trans. 1* **1978**, *74*, 1339–1345.

[S26] H. Östmark, S. Wallin, H. G. Ang, *Propellants Explos. Pyrotech.* **2012**, *37*, 12–23.

[S27] W. Acree, J. S. Chickos, *J. Phys. Chem. Ref. Data* **2010**, *39* (4), 043101.

[S28] W.P.C., d. K. *Thermal Analysis of some Propellants and Explosives with DCS and TG/DTA*; TNO Prins Maurits Laboratory, **1996**.

[S29] G. Bikelytė, M. Härtel, J. Stierstorfer, T. M. Klapötke, A. A. Pimerzin, S. P. Verevkin, *J. Chem. Thermodyn.* **2017**, *111*, 271–278.

[S30] NATO standardization agreement (STANAG) on explosives, impact sensitivity tests, no. 4489, 1st ed., Sept. 17, 1999.

[S31] WIWEB-Standardarbeitsanweisung 4-5.1.02, Ermittlung der Explosionsgefährlichkeit, hier der Schlagempfindlichkeit mit dem Fallhammer, Nov. 8, 2002.

[S32] BAM, http://www.bam.de, (accessed Mai 2022).

[S33] OZM, http://www.ozm.cz, (accessed Mai 2022).

[S34] Military Standard 1751A (MIL-STD-1751A): safety and performance tests for qualification of explosives (high explosives, propellants and pyrotechnics), method 1016, Dec. 11, 2001.

[S35] NATO standardization agreement (STANAG) on explosive, friction sensitivity tests, no. 4487, 1st ed., Aug. 22, 2002.

[S36] WIWEB-Standardarbeitsanweisung 4-5.1.03, Ermittlung der Explosionsgefährlichkeit oder der Reibeempfindlichkeit mit dem Reibeapparat, Nov. 8, 2002.

[S37] UN Model Regulation: Recommendations on the Transport of Dangerous Goods – Manual of Tests and Criteria, section 13.4.2.3.3, 2015.

[S38] Impact: insensitive > 40 J, less sensitive ≥ 35 J, sensitive ≥ 4 J, very sensitive ≤ 3 J; Friction: insensitive > 360 N, less sensitive = 360 N, sensitive < 360 N and > 80 N, very sensitive ≤ 80 N, extremely sensitive ≤ 10 N. According to the UN Recommendations on the Transport of Dangerous Goods, 5th ed., 2009.

[S39] M. Sućeska, EXPLO5 Version 6.05 User's Guide. Zagreb, Croatia: OZM; 2018.

[S40] A. J. Birch, R. A. Massy-Westropp, R. W. Rickards, H. Smith, *J. Chem. Soc.* **1958**, 360–365.

3 1-(Nitratomethyl)tetrazole: A Highly Sensitive Ligand with an Improved Oxygen Balance for Laser Ignitable Coordination Compounds

Moritz Kofen, Vanessa Braun, Simon M. J. Endraß, Thomas M. Klapötke, and Jörg Stierstorfer

published in *Inorganic Chemistry,* **2022**

DOI: 10.1021/acs.inorgchem.2c02805

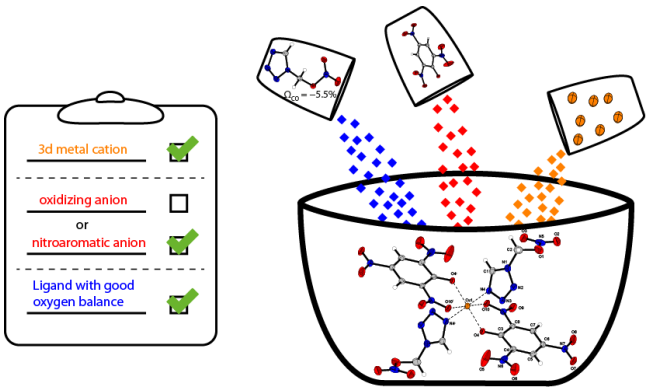

Abstract: For the first time the highly sensitive 1-(Nitratomethyl)tetrazole (1-NAMT) was synthesized, representing the shortest possible 1-(nitratoalkyl)tetrazole with a combined nitrogen and oxygen content of 81.4 %. Compared to its related ethyl-derivative (1-NET) it exhibits an improved oxygen balance, resulting in higher detonation parameters. 1-NAMT was thoroughly analyzed by single-crystal diffraction experiments accompanied by elemental analysis, IR spectroscopy, and multinuclear (^{1}H, ^{13}C, ^{14}N) NMR measurements. The thermal behavior of 1-NAMT was analyzed by Differential Thermal Analysis supported by Thermogravimetric Analysis. Furthermore, energetic coordination compounds of Cu with different inorganic (e.g. nitrate, chlorate, and perchlorate) and nitroaromatic anions (e.g. picrate and styphnate) were synthesized and thoroughly analyzed. It is shown that the formation of energetic coordination compounds with nitroaromatic anions (T_{dec} ~ 180 °C) is a suitable strategy to improve the rather low thermal stability of 1-NAMT (125 °C).

3.1 Introduction

Since the structure elucidation of the DNA by Crick & Watson [1], the importance of N-heterocyclic compounds cannot be questioned. The four nucleobases adenine, guanine, cytosine and thymine (Figure 1) that were found to build up the double helical DNA strands are key examples of N-heterocyclic compounds. Other representatives of important heterocyclic compounds are based on the porphyrin scaffold, which are known for building hemes, the most prominent being heme B, the oxygen transporting iron coordination compound of blood. [2] The application of heterocycles as ligands in coordination compounds offers a nearly infinite amount of possible compounds which chemical and physical properties can be tuned towards their intended use. Prominent examples of heterocycles applied as ligands are found in the Grubbs I [3] and Grubbs II [4] catalysts as well as in the B vitamins with their most prominent representative being vitamin B_{12} [5]. A recently emerged, closely related, field of research is that of energetic coordination compounds (ECCs) used in pyrotechnic mixtures [6], burn rate modifiers [7] and primary explosives [8]. Here, energetic and nitrogen-rich heterocycles are combined with transition metal salts of oxidizing (e.g., nitrate, chlorate and perchlorate) or reducing (e.g. azide) anions. Promising ligands for ECCs should exhibit several characteristics. Like for any energetic material, a high endothermic enthalpy of formation is favorable. Furthermore, the

sensitivities of the pure ligand should be approximately in the range that is desired for the intended use of the resulting ECC. As the formation of ECCs most often leads to an increase in sensitivity [9], it is easily possible to overstate the sensitivities of the resulting ECCs as seen in the work on 1-amino-tetrazole [10] (1-AT) or 1-azidomethyl-tetrazole [11] (AzMT). Among the nitrogen-rich heterocyclic compounds, those based on the 1*H*-tetrazole (Figure 1) motive are promising substances to be applied as ligands. Due to a wide variety of possible substitutions of the tetrazole scaffold, a huge amount of (highly) energetic neutral compounds are feasible. [12] This enables a broad spectrum of potential applications as antitumor-drugs, as low toxic antifungal drugs but also in green energetic coordination compounds, dependent on the size and type of substituents. [13-15] Additionally, the tetrazole scaffold offers a highly endothermic enthalpy of formation (1*H*-tetrazole: 4732 kJ kg^{-1}) due to a very high nitrogen content of the underlying tetrazole moiety (N = 79.98 %). Besides the drawback an acidic proton of 1*H*-tetrazole, the absence of oxygen atoms in the molecular structure leads to an incomplete decomposition into gaseous products as elemental carbon may be produced upon exothermic decomposition. Therefore, increasing the amount of oxygen within the molecular structures improves the overall oxygen balance ($OB_{CO} = \frac{\left[d-a-\frac{b}{2}\right]*1600}{M}$; M = molar mass; formula for $C_aH_bN_cO_d$), which also generally increases the performance of an energetic material. This can be achieved by the functionalization with explosophores such as nitro-, nitramino-, and nitrate ester moieties that all introduce oxygen to the molecular structure (Figure 1). While the direct functionalization of tetrazoles at the 1N position is generally easy, the substitution by a nitro group or a nitrate ester is not reported yet. Here, only the nitramino derivative is known to literature [16].

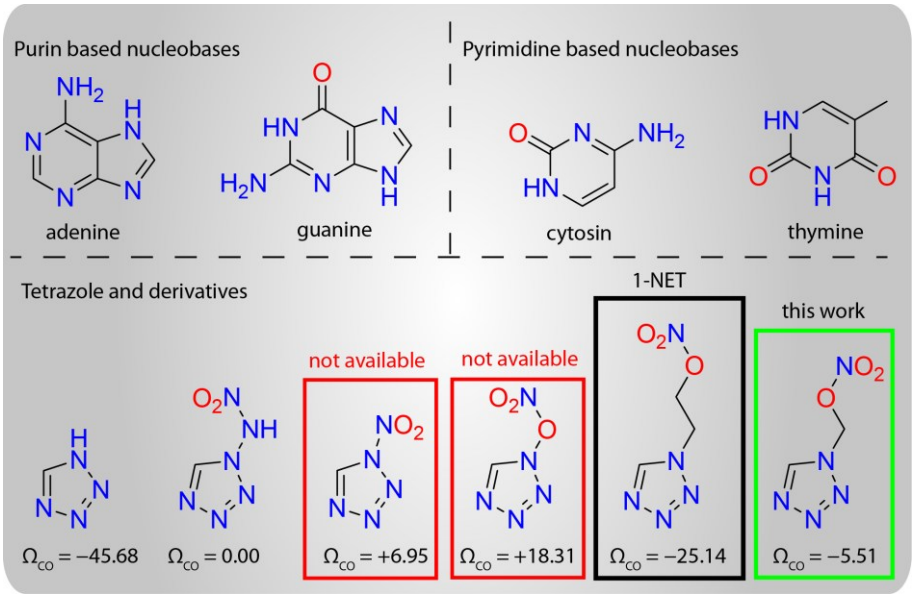

Figure 1. Comparison of oxygen balances between 1*H*-tetrazole and derivatives with different substitution patterns.

Due to the inaccessibility of a direct substitution at the 1*N*-position of tetrazole by a nitrate ester, the introduction of alkyl bridges between the azole and nitrate ester is necessary. Recently, *Klapötke et al.* published the derivative containing a bridging ethyl chain namely 1-(nitratoethyl)-tetrazole [17] (1-NET). This compound exhibits a decreased nitrogen content of 44.0 % compared to pure tetrazole, but an oxygen content of 30.2 %, 1-NET therefore possess an oxygen balance towards the formation of CO of $\Omega_{CO} = -25.1$ %. This drastically increased the oxygen balance compared to 1*H*-tetrazole ($\Omega_{CO} = -45.7$ %). Additionally, the introduction of oxygen atoms in 1-NET (1.55 g cm^{-3}) also increases the density of pure 1*H*-tetrazole (1.41 g cm^{-3}), even though a more sterically demanding substituent is introduced. This increase in density would noticeably be more drastic when comparing 1*H*-tetrazole to the methyl-bridged derivative, which is not published yet. Interestingly, there are only a few examples of methylene-bridged explosophores published [18-20], and even less when focusing solely on 1*N*-subtitution [21]. While the introduction of an ethylene moiety is synthetically rather easy, the challenge to introduce a methylene moiety is to find a suitable starting material that is chemically inert enough to be further functionalized. We recently published a procedure for the synthesis of 1-(hydroxymethyl)-tetrazole (1-HMT), which is at least stable enough to be smoothly converted to the mesylated derivative. Since 1-HMT also represents a suitable precursor for 1-(Nitratomethyl)tetrazole (1-NAMT), we opted to synthesize it for the first time and apply it as ligand for new ECCs. In this work we present the synthesis of 1-(Nitratomethyl)tetrazole (1-NAMT), as well as several new energetic coordination

compounds of 1-NAMT. The ligand was analyzed by multinuclear NMR spectroscopy, and all compounds were analyzed by single crystal X-ray diffraction experiments. Additionally, the physico-chemical properties of all compounds were determined.

3.2 Results and Discussion

3.2.1 Synthesis of 1-NAMT

Warning! The synthetic work described includes the handling of very sensitive compounds such as 1-NAMT (**1**) and ECCs (**2**–**8**). Appropriate protective equipment (leather coat, face shield, Kevlar® wrist protectors, and hearing protection) must be worn at all times when handling these materials!

The synthesis of 1-(Nitratomethyl)tetrazole (**1**) is shown in Scheme 1. The crude isomeric mixture of 1- and 2-(hydroxymethyl)-tetrazole was synthesized according to literature [11]. The isomeric mixture was added to a stirring mixture of acetic anhydride and fuming nitric acid cooled to 5 °C. A previous separation of the isomers is not necessary, due to a complete decomposition of the 2*N* isomer after nitration. The target molecule 1-(Nitratomethyl)tetrazole (**1**) was obtained as a colorless solid by stirring at 5 °C for 1.5h, quenching on ice, adjusting to pH = 6, and extracting into ethyl acetate. To remove trace amounts of spent acid, **1** was purified via column chromatography with a mixture of iso-hexane/ethyl acetate (1/1) as eluting solvent. After removing the solvent *in vacuo,* the resulting oil (**1**) started to solidify after standing undisturbed for 1–2 hours. **1** was obtained as colorless solid in moderate yield of 21 %.

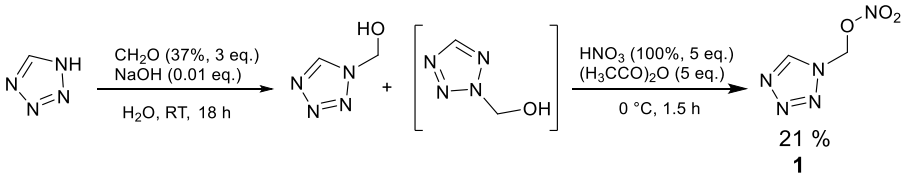

Scheme 1. Synthesis of 1-(Nitratomethyl)tetrazole (**1**), with the hydroxy methylation of 1*H*-tetrazole.

3.2.2 Synthesis of the ECCs

Several energetic coordination compounds with 1-NAMT as a ligand were synthesized according to Schemes 2 and 3. Due to the commercial unavailability of copper(II) chlorate, it was freshly produced according to literature [22]. Generally, compounds **2**–**4** (Scheme 2)

were produced by adding the corresponding copper(II) salt to a solution of **1** in ethanol at elevated temperatures. After stirring for several minutes, the solutions were left to crystallize for up to 3 days. Before complete evaporation of the solvent, the compounds were filtered off and washed with little ice-cold ethanol. The compounds thus obtained were suitable for single crystal X-Ray diffraction experiments without any further recrystallisation necessary.

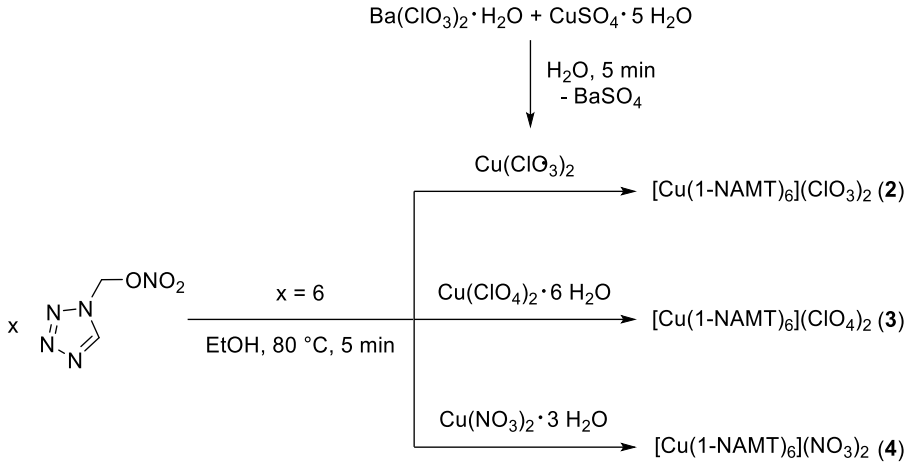

Scheme 2. Preparation of $[Cu(1\text{-}NAMT)_6](ClO_3)_2$ (**2**), $[Cu(1\text{-}NAMT)_6](ClO_4)_2$ (**3**) and $[Cu(1\text{-}NAMT)_6](NO_3)_2$ (**4**).

Compounds **5**–**8** were synthesized by adding the corresponding free nitroaromatic acid to a suspension of basic copper carbonate in water and stirring at 80 °C until a clear solution is obtained (Scheme 3). The solutions are left for crystallization for several days.

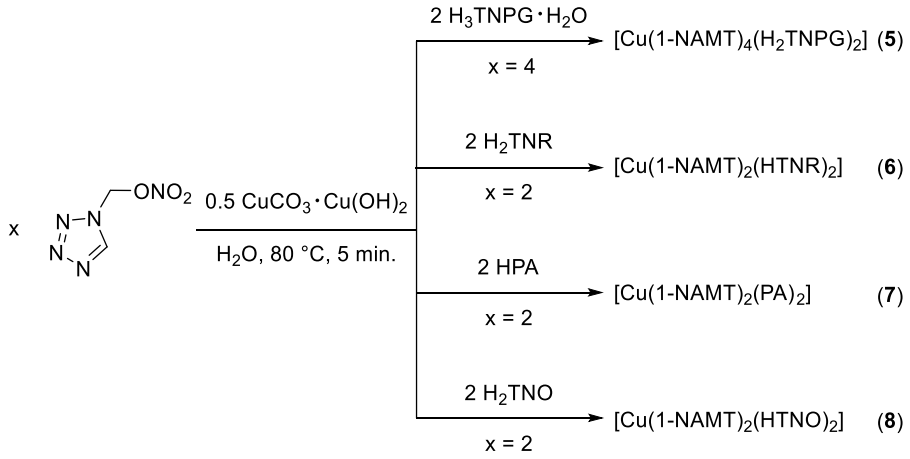

Scheme 3. Preparation of several copper trinitrophenolate complexes of **1** and nitroaromatic acids: Trinitrophloroglucinol monohydrate, $H_3TNPG \bullet H_2O$; Styphnic acid, H_2TNR; Picric Acic, HPA; and Trinitro orcinol, H_2TNO.

3.2.3 Crystal Structures

The obtained compounds were further analyzed by low-temperature single crystal X-Ray diffraction analysis. The low-temperature densities of all compounds are recalculated ($d_{298\,K} = \frac{dT}{1+\alpha_V(298-T_0)}$; $\alpha_V = 1.5 * 10^{-4}K^{-1}$) to their respective density at room temperature. The data and parameters of the measurements as well as the refinements are given in the supporting information Table S1. The crystal datasets are uploaded to the CSD database and can be obtained free of charge with CCDC 2176031 (**1**), 2176030 (**2**), 2176033 (**3**), 2176032 (**4**), 2176035 (**5**), 2176029 (**6**), 2176036 (**7**), 2176034 (**8**). These data can be obtained via https://www.ccdc.cam.ac.uk/structures/, or by emailing data_request@ccdc.cam.ac.uk, or by contacting The Cambridge Crystallographic Data Centre, 12 Union Road, Cambridge CB2 1EZ, UK; fax +44 1223 336033.

Compound **1** crystallizes as colorless platelets in the orthorhombic space group $P2_12_12_1$, with a density of 1.68 g cm^{-3} and four formula units in the unit cell (Figure 2A). The bond lengths within the tetrazole moiety are in the expected range for 1*N*-substituted tetrazoles.[17, 23] The tetrazole unit forms a nearly perfect level plane together with the methylene moiety, which is marginally protruding by 0.3 °. A second plane is also constructed by the methylene carbon atom with the planar nitrate group. Both planes are intersecting at an angle of 111 °, which derives from the sp^3-hybridization of the methylene carbon atom. The bond lengths within the nitrate group are similar to comparable nitrate esters [19, 24] with an elongated bond of 1.42 Å between O1–N5, and two nearly equivalent bonds of 1.20 Å between O2–N5 and O3–N5. Figure 2B shows the crystal packing of **1** along the *c* axis. This highlights the screw axis along *c*, which leads to a slight offset of the methylene groups of two stacked molecules of **1**. This results in a clear distinction of areas of stacked but twisted nitrate units (red blocks) and tetrazole moieties (blue pentagons). Interestingly, there are only non-classical hydrogen bond between two tetrazole rings without any participation in hydrogen bonding of the nitrate moieties. For all ECCs, octahedral coordination of the copper(II) centers are observed. All three ECCs crystallize isotypically in the trigonal space group $\bar{R}3$ with calculated densities of 1.77 g cm^{-3} (**2**) 1.80 g cm^{-3} (**3**), 1.76 g cm^{-3} (**4**) as well as three units per unit cell. In the molecular structures, **2**–**4** (Figures 3–5) show almost perfect octahedral coordination of the copper(II) cation with only slightly

tilted axes but Cu–N distances of 2.12 Å. Due to the symmetry the expected Jahn-Teller distortion (always present for Cu^{2+} d^9 systems) cannot be allocated.

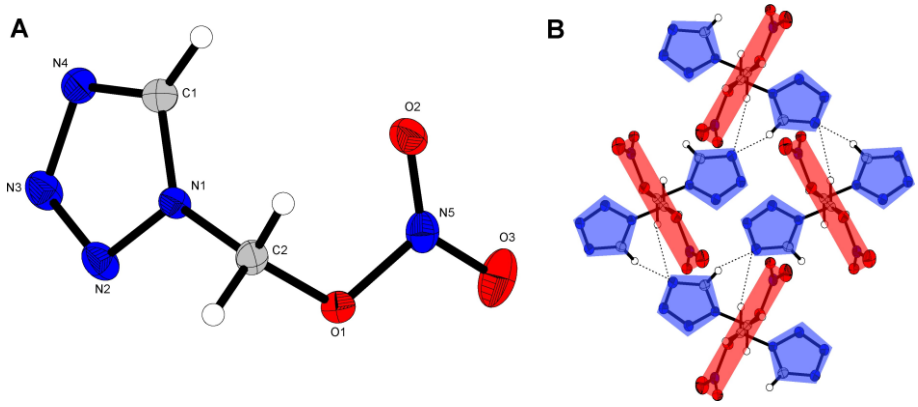

Figure 2. A) Molecular structure of 1-(Nitratomethyl)tetrazole (**1**); B) crystal packing of **1** along the *c* axis highlighting areas of stacked nitro groups (red) and tetrazole moieties (blue); all ellipsoids are shown with a probability of 50 %; selected bond lengths [Å]: N1–C2 1.44(2), O1–C2 1.43(2), O1–N5 1.42(2), O2–N5 1.20(2), O3–N5 1.20(2); Angles [°]: O1–C2–N1 111.00(15), N5–O1–C2 113.46(14), O1–N5–O2 117.83(16), O1–N5–O3 111.50(16); torsion angles [°]: N1–N2–N3–N4 −0.3(2), C2–O1–N5–O2 −6.0(2).

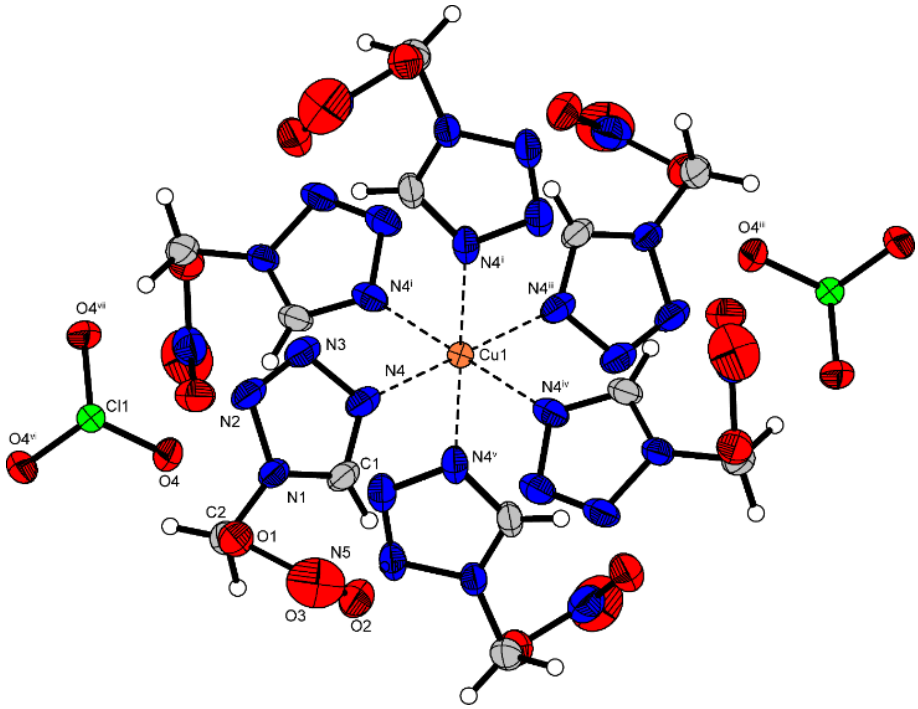

Figure 3. Molecular structure of $[Cu(1\text{-}NAMT)_6](ClO_3)_2$ (**2**). Selected bond lengths [Å]: Cu1–N1 2.13(2); selected bond angles [°]: N1–Cu1–N1^{iii} 92.49(9), N1–Cu1–N1^{v} 180.00, N1–Cu1–N1^{vi} 87.51(9).

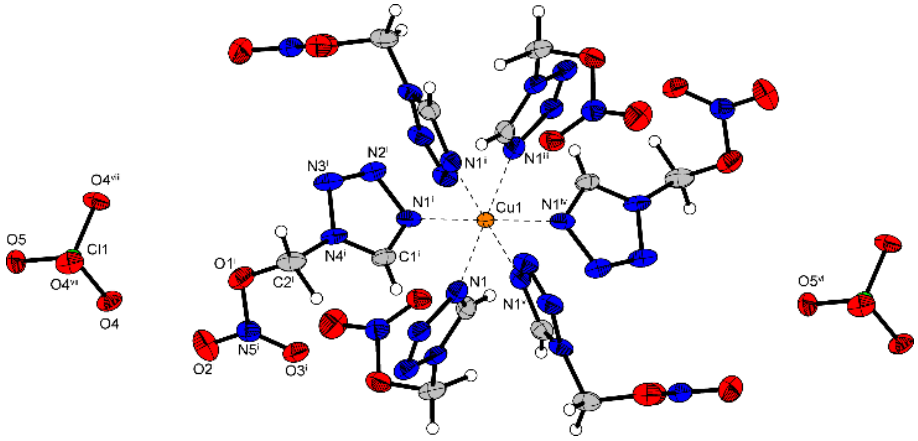

Figure 4. Molecular structure of $[Cu(1\text{-}NAMT)_6](ClO_4)_2$ (**3**). Selected bond lengths [Å]: Cu1–N1 2.12(5); selected bond angles [°]: N1–Cu1–N1^{iv} 91.83(17), N1–Cu1–N1^{vii} 88.16(17), N1–Cu1–N1^{v} 180.00.

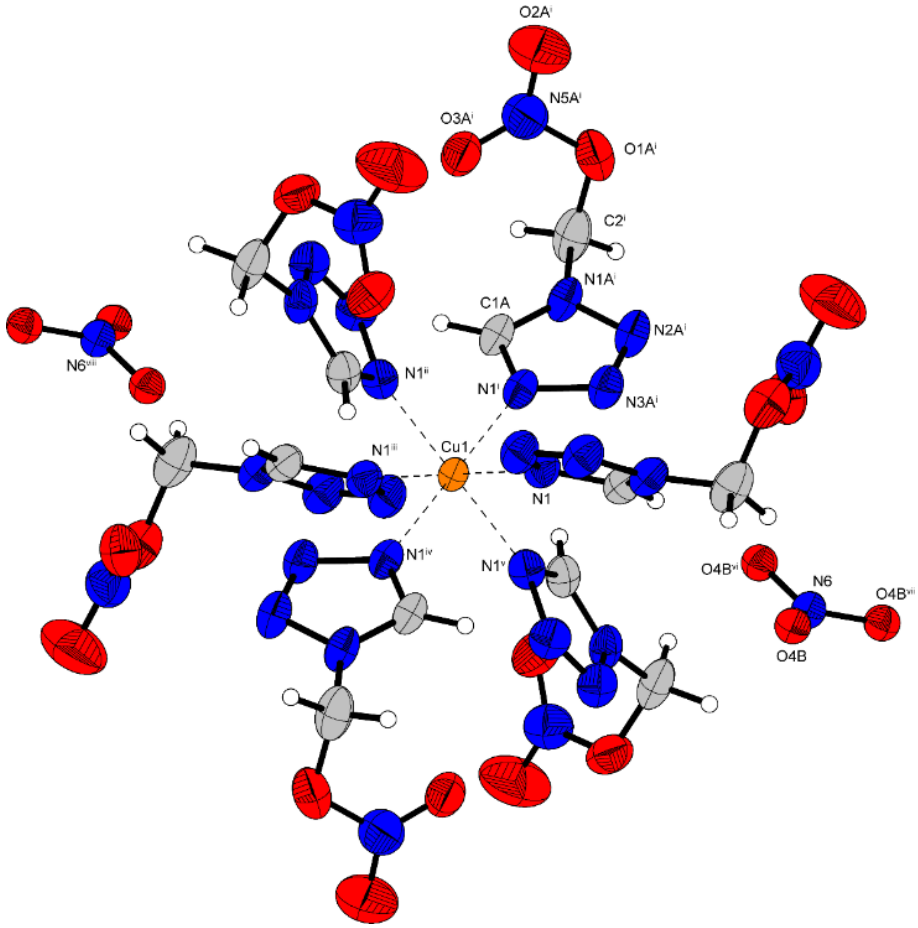

Figure 5. Molecular structure of $[Cu(1\text{-}NAMT)_6](NO_3)_2$ (**4**). Selected bond length (Å): Cu1–N1 2.12(3). Selected bond angles (°): N1–Cu1–N1^{i}, N1–Cu1–N1^{ii}, N1–Cu1–N1^{iii}, N1–Cu1–N1^{iv}, N1–Cu1–N1^{v}.

Compound **5** crystallizes in the triclinic space group *P*−1 with a density of 1.88 g cm^{-3} and one molecular formula in the unit cell (Figure 6). The copper(II) cation is sixfold

coordinated by two single deprotonated trinitro phloroglucinate anions as well as four molecules of **1** forming a distorted octahedron. The four ligands of **1** are positioned in the equatorial plane with bond lengths of 2.00 Å (Cu1–N4) and 2.03 Å (Cu1–N9), with minor deviations of 1.4 ° (N4–Cu1–N9) from the ideal 90 °. The anions are positioned in the axial position with bond lengths of 2.32 Å. This distortion is caused by a high steric demand of the anions together with copper(II) being a d^9 cation with an electronic configuration of $t_{2g}^6e_g^3$, ultimately leading to a degradation of the z^2-orbital. This causes a *Jahn-Teller*-like distortion. As displayed in Figure 6, the trinitro phloroglucinate anions form intermolecular hydrogen bonds between the two hydroxy groups and the *para*-positioned nitro group, which is hence nearly perfectly planar with the aromatic ring. This ultimately leads to a rotation of the two remaining nitro groups out of plane, positioning them in an orientation disfavoring a coordination of the metal center by the nitro groups, as is observed in comparable compounds [11].

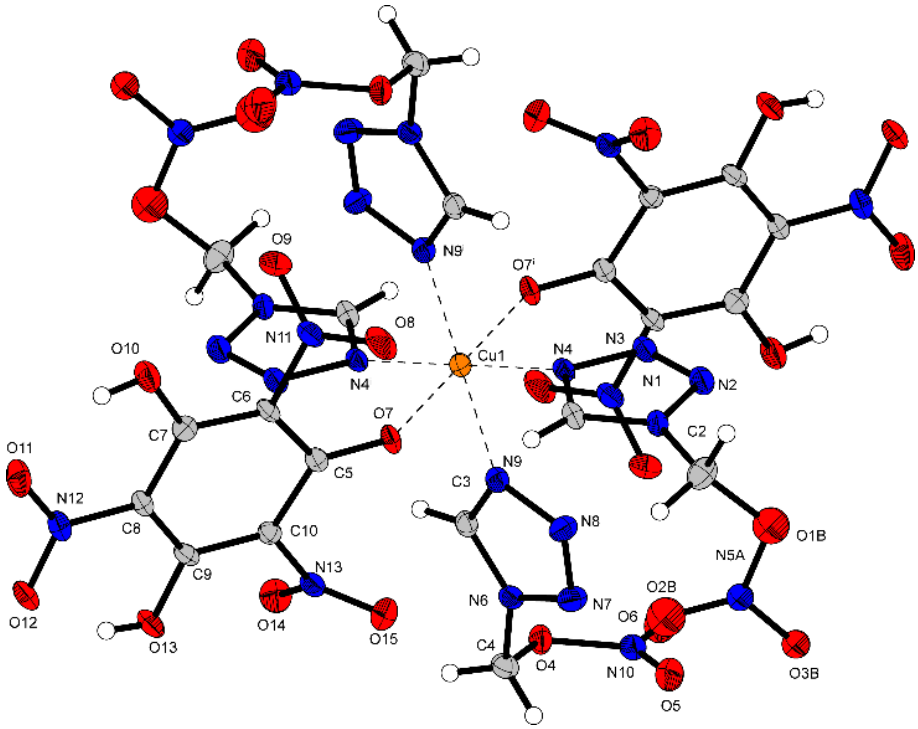

Figure 6. Octahedral coordination in [Cu(1-NAMT)$_4$(H_2TNPG)$_2$] (**5**). Selected bond lengths [Å]: Cu1–O7 2.32(19), Cu1–N4 2.00(3), Cu1–N9 2.03(2); selected bond angles [°]: O7–Cu1–N4 85.05(8), O7–Cu1–N9 89.14(8), N4–Cu1–N9 88.60(10).

Compound **6** (Figure 7) crystallizes in the triclinic space group *P*−1 with a density of 1.88 g cm^{-3} and one formula unit in the unit cell. The copper(II) cation is sixfold coordinated by two single deprotonated anions as well as two molecules of **1** in the form

of a *Jahn-Teller*-like distorted octahedron, like in compound **5**. The equatorial plane is built by the two ligands of **1** with bond lengths of 2.00 Å and the two deprotonated hydroxy groups of the anions with bond lengths of 1.93 Å. The absence of a third hydroxy group, like in the anions of **5**, leads to only one nitro group being rotated out of the aromatic ring plane, which now enables the remaining level nitro group (N6) to additionally coordinate to the metal cation. This results in the occupation of four coordination sites of the copper(II) cation by the anions, thus only two sites remain to be coordinated by molecules of **1**.

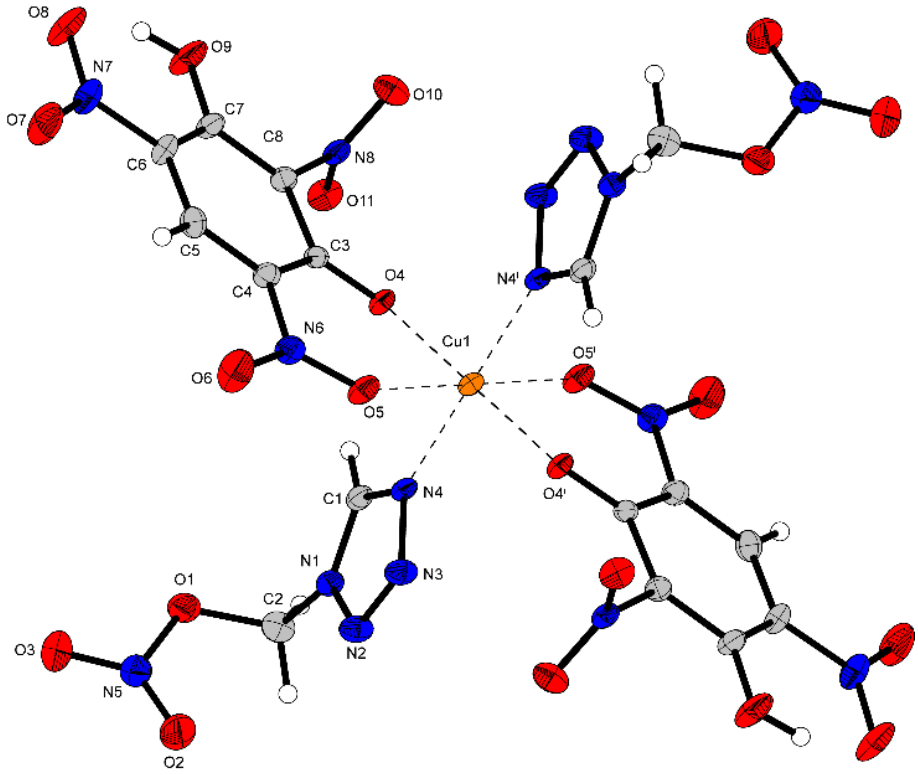

Figure 7. Molecular structure of $[Cu(1\text{-}NAMT)_2(HTNR)_2]$ (**6**) showing a *Jahn-Teller*-like distorted coordination sphere. Selected bond lengths [Å]: Cu1–O4 1.93(16), Cu1–O5 2.33(2), Cu1–N4 2.00(2); selected bond angles [°]: O4–Cu1–O5 81.77(7), O4–Cu1–N4 89.48(7), O5–Cu1–N4 86.14(7).

Compound **7** (Figure 8) crystallizes in the monoclinic space group $P2_1/c$ with two formula units in the unit cell and a density of 1.91 g cm^{-3}, the highest of all herein investigated compounds. Like in **6**, the copper(II) cation is coordinated in a *Jahn-Teller*-like distorted octahedron, with an equatorial plane build by two ligands of **1** and the two deprotonated hydroxy groups of the picrate anions. Here, the bond lengths are similar to those previously observed with a length of 1.90 Å and 2.01 Å, respectively for the deprotonated hydroxy groups and the tetrazole ligands. Like for the styphnate anions, the absence of hydroxy

groups leads to a nearly perfectly planar anion, again enabling the additional coordination of the copper(II) cation by the nitro groups.

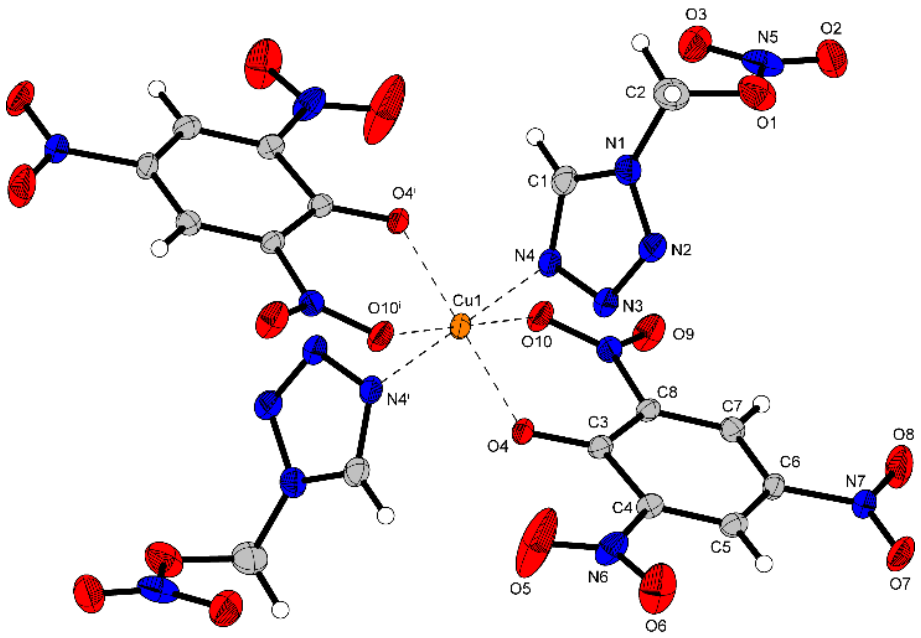

Figure 8. Coordination center of $[Cu(1\text{-NAMT})_2(PA)_2]$ (**7**). Selected bond lengths [Å]: Cu1–O4 1.93(2), Cu1–O10 2.30(3), Cu1–N4 2.01(3); selected bond angles [°]: O4–Cu1–O10 80.27(11), O4–Cu1–N4 92.29(11), O10–Cu1–N4 90.92(12).

Compound **8** crystallizes in the triclinic space group *P*−1 with a density of 1.87 g cm^{-3} and one formula unit in the unit cell. Like in the previously discusses nitroaromatic ECCs, the copper(II) cation is sixfold coordinated in the form of a distorted octahedron. The equatorial plane is again built by two molecules of **1** as well as the deprotonated hydroxy groups, whereas the coordinating nitro groups are positioned in axial position. Here, the bond lengths towards all coordinating atoms are in the same range as previously observed (Figure 9). Interestingly, the introduction of one methyl group to the styphnate anion leads to a slight rotation (14.6 °) of the nitro group (N1), which is normally planar to the aromatic ring due to stabilization by the hydroxy group. A more drastic change is observed for the coordinating nitro group (N2) which is now clearly twisted out of the plane (36.4 °) compared to the coordinating nitro group of the styphnate anions of **6**. Nevertheless, this rotation lead to a slightly decreased Cu(II)–NO_2 (κO) bond length of 2.28 Å compared to that of compounds **6** (2.32 Å) and **7** (2.30 Å).

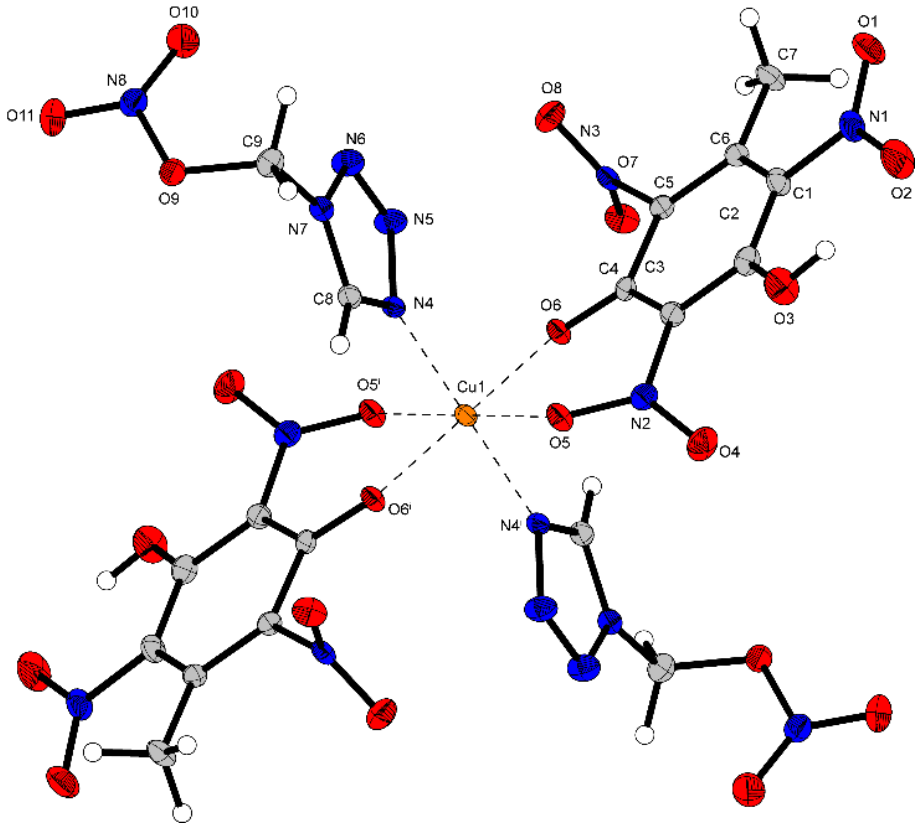

Figure 9. Molecular structure of $[Cu(1\text{-}NAMT)_2(HTNO)_2]$ (**8**). Selected bond lengths [Å]: Cu1–O5 2.28 (14), Cu1–O6 1.92(14), Cu1–N4 2.02(18); selected bond angles [°]: O5–Cu1–O6 83.60(5), O5–Cu1–N4 90.72(6), O6–Cu1–N4 90.37(7).

3.2.4 Physicochemical Properties

3.2.4.1 Characterization of 1-NAMT

Table 1 compares the physical and energetic properties of compound **1** with its structural related compounds 1-(azidomethyl)-tetrazole (AzMT), 1-(nitratoethyl)-tetrazole (1-NET). Here, an increase in density of +0.13 g cm^{-3} is observed when changing from the explosophoric azide (AzMT) functionalization to a nitrate ester. A more drastic change is observed when comparing the enthalpies of formation, where **1** (187 kJ mol^{-1}) is a significantly less endothermic compound than AzMT (655 kJ mol^{-1}), which directly derives from the lack of two N-N double bonds found in the azide functionality. Comparing the energetic properties of all three compounds, calculated with the EXPLO5 [25, 26] program code, a clear increase in performance is observed for the methyl-containing (**1** and AzMT) compounds over the ethyl-containing 1-NET. Compound **1** exhibits a detonation velocity of 8294 m s^{-1}, slightly outperforming AzMT with a detonation velocity of 8124 m s^{-1}, whereas 1-NET does not reach a detonation velocity of over 8000 m s^{-1}. Overall, the nitrate

ester **1** outperforms its structural analogous azides (AzMT), expressing the high importance of a high theoretical maximum density (TMD), which is even able to compensate the lack of enthalpy of formation. Interestingly, 1-NET is completely insensitive towards friction (>360 N) and moderately sensitive towards impact (10 J). By shortening the alkyl-chain the sensitivities are drastically increased, as compound **1** (<1 J, 9 N) exhibits sensitivities in the range of a primary explosive. Even higher sensitivities were reported for AzMT (<1 J, 2 N).

Table 1. Energetic properties of 1-NAMT (**1**), compared to AzMT, and 1-NET.

	1-NAMT (**1**)	AzMT	1-NET
Formula	$C_2H_3N_5O_3$	$C_2H_3N_7$	$C_3H_5N_5O_3$
M [g mol^{-1}]	145.08	125.1	159.1
ρ [g cm^{-3}]	1.68[a]	1.55[a]	1.55[b]
N / N+O [%][c]	48.27 / 81.35	78.38 / 78.38	44.02 / 74.19
Ω_{CO} [%][d]	−5.51	−70.34	−25.14
IS [J][e]	<1	<1	10
FS [N][f]	9	2	>360
ESD [mJ][g]	150	540	n.d.
T_{exo} [°C][h]	119	167	168
$\Delta_f H°$ [kJ mol^{-1}][i]	187	655	174
$\Delta_f H°$ [kJ kg^{-1}][j]	1398	5232	1094
	EXPLO5 V6.05.04		
$-\Delta_{ex}U°$ [kJ kg^{-1}][k]	5301	5127	4861
T_{det} [K][l]	3789	3473	3336
V_0 [L kg^{-1}][m]	451	502	815
P_{CJ} [kbar][n]	280	229	215
V_{det} [m s^{-1}][o]	8294	8124	7583

[a] From single crystal X-ray diffraction analysis recalculated to room temperature. [b] Measured with a gas pycnometer. [c] Nitrogen and combined nitrogen +oxygen content. [d] Oxygen balance towards the formation of CO. [e] Impact sensitivity (BAM drop hammer test). [f] friction sensitivity (BAM friction tester). [g] Electrostatic discharge sensitivity (OZM XSpark10). [h] DTA onset temperature of exothermic decomposition at a heating rate of 5 °C min^{-1}. [i] Calculated enthalpy of formation (CBS-4M + atomization method). [j] Calculated mass related enthalpy of formation. [k] Energy of explosion. [l] Detonation temperature. [m] Volume of detonation products (assuming only gaseous products). [n] Detonation pressure at Chapman-Jouguet point. [o] Detonation velocity.

Hirshfeld surface analysis of compound **1** and AzMT (Figure 10), shows the intermolecular contacts for each type of atoms within the molecules. Here, generally destabilizing N···N, N···O, and O···O contacts are observed for compound **1**, contributing to the surface by 40 %. Contrary, stabilizing contacts such as O···H, and N···H make up 50 % of the Hirshfeld surface, showing a nearly equal distribution of destabilizing to stabilizing contacts for compound **1**. Additionally, all repulsive interactions exhibit very long distances of over 2.9 Å, while for the stabilizing interactions distances of 2.2 Å are observed. For AzMT the Hirshfeld surface consists of 29 % destabilizing contacts, whereas attractive N···H contacts alone build up 63 % of the surface. Here, also long contact

distances of over 3.0 Å are observed for the destabilizing contacts, with distances of 2.4 Å for the destabilizing contacts. Therefore, the stabilizing interactions in **1** seem to be a little stronger than in AzMT, which is correlating with the measured friction sensitivities, showing a more sensitive AzMT (2 N) than 1-NAMT (9 N). The same correlation is not observed for the impact sensitivity, which is mostly due to both compounds exhibiting sensitivities below the limit of measurement of 1 J. Therefore, no distinction between both compounds can be concluded based on their impact sensitivity. Differential thermal analysis (DTA) of compound **1** observed an endothermic event at 57 °C (Figure 11), which was confirmed as a melting point by a conducted thermal gravimetric analysis (TGA). The exothermic event happening in the DTA at 119 °C correlates to the decomposition temperature, confirmed by the TGA measurement, showing a major mass loss of 58.6 % between 123–174 °C. Therefore, 1-NAMT is significantly less thermally stable compared to its azide analogous (167 °C) as well as compared to 1-NET (168 °C).

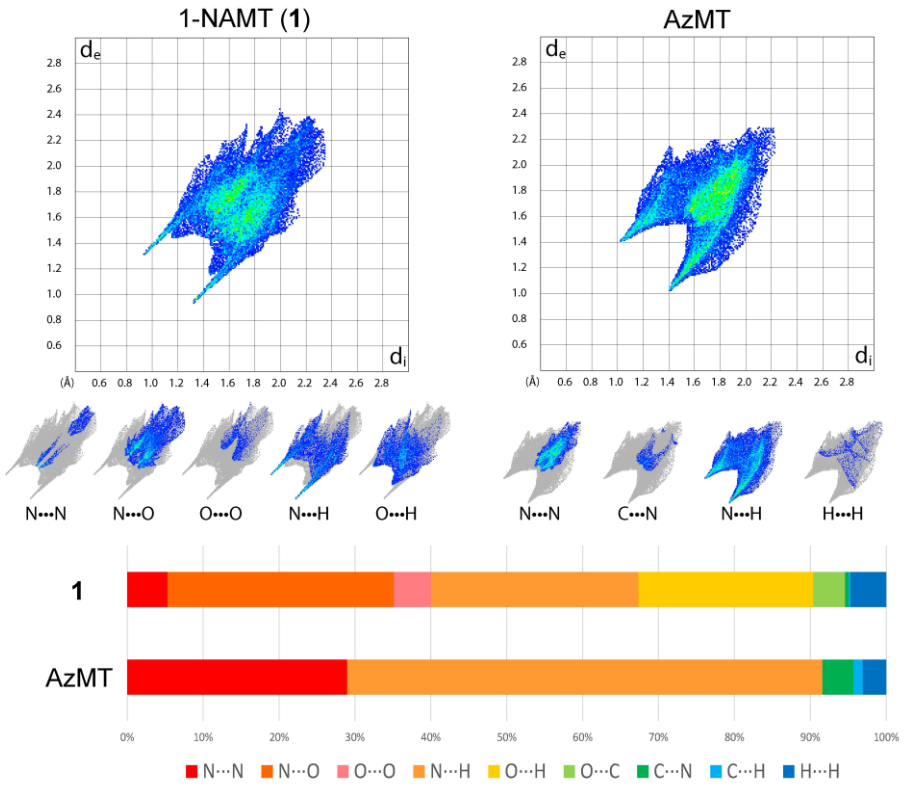

Figure 10. Hirshfeld analysis of compound **1** compared to AzMT. Stabilizing interactions observed in **1** are a shorter, hence stronger than in AzMT.

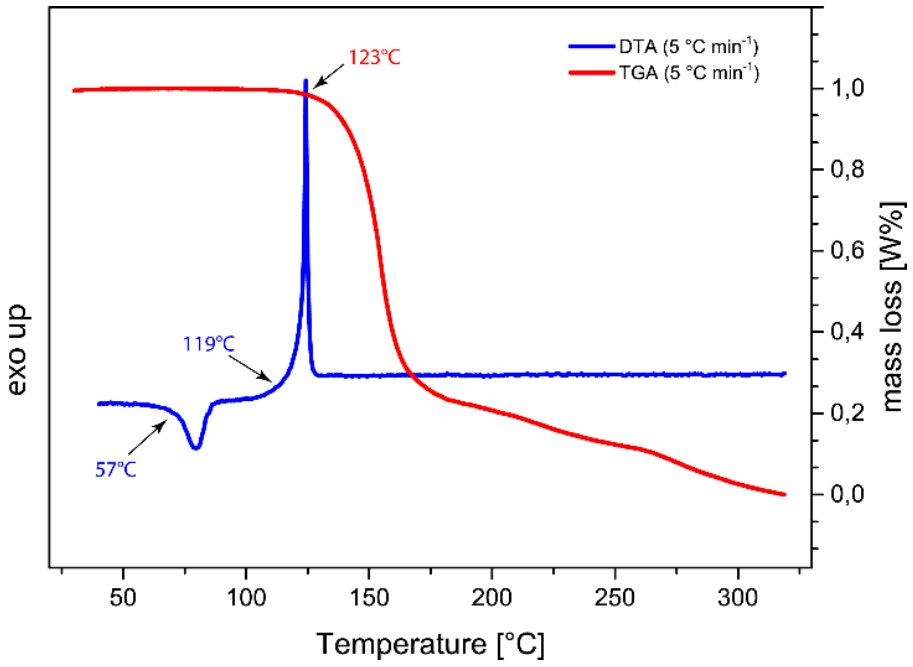

Figure 11. Combined DTA and TGA measurement of compound **1** with heating rates of 5 °C min^{-1}, exhibiting a melting of **1** at 57 °C and an exothermic decomposition at 119 °C.

3.2.4.2 Characterization of the ECCs

The thermal stabilities of all ECCs were analyzed by DTA measurements (Figure 12) with a heating rate of β = 5 °C min^{-1}. Additionally, the sensitivities towards impact, friction and electrostatic discharge were measured according to BAM [27] standards (Table 2). Compound **2** exhibits an exothermic decomposition at 145 °C, while **3** and **4** exhibit exothermic decomposition temperatures of about 120 °C, which is equivalent to that of pure ligand **1**. Additionally, the DTA of **4** shows an endothermic event happening at 102 °C, which derives from a melting of the compound shortly before decomposition, which is confirmed by *Büchi* melting point analysis. For all nitroaromatic ECCs (**5**–**8**), exothermic decomposition, without any endothermic events happening before, was observed. Generally, a significant increase in stability of the ECCs compared to the pure ligand is observed for compounds **6**, **7**, and **8**. Compound **5** exhibits a thermal stability of 135 °C, which is rather low compared to those of **6** (176°C), **7** (181°C) and **8** (161°C). This can be explained by the higher ligand to metal salt ratio of **5** (4:1) compared to the other nitroaromatic compounds (2:1). Therefore, the overall low thermal stability of 1 is inherited to the resulting ECC. On the other hand, the more balanced (2:1) ratio of ligand to metal salt of compounds **6**–**8**, leads to a stabilization of the low thermal stability of **1** by the nitroaromatic anions, which is contrary to previous findings [11, 23, 28]. While a stabilizing

effect was previously observed for some cases [28], it was never as significant as in this study. The drastic increase in thermal stability is most likely owing to the low thermal stability of **1**, resulting in high relative differences between the pure ligand and the resulting ECCs.

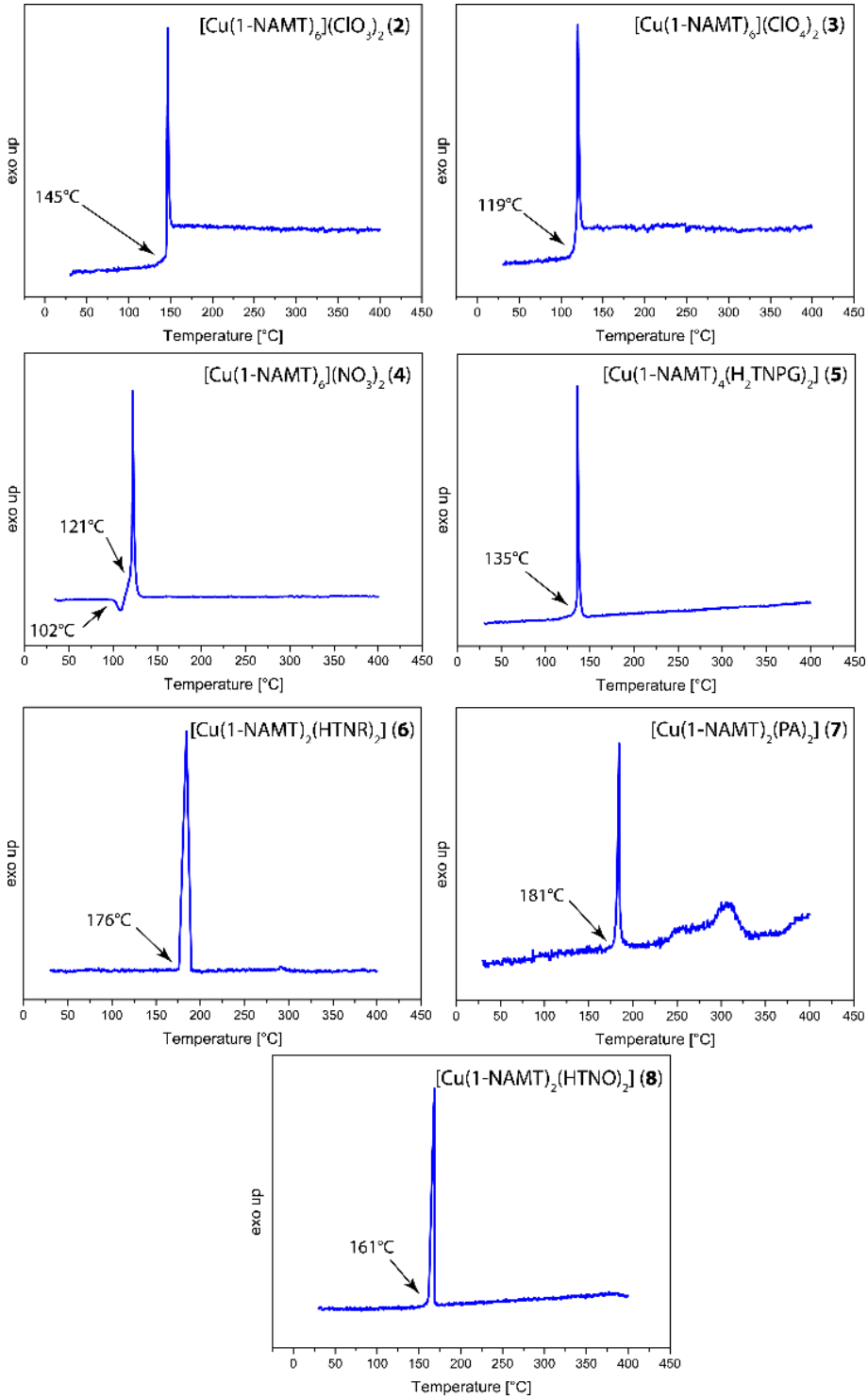

Figure 12. Differential thermal analysis of ECCs **2**–**8** with heating rate of 5 °C min^{-1}.

Following an increment method by Ilyushin [29], it was possible to estimate the detonation velocities of all ECCs, except for **2**, due to the unavailability of data for chlorate anions (Table 2). Detailed information can be found in the Supporting Information. Overall, a slight decrease in detonation velocity compared to the pure ligand is observed. Compounds **3** and **4** exhibit velocities between 7800–7900 m s^{-1}, which is about 300m s^{-1} slower than pure **1**. Generally, for the nitroaromatic ECCs **5**–**8** a more distinct decrease is observed. Compounds **6** and **7** have estimated detonation velocities of below 7800 m s^{-1}, while for **8** a velocity of 7500m s^{-1} was calculated. Interestingly, **5** shows the highest estimated detonation velocity (7918 m s^{-1}) by far surpassing the other nitroaromatic ECCs. Due to the incremental method, a higher contribution of ligand **1** to the detonation velocity is introduced, since the ligand to metal salt ratio differs between **5** (4:1) and **6**–**8** (2:1). Overall, all herein synthesized compounds outperform lead azide (6187 m s^{-1}) as well as lead styphnate (6137 m s^{-1}) by at least 21 %.

3.2.4.3 Sensitivities

According to the UN Recommendation on the Transport of Dangerous Goods [30] compound **1** has to be classified as extremely sensitive with an impact sensitivity of <1 J and a friction sensitivity of 9 N. It is significantly more sensitive towards an electrostatic discharge (150 mJ) compared to AzMT (540 mJ) but less sensitive than typical primaries such as lead azide (Table 2). Compound **2**–**8** are also extremely sensitive towards impact, all exhibiting a sensitivity <1 J, except compound **3**, having an impact sensitivity of 2 J. Therefore, all ECCs exhibit a higher impact sensitivity than lead azide (LA) or lead styphnate (LS). While no clear trend in stability is deriving from the impact sensitivities, the formation of ECCs **2**–**4** results in compounds distinctively more sensitive towards friction than pure compound **1**. While all three compounds are classified as extremely sensitive towards friction, the nitrate compound **4** (5 N), is less sensitive than the chlorate (**2**, 0.4 N) and perchlorate (**3**, 0.75 N) compound, which are on par with LA and LS. The ECCs containing nitroaromatic anions, on the other hand, show a stabilization of **1**, as their friction sensitivities are lowered compared to pure **1**. Interestingly, compound **5** (72 N) is less sensitive than compound **6** (40 N), which is contrary to the higher amount of 1-NAMT in compound **5** than in **6**. While compound **8** exhibits a friction sensitivity (84 N) comparable to that of **5**, compound **7** (120 N) exhibits the lowest friction sensitivity of all herein analyzed compounds, highlighting the high stability of the picrate anion. All ECC exhibit an ESD sensitivity (90–160 mJ) comparable to pure **1** (150 mJ), the only exception

being compound **4** exhibiting a sensitivity of 13 mJ. Nonetheless, all compounds are less sensitive than LA (5–8 mJ) or LS (0.04–1 mJ). [31, 32]

Table 2. Overview of the thermal stability and sensitivity toward external stimuli.

Compound		$T_{endo.}$ [°C][a]	$T_{exo.}$ [°C][b]	*IS* [J][c]	*FS* [N][d]	*ESD* [mJ][e]	V_{det} [m s^{-1}][f]
1-NAMT	**1**	57	119	<1	9	150	8294
$[Cu(1\text{-}NAMT)_6](ClO_3)_2$	**2**	–	145	<1	0.4	139	–[h]
$[Cu(1\text{-}NAMT)_6](ClO_4)_2$	**3**	–	119	2	0.75	13	7910[h]
$[Cu(1\text{-}NAMT)_6](NO_3)_2$	**4**	102	121	<1	5	90	7865[h]
$[Cu(1\text{-}NAMT)_4(H_2TNPG)_2]$	**5**	–	135	<1	72	160	7918[h]
$[Cu(1\text{-}NAMT)_2(HTNR)_2]$	**6**	–	176	<1	40	140	7715[h]
$[Cu(1\text{-}NAMT)_2(PA)_2]$	**7**	–	181	<1	120	90	7767[h]
$[Cu(1\text{-}NAMT)_2(HTNO)_2]$	**8**	–	161	<1	84	90	7507[h]
LA [33, 34]		–	320–350	4	≤0.1	5–8	6187[g]
LS [33, 34]		–	260–310	8	0.45	0.04–1	6138[g]

[a] endothermic peak, which indicates melting of the substance; [b] exothermic peak, which indicates decomposition; [c] impact sensitivity (BAM drop hammer test); [d] friction sensitivity (BAM friction tester); [e] electrostatic discharge sensitivity (OZM XSpark10); [f] Details can be found in the SI. [g] calculated with EXPLO5_V6.05.04. [h] estimated via the incremental method by Ilyushin [29].

3.2.4.4 Initiation Capabilities

To get an insight into the behavior of the sample towards fast heating with and without confinement, hot plate (HP) and hot needle (HN) tests were performed. These tests allow for a first evaluation of their capability to be applied as primary explosives. Detailed procedures for HP and HN tests are given in the Supporting Information. While the HP reflects on the behavior towards fast heating without confinement, the HN test allows for an assessment of the compound's behavior upon fast heating with confinement. Table 3 summarizes the results from HN and HP tests of all compounds. Here, all compounds showed deflagration, except compound **2** showing detonation. Thus only **2** exhibits detonation behavior which is crucial to be applied as detonating primary explosives. While HP and HN tests asses the susceptibility towards initiation by heat and flame, the possibility of ignition by laser impulse cannot be concluded and was additionally tested (Table 4).

Table 3. Results from HN, HP and initiation tests.

Compound	HP	HN
2	def.	det.
3	def.	def.
4	def.	def.
5	def.	def.
6	def.	def.
7	def.	def.
8	def.	def.

def. = deflagration; det. = detonation

All ECCs were directly irradiated by a single-pulsed 45 W InGaAs laser diode. About 25 mg of each compound was pressed into a transparent polycarbonate percussion cap and sealed with UV curing adhesive. The sample was placed in the focused beam path and irradiated with a single laser pulse with a wavelength of 915 nm, a voltage of 4 V, a current of 6–7 A, and a pulse length of 0.1, 1.0, 15, or 30 ms. The results of these experiments are listed in Table 4.

Table 4. Results of laser initiation of compounds 2–8.

Compound	6 A	7 A		
2	τ = 0.1 ms x	τ = 0.1 ms det.	τ = 1 ms det.	–
3	–	τ = 0.1 ms det.	–	–
4	τ = 0.1 ms x	τ = 0.1 ms det.	–	–
5	τ = 0.1 ms x	τ = 1 ms def.	τ = 15 ms def.	τ = 30 ms def.
6	–	τ = 1 ms def.	τ = 15 ms def.	τ = 30 ms def.
7	–	τ = 1 ms x	τ = 15 ms x	τ = 30 ms x
8	–	τ = 1 ms dec.	τ = 15 ms dec.	τ = 30 ms dec.

Operating parameters: current I = 6 and 7 A; voltage U = 4 V; theoretical maximum output power P_{max} = 45 W; theoretical energy E_{max} = 0.1–17 mJ; wavelength λ = 915 nm; pulse length τ = 0.1–1 ms. (– = not tested; x = no ignition; dec. = decomposition; def. = deflagration; det. = detonation).

While compounds **2**–**4** exhibited no ignition at the lowest tested energy of 0.1 mJ, strong detonations were observed for all compounds already at 1.7 mJ, strong enough to destroy parts of the laser setup. The moment of detonation of compound **2** is shown in Figure 13A. Compound **5** showed no ignition at the lowest tested energy, and therefore this energy was not tested for all other nitroaromatic compounds. Nevertheless, **5** and **6** showed

deflagrations already at 17 mJ (Figure 13B/C), as well as at 255 and 510 mJ. Compound **7** shows no ignition at any of the tested energies (17, 255, and 510 mJ) which derives from the lower energetic character of the picrate anions compared to the styphnate and trinitrophloroglucinate anions. Compound **8** shows a slow burning of the material at all tested energies (Figure 13D). Due to the substitution of one hydroxy group of each trinitrophloroglucinate anion by methylene groups, the resulting ECC is lacking energetic performance, thus a self-sustained deflagration is not observed, which is additionally accompanied by the formation of soot.

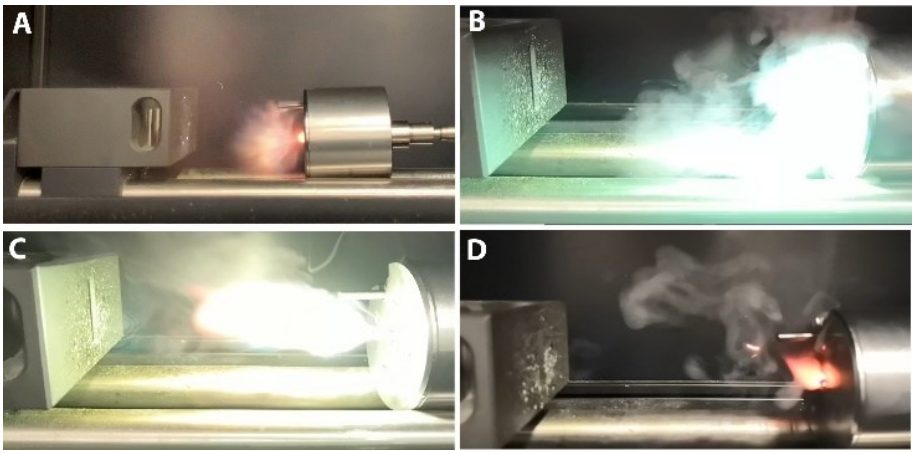

Figure 13. A: Moment of detonation of compound **2** at 1.7 mJ; B/C: moments of deflagration of compounds **5** and **6**; D: burning of compound **8**.

3.3 Conclusion

The synthesis of 1-(Nitratomethyl)tetrazole (1-NAMT, **1**) was possible by the nitration of the literature known isomeric mixture of 1- and 2-(hydroxymethyl)-tetrazole with acetyl nitrate in moderate yield (21 %). 1-NAMT was investigated by low temperature single crystal X-ray diffraction experiments, multinuclear ^{1}H, ^{13}C, ^{14}N NMR spectroscopy as well as elemental analysis and infrared spectroscopy. Differential thermal analysis observed a rather low thermal stability of **1** (119 °C) while BAM sensitivity measurements revealed a high impact (<1 J) and friction (9 N) sensitivity, both in the range of typical primary explosives. Comparing the molecular interactions of **1** with its structural analogous azide (AzMT) on the basis of Hirshfeld analysis, showed stronger stabilizing interactions for **1**, ultimately explaining the differences in friction sensitivities. **1** was further used as ligand for the formation of seven energetic coordination compounds of copper(II) chlorate (**2**), perchlorate (**3**), nitrate (**4**), trinitro phloroglucinolate (**5**), styphnate (**6**), picrate (**7**) and

trinitro-orcinolate (**8**). All ECCs were obtained pure according to elemental analysis and were further analyzed by low temperature single crystal X-ray diffraction experiments, accompanied by differential thermal analysis, infrared spectroscopy and their sensitivities towards external stimuli (IS, FS, and ESD) were measured according to BAM standards. For all ECCs an extremely high impact sensitivity of <1–2 J was observed, while compounds **2**–**4** exhibited increased friction sensitivities (0.4–5 N) compared to pure **1**. The nitroaromatic containing ECCs **5**–**8** exhibited friction sensitivities (40–120 N) in the range of a booster explosive. The thermal stabilities of **2**–**5** are in the same range (119–145 C) as the thermal stability of **1**. Interestingly, the formation of ECCs **6**–**8** led to a drastic increase of the thermal stability of **1**. Hot plate and needle tests revealed deflagration of all compounds, except for **2** showing a violent detonation in the hot needle test. Thus only **2** exhibits a fast DDT, which is necessary to be discussed as primary explosive. Further assessment of laser initiability was positive for compounds **2**–**4** already at low energies (1.7 mJ), while the nitroaromatic compounds showed deflagration or burning at all tested energies. Lastly, detonation velocity predictions suggested velocities of up to 7900 m s^{-1} for all ECCs investigated in this study.

3.4 Acknowledgement

Financial support of this work by the Ludwig Maximilian University of Munich (LMU), the Office of Naval Research (ONR) under grant no. N00014-19-1-2078 is gratefully acknowledged. The authors want to further thank Stefan Huber for sensitivity measurements.

3.5 References

[1] J. D. Watson, F. H. C. Crick, *Nature* **1953**, *171*, 737–738.

[2] G. Thews, Physiologie des Menschen, Eds. Springer Berlin Heidelberg: Berlin, Heidelberg, **1993**.

[3] P. Schwab, R. H. Grubbs, J. W. Ziller, *J. Am. Chem. Soc.* **1996**, *118*, 100–110.

[4] M. Scholl, S. Ding, C. W. Lee, R. H. Grubbs, *Org. Lett.* **1999**, *1*, 953–956.

[5] D. C. Hodgkin, J. Kamper, M. Mackay, J. Pickworth, K. N. Trueblood, J. G. White, *Nature* **1956**, *178*, 64–66.

[6] T. M. Klapötke, Chemistry of High-Energy Materials, 5th. ed., De Gruyter, Berlin, Boston **2019**.

[7] M. A. Ilyushin, I. V. Tselinsky, I. V. Bachurina, L. O. Novoselova, E. N. Konyushenko, A. S. Kozlov, Y. A. Gruzdev, *AIP Conference Proceedings* **2006**, 849, 213–217.

[8] T. M. Klapötke, M. Kofen, L. Schmidt, J. Stierstorfer, M. H. H. Wurzenberger, *Chem. Asian J.* **2021**, *16*, 3001–3012.

[9] M. Kofen, M. Lommel, J. Stierstorfer, T. M. Klapötke, *New Trends in Research of Energetic Materials* Pardubice, Czech Republic, **2022**, 114–118.

[10] N. Szimhardt, M. H. H. Wurzenberger, L. Zeisel, M. S. Gruhne, M. Lommel, J. Stierstorfer, *J. Mater. Chem. A* **2018**, *6*, 16257–16272.

[11] M. Kofen, M. Lommel, M. H. H. Wurzenberger, T. M. Klapötke, J. Stierstorfer, *Chem. Eur. J.* **2022**, *28*, e202200492.

[12] V. A. Ostrovskii, R. E. Trifonov, E. A. Popova, *Russ. Chem. Bull., Int. Ed.* **2012**, *61*, 768–780.

[13] A. E. Popova, V. A. Protas, E. R. Trifonov, E. R., *Anti-Cancer Agents Med. Chem.* **2017**, *17*, 1856–1868.

[14] S.-Q. Wang, Y.-F. Wang, Z. Xu, *Eur. J. Med. Chem.* **2019**, *170*, 225–234.

[15] N. Szimhardt, M. H. H. Wurzenberger, A. Beringer, L. J. Daumann, J. Stierstorfer, *J. Mater. Chem. A* **2017**, *5*, 23753–23765.

[16] M. A. Ilyushin, A. N. Terpigorev, I. V. Tselinskii, *Russ. J. Gen. Chem.* **1999**, *69*, 1645–1657.

[17] M. S. Gruhne, T. Lenz, M. Rösch, M. Lommel, M. H. H. Wurzenberger, T. M. Klapötke, J. Stierstorfer, *Dalton Trans.* **2021**, *50*, 10811–10825.

[18] O. N. Verkhozina, V. N. Kizhnyaev, L. I. Vereshchagin, A. V. Rokhin, A. I. Smirnov, *Russ. J. Org. Chem.* **2003**, *39*, 1792–1796.

[19] T. M. Klapötke, M. Kofen, J. Stierstorfer, *Dalton Trans.* **2021**, *50*, 13656–13660.

[20] Y. Li, W. Liu, S. Pang, *Molecules* **2012**, *17*, 5040–5049.

[21] A. R. Katritzky, C. N. Fali, I. V. Shcherbakova, S. V. Verin, *J. Heterocycl. Chem.* **1996**, *33*, 335–339.

[22] M. H. H. Wurzenberger, N. Szimhardt, J. Stierstorfer, *J. Am. Chem. Soc.* **2018**, *140*, 3206–3209.

[23] M. H. H. Wurzenberger, M. S. Gruhne, M. Lommel, N. Szimhardt, T. M. Klapötke, J. Stierstorfer, *Chem. Asian J.* **2019**, *14*, 2018–2028.

[24] E. C. Johnson, J. J. Sabatini, D. E. Chavez, R. C. Sausa, E. F. C. Byrd, L. A. Wingard, P. E. Guzmàn, *Org. Process Res. Dev.* **2018**, *22*, 736–740.

[25] M. Sućeska, *Propellants Explos. Pyrotech.* **1991**, *16*, 197–202.

[26] M. Sućeska, Explo5 V6.05.02, Zagreb (Croatia), **2018**.

[27] BAM www.bam.de (accessed March 2022).

[28] M. H. H. Wurzenberger, B. R. G. Bissinger, M. Lommel, M. S. Gruhne, N. Szimhardt, J. Stierstorfer, *New J. Chem.* **2019**, *43*, 18193–18202.

[29] M. A. Ilyushin, A. V. Smirnov, A. A. Kotomin, I. V. Tselinskii, *J. Energ. Mater.* **1994**, *2*, 16–20.

[30] W. Beck, J. Evers, M. Göbel, G. Oehlinger, T. M. Klapötke, *Z. Anorg. Allg. Chem.* **2007**, *633*, 1417–1422.

[31] M. B. Talawar, A. P. Agrawal, M. Anniyappan, D. S. Wani, M. K. Bansode, G. M. Gore, *J. Hazard. Mat.* **2006**, *137*, 1074–1078.

[32] K. Raha, J. S. Chhabra, *J. Hazard. Mat.* **1993**, *34* (3), 385–391.

[33] T. M. Klapötke, Energetic Materials Encyclopedia. 2nd ed.; DeGruyter: Berlin/Boston, **2021**; Vol. 1–3.

[34] M. S. Gruhne, M. Lommel, M. H. H. Wurzenberger, N. Szimhardt, T. M. Klapötke, J. Stierstorfer, *Propellants Explos. Pyrotech.* **2020**, *45* (1), 147–153.

3.6 Supporting Information

3.6.1 Compound Overview

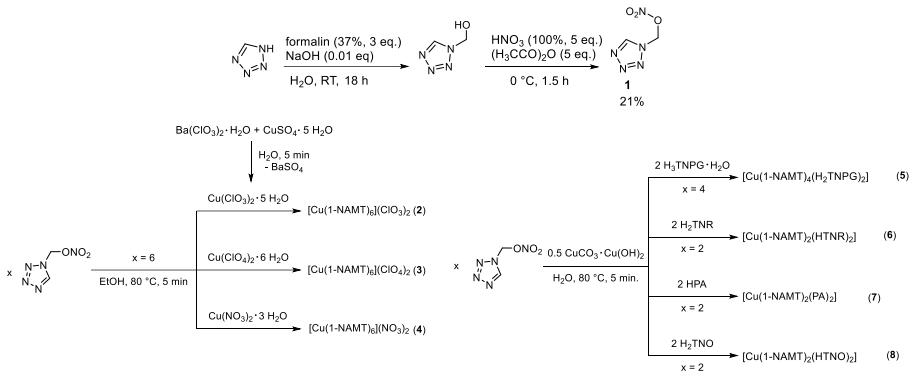

3.6.2 Single Crystal X-Ray Diffraction

For all crystalline compounds an Oxford Xcalibur3 diffractometer with a CCD area detector or Bruker D8 Venture TXS diffractometer equipped with a multilayer monochromator, a Photon 2 detector, and a rotating-anode generator were employed for data collection using Mo-K_α radiation ($\lambda = 0.7107$ Å). On the Oxford device, data collection and reduction were carried out using the CrysAlisPRO software. [S1] On the Bruker diffractometer, the data were collected with the Bruker Instrument Service v3.0.21, the data reduction was performed using the SAINT V8.18C software (Bruker AXS Inc., 2011). The structures were solved by direct methods (SIR-92, [S2] SIR-97, [S3,S4] SHELXS-97[S5,S6] or SHELXT[S7]), refined by full-matrix least-squares on $F2$ (SHELXL[S5,S6]) and finally checked using the PLATON software[S8] integrated in the WinGX[S7,S9] or Olex2[S8] software suite. The non-hydrogen atoms were refined anisotropically and the hydrogen atoms were located and freely refined. The absorptions were corrected by a SCALE3 ABSPACK or SADABS Bruker APEX3 multi-scan method. [S11,S12] All DIAMOND2 plots are shown with thermal ellipsoids at the 50 % probability level and hydrogen atoms are shown as small spheres of arbitrary radius.

Table S1. Crystallographic data and structure refinement details for compounds **1**–**3**.

	1	**2**	**3**
Formula	$C_2H_3N_5O_3$	$C_{12}H_{18}CuN_{30}O_{24}Cl_2$	$C_{12}H_{18}CuN_{30}O_{26}Cl_2$
FW [g mol^{-1}]	145.09	1101.00	1133.00
Crystal system	orthorhombic	trigonal	trigonal
Space group	$P2_12_12_1$ (No. 19)	R-3 (No.148)	R-3 (No.148)
Color / Habit	colorless platelet	blue platelet	colorless block
Size [mm]	0.02 x 0.09 x 0.10	0.05 x 0.30 x 0.35	0.02 x 0.03 x 0.04
a [Å]	6.8187(3)	10.5825(7)	10.5929(5)
b [Å]	8.4487(4)	10.5825(7)	10.5929(5)
c [Å]	9.6666(4)	31.031(4)	31.436(3)
α [°]	90	90	90
β [°]	90	90	90
γ [°]	90	120	120
V [Å^3]	556.89(4)	3009.6(6)	3054.8(5)
Z	4	3	3
$\rho_{calc.}$ [g cm^{-3}]	1.731	1.822	1.848
μ [mm^{-1}]	0.158	0.803	0.797
F(000)	296	1665	1713
$\lambda_{MoK\alpha}$ [Å]	0.71073	0.71073	0.71073
T [K]	102	111	107
θ Min-Max [°]	3.2, 26.4	2.3, 26.3	2.6, 25.4
Dataset	-8:8; -10:10; -12:12	-13:13; -10:13; -38:36	-12:12; -12:12; -37:37
Reflections collected	8145	8370	16560
Independent refl.	1138	1359	1253
R_{int}	0.030	0.041	0.064
Observed reflections	1090	1101	1032
Parameters	91	117	120
R_1 (obs)[a]	0.0257	0.0318	0.0529
wR_2 (all data)[b]	0.0637	0.0838	0.1352
S [c]	1.14	1.06	1.13
Resd. dens [e Å^{-3}]	-0.17, 0.20	-0.21, 0.37	-0.38, 1.41
Device type	Bruker D8 Venture TXS	Oxford Xcalibur3	Bruker D8 Venture TXS
Solution	SHELXT	SHELXT	SHELXT
Refinement	SHELXL-2018	SHELXL-2018	SHELXL-2018
Absorption correction	multi-scan	multi-scan	multi-scan
CCDC	2176031	2176030	2176033

[a]$R_1 = \Sigma||F_0|-|F_c||/\Sigma|F_0|$; [b]$wR_2 = [\Sigma[w(F_0^2-F_c^2)^2]/\Sigma[w(F_0)^2]]^{1/2}$; $w = [\sigma c^2(F_0^2)+(xP)^2+yP]^{-1}$ and $P=(F_0^2+2F_c^2)/3$; [c]$S = \{\Sigma[w(F_o^2-F_c^2)^2]/(n-p)\}^{1/2}$ (n = number of reflections; p = total number of parameters).

Table S2. Crystallographic data and structure refinement details for compounds **4**–**6**.

	4	**5**	**6**
Formula	$C_{12}H_{18}CuN_{32}O_{24}$	$C_{20}H_{16}CuN_{26}O_{30}$	$C_{16}H_{10}CuN_{16}O_{22}$
FW [g mol^{-1}]	1058.12	1164.13	841.94
Crystal system	Trigonal	triclinic	triclinic
Space group	*R*-3 (No.148)	*P*-1 (No. 2)	*P*-1 (No. 2)
Color / Habit	blue block	green block	green block
Size [mm]	0.04 x 0.06 x 0.07	0.10 x 0.25 x 0.50	0.30 x 0.62 x 0.76
a [Å]	10.5666(3)	8.9582(5)	6.2404(6)
b [Å]	10.5666(3)	10.8979(6)	10.9239(10)
c [Å]	30.1912(19)	11.4623(6)	11.0430(11)
α [°]	90	88.678(4)	87.784(8)
β [°]	90	73.117(5)	73.859(9)
γ [°]	120	69.752(5)	86.409(8)
V [Å^3]	2919.3(3)	1000.87(11)	721.52(12)
Z	3	1	1
$\rho_{calc.}$ [g cm^{-3}]	1.806	1.931	1.938
μ [mm^{-1}]	0.692	0.690	0.887
F(000)	1605	587	423
$\lambda_{MoK\alpha}$ [Å]	0.71073	0.71073	0.71073
T [K]	106	101	103
θ Min-Max [°]	3.5, 28.3	2.5, 26.4	2.7, 26.4
Dataset	-14:14; -14:14; -40:40	-11:11; -13:13; -14:14	-6:7; -13:13; -13:13
Reflections collected	23575	11632	4860
Independent refl.	1623	4103	2935
R_{int}	0.039	0.040	0.024
Observed reflections	1463	3204	2573
Parameters	204	370	251
R_1 (obs)[a]	0.0465	0.0431	0.0359
wR_2 (all data)[b]	0.1163	0.1059	0.0942
S [c]	1.06	1.03	1.05
Resd. dens [e Å^{-3}]	-0.46, 0.44	-0.58, 0.40	-0.39, 0.70
Device type	Bruker D8 Venture TXS	Oxford Xcalibur3	Oxford Xcalibur3
Solution	SHELXT	SHELXT	SHELXT
Refinement	SHELXL-2018	SHELXL-2018	SHELXL-2018
Absorption correction	multi-scan	multi-scan	multi-scan
CCDC	2176032	2176035	2176029

[a]$R_1 = \Sigma||F_0|-|F_c||/\Sigma|F_0|$; [b]$wR_2 = [\Sigma[w(F_0^2-F_c^2)^2]/\Sigma[w(F_0)^2]]^{1/2}$; $w = [\sigma c^2(F_0^2)+(xP)^2+yP]^{-1}$ and $P=(F_0^2+2F_c^2)/3$; [c]$S = \{\Sigma[w(F_o^2-F_c^2)^2]/(n-p)\}^{1/2}$ (n = number of reflections; p = total number of parameters).

Table S3. Crystallographic data and structure refinement details for compound **7**–**8**.

	7	**8**
Formula	$C_{16}H_{10}CuN_{16}O_{20}$	$C_{18}H_{14}CuN_{16}O_{22}$
FW [g mol^{-1}]	809.94	869.99
Crystal system	monoclinic	triclinic
Space group	$P2_1/c$ (No. 14)	P-1 (No. 2)
Color / Habit	green plate	green plate
Size [mm]	0.11 x 0.44 x 0.86	0.10 x 0.50 x 0.50
a [Å]	10.0938(5)	6.2429(4)
b [Å]	16.9067(8)	11.0903(6)
c [Å]	8.0880(4)	11.2709(7)
α [°]	90	87.832(5)
β [°]	94.911(5)	74.073(6)
γ [°]	90	87.494(5)
V [Å^3]	1375.17(12)	749.40(8)
Z	2	1
$\rho_{calc.}$ [g cm^{-3}]	1.956	1.928
μ [mm^{-1}]	0.921	0.857
F(000)	814	439
$\lambda_{MoK\alpha}$ [Å]	0.71073	0.71073
T [K]	123	101
θ Min-Max [°]	2.0, 26.4	2.6, 26.4
Dataset	-12:12; -21:21; -10:10	-7:7; -12:13; -14:12
Reflections collected	20148	5684
Independent refl.	2803	3055
R_{int}	0.055	0.019
Observed reflections	2311	2715
Parameters	241	261
R_1 (obs)[a]	0.0569	0.0339
wR_2 (all data)[b]	0.1293	0.0830
S [c]	1.09	1.04
Resd. dens [e Å^{-3}]	-0.51, 1.51	-0.28, 0.43
Device type	Oxford Xcalibur3	Oxford Xcalibur3
Solution	SHELXT	SHELXT
Refinement	SHELXL-2018	SHELXL-2018
Absorption correction	multi-scan	multi-scan
CCDC	2176036	2176034

[a]$R_1 = \Sigma||F_0|-|F_c||/\Sigma|F_0|$; [b]$wR_2 = [\Sigma[w(F_0^2-F_c^2)^2]/\Sigma[w(F_0)^2]]^{1/2}$; $w = [\sigma c^2(F_0^2)+(xP)^2+yP]^{-1}$ and $P=(F_0^2+2F_c^2)/3$; [c]$S = \{\Sigma[w(F_o^2-F_c^2)^2]/(n-p)\}^{1/2}$ (n = number of reflections; p = total number of parameters).

3.6.3 Computations

All calculations were carried out using the Gaussian G09 program package. [S13] The enthalpies (H) and free energies (G) were calculated using the complete basis set (CBS) method of Petersson and coworkers in order to obtain very accurate energies. The CBS models use the known asymptotic convergence of pair natural orbital expressions to extrapolate from calculations using a finite basis set to the estimated complete basis set limit. CBS-4 begins with a HF/3-21G(d) geometry optimization; the zero point energy is computed at the same level. It then uses a large basis set SCF calculation as a base energy, and a MP2/6-31+G calculation with a CBS extrapolation to correct the energy through second order. A MP4(SDQ)/6-31+(d,p) calculation is used to approximate higher order contributions. In this study we applied the modified CBS-4M method (M referring to the use of minimal population localization) which is a re-parametrized version of the original CBS-4 method and also includes some additional empirical corrections. The enthalpies of the gas-phase species M were computed according to the atomization energy method (E1) (Table S4 & 5). [S13–S18]

$$\Delta_f H°_{(g,\,M,\,298)} = H_{(Molecule,\,298)} - \sum H°_{(Atoms,\,298)} + \sum \Delta_f H°_{(Atoms,\,298)} \qquad (E1)$$

Table S4. Literature values for atomic $\Delta H°_f^{298}$ / kcal mol^{-1}

	$-H^{298}$ [a.u.]	NIST[S19]
H	0.50091	52.1
C	37.786156	171.3
N	54.522462	113.0
O	74.991202	59.6

The gas-phase heat of formations were converted to the solid/liquid state ones for neutrals: by subtracting the vaporization/sublimation enthalpies (calculated using the Trouton rule)[S20,21] The calculation results are summarized in Table S7.

$$\Delta U_m = \Delta H_m - \Delta n\ R\ T \qquad (E2)$$

Table S5. CBS-4M results, Gas phase enthalpies of formation, calculated sublimation/vaporization enthalpies and solid-state heat of formation.

Compound	$-H^{298}$ / a.u.	$\Delta_f H°$(g) / kJ mol^{-1}	$\Delta_{s/v} H°$/ kJ mol^{-}	V_m / nm^3	Δn
1	–576.542850	258.0	70.7162		*–5.5*

3.6.4 NMR Spectroscopy

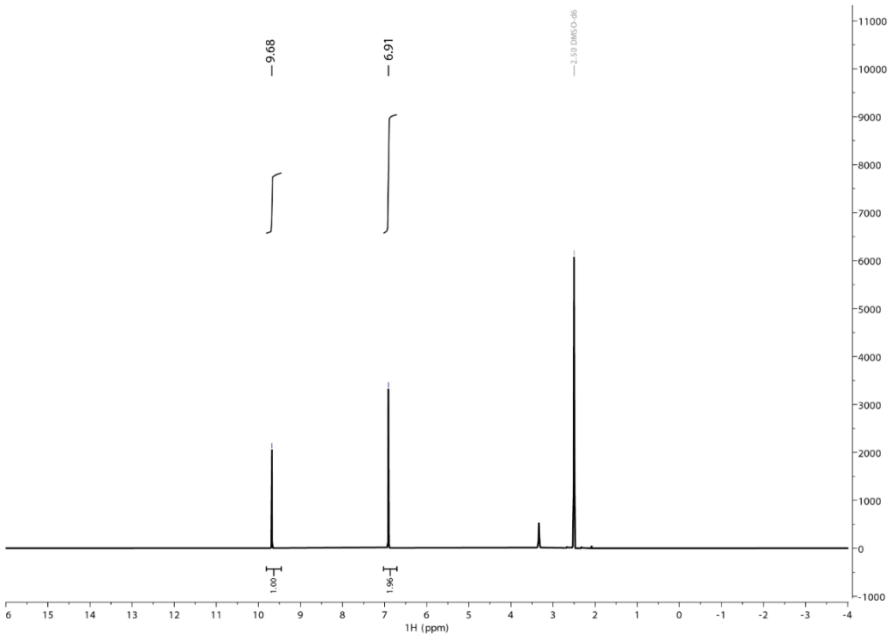

Figure S1. ^{1}H NMR of **1** in DMSO-d_6.

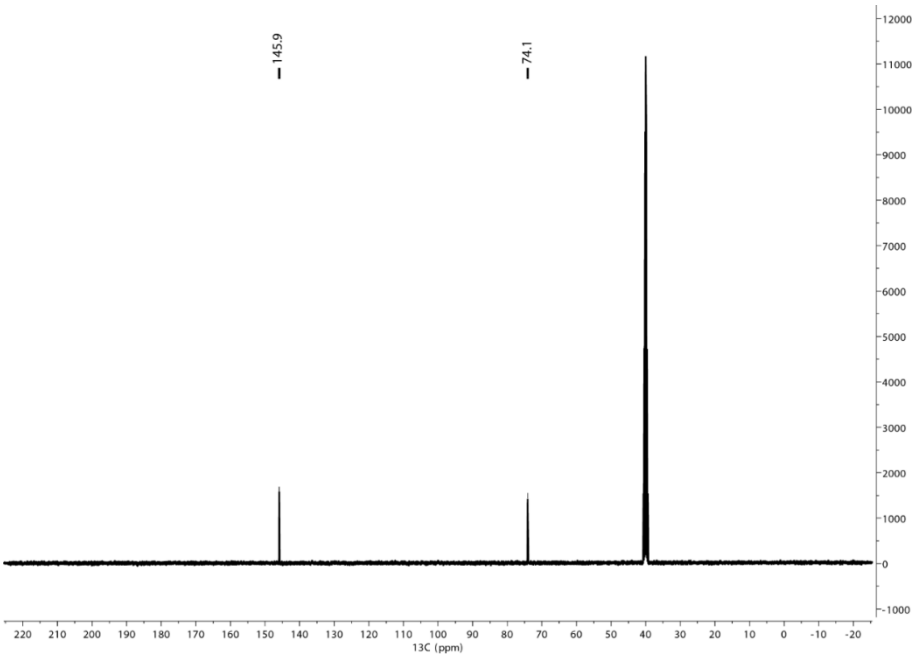

Figure S2. ^{13}C NMR of **1** in DMSO-d_6.

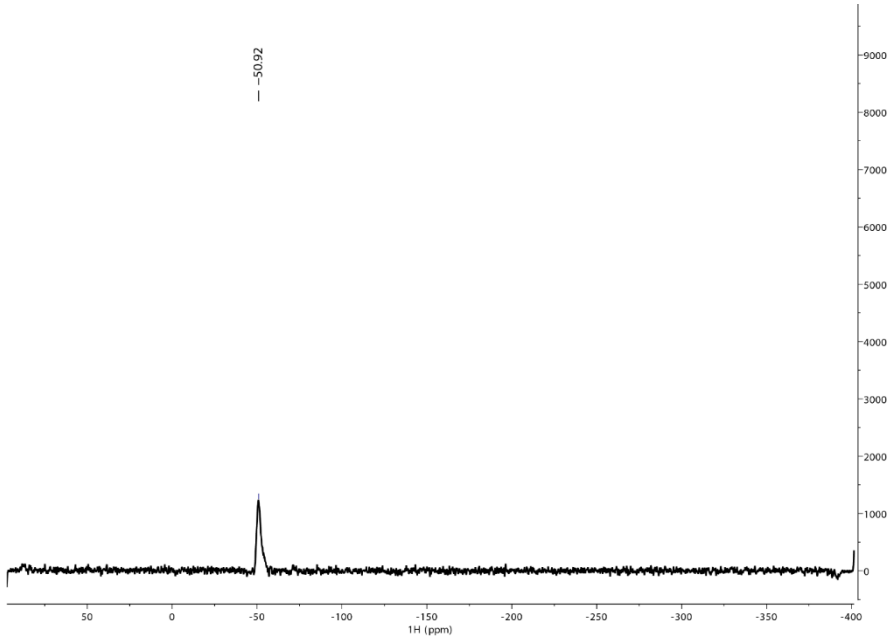

Figure S3. ^{14}N NMR of **1** in DMSO-d_6.

3.6.5 IR Spectroscopy

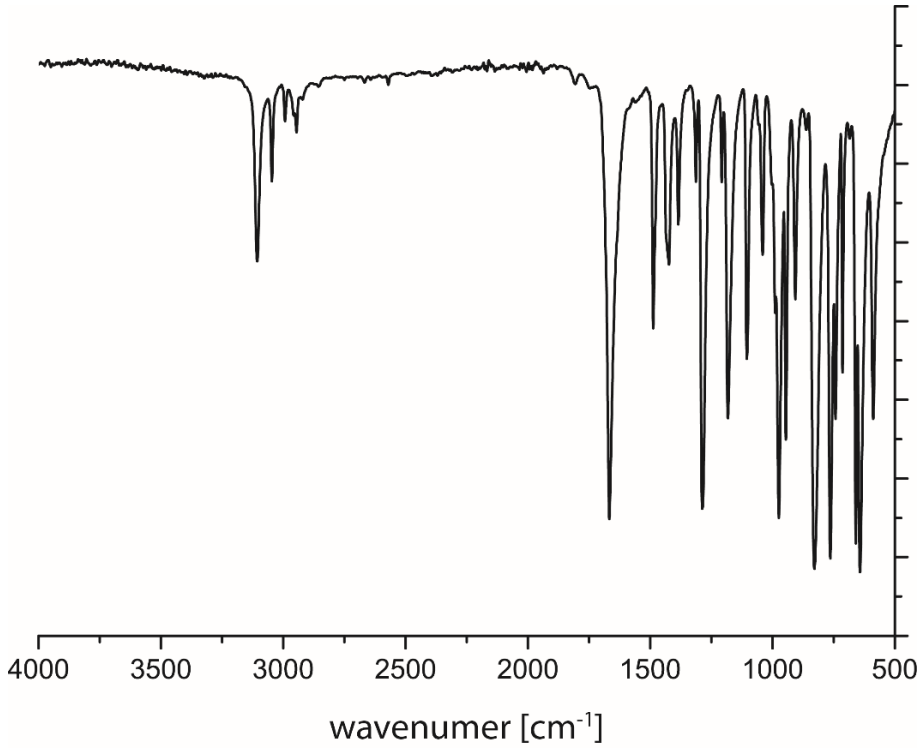

Figure S4. IR spectrum of compound **2**.

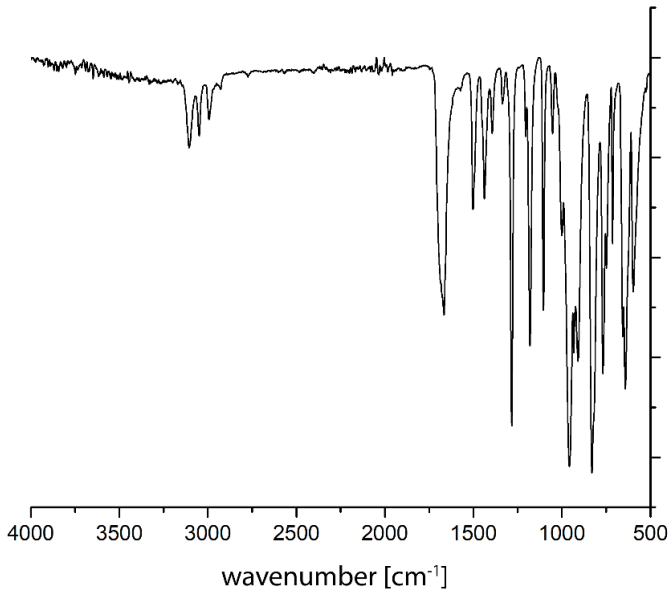

Figure S5. IR spectrum of compound **2**.

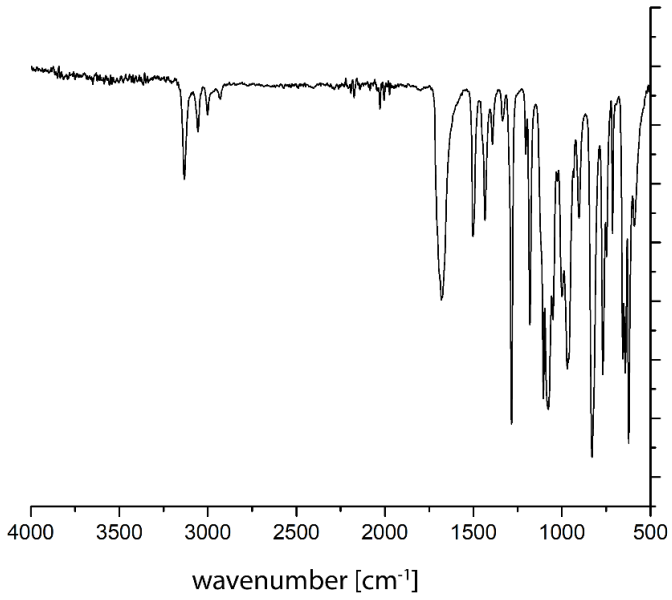

Figure S6. IR spectrum of compound **3**.

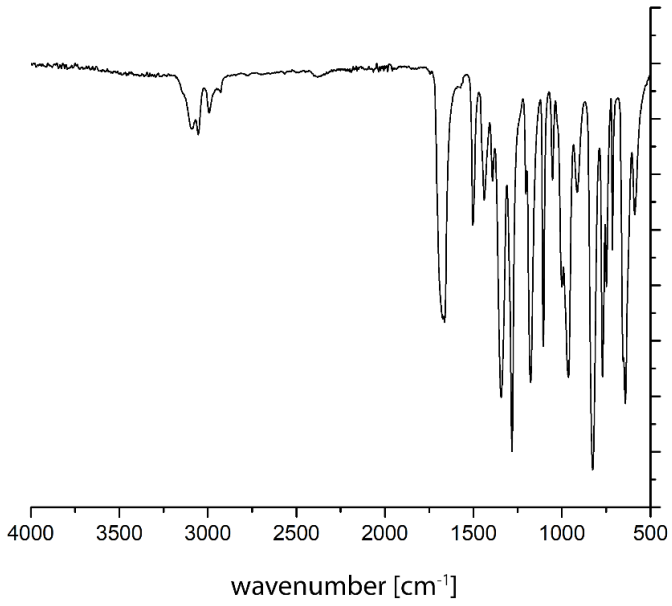

Figure S7. IR spectrum of compound **4**.

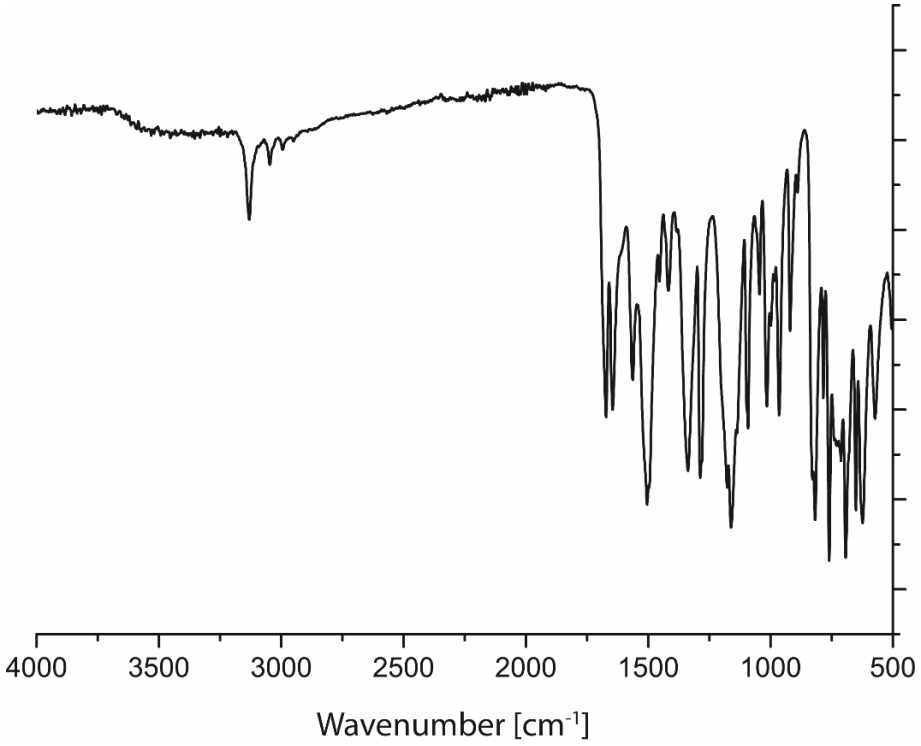

Figure S8. IR spectrum of compound **5**.

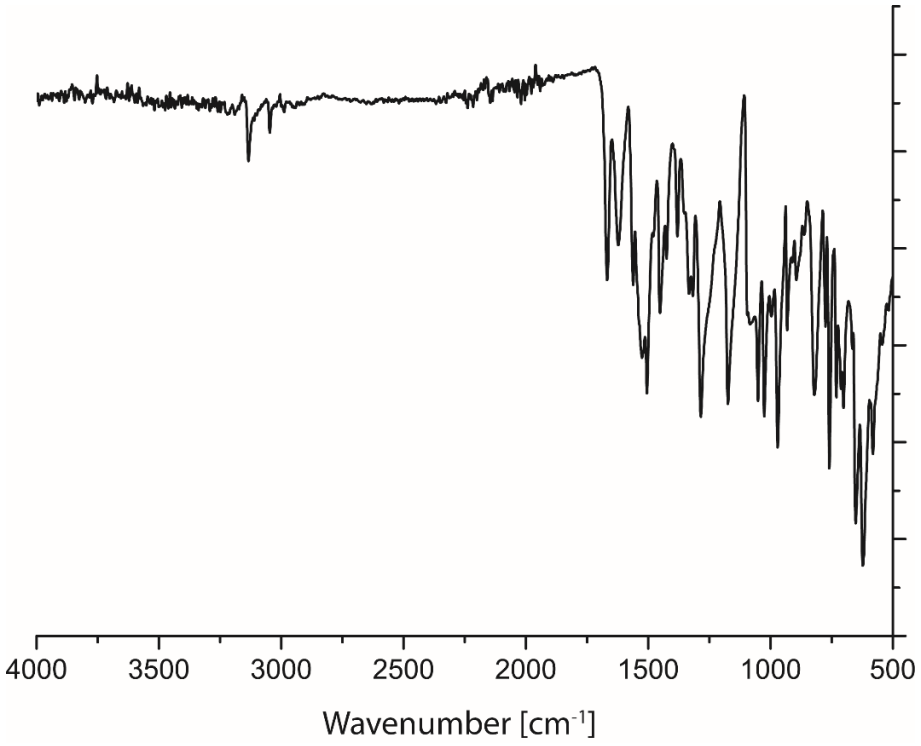

Figure S9. IR spectrum of compound **6**.

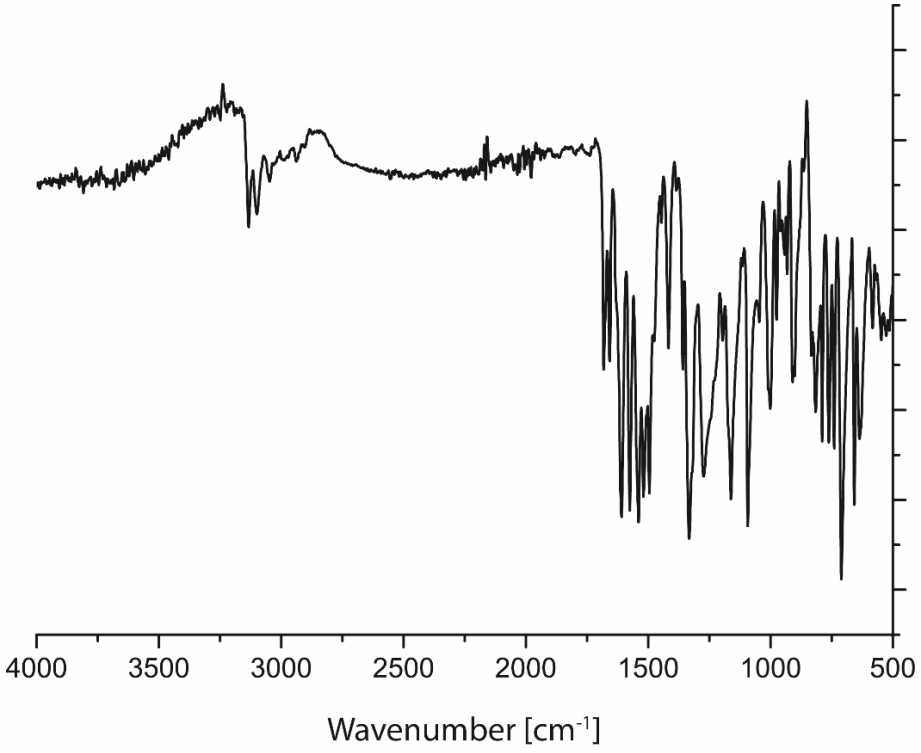

Figure S10. IR spectrum of compound **7**.

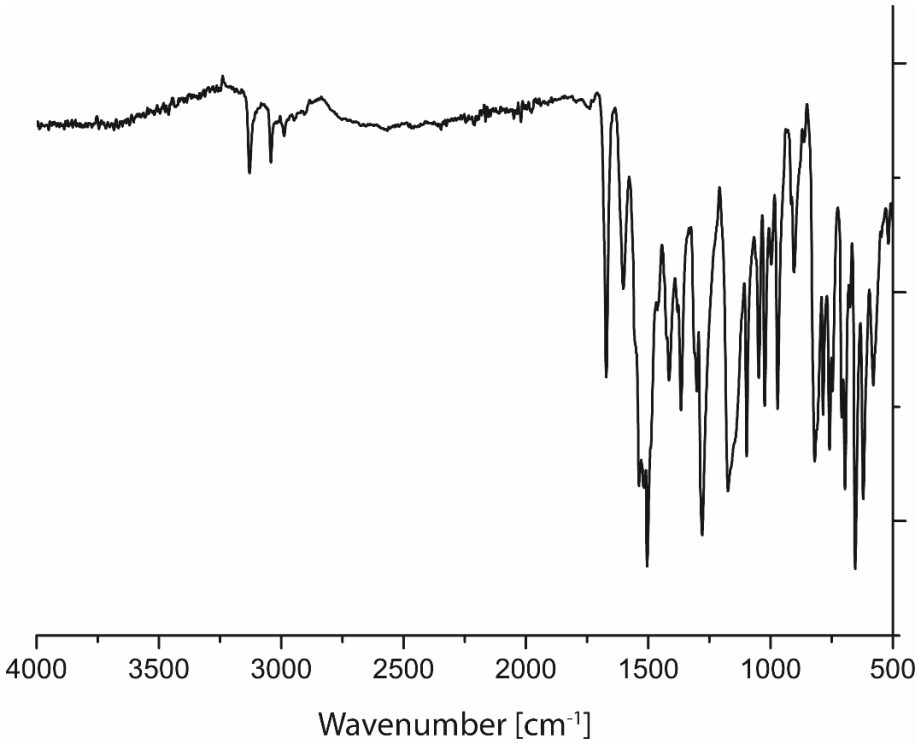

Figure S11. IR spectrum of compound **8**.

3.6.6 Hot Plate and Hot Needle Test

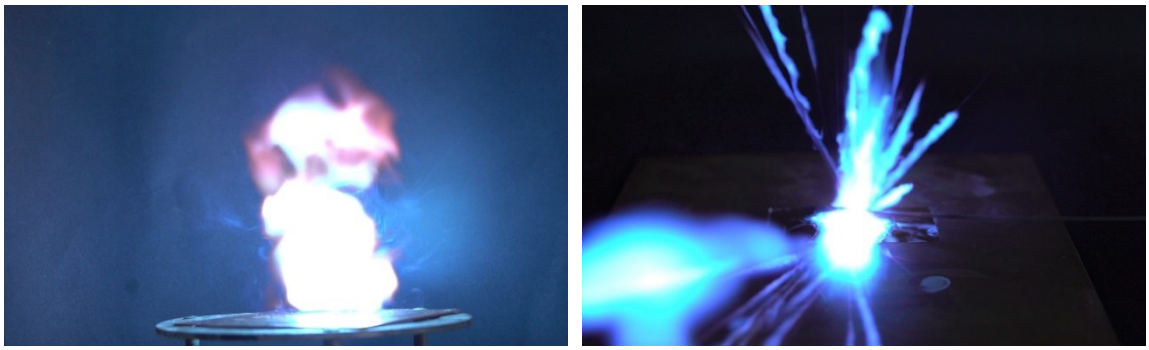

Figure S12. Hot plate (left) and hot needle (right) test of compound **2**.

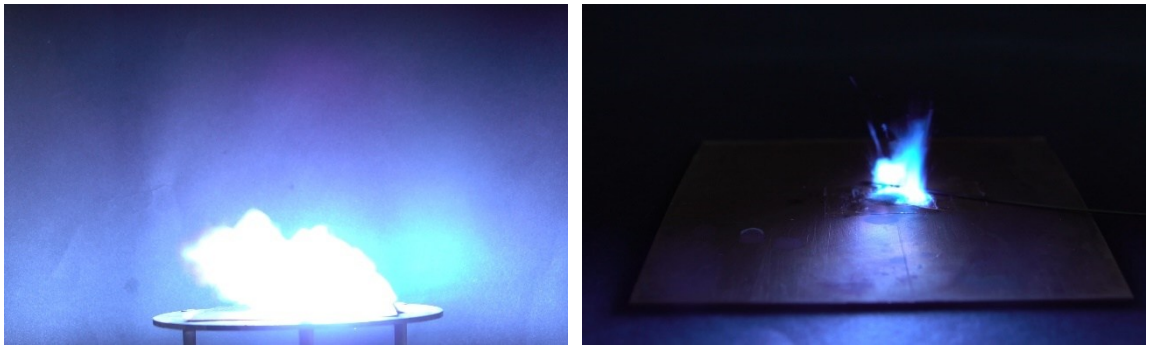

Figure S13. Hot plate (left) and hot needle (right) test of compound **3**.

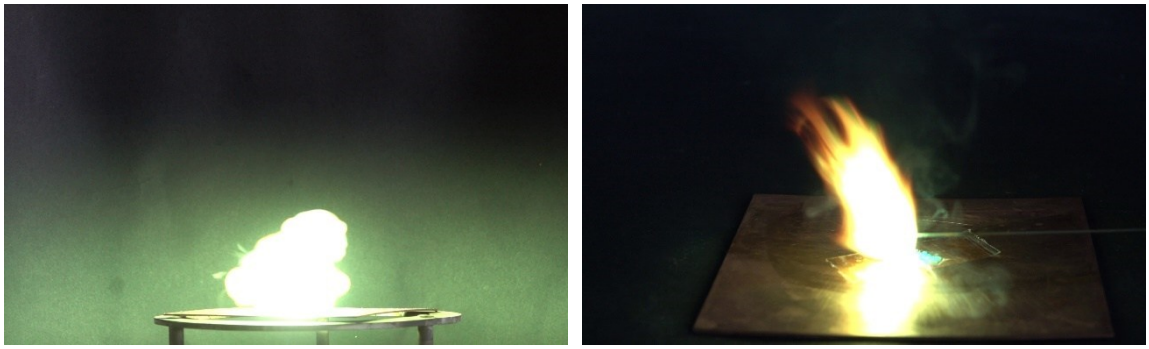

Figure S14. Hot plate (left) and hot needle (right) test of compound **4**.

Figure S15. Hot plate (left) and hot needle (right) test of compound **5**.

Figure S16. Hot plate (left) and hot needle (right) test of compound **6**.

Figure S17. Hot plate (left) and hot needle (right) test of compound **7**.

Figure S18. Hot plate (left) and hot needle (right) test of compound **8**.

3.6.7 General Methods

All chemicals and solvents were employed as received (Sigma-Aldrich, Fluka, Acros, ABCR). ^{1}H, $^{13}C\{^{1}H\}$, ^{14}N, $^{15}N\{^{1}H\}$ spectra were recorded at ambient temperature using a JEOL Bruker 27400, Eclipse 270, JEOL EX 400 or a JEOL Eclipse 400 instrument. The chemical shifts quoted in ppm in the text refer to typical standards such as tetramethylsilane (^{1}H, ^{13}C) nitromethane (^{14}N,^{15}N) in DMSO-d_6, D_2O or acetone-d_6 as the solvent. Endothermic and exothermic events of the described compounds, which indicate melting, loss of crystal water or decomposition, are given as the extrapolated onset temperatures. The samples were measured in a range of 25–400 °C at a heating rate of 5 °C min^{-1} through differential thermal analysis (DTA) with an OZM Research DTA 552-Ex instrument. Infrared spectra were measured with pure samples on a Perkin-Elmer BXII FT-IR system with a Smith DuraSampler IR II diamond ATR. Determination of the carbon, hydrogen, and nitrogen contents was carried out by combustion analysis using an Elementar Vario El (nitrogen values determined are often lower than the calculated ones' due to their explosive behavior). Impact sensitivity tests were carried out according to STANAG 4489[S22] with a modified instruction[S23] using a BAM (Bundesanstalt für Materialforschung) drophammer.[S24] Friction sensitivity tests were carried out according to STANAG 4487[S28] with a modified instruction[S29] using the BAM friction tester. [S24,S25] The classification of the tested compounds results from the "UN Recommendations on the Transport of Dangerous Goods". [S30,S31] Energetic properties have been calculated with the EXPLO5 6.05.04 computer code[S32] using the, to RT converted, X-ray density and calculated solid state heats of formation. These were computed by the atomization method as described in recently published papers. Electronic enthalpies were calculated with the Gaussian09 software[S13] suite using the CBS-4M method.

3.6.8 Detonation Velocity Estimations

The room temperature densities used for calculation of the detonation velocity were obtained by recalculation of the the low temperature densities, obtained by X-ray diffraction experiments. Detonation velocities were calculated according to an increment method, adapted for ECC by Ilyushin. [S33] Analogue to pyrotechnical mixtures, the respective ECCs were divided into an explosive part (anion, ligand) and an inactive ultratispersed metal additive (copper). The active part was further divided into chemical bonds and structural fragments. Corresponding increment values can be found in the literature. [S34] Some of the values are dependent on the hydrogen and oxygen content of the coordination compound, the summarized values for each fragment are listed in Table S6.

Table S6. Values of increments used for fragments.

Fragment	F_i
1-NAMT	453.0
H_2TNPG	716.3
HTNR	666.2
PA	616.1
HTNO	663.1

3.6.9 Experimental Section

All investigated compounds are potentially explosive energetic materials (the compounds lie in the range of primary explosives), which show partly increased sensitivities towards various stimuli (e.g. elevated temperatures, impact, friction or electrostatic discharge). Therefore, proper security precautions (safety glasses, face shield, earthed equipment and shoes, leather jacket, Kevlar gloves, Kevlar sleeves and ear plugs) have to be worn while synthesizing and handling the described compounds. These very sensitive compounds must be handled with great care!

1-(Nitratomethyl)tetrazole (1)

Fuming nitric acid (3.13 mL, 75 mmol) is slowly added to acetic anhydride (8.5 mL, 90 mmol) cooled with an ice-water bath. After complete addition, the mixture is stirred for 30 minutes at 0–5°C. An isomeric mixture of 1- and 2-(hydroxymethyl)tetrazole (1.5 g, 15 mmol), synthesized according to literature[S35], is added while keeping the temperature below 10 °C. The reaction solution is stirred at 0 °C for 1.5 h, quenched on ice water and the solution was adjusted to pH = 6 with sodium hydroxide. The solution is then extracted

into ethyl acetate (3 x 100 mL) and the organic phase in washed with little cold water and dried over magnesium sulfate. After slow evaporation of the solvent by a stream of nitrogen gas, compound **1** is obtained as white solid in moderate yield (455 mg, 3.2 mmol, 21%). **DTA** (5 °C min^{-1}): 57 °C ($_{Tendo}$), 123 °C (T_{exo}); **IR** (ATR, cm^{-1}): $\tilde{\upsilon}$ = 3106 (m), 3046 (w), 2993 (w), 2946 (w), 1667 (s), 1488 (m), 1423 (m), 1385 (m), 1313 (w), 1287 (s), 1208 (w), 1182 (s), 1105 (m), 1040 (m), 989 (m), 975 (s), 946 (s), 907 (m), 862 (w), 829 (vs), 764 (vs), 743 (s), 714 (s), 660 (vs), 643 (vs), 589 (s), 414 (s); **^{1}H NMR** (DMSO-d_6, 25 °C, ppm) δ = 9.67 (s, 1H), 6.91 (s, 2H); **^{13}C NMR** (DMSO-d_6, 25 °C, ppm) δ = 145.9, 74.1; **^{14}N NMR** (DMSO-d_6, 25 °C, ppm) δ = −50.9; **EA** ($C_2H_3N_5O_3$, 145.08) calcd.: C 16.56, H 2.08, N 48.27%, found: C 16.84, H 1.95, N 48.10%; BAM drophammer: <1 J; **BAM friction tester**: 9 N; **ESD**: >1500 mJ (grain size 100–500 µm).

General procedure for ECC 2–4

Barium chlorate monohydrate (145 mg, 0.45 mmol, 1.0 equiv.) and copper(II) sulphate pentahydrate (112 mg, 0.45 mmol, 1.0 equiv.) were dissolved in water (5 mL), combined and stirred for 5 min. The mixture was cooled to 0 °C and the precipitated barium sulphate, filtered off. The solvent was evaporated under reduced pressure and pure copper(II) chlorate was dissolved in ethanol (2 mL).

The respective amounts of copper(II) salt (**2**: $Cu(ClO_3)_2$ 57.6 mg, **3**: $Cu(ClO_4)_2$ 6 H_2O 92.6 mg, **4**: $Cu(NO_3)_2$ 3 H_2O 60.4 mg, 0.25 mmol, 1.0 equiv.) was dissolved in ethanol (2 mL) and added dropwise to the in ethanol dissolved **1** (218 mg, 1.50 mmol, 6.0 equiv.) while stirring at room temperature. The reaction mixture was stirred for 5 min at 80 °C before it was allowed to crystallize at room temperature. Crystallization process took up 1–3 days. The crystalline compounds were filtered off before complete evaporation of the solvent and were washed with cold ethanol. It is also possible to precipitate the compounds by adding a large excess of *n*-hexane to the ethanolic solution. In this case, the powdered compounds were filtered off, washed with n-hexane and dried in air. The powdered compounds were checked for purity with elemental analysis.

$[Cu(1\text{-}NAMT)_6](ClO_3)_2$ (2)

Compound **2** was obtained as blue crystals within 2 h. Yield: 200 mg (0.18 mmol, 73%) **DTA** (5 °C min^{-1}): 145 °C (T_{exo}); **IR** (ATR, cm^{-1}): $\tilde{\upsilon}$ = 3106 (w), 3049 (w), 2994 (w), 1666 (s), 1502 (m), 1438 (m), 1394 (w), 1336 (w), 1284 (s), 1205 (w), 1181 (s), 1105 (s), 1053

(w), 1000 (m), 958 (vs), 933 (s), 909 (s), 831 (vs), 768 (s), 749 (m), 714 (m), 657 (s), 657 (s), 642 (s), 597 (m), 477 (m), 410 (w); **EA** ($C_{12}H_{18}Cl_2CuN_{30}O_{24}$, 1100.91): calc.: C 13.09, H 1.65, N 38.17%, found: C 12.91, H 1.65, N 38.50%; **BAM drophammer**: <1 J, **BAM friction tester**: 0.4 N; **ESD**: 139 mJ (at grain size >1000 µm).

$[Cu(1\text{-}NAMT)_6](ClO_4)_2$ (3)

Compound **3** was obtained as blue crystals within 2 h. Yield: 150 mg (0.13 mmol, 53%). **DTA** (5 °C min^{-1}): 119 °C (T_{exo}); **IR** (ATR, cm^{-1}): $\tilde{\upsilon}$ = 3133 (w), 3056 (w), 3002 (w), 2028 (w), 1682 (m), 1675 (m), 1503 (m), 1435 (m), 1393 (w), 1336 (w), 1285 (vs), 1204 (w), 1181(s), 1105 (s), 1077 (s), 1051 (s), 1026 (w), 1000 (m), 970 (s), 961 (s), 934 (w), 904 (m), 830 (vs), 769 (s), 748 (m), 714 (m), 657 (s), 642 (s), 623 (vs); **EA** ($C_{12}H_{18}Cl_2CuN_{30}O_{26}$, 1132.91): calc.: C 12.72, H 1.60, N 37.09%, found: C 12.67, H 1.63, N 37.35%; **BAM drophammer**: 2 J, **BAM friction tester**: 0.75 N; **ESD**: 13 mJ (at grain size >1000 µm).

$[Cu(1\text{-}NAMT)_6](NO_3)_2$ (4)

Compound **4** was obtained as blue crystals after 3 days. Yield: 160 mg (0.15 mmol, 61%) **DTA** (5 °C min^{-1}): 102 °C (endothermic), 121 °C (exothermic.); **IR** (ATR, cm^{-1}): $\tilde{\upsilon}$ = 3091 (w), 3055 (w), 2993 (w), 2928 (vw), 1673 (s), 1663 (s), 1504 (m), 1439 (m), 1392 (w), 1343 (s), 1282 (vs), 1204 (m), 1177 (s), 1105 (s), 1053 (w), 1000 (m), 963 (s), 914 (m), 826 (vs), 771 (s), 748 (m), 715 (m), 655 (s), 642 (s), 589 (m), 411 (w); **EA** ($C_{12}H_{18}CuN_{32}O_{24}$, 1058.02): calc.: C 13.62, H 1.71, N 42.36%, found: C 13.53, H 1.76, N 43.17%; **BAM drophammer**: <1 J, **BAM friction tester**: 5 N; **ESD**: 90 mJ (at grain size >1000 µm).

General procedure for ECCs 5–8

A suspension of $CuCO_3{\times}Cu(OH)_2$ (27.6 mg, 0.125 mmol, 0.5 eq.) and the corresponding free nitroaromatic acid (0.50 mmol, 2.0 eq.) in 5 mL of water was heated to 80 °C until a clear solution was obtained. To this solution, compound **1** (**5**: 1.0 mmol, 4.0 eq., **6**–**8**: 0.50 mmol, 2.0 eq.) was added. The solution was kept at 80 °C for 5 min. and then left at room temperature to crystallize for 3 weeks. The resulting suspension was filtered off and washed with cold water, ethanol and diethyl ether. Here, a precipitation of the compounds like for **2**–**4** was not possible.

[Cu(1-NAMT)$_4$(H$_2$TNPG)$_2$] (5)

Compound **5** was obtained as a green solid. Yield: 140 mg (0.12 mmol, 48%).

DTA (5 °C min^{-1}): 135 °C (T_{exo}); **IR** (ATR, cm^{-1}): $\tilde{\upsilon}$ = 3130(w), 3046(w), 2995(w), 1672(s), 1645(s), 1563(s), 1505(s), 1496(s), 1454(m), 1418(m), 1384(m), 1338(s), 1287(s), 1280(s), 1177(s), 1161(vs), 1137(s), 1092(s), 1045(m), 1015(s), 999(m), 985(m), 965(s), 920(m), 890(w), 829(s), 818(vs), 784(s), 760(vs), 739(s), 730(s), 719(s), 712(s), 693(vs), 651(s), 624(vs), 573(s), 505(m), 481(m), 470(m), 463(m), 458(m), 417(m). **EA** ($C_{20}H_{16}CuN_{26}O_{30}$, 1164.05) calc.: C 20.64 H 1.39 N 31.29%, found C 20.62 H 1.46 N 31.18%; **BAM drop hammer**: <1 J; **BAM friction tester**: 72 N; **ESD**: 160 mJ (at grain size: 100–500 µm).

[Cu(1-NAMT)$_2$(HTNR)$_2$] (6)

Compound **6** was obtained as a greenish black solid. Yield: 167.9 mg (0.20 mmol, 80%).

DTA (5 °C min^{-1}): 176 °C (T_{exo}); **IR** (ATR, cm^{-1}): $\tilde{\upsilon}$ = 3134(w), 3047(w), 1668(m), 1622(m), 1561(m), 1525(m), 1505(s), 1479(m), 1452(m), 1425(m), 1381(m), 1352(w), 1333(m), 1318(m), 1285(s), 1174(s), 1084(m), 1051(s), 1026(s), 997(m), 971(s), 932(m), 911(m), 895(m), 863(m), 822(s), 775(m), 760(s), 731(s), 713(s); **EA** ($C_{16}H_{10}CuN_{16}O_{22}$, 841.89) calc.: C 22.83 H 1.20 N 26.62%, found C 22.79 H 1.21 N 26.52%; **BAM drop hammer**: <1 J; **BAM friction tester**: 40 N; **ESD**: 140 mJ (at grain size: 100–500 µm).

[Cu(1-NAMT)$_2$(PA)$_2$] (7)

Compound **7** was obtained as a green solid. Yield: 147.5 mg (0.18 mmol, 73%).

DTA (5 °C min^{-1}): 181 °C (T_{exo}); **IR** (ATR, cm^{-1}): $\tilde{\upsilon}$ = 3133(w), 3100(w), 3047(w), 2939(w), 1682(m), 1657(m), 1609(s), 1575(s), 1539(s), 1520(s), 1506(s), 1496(s), 1476(m), 1446(w), 1417(m), 1385(w), 1359(m), 1333(vs), 1274(s), 1196(m), 1162(s), 1093(s), 1046(m), 1009(s), 1001(s), 975(m), 959(w), 943(m), 932(m), 910(s), 902(m), 865(w), 834(m), 816(s), 789(s), 762(s), 740(s), 711(vs), 658(s), 637(s), 583(m), 547(m), 527(m), 789(s), 762(s), 740(s), 711(vs), 658(s), 637(s), 583(m), 547(m), 527(m), 514(m), 503(m), 463(m), 458(m), 435(m), 407(s); **EA** ($C_{16}H_{10}CuN_{16}O_{20}$, 809.89) calc.: C 23.73 H 1.24 N 27.67%, found C 23.68 H 1.26 N 27.80%; **BAM drop hammer**: <1 J. **BAM friction tester**: 120 N; **ESD**: 90 mJ (at grain size: 100–500 µm).

[Cu(1-NAMT)$_2$(HTNO)$_2$] (8)

Compound **8** was obtained as a green solid. Yield: 159.7 mg (0.19 mmol, 73%). **DTA** (5 °C min^{-1}): 161 °C (T_{exo}); **IR** (ATR, cm^{-1}): $\tilde{\upsilon}$ = 3130(w), 3042(w), 2988(w), 2948(vw), 2905(vw), 1671(s), 1602(m), 1538(s), 1520(s), 1516(s), 1505(vs), 1463(m), 1424(m), 1415(s), 1380(m), 1366(s), 1330(m), 1301(s), 1279(vs), 1174(s), 1098(s), 1048(s), 1024(s), 997(m), 971(s), 916(w), 904(m), 864(w), 820(s), 785(s), 759(s), 747(s), 709(s), 696(s), 675(m), 654(vs), 621(s), 580(s), 547(m), 518(m), 497(w), 475(w), 468(w), 675(m), 654(vs), 621(s), 580(s), 547(m), 518(m), 497(w), 475(w), 468(w), 457(w), 448(w), 417(s), 406(m); **EA** ($C_{18}H_{14}CuN_{16}O_{22}$, 869.95) calc.: C 24.85 H 1.62 N 25.76%, found C 24.73 H 1.54 N 25.93%; **BAM drop hammer**: <1 J. **BAM friction tester**: 84 N; **ESD**: 90 mJ (at grain size: 100–500 µm).

3.6.10 References

[S1] CrysAlisPRO (Version 171.33.41), Oxford Diffraction Ltd., **2009**.

[S2] A. Altomare, G. Cascarano, C. Giacovazzo, and A. Guagliardi, *J. Appl. Crystallogr.*, **1992**, *26*, 343.

[S3] A. Altomare, G. Cascarano, C. Giacovazzo, A. Guagliardi, A. G. G. Moliterni, M. C. Burla, G. Polidori, M. Camalli and R. Spagna, SIR97, **2003**.

[S4] A. Altomare, M. C. Burla, M. Camalli, G. L. Cascarano, C. Giacovazzo, A. Guagliardi, A. G. G. Moliterni, G. Polidori and R. Spagna, *J. Appl. Crystallogr.*, **1999**, *32*, 115.

[S5] G. M. Sheldrick, SHELXL-97, University of Göttingen, Germany, **1997**.

[S6] G. M. Sheldrick, *Acta Crystallogr. Sect. A*, **2008**, *64*, 112.

[S7] G. M. Sheldrick, *Acta Cryst. A*, **2015**, *71*, 3–8.

[S8] A. L. Spek, PLATON, Utrecht University, The Netherlands, **1999**.

[S9] L.J. Farrugia, *J. Appl. Cryst.*, **2012**, *45*, 849.

[S10] O. V. Dolomanov, L. J. Bourhis, R. J. Gildea, J. A. K. Howard and H. Puschmann, *J. Appl. Cryst.*, **2009**, *42*, 339–341.

[S11] Empirical absorption correction using spherical harmonics, implemented in SCALE3 ABSPACK scaling algorithm (CrysAlisPro Oxford Diffraction Ltd., Version 171.33.41, **2009**).

[S12] APEX3, Bruker AXS Inc., Madison, Wisconsin, USA.

[S13] M. J. Frisch, G. W. Trucks, H. B. Schlegel, G. E. Scuseria, M. A. Robb, J. R. Cheeseman, G. Scalmani, V.Barone, B. Mennucci, G. A. Petersson, H. Nakatsuji, M. Caricato, X. Li, H.P. Hratchian, A. F. Izmaylov, J. Bloino, G. Zheng, J. L. Sonnenberg, M. Hada, M. Ehara, K. Toyota, R. Fukuda, J. Hasegawa, M. Ishida, T. Nakajima, Y. Honda, O. Kitao, H. Nakai, T. Vreven, J. A. Montgomery, Jr., J. E. Peralta, F. Ogliaro, M. Bearpark, J. J. Heyd, E. Brothers, K. N. Kudin, V. N. Staroverov, R. Kobayashi, J. Normand, K. Raghavachari, A. Rendell, J. C. Burant, S. S. Iyengar, J. Tomasi, M. Cossi, N. Rega, J. M. Millam, M.Klene, J. E. Knox, J. B. Cross, V. Bakken, C. Adamo, J. Jaramillo, R. Gomperts, R. E. Stratmann, O. Yazyev, A. J. Austin, R. Cammi, C. Pomelli, J. W. Ochterski, R. L. Martin, K. Morokuma, V. G. Zakrzewski, G. A. Voth, P. Salvador, J. J. Dannenberg, S. Dapprich, A. D. Daniels, O. Farkas, J.B. Foresman, J. V. Ortiz, J. Cioslowski and D. J. Fox, Gaussian 09 A.02, Gaussian, Inc., Wallingford, CT, USA, **2009**.

[S14] J. W. Ochterski, G. A. Petersson and J. A. Montgomery Jr., *J. Chem. Phys.*, **1996**, *104*, 2598–2619.

[S15] J. A. Montgomery Jr., M. J. Frisch, J. W. Ochterski and G. A. Petersson, *J. Chem. Phys*., **2000**, *112*, 6532–6542.

[S16] L. A. Curtiss, K. Raghavachari, P. C. Redfern and J. A. Pople, J. *Chem. Phys.*, **1997**, *106*, 1063–1079.

[S17] E. F. C. Byrd and B. M. Rice, *J. Phys. Chem. A*, **2006**, *110*, 1005–1013.

[S18] B. M. Rice, S. V. Pai and J. Hare, *Comb. Flame*, **1999**, *118*, 445–458.

[S19] P. J. Lindstrom and W. G. Mallard, NIST Standard Reference Database Number 69, http://webbook.nist.gov/chemistry/, (accessed March 2021).

[S20] M. S. Westwell, M. S. Searle, D. J. Wales and D. H. Williams, *J. Am. Chem. Soc.* **1995**, *117*, 5013–5015.

[S21] F. Trouton, *Philos. Mag*. **1884**, *18*, 54–57.

[S22] NATO standardization agreement (STANAG) on explosives, impact sensitivity tests, no. 4489, 1st ed., Sept. 17, **1999**.

[S23] WIWEB-Standardarbeitsanweisung 4-5.1.02, Ermittlung der Explosionsgefährlichkeit, hier der Schlagempfindlichkeit mit dem Fallhammer, Nov. 8, **2002**.

[S24] BAM, http://www.bam.de, (accessed March 2021).

[S25] OZM, http://www.ozm.cz, (accessed March 2021).

[S26] Military Standard 1751A (MIL-STD-1751A): safety and performance tests for qualification of explosives (high explosives, propellants and pyrotechnics), method 1016, Dec. 11, **2001**.

[S27] M. S. Gruhne, M. Lommel, M. H. H. Wurzenberger, N. Szimhradt, T. M. Klapötke and J. Stierstorfer, *Propellants Explos. Pyrotech.*, **2020**, *45*, 147–153.

[S28] NATO standardization agreement (STANAG) on explosive, friction sensitivity tests, no. 4487, 1st ed., Aug. 22, **2002**.

[S29] WIWEB-Standardarbeitsanweisung 4-5.1.03, Ermittlung der Explosionsgefährlichkeit oder der Reibeempfindlichkeit mit dem Reibeapparat, Nov. 8, **2002**.

[S30] UN Model Regulation: Recommendations on the Transport of Dangerous Goods – Manual of Tests and Criteria, section 13.4.2.3.3, 2015.

[S31] Impact: insensitive > 40 J, less sensitive ≥ 35 J, sensitive ≥ 4 J, very sensitive ≤ 3 J; Friction: insensitive > 360 N, less sensitive = 360 N, sensitive < 360 N and > 80 N, very sensitive ≤ 80 N, extremely sensitive ≤ 10 N. According to the UN Recommendations on the Transport of Dangerous Goods, 5th ed., **2009**.

[S32] M. Sućeska, EXPLO5 Version 6.05 User's Guide. Zagreb, Croatia: OZM; **2018**.

[S33] M. A. Ilyushin, A. V. Smirnov, A. A. Kotomin, I. V. Tselinskii, *Energ. Mater.* **1994**, *2*, 16–20.

[S34] Н.Ю. Сугак, С.В. Мочалов, РАСЧЕТ ВЗРЫВЧАТЫХ ХАРАКТЕРИСТИК ВВ, БТИ АлтГТУ, Бийск, **2013**.

[S35] M. Kofen, M. Lommel, M. H. H. Wurzenberger, T. M. Klapötke, J. Stierstorfer, *Chem. Eur. J.* **2022**, *28*, e202200492.

4 The Adjustability of Physicochemical Properties: Comparison of 1-Vinyltetrazole and 1-Allyltetrazole as Ligands in 3d Metal Energetic Coordination Compounds (ECC)

Markus Rösch, Michael S. Gruhne, Marcus Lommel, Simon M. J. Endraß, and Jörg Stierstorfer

published in *Inorganic Chemistry,* **2023**

DOI: 10.1021/acs.inorgchem.2c03624

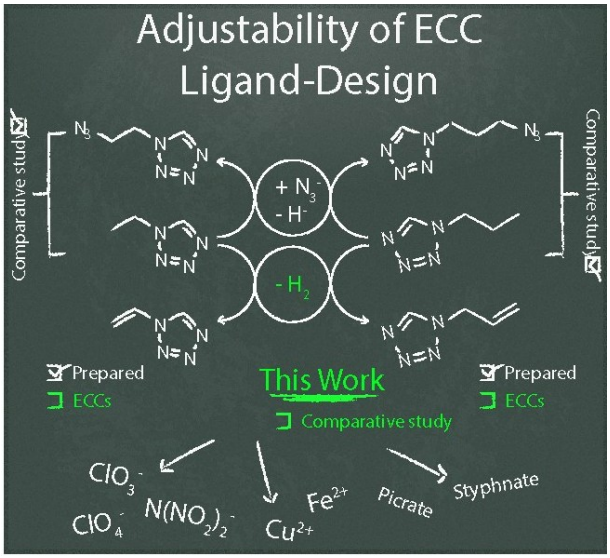

Abstract: Energetic Coordination Compounds (ECC) show promising properties to be used as potential substitutes for highly toxic lead-containing primary explosives or as burn rate catalysts in propellant charges. The concept is to combine the three building blocks: (i) ligand, (ii) transition metal, and (iii) anion, acting as (i) fuel, (ii) matrix, and (iii) oxidizer (e.g., ClO_4^-, NO_3^-, ClO_3^-) or energetic component (e.g., DN^-, N_3^-, picrate, styphnate, trinitrophloroglucinate). By variation of the ligands, the complexes' properties can be adjusted toward their desired performance and sensitivities. In the present study, 1-vinyltetrazole (1-VTZ, **1**) and 1-allyltetrazole (1-ATZ, **2**) were used as nitrogen-rich endothermic ligands to form 3d metal (Mn^{2+}, Fe^{2+}, Cu^{2+}, Zn^{2+}, Co^{2+}, Ni^{2+}) based ECC. The influence of the introduction of an unsaturated C–C bond (1-ETZ *vs.* 1-VTZ and 1-PTZ *vs.* 1-ATZ) on the performance and sensitivity of the complexes are discussed, as is the lengthening of the alkenyl chain (1-VTZ *vs.* 1-ATZ). For further insights, the novel complexes were compared to literature known complexes based on N1-substituted C2- and C3-derived tetrazole ligands, respectively. The ligand 1-VTZ (**1**) was prepared by elimination of hydrogen chloride from 1-(2-chloroethyl)tetrazole in methanolic KOH solution. 1-ATZ (**2**) was obtained by a heterocyclization reaction of allylamine with triethyl orthoformate and sodium azide in an acetic acid medium. All compounds were intensively characterized with analytical methods such as XRD, IR, EA, DTA, TGA, and sensitivity measurements (IS and FS). The energetic performances were visibly evaluated in fast heating experiments. Furthermore, PETN initiation and laser ignition experiments were carried out for promising ECCs.

4.1 Introduction

In the field of energetic materials, the main challenges remain to create compounds that have high performance and thermal stability with low toxicity, in addition to low-cost synthesis. [1] For primary explosives the main substances to be replaced are lead styphnate (LS) and lead azide (LA). In the past, tetrazoles as endothermic nitrogen-rich compounds with a high positive heat of formation have emerged as suitable building blocks for energetic materials. [2-8] Notably, this class of compounds combines the desired properties of endothermicity with kinetic stability as well as forms non-toxic reaction products during decomposition. [1] Up to date, tetrazole-containing compounds are therefore in particular used as 'green' primary [2,7,9-11] and secondary explosives, [3,12] but also binders [13-15] and

energy-rich additives can be found in the literature. [16] Besides these sufficiently known uses, tetrazoles have also found use as ligands in the research of ECC (Chart 1). [17-19] In particular the numerous possibilities to tailor the coordination compounds' chemical and physicochemical properties by varying the central metal, ligand, and anion make this substance class interesting for various purposes. [20]

The introduction of an *N*-substituent onto the tetrazole ring prevents acidic protons and allows to build up neutral complexes with oxidizing anions to synthesize more promising energetic materials. Among others, several monosubstituted [21-24] and disubstituted tetrazoles [25,26] were investigated as ligands in ECC.

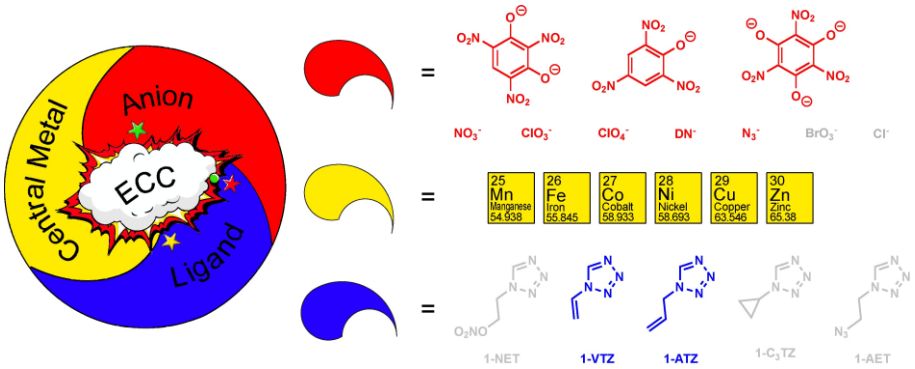

Chart 1. Preliminary (grey colored) and current work using energetic *N*1-substituted tetrazoles in energetic coordination compounds (ECC).

Noteworthy, the energetic character of tetrazole-based ligands is thereby tuned by alteration of the functional groups or their substitution pattern (*N*1-substituted *vs. N*2-substituted *vs. C*5-substituted). In addition to explosophoric groups (e.g., $–NO_2$, $–ONO_2$, $–N_3$), which enhance the density, nitrogen content, and oxygen balance, alkyl chains are introduced to desensitize the complexes. The main challenge is to design ECC with a high heat of detonation as well as low sensitivity (impact, friction, and heat) especially required for special applications in industry (e.g., mining and oil drilling). Unfortunately, there is often a tradeoff between this contradictory relationship. In this context, the ethyl group has proven itself to be very versatile. [27-30] This is not only because of their low-cost availability but also because of the simplicity of implementation. [27]

Every one of the tetrazole derivatives displayed in Figure 1 is known in literature [27,31,32] and were partly used as a ligand in ECC [33] with especially 1-ethyltetrazole (1-ETZ) [23] and 1-propyltetrazole (1-PTZ) [24] showing a lack of performance or were not investigated toward their energetic parameters at all. [34-40] In the present work, 1-VTZ (**1**) and 1-ATZ

(**2**) are used as ligands in energetic 3d transition metal complexes. The gas phase enthalpy of formation was chosen as a comparative criterion for the tetrazole derivatives. The results of the calculations are shown as per unit mass enthalpies of formation in the bar chart in Figure 1.

As shown in Figure 1, the formal reduction of the terminal C–C bond in 1-ETZ ($\Delta_f H°_{(g)}$ = 2727 kJ kg^{-1}) and 1-PTZ ($\Delta_f H°_{(g)}$ = 2138 kJ kg^{-1}) leads to an increase in the gas phase enthalpies of formation in 1-VTZ ($\Delta_f H°_{(g)}$ = 4219 kJ kg^{-1}) and 1-ATZ ($\Delta_f H°_{(g)}$ = 3432 kJ kg^{-1}), respectively.

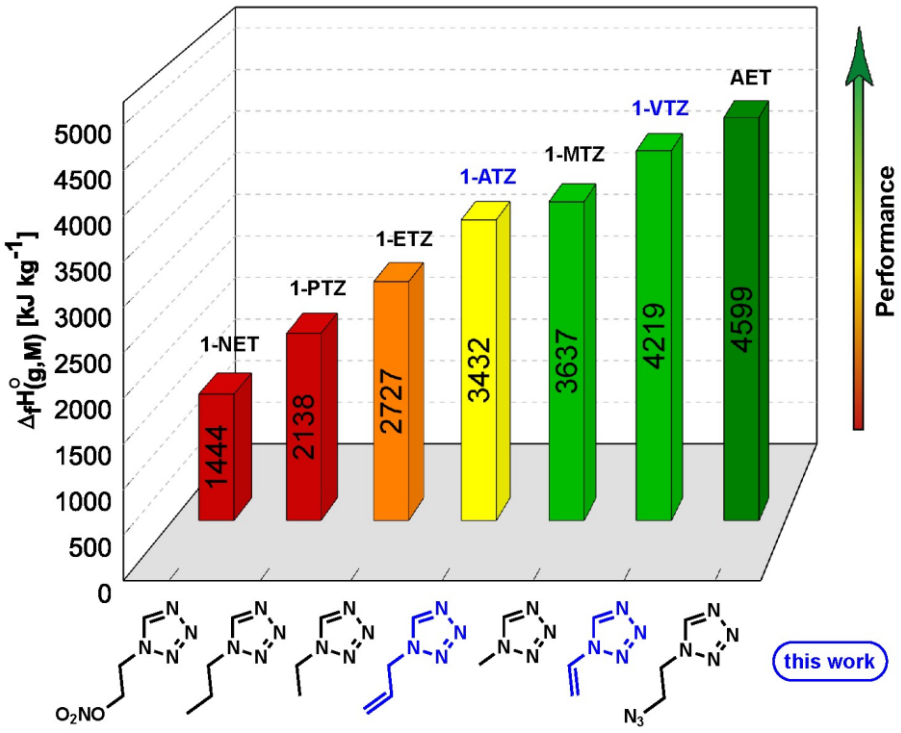

Figure 1. Comparison of the calculated gas-phase enthalpies of formation for various monotetrazole derivatives. Enthalpies of formation were calculated using the atomization method ($\Delta_f H^0_{(g,M)} = H_{(M)} - \Sigma H^0_{(A)} + \Sigma \Delta_f H^0_{(A)}$) using Gaussian09 computed CBS-4M electronic enthalpies.

For 1-VTZ this should, in accordance with hexanitrostilbene (HNS), due to the larger π-system not only result in a higher energetic performance but also higher thermal stability and lower sensitivity of the corresponding ECC. [41] Throughout the sophisticated combination of anion, central metal, and *N*-vinyl or *N*-allyl ligand, the preparation of green ECC, capable of replacing LA or LS, is aimed. Noteworthy, the polymerization of 1-ATZ and 1-VTZ has already been investigated in the early 1960's in an attempt to develop promising energetic polymers. [42]

4.2 Results and Discussion

4.2.1 Synthesis of the Ligands

Initially, the nitrogen-rich heterocycle 1-vinyltetrazole (**1**) was readily prepared *via* a convenient two-step reaction starting from commercially available 2-chloroethylamine hydrochloride (Scheme 1). In the first step, the primary amine salt was converted in a [3+1+1] cyclization to the corresponding 1-substituted alkyl tetrazole upon treatment with an excess of triethyl orthoformate and sodium azide in glacial acetic acid at 100 °C for 3 h. [43] Subsequent elimination of hydrogen chloride from the isolated intermediate 1-(2-chloroethyl)tetrazole (1-ClET) under basic conditions and elevated temperature led to the desired product 1-VTZ (**1**, Scheme 1). An alternative sequence for the preparation of 1-ClET has been published independently by FINNEGAN *et al.* [32] and GAPONIK *et al.,* [31] and involves the formation of 1-(2-hydroxyethyl)tetrazole (1-HET) followed by subsequent chlorination. However, since both approaches require a higher number of reaction steps, the synthesis in Scheme 1 was preferred.

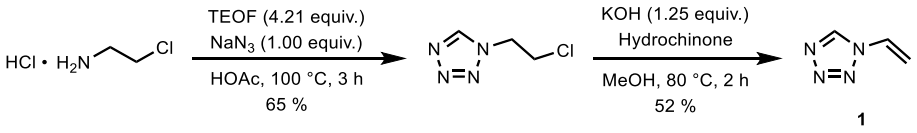

Scheme 1. Synthesis of 1-vinyltetrazole (**1**, 1-VTZ).

1-Allyltetrazole (**1**) was prepared by adapting a literature-known procedure starting from commercially available allylamine (Scheme 2). [27] In analogy to the first reaction step of the 1-VTZ (**1**) synthesis (Scheme 1), a three-component heterocyclization reaction of the free amine with triethyl orthoformate and sodium azide was carried out in an acetic acid medium. The resulting crude product was isolated by column chromatography (EtOAc / hexanes 1:1), yielding the target compound as a pale-yellow liquid (60%).

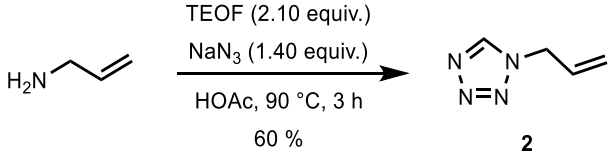

Scheme 2. Synthesis of 1-allyltetrazole (**2**, 1-ATZ).

Retrosynthetically, 1-ATZ (**2**) can also be synthesized starting from 3-chloropropylamine hydrochloride. Following the same synthesis strategy as for 1-VTZ (**1**, Scheme 2), ring closure with subsequent cleavage of hydrogen chloride from the resulting chloropropyltetrazole is possible under basic conditions and elevated temperatures. An alternative approach described in the literature is the substitution reaction of 1*H*-tetrazole and alkyl halides, after which the formed 1- and 2-isomers are separated and purified by vacuum distillation. [44]

Notably, the solid-liquid crude product 1-VTZ (**1**) could be purified by sublimation *in vacuo* (40 °C / 10 mbar) on a cooling finger with solid carbon dioxide-ethanol as coolant. Here we obtained single crystals of 1-VTZ (**1**), which had already been synthesized in 1958 (Fig. 2). [38,45]

4.2.2 Synthesis of the ECCs

To date, several complexes based on 1-VTZ (**1**) and 1-ATZ (**2**) utilizing chloride, nitrate, and thiocyanate as counterion have been reported in the literature but were neither energetically nor structurally investigated. [35-37,46] Apart from structural elucidation, we aimed to investigate the energetic properties of 1-VTZ (**1**) and 1-ATZ (**2**) in various novel transition metal complexes and their potential use as primary explosives, especially aiming for an increase in performance through the implementation of the vinyl or allyl moiety.

As neutral *N*-substituted tetrazoles, the ligands 1-VTZ (**1**) and 1-ATZ (**2**) were incorporated in ECC with anionic oxidizing agents (e.g., perchlorate, chlorate, nitrate, dinitramide), powerful anionic azido ligands or nitrophenolate anions derived from picric acid (HPA), styphnic acid (H_2TNR) or trinitrophloroglucinol (TNPG), leading to powerful energetic materials. The alteration of both the metal(II) center and the counter anion results in ECC with adjustable sensitivity, solubility, and performance parameters. [21] For the preparation of all coordination compounds, water or ethanol were chosen as environmentally friendly solvents. The perchlorate transition metal 1-VTZ complexes **3**–**8** were prepared by slowly adding stoichiometric amounts of liquid 1-VTZ (**1**) to an aqueous solution of the respective metal(II) salt at room temperature (Scheme 3, top). In case of a suspension formed, the reaction mixture was heated until complete dissolution. Both water and ethanol are suitable solvent systems for the preparation of the ECC **3**–**8**, whereby the use of ethanol accelerates the crystallization process at room temperature. All perchlorate 1-VTZ complexes **3**–**8** were

obtained as frequently observed hexacoordinated metal(II) centers without the inclusion of water.

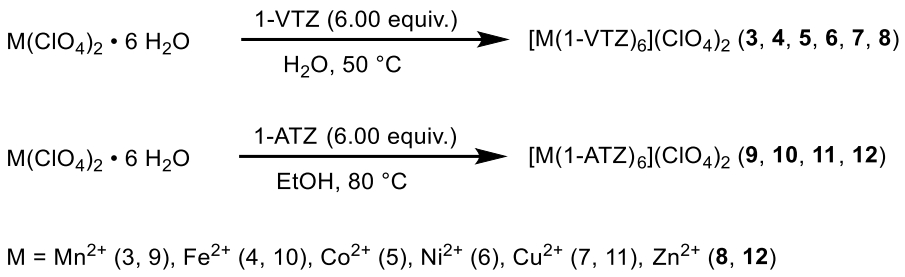

Scheme 3. Synthesis of metal(II) perchlorate-based 1-VTZ (**3**–**8**) and 1-ATZ (**9**–**12**) complexes.

For the synthesis of 1-ATZ (**2**) based perchlorate ECC **9**–**12**, the ligand 1-ATZ (**2**) was added to an ethanolic solution of the corresponding metal(II) salt at elevated temperature (Scheme 3, bottom). All 1-ATZ-based complexes **9**–**12** precipitated from the ethanolic solution, at the least when cooled on ice or by precipitation with an antisolvent in decent to very good yields (49–87%). For crystal growth, small amounts of water were added to the hot ethanolic suspensions until complete dissolution occurred at 80 °C. However, it was difficult to obtain single crystals suitable for X-ray diffraction (XRD), as **9**–**12** show hexagonal plates which are already bent on growing. It was not possible to cut crystals into smaller pieces without introducing many defects. The same phenomenon was reported for hexakis(1-methyltetrazole)iron(II) bis(perchlorate). [47] While crystal structures could be obtained for $[Fe(1\text{-}ATZ)_6](ClO_4)_2$ (**10**) and $[Cu(1\text{-}ATZ)_6](ClO_4)_2$ (**11**), $[Mn(1\text{-}ATZ)_6](ClO_4)_2$ (**9**) and $[Zn(1\text{-}ATZ)_6](ClO_4)_2$ (**12**) were highly disordered and a complete refinement of the data was not feasible. It was nevertheless possible to get an insight into their composition, which was confirmed by elemental analysis (EA).

The copper(II) coordination compound $[Cu(NO_3)_2(H_2O)(1\text{-}VTZ)_2]$ (**13a**) was prepared by applying ligand **1** to an aqueous solution of $Cu(NO_3)_2$, providing the nitrato complex **13a** in 81% yield after seven days of crystallization (Scheme 4). To prevent the incorporation of aqua ligands, the reaction conditions were adapted. Using ethanol as the reaction medium led to the formation of the nitrate complex $[Cu(1\text{-}VTZ)_6](NO_3)_2$ (**13b**). Unfortunately, only a few single crystals suitable for XRD could be isolated. It is assumed that a slow conversion from complex $[Cu(1\text{-}VTZ)_6](NO_3)_2$ to the monohydrate species $[Cu(NO_3)_2(H_2O)(1\text{-}VTZ)_2]$ (**13a**) is taking place. Due to its instability against moisture, no elemental analysis pure sample of **13b** was obtained. In particular, the copper(II) nitrate complex known in the literature with the composition $[Cu(NO_3)_2(1\text{-}VTZ)_4] \cdot H_2O$ was not

obtained in our experiments. [36] As for the complexes of copper(II) nitrate with 1-ATZ, $[Cu(NO_3)_2(1\text{-}ATZ)_2]$ and $[Cu(1\text{-}ATZ)_6](NO_3)_2$ have already been reported by LAVRENOVA *et al.*. [39] By applying the reaction conditions (solvent system, ligand concentration, temperature) as shown in Scheme 4, another species $[Cu(1\text{-}ATZ)_3(NO_3)_2]$ (**14**) could be obtained after two days of crystallization. However, probably due to the co-crystallization of the above-mentioned species, no elemental analysis pure sample of **14** was obtained.

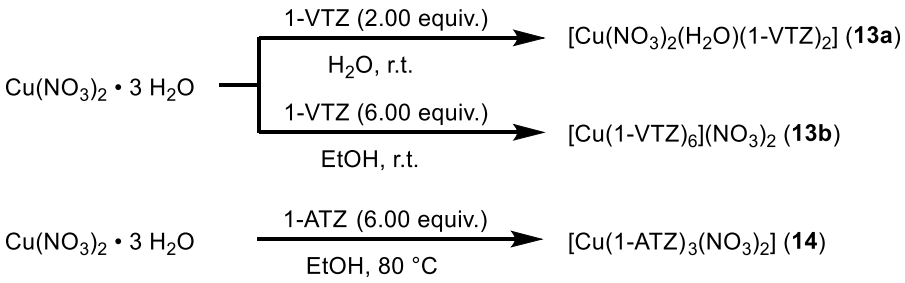

Scheme 4. Synthesis of selected copper(II) nitrate-based 1-VTZ (**13a**, **13b**) and 1-ATZ (**14**) complexes.

Besides the perchlorate, the less toxic, highly oxidizing chlorate anion was used in ECC. In correspondence to a recently published protocol, [48] $[Cu(1\text{-}VTZ)_6](ClO_3)_2$ (**15**) and $[Cu(1\text{-}ATZ)_6](ClO_3)_2$ (**16**) were synthesized by reacting a freshly prepared aqueous solution of copper(II) chlorate with the respective stoichiometric amounts of the nitrogen-rich ligand 1-VTZ (**1**) or 1-ATZ (**2**) (Scheme 5). $Cu(ClO_3)_2$ is formed *in situ* by a metathesis reaction of copper(II) sulfate and barium chlorate. Both complexes were obtained in the form of single crystals in moderate yields (34–60%).

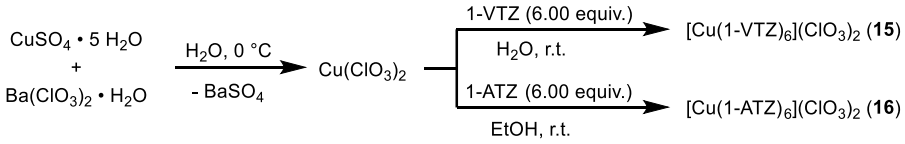

Scheme 5. Formation of the copper(II) 1-VTZ (15) and 1-ATZ (16) chlorate complex.

In the case of the copper(II) dinitramide complexes $[Cu(DN)_2(1\text{-}VTZ)_2]$ (**17**) and $[Cu(DN)_2(1\text{-}ATZ)_2]$ (**18**), stoichiometric amounts of the respective ligand 1-VTZ (**1**) or 1-ATZ (**2**) were combined with a freshly prepared aqueous solution of copper(II) dinitramide (Scheme 6). The mother liquor was left for crystallization at room temperature. Within thirteen days **17** and **18** were obtained as blue crystals in yields of 57% and 72%, respectively. For the *in situ* preparation of $[Cu(H_2O)_x](DN)_2$, dinitraminic acid (HDN) was reacted with basic copper(II) carbonate.

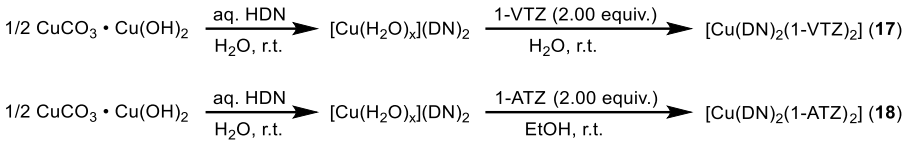

Scheme 6. Synthesis of the energetic copper(II) dinitramide complexes **17** and **18**.

Based on our previously published work, the corresponding copper(II) azide complexes **19** and **20** were prepared. Thus, layering experiments were performed resulting in single crystals of the respective ECC (Scheme 7). The bulk synthesis was attempted by slowly adding an aqueous solution of sodium azide to *in situ* generated complexes of soluble $CuCl_2 \cdot 2\ H_2O$ with **1** or **2** as ligand. [49] Unfortunately, no elemental analysis pure material could be obtained, most likely because of the formation of various unidentified side species.

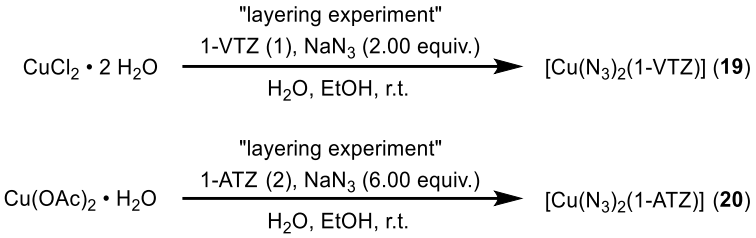

Scheme 7. Single crystal formation of the copper(II) azide complex **19** and **20**.

The commercially unavailable metal(II) precursors for complexes **21**–**23** were prepared by reacting basic copper(II) carbonate with the corresponding acid. [50] To the *in situ* obtained copper(II) trinitrophenolates, the ligand was added dropwise at elevated temperatures and the solutions were left for crystallization at room temperature (Scheme 8). Within several hours or days, all complexes were obtained without aqua ligands or inclusion of crystal water in decent yields (71−84%).

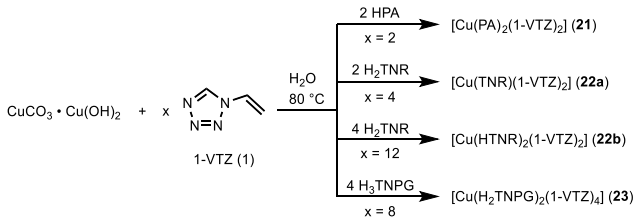

Scheme 8. Synthesis of the trinitrophenolate-based coordination compounds **21**–**23**.

All transition metal complexes were obtained directly from the mother liquor or the solvent layer experiment either by crystallization (**3**–**8**, **13**–**23**) or precipitation (**9**–**12**). The crystals

obtained by slow evaporation were filtered off, washed with small amounts of cold ethanol, and dried in air overnight, not requiring further purification.

4.2.3 Crystal Structures

All ECC **3**–**23** and the ligand 1-vinyltetrazole (**1**, 1-VTZ) were characterized by low-temperature XRD experiments. In the case of **9** and **12,** the measurements allow an indication of the most likely composition, but finalization of the data sets was not possible because of the highly intergrown compounds. Measurement and refinement data are provided in the Supporting Information (Tab. S1–S6). The crystal datasets were uploaded to the CSD database and can be obtained free of charge with the CCDC Nos. 2207191 (**1**), 2207187 (**3**), 2207189 (**4**), 2207252 (**5**), 2207251 (**6**), 2207190 (**7**), 2207194 (**8**), 2207200 (**10a**), 2207254 (**10b**), 2207206 (**11**), 2207205 (**13a**), 2207192 (**13b**), 2207203 (**14**), 2207193 (**15**), 2207199 (**16**), 2207201 (**17**), 2207202 (**18**), 2207204 (**19**), 2207253 (**20**), 2207198 (**21**), 2207207 (**22a**), 2207195 (**22b**), and 2207197 (**23**). Due to the liquid state of 1-allyltetrazole (**2**, 1-ATZ) under ambient conditions, no single crystals could be obtained. Ligand 1-VTZ (**1**) crystallizes in the form of colorless blocks in the monoclinic space group $P2_1/c$ with four formula units per unit cell (Fig. 2). The calculated density of 1-VTZ (**1**, 1.372 g cm^{-3} at 115 K) is higher than the pycnometrically determined density of 1-ATZ (**2**, 1.117 g cm^{-3} at 298 K). The bond lengths and angles of 1-VTZ (**1**) agree well with the geometry of similar literature known *N*1-substituted tetrazole derivatives. All non-hydrogen atoms of ligand 1-VTZ (**1**) are almost perfectly planar (torsion angle N2—N1—C2—C3: –0.1(5)°), indicating a possible interaction between the π-system of the tetrazole ring and the vinyl unit. An insight into the structure of 1-ATZ (**2**) is provided by its transition metal complexes with perchlorate (**10**, **11**), nitrate (**14**), chlorate (**16**), and dinitramide (**18**). In all complexes, the allyl-moiety at the *N*1 position is rotated out of the plane (torsion angle N2—N1—C2—C3: **–**77.7(4)° (**11**), 84.3(3)° (**10**), 92.2(3)° (**14**), –86.2(5)° (**16**) and 122.5(2)° (**18**).

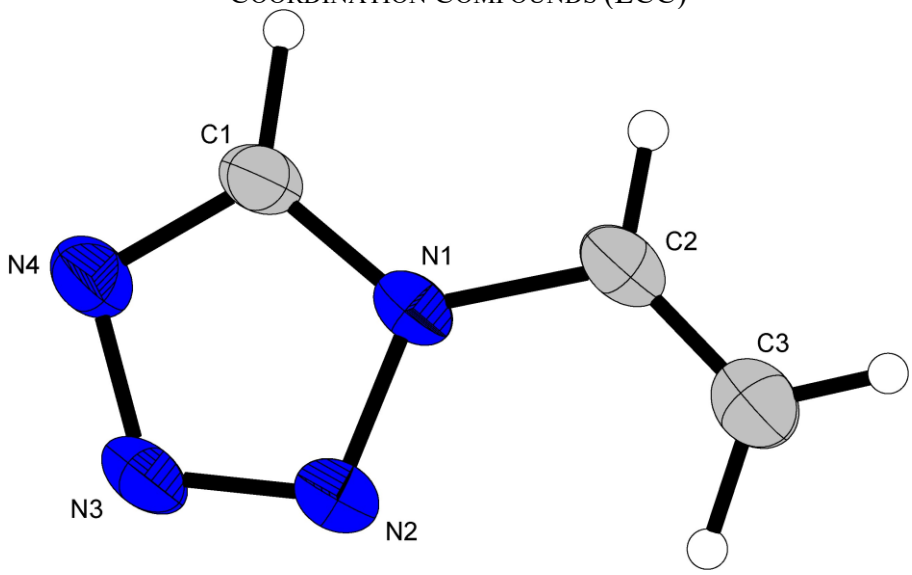

Figure 2. Crystal structure of 1-vinyltetrazole (1-VTZ). Thermal ellipsoids of non-hydrogen atoms in all structures are set to the 50% probability level. Selected bond lengths (Å): N1–N2 1.353(4), N1–C1 1.337(4), N1–C2 1.435(5), N2–N3 1.299(4), N3–N4 1.373(4), N4–C1 1.309(4), C2–C3 1.283(6). Selected bond angles (°): N2–N1–C1 107.9(3), N2–N1–C2 123.4(3), C1–N1–C2 128.7(3), N1–N2–N3 106.0(2), N2–N3–N4 111.2(2), N3–N4–C1 104.7(3), N1–C1–N4 110.2(3), N1–C2–C3 122.8(3).

In the case of 1-VTZ (**1**), the bond lengths and angles of the coordinating ligands in the crystallographically investigated complexes are in the same range as in the non-coordinating molecule. Therefore, they are not part of the discussion in any of the following coordination compounds. However, the torsion angle at which the vinyl group is arranged away from the tetrazole ring system changes with complexation. The relevant torsion angles N2—N1—C2—C3 in the perchlorate complexes **3**–**8** are within 9.4–18.2° and an angle of 5.5° can be found in the chlorate complex $[Cu(1\text{-}VTZ)_6](ClO_3)_2$ (**15**). On the other hand, an angle of 165.5° is found for the dinitramide complex $[Cu(DN)_2(1\text{-}VTZ)_2]$ (**17**). While the torsion angle between the tetrazole plane and the —C═C— plane differ by a maximum of ~7.0° within the perchlorate complexes, the angles in the nitrate complex $[Cu(1\text{-}VTZ)_6](NO_3)_2$ (**13b**) differ significantly from each other (10.2–175.2°).

All copper(II) coordination compounds except the dinitramido (**17**, **18**), nitrato (**14**), and chlorate (**15**, **16**) complexes show an octahedral coordination sphere around the central metal with typical Jahn-Teller distortions along the axial axis. The ligands 1-VTZ (**1**) and 1-ATZ (**2**) show no bridging behavior in transition metal complexes and coordinate exclusively *via* the nitrogen atom at the 4th position of the ring. All prepared 1-VTZ perchlorate complexes **3**–**8** express an octahedral environment, where the central metal is

surrounded by six 1-VTZ ligands and two non-coordinating anions (Fig. 3, left and S1-S5†). All six ECC, except $[Ni(1\text{-}VTZ)_6](ClO_4)_2$ (**6**) (*R*–3), crystallize isotypically in the orthorhombic space group *Pbca* with similar cell volumes (**3**: 3514.3(2) Å^3; **4**: 3476.8(4) Å^3; **5**: 3454.7(4) Å^3; **7**: 3475.5(4) Å^3; **8**: 3488.2(2) Å^3) and parameters (Tab. S1-S2, ESI†).

The unit cell consists of four formula units and the complexes' densities almost increase with increasing atomic number (**3**: 1.570 g cm^{-3} at 111 K; **4**: 1.588 g cm^{-3} at 109 K; **5**: 1.604 g cm^{-3} at 100 K; **6**: 1.552 g cm^{-3} at 96 K; **7**: 1.604 g cm^{-3} at 100 K; **8**: 1.601 g cm^{-3} at 103 K).

Like their 1-VTZ analogs, 1-ATZ-based perchlorate complexes $[Fe(1\text{-}ATZ)_6](ClO_4)_2$ (**10**) and $[Cu(1\text{-}ATZ)_6](ClO_4)_2$ (**11**) show an octahedral coordination sphere formed by a six-fold coordination of the metal center by tetrazole ligands (Fig. 3, right and S6†). Only the copper perchlorate complex $[Cu(1\text{-}ATZ)_6](ClO_4)_2$ (**11**) shows a Jahn-Teller distortion with a typical copper(II) d^9 electronic configuration.

When cooled in liquid nitrogen, the color of $[Fe(1\text{-}ATZ)_6](ClO_4)_2$ (**10**) changes from light beige into light purple (Fig. S39†), indicating a spin-crossover that changes the groundstate from $^5T_{2g}$ to $^1A_{1g}$. [51] Like alkylated tetrazole ligands (MTZ, [52] PTZ, [53] C_3tz, [54] *etc.*) 1-ATZ thus belongs to the compounds of the type $[Fe(R\text{-}TZ)_6]X_2$ (*R*-TZ = 1-alkyl/alkenyl-1*H*-tetrazole, *X* = BF_4, ClO_4, PF_6, CF_3SO_3) as some of the most investigated spin-crossover systems. [47] Therefore, single crystals were measured both at low (**10a**, ρ = 1.588 g cm^{-3} (100 K)) and room temperature (**10b**, ρ = 1.410 g cm^{-3} (297 K)). While the angles hardly change, the HS→LS transition is accompanied by a contraction of the Fe—N4 bond distance (**10a**: ~2.03 Å; **10b**: ~2.18 Å; Fig. S6†) and an increase in density (**10a**: 1.485 g cm^{-3}; **10b**: 1.410 g cm^{-3}). Particularly noteworthy, the corresponding $[Fe(1\text{-}VTZ)_6](ClO_4)_2$ (**4**) complex shows no such behavior. This again proves the strong interdependence between crystal structure and spin-transition features, which both vary drastically with the substituent *R* of the monodentate ligands. [55] All the non-opposing ligands in $[Fe(1\text{-}ATZ)_6](ClO_4)_2$ (**10a**) span angles close to 90° to each other and all the metal-ligand bonds have the same lengths (~2.03 Å), leading to a nearly perfect octahedral environment. Compared to the respective perchlorate complexes of 1-VTZ, $[Cu(1\text{-}ATZ)_6](ClO_4)_2$ (**11**, 1.481 g cm^{-3} at 173 K) and $[Fe(1\text{-}ATZ)_6](ClO_4)_2$ (**10a**, 1.485 g cm^{-3} at 100 K) possess a lower calculated density (~0.1 g cm^{-3}). This is due to the lengthening of the alkenyl chain and the associated higher cell volume of the 1-ATZ ligand.

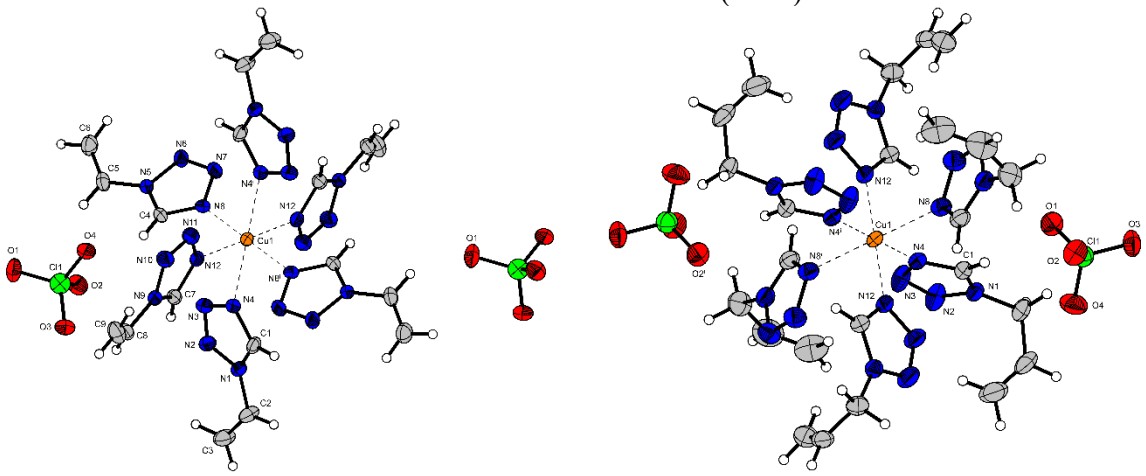

Figure 3. *Left*: Molecular structure of $[Cu(1\text{-}VTZ)_6](ClO_4)_2$ (**7**). Selected bond lengths (Å): Cu1–N4 2.378(3), Cu1–N8 2.031(3), Cu1–N12 2.048(2). Selected bond angles (°): N4–Cu1–N8 88.67(10), N4–Cu1–N12 88.34(9), N8–Cu1–N12 92.17(10). Symmetry code: (i) 1−x, 1−y, 1−z. *Right*: Molecular structure of $[Cu(1\text{-}ATZ)_6](ClO_4)_2$ (**11**). Selected bond lengths (Å): Cu1–N3 2.030(2), Cu1–N8 2.331(3), Cu1–N12 2.060(3). Selected bond angles (°): N3–Cu1–N8 89.54(10), N3–Cu1–N12 89.53(10), N8–Cu1–N12 91.37(11). Symmetry code: (i) –x, −y, −z.

The copper nitrate complex **13a** crystallizes in the orthorhombic space group *Pbcn*. The unit cell consists of four formula units and possesses a calculated density of 1.801 g cm^{-3} at a temperature of 103 K. The coordination sphere of the compound is distorted fivefold square pyramidal (O1—N4—$O1^i$—$N4^i$ = 15.40(13) °) with an aqua ligand at its tip (Fig. 4). The nitrato ligands are shielding the lower coordination position and prevent the formation of an octahedral coordination. Including the very long bond of the nitrato ligands toward the copper center ((O3—Cu1 = 2.815(2) Å) results in a sevenfold coordination sphere. This has already been observed for an alkyl tetrazole-based complex. The anhydrous copper(II) nitrate complex $[Cu(1\text{-}VTZ)_6](NO_3)_2$ (**13b**) also crystallizes as blue blocks in an orthorhombic space group (*Pbca*) with four formula units per unit cell (Fig. 5).

However, the density of 1.580 g cm^{-3} at 102 K is significantly lower than the one of compound **13a**. Like the perchlorate $[Cu(1\text{-}VTZ)_6](ClO_4)_2$ (**7**) the nitrate $[Cu(1\text{-}VTZ)_6](NO_3)_2$ (**13b**) shows the same built-up with six 1-VTZ ligands around the central metal and two noncoordinating anions. The bond distance of the coordinating nitrogen and the metal center is nearly the same ($d_{eq} \approx 2.04$ Å, $d_{ax} \approx 2.38$ Å). The elongation of the N8—Cu1—$N8^i$ axis is caused by a Jahn-Teller distortion along the z-axis of the complex.

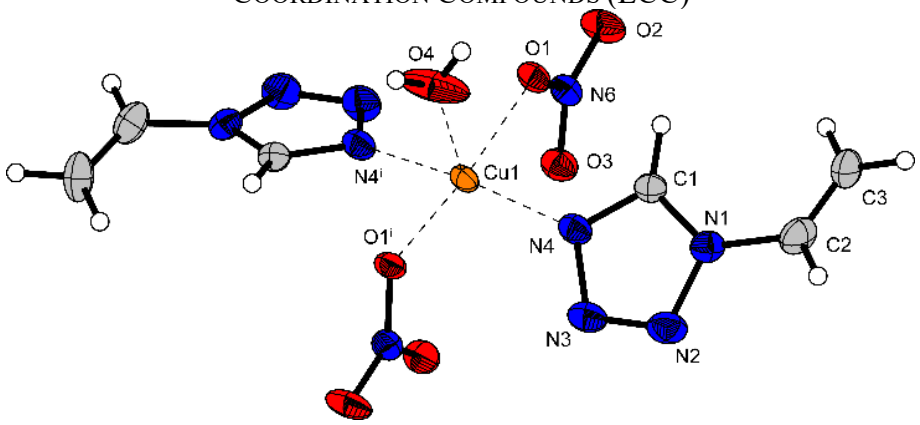

Figure 4. Molecular unit of $[Cu(H_2O)(NO_3)_2(1\text{-}VTZ)_2]$ (**13a**). Selected bond lengths (Å): Cu1–N4 1.985(2), Cu1–O1 1.9787(18), Cu1–O4 2.256(4). Selected bond angles (°): O1–Cu1–N4 89.55(9), N4–Cu1-O4 95.78(8), O4–Cu1–O1 84.86(6), O1–Cu1–O3 50.41(7). Symmetry code: (i) 1−x, y, 0.5−z.

In contrast to $[Cu(1\text{-}VTZ)_6](NO_3)_2$ (**13b**), the coordination sphere of $[Cu(1\text{-}ATZ)_3(NO_3)_2]$ (**14**) consists of three coordinating tetrazole and two nitrato ligands (Fig. 5, right). The copper(II) nitrate complex $[Cu(1\text{-}ATZ)_3](NO_3)_2$ (**14**) crystallizes in the monoclinic space group $P2_1/c$ with four formula units per unit cell and a calculated density of 1.568 g cm^{-3} at 173 K. The coordination sphere could either be interpreted as a distorted fivefold trigonal bipyramidal (O1—Cu1—O4 127.58(6)°, O4—Cu1—N12 89.35(7)°) or as a distorted seven-fold pentagonal bipyramidal depending on whether the longer Cu—O bonds between the central metal and nitrato ligands are included (Cu1—O2 2.6213(17) Å, Cu1—O6 2.916(2) Å). In every case, the equatorial positions are occupied by the anionic nitrato ligands, and one ligand moiety (Fig. 5, right). This coordination geometry has already been observed for $[Cu(1\text{-}NET)_3(NO_3)_2]$[33] and $[Cu(C_4tz)_3(NO_3)_2]$. [54]

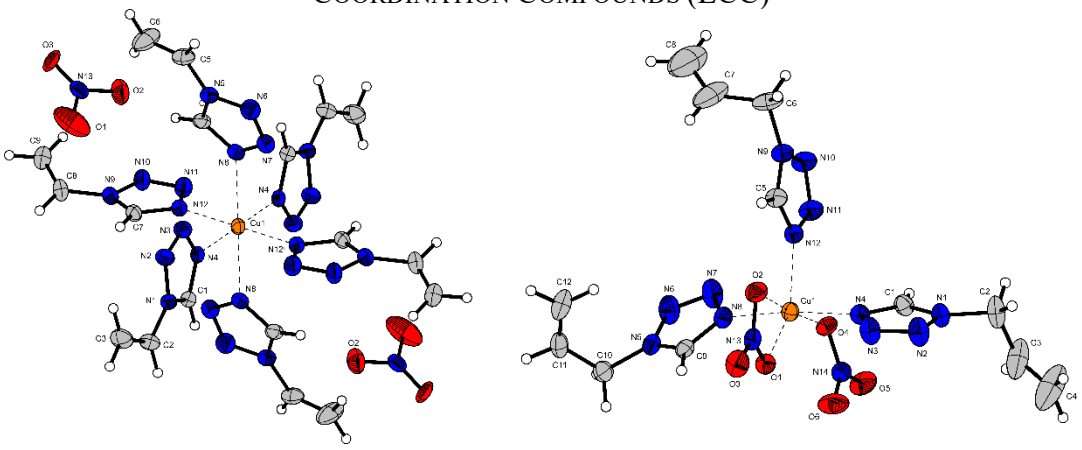

Figure 5. *Left:* Molecular structure of $[Cu(1\text{-}VTZ)_6](NO_3)_2$ (**13b**). Selected bond lengths (Å): Cu1–N4 2.017(2), Cu1–N8 2.379(2), Cu1–N12 2.054(2). Selected bond angles (°): N4–Cu1–N8 89.52(8), N4–Cu1–N12 91.34(9), N8–Cu1–N12 90.35(8). Symmetry code: (i) 1−x, 1−y, 1−z. *Right*: Molecular structure of $[Cu(1\text{-}ATZ)_3(NO_3)_2]$ (**14**). Selected bond lengths (Å): Cu1–O1 2.0192(16), Cu1–O2 2.6213(17), Cu1–O4 2.1805(15), Cu1–O6 2.916(2), Cu1–N4 1.998(2), Cu1–N8 1.978(2), Cu1–N12 2.0712(18), Cu1–N13 2.711(2). Selected bond angles (°): O1–Cu1–O2 54.04(6), O1–Cu1–O4 127.58(6), O1–Cu1–O6 80.78(6), O1–Cu1–N4 89.99(8), O1–Cu1–N8 87.96(8), O1–Cu1–N12 143.04(7), O1–Cu1–N13 27.25(6).

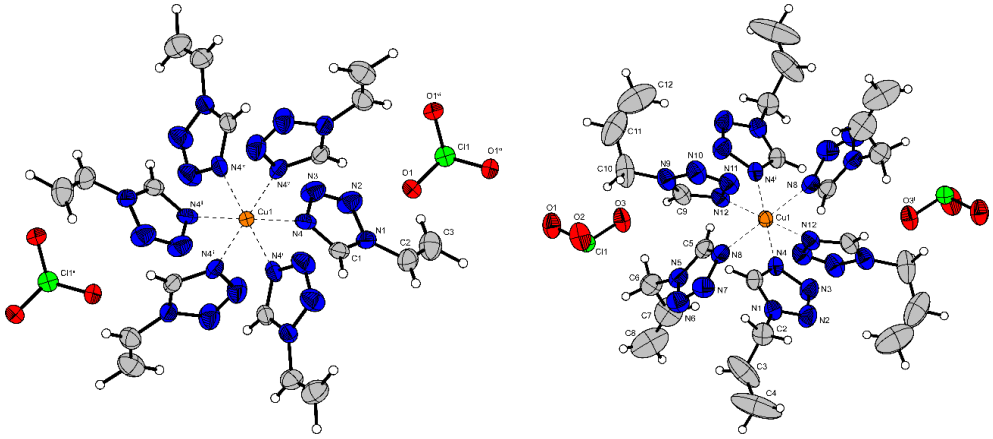

Figure 6. *Left*: Molecular structure of $[Cu(1\text{-}VTZ)_6](ClO_3)_2$ (**15**). Selected bond lengths (Å): Cu1–N4 2.128(3). Selected bond angles (°): N4–Cu1–N4^{i} 90.81(13), N4–Cu1–N4^{iv} 89.19(13). Symmetry code: (i) −y, x−y, z; (ii) −x+y, −x, z; (iii) −x, −y, 1−z; (iv) y, −x+y, 1−z; and (v) x−y, x, 1−z. *Right*: Molecular structure of $[Cu(1\text{-}ATZ)_6](ClO_3)_2$ (**16**). Selected bond lengths (Å): Cu1–N4 2.083(2), Cu1–N8 2.179(3), Cu1–N12 2.143(3). Selected bond angles (°): N4–Cu1–N8 90.56(11), N4–Cu1–N12 88.67(11), N8–Cu1–N12 89.60(11). Symmetry code: (i) 1−x, 1−y, 1−z.

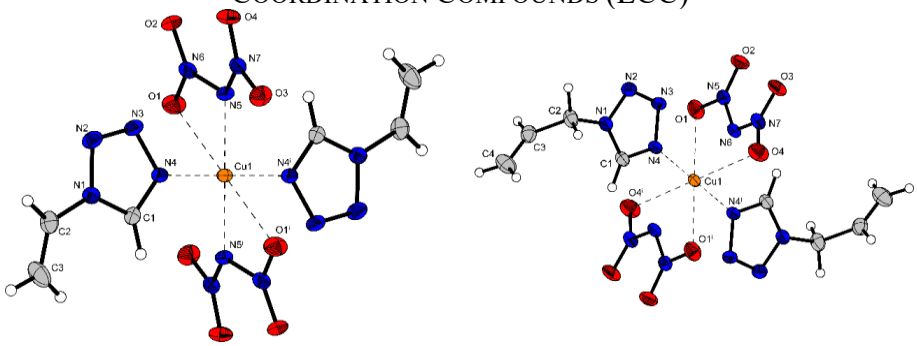

Figure 7. *Left*: Molecular structure of $[Cu(DN)_2(1\text{-}VTZ)_2]$ (**17**). Selected bond lengths (Å): Cu1–O1 2.736(2), Cu1–O3 2.911(2), Cu1–N4 1.986(3), Cu1–N5 1.992(2). Selected bond angles (°): O1–Cu1–O3 98.52(7), O1–Cu1–N4 90.98(9), O1–Cu1–N5 51.32(8), O3–Cu1–N4 79.84(8), O3–Cu1–N5 47.98(8), N4–Cu1–N5 89.92(11). Symmetry code: (i) 1−x, 1−y, 1−z. *Right*: Molecular structure of $[Cu(DN)_2(1\text{-}ATZ)_2]$ (**18**). Selected bond lengths (Å): Cu1–O1 2.8041(18), Cu1–O4 2.845(2), Cu1–N4 1.976(2), Cu1–N6 1.9830(17). Selected bond angles (°): O1–Cu1–O4 98.26(6), O1–Cu1–N4 88.25(6), O1–Cu1–N6 50.03(7), O4–Cu1–N4 83.77(7), O4–Cu1–N6 48.77(7), N4–Cu1–N6 89.84(8). Symmetry code: (i) 1−x, 1−y, 1−z.

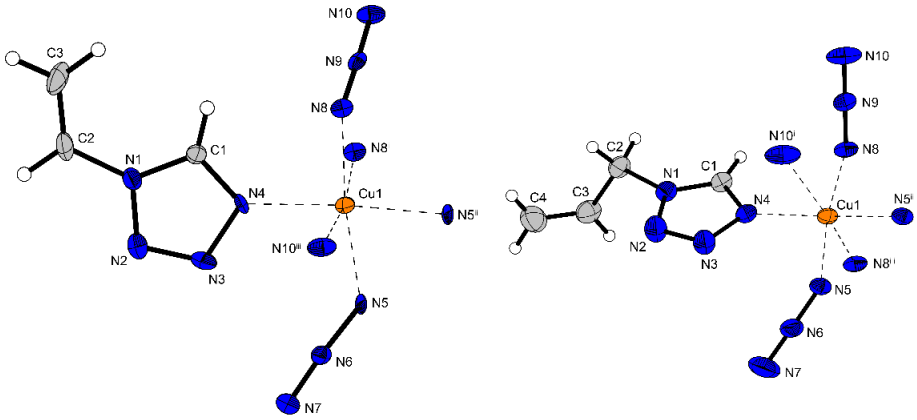

Figure 8. *Left:* Molecular structure of $[Cu(N_3)_2(1\text{-}VTZ)]$ (**19**). Selected bond lengths (Å): Cu1–N4 1.997(7), Cu1–N5 2.005(7), Cu1–N8 2.014(7), Cu1–$N5^{ii}$ 1.983(7), Cu1–$N10^{iii}$ 2.557(8), Cu1–$N8^{i}$ 2.568(7). Selected bond angles (°): N4–Cu1–N8 90.4(3), $N10^{iii}$–Cu1–$N5^{ii}$ 92.9(3), $N10^{iii}$–Cu1–N8 85.8(3). Symmetry codes: (i) 0.5+x, 0.5−y, −z; (ii) 2−x, 1−y, −z; (iii) −0.5+x, 0.5−y, −z. *Right:* Molecular structure of $[Cu(N_3)_2(1\text{-}ATZ)]$ (**20**). Selected bond lengths (Å): Cu1–N4 2.0024(15), Cu1–N5 1.9982(12), Cu1–N8 1.9782(12), Cu1–$N5^{ii}$ 2.0105(14), Cu1–$N10^{i}$ 2.6546(17), Cu1–$N8^{iii}$ 2.4401(13). Selected bond angles (°): N4–Cu1–N8 90.83(6), $N10^{i}$–Cu1–$N5^{ii}$ 89.56(6), $N10^{i}$–Cu1–N8 94.11(5). Symmetry codes: (i) 1−x, −0.5+y, 1.5−z; (ii) 1−x, −y, 1−z; (iii) 1−x, 1−y, 1−z.

Like the $[Cu(1\text{-}ETZ)_6](ClO_3)_2$ complex (CCDC 1898541) [23] the copper chlorate complex $[Cu(1\text{-}VTZ)_6](ClO_3)_2$ (**15**) crystallizes in the hexagonal space group *R*–3 with three formula units per unit cell. The compounds calculated density of 1.499 g cm^{-3} at 101 K is significantly lower than the densities observed for the corresponding perchlorate complex $[Cu(1\text{-}VTZ)_6](ClO_4)_2$ (**7**). The coordination sphere is built up octahedrally by six ligand

moieties, whereas no Jahn-Teller distortion is observed because of the compound's hexagonal space group. Deviating therefrom, the 1-ATZ-based complex $[Cu(1\text{-}ATZ)_6](ClO_3)_2$ (**16**) crystallizes in the monoclinic space group No. 15 (*C*2/*c*) with four formula units per unit cell and a calculated density of 1.455 g cm^{-3} at 173 K.

Both copper(II) dinitramide coordination compounds $[Cu(DN)_2(1\text{-}VTZ)_2]$ (**17**) and $[Cu(DN)_2(1\text{-}ATZ)_2]$ (**18**) crystallize isotypically in the monoclinic space group No. 14 ($P2_1/c$, $P2_1/n$) with two formula units per unit cell. The coordination sphere is built up of two ligand moieties and two coordinating dinitrimido anions (Fig. 7). The calculated density of 1.842 g cm^{-3} at 103 K (**17**) and 1.774 g cm^{-3} at 101 K (**18**) are among the highest observed for coordination compounds based on ligands 1-VTZ and 1-ATZ. The rather uncommon coordination geometry has already been observed for $[Cu(DN)_2(1\text{-}NET)_2]$[33] and can either be interpreted as eightfold, considering the very long Cu—O bonds (**17**: Cu1—O3 = 2.911(2) Å, Cu1—O1 = 2.736(2) Å; **18**: Cu1—O1 = 2.8041(18) Å, Cu1—O4 = 2.845(2) Å), or as double square planar coordination.

Copper azide complex **19** crystallizes in the form of brown platelets in the orthorhombic space group *Pbca* with eight formula units per unit cell and shows the highest density of all investigated complexes (1.992 g cm^{-3} at 123 K), whereas $[Cu(N_3)_2(1\text{-}ATZ)]$ (**20**) crystallizes in the monoclinic space group $P2_1/c$ with four formula units per unit cell and a calculated density of 1.768 g cm^{-3} at 173 K. The molecular unit of both are built up similar to copper(II) azide coordination compounds based on 1-alkyl tetrazoles. [33,49,54] It consists of one copper(II) central metal coordinated by one vinyl tetrazole ligand in the equatorial position and five azido anions (Fig. 8). Overall, two different coordination modes of azido ligands are observed in the structure. The N5 nitrogen atoms bridge between the same copper centers, while the N7 nitrogen atoms do not coordinate at all. The remaining anion bridges twice *via* the N8 nitrogen and once *via* the N10 nitrogen to different copper centers. These two different bridging modes lead to the formation of 2D layers (Fig. 9).

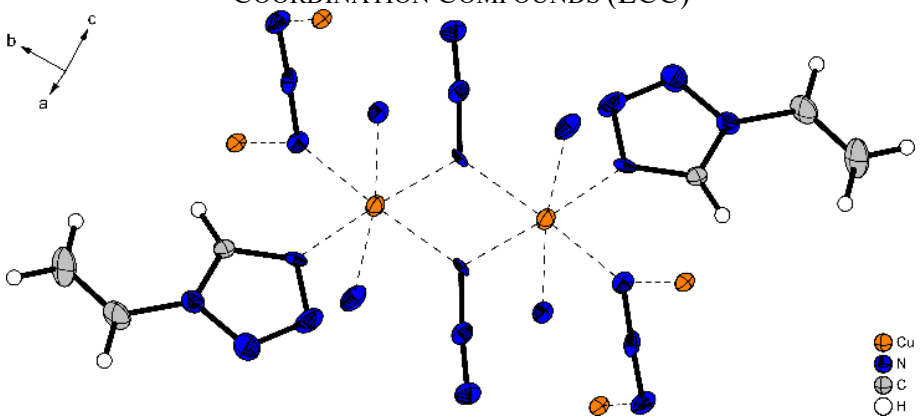

Figure 9. The coordination environment of the copper(II) azide complex **19**.

The coordination compounds $[Cu(PA)_2(1\text{-}VTZ)_2]$ (**21**) and $[Cu(HTNR)_2(1\text{-}VTZ)_2]$ (**22a**) crystallize in the monoclinic space group $P2_1/c$ and the triclinic space group $P\bar{1}$, respectively. Despite the compounds' different space groups, the densities of both ECC are roughly the same (**21**: 1.801 g cm^{-3} at 123 K; **22a**: 1.862 g cm^{-3} at 123 K). A reason for this is most likely the similar coordination geometry both compounds possess. The copper center in complex **21** is coordinated by two picrato ligands with the Cu1—O1 bond (1.9294(1) Å) formed by the hydroxy group of the anion, in the equatorial positions (Fig. 10, left). The Cu1—O7 bond (2.3809(2) Å) between the central metal and a nitrate group of the anion is located in the axial positions. The remaining equatorial binding sites are occupied by 1-VTZ moieties.

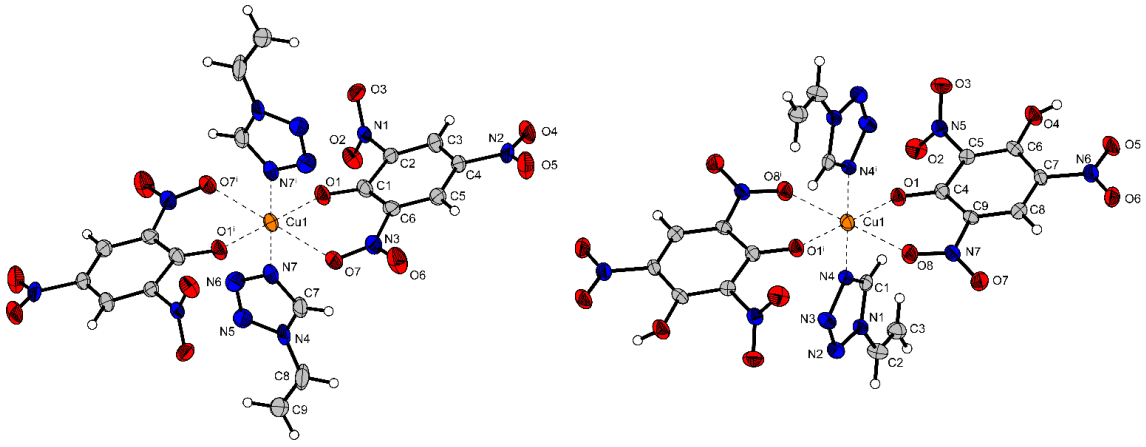

Figure 10. *Left*: Molecular unit of the picrate ECC $[Cu(PA)_2(1\text{-}VTZ)_2]$ (**21**). Selected bond lengths (Å): Cu1–O1 1.9294(1), Cu1–O7 2.3809(2), Cu1–N7 2.0005(2). Selected bond angles (°): N7–Cu1–O7 86.99(15), O1–Cu1–O7 78.51(12). Symmetry code: (i) −x, 1y, 1−z. *Right*: Molecular unit of the styphnate complex $[Cu(HTNR)_2(1\text{-}VTZ)_2]$ (**22a**). Selected bond lengths (Å): Cu1–O1 1.9238(2), Cu1–O8 2.3427(2), Cu1–N4 2.0071(2). Selected bond angles (°): O1–Cu1–N4 89.27(9), O1–Cu1–O8 81.20(8), O8–Cu1–N4 92.05(9). Symmetry code: (i) 1−x, 1−y, −z.

This coordination pattern has already been observed for several tetrazole complexes based on copper picrate. [50,56] The coordination sphere of **22a** (Fig. 10, right) is arranged in the same way as that of **21**, the major difference here being the O1—Cu1—N4—C1 torsion angle (**21**: 68.1(4) °, **22a**: –13.3(3) °). The copper styphnate complex **22b** crystallizes in the orthorhombic space group *Fddd* with 16 formula units per unit cell. The observed density of 1.804 g cm^{-3} (at 103 K) is in the middle range of the values obtained for the trinitrophenolate ECC. The copper cation is coordinated by two 1-VTZ ligands and two bridging styphnate moieties. The tetrazole ligands and the anions are in this case *cis* arranged (Fig. 11).

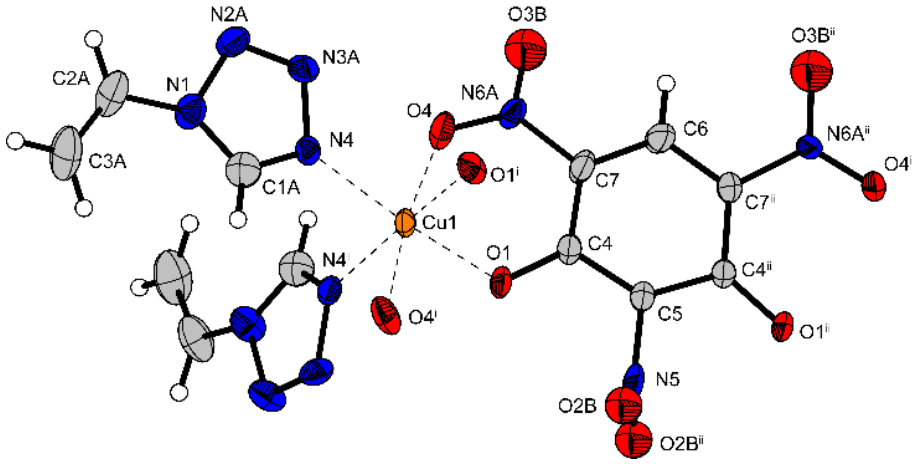

Figure 11. Coordination environment of [Cu(TNR)(1-VTZ)$_2$] (**22b**). Selected bond lengths (Å): Cu1–N4 2.008(3), Cu1–O1 1.944(2), Cu1–O4 2.272(3). Selected bond angles (°): O1–Cu1–O4 81.82(10), O4–Cu1–N4 89.25(10), N4–Cu1–O1 170.79(11). Symmetry codes: (i): 0.75−x, 0.75−y, z; (ii) 1.25−x, y, 1.25−z.

The bridging character of the TNR^{2-} anion leads to the formation of 1D polymeric chains (Fig. 12).

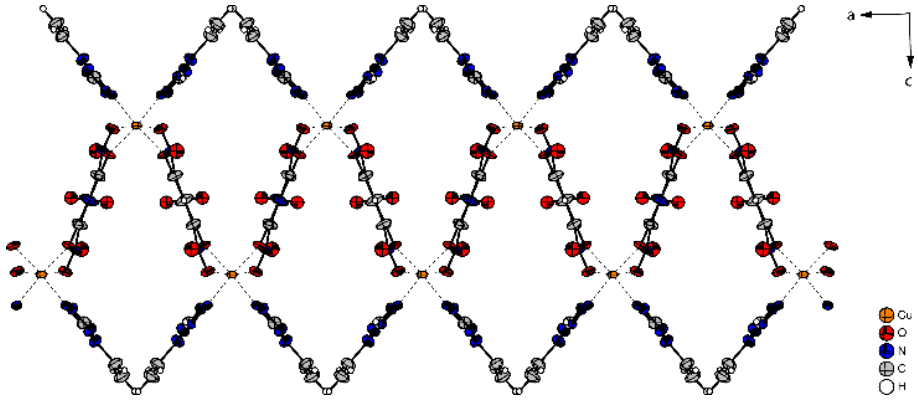

Figure 12. One-dimensional polymeric chains built up by compound **22b**, displayed along the *b* axis.

The ECC $[Cu(H_2TNPG)_2(1\text{-}VTZ)_4]$ (**23**) crystallizes in the form of green prisms in the triclinic space group *P*−1 with a calculated density of 1.767 g cm^{-3} (at 112 K). The unit cell consists of only one formula unit. The octahedral coordination sphere is arranged in a typical manner for the H_2TNPG^- anion.[50] Four 1-VTZ ligands are occupying the equatorial positions, whereas the anions are located in the axial position (Fig. 13).

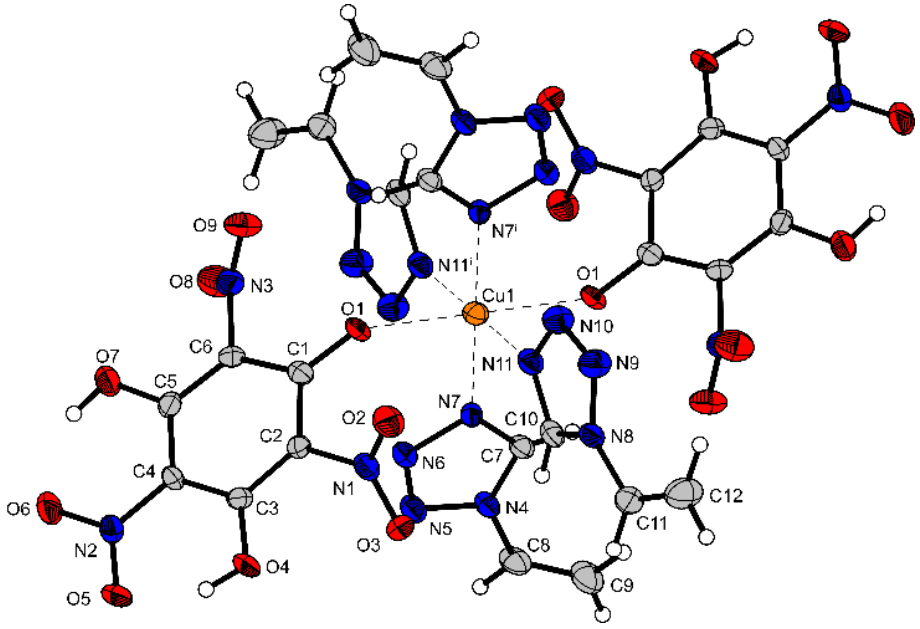

Figure 13. Molecular unit of $[Cu(H_2TNPG)_2(1\text{-}VTZ)_4]$ (**23**). Selected bond lengths (Å): Cu1–N7 2.0100(2), Cu1-N11 2.0201(3), Cu1-O1 2.3331(2). Selected bond angles (°): N7–Cu1–N11 91.224(8), N7–Cu1–O1 94.998(6), O1–Cu1–N11 90.673(6). Symmetry code: (i): 1−x, 1−y, 1−z.

4.2.4 Thermal Stability and Sensitivity Data of the ECCs

Thermal stability measurements were carried out using differential thermal analysis (DTA) in the range from 25 °C to 400 °C at a heating rate of 5 °C min^{-1}. The ligands 1-VTZ (**1**) and 1-ATZ (**2**) together with the compounds **3**–**13a**, **15**–**18**, and **21**–**23** were investigated regarding their stability toward heat. Compounds **13b**, **14, 19,** and **20**, which could not be obtained elemental analysis pure, were not further analyzed. Endothermic events indicating melting, phase transition, or dehydration, together with exothermic events indicating decomposition, are given as the extrapolated onset temperatures. The results of the DTA measurements are summarized in Table 1. Plots of every DTA spectrum measured can be found in the Supporting Information (Fig. S13–S15†).

To further verify endothermic processes that occurred during DTA measurements, thermogravimetric (TG) analysis was applied at a heating rate of 5 °C min^{-1} in the range

from 30 to 400 °C. The TG plots of complexes **3**, **5**, and **9**–**12** can be found in the ESI (Fig. S16 and S17†).

For all metal(II) perchlorate 1-ATZ complexes **9**–**12**, the first endothermic process indicates phase transitions, as no mass loss was observed during TGA and melting could be ruled out visually with a BÜCHI Melting Point B-540 instrument (Fig. S17†). In contrast to $[Fe(1\text{-}ATZ)_6](ClO_4)_2$ (**10**), which decomposes exothermically over a narrow temperature range, thermal decomposition of **9**, **11**, and **12** proceeds endothermically at first, directly followed by an exothermic event (Fig. S15†). This endothermic stage is characterized by a continuous mass loss (**9**: 45%, **11**: 37%, **12**: 41%), indicating the elimination of volatile 1-ATZ from the melt (Fig. S17†). This is confirmed by the weight loss being close to that calculated for the removal of 1-ATZ equivalents (**9**: 48%, **11**: 36%, **12**: 36%). For $[Fe(1\text{-}ATZ)_6](ClO_4)_2$ (**10**) the TG plot exhibits a continuous mass loss (25%) followed by a sharp disintegration event accompanied by complete decomposition (residual mass of 0.2%) (Fig. S17†).

As verified by TGA and BÜCHI experiments, the endothermic event of $[Co(1\text{-}VTZ)_6](ClO_4)_2$ (**5**) at 118°C represents its phase transition (Fig. S16†). Before compounds' **5** complete decomposition (196 °C), the detected mass loss during the TG measurement can be assumed to be the loss of one molecule of 1-VTZ (Fig. S16†). In consistency with the observed hygroscopicity of **3** under ambient conditions, the observed mass loss starting at 98 °C (5.07%) can be assigned to dehydration (Fig. S16†). Thereafter, **3** exhibits distinct disintegration events. One major step of decomposition is identified by an exothermic event at 250 °C.

The melting point of 1-VTZ (**1**, T_{endo} = 18 °C) is slightly higher than given in the literature (15–16 °C). [31] Overall, most of the coordination compounds based on oxidizing anions (**3**–**13a**, **15**–**18**) hardly exceed the thermal stability of the ligand they are based on (Tab. 1). When it comes to coordination compounds based on trinitrophenolate anions, compounds **21**, **22a**, and **22b** possess better thermal stabilities. According to literature, [20,21,23,33] the exothermic events of the nitrate (**13a**), dinitramide (**17**, **18**), and chlorate [48] complexes (**15**, **16**) at rather low temperatures are caused by the anion. Another effect of the anion on the complexes' thermal stability described in the literature is seen in the compounds **21** (T_{exo} = 191 °C) to **23** (T_{exo} = 158 °C). With an increasing number of hydroxy groups, the thermal stability is decreasing. [50] ECC **22b** (T_{exo} = 191 °C) is an exception because of its structure. The double deprotonated styphnate anion is bridging two copper centers and

therefore increasing the stability of the complex. Concluding, the thermal stability within the $[Cu(1\text{-}VTZ)_x(A)_y](A)_z$ complexes decrease in the following sequence: PA^- (191 °C) = TNR^{2-} (191 °C) > $HTNR^-$ (184 °C) > H_2TNPG^- (158 °C) > ClO_4^- (154 °C) > $N(NO_2)_2^-$ (115 °C) > ClO_3^- (107 °C). As expected, the same order is found within the $[Cu(1\text{-}ATZ)_x(A)_y](A)_z$ coordination compounds: ClO_4^- (176 °C) > $N(NO_2)_2^-$ (127 °C) > ClO_3^- (113 °C). It can be stated that the perchlorate complexes **3**–**8** (T_{exo} = 154–207 °C) and **9**–**12** (T_{exo} = 176–222 °C) possess good exothermic decomposition temperatures.

By variation of the central metal in $[M^{II}(1\text{-}VTZ)_6](ClO_4)_2$ complexes **3**–**8** the thermal stability increases in the following order (Tab. 1): Cu^{2+} (154 °C) < Fe^{2+} (165 °C) < Zn^{2+} (174 °C) < Co^{2+} (196 °C) < Ni^{2+} (207 °C) < Mn^{2+} (250 °C). The same tunability is observed in the row of $[M^{II}(1\text{-}ATZ)_6](ClO_4)_2$ complexes **9**–**12** (Fig. 14): Cu^{2+} (176 °C) < Fe^{2+} (201 °C) < Zn^{2+} (194 °C) < Mn^{2+} (222 °C). A similar trend has already been reported for 1-MTZ [21], 1,1-dtp [57] and 1-AT [22] based perchlorate complexes.

Varying the ligand also affects thermal stability. Comparing the $[M^{II}(1\text{-}VTZ)_6](ClO_4)_2$ (**4**, **7**, **8**) with the corresponding $[M^{II}(1\text{-}ATZ)_6](ClO_4)_2$ complexes (**10**–**12**), the elongation of the *N*1-substituted alkenyl moiety leads to higher thermal stability (Fig. 14). Thus, an increase in decomposition temperature is observed from 1-VTZ to 1-ATZ in the respective $[M^{II}(L)_6](ClO_4)_2$ compounds (ΔT_{dec} for Fe^{2+}: 36 °C, Cu^{2+}: 22 °C, Zn^{2+}: 20 °C), which corresponds approximately to the decomposition temperature difference of the free ligands (ΔT_{dec} = 34 °C) (Fig. 14). A comparison of the analogs **3** and **9** is difficult due to their different decomposition behavior. Within $[Cu(L)_6](ClO_3)_2$ analogs the introduction of an additional carbon atom at the ligands' *N*1 position increased the thermal stability (**15**: 107 °C, **16**: 113 °C).

Similarly, an increase in decomposition temperature from 1-VTZ (**17**: 115 °C) to 1-ATZ (**18**: 127 °C) is observed for the $[Cu(DN)_2(L)_2]$ cognates. A similar study on the influence of the alkyl-bridge carbon content in ditetrazole ligands (1,1-dte, 1,1-dtp, 1,1-dtp) supports these findings. [58]

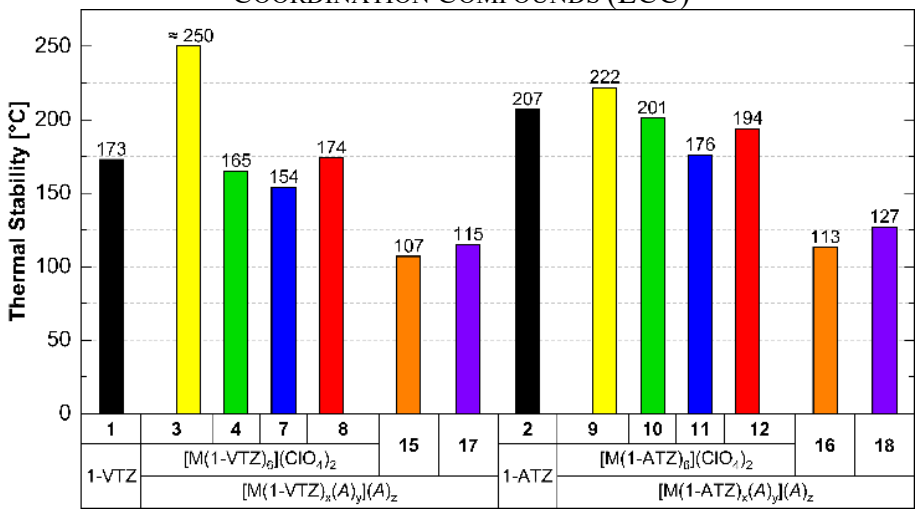

Figure 14. Comparison of the thermal stability of 1-VTZ (**1**) and 1-ATZ (**2**) based complexes with different anions (*A*) and transition metals (*M*), confirming the lower stability of $[M(1\text{-ATZ})_x(A)_y](A)_z$ analogs toward heat.

One of the most important parameters for energetic materials, apart from thermal stability and performance, is their sensitivity to mechanical stimuli as well as electrostatic discharge. Therefore, all pure analytical substances obtained (except the most toxic **5** and **6**) were comprehensively characterized in terms of their sensitivities toward impact, friction as well as electrostatic discharge (Tab. 1). For the energetically more promising 1-VTZ complexes the sensitivity toward ball drop impact was additionally measured (Tab. 1). For BAM friction, [59,61] BAM impact, [62-65] and BAM electrostatic discharge [65] sensitivity measurements, the BAM 1-out of-6 method was applied to determine the lowest ignition force or energy. For the ligands 1-VTZ (**1**) and 1-ATZ (**2**), a characterization of ball drop impact (OZM BIT-132) and electrostatic discharge (OZM XSpark10) was waived because of the compounds' low melting point (**1**) or liquid state (**2**).

Considering the sensitivities of the *N*1-alkenylated tetrazoles **1** (*IS* = 15 J, *FS* = > 360 N) and **2** (*IS* = > 40 J, *FS* = > 360 N), the lengthening of the alkenyl chain decreases sensitivity toward impact. Whilst the *N*1-allyl-substituted tetrazole **2** can be categorized as insensitive toward both friction and impact, **1** is sensitive to impact. [66] In either case, subsequent complexation leads to more sensitive compounds than with the neutral ligands.

Amidst the 1-VTZ-based ECC, the dinitramide complex **17** (*IS* ≤ 1 J) is the most impact sensitive compound with no-fire-level being determined (Tab. 2 and Fig. 15). This is followed by most of the chlorate and perchlorate complexes with impact sensitivities between 2 and 4 J, as well as the styphnate and trinitrophloroglucinate complexes **22**–**23** (Tab. 1). The zinc perchlorate **8** (*IS* = 6 J), copper nitrate **13a** (*IS* = 6 J) and ultimately the

copper picrate complex **20** (*IS* = 10 J) possess the lowest sensitivities. The friction sensitivity measurements on the other hand indicated that the copper chlorate complex **15** is the most sensitive compound (*FS* = 2 N) (Tab. 1 and Fig. 16).

Table 1. Summary of the compounds' thermal stability[a] as well as sensitivities toward various external stimuli.

Compound	No.	$T_{endo.}$ (°C)[b]	$T_{exo.}$ (°C)[c]	*IS* (J)[d]	*FS* (N)[e]	*ESD* (mJ)[f]	*BDIS* (mJ)[g]
1-VTZ	**1**	18	173	15	> 360	n.d.	n.d.
1-ATZ	**2**	—	207	> 40	> 360	n.d.	n.d.
$[Mn(1\text{-}VTZ)_6](ClO_4)_2$	**3**	115[h]	115[h], ≈ 250	2	20	1080	> 200
$[Fe(1\text{-}VTZ)_6](ClO_4)_2$	**4**	120	165	4	3	480	41
$[Co(1\text{-}VTZ)_6](ClO_4)_2$	**5**	118	196	n.d.	n.d.	n.d.	n.d.
$[Ni(1\text{-}VTZ)_6](ClO_4)_2$	**6**	—	207	n.d.	n.d.	n.d.	n.d.
$[Cu(1\text{-}VTZ)_6](ClO_4)_2$	**7**	154[h]	154[h]	2	7	317	194
$[Zn(1\text{-}VTZ)_6](ClO_4)_2$	**8**	100, 174[h]	174[h]	6	10	1500	> 200
$[Mn(1\text{-}ATZ)_6](ClO_4)_2$	**9**	61, 187	222	20	216	1500	n.d.
$[Fe(1\text{-}ATZ)_6](ClO_4)_2$	**10**	77	201	5	96	480	n.d.
$[Cu(1\text{-}ATZ)_6](ClO_4)_2$	**11**	76, 176[h]	176[h]	5	72	420	n.d.
$[Zn(1\text{-}ATZ)_6](ClO_4)_2$	**12**	89, 194[h]	194[h]	25	168	1500	n.d.
$[Cu(NO_3)_2(H_2O)(1\text{-}VTZ)_2]$	**13a**	78, 110[h]	110[h]	6	160	> 1500	> 200
$[Cu(1\text{-}VTZ)_6](ClO_3)_2$	**15**	79	107	4	2	480	≤ 4
$[Cu(1\text{-}ATZ)_6](ClO_3)_2$	**16**	58	113	3	36	600	n.d.
$[Cu(DN)_2(1\text{-}VTZ)_2]$	**17**	—	115	≤ 1	9	250	28
$[Cu(DN)_2(1\text{-}ATZ)_2]$	**18**	—	127	2	48	480	n.d.
$[Cu(PA)_2(1\text{-}VTZ)_2]$	**21**	—	191	10	288	750	> 200
$[Cu(HTNR)_2(1\text{-}VTZ)_2]$	**22a**	—	184	2	96	1080	> 200
$[Cu(TNR)(1\text{-}VTZ)_2]$	**22b**	—	191	2	144	750	180
$[Cu(H_2TNPG)_2(1\text{-}VTZ)_4]$	**23**	—	158	3	84	1080	> 200

[a] Onset temperature at a heating rate of 5 °C min^{-1} measured by DTA. [b] Endothermic peak, which indicates melting, dehydration, loss of aqua ligands, or phase transition. [c] Exothermic peak, which indicates decomposition. [d] Impact sensitivity according to the BAM drophammer (method 1 out of 6). [e] Friction sensitivity according to the BAM friction tester (method 1 out of 6). [f] Electrostatic discharge sensitivity (OZM XSpark10, method 1 out of 6). [g] Ball drop impact sensitivity (OZM BIT-132). [67] [h] Endothermic signal followed by an exothermic signal; n.d.: not determined.

Nevertheless, the dinitramide complex (**17**, *FS* = 9 N) together with the copper (**7**, *FS* = 7 N) and iron perchlorate complexes (**4**, *FS* = 3 N) is still among the most sensitive compound regarding friction sensitivity. Worth mentioning is the higher frictional sensitivity of the manganese perchlorate coordination compound **3** (*FS* = 20 N) and the trinitrophenolate complexes **22**–**23**, which are ranked among the most sensitive compounds regarding impact sensitivity. In terms of sensitivity to electrostatic discharge, the dinitramide compound **17** (*ESD* = 250 mJ) is again the most sensitive of the ECC studied (Tab. 1 and Fig. 17). With copper and iron being more sensitive than manganese and zinc in the transition metal complexes $[M^{II}(1\text{-}VTZ)_6](ClO_4)_2$ (Fig. 17), the sensitivity of **4** (*ESD* = 480 mJ) and **7** (*ESD* = 317 mJ) are in the same order of magnitude as the chlorate

complex **15** (*ESD* = 480 mJ). This is followed by ECC with oxidizing anions like picrate, trinitroresorcinates or trinitrophloroglucinate (**21**-**23**, *ESD* = 780-1080 mJ), subsequent to $[Mn^{II}(1\text{-VTZ})_6](ClO_4)_2]$ (**3**, *ESD* = 1080 mJ) and $[Zn^{II}(1\text{-VTZ})_6](ClO_4)_2]$ (**8**, *ESD* = 1500 mJ) as the least sensitive compounds.

When it comes to 1-ATZ-based ECC, the perchlorate complexes **9**–**12** are sensitive toward impact (5 – 25 J) and vary from sensitive to very sensitive against friction (72 – 216 N). Among the $[M^{II}(1\text{-ATZ})_6](ClO_4)_2$ complexes, the impact sensitivity increases in the order: Zn^{2+} (25 J) < Mn^{2+} (20 J) < Cu^{2+} (5 J) = Fe^{2+} (5 J) and in the following order toward friction: Mn^{2+} (216 N) < Zn^{2+} (168 N) < Fe^{2+} (96 N) < Cu^{2+} (72 N). Similar trends have been observed in the literature for $[M(L)_6](ClO_4)_2$ (*e.g. L*: 1-MTZ [21], 1-AT [22], 1-APT [24], 1-AMT [68], 1,1-dtp [57]) complexes, with manganese(II) and copper(II) being less sensitive than iron(II) and copper(II) coordination compounds. Compared to the perchlorate complexes **9**–**12** (Fig. 15 and 16), the chlorate (**16**, *IS* = 3 J, *FS* = 36 N) and dinitramide complexes (**18**, *IS* = 2 J, *FS* = 48 N) show an increased sensitivity towards impact and friction, after which they can be classified as very sensitive. ESD sensitivity measurements (Fig. 17) showed comparable values for the copper and iron perchlorate (**10**: 480 mJ; **11**: 420 mJ), chlorate (**16**: 600 mJ), and dinitramide complexes (**18**: 480 mJ). Manganese(II) and zinc(II) in $[M^{II}(1\text{-ATZ})_6](ClO_4)_2$ again seem to less catalyze the compounds' decomposition, leading to a lower sensitivity (**9**, **12**: 1500 mJ).

Comparing analogous complexes based on the different ligands 1-VTZ (**1**) and 1-ATZ (**2**), there is a clear trend of higher stability (IS, FS, ESD) for $[M(1\text{-ATZ})_x(A)_y](A)_z$ correlates (Fig. 15-17). While the free nitrogen-rich ligands show an impact sensitivity difference of about 25 J (Fig. 15), the greatest difference within the perchlorate complexes after formal ligand exchange is observed for manganese(II) (**9**→**3**: Δ*IS* = 18 J) and zinc(II) (**12**→**8**: Δ*IS* = 19 J). Compared to the thermal behavior, the elongation of the alkenyl chain has the least influence on the impact sensitivity of the iron(II) (**10**→**4**: Δ*IS* = 1 J) and copper(II) (**11**→**7**: Δ*IS* = 3 J) complexes. With chlorate and dinitramide as a counter anion, almost no difference in sensitivity can be observed (**16**→**15**: Δ*IS* = −1 J; **18**→**17**: Δ*IS* = 1 J). The same correlations between carbon content (1-VTZ *vs.* 1-ATZ) and desensitization of the complexes can be drawn with regard to friction sensitivity and sensitivity to electrostatic discharge: (i) Manganese(II) (**9**→**3**: Δ*FS* = 196 N, Δ*ESD* = 420 mJ) and zinc(II) perchlorate complexes (**12**→**8**: Δ*FS* = 158 N) are more desensitized than the iron(II) (**10**→**4**: Δ*FS* = 93 N, Δ*ESD* = 0 mJ) and copper(II) analogues (**11**→**7**: Δ*FS* = 65 N, Δ*ESD* = 103 mJ). (ii)

Independent of the varied anions (DN^-, ClO_3^-, ClO_4^-) the copper complexes show desensitization of similar magnitude (ΔFS: 65 N (**11**→**7**), 34 N (**16**→**15**), 39 N (**18**→**17**); ΔESD: 103 mJ (**11**→**7**), 120 mJ (**16**→**15**), 230 mJ (**18**→**17**)), indicating the important role of the central metal. As a consequence, according to the UN Recommendations on the Transport of Dangerous Goods, [66] 1-VTZ complexes (**3**, **4**, **7**, **8**) can be classified as very to extremely sensitive, while 1-ATZ compounds (**9**–**12**) are rated sensitive and are therefore not suitable as future primary explosives.

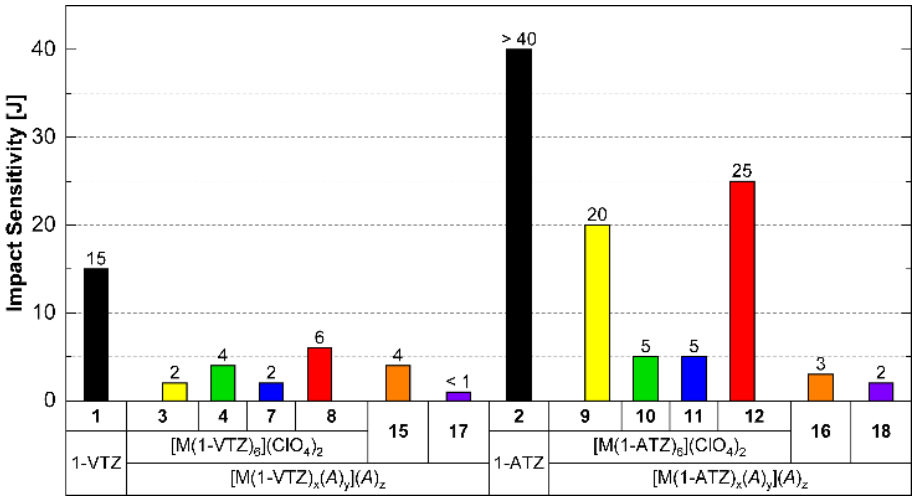

Figure 15. Comparison of the impact sensitivity of 1-VTZ (**1**) and 1-ATZ (**2**) based complexes with different anions (*A*) and transition metals (*M*), confirming the lower stability of $[M(1\text{-ATZ})_x(A)_y](A)_z$ analogs toward impact.

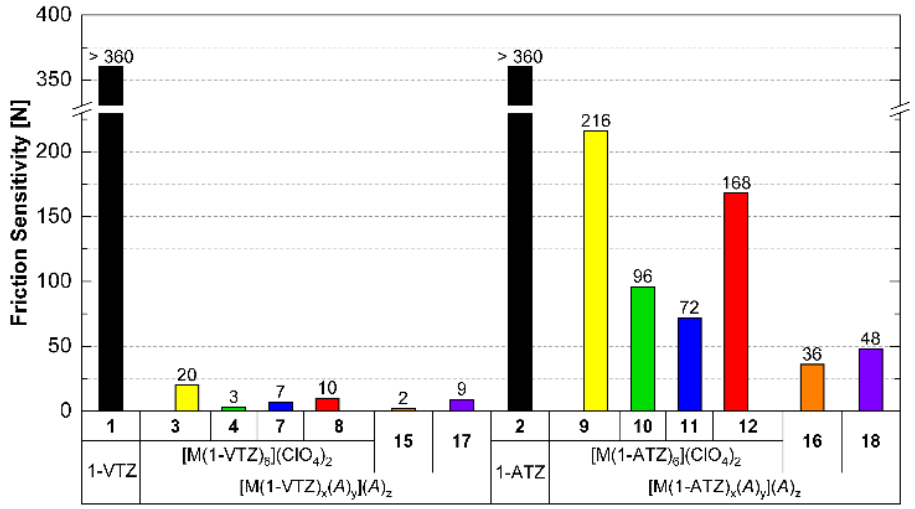

Figure 16. Comparison of the friction sensitivity of 1-VTZ (**1**) and 1-ATZ (**2**) based complexes with different anions (*A*) and transition metals (*M*), confirming the lower stability of $[M(1\text{-ATZ})_x(A)_y](A)_z$ analogs toward friction.

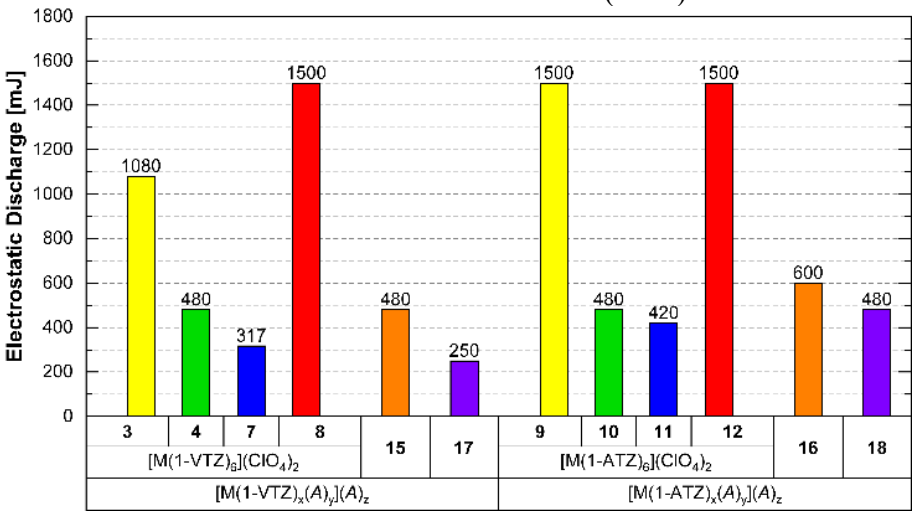

Figure 17. Comparison of the electrostatic discharge sensitivity of 1-VTZ (**1**) and 1-ATZ (**2**) based complexes with different anions (*A*) and transition metals (*M*), confirming the lower stability of $[M(1\text{-ATZ})_x(A)_y](A)_z$ analogs toward electrostatic discharge.

In general, the trends found for both the 1-VTZ and 1-ATZ-based ECC are largely expected and are therefore described in the literature. This is especially relevant for the chlorate complexes, which are known to be among the most sensitive compounds, especially compared to perchlorates (Fig. 14). [33,48] Also extensively studied are the perchlorate monosubstituted tetrazole complexes of the 3d metals manganese, iron, copper, and zinc. In these extensive studies, [21,22,24] the iron and copper perchlorates were found to be more sensitive than the respective manganese and zinc analogs. This tendency also applies predominantly to the compounds $[M^{II}(1\text{-VTZ})_6](ClO_4)_2$ and $[M^{II}(1\text{-ATZ})_6](ClO_4)_2$ (Fig. 15-17). Deviations in impact sensitivity are less significant, as the drop hammer test is known to suffer from inadequacies such as hotspot formation. [69]

Among other things, because of these limitations, an alternative method of impact sensitivity determination, the ball drop impact sensitivity (BDIS), [67] was used in this work to investigate the more sensitive 1-VTZ-based ECC (Tab. 2). The resulting data are in large parts in accordance with our previous work, indicating that a high sensitivity toward friction also comes with high sensitivity toward ball drop impact. [23,33,70] It is also worth mentioning that again no correlations can be drawn between BAM IS and BDIS. Good examples of the correlation between friction and ball drop impact are the copper chlorate complex **15** (*FS* = 2 N; *BDIS* ≤ 4 mJ) and the copper dinitramide ECC **17** (*FS* = 9 N; *BDIS* = 28 mJ). Both compounds were tested extremely sensitive during both measurement types. Furthermore, the trinitrophenolate-based ECC also show a correlation. In these cases, the

complexes tend to be less sensitive toward both methods, as in the case of picrate **21** (*FS* = 288 N; *BDIS* > 200 mJ). Of course, there are exceptions again in this study, especially in the area of perchlorate complexes (**7**, *FS* = 7 N; *BDIS* = 194 mJ). However, since these primary explosives cannot be sieved before testing due to their sensitivity, grain size effects are significantly involved in a reduction in sensitivity here.

Conclusively, every compound was ranked according to the UN Recommendations on the Transport of Dangerous Goods. [66] According to this document, every 1-VTZ-based coordination compound has to be either classified as very sensitive (**3**, **7**, **17**, **22a**, **22b**, **23**) or sensitive (**4**, **8**, **15**, **21**, **13a**) to impact. The 1-ATZ-based transition metal complexes can also be rated as very sensitive (**16**, **18**) or sensitive (**9**–**12**). When it comes to friction sensitivity, only the neutral ligands **1** and **2** are tested to be insensitive. The compounds based on 1-VTZ as ligand are classified at least as sensitive (**13a**, **21**–**23**), very sensitive (**3**), or in the majority even as extremely sensitive (**4**, **7**, **8**, **15**, **17**). With 1-ATZ as ligand the complexes can be only rated very sensitive (**11**, **16**, **18**) or sensitive (**9**, **10**, **12**).

4.2.5 Hot Plate (HP) and Hot Needle (HN) Experiments

The enthalpies of formation of 1-VTZ (**1**), 1-ATZ (**2**), and TNT were calculated at the CBS-4M level of theory for a better comparison, using the atomization energy method and utilizing experimental data. The results are summarized in Table 2.

Table 2. Physicochemical and calculated properties for compounds 1–2 compared to TNT.

	1	**2**	TNT
ρ (298 K) [g cm^{-3}][a]	1.34	1.12 [32]	1.65
N [%][b]	58.3	50.9	18.5
Ω_{CO2} [%][c]	−133.2	−159.8	−74.0
Ω_{CO} [%][d]	−83.3	−101.7	−24.7
T_{endo}[e]/T_{exo}[f] [°C]	18/173	—/207	80/290
$\Delta_f H°$ [kJ mol^{-1}][g]	350.6	334.8	−59.3
Calculated detonation parameters (EXPLO V6.05.04)			
$-\Delta_{Ex}U°$ [kJ kg^{-1}][h]	3712	3472	4406
T_{det} [K][i]	2584	2189	3177
P_{CJ} [kbar][j]	154	82.4	183
V_{det} [m s^{-1}][k]	6503	5702	6798
V_0 [L kg^{-1}][l]	725	751	640

[a] Measured X-ray densities converted to RT. [b] Nitrogen content. [c] Oxygen balance with respect to CO_2 (Ω_{CO2}=((*x*O−2*y*C−1/2*z*H)·1600)/M). [d] Oxygen balance with respect to CO (Ω_{CO}=((*x*O−*y*C−1/2*z*H)·1600)/M). [e] Endothermic peak, which indicates melting. [f] Exothermic peak, which indicates decomposition. [g] Calculated enthalpy of

formation at 298.15 K. [h] Energy of explosion. [i] Detonation temperature. [j] Detonation pressure at the Chapman-Jouguet point. [k] Detonation velocity. [l] Volume of detonation products (assuming only gaseous products).

Both *N*1-alkenyl substituted tetrazoles exhibit highly endothermic enthalpies of formation (**1**: 350.6 kJ mol^{-1}; **2**: 334.6 kJ mol^{-1}), by far surpassing TNT (−59.3 kJ mol^{-1}). To estimate the detonation performances of the prepared ligands, selected key parameters were calculated using EXPLO5 (version 6.05.04), [71] and compared to TNT. The program is based on the chemical equilibrium steady-state model of detonation. It uses the Becker-Kistiakowsky-Wilson equation of state (BKW EOS) for gaseous detonation products and the Cowan-Fickett equation of state for solid carbon. For these calculations, the low-temperature XRD density of 1-VTZ was converted to a room temperature value with the equation $\rho_{298\,K} = \rho_T / (1+\alpha_V(298-T_0)$; $\alpha_V = 1.5\times10^{-4}$ K^{-1} and the density of liquid 1-ATZ was measured with a helium gas pycnometer at room temperature, which is equivalent to the literature value. [32] Noteworthy, a high density is vital for the performance of an energetic material, as the detonation pressure is proportional to the square of its density. [72] Therefore, **1** (6503 m s^{-1}) and **2** (5702 m s^{-1}) both show lower detonation velocity values compared to TNT (6798 m s^{-1}). Having both a higher enthalpy of formation as well as a higher density, 1-VTZ (**1**) shows better detonation parameters than 1-ATZ (**2**).

The 1-VTZ (**3**, **4**, **7**, **8**) and 1-ATZ (**7**–**10**) based perchlorate complexes were tested for their capability of being primary explosives by applying some basic heating tests. A small amount (~5 mg) of the respective ECC was therefore heated on a spatula by a lighter without direct flame contact. All prepared compounds deflagrated upon reaching their ignition temperatures. Next, HP tests were performed for every coordination compound by heating an unconfined sample (again ~30 mg) on a copper plate with a Bunsen burner (Fig. 18). The results are supposed to give insights into a compound's behavior during fast heating. All four 1-ATZ complexes melt before their deflagration. This can also be observed for almost all 1-VTZ analogs, except for $[Fe(1\text{-VTZ})_6](ClO_4)_2$ (**4**), which deflagrates without melting first. The results are summarized in Table 3. Additional images can be found in the Supporting Information (Fig. S18–S34†). Finally, a small sample (again ~30 mg) was fixed and confined onto a surface (copper plate) with a bit of transparent tape and poked by a preheated needle (HN test). The result, preferably a detonation, shows the compound's behavior under slight confinement and is intended to indicate the deflagration-detonation transition (DDT). Only decomposition can be observed with the thermally stable (176-222 °C) 1-ATZ perchlorate complexes. A possible reason is the rapid cooling of the

needle below the necessary ignition temperature. In contrast, the corresponding thermally more unstable (154-174 °C) 1-VTZ compounds show either deflagration or detonation. During HP tests every compound showed deflagration reactions. However, when it comes to HN tests also detonations were observed for compounds **4**, **17**, and **18**. Because of this behavior, these particular compounds are of considerable interest in pentaerythritol tetranitrate (PETN) initiation experiments. Compounds **7** and **15** were also selected for further characterization concerning their initiation capability, as their overall performance during Hot Needle testing, despite the lack of detonation, was also satisfying.

Table 3. Results of the hot plate, hot needle, and PETN initiation tests as well as of laser ignition experiments[a]

Compound	No.	HP	HN	PETN initiation	Laser energy, E^b (mJ)		
					1.7	25.5	51.0
$[Mn(1\text{-}VTZ)_6](ClO_4)_2$	**3**	defl.	defl.	—	—	—	—
$[Fe(1\text{-}VTZ)_6](ClO_4)_2$	**4**	defl.	det.	negative	—	—	—
$[Cu(1\text{-}VTZ)_6](ClO_4)_2$	**7**	defl.	defl.	negative	det.	det.	—
$[Zn(1\text{-}VTZ)_6](ClO_4)_2$	**8**	defl.	defl.	—	—	—	—
$[Mn(1\text{-}ATZ)_6](ClO_4)_2$	**9**	defl.	dec.	—	—	—	—
$[Fe(1\text{-}ATZ)_6](ClO_4)_2$	**10**	defl.	dec.	—	—	—	—
$[Cu(1\text{-}ATZ)_6](ClO_4)_2$	**11**	defl.	dec.	—	✗	✗	✗
$[Zn(1\text{-}ATZ)_6](ClO_4)_2$	**12**	defl.	dec.	—	—	—	—
$[Cu(NO_3)_2(H_2O)(1\text{-}VTZ)_2]$	**13a**	defl.	defl.	—	—	dec.	dec.
$[Cu(1\text{-}VTZ)_6](ClO_3)_2$	**15**	defl.	defl.	negative	det.	det.	—
$[Cu(1\text{-}ATZ)_6](ClO_3)_2$	**16**	defl.	dec.	—	✗	dec.	dec.
$[Cu(DN)_2(1\text{-}VTZ)_2]$	**17**	defl.	det.	negative	det.	defl.	—
$[Cu(DN)_2(1\text{-}ATZ)_2]$	**18**	defl.	det.	negative	defl.	defl.	defl.
$[Cu(PA)_2(1\text{-}VTZ)_2]$	**21**	defl.	dec.	—	—	dec.	dec.
$[Cu(HTNR)_2(1\text{-}VTZ)_2]$	**22a**	defl.	defl.	—	—	dec.	comb.
$[Cu(TNR)(1\text{-}VTZ)_2]$	**22b**	defl.	dec.	—	—	comb.	comb.
$[Cu(H_2TNPG)_2(1\text{-}VTZ)_4]$	**23**	defl.	dec.	—	—	dec.	comb.

[a] —: not tested, ✗: no ignition, dec.: decomposition, defl.: deflagration, det.: detonation, comb.: combustion. [b] Operating parameters: current $I = 7$ A; voltage $U = 4$ V; theoretical maximal output power $P_{max} = 45$ W; theoretical energy $E_{max} = 1.7$–51.0 mJ; wavelength $\lambda = 915$ nm; pulse length $\tau = 1.0$–30 ms.

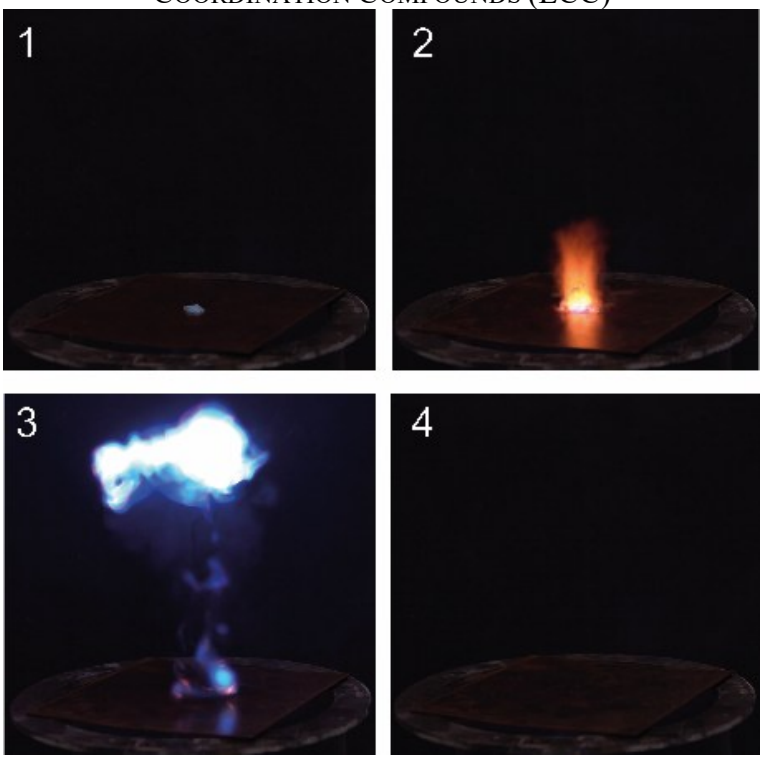

Figure 18. Hot Plate test of compound **9** shown as a sequence.

4.2.6 PETN Initiation Experiments

Following on from the preliminary tests (HP, HN), the most promising compounds were tested to ascertain whether they could ignite a secondary explosive and thus be considered as a potential substitute for lead azide. Showing either sharp deflagrations or even detonations during hot plate and hot needle tests, the dinitramide coordination compounds **17** and **18**, the ECC **4** and **7**, and the copper(II) chlorate complex **15** were tested for their capability of initiating PETN. For this purpose, a 200 mg booster charge of PETN was loaded into a copper shell and the potential primary explosive to be tested was filled on top. More detailed information on the test setup can be found in the general methods of the ESI.† In case of a positive DDT from the primary explosive toward PETN a hole in the copper witness plate and the fragmentation of the copper shell is evident. Of the five tested complexes, none of them were able to initiate PETN. An overview of the test results can be found in Table 3. However, in the case of [Cu(DN)2(1-VTZ)2] (**17**) fragmentation of the shell was observed (S38†).

4.2.7 Laser Ignition Experiments

Besides classic ignition through heat, mechanical stimuli or electric discharge, laser ignition is getting increased attention over the last years. [73-75] This is especially because of the ignition itself. One of the most common ignition methods for pyrotechnic mixtures are primer caps. These are ignited by a hit from the firing pin and the ignition, in the end, is caused by friction within the primer cap. Using laser irradiation for ignition makes the compound's sensitivity toward friction, which is needed for classic ignition, obsolete, and is simultaneously opening the field for less sensitive compounds. This has implications not only for safety but also for the processing and storage of the mixtures and compounds.

Laser ignition experiments were carried out for the copper 1-VTZ and 1-ATZ complexes only. The manganese (**3**, **9**), iron (**4**, **10**), and zinc (**8**, **12**) complexes were waived, as only colored complexes are known to react toward laser irradiation. [22,23] Details on the experiment and setup can be found in the experimental section of the Supporting Information. The outcome of each test is summarized in Table 3.

The most convincing results were obtained for the ECC **7**, **15**, and **17**, showing detonations at an energy level of 1.7 mJ. High-speed images of selected experiments are shown in Fig. 19. As already known from former investigations, [21-23,33] these results again underpin the special suitability of the anions ClO_4^-, ClO_3^-, and DN^- in future laser ignitable ECC. Unsurprisingly, the compounds based on trinitrophenolate anions (**21**–**23**) or the complex of type $[Cu(NO_3)_2(H_2O)(1\text{-VTZ})_2]$ mainly show decomposition reactions and are therefore rather not interesting as laser ignitable energetic materials. Nevertheless, this behavior indicates a correlation between the compounds' performance during HN tests and laser ignition experiments. ECC that exhibit detonation or strong deflagration tend to detonate during laser experiments, while weaker reacting or water-containing compounds usually only decompose. A reason for this correlation is most likely that both experiments were carried out under the confinement of the samples.

The formal introduction of an additional CH_2-group when replacing the *N*1-vinyl with an *N*1-allyl moiety is accompanied by a significant increase in the initiation threshold. While the coordination compounds based on the more energetic ligand **1** detonate at 1.7 mJ (**7**, **15**, **17**), the complementary complexes based on ligand **2** (**11**, **16**, **18**) show either no or only weak reactions, which is within expectations considering the corresponding HN tests.

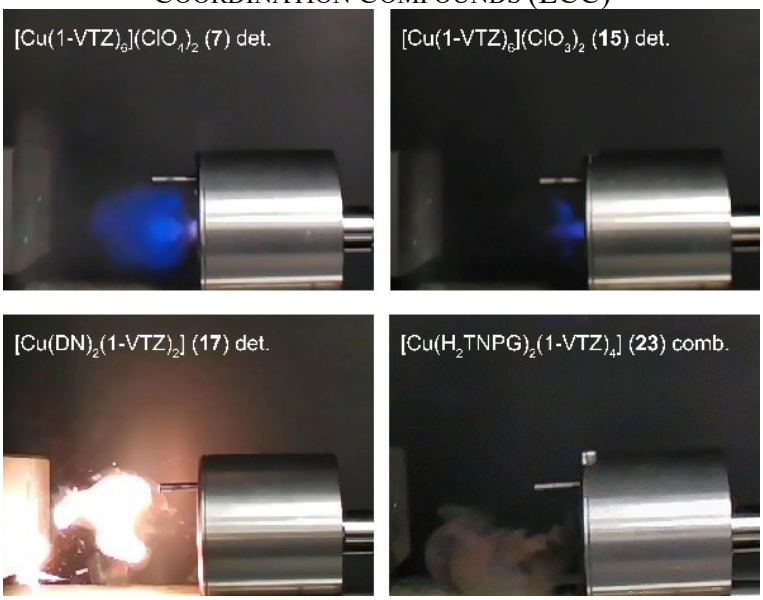

Figure 19. High-speed images of the detonations (det.) of the ECC **7**, **15**, and **17** together with the combustion (comb.) of complex **23** during laser ignition experiments.

4.2.8 Comparison of 1-Ethyltetrazole-based and 1-Propyl-tetrazole-based ECCs

A main target of this work was not only to incorporate vinyl or allyl tetrazoles in energetic coordination compounds but also to investigate the complexes' properties. These properties have been discussed in detail in the sections above, however, these results should be put in relation to already known, similarly arranged complexes. For this purpose, the ligands of this work (**1**, **2**) were subdivided according to their *N*1-substitution pattern and compared with three ligands of the same carbon number (Chart 2). Exactly these ligands, recently published by our group, were chosen on purpose, as it can be assumed that all experiments were performed similarly.

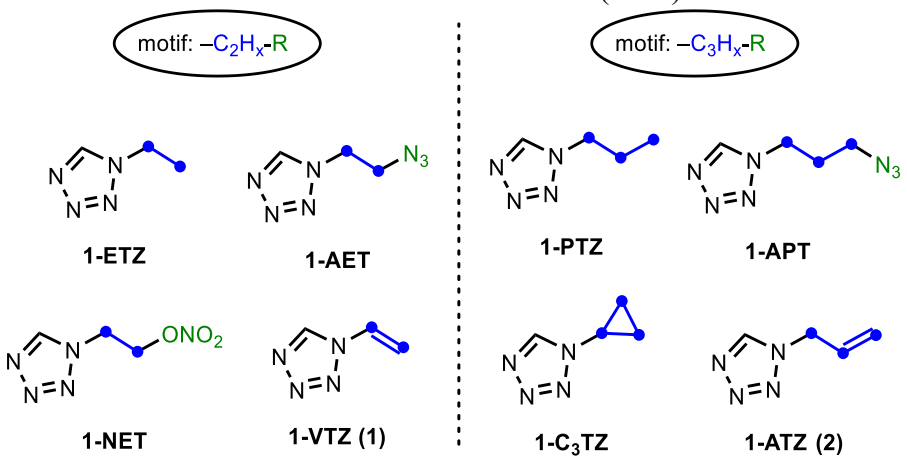

Chart 2. Overview of the ligands used for comparison subdivided according to their structural motif (C_2/C_3-chain/ring).

Unfortunately, we are restricted to a comparison of the ligands themselves and copper as the central metal and chlorate, perchlorate, dinitramide, and picrate as anions. This is mainly because, for example, nitrate or styphnate complexes in many cases have a different composition or coordination geometry, and in many cases, the complexes cannot be isolated when metals other than copper were used. Thermal stability, as well as sensitivity to BAM drop hammer and friction tester, were chosen as comparative variables. Since Hot Plate and Hot Needle tests are considered important preliminary tests for primary explosives, they were used to visualize the compounds' performance. The sensitivity data of the respective ligands and ECC is summarized in Table 4.

Starting with the ligands of the *N*1 substitution pattern —C_2H_x-R, every molecule is insensitive toward friction, which is most likely caused by the liquid state of the compounds. Therefore, no conclusions about ECC can be drawn from this point. The thermal stability on the other hand is the lowest for 1-NET and is again limited by the energetic group (—ONO_2). Consequently, the complexes based on the 1-NET ligand should have the lowest thermal stability. However, it is found that for the dinitramide and picrate complexes the thermal stability is similar (Fig. 19). The same applies to the perchlorate complexes except for the 1-ETZ complex (T_{exo} = 210 °C). Only in the case of $[Cu(1\text{-VTZ})_6](ClO_3)_2$ (**15**, T_{exo} = 107 °C) a significantly lower thermal stability was observed compared to the other complexes.

When it comes to impact sensitivity, the perchlorate, chlorate, and dinitramide ECC based on 1-nitratoehyltetrazole, 1-azidoethyltetrazole, and 1-vinyltetrazole are roughly within the same area of about 1-4 J. Only the coordination compounds having 1-ethyltetrazole as a

ligand are less sensitive (7–10 J). The picrate anion does not allow such a clear pattern since the sensitivities are much more widely scattered. A comparison of the friction sensitivity data indicates, that ECC based on 1-ETZ are the least sensitive complexes.

Table 4. Thermal stability[a], BAM impact, and friction sensitivity together with a hot plate and hot needle test outcome for several ECC based on 1-ethyltetrazole and 1-propyltetrazole ligand derivatives.

*N*1 subst. pattern[b]	Compound	No.	T_{exo} (°C)[c]	IS (J)[d]	FS (N)[e]	HP[f]	HN[f]	Ref.
–C_2H_x–R	1-ETZ		208	> 40	> 360	n.d.	n.d.	[23]
	1-AET		193	9	> 360	n.d.	n.d.	[23]
	1-NET		168	10	> 360	n.d.	n.d.	[33]
	1-VTZ	**1**	172	15	> 360	n.d.	n.d.	
	$[Cu(1\text{-}ETZ)_6](ClO_4)_2$		210	10	120	defl.	defl.	[23]
	$[Cu(1\text{-}AET)_6](ClO_4)_2$		158	< 1	15	defl.	det.	[23]
	$[Cu(1\text{-}NET)_6](ClO_4)_2$		165	3	25	defl.	defl.	[33]
	$[Cu(1\text{-}VTZ)_6](ClO_4)_2$	**7**	154	2	7	defl.	defl.	
	$[Cu(1\text{-}ETZ)_6](ClO_3)_2$		158	7	60	defl.	defl.	[23]
	$[Cu(1\text{-}AET)_6](ClO_3)_2$		146	2.5	4	defl.	det.	[23]
	$[Cu(1\text{-}NET)_6](ClO_3)_2$		149	2	15	defl.	defl.	[33]
	$[Cu(1\text{-}VTZ)_6](ClO_3)_2$	**15**	107	4	2	defl.	defl.	
	$[Cu(1\text{-}AET)_2(DN)_2]$		106	2	5	defl.	defl.	[76]
	$[Cu(1\text{-}NET)_2(DN)_2]$		110	2	7	defl.	defl.	[33]
	$[Cu(1\text{-}VTZ)_2(DN)_2]$	**17**	115	1	9	defl.	det.	
	$[Cu(PA)_2(1\text{-}AET)_2]$		183	3	252	defl.	defl.	[23]
	$[Cu(PA)_2(1\text{-}NET)_2]$		197	20	> 360	defl.	dec.	[33]
	$[Cu(PA)_2(1\text{-}VTZ)_2]$	**21**	191	10	288	defl.	dec.	
–C_3H_x–R	1-PTZ		206	> 40	> 360	n.d.	n.d.	[24]
	1-APT		195	> 40	> 360	n.d.	n.d.	[24]
	1-C_3TZ		200	> 40	> 360	inf.	dec.	[54]
	1-ATZ	**2**	207	> 40	> 360	n.d.	n.d.	
	$[Cu(1\text{-}PTZ)_6](ClO_4)_2$		209	30	240	dec.	dec.	[24]
	$[Cu(1\text{-}APT)_6](ClO_4)_2$		165	2.5	32	defl.	defl.	[24]
	$[Cu(1\text{-}C_3TZ)_6](ClO_4)_2$		183	4	80	defl.	dec.	[54]
	$[Cu(1\text{-}ATZ)_6](ClO_4)_2$	**11**	176	5	72	defl.	dec.	
	$[Cu(1\text{-}PTZ)_6](ClO_3)_2$		152	> 40	168	dec.	dec.	[24]
	$[Cu(1\text{-}APT)_6](ClO_3)_2$		151	2.5	24	defl.	defl.	[24]
	$[Cu(1\text{-}C_3TZ)_6](ClO_3)_2$		156	2	32	defl.	dec.	[54]
	$[Cu(1\text{-}ATZ)_6](ClO_3)_2$	**16**	113	3	36	defl.	dec.	

[a] Onset temperature at a heating rate of 5 °C min^{-1} measured by DTA. [b] R = H, ONO_2, N_3. [c] Exothermic peak, which indicates decomposition. [d] Impact sensitivity according to the BAM drophammer (method 1 out of 6). [e] Friction sensitivity according to the BAM friction tester (method 1 out of 6). [f] dec.: decomposition; inf.: inflammation; defl.: deflagration; det.: detonation; n.d.: not determined.

This is followed by the 1-NET complexes, with the dinitramide complexes being a slight exception here. 1-AET and 1-VTZ coordination compounds together form the most

sensitive of the investigated complexes. The fact that in some cases no patterns are discernible, or exceptions occur is probably due to grain size effects.

The HP and HN data of all complexes based on *N*1-substituted C_2-derived ligands indicate sufficient performance, except the picrate compounds. Deflagrations were observed in the majority of the tests carried out. However, the best results (detonations) were observed for 1-AET-based coordination compounds and in one case for a the 1-VTZ-based complex (**17**). Overall, it can be stated, that ECC based on 1-vinyltetrazole possesses comparable or better thermal stability than ECC based on 1-AET or 1-NET as ligand. In most of the cases, the compounds' friction and impact sensitivity is lower than the ones for 1-AET complexes, whilst having comparable performance data.

Focusing on the tetrazoles with a C_3-based substitution pattern at *N*1, 1-PTZ as the least endothermic ligand forms both the most thermally stable and the least sensitive (*IS*, *FS*) perchlorate complex (Fig. 21). As the endothermicity of the ligands increases, the complexes' thermal stability decreases and their sensitivity increases: 1-C_3TZ (T_{exo} = 183 °C, *IS* = 4 J, *FS* = 80 N) > 1-ATZ (T_{exo} = 176 °C, *IS* = 5 J, *FS* = 72 N) > 1-APT (T_{exo} = 165 °C, *IS* = 2.5 J, *FS* = 32 N). In terms of performance, the HP tests state that starting from the parent 1-PTZ structural motif, formal cyclization (1-C_3TZ) or reduction (1-ATZ) is sufficient for the perchlorate complexes to deflagrate, whereas HN experiments need the azide-substituted ligand (1-APT) for the same outcome.

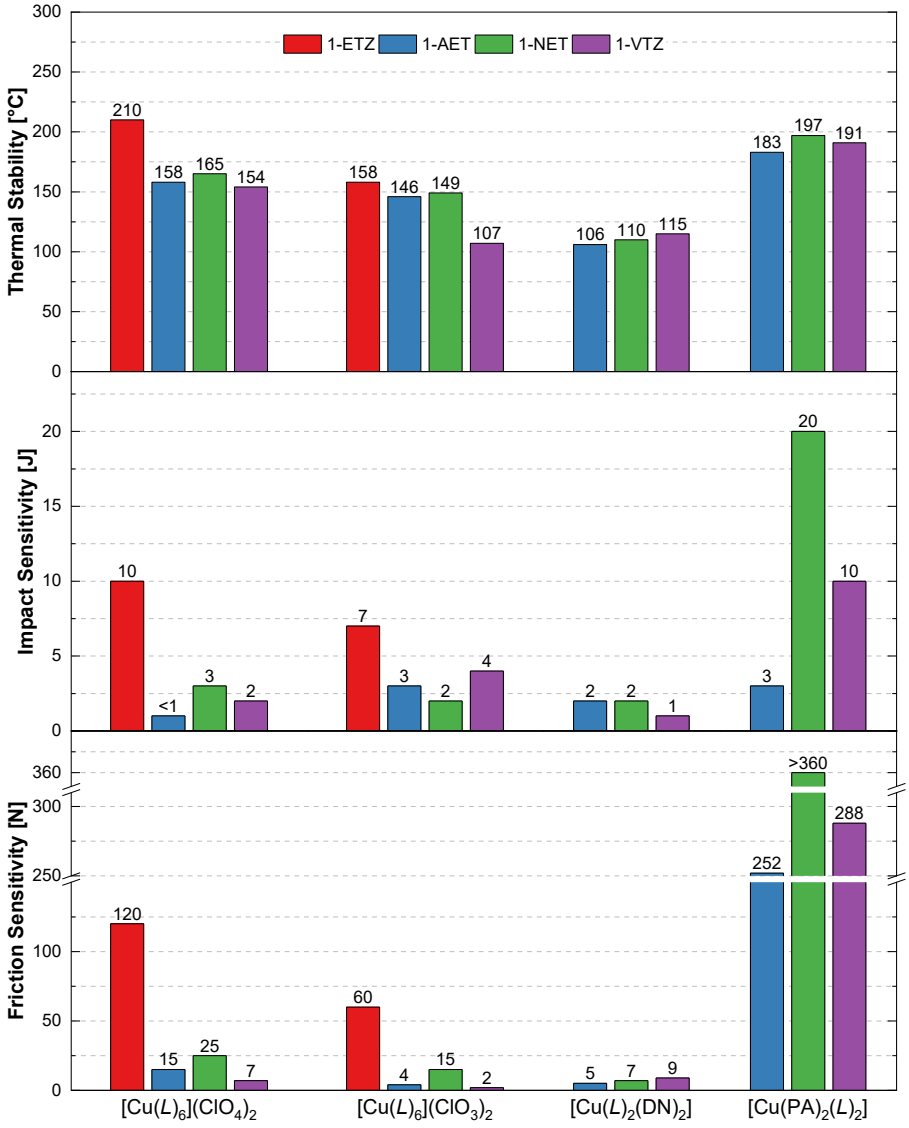

Figure 19. Comparison of the sensitivities and thermal stability of several ECCs based on different *N*1-substituted C_2-derived ligands (*L*).

This observation also applies to the complementary chlorate complexes (Fig. 22). Accordingly, it is not surprising that $[Cu(1\text{-APT})_6](ClO_3)_2$ is the most friction-sensitive ECC, although it should be mentioned that the sensitivities for 1-C_3TZ and 1-ATZ based chlorate complexes are also of approximately the same order of magnitude. Only $[Cu(1\text{-PTZ})_6](ClO_3)_2$ exhibits a significantly lower sensitivity (*IS* = > 40 J, *FS* = 168 N). Contrary to expectations, however, the thermal stabilities of the chlorate complexes based on 1-PTZ (T_{exo} = 152 °C), 1-APT (T_{exo} = 151 °C) and 1-C_3TZ (T_{exo} = 156 °C) are almost identical, while the decomposition temperature for **16** (T_{exo} = 113 °C) is significantly lower. When looking at the uncoordinated *N*1-substituted C_3-derived tetrazole ligands themselves,

all of them can be classified as insensitive to mechanical stimuli. On the whole, this comparative study illustrates (Fig. 21 and 22) that – as is often the case – higher performance goes hand in hand with higher sensitivity.

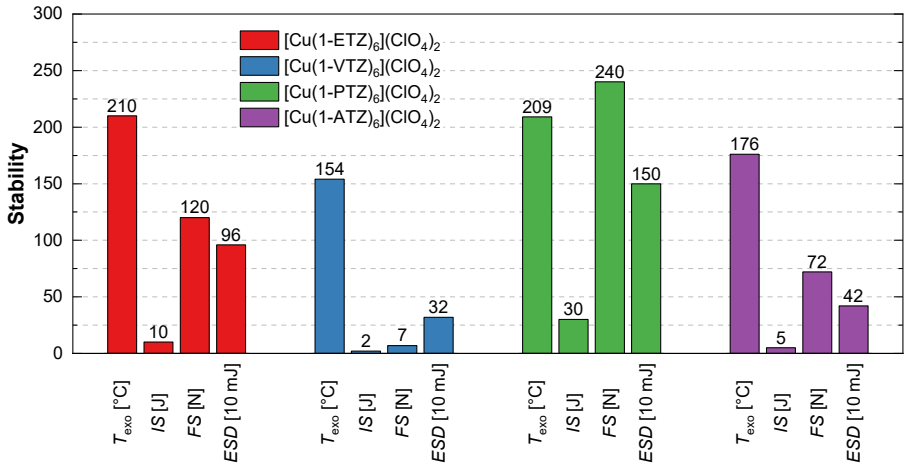

Figure 20. Graphical representation of the influence of the introduction of an unsaturated C—C bond.

If we compare the 1-VTZ-based copper perchlorate complex $[Cu(1\text{-}VTZ)_6](ClO_4)_2$ (**5**) with the corresponding $[Cu(1\text{-}ETZ)_6](ClO_4)_2$ we observe that the introduction of an unsaturated bond leads to an increase in the sensitivities (IS, FS, ESD) on the one hand and to lower thermal stability on the other (Fig. 20).

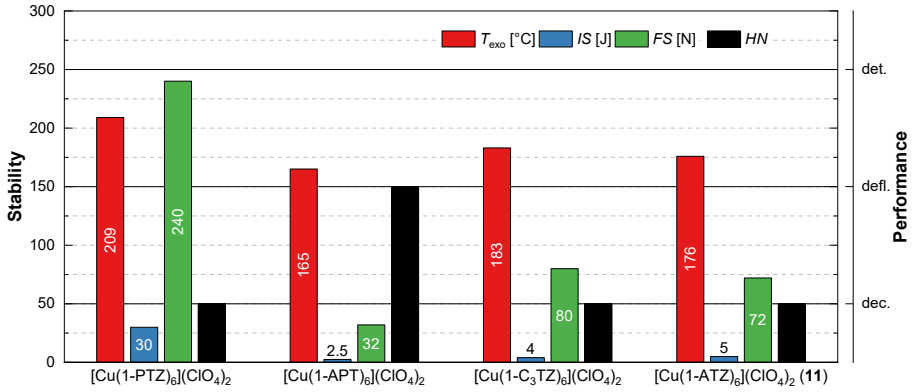

Figure 21. Comparison of the stabilities (T_{exo}, *IS*, *FS*) and performance (*HN*) of the copper(II) perchlorate complexes based on different *N*1-substituted C_3-derived tetrazole ligands.

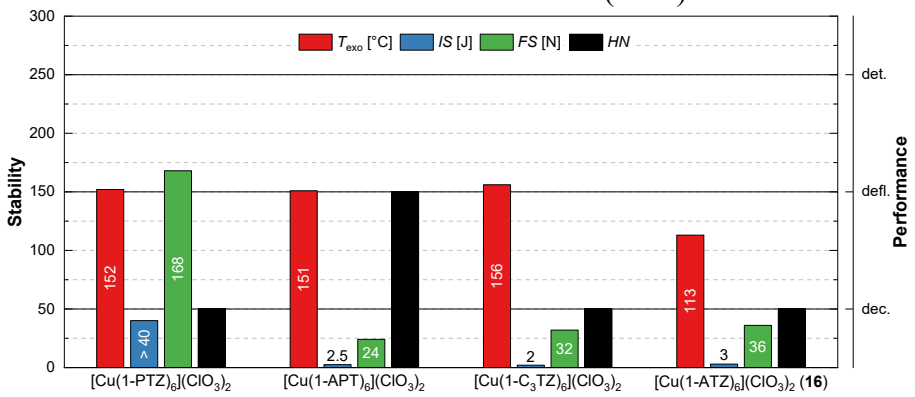

Figure 22. Comparison of the stabilities (T_{exo}, *IS*, *FS*) and performance (*HN*) of the copper(II) chlorate complexes based on different *N*1-substituted C_3-derived tetrazole ligands.

The same applies to the comparison of the 1-ATZ-based energetic coordination compound $[Cu(1\text{-}ATZ)_6](ClO_4)_2$ (**9**) with the respective 1-PTZ complex (Fig. 20). This fact is consistent with the higher heat of formation of the unsaturated compounds.

4.3 Conclusion

The goal of the present study has been the preparation of the nitrogen-rich neutral ligands 1-VTZ (**1**) and 1-ATZ (**2**) and their incorporation into ECC aiming for green primary explosives capable of replacing LA and LS. Of particular interest was the investigation of the influence of the alkenyl chain lengthening by comparing analogous ECC based on 1-VTZ (**1**) and 1-ATZ (**2**). Besides, the influence of the increased endothermicity by introducing an unsaturated C—C bond (1-ETZ *vs.* 1-VTZ and 1-PTZ *vs.* 1-ATZ) is discussed. Starting from commercially available precursors, the ligand 1-vinyltetrazole (**1**, 1-VTZ) was synthesized in a two-step reaction with an overall yield of 34%, whereas ligand 1-allyltetrazole (**2**, 1-ATZ) was accessible in a straightforward one-step synthesis (Yield: 60%). For characterization of the tetrazole derivatives various analytical methods, including EA, NMR spectroscopy, and IR spectroscopy as well as DTA and sensitivity measurements (IS, FS, ESD, and BDIS) were used. As expected, the lengthening of the alkenyl chain leads to increased thermal stability (**1**: 173 °C (T_{dec}), **2**: 207 °C (T_{dec}) and decreased impact sensitivity (**1**: 15 J, **2**: > 40J) of the uncoordinated ligands. For the first time, it was possible to obtain a single crystal structure of 1-VTZ.

The ligands were successfully applied for the synthesis of 23 new coordination compounds based on toxic (Co, Ni) and less or nontoxic 3d transition metals (Mn, Fe, Cu, and Zn) and

oxidizing anions (perchlorate, nitrate, chlorate, and dinitramide) or trinitrophenolate anions. In the present work, a comprehensive comparative study of the physicochemical properties of the obtained 1-VTZ and 1-ATZ-based ECCs was conducted, which were partly also tested for their capability of initiating PETN or being laser ignitable. In all cases, the introduction of an additional carbon atom increased the thermal stability and decreased the complex sensitivity toward various mechanical stimuli.

Furthermore, the synthesized ligands 1-VTZ (**1**) and 1-ATZ (**2**) and their ECCs are put in relation to already published *N*1-substituted C_2-derived and C_3-derived tetrazole-based ECCs, respectively. Comparison of $[Cu(1\text{-}VTZ)_6](ClO_4)_2$ (**7**) with the literature known $[Cu(1\text{-}ETZ)_6](ClO_4)_2$ proves that the introduction of an unsaturated bond leads to more sensitive and less thermally stable ECC. The same observation is made in the case of $[Cu(1\text{-}ATZ)_6](ClO_4)_2$ (**11**) and $[Cu(1\text{-}PTZ)_6](ClO_4)_2$.

4.4 Acknowledgement

For financial support of this work by Ludwig-Maximilian University (LMU), the Office of Naval Research (ONR) under grant no. ONR N00014-19-1-2078 and the Strategic Environmental Research and Development Program (SERDP) under contract no. W912HQ19C0033 is gratefully acknowledged. The authors would also like to thank Prof. Dr. Konstantin Karaghiosoff for the measurement of the two-dimensional ^{1}H-^{15}N HMBC NMR spectra.

4.5 References

[1] T. M. Klapötke, *Chemistry of* High-*Energy Materials*, Walter de Gruyter, Berlin/Boston, **2019**.

[2] J. W. Fronabarger, M. D. Williams, W. B. Sanborn, J. G. Bragg, D. A. Parrish, M. Bichay, *Propellants, Explos., Pyrotech.* **2011**, *36*, 541–550.

[3] N. Fischer, D. Fischer, T. M. Klapötke, D. G. Piercey, J. Stierstorfer, *J. Mater. Chem.* **2012**, *22*, 20418–20422.

[4] H. Wei, J. Zhang, J. M. Shreeve, *Chem. Asian J.* **2015**, *10*, 1130–1132.

[5] Q. Yu, G. H. Imler, D. A. Parrish, J. M. Shreeve, *Org. Lett.* **2019**, *21*, 4684–4688.

[6] D. E. Chavez, D. A. Parrish, L. Mitchell, G. H. Imler, *Angew. Chem., Int. Ed.* **2017**, *56*, 3575–3578.

[7] M. L. Gettings, M. T. Thoenen, E. F. C. Byrd, J. J. Sabatini, M. Zeller, D. G. Piercey, *Chem. Eur. J.* **2020**, *26*, 14530–14535.

[8] R. V. Kent, R. A. Wiscons, P. Sharon, D. Grinstein, A. A. Frimer, A. J. Matzger, *Cryst. Growth Des.* **2018**, *18*, 219–224.

[9] Q. Zhang, D. Chen, D. Jing, G. Fan, L. He, H. Li, W. Wang, F. Nie, *Green Chem.* **2019**, *21*, 1947–1955.

[10] D. Fischer, T. M. Klapötke, J. Stierstorfer, *Angew. Chem., Int. Ed.* **2014**, *53*, 8172–8175.

[11] W. Huang, Y. Tang, G. H. Imler, D. A. Parrish, J. M. Shreeve, *J. Am. Chem. Soc.* **2020**, *142*, 3652–3657.

[12] Q. Wang, Y. Shao, M. Lu, *Chem. Commun. (Cambridge, U. K.)* **2019**, *55*, 6062–6065.

[13] T. Cheng, *Des. Monomers Polym.* **2019**, *22*, 54–65.

[14] F. M. Betzler, R. Boller, A. Grossmann, T. M. Klapötke, *Z. Naturforsch. B* **2013**, *68*, 714–718.

[15] M.-R. Huang, X.-G. Li, S.-X. Li, W. Zhang, *React. Funct. Polym.* **2004**, *59*, 53–61.

[16] D. B. Lempert, A. I. Kazakov, S. I. Soglasnova, I. L. Dalinger, A. B. Sheremetev, *Russ. Chem. Bull.* **2018**, *67*, 1580–1588.

[17] T.-A. D. Nguyen, J. M. Veauthier, D. E. Chavez, B. C. Tappan, A. H. Mueller, B. L. Scott, D. A. Parrish, *Inorg. Chem.* **2020**, *59*, 16109–16116.

[18] M. Joas, T. M. Klapötke, N. Szimhardt, *Eur. J. Inorg. Chem.* **2014**, *2014*, 493–498.

[19] M. A. Ilyushin, A. S. Tver'yanovich, Y. S. Tver'yanovich, G. O. Abdrashitov, A. O. Aver'yanov, M. D. Bal'makov, *Glass Phys. Chem.* **2018**, *44*, 120–122.

[20] V. P. Sinditskii, V. V. Serushkin, *DSJ* **1996**, *46*, 371–383.

[21] N. Szimhardt, M. H. H. Wurzenberger, A. Beringer, L. J. Daumann, J. Stierstorfer, *J. Mater. Chem. A* **2017**, *5*, 23753–23765.

[22] N. Szimhardt, M. H. H. Wurzenberger, L. Zeisel, M. S. Gruhne, M. Lommel, J. Stierstorfer, *J. Mater. Chem. A* **2018**, *6*, 16257–16272.

[23] M. H. H. Wurzenberger, M. S. Gruhne, M. Lommel, N. Szimhardt, T. M. Klapötke, J. Stierstorfer, *Chem. Asian J.* **2019**, *14*, 2018–2028.

[24] M. H. H. Wurzenberger, S. M. J. Endraß, M. Lommel, T. M. Klapötke, J. Stierstorfer, *ACS Appl. Energy Mater.* **2020**, *3*, 3798–3806.

[25] M. Freis, T. M. Klapötke, J. Stierstorfer, N. Szimhardt, *Inorg. Chem.* **2017**, *56*, 7936–7947.

[26] J. Evers, I. Gospodinov, M. Joas, T. M. Klapötke, J. Stierstorfer, *Inorg. Chem.* **2014**, *53*, 11749–11756.

[27] P. N. Gaponik, V. P. Karavai, Y. V. Grigorev, *Khim. Geterotsikl. Soedin.* **1985**, 1521–1524.

[28] N. Fischer, T. M. Klapötke, J. Stierstorfer, C. Wiedemann, *Polyhedron* **2011**, *30*, 2374–2386.

[29] J. Stierstorfer, K. R. Tarantik, T. M. Klapötke, *Chem. – Eur. J.* **2009**, *15*, 5775–5792.

[30] T. M. Klapötke, B. Krumm, T. Reith, C. C. Unger, *J. Org. Chem* **2018**, *83*, 10505–10509.

[31] P. N. Gaponik, V. P. Karavai, *Chem. Heterocycl. Compd.* **1985**, *21*, 1172–1174.

[32] W. G. Finnegan, R. A. Henry, *J. Org. Chem.* **1959**, *24*, 1565–1567.

[33] M. S. Gruhne, T. Lenz, M. Rösch, M. Lommel, M. H. H. Wurzenberger, T. M. Klapötke, J. Stierstorfer, *Dalton Trans.* **2021**, *50*, 10811–10825.

[34] Y. Shvedenkov, M. Bushuev, G. Romanenko, L. Lavrenova, V. Ikorskii, P. Gaponik, S. Larionov, *Eur. J. Inorg. Chem.* **2005**, 1678–1682.

[35] V. N. Kizhnyaev, V. A. Kruglova, *J. Appl. Chem. USSR* **1992**, *65*, 1523–1527.

[36] L. G. Lavrenova, A. N. Bogatikov, V. N. Ikorskii, L. A. Sheludyakova, E. G. Boguslavskii, P. N. Gaponik, S. V. Larionov, *Russ. J. Inorg. Chem.* **1996**, *41*, 406–409.

[37] P. N. Gaponik, O. A. Ivashkevich, M. M. Degtyarik, *Izv. Vyssh. Uchebn. Zaved., Khim. Khim. Tekhnol.* **1985**, *28*, 43–46.

[38] V. N. Kizhnyaev, L. I. Vereshchagin, *Russ. Chem. Rev.* **2003**, *72*, 143–164.

[39] L. G. Lavrenova, A. N. Bogatikov, L. A. Sheludyakova, V. N. Ikorskii, S. V. Larionov, P. N. Gaponik, *Russ. J. Inorg. Chem.* **1991**, *36*, 693–696.

[40] L. G. Lavrenova, V. N. Ikorskii, S. V. Larionov, A. N. Bogatikov, P. N. Gaponik, *Russ. J. Inorg. Chem.* **1993**, *38*, 1416–1417.

[41] J. P. Agrawal, *Cent. Eur. J. Energ. Mater.* **2012**, 273–290.

[42] W. G. Finnegan, R. A. Henry, S. Sol, US 3004959 A, **1959**.

[43] A. F. Stassen, E. Dova, R. Ensling, H. Schenk, P. Gutlich, J. G. Haasnoot, J. Reedijk, *Inorg. Chim. Acta* **2002**, *335*, 61–68.

[44] P. N. Gaponik, O. A. Ivashkevich, O. N. Bubel, M. M. Degtyarik, V. N. Naumenko, *Theor. Exp. Chem.* **1989**, *25*, 33–40.

[45] W. G. Finnegan, R. A. Henry, S. Sol, US 3055911 A, **1958**.

[46] P. N. Gaponik, S. V. Voitekhovich, O. A. Ivashkevich, *Russ. Chem. Rev.* **2006**, *75*, 569–603.

[47] L. Wiehl, *Acta Crystallogr., Sect. B: Struct. Sci.* **1993**, *49*, 289–303.

[48] M. H. H. Wurzenberger, N. Szimhardt, J. Stierstorfer, *J. Am. Chem. Soc.* **2018**, *140*, 3206–3209.

[49] M. H. H. Wurzenberger, M. Lommel, M. S. Gruhne, N. Szimhardt, J. Stierstorfer, *Angew. Chem., Int. Ed.* **2020**, *59*, 12367–12370.

[50] M. H. H. Wurzenberger, B. R. G. Bissinger, M. Lommel, M. S. Gruhne, N. Szimhardt, J. Stierstorfer, *New J. Chem.* **2019**, *43*, 18193–18202.

[51] P. Gütlich, A. Hauser, H. Spiering, *Angew. Chem., Int. Ed.* **1994**, *33*, 2024–2054.

[52] A. F. Stassen, O. Roubeau, I. Ferrero Gramage, J. Linarès, F. Varret, I. Mutikainen, U. Turpeinen, J. G. Haasnoot, J. Reedijk, *Polyhedron* **2001**, *20*, 1699–1707.

[53] P. L. Franke, J. G. Haasnoot, A. P. Zuur, *Inorg. Chim. Acta* **1982**, *59*, 5–9.

[54] V. Braun, M. H. H. Wurzenberger, V. Weippert, J. Stierstorfer, *New J. Chem.* **2021**, *45*, 11042–11050.

[55] A. Hauser, P. Gütlich, R. Hinek, H. Spiering, D. Schollmeyer, *Chem. Asian J.* **1996**, *2*, 1427–1434.

[56] Y.-G. Bi, Y.-A. Feng, Y. Li, B.-D. Wu, T.-L. Zhang, *J. Coord. Chem.* **2015**, *68*, 181–194.

[57] N. Szimhardt, M. H. H. Wurzenberger, T. M. Klapötke, J. T. Lechner, H. Reichherzer, C. C. Unger, J. Stierstorfer, *J. Mater. Chem. A* **2018**, *6*, 6565–6577.

[58] M. B. Joas, *Dissertation*, Ludwig-Maximilians-Universität, **2014**.

[59] NATO, *Standardization Agreement (STANAG). explosives, friction sensitivity tests*, **2009**.

[60] *Manual of Tests and Criteria*, United Nations Publication, New York, Geneva, **2019**.

[61] WIWEB, *Standardarbeitsanweisung 4–5.1.03. Ermittlung der Explosionsgefährlichkeit oder der Reibeempfindlichkeit mit dem Reibeapparat*, **2002**.

[62] NATO, *Standardization Agreement (STANAG). explosives, impact sensitivity tests*, **1999**.

[63] *Manual of Tests and Criteria*, United Nations Publication, New York, Geneva, **2019**.

[64] WIWEB, *Standardarbeitsanweisung 4–5.1.02. Ermittlung der Explosionsgefährlichkeit, hier der Schlagempfindlichkeit mit dem Fallhammer*, **2002**.

[65] NATO, *Standardization Agreement (STANAG). explosives, electrostatic discharge sensitivity tests*, **2001**.

[66] *Manual of Tests and Criteria*, United Nations Publication, New York, Geneva, **2019**.

[67] DOD, *Military Standard 1751A (MIL-STD-1751A). safety and performance tests for the qualification of explosives (high explosives, propellants, and pyrotechnics)*, **2001**.

[68] M. H. H. Wurzenberger, M. S. Gruhne, M. Lommel, J. Stierstorfer, *Propellants, Explos., Pyrotech.* **2021**, *46*, 207–213.

[69] John G. Reynolds, Peter C. Hsu, Gary A. Hust, Stephen A. Strout, H. Keo Springer, *Propellants, Explos., Pyrotech.* **2017**, *42*, 1303–1308.

[70] M. S. Gruhne, M. Lommel, M. H. H. Wurzenberger, N. Szimhardt, T. M. Klapotke, J. Stierstorfer, *Propellants, Explos., Pyrotech.* **2020**, *45*, 147–153.

[71] M. Sućeska, *EXPLO5*, Brodarski Institute, Zagreb, Croatia, **2014**.

[72] T. Fendt, N. Fischer, T. M. Klapötke, J. Stierstorfer, *Inorg. Chem.* **2011**, *50*, 1447–1458.

[73] T. W. Myers, J. A. Bjorgaard, K. E. Brown, D. E. Chavez, S. K. Hanson, R. J. Scharff, S. Tretiak, J. M. Veauthier, *J. Am. Chem. Soc.* **2016**, *138*, 4685–4692.

[74] T. W. Myers, K. E. Brown, D. E. Chavez, R. J. Scharff, J. M. Veauthier, *Inorg. Chem.* **2017**, *56*, 2297–2303.

[75] M. A. Ilyushin, A. A. Kotomin, S. A. Dushenok, *Russ J. Phys. Chem. B* **2019**, *13*, 119–138.

[76] M. S. Gruhne, M. H. H. Wurzenberger, M. Lommel, J. Stierstorfer, *Chem. – Eur. J.* **2021**, *27*, 9112–9123.

4.6 Supporting Information

4.6.1 Compound Overview

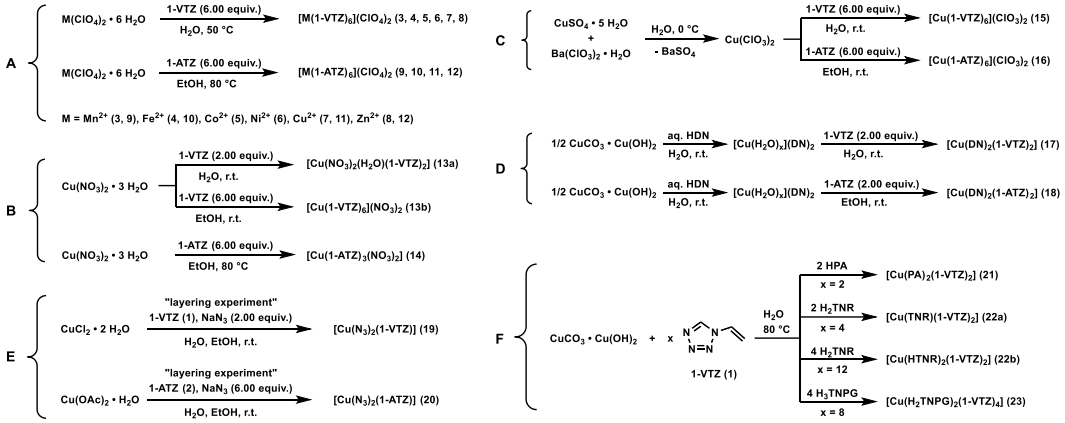

Chart S1. (**A**) Synthesis of the metal(II) perchlorate based 1-VTZ (**3**–**8**) and 1-ATZ (**9**–**12**) complexes. (**B**) Synthesis of selected copper(II) nitrate based 1-VTZ (**13a**, **13b**) and 1-ATZ (**14**) complexes. (**C**) Formation of the copper(II) 1-VTZ (**15**) and 1-ATZ (**16**) chlorate complex. (**D**) Synthesis of the energetic copper(II) dinitramide complexes **17** and **18**. (**E**) Single crystal formation of the copper(II) azide complexes **19** and **20**. (**F**) Synthesis of the trinitrophenolate-based coordination compounds **21**–**23**.

4.6.2 Mechanistic Proposal for the Synthesis of 1-ClET

Although the detailed mechanism has not yet been fully elucidated, the literature suggests that tetrazoles form by cyclization of the imidoyl azides (**C**, Scheme 1), which in turn originate from the corresponding imino ethers (**B**, Scheme 1).[S1–5] The multicomponent heterocyclization process can thus be rationalized as shown in Scheme 1. Proposedly, the orthoester is first protonated under acidic conditions. Subsequent E1 elimination of ethanol leads to the formation of a carboxonium ion **A**, which simplifies the following nucleophilic substitution by 2-chloroethylamine hydrochloride. The nucleophilic attack of the amine produces the disubstituted imino ether **B** as an intermediate, which then reacts with the azide ion to form azidoazomethine **C**. Ultimately, a 1,5-dipolar cyclization reaction takes place affording the desired tetrazole.

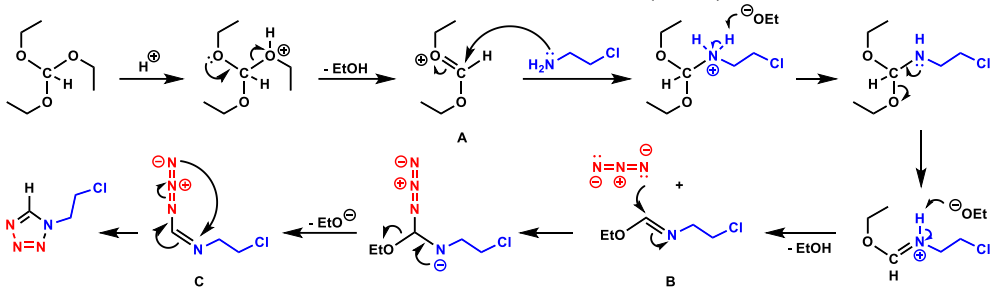

Scheme 1. Mechanistic proposal for the synthesis of 1-(2-chloroethyl)-tetrazole (1-ClET)).

4.6.3 Single Crystal X-Ray Diffraction

For all crystalline compounds, an Oxford Xcalibur3 diffractometer with a CCD area detector or Bruker D8 Venture TXS diffractometer equipped with a multilayer monochromator, a Photon 2 detector and a rotating-anode generator were employed for data collection using Mo-K_α radiation ($\lambda = 0.7107$ Å). On the Oxford device, data collection and reduction were carried out using the CrysAlisPRO software.[S6] On the Bruker diffractometer, the data were collected with the Bruker Instrument Service v3.0.21, the data reduction was performed using the SAINT V8.18C software (Bruker AXS Inc., 2011). The structures were solved by direct methods (SIR-92,[S7] SIR-97,[S8,S9] SHELXS-97[S10,S11] or SHELXT[S12]) and refined by full-matrix least-squares on $F2$ (SHELXL[S10,11]) using the software suites WinGX[S13] or OLEX2[S14] and finally checked using the PLATON software.[S15] The non-hydrogen atoms were refined anisotropically and the hydrogen atoms were located and freely refined. The absorptions were corrected by a SCALE3 ABSPACK or SADABS Bruker APEX3 multi-scan method.[S16,S17] All DIAMOND2 plots are shown with thermal ellipsoids at the 50% probability level and hydrogen atoms are shown as small spheres of arbitrary radius.

Table S1. Crystallographic data of the ligand **1** and of the complexes **3** and **4**.

	1 (1-VTZ)	**3**	**4**
Formula	$C_3H_4N_4$	$C_{18}H_{24}Cl_2MnN_{24}O_8$	$C_{18}H_{24}Cl_2FeN_{24}O_8$
FW [g mol^{-1}]	96.10	830.45	831.36
Crystal system	monoclinic	orthorhombic	orthorhombic
Space group	$P2_1/c$ (14)	*Pbca* (61)	*Pbca* (61)
Color / Habit	colorless block	colorless plate	colorless plate
Size [mm]	0.12 x 0.25 x 0.39	0.05 x 0.30 x 0.40	0.18 x 0.35 x 0.50
a [Å]	3.7826(6)	17.1183(5)	17.0737(13)
b [Å]	14.4852(19)	10.5381(4)	10.5063(5)
c [Å]	8.6509(17)	19.4810(10)	19.3823(18)
α [°]	90	90	90
β [°]	101.035(17)	90	90
γ [°]	90	90	90
V [Å^3]	465.23(14)	3514.3(2)	3476.8(4)
Z	4	4	4
$\rho_{calc.}$ [g cm^{-3}]	1.372	1.570	1.588
μ [mm^{-1}]	0.099	0.606	0.667
F(000)	200	1692	1696
$\lambda_{MoK\alpha}$ [Å]	0.71073	0.71073	0.71073
T [K]	112	111	109
θ Min-Max [°]	2.8–26.4	2.1–26.4	2.1–26.4
Dataset	-4:4; -12:18; -10:10	-21:21; -13:13; -24:24	-21:18; -13:13; -24:23
Reflections collected	2670	33486	31896
Independent refl.	948	3590	3550
R_{int}	0.078	0.093	0.088
Observed reflections	562	2571	2568
Parameters	80	289	289
R_1 (obs)[a]	0.0735	0.0444	0.0475
wR_2 (all data)[b]	0.2071	0.0996	0.1052
GooF[c]	1.021	1.064	1.081
Resd. Dens. [e Å^{-3}]	−0.224, 0.330	−0.272, 0.378	−0.283, 0.396
Absorption correction	multi-scan	multi-scan	Multi-scan
Device type	Oxford Xcalibur3	Oxford Xcalibur3	Oxford Xcalibur3
CCDC	2207191	2207187	2207189

a) $R_1 = \Sigma||F_0|-|F_c||/\Sigma|F_0|$; b) $wR_2 = [\Sigma[w(F_0^2-F_c^2)^2]/\Sigma[w(F_0)^2]]^{1/2}$; $w = [\sigma c^2(F_0^2)+(xP)^2+yP]^{-1}$ and $P = (F_0^2+2F_c^2)/3$; c) GooF = $\{\Sigma[w(F_o^2-F_c^2)^2]/(n-p)\}^{1/2}$ (n = number of reflections; p = total number of parameters).

Table S2. Crystallographic data of the perchlorate complexes **5**, **6**, **7**, and **8**.

	5	**6**	**7**	**8**
Formula	$C_{18}H_{24}Cl_2CoN_{24}O_8$	$C_{18}H_{24}Cl_2N_{24}NiO_8$	$C_{18}H_{24}Cl_2CuN_{24}O_8$	$C_{18}H_{24}Cl_2N_{24}O_8Zn$
FW [g mol^{-1}]	834.44	834.22	839.05	840.88
Crystal system	orthorhombic	trigonal	orthorhombic	orthorhombic
Space group	*Pbca* (61)	*R*–3 (148)	*Pbca* (61)	*Pbca (61)*
Color / Habit	light-yellow plate	light-violet plate	blue block	colorless block
Size [mm]	0.15 x 0.50 x 0.50	0.50 x 0.25 x 0.10	0.12 x 0.25 x 0.37	0.26 x 0.50 x 0.50
a [Å]	17.0746(13)	10.1248(4)	17.0338(12)	17.0896(5)
b [Å]	10.4861(7)	10.1248(4)	10.5877(7)	10.4969(4)
c [Å]	19.2951(13)	30.1685(17)	19.2708(14)	19.4453(7)
α [°]	90	90	90	90
β [°]	90	90	90	90
γ [°]	90	120	90	90
V [Å^3]	3454.7(4)	2678.3(3)	3475.5(4)	3488.2(2)
Z	4	3	4	4
$\rho_{calc.}$ [g cm^{-3}]	1.604	1.552	1.604	1.601
μ [mm^{-1}]	0.732	0.770	0.862	0.937
F(000)	1700	1278	1708	1712
$\lambda_{MoK\alpha}$ [Å]	0.71073	0.71073	0.71073	0.71073
T [K]	100	96	100	103
θ Min-Max [°]	2.1–32.6	2.0–26.4	2.1–26.4	2.4–26.4
Dataset	-24:24; -15:14; -27:28	-12:12; -12:12; -37:37	-21:21; -13:13; -24:16	-21:21; -13:13; -24:24
Reflections collected	31632	14671	31531	50999
Independent refl.	5869	1230	3543	3562
R_{int}	0.049	0.047	0.116	0.040
Observed reflections	3887	1040	2302	3015
Parameters	241	145	289	278
R_1 (obs)[a]	0.0542	0.0592	0.0498	0.0352
wR_2 (all data)[b]	0.1487	0.1440	0.1120	0.0901
GooF[c]	1.054	1.063	1.026	1.159
Resd. Dens. [e Å^{-3}]	−0.477, 0.758	−0.942, 1.804	−0.323, 0.501	−0.328, 0.366
Absorption correction	multi-scan	multi-scan	multi-scan	multi-scan
Device type	Oxford Xcalibur3	Oxford Xcalibur3	Oxford Xcalibur3	Oxford Xcalibur3
CCDC	2207252	2207251	2207190	2207194

a) $R_1 = \Sigma||F_0|-|F_c||/\Sigma|F_0|$; b) $wR_2 = [\Sigma[w(F_0^2-F_c^2)^2]/\Sigma[w(F_0)^2]]^{1/2}$; $w = [\sigma c^2(F_0^2)+(xP)^2+yP]^{-1}$ and $P = (F_0^2+2F_c^2)/3$; c) GooF = $\{\Sigma[w(F_o^2-F_c^2)^2]/(n-p)\}^{1/2}$ (n = number of reflections; p = total number of parameters).

Table S3. Crystallographic data of the complexes **10a**, **10b**, **11**, and **13a**.

	10a	**10b**	**11**	**13a**
Formula	$C_{24}H_{36}Cl_2FeN_{24}O_8$	$C_{24}H_{36}Cl_2FeN_{24}O_8$	$C_{24}H_{36}Cl_2CuN_{24}O_8$	$C_6H_{10}CuN_{10}O_7$
FW [g mol^{-1}]	915.52	915.52	923.21	397.78
Crystal system	monoclinic	monoclinic	triclinic	orthorhombic
Space group	$P2_1/c$ (14)	$P2_1/c$ (14)	$P\bar{1}$ (2)	*Pbcn*
Color / Habit	light-violet platelet	colorless plate	blue block	blue block
Size [mm]	0.05 x 0.40 x 0.50	0.03 x 0.12 x 0.15	0.12 x 0.15 x 0.20	0.30 x 0.50 x 0.50
a [Å]	12.0103(8)	12.2123(5)	10.2785(6)	19.5975(15)
b [Å]	17.6452(8)	18.0219(6)	12.0894(8)	6.3507(5)
c [Å]	10.2989(6)	10.4115(4)	17.7245(10)	11.7866(8)
α [°]	90	90	87.641(2)	90
β [°]	110.249(7)	109.792(1)°	89.349(2)	90
γ [°]	90	90	70.167(2)	90
V [Å^3]	2047.7(2)	2156.09(14)	2070.1(2)	1466.94(19)
Z	2	2	2	4
$\rho_{calc.}$ [g cm^{-3}]	1.485	1.410	1.481	1.801
μ [mm^{-1}]	0.574	0.545	0.731	1.548
F(000)	944	944	950	804
$\lambda_{MoK\alpha}$ [Å]	0.71073	0.71073	0.71073	0.71073
T [K]	100	297	173	103
θ Min-Max [°]	2.1–29.3	2.1–25.4	2.1–26.4	2.1–26.4
Dataset	-16:16; -22:24; -14:13	-14:14; -21:21; -12:12	-12:12; -15:15; -22:22	-24:24; -7:7; -14:14
Reflections collected	34292	25182	35054	9396
Independent refl.	5162	3953	8425	1500
R_{int}	0.062	0.053	0.044	0.107
Observed reflections	3209	3038	6514	1256
Parameters	305	336	608	130
R_1 (obs)[a]	0.0505	0.0439	0.0534	0.0413
wR_2 (all data)[b]	0.1309	0.1325	0.1580	0.1143
GooF[c]	1.024	1.112	1.063	1.105
Resd. Dens. [e Å^{-3}]	−0.344, 0.554	−0.324, 0.339	−0.497, 1.534	-0.418, 0.728
Absorption correction	multi-scan	multi-scan	multi-scan	multi-scan
Device type	Oxford Xcalibur3	Bruker D8 Venture TXS	Bruker D8 Venture TXS	Oxford Xcalibur3
CCDC	2207200	2207254	2207206	2207205

a) $R_1 = \Sigma||F_0|-|F_c||/\Sigma|F_0|$; b) $wR_2 = [\Sigma[w(F_0^2-F_c^2)^2]/\Sigma[w(F_0)^2]]^{1/2}$; $w = [\sigma c^2(F_0^2)+(xP)^2+yP]^{-1}$ and $P = (F_0^2+2F_c^2)/3$; c) GooF = $\{\Sigma[w(F_o^2-F_c^2)^2]/(n-p)\}^{1/2}$ (n = number of reflections; p = total number of parameters).

Table S4. Crystallographic data of the complexes **13b**–**16**.

	13b	**14**	**15**	**16**
Formula	$C_{18}H_{24}CuN_{26}O_6$	$C_{12}H_{18}CuN_{14}O_6$	$C_{18}H_{24}Cl_2CuN_{24}O_6$	$C_{24}H_{36}Cl_2CuN_{24}O_6$
FW [g mol^{-1}]	764.17	517.94	807.05	891.22
Crystal system	orthorhombic	monoclinic	trigonal	monoclinic
Space group	*Pbca (61)*	$P2_1/c$ (14)	$R\bar{3}$ (148)	$C2/c$ (15)
Color / Habit	blue block	blue plate	blue plate	blue platelet
Size [mm]	0.21 x 0.47 x 0.50	0.03 x 0.08 x 0.12	0.12 x 0.50 x 0.50	0.02 x 0.07 x 0.11
a [Å]	16.7779(11)	12.5071(3)	10.6485(10)	18.2728(13)
b [Å]	10.3807(5)	17.8674(4)	10.6485(10)	10.7055(7)
c [Å]	18.4428(12)	10.8881(2)	27.320(4)	21.829(2)
α [°]	90	90	90	90
β [°]	90	115.6110(10)	90	107.656(2)
γ [°]	90	90	120	90
V [Å^3]	3212.1(3)	2194.10(8)	2682.8(7)	4069.1(5)
Z	4	4	3	4
$\rho_{calc.}$ [g cm^{-3}]	1.580	1.568	1.499	1.455
μ [mm^{-1}]	0.760	1.057	0.830	0.737
F(000)	1564	1060	1233	1836
$\lambda_{MoK\alpha}$ [Å]	0.71073	0.71073	0.71073	0.71073
T [K]	102	173	101	173
θ Min-Max [°]	2.2–26.4	2.1–26.4	2.2–26.4	2.3–26.8
Dataset	-20:13; -12:12; -23:15	-15:14; -22:22; -12:13	-13:13; -13:13; -29:34	-23:23; -13:13; -27:27
Reflections collected	9758	24517	7180	34738
Independent refl.	3284	4495	1223	4350
R_{int}	0.031	0.034	0.093	0.048
Observed reflections	2367	3844	975	3418
Parameters	260	298	94	259
R_1 (obs)[a]	0.0443	0.0340	0.0500	0.0553
wR_2 (all data)[b]	0.1156	0.0813	0.1375	0.1081
GooF[c]	1.034	1.065	1.103	1.189
Resd. Dens. [e Å^{-3}]	−0.384, 0.713	−0.418, 0.871	−0.417, 1.050	−0.291, 0.277
Absorption correction	multi-scan	multi-scan	multi-scan	multi-scan
Device type	Oxford Xcalibur3	Bruker D8 Venture TXS	Oxford Xcalibur3	Bruker D8 Venture TXS
CCDC	2207192	2207203	2207193	2207199

a) $R_1 = \Sigma||F_0|-|F_c||/\Sigma|F_0|$; b) $wR_2 = [\Sigma[w(F_0^2-F_c^2)^2]/\Sigma[w(F_0)^2]]^{1/2}$; $w = [\sigma c^2(F_0^2)+(xP)^2+yP]^{-1}$ and $P = (F_0^2+2F_c^2)/3$; c) GooF = $\{\Sigma[w(F_o^2-F_c^2)^2]/(n-p)\}^{1/2}$ (n = number of reflections; p = total number of parameters).

Table S5. Crystallographic data of the coordination compounds **17–20**.

	17	**18**	**19**	**20**
Formula	$C_6H_8CuN_{14}O_8$	$C_8H_{12}CuN_{14}O_8$	$C_3H_4CuN_{10}$	$C_4H_6CuN_{10}$
FW [g mol^{-1}]	467.80	495.87	243.70	257.73
Crystal system	monoclinic	monoclinic	orthorhombic	monoclinic
Space group	$P2_1/c$ (14)	$P2_1/n$ (14)	*Pbca (61)*	$P2_1/c$ (14)
Color / Habit	blue needles	blue block	brown platelet	brown platelet
Size [mm]	0.04 x 0.15 x 0.50	0.20 x 0.30 x 0.50	0.02 x 0.15 x 0.15	0.03 x 0.08 x 0.14
a [Å]	9.6062(9)	7.1586(10)	6.2328(8)	14.3501(4)
b [Å]	7.8718(6)	16.854(3)	10.7924(9)	5.69380(10)
c [Å]	11.5874(12)	7.8678(9)	24.161(2)	13.0705(3)
α [°]	90	90	90	90
β [°]	105.739(10)	102.078(13)	90	114.9550(10)
γ [°]	90	90	90	90
V [Å^3]	843.37(14)	928.3(2)	1625.2(3)	968.24(4)
Z	2	2	8	4
$\rho_{calc.}$ [g cm^{-3}]	1.842	1.774	1.992	1.768
μ [mm^{-1}]	1.373	1.253	2.664	2.241
F(000)	470	502	968	516
$\lambda_{MoK\alpha}$ [Å]	0.71073	0.71073	0.71073	0.71073
T [K]	103	101	123	173
θ Min-Max [°]	3.2–26.4	2.4–32.7	3.4–26.0	3.1–27.5
Dataset	-11:12; -9:9; -14:7	-10:10; -25:25; -10:11	-7:6; -13:10; -29:28	-18:18; -7:7; -16:16
Reflections collected	5455	10938	9429	16177
Independent refl.	1715	3164	1600	2223
R_{int}	0.045	0.043	0.099	0.027
Observed reflections	1310	2386	1192	2061
Parameters	133	142	127	136
R_1 (obs)[a]	0.0388	0.0466	0.0805	0.0197
wR_2 (all data)[b]	0.0820	0.1140	0.1877	0.0513
GooF[c]	1.055	1.079	1.203	1.12
Resd. Dens. [e Å^{-3}]	−0.411, 0.509	−0.373, 0.838	−0.909, 0.203	−0.273, 0.271
Absorption correction	multi-scan	multi-scan	multi-scan	multi-scan
Device type	Oxford Xcalibur3	Oxford Xcalibur3	Oxford Xcalibur3	Bruker D8 Venture TXS
CCDC	2207201	2207202	2207204	2207253

a) $R_1 = \Sigma||F_0|-|F_c||/\Sigma|F_0|$; b) $wR_2 = [\Sigma[w(F_0^2-F_c^2)^2]/\Sigma[w(F_0)^2]]^{1/2}$; $w = [\sigma c^2(F_0^2)+(xP)^2+yP]^{-1}$ and $P = (F_0^2+2F_c^2)/3$; c) GooF = $\{\Sigma[w(F_o^2-F_c^2)^2]/(n-p)\}^{1/2}$ (n = number of reflections; p = total number of parameters).

Table S6. Crystallographic data of the ECCs **21–23**.

	21	**22a**	**22b**	**23**
Formula	$C_{18}H_{12}CuN_{14}O_{14}$	$C_{18}H_{12}CuN_{14}O_{16}$	$C_{12}H_9CuN_{11}O_8$	$C_{24}H_{20}CuN_{22}O_{18}$
FW [g mol^{-1}]	711.96	743.96	498.84	968.16
Crystal system	monoclinic	triclinic	orthorhombic	triclinic
Space group	$P2_1/c$ (14)	$P\bar{1}$ (2)	$Fddd$ (70)	$P\bar{1}$ (2)
Color / Habit	green needle	green block	green needle	green prism
Size [mm]	0.07 x 0.19 x 0.50	0.25 x 0.30 x 0.35	0.08 x 0.08 x 0.50	0.07 x 0.16 x 0.42
a [Å]	10.5417(8)	7.6375(6)	8.8897(5)	8.9566(8)
b [Å]	6.2506(6)	8.1622(6)	19.6728(9)	10.1965(10)
c [Å]	20.028(2)	11.4581(9)	42.007(2)	11.7791(12)
α [°]	90	72.852(6)	90	78.329(8)
β [°]	95.940(9)	77.378(7)	90	69.692(9)
γ [°]	90	81.574(6)	90	64.653(9)
V [Å^3]	1312.6(2)	663.45(9)	7346.4(6)	909.92(17)
Z	2	1	16	1
$\rho_{calc.}$ [g cm^{-3}]	1.801	1.862	1.804	1.767
μ [mm^{-1}]	0.933	0.933	1.263	0.713
F(000)	718	375	4016	491
$\lambda_{MoK\alpha}$ [Å]	0.71073	0.71073	0.71073	0.71073
T [K]	123	123	103	112
θ Min-Max [°]	1.9–26.4	2.6–26.4	2.6–26.4	2.2–26.4
Dataset	-13:13; -7:7; -25:25	-8:9; -10:10; -12:14	-10:11; -19:24; -40:52	-11:11; -12:12; -14:14
Reflections collected	17469	5090	11529	6825
Independent refl.	2687	2711	1891	3715
R_{int}	0.102	0.037	0.035	0.043
Observed reflections	2055	2010	1648	2502
Parameters	214	223	184	297
R_1 (obs)[a]	0.0705	0.0507	0.0481	0.0554
wR_2 (all data)[b]	0.1803	0.0943	0.1106	0.1113
GooF[c]	1.149	1.060	1.052	1.035
Resd. Dens. [e Å^{-3}]	−1.015, 0.863	−0.382, 0.622	−0.685, 1.268	−0.434, 0.870
Absorption correction	multi-scan	multi-scan	multi-scan	multi-scan
Device type	Oxford Xcalibur3	Oxford Xcalibur3	Oxford Xcalibur3	Oxford Xcalibur3
CCDC	2207198	2207207	2207195	2207197

a) $R_1 = \Sigma||F_0|-|F_c||/\Sigma|F_0|$; b) $wR_2 = [\Sigma[w(F_0^2-F_c^2)^2]/\Sigma[w(F_0)^2]]^{1/2}$; $w = [\sigma c^2(F_0^2)+(xP)^2+yP]^{-1}$ and $P = (F_0^2+2F_c^2)/3$; c) GooF = $\{\Sigma[w(F_o^2-F_c^2)^2]/(n-p)\}^{1/2}$ (n = number of reflections; p = total number of parameters).

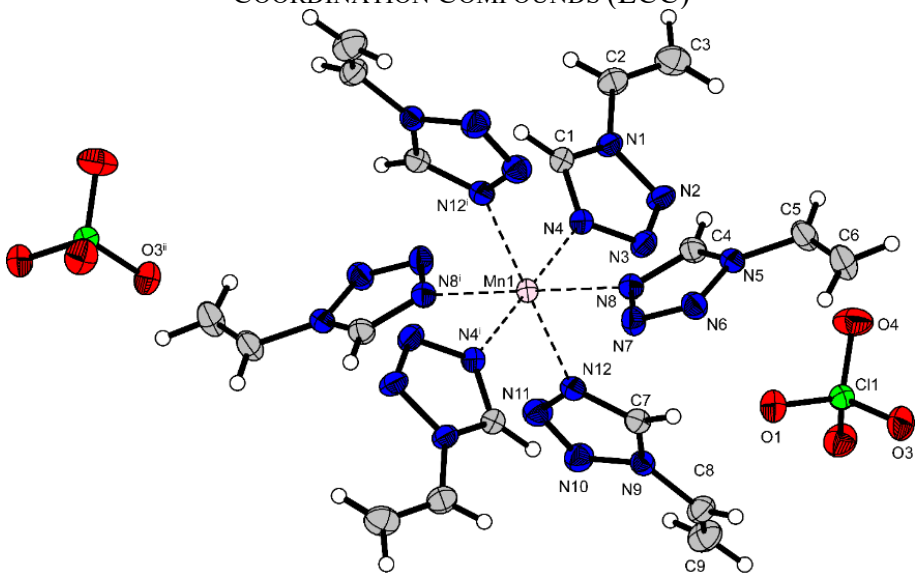

Figure S1. Molecular structure of $[Mn(1\text{-}VTZ)_6](ClO_4)_2$ (**3**). Selected bond lengths (Å): Mn1–N4 2.247(2), Mn1–N8 2.269(2), Mn1–N12 2.253(2). Selected bond angles (°): N4–Mn1–N8 89.99(8), N4–Mn1–N12 86.61(8), N8–Mn1–N12 89.11(8). Symmetry code: (i) 1–x, 1–y, 1–z.

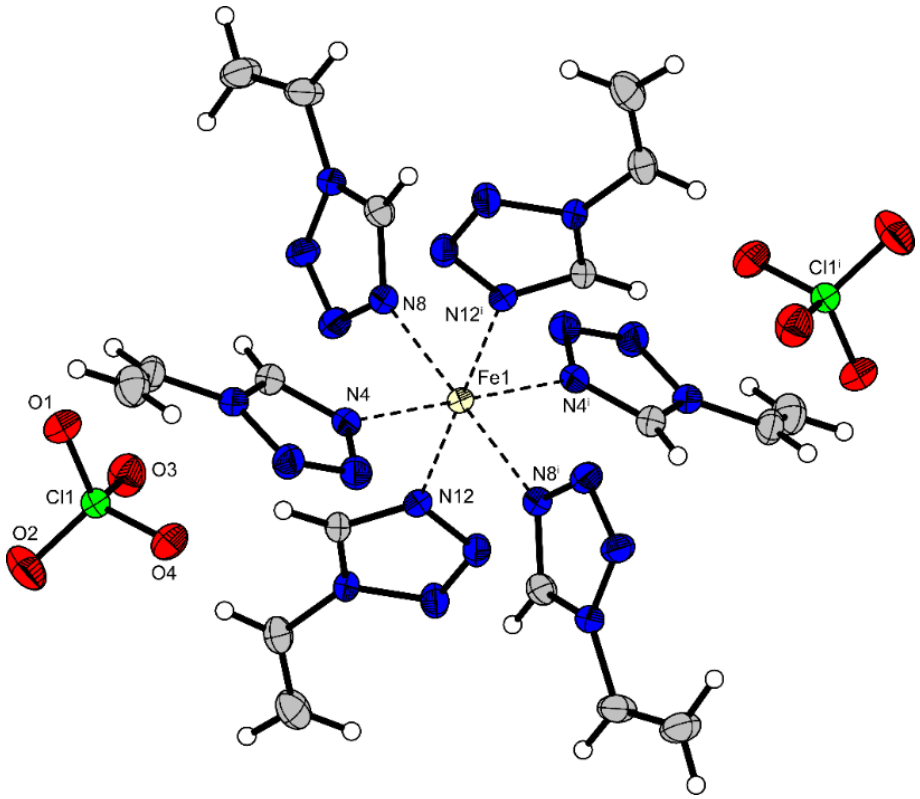

Figure S2. Molecular structure of $[Fe(1\text{-}VTZ)_6](ClO_4)_2$ (**4**). Selected bond lengths (Å): Fe1-N4 2.189(2), Fe1-N8 2.205(2), Fe1-N12 2.185(2). Selected bond angles (°): N4-Fe1-N8 90.23(9), N4-Fe1-N12 93.40(9), N8-Fe1-N12 90.12(9). Symmetry code: (i) 1–x, 1–y, 1–z.

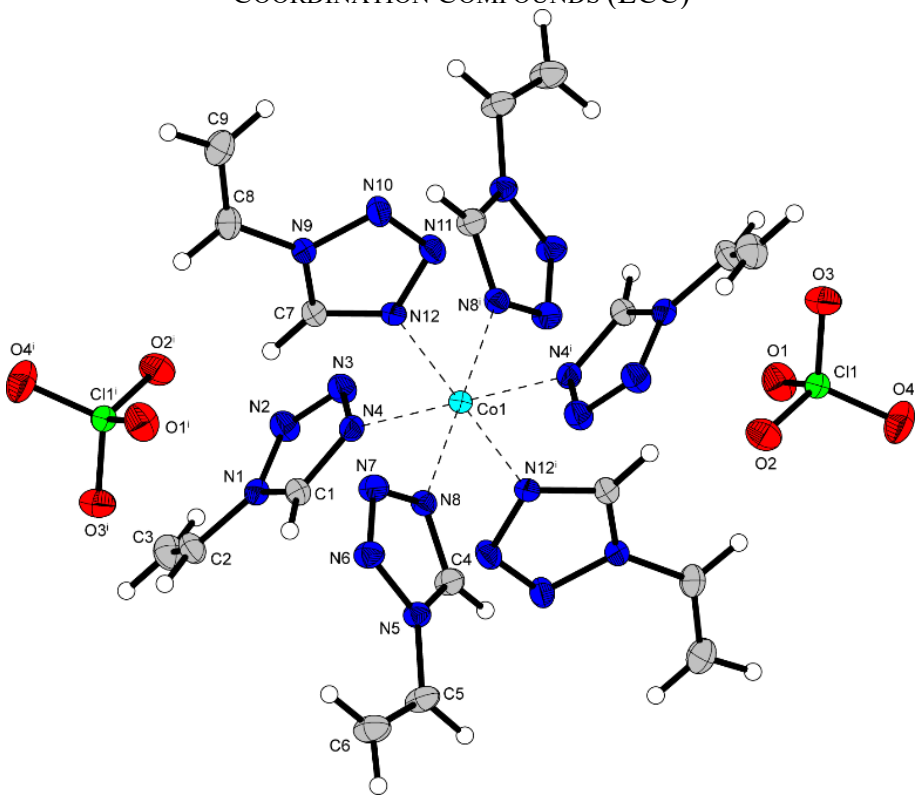

Figure S3. Molecular structure of $[Co(1\text{-}VTZ)_6](ClO_4)_2$ (**5**). Selected bond lengths (Å): Co1-N4 2.141(2), Co1-N8 2.168(2), Co1-N12 2.131(2). Selected bond angles (°): N4-Co1-N8 89.25(8), N4-Co1-N12 92.76(8), N8-Co1-N12 89.99(8). Symmetry code: (i) 1–x, 1–y, 1–z.

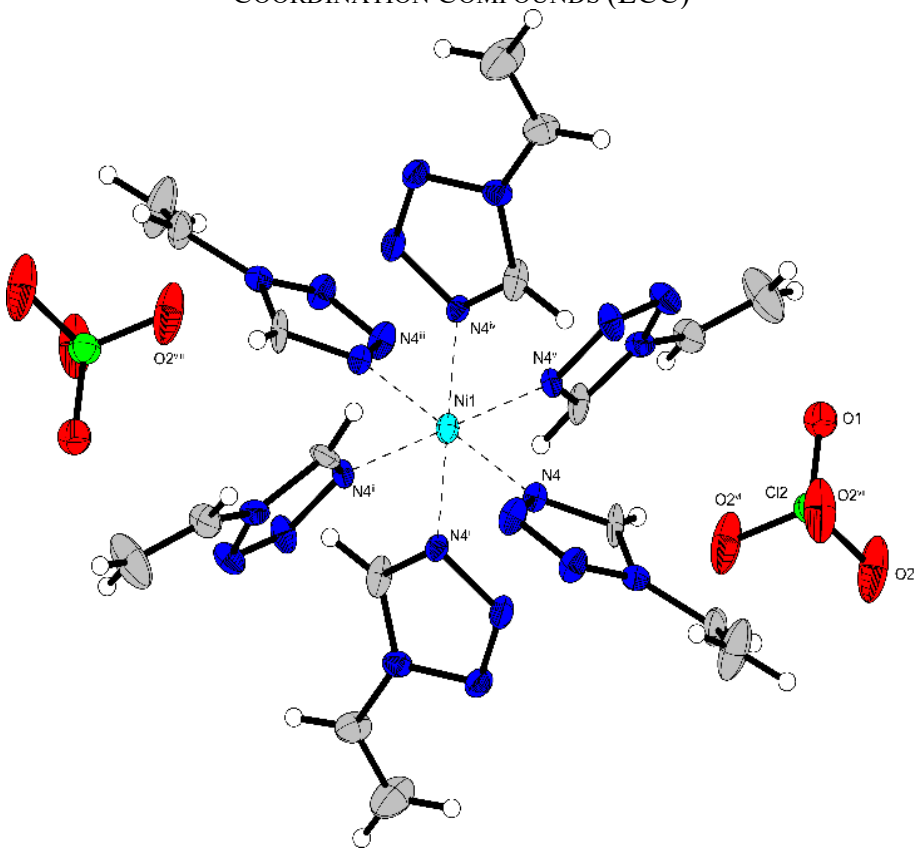

Figure S4. Molecular structure of $[Ni(1\text{-}VTZ)_6](ClO_4)_2$ (**6**). Selected bond lengths (Å): Ni1-N4 2.107(8). Selected bond angles (°): N4-Ni1-N4^{i} 90.3(4), N4-Ni1-N4^{iii} 180.00, N4-Ni1-N4^{v} 89.7(4). Symmetry codes: (i) –y, x–y, z; (ii) –x+y, –x, z; (iii) –x, –y, 1–z; (iv) y, –x+y, 1–z; (v) x–y, x, 1–z.

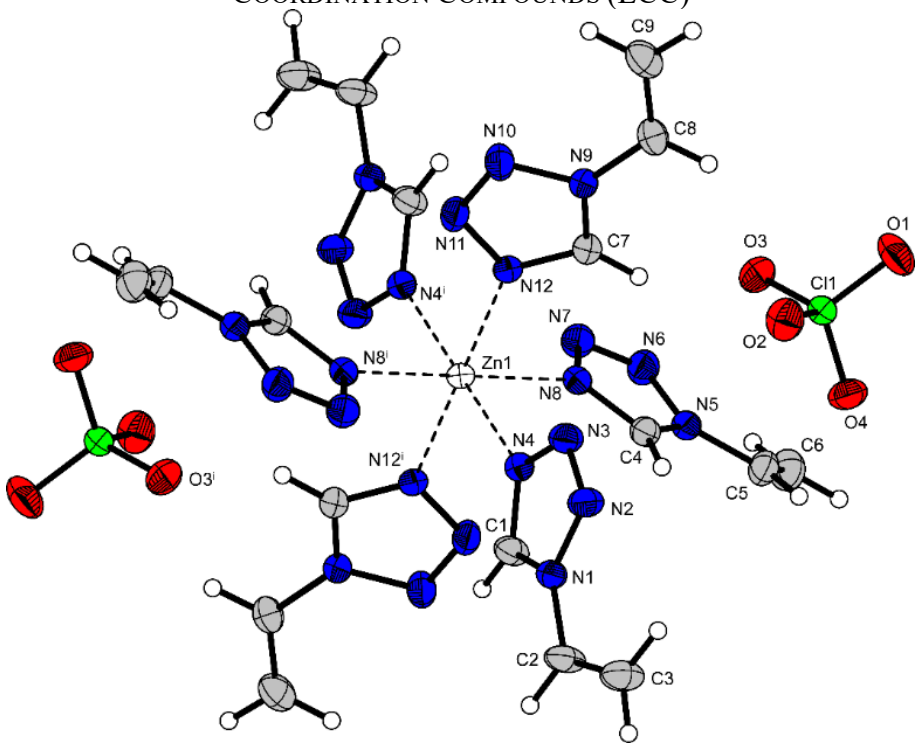

Figure S5. Molecular structure of $[Zn(1\text{-}VTZ)_6](ClO_4)_2$ (**8**). Selected bond lengths (Å): Zn1-N4 2.1878(19), Zn1-N8 2.1720(19), Zn1-N12 2.1526(19). Selected bond angles (°): N4-Zn1-N8 89.70(7), N4-Zn1-N12 89.78(7), N8-Zn1-N12 92.72(7). Symmetry code: (i) 1–x, 2–y, 1–z.

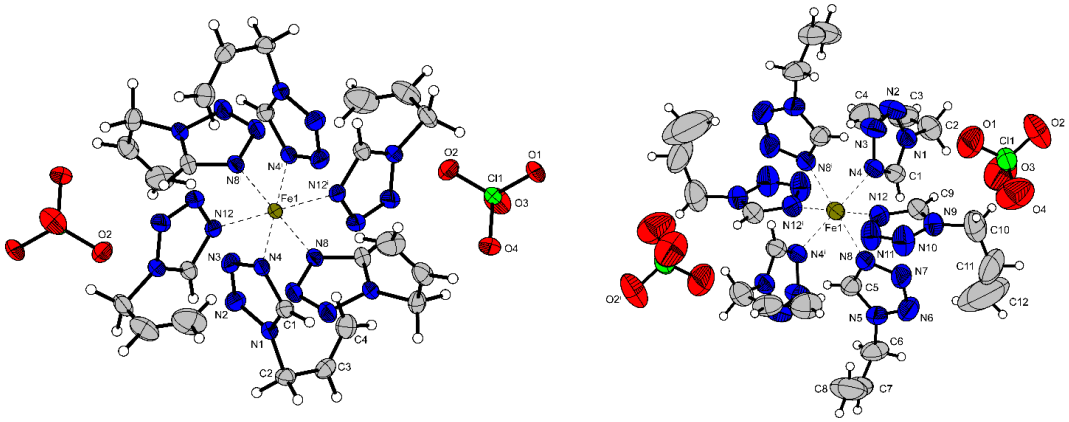

Figure S6. *Left:* Molecular structure of $[Fe(1\text{-}ATZ)_6](ClO_4)_2$ (**10a**) at 100 K. Selected bond lengths (Å): Fe1-N4 2.038(2), Fe1-N8 2.028(2), Fe1-N12 2.035(2). Selected bond angles (°): N4-Fe1-N8 90.27(8), N4-Fe1-N12 90.51(8), N8-Fe1-N12 89.30(9). Symmetry code: (i) 1–x, 1–y, 1–z. *Right:* Molecular structure of $[Fe(1\text{-}ATZ)_6](ClO_4)_2$ (**10b**) at 297 K: Selected bond lengths (Å): Fe1-N4 2.182(2), Fe1-N8 2.183(2), Fe1-N12 2.183(7). Selected bond angles (°): N4-Fe1-N8 90.23(0), N4-Fe1-N12 90.64(1), N8-Fe1-N12 89.46(4). Symmetry code: (i) 1–x, 1–y, 1–z.

4.6.4 NMR Spectroscopy of 1-ClET, 1-VTZ (1) and 1-ATZ (2)

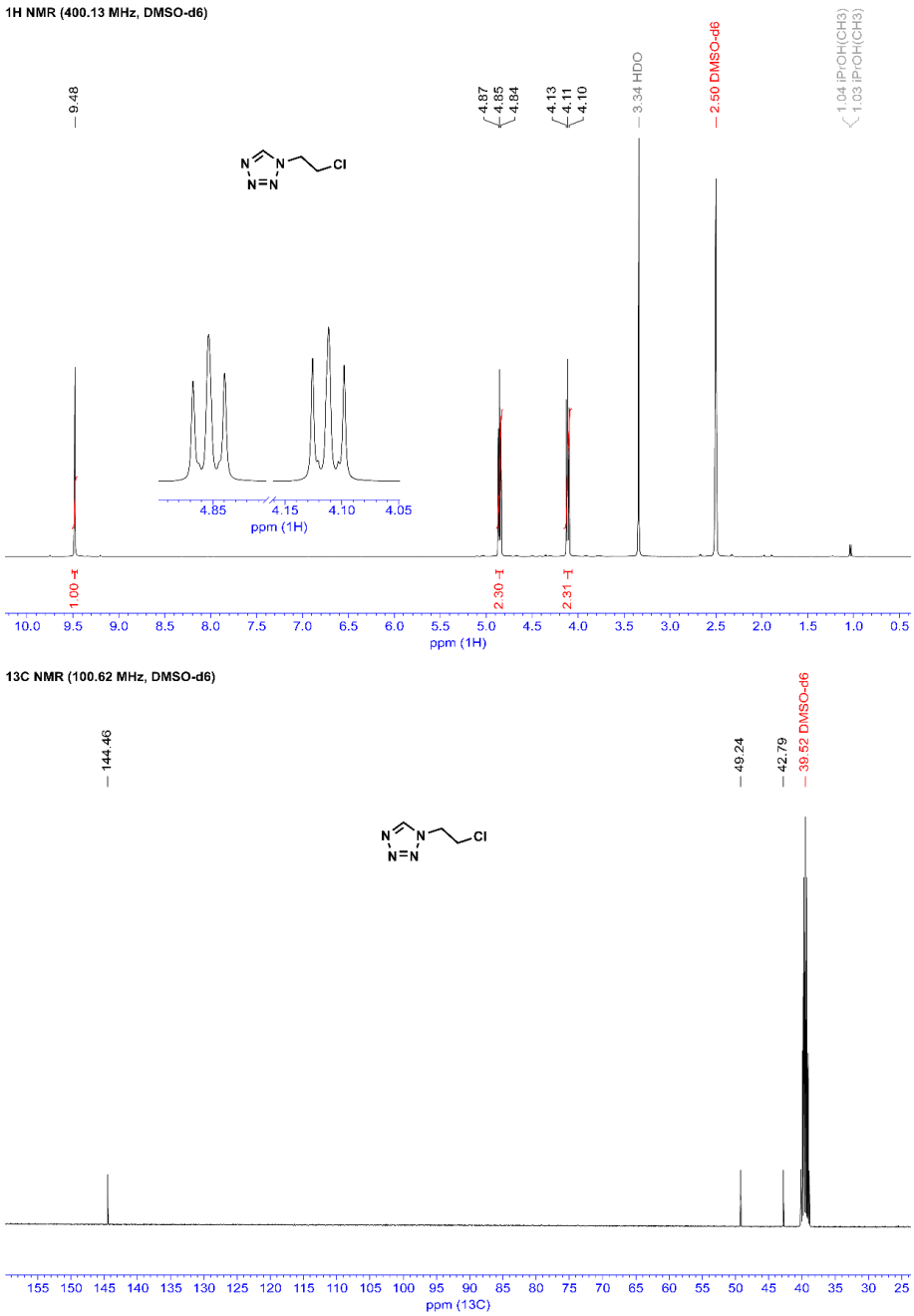

Figure S7. ^{1}H and ^{13}C NMR spectra of 1-ClET with inset structure.

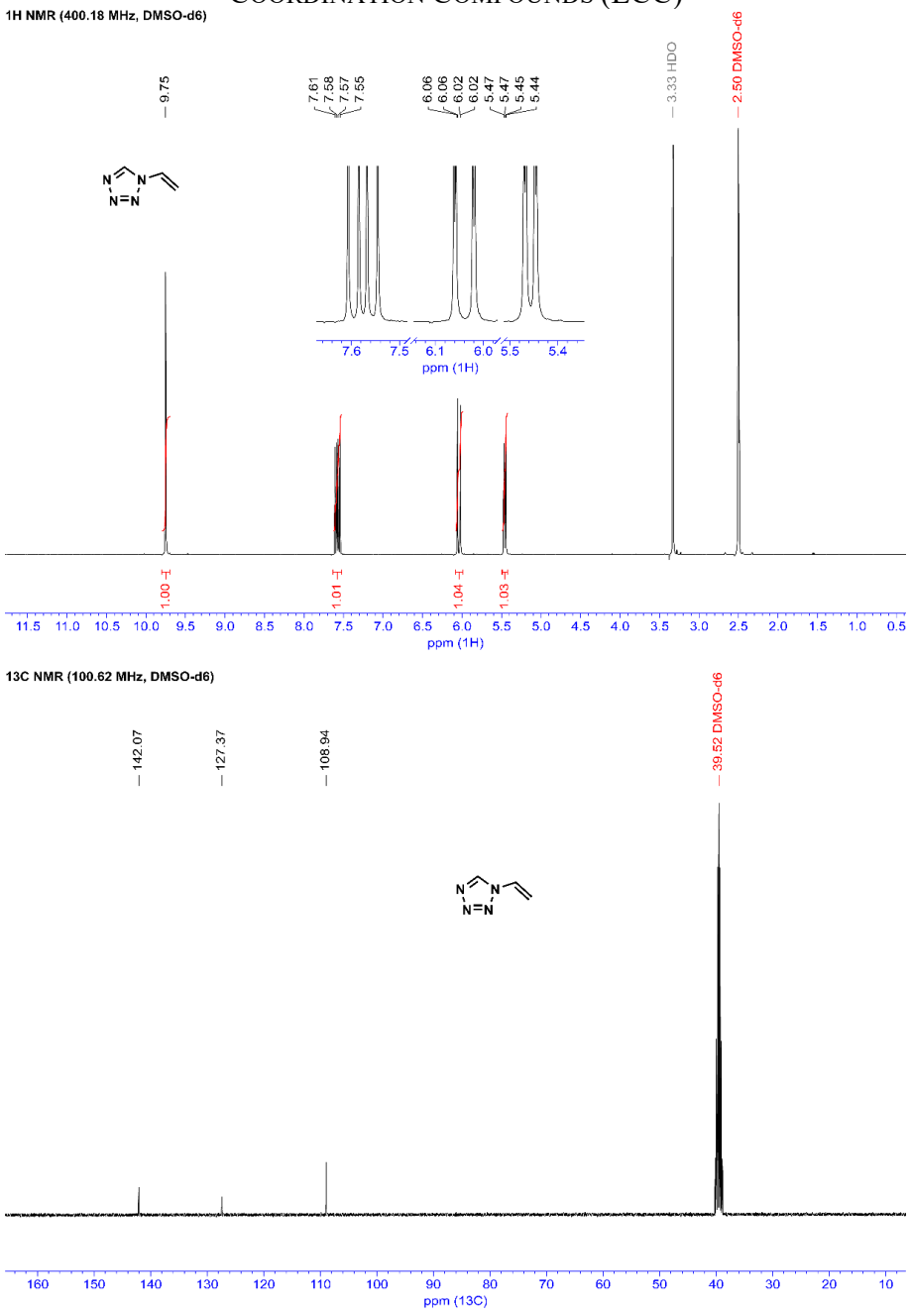

Figure S8. ^{1}H and ^{13}C NMR spectra of 1-VTZ (**1**) with inset structure.

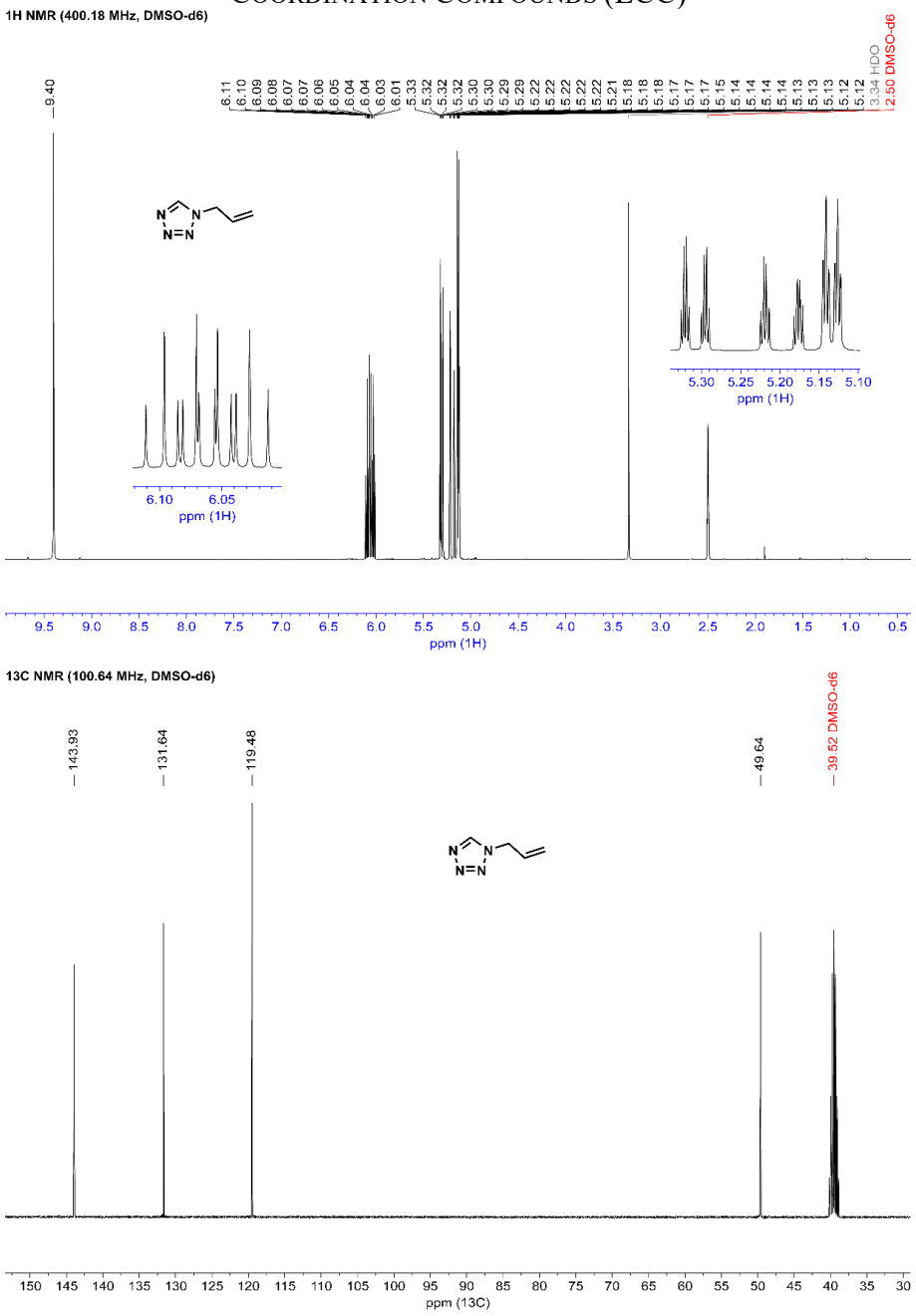

Figure S9. ^{1}H and ^{13}C NMR spectra of 1-ATZ (**2**) with inset structure.

4.6.5 IR Spectroscopy of 1–12, 13a, 15–18, and 21–23

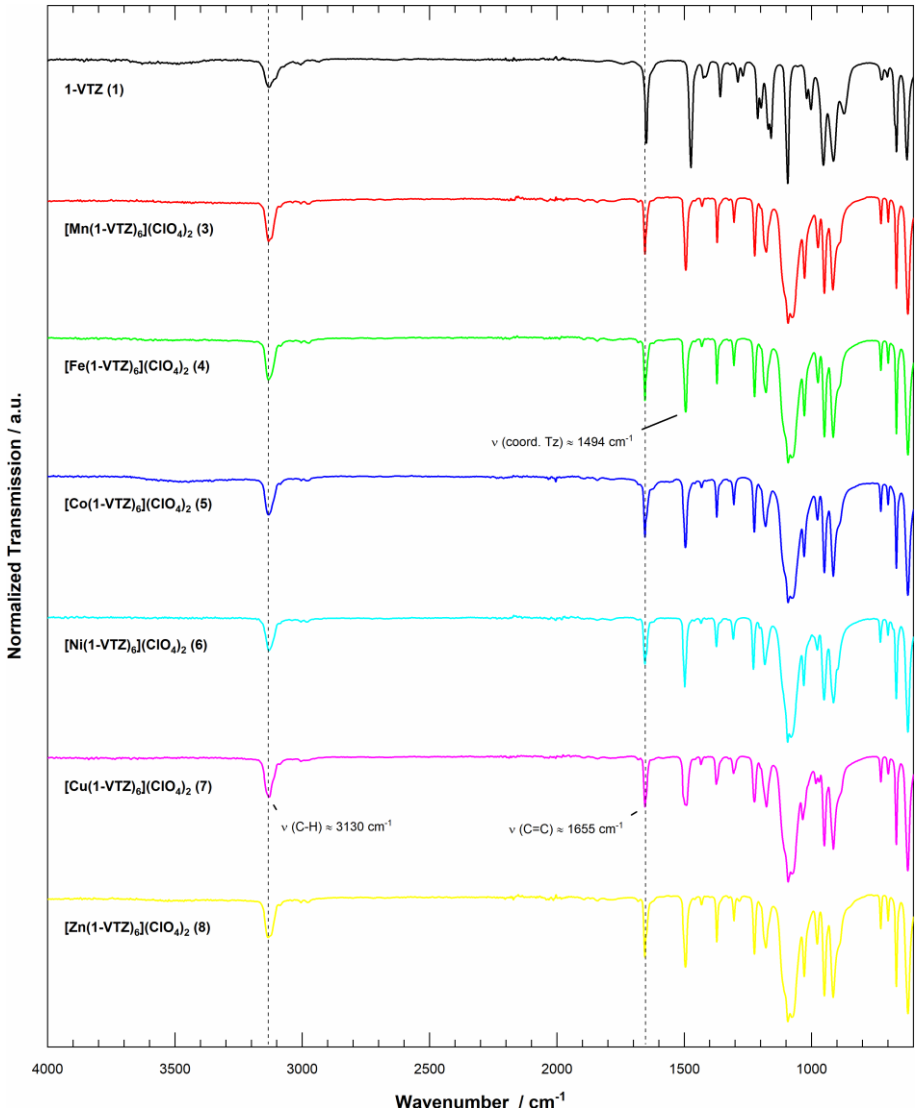

Figure S10. Fourier-transform infrared (FT-IR) spectra of the 1-VTZ ligand **1** as well as its metal(II) perchlorate complexes **3**–**8**. Band assignments were made with the help of literature.[S18–S20]

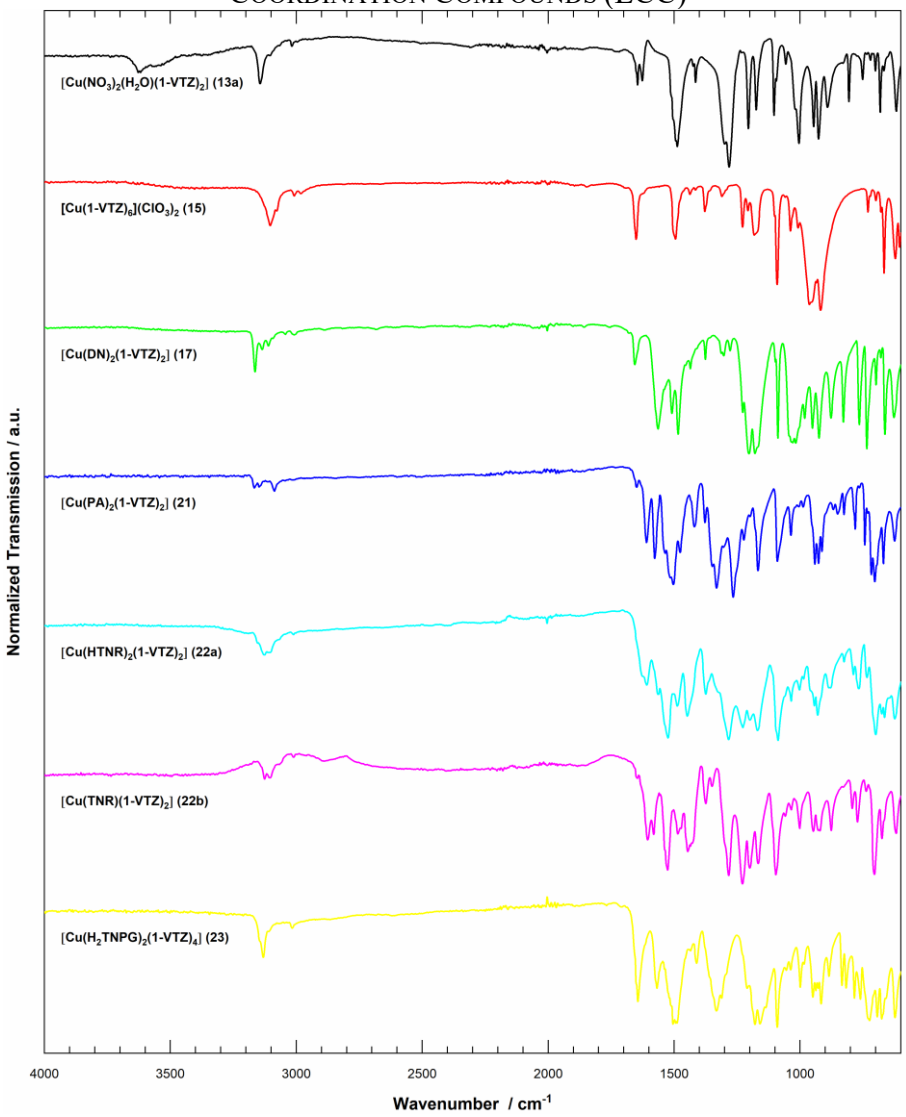

Figure S11. Fourier-transform infrared (FT-IR) spectra of the copper(II) complexes **13a**, **15**, **17**, and **21**–**23**.

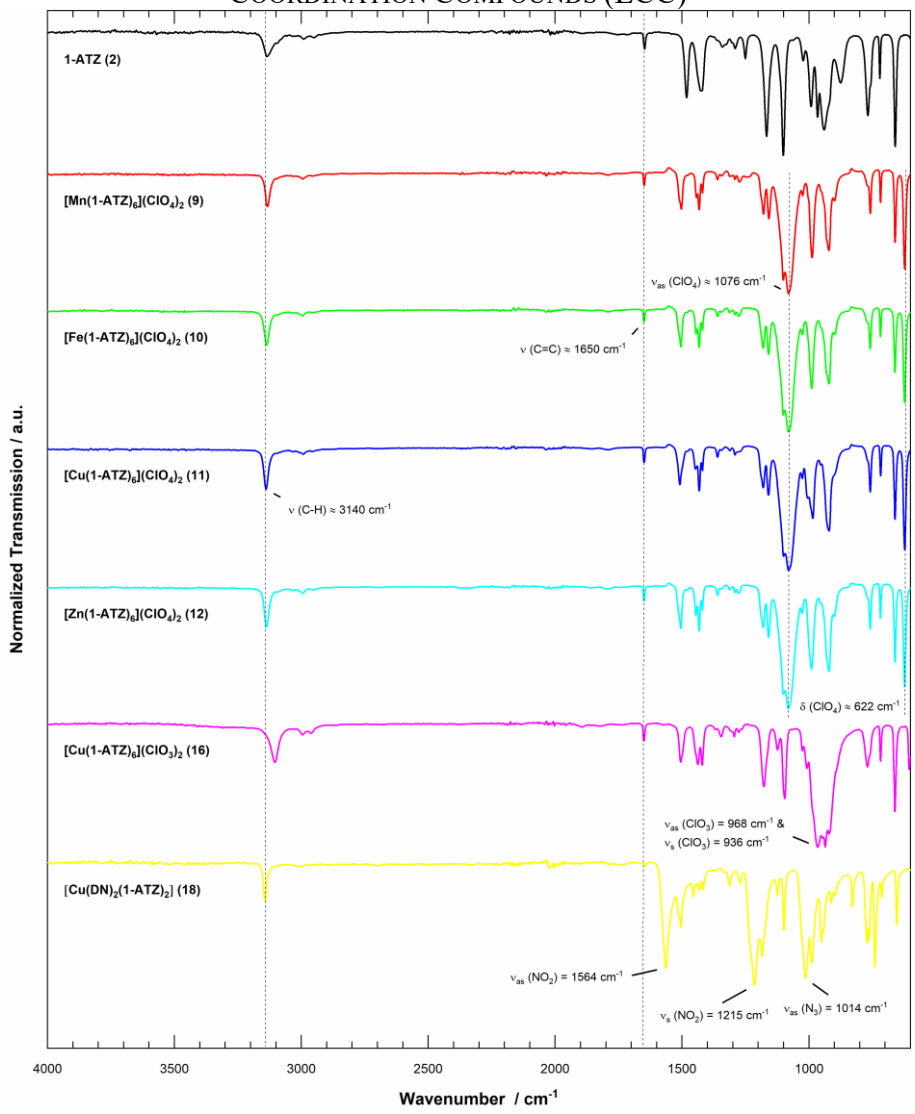

Figure S12. Fourier-transform infrared (FT-IR) spectra of the 1-ATZ ligand **2** as well as its metal(II) complexes **9**–**12**, **16**, and **18**. Band assignments were made with the help of literature.[S18–S20] As a result of complexation, typical dinitramide vibrations of **18** ($\tilde{\nu}_{as}$ (NO_2) = 1564 cm^{-1}, $\tilde{\nu}_{s}$(NO_2) = 1215 cm^{-1}, and $\tilde{\nu}_{as}$ (N_3) = 1014 cm^{-1}) are redshifted compared to those of noncoordinating dinitramide anions.[S21]

4.6.6 DTA Plots of 1–12, 13a, 15–18, 21–23

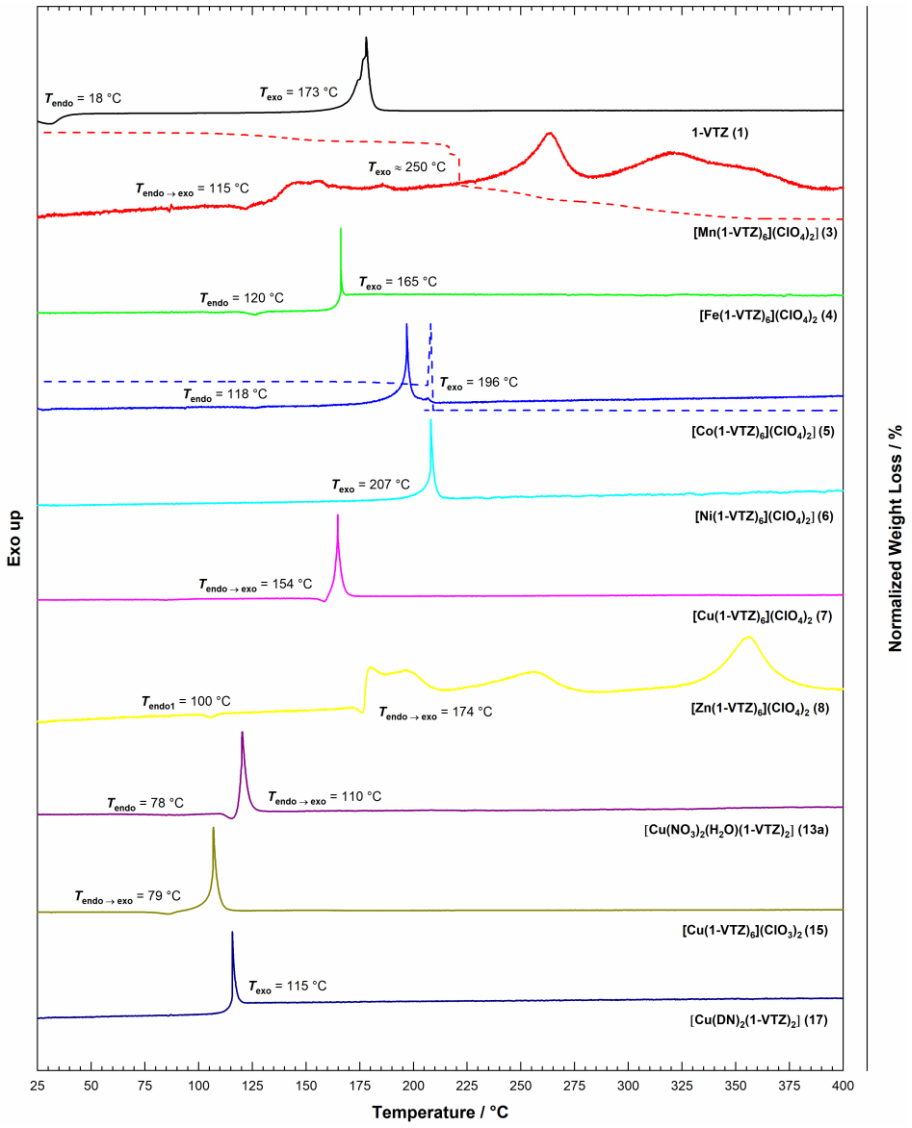

Figure S13. Normalized DTA (solid line, 5 °C min^{-1}) and TGA curves (dashed line, 5 °C min^{-1}) of the compounds **1**, **3**–**8**, **13a**, **15**, and **17**.

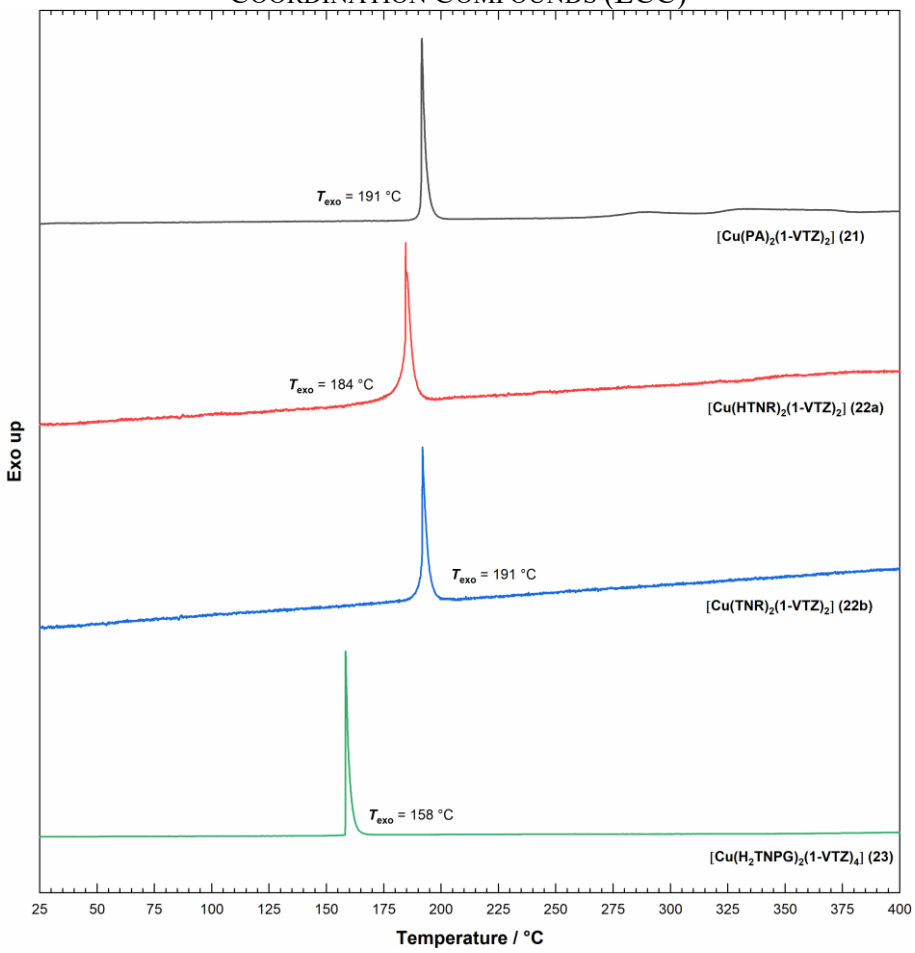

Figure S14. Normalized DTA (solid line, 5 °C min^{-1}) curves of the compounds **21**–**23**.

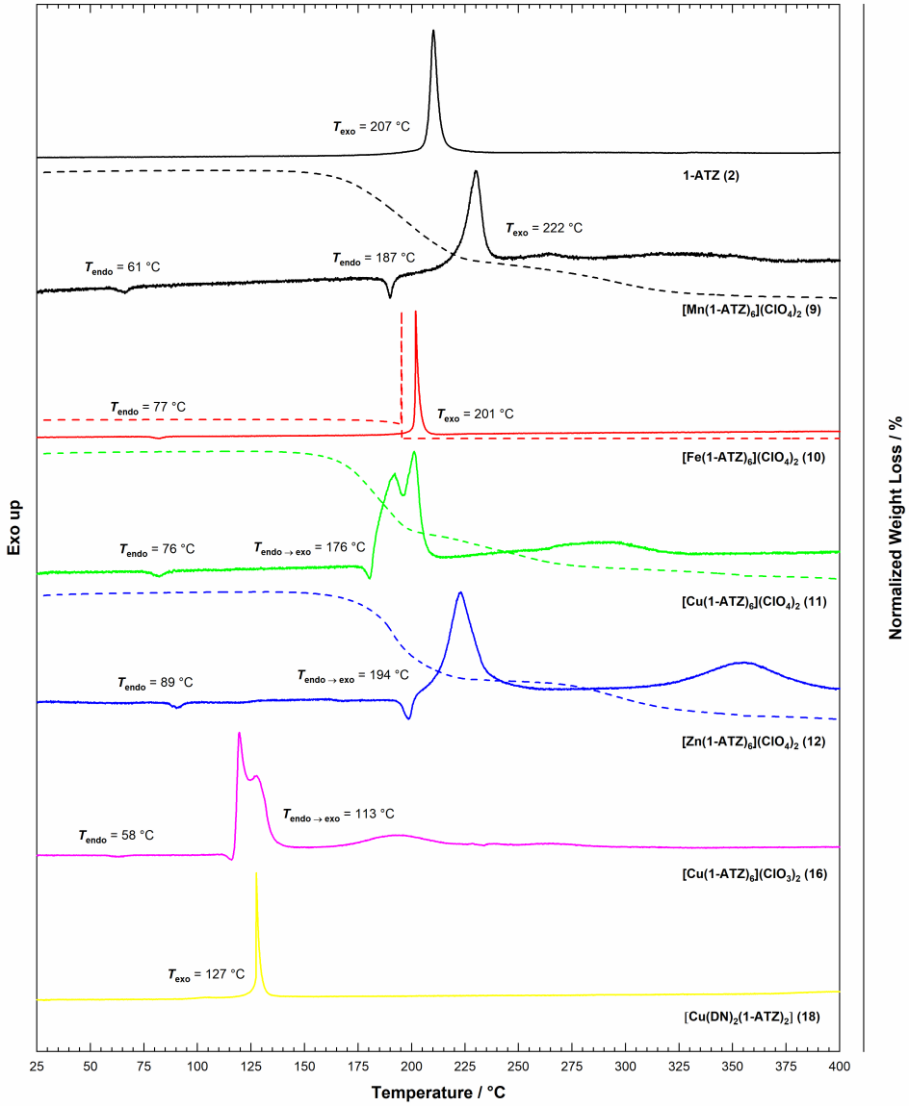

Figure S15. Normalized DTA (solid line, 5 °C min^{-1}) and TGA curves (dashed line, 5 °C min^{-1}) of the 1-ATZ ligand **2** and the ECC **9**–**12**, **16**, and **18**.

4.6.7 TGA Plot of 3, 5, 9–12

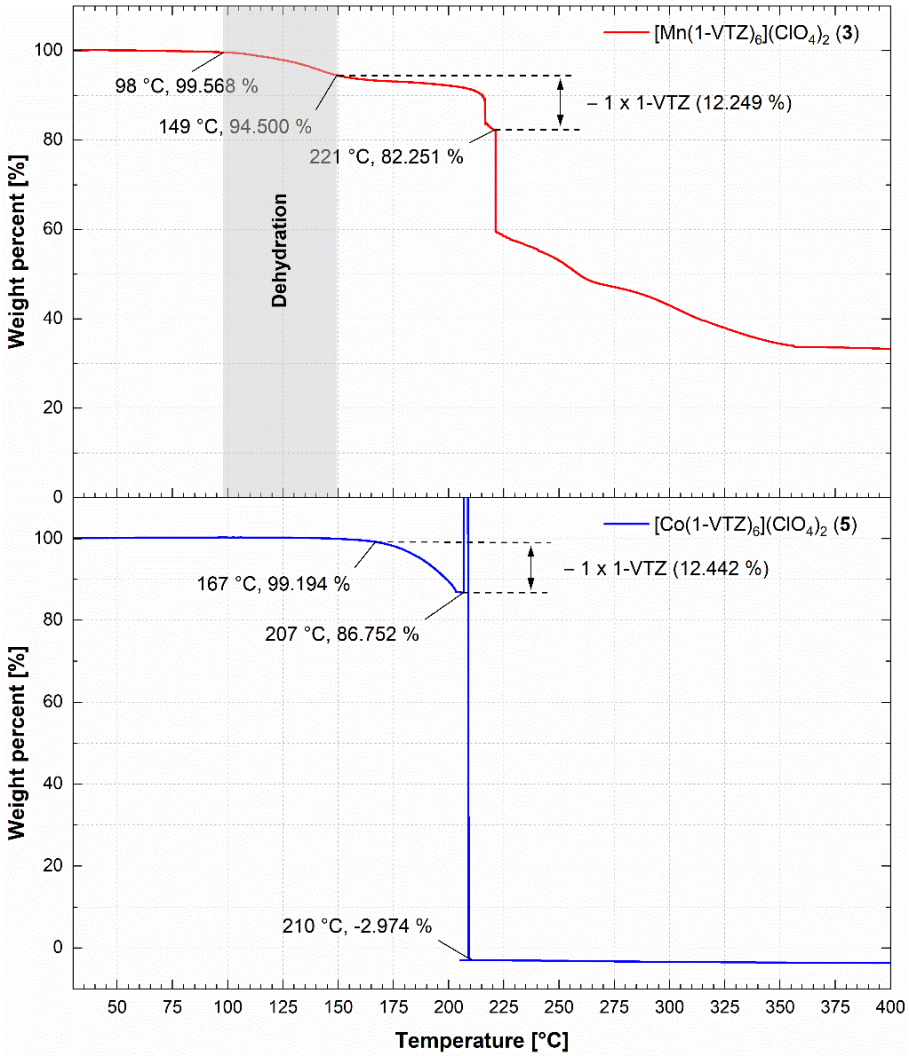

Figure S16. TGA plots (5 °C min^{-1}) of the $[M^{II}(1\text{-VTZ})_6](ClO_4)_2$ complexes **3** and **5**.

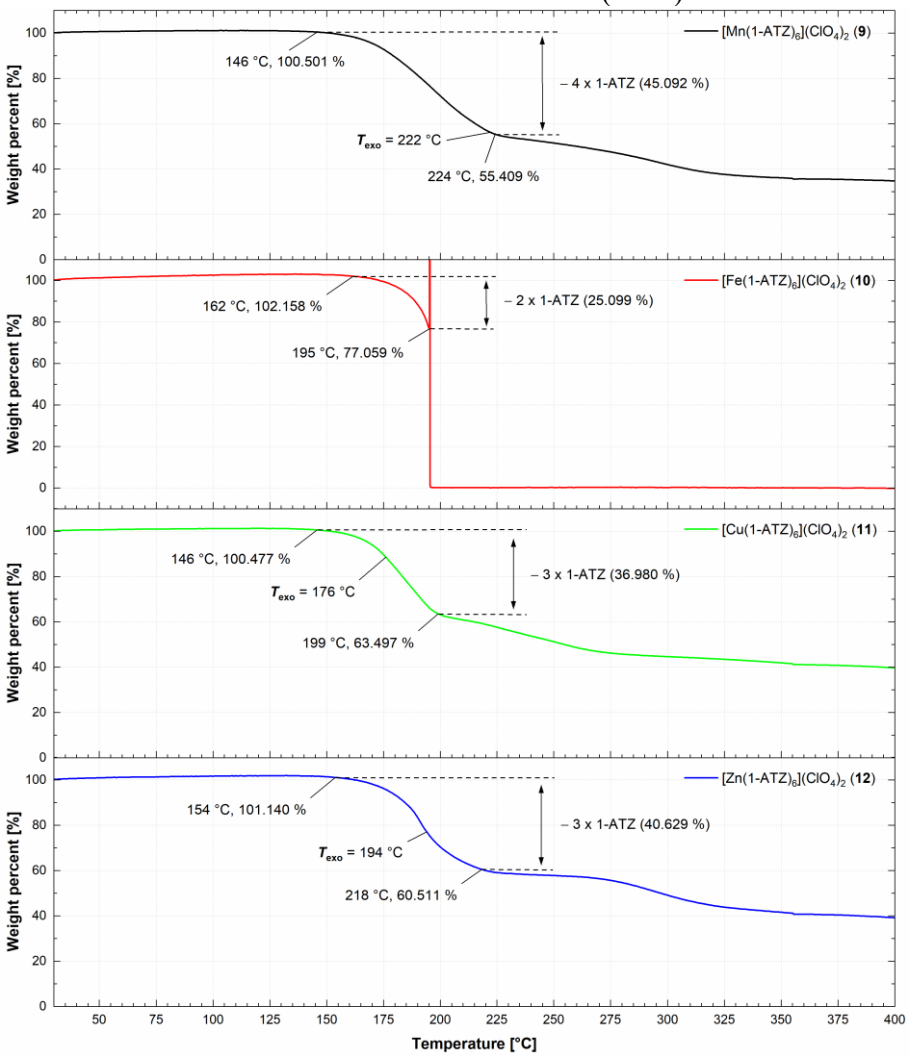

Figure S17. TGA plots (5 °C min^{-1}) of the $[M^{II}(1\text{-ATZ})_6](ClO_4)_2$ complexes **9**–**12**.

4.6.8 Hot Plate & Hot Needle Tests of 3, 4, 7–13a, 15–18, and 21–23

Figure S18. Deflagration of $[Mn(1\text{-}VTZ)_6](ClO_4)_2$ (**3**) during hot plate (left) and hot needle test (right).

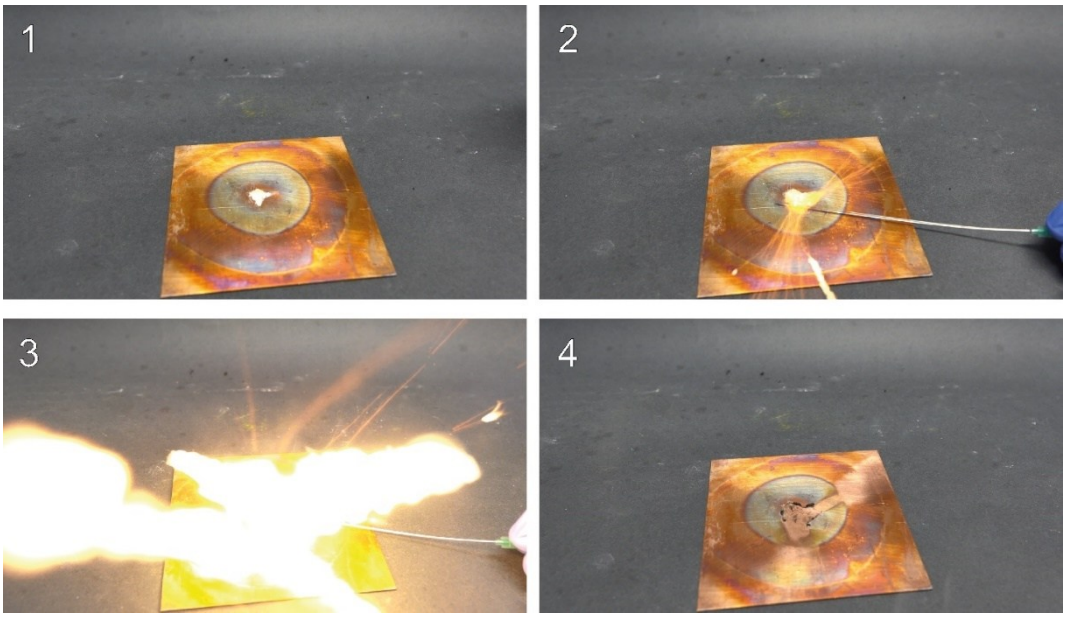

Figure S19. Detonation of $[Fe(1\text{-}VTZ)_6](ClO_4)_2$ (**4**) during the hot needle test, displayed in a sequence.

Figure S20. Behavior of $[Cu(1\text{-}VTZ)_6](ClO_4)_2$ (**7**) while hot plate (left) and hot needle testing (right).

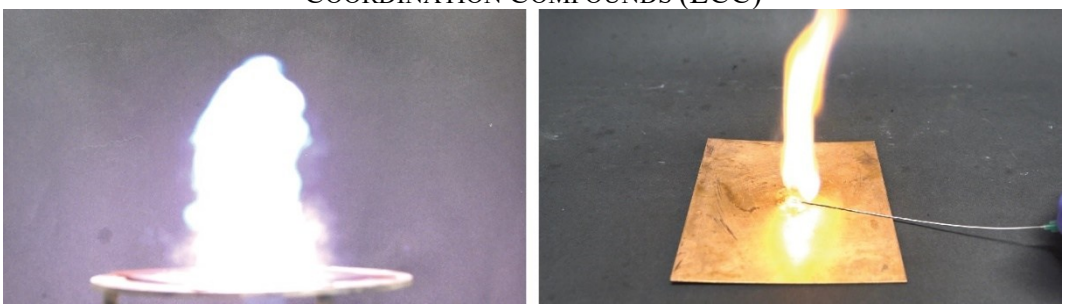

Figure S21. Hot plate (left) and hot needle tests (right) of $[Zn(1\text{-}VTZ)_6](ClO_4)_2$ (**8**).

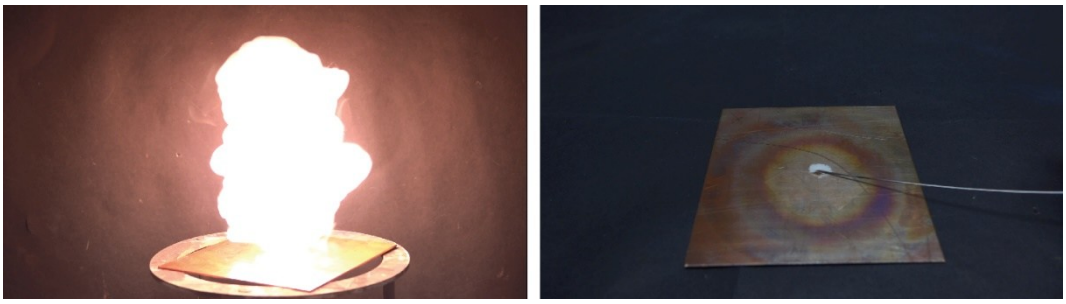

Figure S22. Hot plate (left) and hot needle tests (right) of $[Mn(1\text{-}ATZ)_6](ClO_4)_2$ (**9**).

Figure S23. Behavior of $[Fe(1\text{-}ATZ)_6](ClO_4)_2$ (**10**) while hot plate (left) and hot needle testing (right).

Figure S24. Behavior of $[Cu(1\text{-}ATZ)_6](ClO_4)_2$ (**11**) while hot plate (left) and hot needle testing (right).

Figure S25. Behavior of $[Zn(1\text{-}ATZ)_6](ClO_4)_2$ (**12**) while hot plate (left) and hot needle testing (right).

Figure S26. Reaction of compound of $[Cu(NO_3)_2(H_2O)(1\text{-}VTZ)_2]$ (**13a**) while hot plate (left) and hot needle testing (right).

Figure S27. Deflagration of $[Cu(1\text{-}VTZ)_6](ClO_3)_2$ (**15**) during the hot plate test (left) and hot needle test (right).

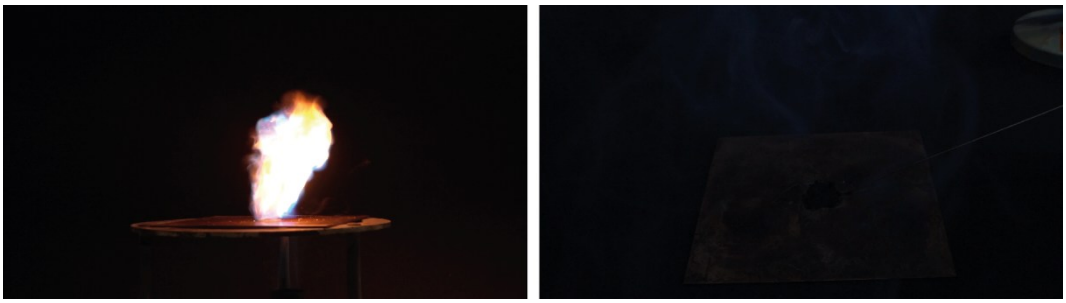

Figure S28. Deflagration of $[Cu(1\text{-}ATZ)_6](ClO_3)_2$ (**16**) during the hot plate test (left) and decomposition during the hot needle test (right).

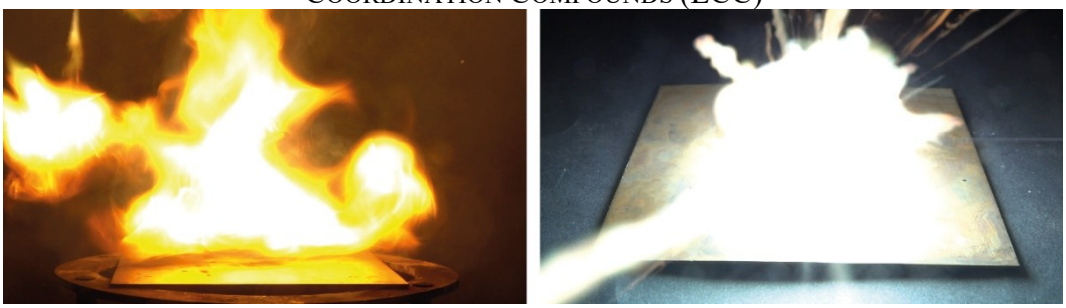

Figure S29. Hot plate (left) and hot needle tests (right) of $[Cu(DN)_2(1\text{-}VTZ)_2]$ (**17**).

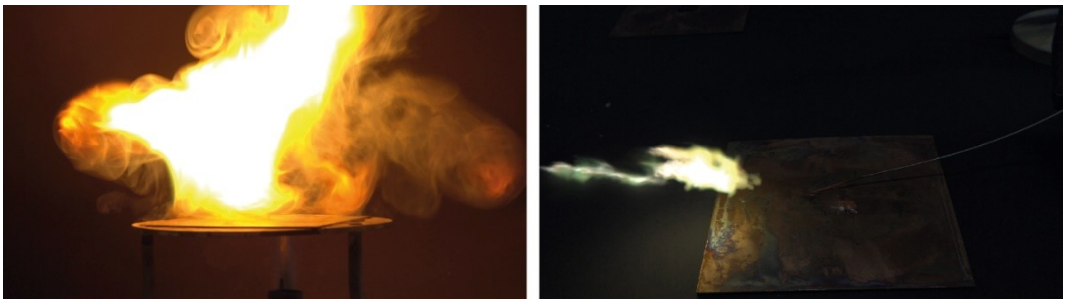

Figure S30. Hot plate (left) and hot needle tests (right) of $[Cu(DN)_2(1\text{-}ATZ)_2]$ (**18**).

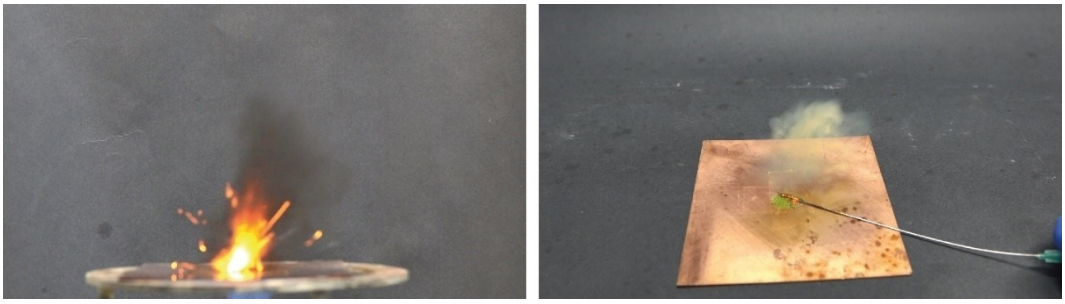

Figure S31. Hot plate (left) and hot needle tests (right) of $[Cu(PA)_2(1\text{-}VTZ)_2]$ (**21**).

Figure S32. Hot plate (left) and hot needle test (right) of ECC $[Cu(HTNR)(1\text{-}VTZ)_2]$ (**22a**).

Figure S33. Hot plate (left) and hot needle test (right) of ECC $[Cu(TNR)(1\text{-}VTZ)_2]$ (**22b**).

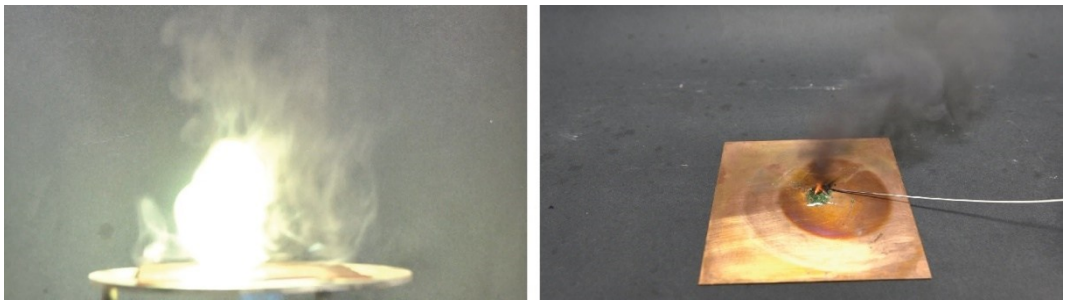

Figure S34. Hot plate (left) and hot needle test (right) of ECC $[Cu(H_2TNPG)_2(1\text{-}VTZ)_4]$ (**23**).

4.6.9 Laser Initiation Tests of 16, 18, 22b

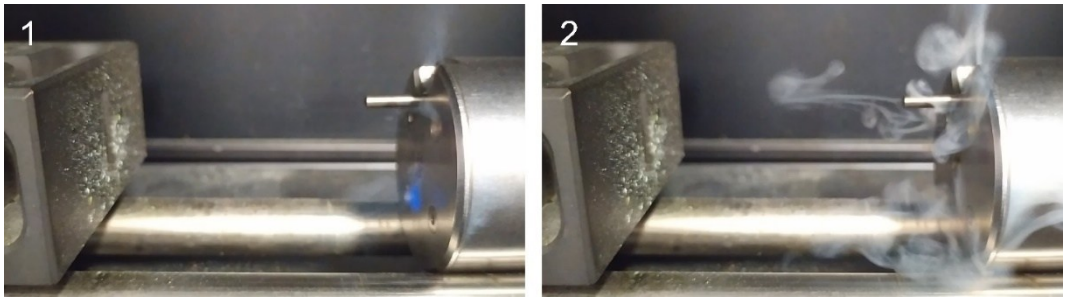

Figure S35. Decomposition of $[Cu(1\text{-}ATZ)_6](ClO_3)_2$ (**16**) shown as a sequence.

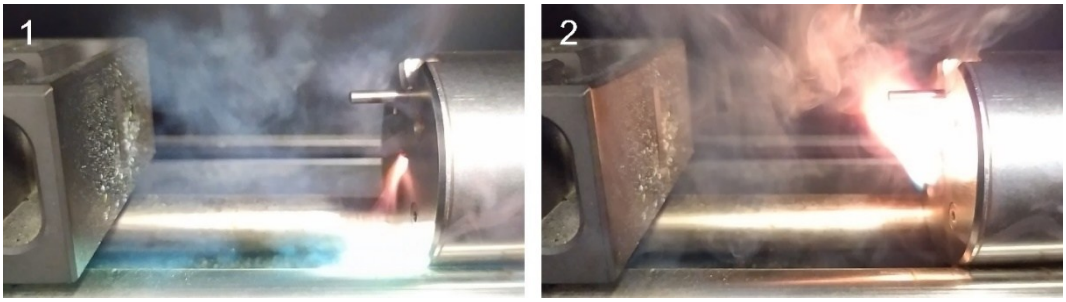

Figure S36. Deflagration of $[Cu(DN)_2(1\text{-}ATZ)_2]$ (**18**) shown as a sequence.

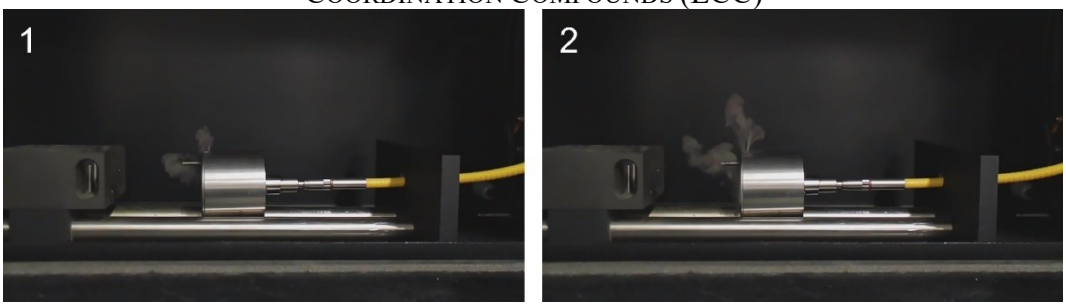

Figure S37. Combustion of [Cu(TNR)(1-VTZ)$_2$] (**22b**) shown as a sequence.

4.6.10 Initiation Capability Tests

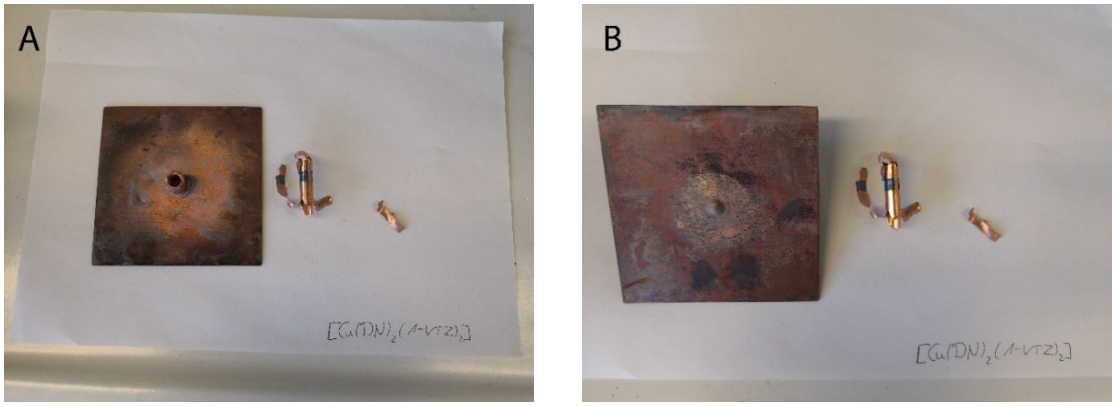

Figure S38. Result of the initiation experiment of compound [Cu(DN)$_2$(1-VTZ)$_2$] (**17**) toward PETN with the front side (A) and the back side (B) of the copper witness plate.

4.6.11 Magnetic Properties

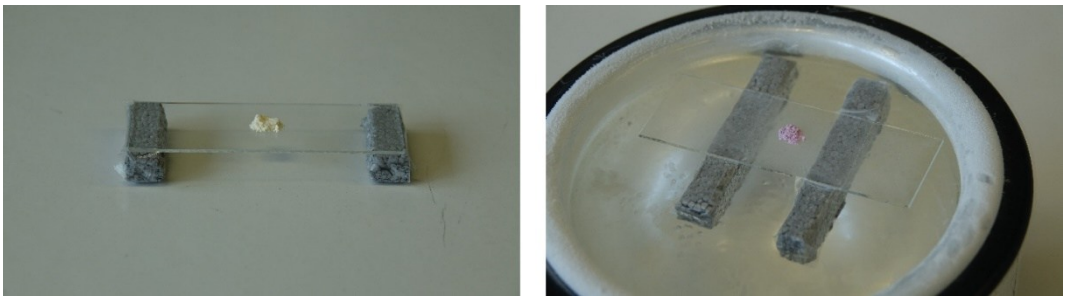

Figure S39. [Fe(1-ATZ)$_6$](ClO$_4$)$_2$ (**10**) at room temperature (left) and cooled with liquid nitrogen (right) revealing a thermochromic effect.

4.6.12 Experimental Part and General Methods

All chemicals and solvents were employed as received (Sigma-Aldrich, Fluka, Acros, ABCR). ^{1}H and ^{13}C spectra were recorded at ambient temperature using a JEOL Bruker 27400, Eclipse 270, JEOL EX 400 or a JEOL Eclipse 400 instrument. The chemical shifts quoted in ppm in the text refer to typical standards such as tetramethyl silane (^{1}H, ^{13}C) in DMSO-d_6 as the solvent. Endothermic and exothermic events of the described compounds, which indicate melting, loss of aqua ligands, or decomposition, are given as the extrapolated onset temperatures. The samples were measured in a range of 25–400 °C at a heating rate of 5 °C min^{-1} through differential thermal analysis (DTA) with an OZM Research DTA 552-Ex instrument and in some cases additionally by thermal gravimetric analysis (TGA) with a PerkinElmer TGA4000. Infrared spectra were measured with neat samples on a Perkin-Elmer BXII FT-IR system with a Smith DuraSampler IR II diamond ATR. Determination of the carbon, hydrogen and nitrogen contents was carried out by combustion analysis using an Elementar Vario El (nitrogen values determined are often lower than the calculated ones' due to their explosive behavior). Impact sensitivity tests were carried out according to STANAG 4489[S22] with a modified instruction[S23] using a BAM (Bundesanstalt für Materialforschung) drophammer.[S24,S25] Ball drop impact sensitivity tests were determined for selected compounds on an OZM ball drop machine (BIT-132), following MIL-STD-1751A (method 1016) by dropping a free-falling steel ball onto the explosive compound.[S24,S26] Friction sensitivity tests were carried out according to STANAG 4487[S27] with a modified instruction[S28] using the BAM friction tester.[S24,S25] The classification of the tested compounds results from the "UN Recommendations on the Transport of Dangerous Goods".[S29,S30] Additionally, all compounds were tested upon the sensitivity toward electrical discharge using the OZM Electric Spark XSpark10 device.[S24] Hot plate and hot needle tests were performed in order to evaluate the potential initiation capability of selected complexes. The samples were fixed on a copper plate underneath adhesive tape and initiated by a red-hot needle. Strong deflagration or detonation of the compound usually indicates a valuable primary explosive. The safe and straightforward hot plate test only shows the behavior of the unconfined sample toward fast heating on a copper plate. It does not necessarily allow any conclusions on a compound's capability as a suitable primary explosive. Initiation capability tests of the newly investigated complexes toward pentaerythritol tetranitrate (PETN) were carried out in a copper shell with a diameter of

7 mm and length of 88 mm filled with 200 mg of sieved secondary explosive (grain size < 100 µm). First, the secondary explosive was pressed with a weight of 8 kg, then the primary explosive to be investigated was subsequently filled on top of the main charge and pressed with the same pressure force. The shell was sealed by an insulator, placed in a retaining ring, which was soldered to a copper witness plate with a thickness of 1 mm and finally initiated by a type A electric igniter. A positive test is indicated by a hole in the copper plate and fragmentation of the shell caused by a deflagration-to-detonation transition (DDT) of PETN. The laser initiation experiments were performed with a 45 W InGaAs laser diode operating in the single-pulsed mode. The diode is attached to an optical fiber with a core diameter of 400 µm and a cladding diameter of 480 µm. The optical fiber is connected via a SMA type connecter directly to the laser and to a collimator. This collimator is coupled to an optical lens, which was positioned in its focal distance (f = 29.9 mm) to the sample. The lens is shielded from the explosive by a sapphire glass. Approximately 15 mg of the carefully pestled compound to be investigated was filled into a transparent plastic cap, pressed with a pressure force of 1 kN and sealed by a UV-curing adhesive. The confined samples were irradiated at a wavelength of 915 nm, a voltage of 4 V, a current of 7 A and pulse lengths of 1–30 ms. The combined currents and pulse lengths result in an energy output of 1.7–51 mJ.

The obtained coordination compounds were washed with cold ethanol when stated, dried overnight in air, and used for analytics without further purification.

CAUTION! *All investigated compounds are* potentially *explosive energetic materials, which show partly increased sensitivities toward various stimuli (e.g., elevated temperatures, impact, friction, or electrostatic discharge). Therefore, proper security precautions (safety glass, face shield, earthed equipment, and shoes, leather coat, Kevlar gloves, Kevlar sleeves, and ear plugs) have to be applied while synthesizing and handling the described compounds.*

1-(2-Chloroethyl)tetrazole (1-ClET)

In correspondence to a literature procedure,[S31] 2-chloroethylamine hydrochloride (60.0 g, 517 mmol, 1.00 equiv.) and sodium azide (33.6 g, 517 mmol, 1.00 equiv.) were suspended in triethyl orthoformate (362 mL, 2.18 mol, 4.21 equiv.). In the following, glacial acetic acid (207 mL, 3.62 mol, 7.00 equiv.) was added dropwise and the resulting reaction

mixture was refluxed for 3 h at 100 °C. Afterwards, the white suspension formed was filtrated and excess reagents and the solvent removed under reduced pressure. To the white residue 2-propanol was added (200 mL) and the obtained mixture was heated and filtrated while hot. The target compound 1-ClET crystallizes in 2-propanol after several hours as colorless crystals (44.8 g, 338 mmol, 65%). Analytical data are consistent with previously reported results.[S32,S33]

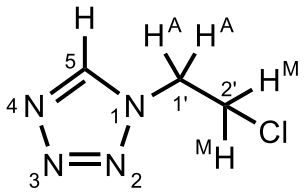

DTA (5 °C min^{-1}) onset: 51 °C (endothermic), 186 °C (exothermic). **^{1}H NMR** (400.13 MHz, DMSO-d_6) δ [ppm]: 9.47 (s, 1H, C5-*H*), 4.85 (t, $^{3}J_{H1'\text{-}H2'}$ = 5.70 Hz, 2H, C1'-H_2), 4.11 (t, $^{3}J_{H2'\text{-}H1'}$ = 5.67 Hz, 2H, C2'-H_2). **^{13}C NMR** (100.62 MHz, DMSO-d_6) δ [ppm]: 144.4 (*C5*), 49.2 (*C1'*), 42.7 (*C2'*). **IR** (ATR, cm^{-1}): 3143 (m, ν̃ tetrazole), 3035 (vw), 3011 (vw), 2976 (w), 1746 (w), 1560 (vw, ν̃ C=N), 1487 (s, ν̃ N=N, *et al.*), 1435 (m), 1423 (s), 1359 (w), 1317 (w), 1282 (m), 1256 (m), 1202 (w), 1176 (vs), 1130 (w), 1101 (vs), 1043 (w), 1023 (w), 971 (vs), 948 (m), 915 (s), 875 (s), 722 (w), 677 (m), 664 (s), 640 (s). **HRMS** (GC/EI): *m/z* calc. for $C_3H_5ClN_4$ $[M]^+$ 132.020; found 132.0196. **EA**: ($C_3H_5ClN_4$, 132.55) calc.: C 27.18, H 3.80, N 42.27%; found: C 27.13, H 3.68, N 42.34%. **Ball drop impact sensitivity**: > 200 mJ. **BAM friction sensitivity**: > 360 N (at grain size > 1000 µm). **ESD**: 1500 mJ (at grain size > 1000 µm).

1-Vinyltetrazole (1, 1-VTZ)

According to a modified procedure from GAPONIK *et al.*,[S34] 1-ClET (6.00 g, 45.3 mmol, 1.00 equiv.) was suspended in methanol (10.9 mL) and hydroquinone (30.0 mg, 272 µmol, 0.006 equiv.) was added to prevent polymerization. Under vigorous stirring a solution of potassium hydroxide (3.18 g, 56.6 mmol, 1.25 equiv.) in methanol (10.9 mL) was added dropwise over a time period of 5 min, whereupon a color change from colorless to yellow and finally orange could be observed. After addition of water (6.82 mL) the reaction mixture was refluxed for 2 h, cooled down and the resulting brownish suspension filtrated. The filtrate was evaporated to dryness, the residue dissolved in water followed by extraction of the aqueous phase with dichloromethane (3 × 100 mL). The combined organic

layers were washed with brine (100 mL), dried over magnesium sulfate, filtered and the solvent removed in vacuo. The resulting crude product was purified through vacuum distillation (2.7×10^{-2} mbar, 50 °C) to yield ligand **1** (2.24 g, 23.3 mmol, 52%) as a colorless product with a melting point of 18 °C. Analytical data are consistent with previously reported results.[S35]

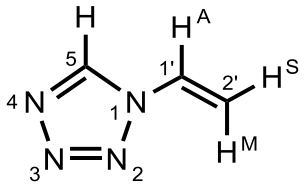

DTA (5 °C min^{-1}) onset: 18 °C (endothermic), 172 °C (exothermic). **^{1}H NMR** (400.13 MHz, DMSO-*d*$_6$) δ [ppm]: 9.76 (s, 1H, C5-*H*), 7.58 (dd, $^{3}J_{H1'\text{-}H2'M}$ = 15.8 Hz, $^{3}J_{H1'\text{-}H2'S}$ = 9.0 Hz, 1H, C1'-*H*), 6.04 (dd, $^{3}J_{\text{H2'M-H1'}}$ = 15.8 Hz, $^{2}J_{H2'M\text{-}H2'S}$ = 1.7 Hz, 1H, C2'-H^{M}), 5.46 (dd, $^{3}J_{H2'S\text{-}H1'}$ = 8.9 Hz, $^{2}J_{H2'S\text{-}H2'M}$ = 1.6 Hz, 1H, C2'-H^{S}). **^{13}C NMR** (100.62 MHz, DMSO-*d*$_6$) δ [ppm]: 142.1 (*C5*), 127.4 (*C1'*), 108.9 (*C2'*). **IR** (ATR, cm^{-1}): 3131 (w, ṽ tetrazole C–H), 3106 (w), 3075 (vw), 3006 (vw), 2934 (vw), 1650 (s, ṽ C═C), 1474 (s, ṽ tetrazole), 1425 (w), 1417 (w), 1360 (m), 1320 (vw), 1290 (w), 1271 (w), 1212 (m), 1198 (m), 1171 (m), 1160 (s), 1094 (vs, ṽ tetrazole), 1020 (m), 1003 (m), 954 (s), 915 (s), 874 (m), 726 (w), 703 (w), 667 (s), 626 (s). **HRMS** (GC/EI): *m/z* calc. for $C_3H_4N_4$ $[M]^+$ 96.0436; found 96.0424. **EA**: ($C_3H_4N_4$, 96.09) calc.: C 37.50, H 4.20, N 58.31%; found: C 36.39, H 4.14, N 56.91%. **BAM impact sensitivity**: 15 J. **BAM friction sensitivity**: > 360 N.

1-Allyltetrazole (2, 1-ATZ)

Adapting the literature,[S1,S2,S36] sodium azide (7.97 g, 123 mmol, 1.40 equiv.) was suspended in a colorless solution of allylamine (6.56 mL, 87.6 mmol, 1.00 equiv.) in triethyl orthoformate (30.6 mL, 184 mmol, 2.10 equiv.). In the following, glacial acetic acid (43.6 mL, 762 mmol, 8.70 equiv.) was added dropwise and the resulting reaction mixture was refluxed for 3 h at 90 °C. TLC control (SiO_2 / 50% MeOH in DCM, stained with $KMnO_4$): R_f = 0.90 (product), R_f = 0.19 (starting material). Upon being cooled to room temperature, the precipitated sodium acetate was removed by filtration and excess reagents and the solvent removed under reduced pressure. The residue was taken up in water (100 mL) and the slightly yellow solution carefully neutralized with K_2CO_3. After

concentration *in vacuo*, the white precipitate was suspended in acetone (100 mL), filtered off and the organic solvent removed on a rotavapor (bath temperature 40 °C). The resulting crude product was isolated by column chromatography (SiO_2, EtOAc / hexanes 1:1, h = 31 cm, d = 3.5 cm, 20 mL tubes, Fr 21-54) yielding the target compound 1-ATE as a pale-yellow liquid (5.82 mg, 52.8 mmol, 60%). Analytical data are consistent with previously reported results.

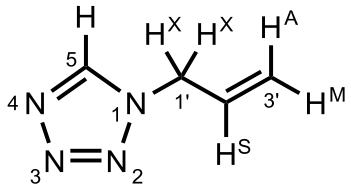

^{1}H NMR (400.13 MHz, DMSO-d_6) δ [ppm]: 9.40 (s, 1H, C5-*H*), 6.06 (ddt, 1H, $^3J_{H2'-H3'A}$ = 17.04 Hz, $^3J_{H2'-H3'M}$ = 10.29 Hz, $^3J_{H2'-H1'}$ = 5.97 Hz, C2'-*H*), 5.31 (ddt, $^3J_{H3'M-H2'}$ = 10.18Hz, $^2J_{H3'M-H3'A}$ = $^4J_{H3'M-H1'}$ = 1.26 Hz, C3'-H^M), 5.20 (ddt, 1H, $^3J_{H3'A-H2'}$ = 17.11 Hz, $^2J_{H3'A-H3'M}$ = 1.21 Hz, $^4J_{H3'A-H1'}$ = 1.65 Hz, C3'-H^A), 5.13 (ddd, 2H, $^3J_{H1'-H2'}$ = 5.91 Hz, $^4J_{H1'-H3'A}$ = 1.65 Hz, $^4J_{H1'-H3'M}$ = 1.29 Hz, C1'-H_2). **^{13}C NMR** (100.62 MHz, DMSO-d_6) δ [ppm]: 143.93 (*C5*), 131.64 (*C2'*), 119.48 (*C3'*), 49.72 (*C1'*). **DTA** (5 °C min^{-1}) onset: 207 °C (exothermic). **IR** (ATR, cm^{-1}): 3135 (w, ν̃ tetrazole C–H), 2991 (vw), 2951 (vw), 1648 (w, ν̃ C=C), 1482 (m), 1426 (m), 1341 (w), 1291 (w), 1251 (w), 1167 (s), 1102 (vs), 1023 (w), 992 (s), 967 (s), 941 (s), 876 (m), 768 (s), 721 (m), 660 (vs). **BAM impact sensitivity**: > 40 J. **BAM friction sensitivity**: > 360 N.

General procedure for the preparation of the metal(II) (Mn^{II}, Fe^{II}, Co^{II}, Ni^{II}, Cu^{II}, Zn^{II}) 1-VTZ perchlorate complexes (3, 4, 5, 6, 7, 8):

To a mechanically stirred aqueous solution (2 mL) of the corresponding metal(II) perchlorate salt (**3**: $Mn(ClO_4)_2 \cdot 6\,H_2O$ (90.5 mg, 0.25 mmol, 1.00 equiv.); **4**: $Fe(ClO_4)_2 \cdot 6\,H_2O$ (90.7 mg, 0.25 mmol, 1.00 equiv.); **5**: $Co(ClO_4)_2 \cdot 6\,H_2O$ (91.5 mg, 0.25 mmol, 1.00 equiv.); **6**: $Ni(ClO_4)_2 \cdot 6\,H_2O$ (91.4 mg, 0.25 mmol, 1.00 equiv.) **7**: $Cu(ClO_4)_2 \cdot 6\,H_2O$ (92.6 mg, 0.25 mmol, 1.00 equiv.); **8**: $Zn(ClO_4)_2 \cdot 6\,H_2O$ (93.1 mg, 0.25 mmol, 1.00 equiv.)), an aqueous solution (1 mL) of the ligand (144 mg, 1.50 mmol, 6.00 equiv.) was added dropwise. For complete dissolution the resulting suspension was heated to 50 °C and left for crystallization at ambient temperature.

[Mn(1-VTZ)$_6$](ClO$_4$)$_2$ (3)

From a pale-yellow solution the manganese(II) complex **3** was obtained after forty-one days in the form of crystals suitable for X-ray diffraction (12.1 mg, 14.6 µmol, 6%). **IR** (ATR, cm^{-1}): 3132 (m, ṽ tetrazole C–H), 3086 (vw), 3038 (vw), 3006 (vw), 2979 (vw), 1655 (m, ṽ C═C), 1494 (m, ṽ coord. tetrazole), 1431 (vw), 1371 (m), 1305 (w), 1224 (m), 1179 (m), 1093 (vs), 1076 (vs, ṽ ClO$_4$), 1028 (s), 975 (m), 950 (s), 917 (s), 728 (w), 699 (w), 667 (s), 622 (vs, δ ClO$_4$). **EA**: ($C_{18}H_{24}Cl_2MnN_{24}O_8$, 830.39) calc.: C 26.04, H 2.91, N 40.48%; found: C 25.84, H 2.90, N 40.61%. **BAM impact sensitivity**: 2 J (at grain size > 1000 µm). **Ball drop impact sensitivity**: > 200 mJ. **BAM friction sensitivity**: 20 N (at grain size > 1000 µm). **ESD**: 1080 mJ (at grain size > 1000 µm).

[Fe(1-VTZ)$_6$](ClO$_4$)$_2$ (4)

Resulting from subsequent crystallization at room temperature, [Fe(1-VTZ)$_6$](ClO$_4$)$_2$ (**4**, 122.4 mg, 147 µmol, 59%) was obtained as brown crystals within five days, which were filtered off and washed with cold ethanol. **DTA** (5 °C min^{-1}) onset: 120 °C (endothermic), 165 °C (exothermic). **IR** (ATR, cm^{-1}): 3133 (m, ṽ tetrazole C–H), 3086 (vw), 3037 (vw), 3004 (vw), 2975 (vw), 1655 (m, ṽ C═C), 1494 (m, ṽ coord. tetrazole), 1431 (vw), 1372 (m), 1305 (w), 1224 (m), 1180 (m), 1092 (vs), 1078 (vs, ṽ ClO$_4$), 1029 (s), 976 (m), 950 (s), 916 (s), 729 (w), 700 (w), 667 (s), 622 (vs, δ ClO$_4$). **EA**: ($C_{18}H_{24}Cl_2FeN_{24}O_8$, 831.30) calc.: C 26.01, H 2.91, N 40.44%; found: C 25.81, H 2.89, N 40.48%. **BAM impact sensitivity**: 4 J (at grain size > 1000 µm). **Ball drop impact sensitivity**: 41 mJ. **BAM friction sensitivity**: 3 N (at grain size > 1000 µm). **ESD**: 480 mJ (at grain size > 1000 µm).

[Co(1-VTZ)$_6$](ClO$_4$)$_2$ (5)

From an ochre-colored solution the cobalt(II) complex **5** crystallized within six days in the form of light-yellow plates (129 mg, 154 µmol, 62%). **DTA** (5 °C min^{-1}) onset: 196 °C (exothermic). **IR** (ATR, cm^{-1}): 3133 (m), 3086 (vw), 3004 (vw), 2980 (vw), 1892 (vw), 1842 (vw), 1678 (vw), 1655 (m), 1625 (w), 1496 (m), 1459 (vw), 1432 (vw), 1373 (m), 1324 (vw), 1306 (w), 1225 (m), 1181 (m), 1093 (vs), 1078 (vs), 1030 (s), 977 (m), 950 (s), 915 (s), 729 (w), 700 (w), 667 (s), 622 (vs). **EA**: ($C_{18}H_{24}Cl_2CoN_{24}O_8$, 833.09) calc.: C 25.91, H 2.90, N 40.29%; found: C 25.75, H 3.05, N 40.01%.

[Ni(1-VTZ)$_6$](ClO$_4$)$_2$ (6)

The light-violet solution was left to crystallize at room room temperature, the solid was filtered off, washed with acetone and diethyl ether and dried in air. Coordination compound **6** (85.8 mg, 103 µmol, 42%) was obtained after twelve days in the form of light-violet plates suitable for X-ray diffraction. **DTA** (5 °C min^{-1}) onset: 207 °C (exothermic). **IR** (ATR, cm^{-1}): 3131 (w), 3087 (vw), 3041 (vw), 3005 (vw), 2980 (vw), 1842 (vw), 1790 (vw), 1681 (vw), 1655 (m), 1498 (m), 1461 (vw), 1434 (vw), 1374 (w), 1308 (w), 1229 (m), 1203 (w), 1184 (m), 1094 (vs), 1081 (vs), 1031 (m), 978 (w), 951 (s), 914 (s), 898 (m), 731 (w), 700 (w), 667 (s), 622 (vs). **EA**: ($C_{18}H_{24}Cl_2N_{24}NiO_8$, 832,09) calc.: C 25.92, H 2.90, N 40.30%; found: C 25.80, H 2.77, N 40.32%.

[Cu(1-VTZ)$_6$](ClO$_4$)$_2$ (7)

The blue-colored solution was left to crystallize, the solid was filtered off, washed with cold ethanol and dried in air. Coordination compound **5** (147 mg, 175 µmol, 70%) was obtained after three days in the form of blue crystals suitable for X-ray diffraction. **DTA** (5 °C min^{-1}) onset: 154 °C (endothermic, followed by exothermic). **IR** (ATR, cm^{-1}): 3130 (m, ν̃ tetrazole C–H), 3089 (vw), 3039 (vw), 3005 (vw), 1655 (m, ν̃ C═C), 1491 (m, ν̃ coord. tetrazole), 1435 (vw), 1375 (w), 1307 (w), 1225 (m), 1178 (m), 1092 (vs), 1077 (vs, ν̃ ClO$_4$), 1035 (m), 983 (w), 971 (w), 950 (s), 915 (s), 729 (w), 699 (w), 667 (s), 622 (vs, δ ClO$_4$). **EA**: ($C_{18}H_{24}Cl_2CuN_{24}O_8$, 839.00) calc.: C 25.77, H 2.88, N 40.07%; found: C 25.67, H 2.94, N 40.15%. **BAM impact sensitivity**: 2 J (at grain size 500–1000 µm). **Ball drop impact sensitivity**: 194 mJ. **BAM friction sensitivity**: 7 N (at grain size 500–1000 µm). **ESD**: 317 mJ (at grain size 500–1000 µm).

[Zn(1-VTZ)$_6$](ClO$_4$)$_2$ (8)

From a light-yellow solution, crystals suitable for X-ray diffraction of the zinc(II) complex **6** were obtained within fourty-five days (69.0 mg, 82.1 µmol, 33%). **DTA** (5 °C min^{-1}) onset: 100 °C (endothermic), 174 °C (endothermic, followed by exothermic). **IR** (ATR, cm^{-1}): 3134.00 (m, ν̃ tetrazole C–H), 3087 (vw), 3040 (vw), 3005 (vw), 2980 (vw), 1655 (m, ν̃ C═C), 1495 (m, ν̃ coord. tetrazole), 1432 (vw), 1373 (m), 1305 (w), 1225 (m), 1180 (m), 1094 (vs), 1078 (vs, ν̃ ClO$_4$), 1030 (s), 978 (m), 950 (s), 916 (s), 729 (w), 700 (w), 667 (s), 622 (vs, δ ClO$_4$). **EA**: ($C_{18}H_{24}Cl_2N_{24}O_8Zn$, 840.83) calc.: C 25.71, H 2.88, N 39.98%;

found: C 25.57, H 2.98, N 40.07%. **BAM impact sensitivity**: 6 J (at grain size > 1000 µm). **Ball drop impact sensitivity**: > 200 mJ. **BAM friction sensitivity**: 10 N (at grain size > 1000 µm). **ESD**: 1500 mJ (at grain size > 1000 µm).

General procedure for the preparation of metal(II) (Mn^{II}, Fe^{II}, Cu^{II}, Zn^{II}) 1-ATZ perchlorate complexes (9, 10, 11, 12):

The corresponding metal(II) perchlorate salt [**9**: $Mn(ClO_4)_2 \cdot 6\ H_2O$ (362 mg, 1.00 mmol, 1.00 equiv.); **10**: $Fe(ClO_4)_2 \cdot 6\ H_2O$ (363 mg, 1.00 mmol, 1.00 equiv.); **11**: $Cu(ClO_4)_2 \cdot 6\ H_2O$ (371 mg, 1.00 mmol, 1.00 equiv.); **12**: $Zn(ClO_4)_2 \cdot 6\ H_2O$ (372 mg, 1.00 mmol, 1.00 equiv.)] was dissolved in ethanol (2 mL) and heated to 80 °C. While stirring, an ethanolic solution (2 mL) of the ligand (**2**, 661 mg, 6.00 mmol, 6.00 equiv.) was added dropwise. The complexes either precipitated immidiately from the ethanolic solution (**11**), or at the least when cooled on ice (**12**) or by precipitation with diethyl ether as an antisolvent (**9**, **10**). The powders were filtered off and washed with cold iPrOH an Et_2O. For crystal growth, water was added dropwise to the hot ethanolic suspensions until a complete dissolution occurred at 80 °C. After cooling and standing in air the compounds crystallized within 1–6 days.

Figure S40. Picture of the precipitated complexes **9** (MR177), **10** (MR176), **11** (MR175) and **12** (MR178).

$[Mn(1\text{-}ATZ)_6](ClO_4)_2$ (9)

Compound **7** was obtained as colorless powder (444 mg, 0.49 mmol, 49%). **DTA** (5 °C min^{-1}) onset: 61 °C (endothermic), 187 °C (endothermic), 222 °C (exothermic). **IR** (ATR, cm^{-1}): 3134 (m, ṽ tetrazole C–H), 3034 (vw), 2994 (vw), 2955 (vw), 1793 (vw), 1649 (w, ṽ C═C), 1503 (m), 1443 (w), 1433 (m), 1420 (w), 1361 (vw), 1344 (vw), 1312 (vw), 1292 (vw), 1274 (w), 1180 (m), 1158 (m), 1102 (s), 1081 (vs, ṽ ClO_4), 1025 (w), 988 (s), 922 (s), 899 (w), 759 (m), 718 (w), 661 (m), 623 (s, δ ClO_4). **BAM impact sensitivity**: 20 J (at grain size 500–1000 µm). **BAM friction sensitivity**: 216 N (at grain size 500–1000 µm). **ESD**: 1500 mJ (at grain size 500–1000 µm).

$[Fe(1\text{-}ATZ)_6](ClO_4)_2$ (10)

ECC **8** was received in the form of a light beige powder (536 mg, 0.59 mmol, 59%). **DTA** (5 °C min^{-1}) onset: 77 °C (endothermic), 201 °C (exothermic). **IR** (ATR, cm^{-1}): 3137 (m, ṽ tetrazole C–H), 3033 (vw), 2995 (vw), 2956 (vw), 1789 (vw), 1650 (w, ṽ C═C), 1505 (m), 1445 (w), 1433 (m), 1420 (w), 1361 (vw), 1345 (vw), 1313 (vw), 1292 (vw), 1277 (vw), 1181 (m), 1159 (m), 1101 (s), 1081 (vs, ṽ ClO_4), 1026 (w), 989 (s), 921 (s), 899 (w), 759 (m), 719 (w), 661 (m), 623 (s, δ ClO_4). **BAM impact sensitivity**: 5 J (at grain size 500–1000 µm). **BAM friction sensitivity**: 96 N (at grain size 500–1000µm). **ESD**: 480 mJ (at grain size 500–1000 µm).

$[Cu(1\text{-}ATZ)_6](ClO_4)_2$ (11)

Complex compound **9** precipitated as light blue powder (803 mg, 0.87 mmol, 87%). **DTA** (5 °C min^{-1}) onset: 76 °C (endothermic), 176 °C (exothermic). **IR** (ATR, cm^{-1}): 3139 (m, ṽ tetrazole C–H), 3034 (vw), 2993 (vw), 2957 (vw), 1793 (vw), 1650 (w, ṽ C═C), 1509 (m), 1447 (w), 1433 (m), 1420 (w), 1361 (w), 1345 (vw), 1312 (vw), 1292 (vw), 1181 (m), 1160 (m), 1100 (s), 1080 (vs, ṽ ClO_4), 1027 (w), 985 (m), 954 (w), 921 (s), 759 (m), 718 (w), 661 (m), 623 (s, δ ClO_4). **BAM impact sensitivity**: 5 J (at grain size 500–1000 µm). **BAM friction sensitivity**: 72 N (at grain size 500–1000 µm). **ESD**: 420 mJ (at grain size 500–1000 µm).

$[Zn(1\text{-}ATZ)_6](ClO_4)_2$ (12)

Product **10** precipitated as colorless powder (733 mg, 0.79 mmol, 79%). **DTA** (5 °C min^{-1}) onset: 89 °C (endothermic), 194 °C (endothermic, followed by exothermic). **IR** (ATR, cm^{-1}): 3138 (m, ṽ tetrazole C–H), 3033 (vw), 2994 (vw), 2955 (vw), 1790 (vw), 1649 (w, ṽ C═C), 1506 (m), 1480 (vw), 1446 (w), 1433 (m), 1420 (w), 1361 (vw), 1345 (vw), 1314 (vw), 1292 (vw), 1278 (vw), 1181 (m), 1159 (m), 1102 (s), 1082 (vs, ṽ ClO_4), 1027 (w), 990 (s), 953 (w), 921 (s), 900 (w), 759 (m), 719 (w), 661 (s), 623 (s, δ ClO_4). **BAM impact sensitivity**: 25 J (at grain size 500–1000 µm). **BAM friction sensitivity**: 168 N (at grain size 500–1000 µm). **ESD**: 1500 mJ (at grain size 500–1000 µm).

$[Cu(NO_3)_2(H_2O)(1\text{-}VTZ)_2]$ (13a)

1-Vinyltetrazole (**1**, 192 mg, 2.00 mmol, 2.00 equiv.) was added to an aqueous solution (2 mL) of copper(II) nitrate trihydrate (242 mg, 1.00 mmol, 1.00 equiv.). In the course of crystallization and purification, and within seven days, the product was obtained in the form of blue blocks (644 mg, 1.62 mmol, 81%). **DTA** (5 °C min^{-1}) onset: 78 °C (endothermic), 111 °C (endothermic, followed by exothermic). **IR** (ATR, cm^{-1}): 3618 (w, ṽ O–H), 3556 (w, ṽ O–H), 3144 (m, ṽ tetrazole C–H), 3105 (w), 3017 (vw), 1727 (w, ṽ + δ NO_3), 1646 (m, ṽ C═C), 1627 (m, δ O–H), 1488 (s, ṽ coord. tetrazole), 1425 (w), 1415 (m), 1300 (s, ṽ NO_3), 1282 (vs, ṽ NO_3), 1206 (s), 1175 (m), 1104 (s), 1094 (m), 1057 (w), 1019 (m), 1005 (s), 947 (s), 927 (s), 891 (m), 806 (m, γ NO_3), 752 (m), 721 (w), 701 (w), 682 (m), 668 (w), 619 (m). **EA**: ($C_6H_{10}CuN_{10}O_7$, 397.76) calc.: C 18.12, H 2.53, N 35.22%; found: C 18.33, H 2.40, N 35.21%. **BAM impact sensitivity**: 6 J. **Ball drop impact sensitivity**: > 200 mJ. **BAM friction sensitivity**: 160 N (at grain size > 1000 µm). **ESD**: > 1500 mJ (at grain size > 1000 µm).

$[Cu(1\text{-}VTZ)_6](NO_3)_2$ (13b)

The ligand 1-vinyltetrazole (**1**, 577 mg, 6.00 mmol, 6.00 equiv.) was added to a solution of copper nitrate trihydrate (242 mg, 1.00 mmol, 1.00 equiv.) dissolved in warm ethanol (2 mL). The obtained solution was left for crystallization at room temperature. After four days, a few blue crystals suitable for X-ray determination were obtained. It is assumed that a slow hydrolysis of the compound caused by air moisture is taking place, preventing an elemental analysis pure isolation.

[Cu(1-ATZ)$_3$(NO$_3$)$_2$] (14)

A solution of 1-ATZ (165 mg, 1.50 mmol, 6.00 equiv.) in ethanol (2 mL) was added to an ethanolic solution (1 mL) of copper nitrate trihydrate (60.4 mg, 0.25 mmol, 1.00 equiv.) heated to 80 °C. Since the product did not precipitate upon cooling on ice, the reaction mixture was left at room temperature to crystallize. After two days, a few blue platelet-shaped crystals suitable for X-ray diffraction could be obtained.

[Cu(1-VTZ)$_6$](ClO$_3$)$_2$ (15)

According to a modified literature procedure from WURZENBERGER *et al.*,[S37] aqueous solutions (2 mL) of barium(II) chlorate monohydrate (80.6 mg, 0.25 mmol, 1.00 equiv.) and copper(II) sulfate pentahydrate (62.4 mg, 0.25 mmol, 1.00 equiv.) were combined. After mechanically stirring and cooling in an ice bath for 5 min, the precipitated barium(II) sulfate was filtrated off using a syringe filter. In the following, the ligand (**1**, 144 mg, 1.50 mmol, 6.00 equiv.) was added and the resulting mixture again filtrated using a syringe filter. After one week single crystals of **13** were isolated (121 mg, 0.15 mmol, 60%). **DTA** (5 °C min^{-1}) onset: 79 °C (endothermic), 107 °C (exothermic). **IR** (ATR, cm^{-1}): 3104 (m, ṽ tetrazole C–H), 3078 (w), 3008 (w), 2981 (w), 1652 (m, ṽ C═C), 1495 (m, ṽ coord. tetrazole), 1437 (w), 1415 (vw), 1378 (w), 1310 (w), 1229 (m), 1207 (w), 1182 (m), 1102 (w), 1091 (s), 1039 (m), 1009 (m), 963 (vs, ṽ ClO$_3$), 935 (s, ṽ ClO$_3$), 919 (vs), 731 (w), 699 (w), 679 (w), 667 (s), 622 (s, δ ClO$_3$), 605 (m). **EA**: ($C_{18}H_{24}Cl_2CuN_{24}O_6$, 807.00) calc.: C 26.79, H 3.00, N 41.66%; found: C 26.37, H 2.91, N 40.96%. **BAM impact sensitivity**: 4 J (at grain size 500–1000 µm). **Ball drop impact sensitivity**: ≤ 4 mJ. **BAM friction sensitivity**: 2 N (at grain size 500–1000 µm). **ESD**: 480 mJ (at grain size 500–1000 µm).

[Cu(1-ATZ)$_6$](ClO$_3$)$_2$ (16)

According to a modified literature procedure from WURZENBERGER *et al.*,[S37] aqueous solutions (1 mL) of barium(II) chlorate monohydrate (80.6 mg, 0.25 mmol, 1.00 equiv.) and copper(II) sulfate pentahydrate (62.4 mg, 0.25 mmol, 1.00 equiv.) were combined. After mechanically stirring and cooling in an ice bath for 5 min, the precipitated barium(II) sulfate was filtrated off using a syringe filter. In the following, an ethanolic solution (2 mL) of the ligand (**2**, 165 mg, 1.50 mmol, 6.00 equiv.) was added and the reaction mixture left to crystallize at ambient temperature. After eleven days ECC **14** was obtained as blue

platelet-shaped crystals (75.3 mg, 84.5 µmol, 34%). **DTA** (5 °C min^{-1}) onset: 58 °C (endothermic), 113 °C (exothermic). **IR** (ATR, cm^{-1}): 3105 (m, ṽ tetrazole C–H), 2995 (w), 2962 (vw), 1892 (vw), 1823 (vw), 1650 (w, ṽ C═C), 1573 (vw), 1506 (m), 1438 (m), 1421 (m), 1368 (vw), 1347 (w), 1295 (w), 1276 (vw), 1178 (m), 1124 (w), 1096 (s), 1026 (w), 1009 (m), 966 (vs, ṽ ClO_3), 945 (vs), 936 (vs, ṽ ClO_3), 922 (s), 770 (m), 718 (m), 661 (s), 605 (m). **EA**: ($C_{24}H_{36}Cl_2CuN_{24}O_6$, 891.16) calc.: C 32.35, H 4.07, N 37.72%; found: C 32.08, H 4.14, N 37.92%. **BAM impact sensitivity**: 3 J (at grain size 100–500 µm). **BAM friction sensitivity**: 36 N (at grain size 100–500 µm). **ESD**: 600 mJ (at grain size 100–500 µm).

[Cu(DN)$_2$(1-VTZ)$_2$] (17)

According to a recently published protocol by GRUHNE *et al.*,[S38] basic copper(II) carbonate (221 mg, 1.00 mmol, 1.00 equiv.) was dissolved in dinitraminic acid (8 mL) with stirring. After a clear solution was obtained, **1** (384 mg, 4.00 mmol, 4.00 equiv.) was added and the reaction mixture left to crystallize. The solids were filtrated off, washed with cold water (2 mL) and dried in air, yielding the title complex **15** (535 mg, 1.14 mmol, 57%) as blue needles (< 500 µm). **DTA** (5 °C min^{-1}) onset: 115 °C (exothermic). **IR** (ATR, cm^{-1}): 3164 (m, ṽ tetrazole C–H), 3136 (w), 3111 (w), 1657 (m, ṽ C═C), 1564 (s, $\tilde{\nu}_{as}$ NO_2), 1539 (m), 1509 (s), 1485 (s), 1456 (m), 1436 (m), 1376 (w), 1313 (w), 1304 (w), 1278 (w), 1228 (s), 1203 (vs, $\tilde{\nu}_s$ NO_2), 1179 (vs), 1099 (w), 1088 (s), 1044 (s), 1036 (vs), 1029 (vs), 1018 (vs, $\tilde{\nu}_{as}$ N_3), 982 (s), 951 (s), 925 (s), 878 (s), 828 (s), 765 (s), 735 (vs), 699 (m), 679 (w), 663 (s), 628 (s). **EA**: ($C_6H_8CuN_{14}O_8$, 467.77) calc.: C 15.41, H 1.72, N 41.92%; found: C 15.47, H 1.80, N 42.03%. **BAM impact sensitivity**: ≤ 1 J. **Ball drop impact sensitivity**: 28 mJ. **BAM friction sensitivity**: 9 N (at grain size 500–1000 µm). **ESD**: 250 mJ (at grain size 500–1000 µm).

[Cu(DN)$_2$(1-ATZ)$_2$] (18)

According to a literature procedure recently published by GRUHNE *et al.*,[S38] basic copper(II) carbonate (55.3 mg, 0.25 mmol, 1.00 equiv.) and an aqueous solution of HDN (4.00 mL, 0.25 mol L^{-1}, 1.00 mmol, 4.00 equiv.) were stirred mechanically until a clear solution was obtained. Stoichiometric amounts of an ethanolic solution (1 mL) of the ligand 1-ATE (110 mg, 1.00 mmol, 4.00 equiv.) were added under continuous stirring and the

reaction mixture left to crystallize. Dark-blue crystals of target compound **16** were isolated within thirteen days (178 mg, 0.36 mmol, 72%). **DTA** (5 °C min^{-1}) onset: 127 °C (exothermic). **IR** (ATR, cm^{-1}): 3144 (m, ṽ tetrazole C–H), 1647 (vw, ṽ C═C), 1564 (s, $\tilde{\nu}_{as}$ NO_2), 1505 (m), 1456 (w), 1443 (w), 1433 (w), 1417 (w), 1332 (w), 1314 (w), 1272 (w), 1215 (vs, $\tilde{\nu}_{s}$ NO_2), 1185 (s), 1125 (w), 1099 (m), 1014 (vs, $\tilde{\nu}_{as}$ N_3), 988 (s), 951 (s), 943 (m), 913 (m), 897 (w), 829 (m), 771 (s), 763 (s), 740 (s), 714 (m), 654 (m). **EA**: ($C_8H_{12}CuN_{14}O_8$, 495.82) calc.: C 19.38, H 2.44, N 39.55%; found: C 19.20, H 2.45, N 39.75%. **BAM impact sensitivity**: 2 J (at grain size 100–500 µm). **BAM friction sensitivity**: 48 N (at grain size 100–500 µm). **ESD**: 480 mJ (at grain size 100–500 µm).

[Cu(N$_3$)$_2$(1-VTZ)] (19)

Adapting a literature procedure,[S39] a solution of sodium azide (32.5 mg, 0.50 mmol, 2.00 eq.) and 1-vinyltetrazole (24.0 mg, 0.25 mmol, 1.00 eq.) in water (6 mL) was layered with a mixture of water and ethanol (4 mL, 50:50). Subsequently, a layer of copper(II) chloride dihydrate (42.6 mg, 0.25 mmol, 1.00 eq.) in ethanol (6 mL) was added. After several days, small brown, platelet-shaped crystals suitable for X-ray determination could be obtained. An elemental analysis pure isolation was not possible, most likely due to the formation of side species.

[Cu(N$_3$)$_2$(1-ATZ)] (20)

Adapting a literature procedure,[S39] a solution of sodium azide (32.5 mg, 0.50 mmol, 2.00 eq.) and 1-allyltetrazole (165 mg, 1.50 mmol, 6.00 eq.) in water (4 mL) was layered with a mixture of water and ethanol (4 mL, 50:50). Subsequently, a layer of copper(II) acetate monohydrate (49.9 mg, 0.25 mmol, 1.00 eq.) in ethanol (4 mL) was added. Within one day, small brown, platelet-shaped crystals suitable for X-ray determination could be obtained.

General procedure for the preparation of the trinitrophenolate complexes 21–23

Following a literature procedure,[S40] basic copper(II) carbonate (0.50 mmol, 1.00 equiv.) was reacted with an aqueous solution (4 mL) of picric acid (**21**: 458 mg, 2.00 mmol, 4.00 equiv.), styphnic acid (**22a**: 490 mg, 2.00 mmol, 4.00 equiv.; **22b**: 245 mg,

1.00 mmol, 2.00 equiv.) or trinitrophloroglucinol monohydrate (**23**: 558 mg, 2.00 mmol, 4.00 equiv.). The mixtures were heated to 80 °C until complete dissolution. Subsequently stoichiometric amounts of the ligand **1** (**21**, **22a**, **22b**: 192 mg, 2.00 mmol, 4.00 equiv.; **23**: 384 mg, 4.00 mmol, 8.00 equiv.) in water (2 ml) were added. Stirring was continued for 5 min and the resulting clear solutions were left for crystallization.

[Cu(PA)$_2$(1-VTZ)$_2$] (21)

Green needles of complex **21**, suitable for single crystal X-ray diffraction were obtained within a day (150 mg, 0.21 mmol, 84%). **DTA** (5 °C min^{-1}) onset: 191 °C (exothermic). **IR** (ATR, cm^{-1}): 3147 (w), 3087 (w), 1649 (w), 1610 (m), 1577 (s), 1536 (s), 1516 (s), 1503 (vs), 1476 (s), 1420 (m), 1378 (m), 1348 (s), 1332 (vs), 1305 (m), 1266 (vs), 1223 (m), 1199 (m), 1168 (s), 1090 (s), 1037 (m), 1006 (w), 988 (w), 942 (s), 927 (s), 914 (m), 868 (w), 852 (w), 826 (w), 782 (m), 743 (m), 732 (w), 718 (s), 704 (s), 669 (s), 625 (m). **EA**: ($C_{18}H_{12}CuN_{14}O_{14}$, 711.92) calc.: C 30.37, H 1.70, N 27.54%; found: C 30.19, H 1.79, N 27.47%. **BAM impact sensitivity**: 10 J. **Ball drop impact sensitivity**: > 200 mJ. **BAM friction sensitivity**: 288 N. **ESD**: 750 mJ (at grain size < 100 µm).

[Cu(HTNR)$_2$(1-VTZ)$_2$] (22a)

After one day, the complex **22a** started to crystallize in the form of green blocks, which were filtered off and dried in air (141 mg, 0.19 mmol, 76%). **DTA** (5 °C min^{-1}) onset: 184 °C (exothermic). **IR** (ATR, cm^{-1}): 3126 (w), 3106 (w), 1609 (m), 1564 (s), 1525 (vs), 1488 (s), 1448 (s), 1375 (s), 1284 (vs), 1228 (s), 1200 (s), 1170 (s), 1088 (vs), 1036 (s), 1003 (m), 986 (m), 944 (s), 930 (s), 886 (m), 880 (m), 789 (m), 767 (m), 735 (m), 700 (s), 676 (s), 665 (s), 625 (s). EA: ($C_{18}H_{12}CuN_{14}O_{16}$, 743.92) calc.: C 29.06, H 1.63, N 26.36%; found: C 29.14, H 1.81, N 28.92%. **BAM impact sensitivity**: 2 J. **Ball drop impact sensitivity**: > 200 mJ. **BAM friction sensitivity**: 96 N. **ESD**: 1080 mJ (at grain size 100–500 µm).

[Cu(TNR)(1-VTZ)$_2$] (22b)

Single crystals of ECC **22b**, suitable for X-ray diffraction were obtained in the form of green block after a few days (90 mg, 0.18 mmol, 72%). **DTA** (5 °C min^{-1}) onset: 191 °C (exothermic). **IR** (ATR, cm^{-1}): 3126 (w), 3105 (w), 3068 (vw), 3010 (vw), 2889 (vw), 1647

(w), 1605 (s), 1582 (s), 1558 (m), 1526 (s), 1506 (m), 1486 (s), 1472 (m), 1446 (s), 1435 (s), 1429 (s), 1374 (m), 1349 (w), 1283 (vs), 1230 (vs), 1200 (s), 1167 (s), 1096 (vs), 1059 (m), 1035 (m), 1002 (m), 948 (m), 928 (m), 922 (m), 877 (m), 829 (w), 793 (m), 772 (m), 738 (w), 705 (vs), 675 (s), 619 (s). **EA**: ($C_{12}H_9CuN_{11}O_8$, 498.82) calc.: C 28.89, H 1.82, N 30.89%; found: C 28.98, H 1.50, N 27.11%. **BAM impact sensitivity**: 2 J. **Ball drop impact sensitivity**: 180 mJ. **BAM friction sensitivity**: 144 N. **ESD**: 750 mJ (at grain size < 100 μm).

[Cu(H$_2$TNPG)$_2$(1-VTZ)$_4$] (23)

Resulting from slow evaporation of the solvent at room temperature, complex **23** was obtained after one hour in the form of green needles suitable for X-ray diffraction. (194 mg, 0.20 mmol, 80%). **DTA** (5 °C min^{-1}) onset: 158 °C (exothermic). **IR** (ATR, cm^{-1}): 3131 (m), 3110 (w), 3016 (w), 1645 (s), 1568 (s), 1538 (m), 1505 (vs), 1495 (vs), 1489 (vs), 1435 (m), 1411 (m), 1332 (s), 1312 (s), 1210 (s), 1179 (vs), 1159 (vs), 1137 (s), 1091 (vs), 1055 (m), 1038 (m), 999 (s), 985 (m), 950 (s), 938 (s), 928 (s), 917 (s), 886 (s), 834 (s), 818 (s), 785 (s), 761 (s), 725 (vs), 694 (vs), 676 (vs), 660 (s), 624 (vs). **EA**: ($C_{24}H_{20}CuN_{22}O_{18}$, 968.11) calc.: C 29.78, H 2.08, N 31.83%; found: C 29.57, H 2.06, N 31.78%. **BAM impact sensitivity**: 3 J. **Ball drop impact sensitivity**: > 200 mJ. **BAM friction sensitivity**: 84 N. **ESD**: 1080 mJ (at grain size > 1000 μm).

4.6.13 References

[S1] P. N. Gaponik, V. P. Karavai, Y. V. Grigorev, *Khim. Geterotsikl. Soedin.* **1985**, 1521–1524.

[S2] Y. V. Grigoriev, S. V. Voitekhovich, V. P. Karavai, O. A. Ivashkevich, *Chem. Heterocycl. Compd.* **2017**, *53*, 670–681.

[S3] V. A. Ostrovskii, G. I. Koldobskii, R. E. Trifonov in *Other five-membered rings with three or more heteroatoms, and their fused carbocyclic derivatives*, *Vol. 6* (Eds.: A. R. Katritzky, E. F. V. Scriven, C. A. Ramsden, R. J. K. Taylor), Elsevier, Amsterdam, **2008**, pp. 257–423.

[S4] S. V. Voitekhovich, O. A. Ivashkevich, P. N. Gaponik, *Russ J Org Chem* **2013**, *49*, 635–654.

[S5] A. Sebris, M. Turks, *Chem. Heterocycl. Compd.* **2019**, *55*, 1041–1043.

[S6] *CrysAlisPRO (Version 171.33.41)*, Oxford Diffraction Ltd., Abingdon, U.K., **2009**.

[S7] A. Altomare, G. Cascarano, C. Giacovazzo, A. Guagliardi, *J. Appl. Cryst.* **1993**, *26*, 343–350.

[S8] A. Altomare, G. Cascarano, A. Giacovazzo, A. Guagliardi, A. G. G. Moliterni, M. C. Burla, G. Polidori, M. Camalli, R. Spagna, *SIR97*, Italy, **1997**.

[S9] A. Altomare, M. C. Burla, M. Camalli, G. L. Cascarano, C. Giacovazzo, A. Guagliardi, A. G. G. Moliterni, G. Polidori, R. Spagna, *J. Appl. Cryst.* **1999**, *32*, 115–119.

[S10] G. M. Sheldrick, *SHELXL-97*, University of Göttingen, Germany, **1997**.

[S11] G. M. Sheldrick, *Acta Crystallogr., Sect. A* **2008**, *64*, 112–122.

[S12] G. M. Sheldrick, *Acta Crystallogr., Sect. A* **2015**, *71*, 3–8.

[S13] L. J. Farrugia, *J. Appl. Cryst.* **2012**, *45*, 849–854.

[S14] O. V. Dolomanov, L. J. Bourhis, R. J. Gildea, J. A. K. Howard, H. Puschmann, *J. Appl. Cryst.* **2009**, *42*, 339–341.

[S15] A. L. Spek, *PLATON*, Utrecht University, Utrecht, The Netherlands, **1999**.

[S16] *SCALE3 ABSPACK*, Oxford Diffraction Ltd., Abingdon, U.K., **2005**.

[S17] *APEX3*, Bruker AXS Inc., Madison, Wisconsin, USA.

[S18] N. He, Y. Ni, J. Teng, H. Li, L. Yao, P. Zhao, *Spectrochim. Acta, Part A* **2019**, *221*, 117164.

[S19] K. Nosratzadegan, M. Mahdavi, K. Ghani, K. Barati, *Propellants, Explos., Pyrotech.* **2019**, *44*, 830–836.

[S20] G. Socrates, *Infrared and Raman Characteristic Group Frequencies*. *Tables and Charts*, John Wiley & Sons, Chichester, **2004**.

[S21] H.-G. Ang, W. Fraenk, K. Karaghiosoff, T. M. Klapötke, P. Mayer, H. Nöth, J. Sprott, M. Warchhold, *Z. Anorg. Allg. Chem.* **2002**, *628*, 2894–2900.

[S22] NATO, *Standardization Agreement (STANAG)*. *explosives, impact sensitivity tests*, **1999**.

[S23] WIWEB, *Standardarbeitsanweisung 4–5.1.02*. *Ermittlung der Explosionsgefährlichkeit, hier der Schlagempfindlichkeit mit dem Fallhammer*, **2002**.

[S24] OZM, can be found under https://www.ozm.cz/, **2022**.

[S25] BAM, can be found under https://www.bam.de/, **2022**.

[S26] DOD, *Military Standard 1751A (MIL-STD-1751A). safety and performance tests for the qualification of explosives (high explosives, propellants, and pyrotechnics)*, **2001**.

[S27] NATO, *Standardization Agreement (STANAG). explosives, friction sensitivity tests*, **2009**.

[S28] WIWEB, *Standardarbeitsanweisung 4–5.1.03. Ermittlung der Explosionsgefährlichkeit oder der Reibeempfindlichkeit mit dem Reibeapparat*, **2002**.

[S29] *Recommendations on the Transport of Dangerous Goods. Model Regulations*. ST/SG/AC.10/1/Rev.22, United Nations Publication, New York, Geneva, **2021**.

[S30] *Manual of Tests and Criteria*, United Nations Publication, New York, Geneva, **2019**.

[S31] A. F. Stassen, M. Grunert, E. Dova, M. Müller, P. Weinberger, G. Wiesinger, H. Schenk, W. Linert, J. G. Haasnoot, J. Reedijk, *Eur. J. Inorg. Chem.* **2003**, 2273–2282.

[S32] A. F. Stassen, E. Dova, R. Ensling, H. Schenk, P. Gutlich, J. G. Haasnoot, J. Reedijk, *Inorg. Chim. Acta* **2002**, *335*, 61–68.

[S33] C. M. Grunert, P. Weinberger, J. Schweifer, C. Hampel, A. F. Stassen, K. Mereiter, W. Linert, *J. Mol. Struct.* **2005**, *733*, 41–52.

[S34] P. N. Gaponik, V. P. Karavai, *Chem. Heterocycl. Compd.* **1985**, *21*, 1172–1174.

[S35] N. I. Sushko, N. I. Makarevich, N. A. Matveeva, O. A. Ivashkevich, P. N. Gaponik, *J. Appl. Spectrosc.* **1991**, *54*, 549–558.

[S36] R. A. Bunce, *ARKIVOC* **2020**, 400–436.

[S37] M. H. H. Wurzenberger, N. Szimhardt, J. Stierstorfer, *J. Am. Chem. Soc.* **2018**, *140*, 3206–3209.

[S38] M. S. Gruhne, M. H. H. Wurzenberger, M. Lommel, J. Stierstorfer, *Chem. –Eur. J.* **2021**, *27*, 9112–9123.

[S39] M. H. H. Wurzenberger, M. Lommel, M. S. Gruhne, N. Szimhardt, J. Stierstorfer, *Angew. Chem. Int. Ed.* **2020**, *59*, 12367–12370.

[S40] M. H. H. Wurzenberger, B. R. G. Bissinger, M. Lommel, M. S. Gruhne, N. Szimhardt, J. Stierstorfer, *New J. Chem.* **2019**, *43*, 18193–18202.

5 Application of 1- and 2-Propargyltetrazole in Laser-Ignitable Energetic Coordination Compounds

Simon M. J. Endraß, Thomas M. Klapötke, Jasmin T. Lechner and Jörg Stierstorfer

published in *FirePhysChem,* **2023**

DOI: 10.1016/j.fpc.2023.03.005

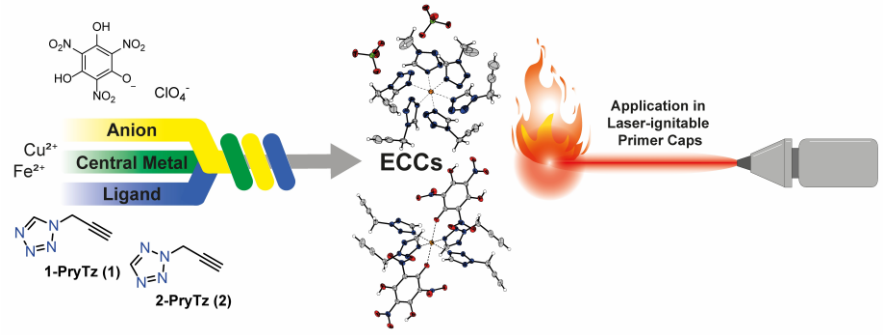

Abstract: 1- and 2-Propargyl-tetrazole (1- and 2-PryTz) were synthesized by reaction of propargyl bromide with sodium tetrazolate and used as ligands in energetic coordination compounds (ECCs) and evaluated concerning their thermal and mechanical sensitivities. Furthermore, the two nitrogen-rich compounds 1-((1*H*-1,2,3-triazol-4-yl)methyl)-1*H*-tetrazole (TriMT, **3**) and 1-((1-(2-(1*H*-tetrazol-1-yl)ethyl)-1*H*-1,2,3-triazol-4-yl)methyl)-1*H*-tetrazole (TriMTET, **4**) were prepared. Both were characterized by IR spectroscopy, NMR measurements, and low-temperature X-Ray diffraction analysis. Due to the highly endothermic enthalpy of formation of the propargyl-tetrazole ligands, powerful, yet relatively safe to handle, laser-ignitable ECCs were obtained.

5.1 Introduction

Coordination compounds have gained interest within multiple fields such as anti-cancer drugs [1, 2], hypergolic propellants [3-6], catalysts [7], and chemical sensors [8] but also as potential replacement candidates for the very commonly used, but highly toxic primary explosives lead azide (LA) and lead styphnate (LS) [9, 10]. One structural motif which can be found among these classes of applications is the tetrazole ring. [11, 12] While in the case of drug candidates, the interest is a result of the very specific biological activity of differently substituted tetrazoles [13-15], the favorability of tetrazoles for energetic coordination compounds (ECCs) can be explained by their endothermicity and potential for modification which seems to result in fast deflagration to detonation transitions (DDT) [16, 17]. In this field, the interesting application as ligands in laser ignitable primary explosives arose and multiple publications proved the feasibility of the concept with various compounds. [17-22] Figure 1 shows the calculated heat of formation (HOF) of the gas phase of several 1*N*-substituted tetrazoles. As the figure indicates, the enthalpy of formation is raised not only by shortening the chain length, or introducing an azide residue, but also by formal oxidation of carbon-carbon bonds. Especially the comparison between 1-propyl-, 1-allyl-, and 1-propargyl-tetrazole shows the strong increase of the endothermicity that is accompanied by the unsaturated side-chain, which is also one reason for its consideration as a ligand within hypergolic mixtures, that were reported in the literature. [23] The enthalpies of formation of 1- and 2-PryTz can therefore compete with compounds such as 1-amino-tetrazole, 1-azidoethyl-tetrazole, and 1-azidomethyl-tetrazole, which all possess nitrogen contents of above 70 % and are known to be applicable in ECCs which are laser

ignitable and initiate compressed PETN. [16, 20, 24] This makes propargyl bromide an interesting alkylation agent for the synthesis of N-heterocycles with a positive HOF.

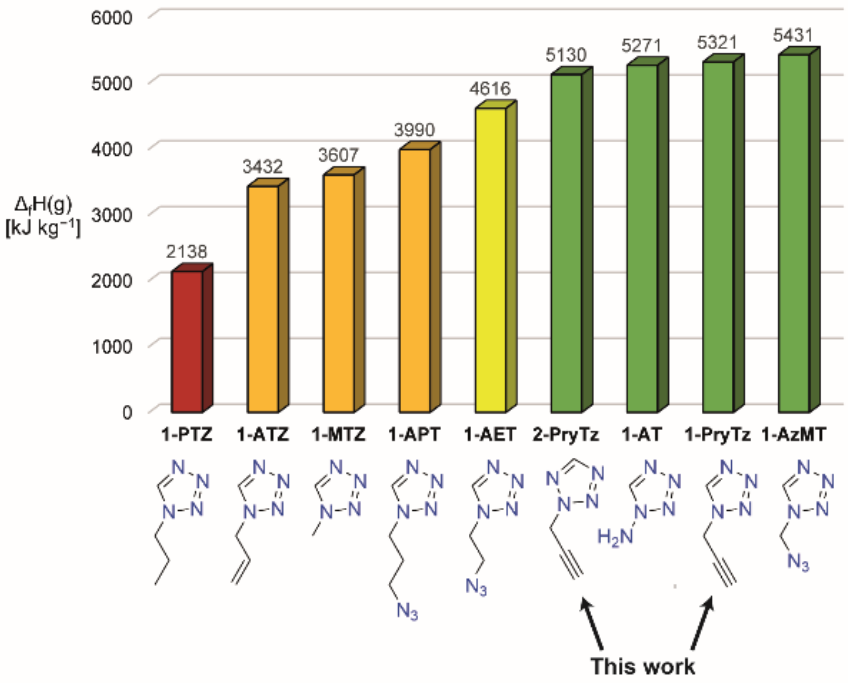

Figure 1. Comparison of some selected compounds concerning their calculated (CBS-4M and atomization method) gas phase enthalpies of formation. [20, 24-26]

In this work ECCs with 1- and 2-propargyl-tetrazole ligands, as well as further nitrogen-rich compounds which are derived from the propargyl-unit are synthesized and described. Hereby an insight in the potential of unsaturated bonds for the formation of ECCs is generated, by elaborating their sensitivities, structures and applicability in laser initiation setups.

5.2 Results and Discussion

5.2.1 Synthesis

As depicted in Scheme 1, 1- and 2-propargyl-tetrazole (1-PryTz, **1** and 2-PryTz, **2**) were prepared according to a modified literature procedure by alkylation of sodium tetrazolate with propargyl bromide. [27] It should be noted, that **1** can be accessed by direct ring closure on prop-2-yn-1-amine hydrochloride. [28] Also, two other nitrogen-rich compounds were synthesized. By applying the Banert-cascade and further tetrazole ring closure, it was possible to yield 1-((1*H*-1,2,3-triazol-4-yl)methyl)-1*H*-tetrazole (TriMT, **3**). [29, 30] In addition, 1-PryTz was

further reacted with 1-(azidoethyl)-tetrazole in a copper(I)-catalyzed cycloaddition with water as reaction medium to form 1-((1-(2-(1*H*-tetrazol-1-yl)ethyl)-1*H*-1,2,3-triazol-4-yl)-methyl)-1*H*-tetrazole (TriMTET, **4**). [31]

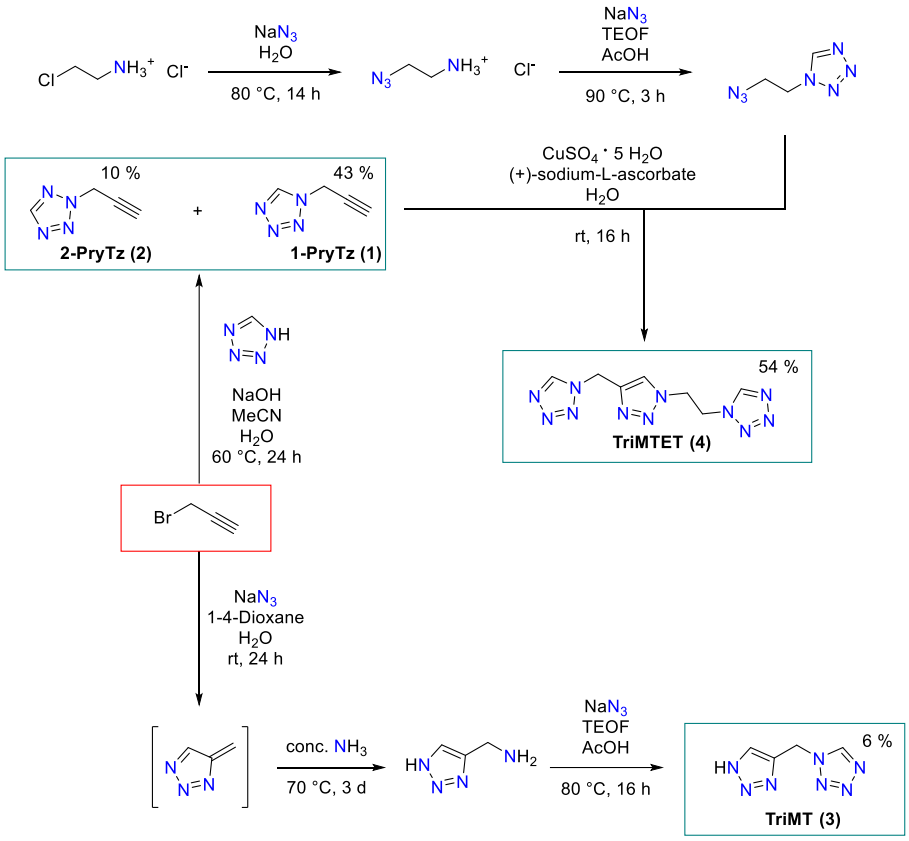

Scheme 1. Reaction pathways for the formation of propargyl bromide-based compounds **1–4**. [20, 29-31]

1-PryTz was used as a ligand to create three perchlorate complexes, and one copper(II) dicyanamide complex. As seen in Scheme 2 $[Cu(1\text{-}PryTz)_6](ClO_4)_2$ (**5**) and $[Cu(DCA)_2(1\text{-}PryTz)_2]$ (**17**) were obtained without further crystal water, while $[Fe(1\text{-}PryTz)_6](ClO_4)_2 \cdot H_2O$ (**6**) and $[Zn(1\text{-}PryTz)_6](ClO_4)_2 \cdot H_2O$ (**7**) both contain one water per unit. In addition, the silver salt Ag(1-PryTz) was produced by applying a modified literature procedure for silver acetylides. [32] Apart from elemental analysis, differential thermal analysis and IR spectrometry, this compound was not further investigated due to its rapid decomposition, even under exclusion of light at room temperature.

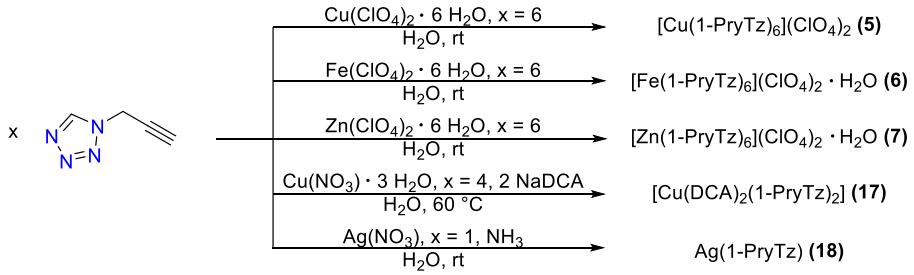

Scheme 2. Synthesis of coordination compounds **5**, **6**, **7**, **17** and **18**.

The structures of all coordinating anions are given in Scheme 3. These anions were obtained by deprotonation of the respective neutral compounds (H_3TNPG: trinitrophloro-glucinol, H_2TNR: styphnic acid, HPA: picric acid, HTNO: trinitro-orcinol), or as in **17** by utilization of sodium dicyanamide.

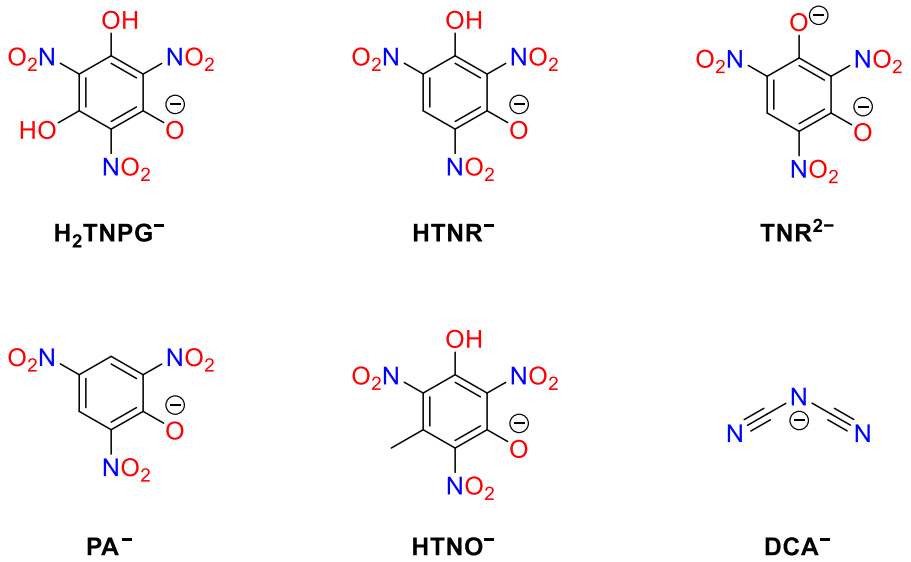

Scheme 3. Structures of the coordinating anions, which were used for the complexation of 1- and 2-propargyl-tetrazole.

Scheme 4 shows the ECCs with nitroaromatic anions that were created by treating the respective nitroaromatic compound with basic copper carbonate. 1-PryTz was then added to the resulting aqueous solutions. After cooling to room temperature all compounds crystallized within days, except for compound **10**, which precipitated immediately upon cooling.

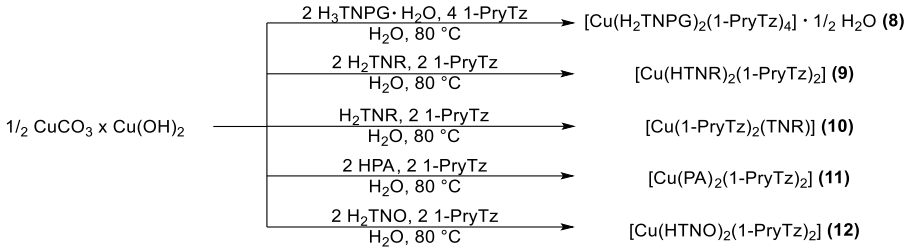

Scheme 4. Synthesis of the ECCs **8**–**12**, which carry the 1-PryTz ligand and a nitroaromatic anion.

As seen in Scheme 5, a similar approach was used for compounds **13**–**16**, which carry the 2-PryTz ligand. However, due to its lower polarity, a mixture of water and ethanol (3:2) was selected as the suitable solvent mixture.

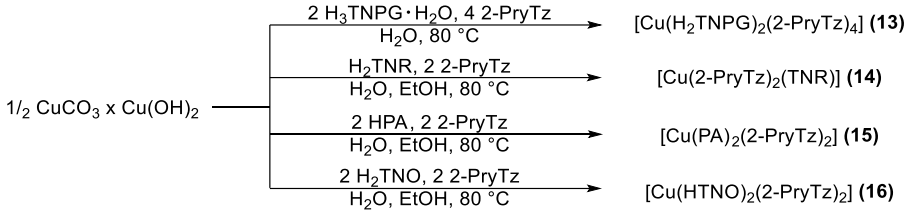

Scheme 5. Synthesis of the ECCs **13–16**, which carry the 2-PryTz ligand and a nitroaromatic anion.

All compounds, except for 1-PryTz, which was obtained with minor impurities, that did not influence the formation of the ECCs and was therefore not considered relevant for further reactions, were obtained clean according to elemental analysis. In summary, the two nitrogen-rich compounds TriMT and TriMTET, one silver(I) propargylide, as well as 13 energetic coordination compounds that carry the ligands 1- and 2-PryTz were produced. Attempts to generate ECCs of **3** and **4** were not successful as they precipitated or crystallized again without coordinative behavior.

5.2.2 Energetic Properties of 1–4

Compounds **1**–**4** were characterized concerning their enthalpy of formation by applying the atomization method from each room temperature CBS-4M enthalpy. This was used to calculate the energetic properties of the respective compounds with EXPLO5 program code. [33] Selected output parameters of the calculations are shown in Table 1. The results of the CBS-4M calculations are given in the Supporting Information. The thermal stabilities of compounds **1**–**4** compete with those of very stable tetrazoles such as 1,1-ditetrazolyl-propane (205 °C) and 1-

amino-5-methyltetrazole (190 °C), which are insensitive toward mechanical stimuli, just as TriMT and TriMTET. [19, 34] As reported for other tetrazoles, the 2-isomer shows a significantly higher impact sensitivity than the 1-isomer. [35, 36]

Table 1. Physicochemical properties of compounds **1–4**.

	1-PryTz	2-PryTz	TriMT	TriMTET
Formula	$C_4H_4N_4$	$C_4H_4N_4$	$C_4H_5N_7$	$C_7H_9N_{11}$
M [g mol^{-1}]	108.10	108.10	151.13	247.23
IS [J][a]	20	<1	>40	>40
FS [N][b]	>360	>360	>360	>360
ESD [J][c]	-	-	>1.5	1.0
T_{endo}/T_{exo}	-/187	195/195	131/192	101/194
ρ [g cm^{-3}]	1.22[d]	1.17[d]	1.54[e]	1.47[e]
N [%][f]	51.83	51.83	64.88	62.32
$\Delta_f H°$ [kJ mol^{-1}][g]	533.8	512.6	493.7	819.1
Explo5 V6.05.04				
$-\Delta_{Ex}U$ [kJ kg^{-1}][h]	4831	4630	3266	3347
$T_{det.}$ [K][i]	2959	2888	2332	2333
V_0 [L kg^{-1}][j]	677	683	734	732
P_{CJ} [kbar][k]	104	90	165	146
$V_{det.}$ [m s^{-1}][l]	6095	5774	7124	6816

[a] Impact sensitivity (BAM drophammer (1 of 6)). [b] Friction sensitivity (BAM friction tester (1 of 6)). [c] Electrostatic discharge devise (OZM XSpark10). [d] Pycnometrically determined [e] From X-Ray diffraction analysis recalculated to 298 K. [f] Nitrogen content. [g] Enthalpy of formation. [h] Energy of explosion. [i] Detonation temperature. [j] Volume of detonation products (assuming only gaseous products). [k] Detonation pressure at the *Chapman–Jouguet* point. [l] Detonation velocity.

5.2.3 Crystal Structures

Compounds **3**–**5**, **8**, **9**, and **11**–**17** were analyzed by low temperature X-ray diffraction. The data, measurement and refinement parameters are given in the Supporting Information Tables S1–4. The thermal ellipsoids of non-hydrogen atoms in all structures are set to the 50 % probability level. Measurement and refinement data sets were uploaded to the CSD database (CCDC 2241739 (**3**), 2241731 (**4**), 2241732 (**5**), 2241736 (**8**), 2241730 (**9**), 2241737 (**11**), 2241735 (**12**), 2241733 (**13**), 2241738 (**14**), 2241813 (**15**), 2241814 (**16**), 2241734 (**17**)). TriMT (Figure 2a) crystallized in the orthorhombic space group *Pbca* with a density of 1.59 g cm^{-3} at 99 K and eight formula units per unit cell. TriMTET (Figure 2b) crystallized in the monoclinic space group *Pn* in the form of colorless rods. The compound showed a density of 1.49 g cm^{-3} at 173 K and six formula units per unit cell. The single crystals of both compounds were obtained by crystallization from water.

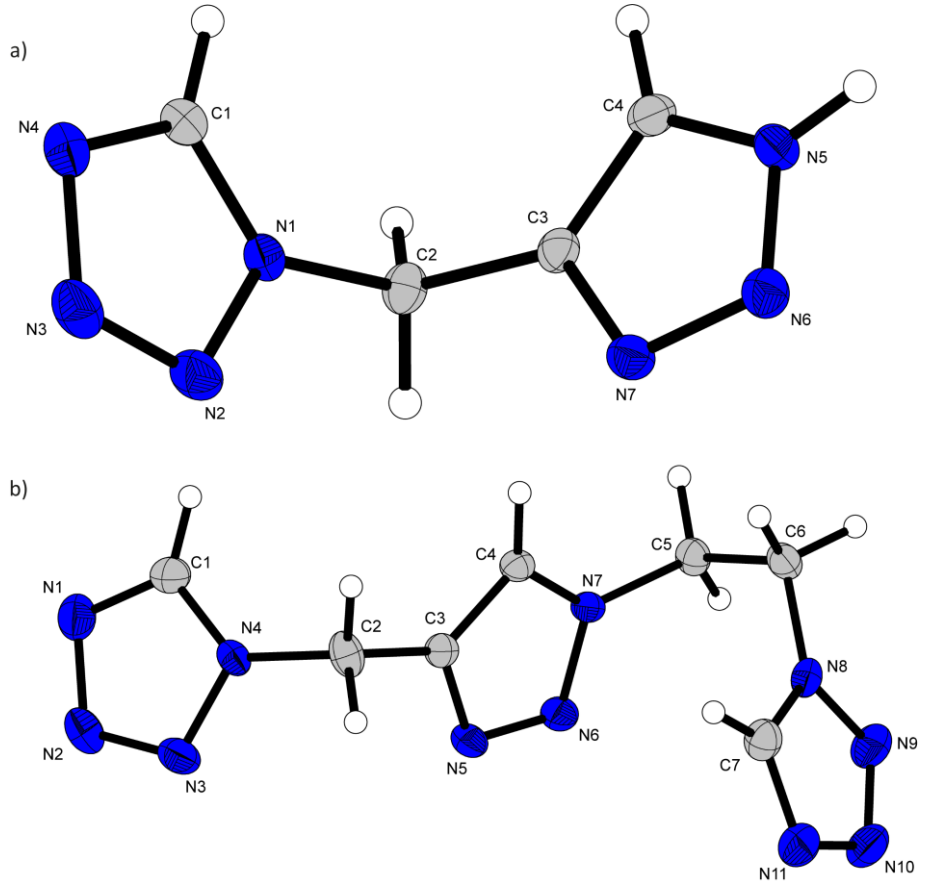

Figure 2a) Crystal structure of compound **3**. Selected bond lengths [Å]: N1–N2 1.3470(18), N7–C3 1.3650(18), N1–C1 1.3338(19), C2–C3 1.4939(19), N1–C2 1.4676(18), C3–C4 1.374(2), N2–N3 1.301(2), N5–H5 0.872(19), N3–N4 1.3627(19), N4–C1 1.316(2), N5–N6 1.3422(19), N5–C4 1.3376(19), N6–N7 1.3203(17); Selected bond angles [°]: N1–C2–C3 112.13(11), C1–N1–C2 130.33(13), C2–C3–C4 129.58(13), N2–N1–C2 121.28(12), N7–C3–C2 121.83(13). **b)** Crystal structure of compound **4**. Selected s bond lengths [Å]: N1–N2 1.357(4), N1–C1 1.304(5), N2–N3 1.299(4), N3–N4 1.339(4), N4–C1 1.327(4), N5–N6 1.315(4), N6–N7 1.348(3), N4–C2 1.478(4), N7–C5 1.457(4), N8–C6 1.456(4), N9–N10 1.296(5), N10–N11 1.366(4); Selected bond angles [°]: N4–C2–C3 112.6(2), N7–C5–C6 110.2(2), N8–C6–C5 110.7(2).

Figure 3 shows the coordination sphere of $[Cu(1\text{-PryTz})_6](ClO_4)_2$. The compound crystallized in the monoclinic space group $P2_1/n$ with a calculated density of 1.52 g cm^{-3} at 173 K and four formula units per unit cell. The crystal structure shows the expected *Jahn-Teller* distortion which is expected for the d^9-Cu^{2+} coordination center, which leads to the coordination in form of an elongated octahedron.

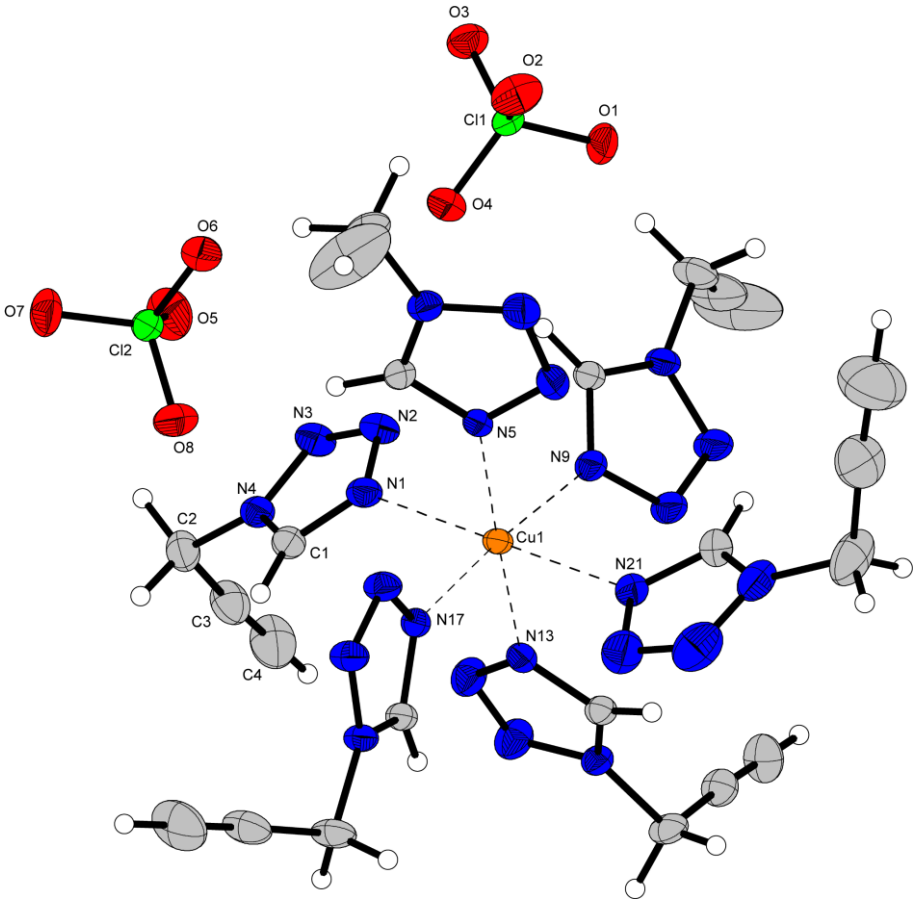

Figure 3. Molecular structure of compound **5** determined by XRD. Selected bond lengths [Å]: Cu1–N1 2.364(2), Cu1–N5 2.025(2), Cu1–N9 2.028(2), Cu1–N13 2.036(2), Cu1–N17 2.0283(19), Cu1–N21 2.417(2); Selected bond angles [°]: N1–Cu1–N5 88.74(8), N1–Cu1–N9 91.59(8), N1–Cu1–N13 91.38(8), N1–Cu1–N17 93.71(7), N1–Cu1–N21 178.22(7), N5–Cu1–N9 89.63(8), N5–Cu1–N13 177.72(8), N5–Cu1–N17 91.22(8), N5–Cu1–N21 89.92(8), N9–Cu1–N13 88.09(8), N9–Cu1–N17 174.65(8), N9–Cu1–N21 89.56(8), N13–Cu1–N17 91.05(8), N13–Cu1–N21 90.02(8), N17–Cu1–N21 85.15(7).

Figure 4 shows the crystal structures of compounds **8**, **9** and **12**, which carry nonbridging nitroaromatic anions. Compounds **8** and **12** crystallized in the monoclinic space group $P2_1/n$, while **9** crystallized in the triclinic space group $P\bar{1}$ (one formula unit). The three compounds show densities of 1.71–1.82 g cm^{-3} within the temperature ranges of their measurements (99–112 K) and coordination as expected for the nitrophenolato complexes. While in the case of **8** four 1-PryTz ligands are arranged around the copper(II) center in the *xy* plane, the z^2-axis is occupied by the trinitrophloroglucinate anions.

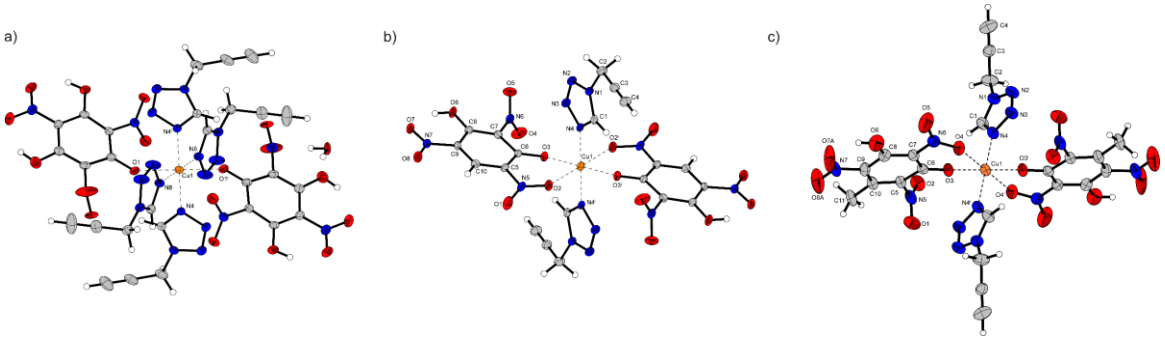

Figure 4a) Crystal structure of compound **8** including the crystal water. Selected bond lengths [Å]: Cu1–O1 2.3186(18), Cu1–N4 2.0257(19), Cu1–N8 2.011(2); Selected bond angles [°]: O1–Cu1–N4 81.95(7), O1–Cu1–N8 89.97(7); Symmetry codes: (i) 1−x, 1−y, 1−z. **b)** Crystal structure of compound **9**. Selected bond lengths [Å]: Cu1–O2 2.311(2), Cu1–O3 1.939(2), Cu1–N4 2.013(3); Selected bond angles [°]: O2–Cu1–O3 82.22(9), O2–Cu1–N4 89.54(11); Symmetry codes: (i) 2−x, 1−y, 1−z. **c)** Crystal structure of compound **12**. Selected bond lengths [Å]: Cu1–O3 1.941(3), Cu1–O4 2.313(3), Cu1–N4 1.996(3); Selected bond angles [°]: O3–Cu1–O4 79.95(11), O–Cu1–N4 88.12(14); Symmetry codes: (i) 1−x, 2−y, 1−z.

Unlike in the case of **8**, compounds **9** and **12** carry only two 1-PryTz ligands per copper(II) center. In both cases, those two ligands share the *xy* plane with the deprotonated hydroxy group, while their z^2-axes are occupied by the coordinating nitro groups of the respective anion. As described in earlier publication, the coordinating nitro groups differs concerning the position on the ring. [37] While the $HTNR^-$ anion prefers coordination *via* the nitro group *ortho* to the ring proton, the $HTNO^-$ anion preferably coordinates by the *para*-NO_2. Figure 5 shows the crystal structures of the metal-organic-frameworks **14** and **17**. Both compounds crystallized in the monoclinic space group $P2_1/c$. In the case of **14** (a), the alternating orientation and tilt of the styphnate anions leads to a 1D polymeric coordination chain in which each styphnate bridges two copper(II) centers. The outer edges of the chain are then blocked by the coordinating 2-PryTz ligands. Meanwhile, the bridging behavior of the dicyanamide anion in compound **17** (b), which coordinates via the central and one terminal nitrogen atom, leads to the formation of a 2D polymeric structure, in which the faces of the layer are occupied by the 1-PryTz ligands.

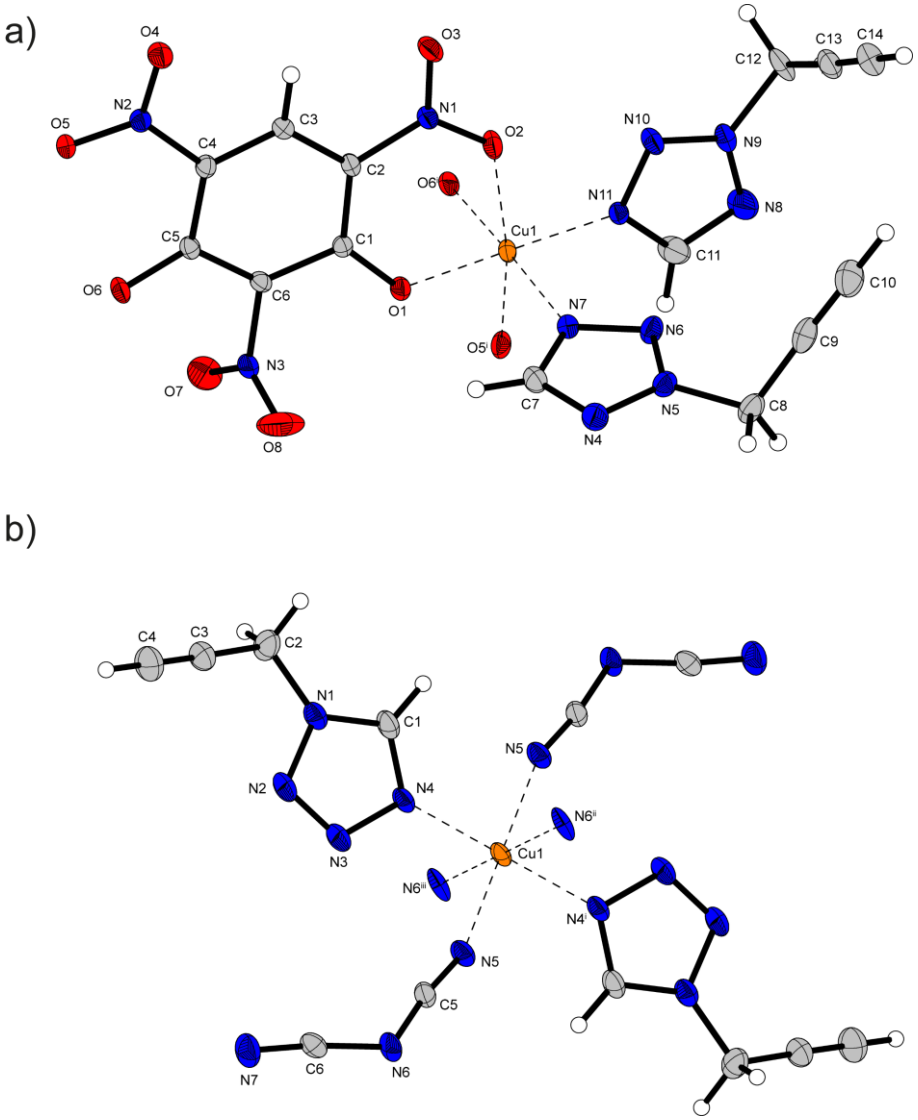

Figure 5a) Crystal structure of compound **14**. Selected bond lengths [Å]: Cu1–O1 1.9350(16), Cu1–O2 2.2053(17), Cu1–N7 2.0298(18), Cu1–N11 1.9947(19), Cu1–O5^{i} 2.2798(17), Cu1–O6^{i} 1.9768(17); Selected bond angles [°]: O1–Cu1–O2 84.57(6), O1–Cu1–N7 88.58(7), O1–Cu1–N11 178.54(7), O1–Cu1–O5^{i} 92.71(6), O1–Cu1–O6^{i} 91.86(7), O2–Cu1–N7 95.65(7), O2–Cu1–N11 95.05(7), O2–Cu1–O5^{i} 167.13(6), O2–Cu1–O6^{i} 88.39(7); Symmetry codes: (i) −x, 1/2+y, 1/2−z. **b)** Crystal structure of compound **17**. Selected bond lengths [Å]: Cu1–N4 2.023(2), Cu1–N5 1.954(3), Cu1–N6^{ii} 2.458(2); Selected bond angles [°]: N4–Cu1–N5 89.89(11), N4–Cu1–N6^{ii} 92.94(9), N5–Cu1–N6^{ii} 89.87(9); Symmetry codes: (i) 2−x, −y, 1−z, (ii) 2−x, 1/2+y, 1/2−z, (iii) x, −1/2−y, 1/2+z.

5.2.4 Physicochemical Properties

All compounds were examined concerning their thermal stability by differential thermal analysis (DTA) within a range of 25–400 °C at a heating rate of 5 °C min^{-1}. In cases, where endothermic events were observed, further investigation by thermogravimetric analysis (TGA) was carried out in a range of 30–400 °C and additionally characterized as melting of the

samples with a BÜCHI Melting Point B-540 instrument. While the gathered exothermal signals of the DTA measurements, which can be found in Table 2 indicate a stabilizing effect, of the nitroaromatic anions compared to **5** (T_{exo}: 135 °C), only [Cu(HTNR)$_2$(1-PryTz)$_2$] (T_{exo}: 172 °C) and [Cu(HTNO)$_2$(1-PryTz)$_2$] (T_{exo}: 177 °C) exceed the thermal stabilities of the iron(II) (T_{exo}: 168 °C) and zink(II) perchlorate (T_{exo}: 164 °C) complexes of **1**. This might be explained by a stabilizing effect of the water, which is still contained in compounds **6** and **7**. In the case of compound **2** no evaluation by TGA was possible due to rapid mass loss already at low temperatures, which can most likely be explained by a high vapor pressure of the liquid 2-PryTz. All plots of the measurements can be found in the Supporting Information.

Table 2. Thermal stability and sensitivities to mechanical and electrical stimuli of compounds **5–17**.

Compound	No.	T_{endo}[a] [°C]	T_{exo}[b] [°C]	IS[c] [J]	FS[d] [N]	ESD[e] [mJ]	HP[f]	HN[g]
[Cu(1-PryTz)$_6$](ClO$_4$)$_2$	**5**	79	135	2	5	25	def.	det.
[Fe(1-PryTz)$_6$](ClO$_4$)$_2$ · H$_2$O	**6**	74	168	2	6	50	def.	det.
[Zn(1-PryTz)$_6$](ClO$_4$)$_2$ · H$_2$O	**7**	70	164	2	15	50	def.	def.
[Cu(H$_2$TNPG)$_2$(1-PryTz)$_4$] · ½ H$_2$O	**8**	-	145	<1	80	160	def.	dec.
[Cu(HTNR)$_2$(1-PryTz)$_2$]	**9**	-	172	<1	96	160	def.	dec.
[Cu(1-PryTz)$_2$(TNR)]	**10**	-	150	<1	40	250	det.	det.
[Cu(PA)$_2$(1-PryTz)$_2$]	**11**	86	157	2	160	250	dec.	dec.
[Cu(HTNO)$_2$(1-PryTz)$_2$]	**12**	-	177	<1	120	90	def.	def.
[Cu(H$_2$TNPG)$_2$(2-PryTz)$_4$]	**13**	123[h]	123[h]	<1	40	250	def.	dec.
[Cu(2-PryTz)$_2$(TNR)]	**14**	-	150	<1	48	200	def.	det.
[Cu(PA)$_2$(2-PryTz)$_2$]	**15**	-	142	2	120	160	def.	dec.
[Cu(HTNO)$_2$(2-PryTz)$_2$]	**16**	-	164	<1	72	200	def.	dec.
[Cu(DCA)$_2$(1-PryTz)$_2$]	**17**	-	120	4	>360	90	dec.	dec.
Ag(1-PryTz)	**18**	-	124	-	-	-	-	-
LA (RD-1333) [10, 38, 39]		-	320–350	4	≤0.1	0.007–5	det.	det.

[a] Onset temperature of endothermic event in the DTA (heating rate of 5 °C min^{-1}), indicating a melting point of the compound. [b] Onset of exothermic event in the DTA. [c] Impact sensitivity (BAM drophammer (1 of 6)). [d] Friction sensitivity (BAM friction tester (1 of 6)). [e] Electrostatic discharge devise (OZM XSpark10). [f] Hot plate test (det.: detonation, def.: deflagration, dec.: decomposition). [g] Hot needle test (det.: detonation, def.: deflagration, dec.: decomposition). [h] endo-to-exo-transition.

Except for compound **1**, which is classified as *sensitive*, compounds **3** and **4**, which were determined to be *insensitive*, and compound **18** which was not investigated due to its rapid decomposition, all other compounds of this work have to be described as *very sensitive* toward impact in the sense of the "UN Recommendations on the Transport of Dangerous Goods". [40] According to this, compounds **1**–**4** and **17** are considered *insensitive*, **9**, **11**, **12** and **15** are *sensitive*, **7**, **8**, **10**, **13**, and **16** are *very sensitive* and only compounds **5** and **6** are *extremely sensitive* toward friction.

The observed sensitivities of $[Fe(1\text{-}PryTz)_6](ClO_4)_2 \cdot H_2O$ are especially surprising, since $[Fe(1\text{-}PryTz)_6](ClO_4)_2$ was earlier reported in the literature as insensitive to impact energies up to 14.7 J. [41] In direct comparison with lead azide, all ECCs were less sensitive toward friction and electrostatic discharge. Furthermore, the ECCs were tested concerning their reaction towards rapid heating under open and slight contained conditions. By performing the hot plate and hot needle test, a first estimation of whether or not a substance undergoes a deflagration-to-detonation transition (DDT) is possible. The results are summarized in Table 2. A rapid detonation was observed under the circumstances of the hot needle test for compounds **5**, **6**, **10** and **14**. These compounds were therefore tested in initiation experiments for their capability to ignite 200 mg of compressed PETN (grain size <100 μm) within a copper shell. Unfortunately, none of the four compounds were able to initiate the PETN samples. Figure 6 shows the output of the laser initiation of compounds **5**, **6** and **13**, which were successfully brought to detonation by irradiation 45 W InGaAs laser diode working in single-pulse mode at a wavelength of 915 nm. The detailed laser conditions of the experiments are summarized in Table 3.

Table 3. Reaction of the produced ECCs (**5**–**17**) toward thermal stimulation as well as initiation and laser ignitability assessment.

Compound	No.	PETN initiation	Laser parameters[a] 7 A, 15 ms	8 A, 15 ms	7 A, 30 ms	8 A, 30 ms	10 A, 30 ms
$[Cu(1\text{-}PryTz)_6](ClO_4)_2$	**5**	Negative	det.	-	-	-	-
$[Fe(1\text{-}PryTz)_6](ClO_4)_2 \cdot H_2O$	**6**	Negative	neg.	det.	-	det.	-
$[Zn(1\text{-}PryTz)_6](ClO_4)_2 \cdot H_2O$	**7**	-	-	-	-	-	-
$[Cu(H_2TNPG)_2(1\text{-}PryTz)_4] \cdot ¼\ H_2O$	**8**	-	-	-	neg.	dec.	dec.
$[Cu(HTNR)_2(1\text{-}PryTz)_2]$	**9**	-	-	-	neg.	dec.	dec.
$[Cu(1\text{-}PryTz)_2(TNR)]$	**10**	Negative	-	-	-	-	neg.
$[Cu(PA)_2(1\text{-}PryTz)_2]$	**11**	-	-	-	-	-	neg.
$[Cu(HTNO)_2(1\text{-}PryTz)_2]$	**12**	-	-	-	-	neg.	dec.
$[Cu(H_2TNPG)_2(2\text{-}PryTz)_4]$	**13**	-	-	-	det.	det.	det.
$[Cu(2\text{-}PryTz)_2(TNR)]$	**14**	Negative	-	-	-	neg.	dec.
$[Cu(PA)_2(2\text{-}PryTz)_2]$	**15**	-	-	-	-	-	neg.
$[Cu(HTNO)_2(2\text{-}PryTz)_2]$	**16**	-	-	-	-	-	neg.
$[Cu(DCA)_2(1\text{-}PryTz)_2]$	**17**	-	-	-	dec.	dec.	dec.

[a] Operating parameters: voltage U = 4 V, current I = 7–10 A pulse length τ = 15–30 ms, theoretical maximal output power P_{max} = 45 W, wavelength λ = 915 nm (det.: detonation, def.: deflagration, dec.: decomposition, neg.: negative).

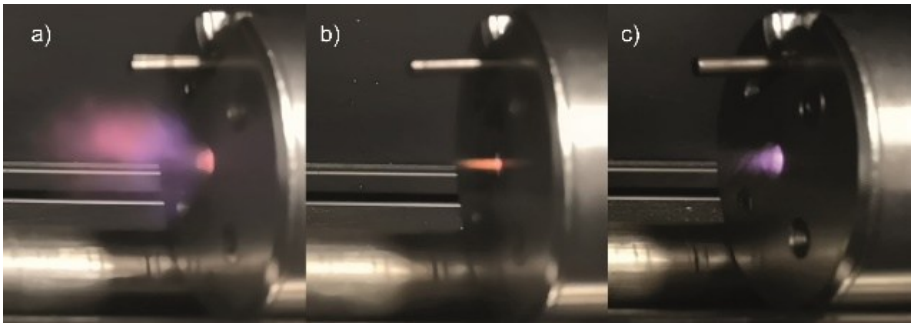

Figure 6. Detonation of **a)** $[Cu(1\text{-}PryTz)_6](ClO_4)_2$, **b)** $[Fe(1\text{-}PryTz)_6](ClO_4)_2 \cdot H_2O$ and **c)** $[Cu(H_2TNPG)_2(2\text{-}PryTz)_4]$ during laser irradiation.

5.3 Conclusion

Alkylation of sodium tetrazolate with propargyl bromide yielded 1- and 2-propargyl-tetrazole. Interestingly, 2-propargyl-tetrazole shows an extremely high sensitivity toward impact and therefore should be handled with caution. Both propargyl-tetrazoles were used for the formation of 13 energetic coordination compounds, which were obtained in moderate to high yields. This includes the perchlorates $[Cu(1\text{-}PryTz)_6](ClO_4)_2$ and $[Fe(1\text{-}PryTz)_6](ClO_4)_2 \cdot H_2O$ as well as $[Cu(H_2TNPG)_2(2\text{-}PryTz)_4]$, which were successfully brought to initiation by laser irradiation. In summary, the benefits of 1-PryTz over 2-PryTz, of its higher enthalpy of formation, better solubility in water, direct accessibility and lower impact sensitivity of the neat ligand prevail.

5.4 Acknowledgement

The Ludwig Maximilian University of Munich (LMU) is gratefully acknowledged for providing financial support for this work. The authors would like to thank Prof. Dr. Konstantin Karaghiosoff and Dr. Burkhard Krumm for NMR spectroscopy and Stefan Huber for sensitivity measurements.

5.5 References

[1] F. Trudu, F. Amato, P. Vaňhara, T. Pivetta, E. M. Peña-Méndez, J. Havel, *J. Appl. Biomed.* **2015**, *13*, 79–103.

[2] A. E. Popova, V. A. Protas, E. R. Trifonov, *Anti-Cancer Agents Med. Chem.* **2017**, *17*, 1856–1868.

[3] Z.-M. Li, Y.-Q. Xu, C. Wang, G.-R. Lei, R. Zhang, L. Zhang, J.-H. Chen, J.-G. Zhang, T.-L. Zhang, Q.-Y. Wang, *J. Mater. Chem. A* **2022**, *10*, 2795–2799.

[4] L. Liang, Y. Zhong, J. Chen, J. Zhang, T. Zhang, Z. Li, *Inorg. Chem.* **2022**.

[5] P. D. McCrary, G. Chatel, S. A. Alaniz, O. A. Cojocaru, P. A. Beasley, L. A. Flores, S. P. Kelley, P. S. Barber, R. D. Rogers, *Energy & Fuels* **2014**, *28*, 3460–3473.

[6] S. V. Khomik, S. V. Usachev, S. P. Medvedev, A. A. Cherepanov, S. V. Stovbun, V. N. Mikhalkin, G. L. Agafonov, *Proc. Combust. Inst.* **2019**, *37*, 3311–3317.

[7] M. Yoon, R. Srirambalaji, K. Kim, *Chem. Rev.* **2012**, *112*, 1196–1231.

[8] S. E. Angell, C. W. Rogers, Y. Zhang, M. O. Wolf, W. E. Jones, *Coord. Chem. Rev.* **2006**, *250*, 1829–1841.

[9] J. W. Fronabarger, M. D. Williams, W. B. Sanborn, J. G. Bragg, D. A. Parrish, M. Bichay, *Propellants, Explos. Pyrotech.* **2011**, *36*, 541–550.

[10] K. D. Oyler, in *Green Energetic Materials*, **2014**, pp. 103–132.

[11] V. A. Ostrovskii, E. A. Popova, R. E. Trifonov, in *Advances in Heterocyclic Chemistry, Vol. 123* (Eds.: E. F. V. Scriven, C. A. Ramsden), Academic Press, **2017**, pp. 1–62.

[12] S.-Q. Wang, Y.-F. Wang, Z. Xu, *Eur. J. Med. Chem.* **2019**, *170*, 225–234.

[13] A. Verma, B. Kaur, S. Venugopal, P. Wadhwa, S. Sahu, P. Kaur, D. Kumar, A. Sharma, *Chem. Biol. Drug Des.* **2022**, *100*, 419–442.

[14] H. A. Soliman, A. Kalmouch, H. M. Awad, N. A. M. Abdel Wahed, *Russ. J. Gen. Chem.* **2018**, *88*, 1726–1733.

[15] L. V. Myznikov, A. Hrabalek, G. I. Koldobskii, *Chem. Heterocycl. Compd.* **2007**, *43*, 1–9.

[16] N. Szimhardt, M. H. H. Wurzenberger, L. Zeisel, M. S. Gruhne, M. Lommel, J. Stierstorfer, *J. Mater. Chem. A* **2018**, *6*, 16257–16272.

[17] M. Kofen, V. Braun, S. M. J. Endraß, T. M. Klapötke, J. Stierstorfer, *Inorg. Chem.* **2022**, *61*, 17212–17225

[18] M. Joas, T. M. Klapötke, N. Szimhardt, *Eur. J. Inorg. Chem.* **2014**, *2014*, 493–498.

[19] N. Szimhardt, M. H. H. Wurzenberger, T. M. Klapötke, J. T. Lechner, H. Reichherzer, C. C. Unger, J. Stierstorfer, *J. Mater. Chem. A* **2018**, *6*, 6565–6577.

[20] M. H. H. Wurzenberger, M. S. Gruhne, M. Lommel, N. Szimhardt, T. M. Klapötke, J. Stierstorfer, *Chem. Asian J.* **2019**, *14*, 2018–2028.

[21] M. H. H. Wurzenberger, M. S. Gruhne, M. Lommel, N. Szimhardt, J. Stierstorfer, *Materials Advances* **2022**, *3*, 579–591.

[22] T. W. Myers, J. A. Bjorgaard, K. E. Brown, D. E. Chavez, S. K. Hanson, R. J. Scharff, S. Tretiak, J. M. Veauthier, *J. Am. Chem. Soc.* **2016**, *138*, 4685–4692.

[23] Y. Zhang, Y.-Y. Xing, C. Wang, R. Pang, W.-W. Ren, S. Wang, Z.-M. Li, L. Yang, W.-C. Tong, Q.-Y. Wang, S.-Q. Zang, *ACS Appl. Energy Mater.* **2022**, *14*, 23909–23915.

[24] M. Kofen, M. Lommel, M. H. H. Wurzenberger, T. M. Klapötke, J. Stierstorfer, *Chem. Eur. J.* **2022**, e202200492.

[25] M. Rösch, M. S. Gruhne, M. Lommel, S. M. J. Endraß, J. Stierstorfer, *Inorg. Chem.* **2023**, *62*, 1488–1507.

[26] M. H. H. Wurzenberger, S. M. J. Endraß, M. Lommel, T. M. Klapötke, J. Stierstorfer, *ACS Appl. Energy Mater.* **2020**, *3*, 3798–3806.

[27] E. A. Popova, G. K. Ovsepyan, A. V. Protas, E. B. Erkhitueva, M. K. Kukhanova, Y. L. Yesaulkova, V. V. Zarubaev, G. L. Starova, R. V. Suezov, A. V. Eremin, V. A. Ostrovskii, R. E. Trifonov, *Nucleosides, Nucleotides & Nucleic Acids* **2019**, *38*, 713–731.

[28] M. Muttenthaler, M. Bartel, P. Weinberger, G. Hilscher, W. Linert, *J. Mol. Struct.* **2005**, *741*, 159–169.

[29] K. Banert, *Chem. Ber.* **1989**, *122*, 911–918.

[30] K. Banert, M. Hagedorn, C. Hemeltjen, A. Ihle, K. Weigand, H. Priebe, *ARKIVOC* **2016**, *2016*, 338–361.

[31] F. Himo, T. Lovell, R. Hilgraf, V. V. Rostovtsev, L. Noodleman, K. B. Sharpless, V. V. Fokin, *J. Am. Chem. Soc.* **2005**, *127*, 210–216.

[32] R. Matyáš, J. Šelešovský, T. Musil, *J. Hazard. Mat.* **2012**, *213–214*, 236–241.

[33] *EXPLO5* V7.01.01, M. Sućeska, Zagreb, **2023**.

[34] M. H. H. Wurzenberger, M. S. Gruhne, M. Lommel, J. Stierstorfer, *Propellants, Explos. Pyrotech.* **2021**, *46*, 207–213.

[35] M. S. Gruhne, T. Lenz, M. Rösch, M. Lommel, M. H. H. Wurzenberger, T. M. Klapötke, J. Stierstorfer, *Dalton Trans.* **2021**, *50*, 10811–10825.

[36] J. Bauer, M. Benz, T. M. Klapoetke, J. Stierstorfer, *Dalton Trans.* **2022**.

[37] S. M. J. Endraß, A. Neuer, T. M. Klapötke, J. Stierstorfer, *ChemistrySelect* **2022**, *7*, e202203140.

[38] M. S. Gruhne, M. Lommel, M. H. H. Wurzenberger, N. Szimhardt, T. M. Klapötke, J. Stierstorfer, *Propellants, Explos. Pyrotech.* **2020**, *45*, 147–153.

[39] T. M. Klapötke, *Energetic Materials Encyclopedia, Vol. 1–3*, 2nd ed., DeGruyter, Berlin/Boston, **2021**.

[40] Impact: insensitive > 40 J, less sensitive ≥ 35 J, sensitive ≥ 4 J, very sensitive ≤ 3 J; Friction: insensitive > 360 N, less sensitive = 360 N, sensitive < 360 N and > 80 N, very sensitive ≤ 80 N, extremely sensitive ≤ 10 N, **1999**.

[41] M. Seifried, C. Knoll, G. Giester, M. Reissner, D. Müller, P. Weinberger, *Magnetochemistry* **2016**, *2*, 1–13.

5.6 Supporting Information

5.6.1 Compound Overview

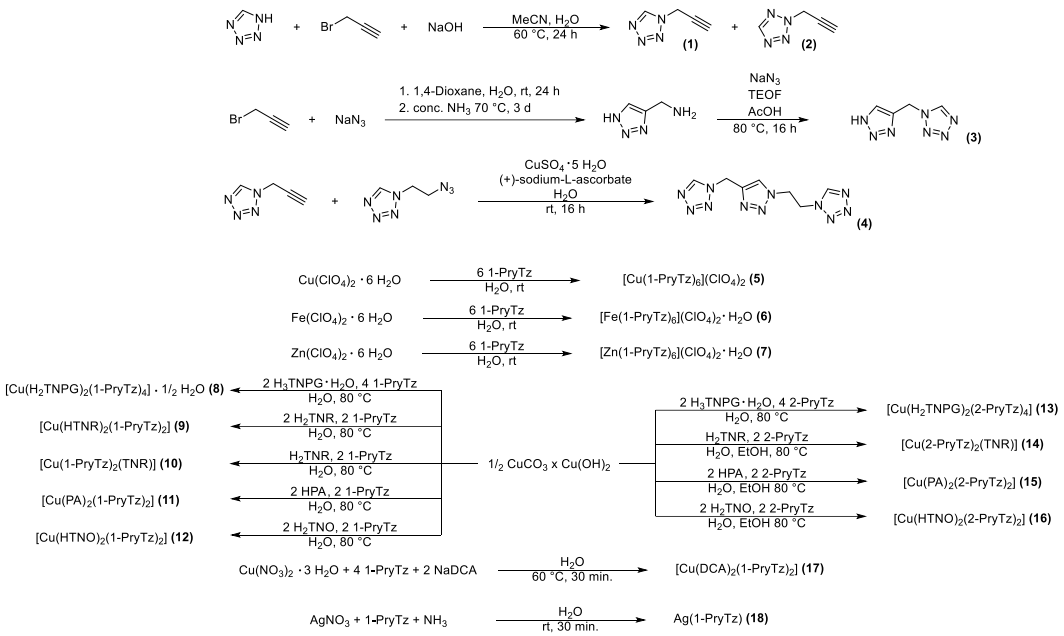

5.6.2 Single Crystal X-Ray Diffraction

For all crystalline compounds an Oxford Xcalibur3 diffractometer with a CCD area detector or Bruker D8 Venture TXS diffractometer equipped with a multilayer monochromator, a Photon 2 detector, and a rotating-anode generator were employed for data collection using Mo-Kα radiation (λ = 0.7107 Å). On the Oxford device, data collection and reduction were carried out using the CrysAlisPRO software.[S1] On the Bruker diffractometer, the data were collected with the Bruker Instrument Service v3.0.21, the data reduction was performed using the SAINT V8.18C software (Bruker AXS Inc., 2011). The structures were solved by direct methods (SIR-92, [S2] SIR-97, [S3,S4] SHELXS-97[S5,S6] or SHELXT[S7]), refined by full-matrix least-squares on *F2* (SHELXL[S5,S6]) and finally checked using the PLATON software[S8] integrated in the WinGX[S7,S9] or Olex2[S8] software suite. The non-hydrogen atoms were refined anisotropically and the hydrogen atoms were located and freely refined. The absorptions were corrected by a SCALE3 ABSPACK or SADABS Bruker APEX3 multi-scan method. [S11,S12] All DIAMOND2 plots are shown with thermal ellipsoids at the 50% probability level and hydrogen atoms are shown as small spheres of arbitrary radius.

Table S1. Crystallographic data and crystal structure refinement details of compounds **3**, **4** and **5**.

	TriMT **(3)**	**TriMTET** **(4)**	**$[Cu(1\text{-}PryTz)_6](ClO_4)_2$** **(5)**
Formula	$C_4H_5N_7$	$C_7H_9N_{11}$	$C_{24}H_{24}CuCl_2N_{24}O_8$
FW [g mol^{-1}]	151.15	247.25	911.11
Crystal system	Orthorhombic	monoclinic	monoclinic
Space Group	*Pbca*	*Pn* (No. 7)	$P2_1/n$ (No. 14)
Color / Habit	Colorless platelet	Colorless rod	Blue platelet
Size [mm]	0.05×0.25×0.50	0.04×0.05×0.15	0.03×0.14×0.16
a [Å]	6.5167(5)	9.1479(4)	10.0460(4)
b [Å]	10.0554(9)	5.4751(2)	17.5118(7)
c [Å]	19.3075(17)	33.0038(12)	23.0673(9)
α [°]	90	90	90
β [°]	90	91.855(1)	100.044(2)
γ [°]	90	90	90
V [Å^3]	1265.18(19)	1652.15(11)	3995.9(3)
Z	8	6	4
$\rho_{calc.}$ [g cm^{-3}]	1.587	1.491	1.515
μ [mm^{-1}]	0.118	0.110	0.757
F(000)	624	768	1852
$\lambda_{MoK\alpha}$ [Å]	0.71073	0.71073	0.71073
T [K]	99	173	173
θ Min–Max [°]	2.1, 32.8	2.5, 26.4	2.7, 26.4
Dataset	−9:9; −15:10; −27:28	−11:11; −6:6; −41:41	−12:12; −21:21; −28:28
Reflections collected	14059	26317	65915
Independent refl.	2204	6479	8169
Rint	0.059	0.031	0.049
Observed reflections	1471	6310	6572
Parameters	104	488	532
R_1 (obs)[a]	0.0535	0.0364	0.0406
wR_2 (all data)[b]	0.1358	0.0926	0.1464
GooF[c]	1.04	1.14	1.10
Resd. Dens. [e Å^{-3}]	−0.23, 0.33	−0.22, 0.18	−0.79, 0.39
Absorption correction	Multi-scan	Multi-scan	Multi-scan
CCDC	2241739	2241731	2241732

[a]$R_1 = \Sigma||F_0|-|F_c||/\Sigma|F_0|$; [b]$wR_2 = [\Sigma[w(F_0^2-F_c^2)^2]/\Sigma[w(F_0)^2]]^{1/2}$; $w = [\sigma c^2(F_0^2)+(xP)^2+yP]^{-1}$ and $P=(F_0^2+2F_c^2)/3$; [c]$S = \{\Sigma[w(F_o^2-F_c^2)^2]/(n-p)\}^{1/2}$ (n = number of reflections; p = total number of parameters).

Table S2. Crystallographic data and crystal structure refinement details of compounds **8**, **9** and **11**.

	[Cu(H$_2$TNPG)$_2$(1-PryTz)$_4$] · ½ H$_2$O (8)	**[Cu(HTNR)$_2$(1-PryTz)$_2$] (9)**	**[Cu(PA)$_2$(1-PryTz)$_2$] (11)**
Formula	$C_{56}H_{42}Cu_2N_{44}O_{37}$	$C_{20}H_{12}CuN_{14}O_{16}$	$C_{20}H_{12}CuN_{14}O_{14}$
FW [g mol^{-1}]	2050.44	767.98	735.98
Crystal system	monoclinic	triclinic	monoclinic
Space Group	$P2_1/n$ (No. 14)	$P\bar{1}$ (No. 2)	$P2_1/c$ (No. 14)
Color / Habit	Green rod	Green block	Green block
Size [mm]	0.10×0.20×0.50	0.25×0.40×0.40	0.20×0.50×0.50
a [Å]	8.9758(8)	8.2748(6)	12.0728(10)
b [Å]	16.1298(18)	8.3290(7)	10.0977(6)
c [Å]	13.7742(13)	11.2972(10)	12.2909(10)
α [°]	90	76.725(7)	90
β [°]	92.469(8)	73.305(7)	115.698(11)
γ [°]	90	71.648(7)	90
V [Å^3]	1992.4(3)	699.52(11)	1350.2(2)
Z	1	1	2
$\rho_{calc.}$ [g cm^{-3}]	1.709	1.823	1.810
μ [mm^{-1}]	0.657	0.888	0.911
F(000)	1040	387	742
$\lambda_{MoK\alpha}$ [Å]	0.71073	0.71073	0.71073
T [K]	102	99	105
θ Min–Max [°]	2.5, 29.3	1.9, 26.4	2.7, 26.4
Dataset	−11:12; −19:22; −18:18	−9:10; −10:8; −11:14	−14:15; −12:11; −15:15
Reflections collected	17125	5510	9911
Independent refl.	4770	2856	2760
Rint	0.038	0.035	0.028
Observed reflections	3487	2220	2312
Parameters	346	233	223
R_1 (obs)[a]	0.0472	0.0518	0.0331
wR_2 (all data)[b]	0.1158	0.1247	0.0845
GooF[c]	1.04	1.04	1.03
Resd. Dens. [e Å^{-3}]	−0.32, 0.50	−0.43, 0.75	−0.34, 0.34
Absorption correction	Multi-scan	Multi-scan	Multi-scan
CCDC	2241736	2241730	2241737

[a]$R_1 = \Sigma||F_0|-|F_c||/\Sigma|F_0|$; [b]$wR_2 = [\Sigma[w(F_0^2-F_c^2)^2]/\Sigma[w(F_0)^2]]^{1/2}$; $w = [\sigma c^2(F_0^2)+(xP)^2+yP]^{-1}$ and $P=(F_0^2+2F_c^2)/3$; [c]$S = \{\Sigma[w(F_o^2-F_c^2)^2]/(n-p)\}^{1/2}$ (n = number of reflections; p = total number of parameters).

Table S3. Crystallographic data and crystal structure refinement details of compounds **12**, **13** and **14**.

	[Cu(HTNO)$_2$(1-PryTz)$_2$] **(12)**	**[Cu(H$_2$TNPG)$_2$(2-PryTz)$_4$]** **(13)**	**[Cu(2-PryTz)$_2$(TNR)]** **(14)**
Formula	$C_{22}H_{16}CuN_{14}O_{16}$	$C_{28}H_{20}CuN_{22}O_{18}$	$C_{14}H_9CuN_{11}O_8$
FW [g mol^{-1}]	796.03	1016.20	522.86
Crystal system	monoclinic	triclinic	monoclinic
Space Group	$P2_1/n$ (No. 14)	$P\bar{1}$ (No. 2)	$P2_1/c$ (No. 14)
Color / Habit	Blue plate	Green block	Green block
Size [mm]	0.05×0.25×0.70	0.40×0.50×0.50	0.30×0.50×0.50
a [Å]	6.4060(5)	9.1372(5)	14.3445(5)
b [Å]	10.6849(12)	9.4423(5)	8.3704(4)
c [Å]	22.041(2)	11.7964(8)	16.9128(7)
α [°]	90	97.882(5)	90
β [°]	96.799(8)	91.371(5)	101.283(4)
γ [°]	90	105.674(5)	90
V [Å^3]	1498.0(2)	968.66(10)	1991.46(15)
Z	2	1	4
$\rho_{calc.}$ [g cm^{-3}]	1.765	1.742	1.744
μ [mm^{-1}]	0.833	0.674	1.169
F(000)	806	515	1052
$\lambda_{MoK\alpha}$ [Å]	0.71073	0.71073	0.71073
T [K]	112	95	113
θ Min–Max [°]	2.7, 26.4	2.3, 29.2	2.5, 29.2
Dataset	−7:8; −13:13; −27:24	−12:11; −11:12; −13:14	−16:19; −11:11; −22:23
Reflections collected	11596	8126	17532
Independent refl.	3049	4411	4782
Rint	0.055	0.024	0.032
Observed reflections	2222	3644	3894
Parameters	256	321	307
R_1 (obs)[a]	0.0654	0.0391	0.0384
wR_2 (all data)[b]	0.1562	0.1008	0.0982
GooF[c]	1.04	1.03	1.05
Resd. Dens. [e Å^{-3}]	−0.88, 0.72	−0.31, 0.40	−0.43, 0.65
Absorption correction	Multi-scan	Multi-scan	Multi-scan
CCDC	2241735	2241733	2241738

[a]$R_1 = \Sigma||F_0|-|F_c||/\Sigma|F_0|$; [b]$wR_2 = [\Sigma[w(F_0^2-F_c^2)^2]/\Sigma[w(F_0)^2]]^{1/2}$; $w = [\sigma c^2(F_0^2)+(xP)^2+yP]^{-1}$ and $P=(F_0^2+2F_c^2)/3$; [c]$S = \{\Sigma[w(F_o^2-F_c^2)^2]/(n-p)\}^{1/2}$ (n = number of reflections; p = total number of parameters).

Table S4. Crystallographic data and crystal structure refinement details of compounds **15**, **16** and **17**.

	$[Cu(PA)_2(2\text{-}PryTz)_2]$ (15)	**$[Cu(HTNO)_2(2\text{-}PryTz)_2]$ (16)**	**$[Cu(DCA)_2(1\text{-}PryTz)_2]$ (17)**
Formula	$C_{20}H_{12}CuN_{14}O_{14}$	$C_{22}H_{16}CuN_{14}O_{16}$	$C_{12}H_8CuN_{14}$
FW [g mol^{-1}]	735.98	796.03	411.87
Crystal system	monoclinic	triclinic	monoclinic
Space Group	$P2_1/c$ (No. 14)	$P\bar{1}$ (No. 2)	$P2_1/c$ (No. 14)
Color / Habit	Green block	Green block	Blue block
Size [mm]	0.30×0.40×0.40	0.10×0.30×0.50	0.10×0.25×0.30
a [Å]	6.1159(4)	6.3812(3)	12.3458(9)
b [Å]	23.7395(13)	9.4567(5)	7.1401(4)
c [Å]	9.9012(6)	12.4667(7)	9.4656(7)
α [°]	90	96.550(5)	90
β [°]	105.429(6)	92.150(4)	96.263(7)
γ [°]	90	95.608(4)	90
V [Å^3]	1385.73(15)	742.92(7)	829.42(10)
Z	2	1	2
$\rho_{calc.}$ [g cm^{-3}]	1.764	1.779	1.649
μ [mm^{-1}]	0.887	0.840	1.350
F(000)	742	403	414
$\lambda_{MoK\alpha}$ [Å]	0.71073	0.71073	0.71073
T [K]	99	97	94
θ Min–Max [°]	2.3, 32.6	2.2, 32.6	3.3, 26.4
Dataset	−8:8; −35:34; −14:14	−8:9; −13:12; −18:17	−15:14; −8:8; −10:11
Reflections collected	15927	9197	7003
Independent refl.	4662	4882	1690
Rint	0.046	0.035	0.051
Observed reflections	3312	3618	1355
Parameters	223	246	124
R_1 (obs)[a]	0.0543	0.0518	0.0433
wR_2 (all data)[b]	0.1341	0.1340	0.1155
GooF[c]	1.07	1.05	1.08
Resd. Dens. [e Å^{-3}]	−0.39, 0.62	−0.48, 0.93	−0.42, 1.12
Absorption correction	Multi-scan	Multi-scan	Multi-scan
CCDC	2241813	2241814	2241734

[a] $R_1 = \Sigma||F_0|-|F_c||/\Sigma|F_0|$; [b] $wR_2 = [\Sigma[w(F_0^2-F_c^2)^2]/\Sigma[w(F_0)^2]]^{1/2}$; $w = [\sigma c^2(F_0^2)+(xP)^2+yP]^{-1}$ and $P=(F_0^2+2F_c^2)/3$; [c] $S = \{\Sigma[w(F_o^2-F_c^2)^2]/(n-p)\}^{1/2}$ (n = number of reflections; p = total number of parameters).

$[Cu(PA)_2(1\text{-PryTz})_2]$ crystallized in the monoclinic space group $P2_1/c$ with two formula units per unit cell and a density of 1.81 g cm^{-3} at 105 K. As depicted in Figure S1, the coordination sphere is again realized in form of a *Jahn-Teller*-like distorted octahedron.

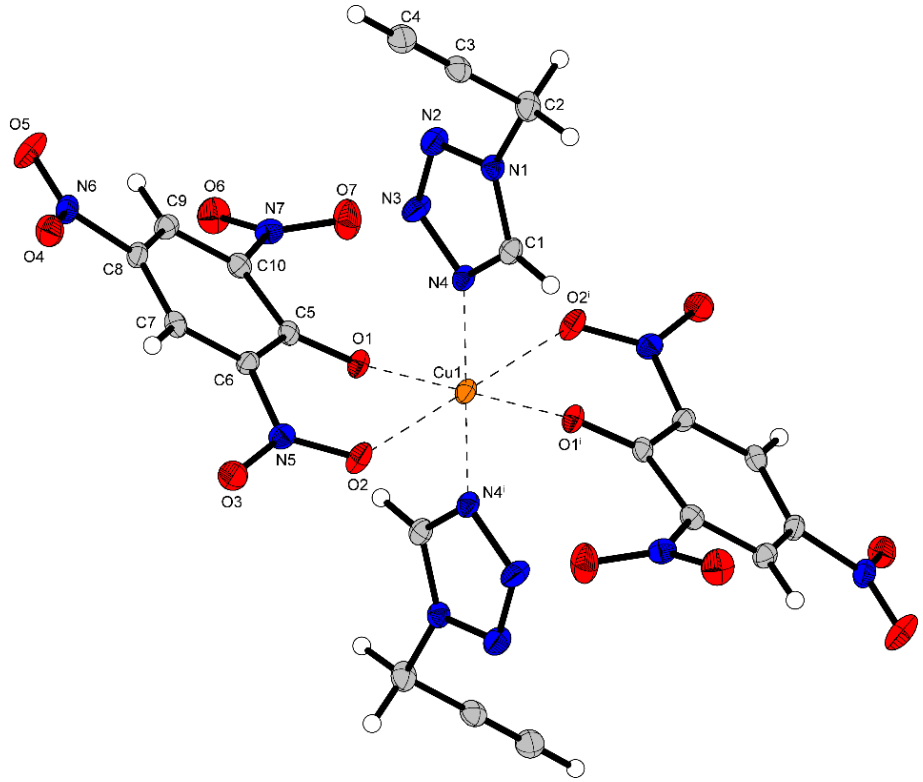

Figure S1. Crystal structure of compound **11**. Selected bond lengths [Å]: Cu1–O1 1.9734(15), Cu1–O2 2.3387(19), Cu1–N4 1.9859(18); Selected bond angles [°]: O1–Cu1–O2 78.02(6), O1–Cu1–N4 92.21(7); Symmetry codes: (i) 2−x, 1−y, 1−z.

$[Cu(H_2TNPG)_2(2\text{-PryTz})_4]$ crystallized in the triclinic space group *P*−1 with a calculated density of 1.74 g cm^{-3} at 95 K. The copper(II) center is coordinated octahedrally with the anion in the *Jahn-Teller*-like distorted z^2-axis.

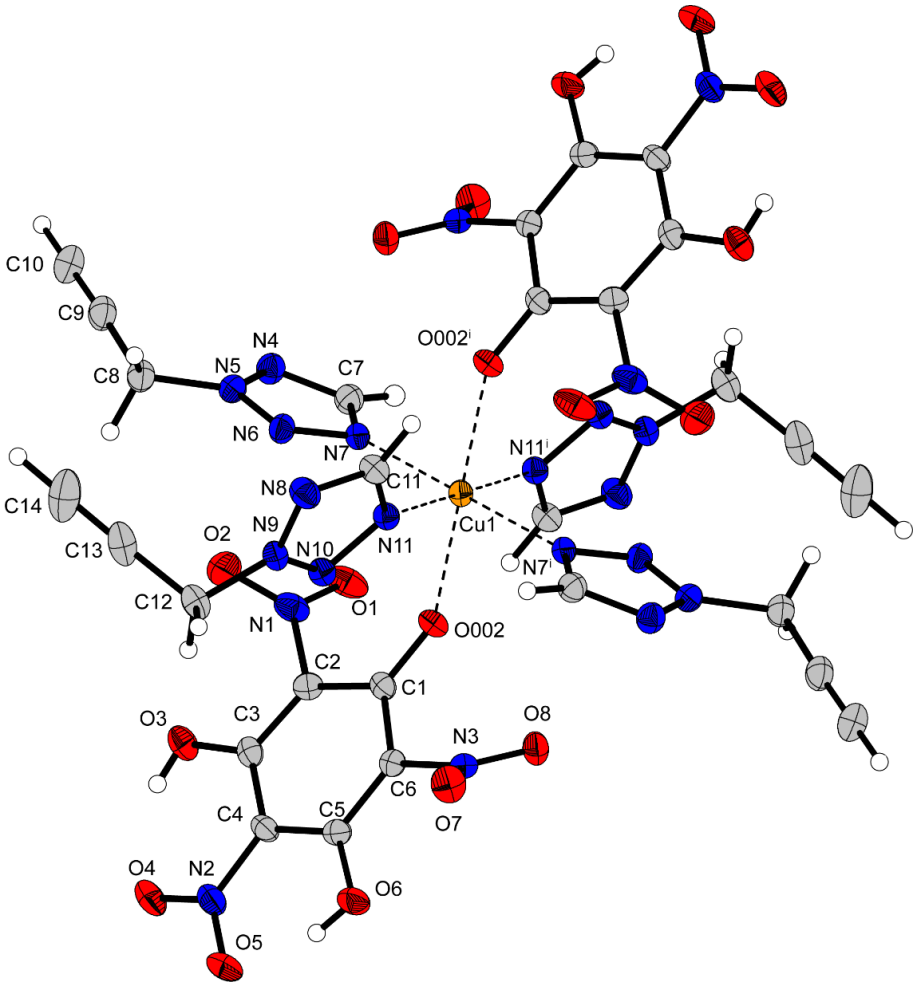

Figure S2. Crystal structure of compound **13**. Selected bond lengths [Å]: Cu1–O002 2.2890(15), Cu1–N7 2.0509(17), Cu1–N11 2.0003(17); Selected bond angles [°]: O002–Cu1–N7 87.17(6), O002–Cu1–N11 86.05(6); Symmetry codes: (i) 1−x, 1−y, 1−z.

Similar to compound **11**, compound **15** crystallized in the monoclinic space group $P2_1/c$ with a calculated density of 1.76 g cm^{-3} at 99 K. The coordination follows the expected pattern of a d^9-Cu^{2+} center.

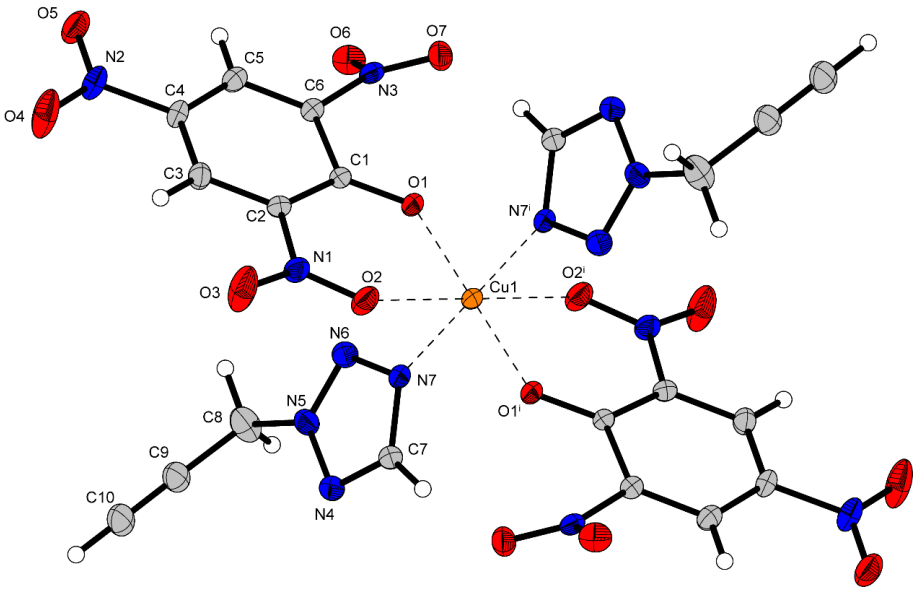

Figure S3. Crystal structure of compound **15**. Selected bond lengths [Å]: Cu1–O1 1.9231(18), Cu1–O2 2.3164(19), Cu1–N7 2.0092(19); Selected bond angles [°]: O1–Cu1–O2 81.00(7), O1–Cu1–N7 93.08(8); Symmetry codes: (i) 1−x, 1−y, 1−z.

[Cu(HTNO)$_2$(2-PryTz)$_2$] (Figure S4**Figure S**) crystallized in the triclinic space group $P\bar{1}$ with a density of 1.78 g cm^{-3} at 94 K. The compound shows the expected coordination pattern with two anions and two ligands, in which the elongated z^2-axis of the octahedra is occupied by the oxygen of the nitro groups in para position to the methyl group.

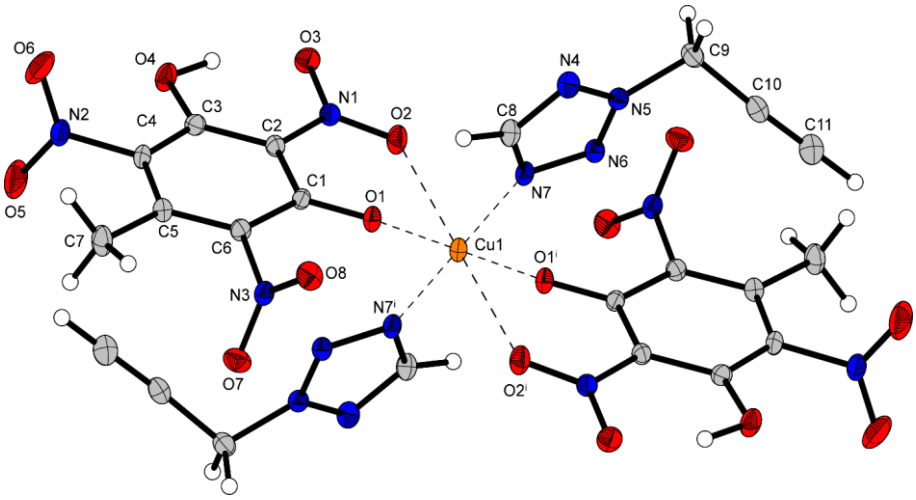

Figure S4. Crystal structure of compound **16**. Selected bond lengths [Å]: Cu1–O1 1.9285(15), Cu1–O2 2.4239(18), Cu1–N7 1.9928(19); O1–Cu1–O2 75.55(6), O1–Cu1–N7 87.98(7); Symmetry codes: (i) 1−x, 1−y, 1−z.

5.6.3 Computations

All calculations were carried out using the Gaussian G09 program package. [S13] The enthalpies (H) and free energies (G) were calculated using the complete basis set (CBS) method of Petersson and coworkers in order to obtain very accurate energies. The CBS models use the known asymptotic convergence of pair natural orbital expressions to extrapolate from calculations using a finite basis set to the estimated complete basis set limit. CBS-4 begins with a HF/3-21G(d) geometry optimization; the zero point energy is computed at the same level. It then uses a large basis set SCF calculation as a base energy, and a MP2/6-31+G calculation with a CBS extrapolation to correct the energy through second order. A MP4(SDQ)/6-31+(d,p) calculation is used to approximate higher order contributions. In this study we applied the modified CBS-4M method (M referring to the use of minimal population localization) which is a re-parametrized version of the original CBS-4 method and also includes some additional empirical corrections. The enthalpies of the gas-phase species M were computed according to the atomization energy method (E1) (Table S5 & Table S6). [S13–18]

$$\Delta_f \mathrm{H}^\circ_{(g,M,298)} = H_{(Molecule,298)} - \sum H^\circ_{(Atoms,298)} + \sum \Delta_f H^\circ_{(Atoms,298)} \qquad \text{(E1)}$$

Table S5. Literature values for atomic $\Delta \boldsymbol{H^\circ_f}^{\mathbf{298}}$ / kcal mol^{-1}.

	$-H^{298}$ [a.u.]	NIST [S19]
H	0.50091	52.1
C	37.786156	171.3
N	54.522462	113.0
O	74.991202	59.6

The gas-phase heat of formations were converted to the solid/liquid state ones for neutrals: by subtracting the vaporization/sublimation enthalpies (calculated using the Trouton rule). [S20,21] The calculation results are summarized in Table S6.

$$\Delta U_m = \Delta H_m - \Delta n\, R\, T \qquad \text{(E2)}$$

Table S6. CBS-4M results.

Compound	$-H^{298}$[a] [a.u.]	$\Delta_f H^\circ(g,M)$[b] [kJ mol^{-1}]	$\Delta_f H^\circ(l)$[c] [kJ mol^{-1}]	Δn[d]	$\Delta_f U(l)$[e] [kJ mol^{-1}]
1-PryTz	−373.163492	575.2	533.8	−4.0	5029.6
2-PryTz	−373.171341	554.6	512.6	−4.0	4833.1
1-AT	−313.152885	448.4	407.4	−4.0	4906.2

[a] CBS-4M electronic enthalpy; [b] gas phase enthalpy of formation; [c] standard liquid state enthalpy of formation; [d] Δn being the change of moles of gaseous components when formed; [e] solid state energy of formation.

Hirshfeld analysis was carried out with the CRYSTAL EXPLORER code. [S22] Figure S5 shows, that 10.4 % of TriMT and 5.1 % of TriMTET are destabilizing N···N interactions, while the majority (64.8 % for TriMT and 75.4 % for TriMTET) are stabilizing N···H interactions.

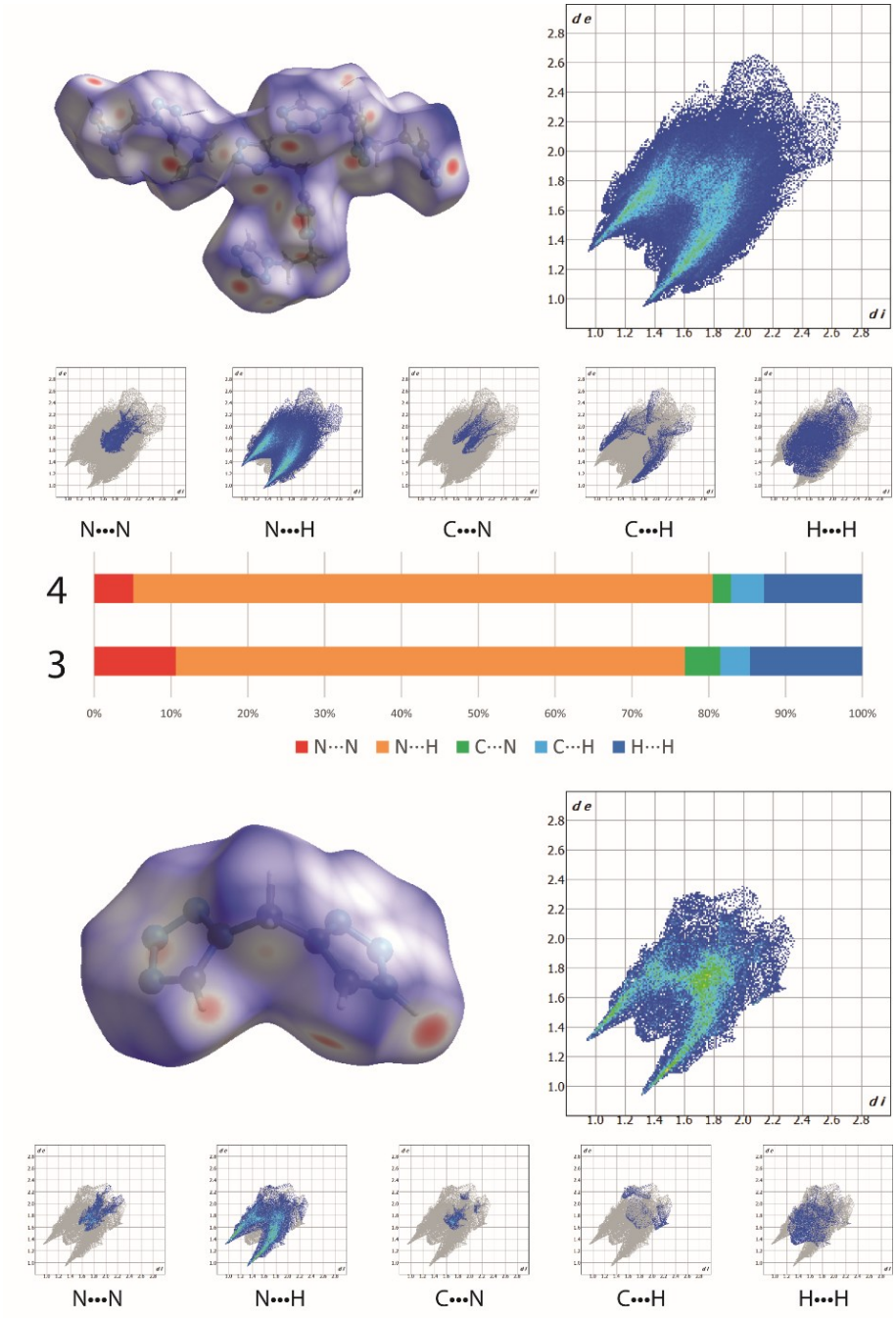

Figure S5. Hirshfeld analysis of compounds **3** and **4**.

5.6.4 NMR Spectroscopy of 1–4

1-Propargyltetrazole

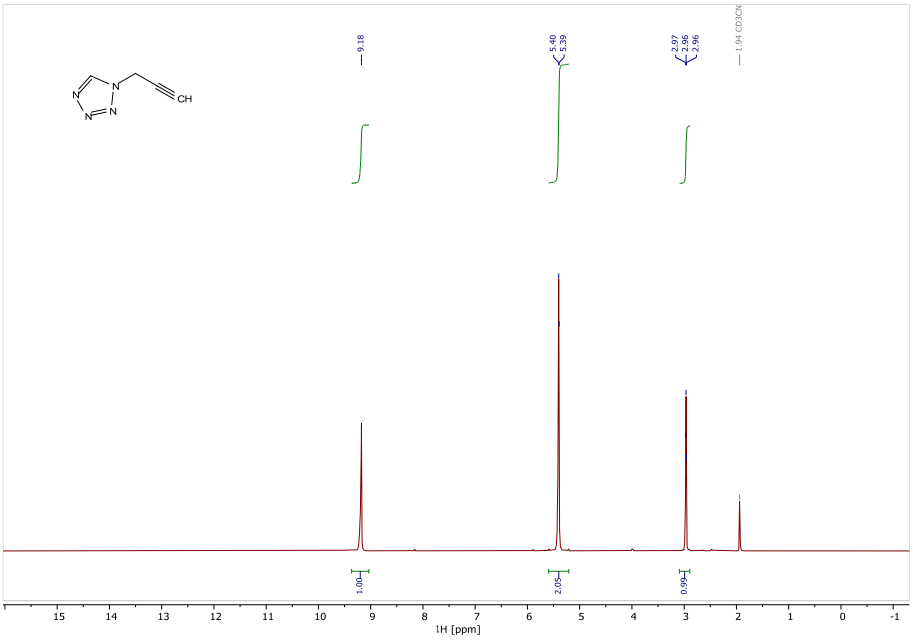

Figure S6. [1]H NMR of 1-Propargyltetrazole.

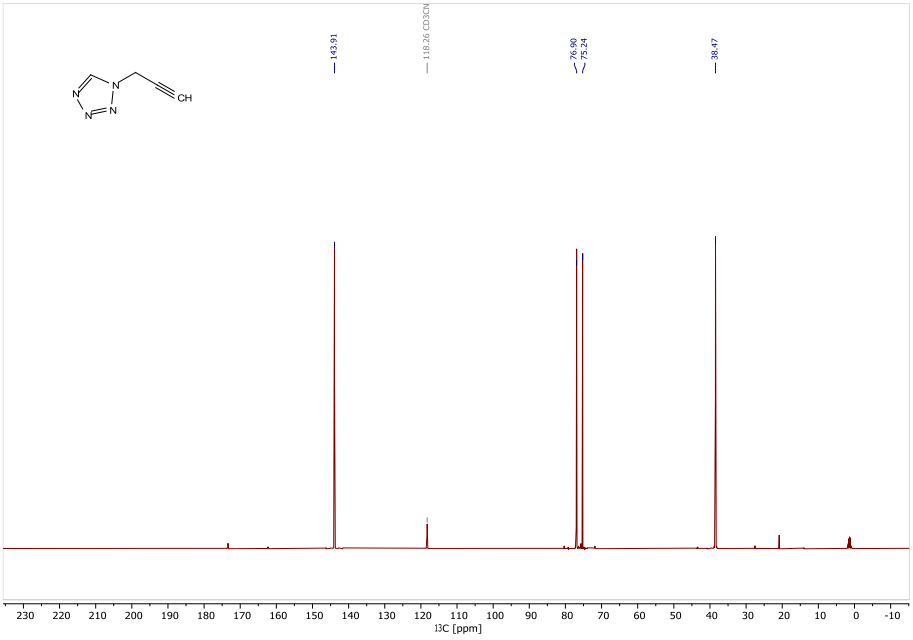

Figure S7. [13]C NMR of 1-Propargyltetrazole.

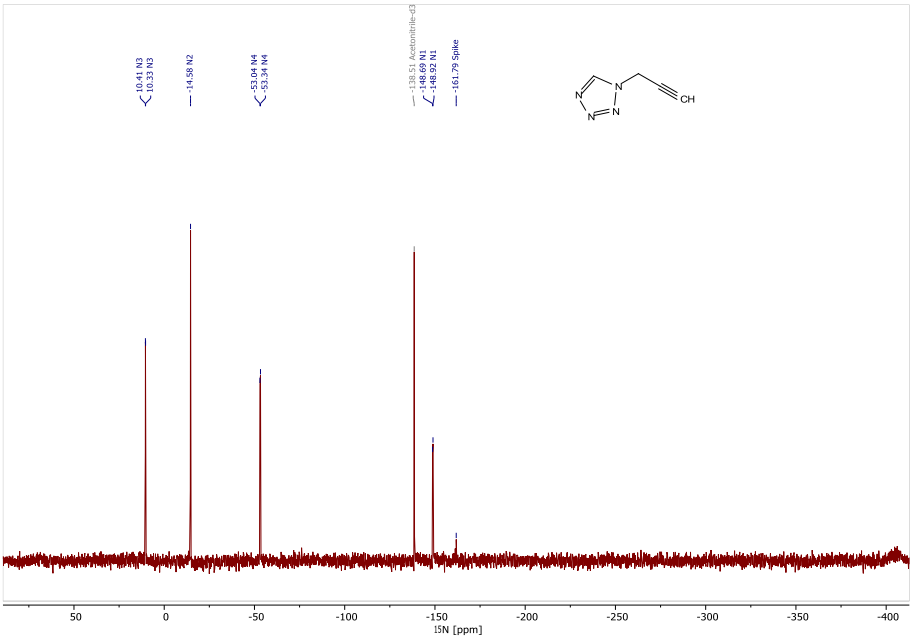

Figure S8. ^{15}N NMR of 1-Propargyltetrazole.

2-Propargyltetrazole

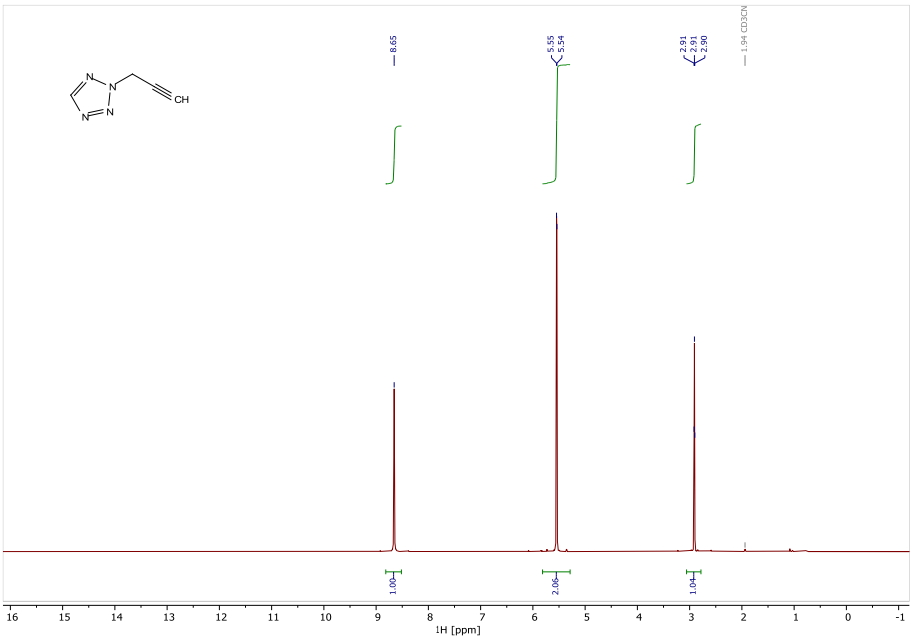

Figure S9. ^{1}H NMR of 2-Propargyltetrazole.

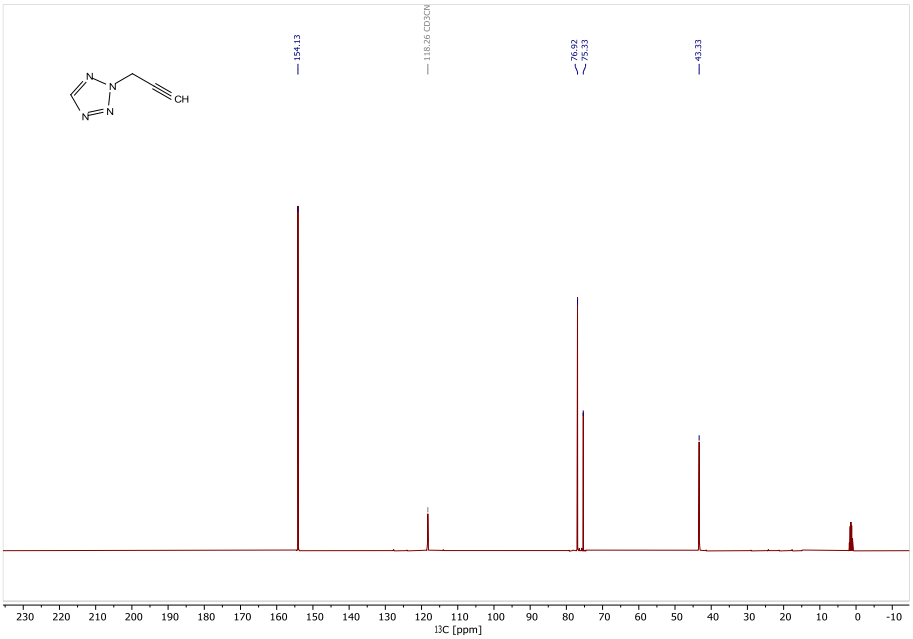

Figure S10. ^{13}C NMR of 2-Propargyltetrazole.

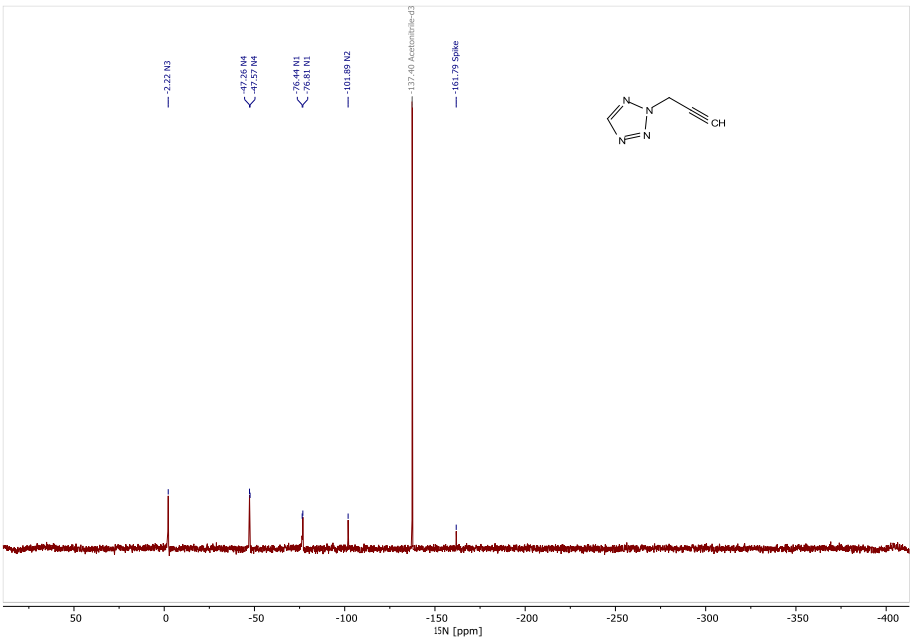

Figure S11. ^{15}N NMR of 2-Propargyltetrazole.

1-((1*H*-1,2,3-triazol-4-yl)methyl)-1*H*-tetrazole (3)

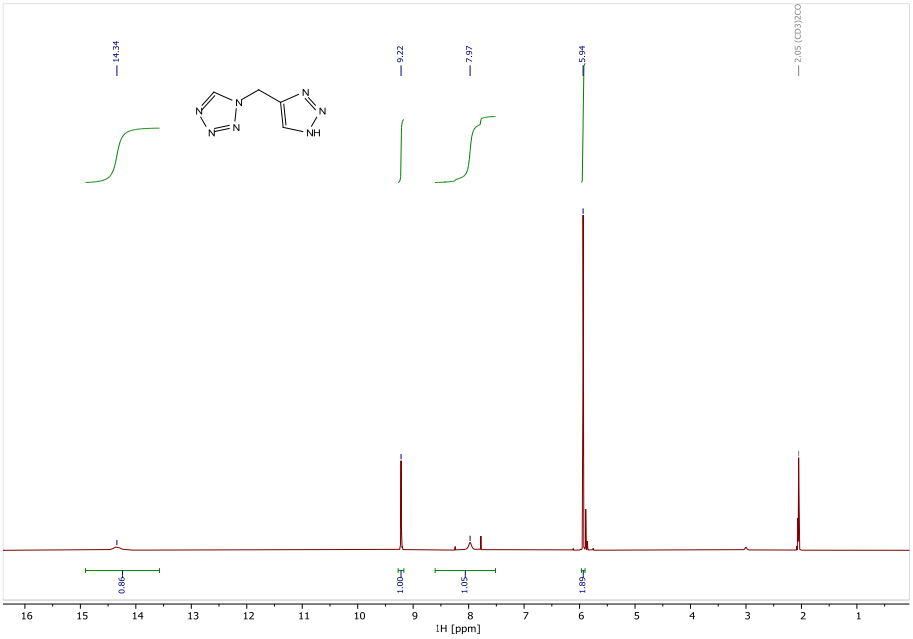

Figure S12. ^{1}H NMR of compound **3**.

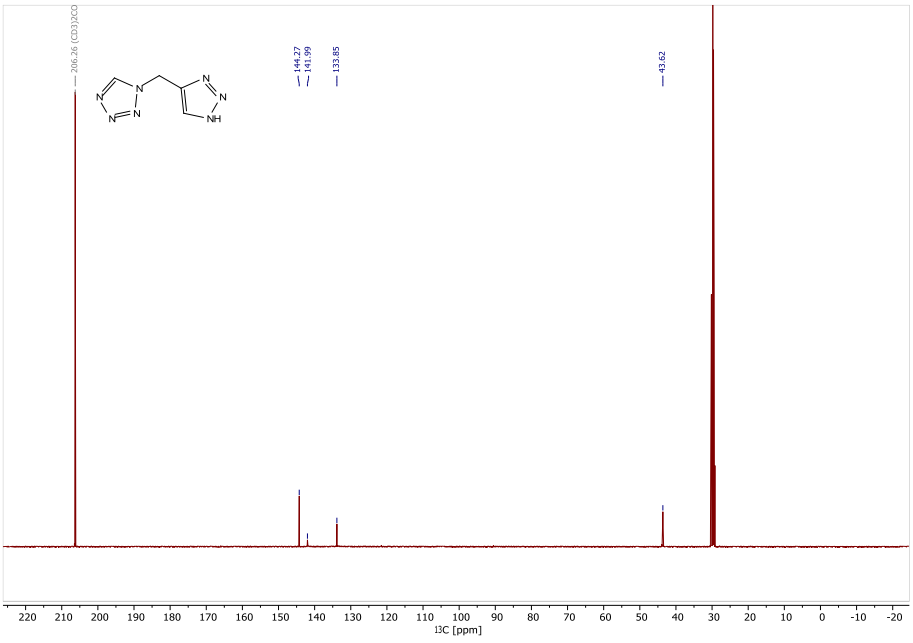

Figure S13. ^{13}C NMR of compound **3**.

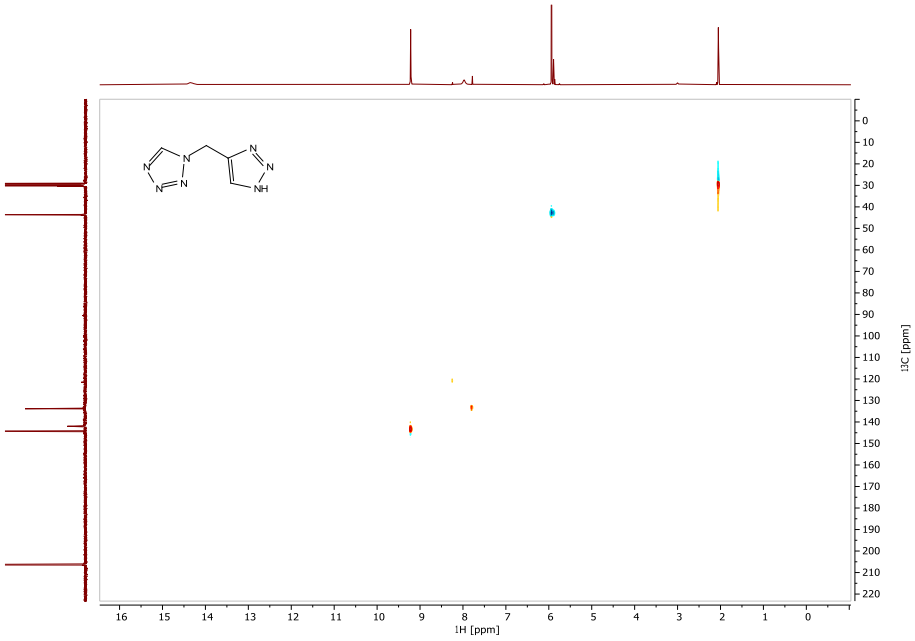

Figure S14. ^{1}H-^{13}C HSQC of compound **3**.

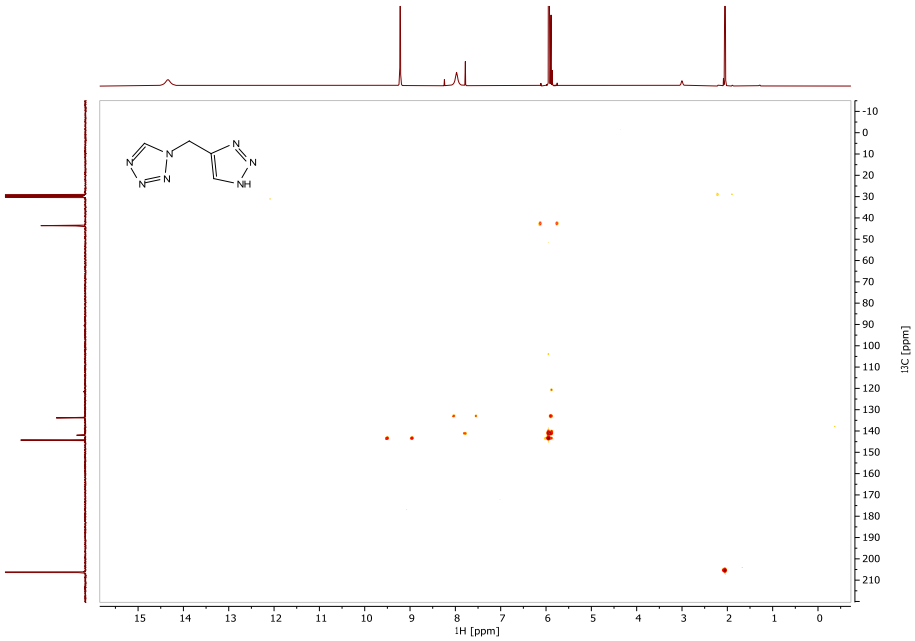

Figure S15. ^{1}H-^{13}C HMBC of compound **3**.

1-((1-(2-(1*H*-tetrazol-1-yl)ethyl)-1*H*-1,2,3-triazol-4-yl)methyl)-1*H*-tetrazole (4)

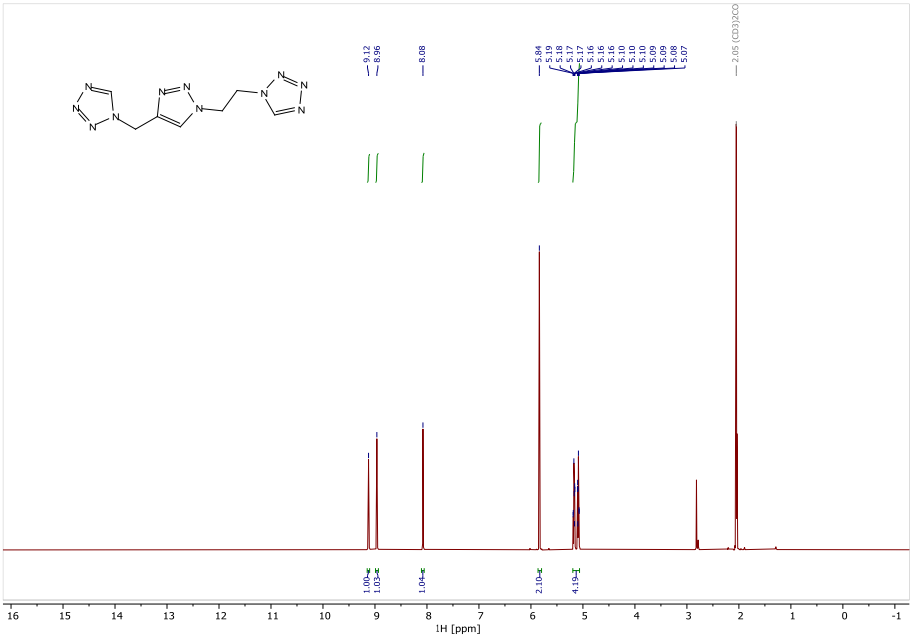

Figure S16. ^{1}H NMR of compound **4**.

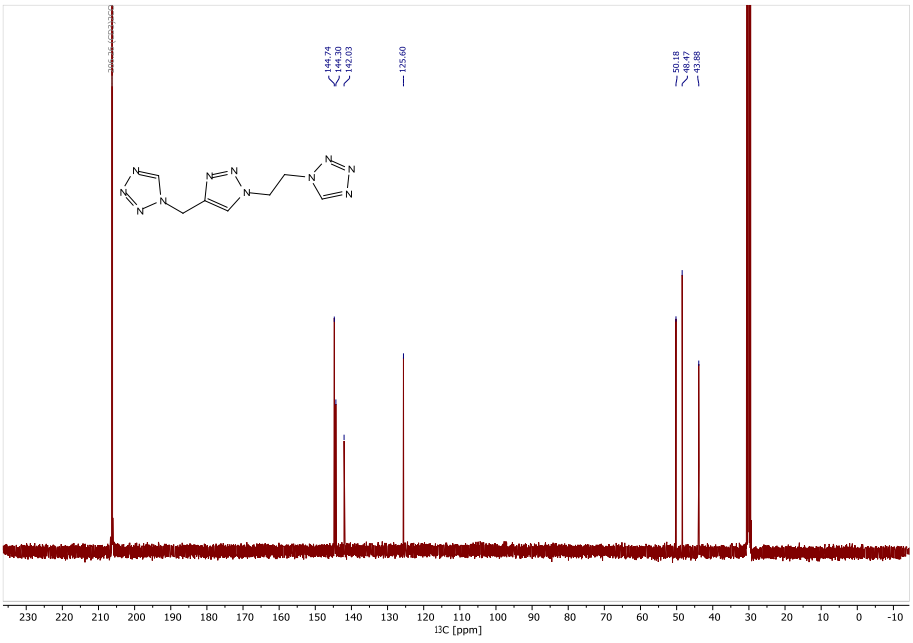

Figure S17. ^{13}C NMR of compound **4**.

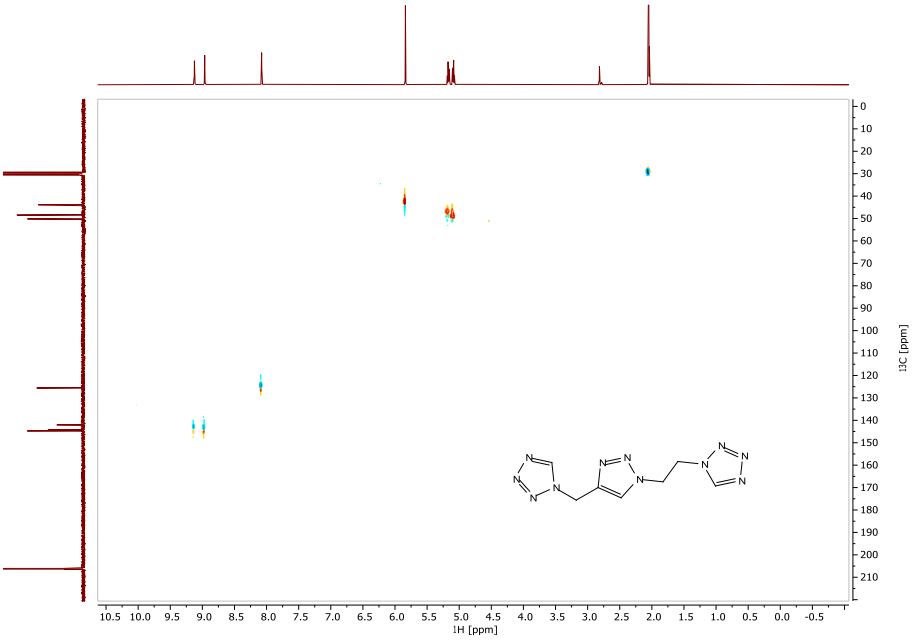

Figure S18. ^{1}H-^{13}C HSQC of compound **4**.

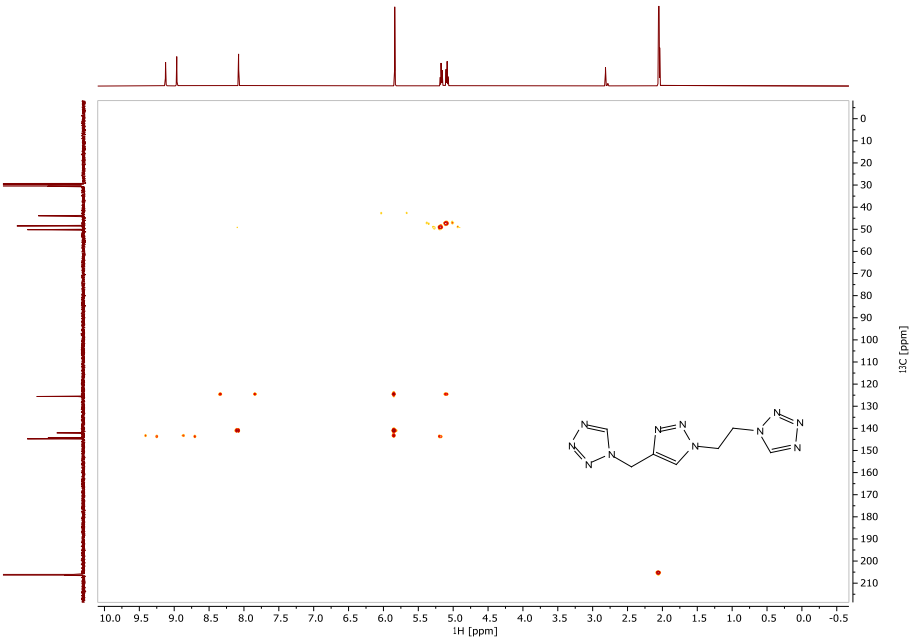

Figure S19. ^{1}H-^{13}C HMBC of compound **4**.

5.6.5 IR Spectroscopy of 1–18

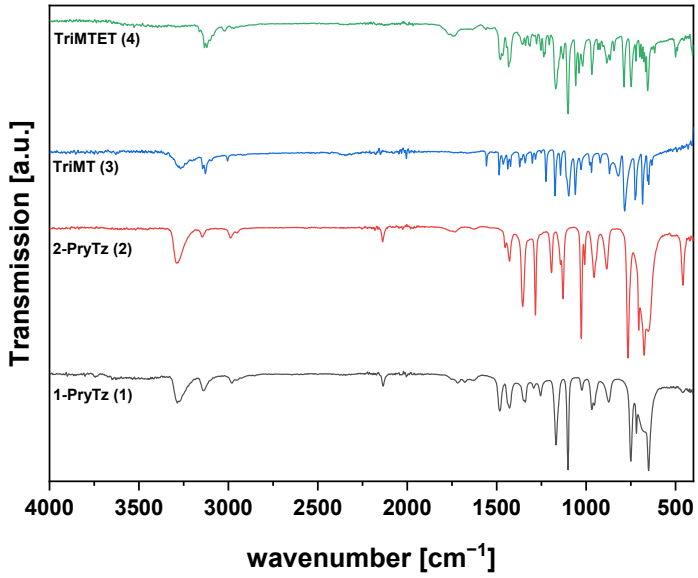

Figure S20. IR spectrum of 1-PryTz, 2-PryTz, TriMT and TriMTET.

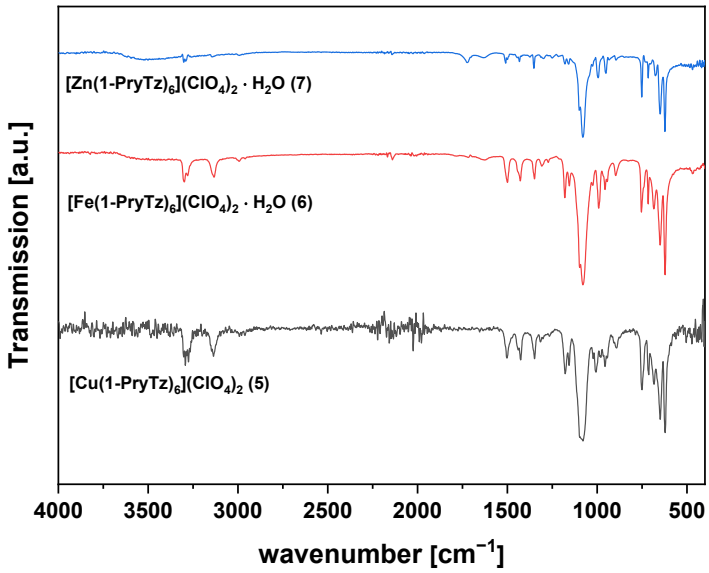

Figure S21. IR spectra of compounds **5**–**7**.

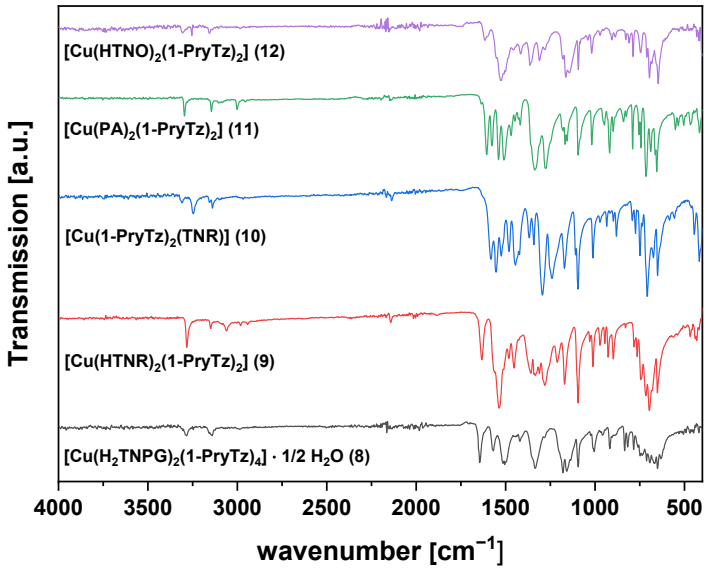

Figure S22. IR spectra of compounds **8**–**12**.

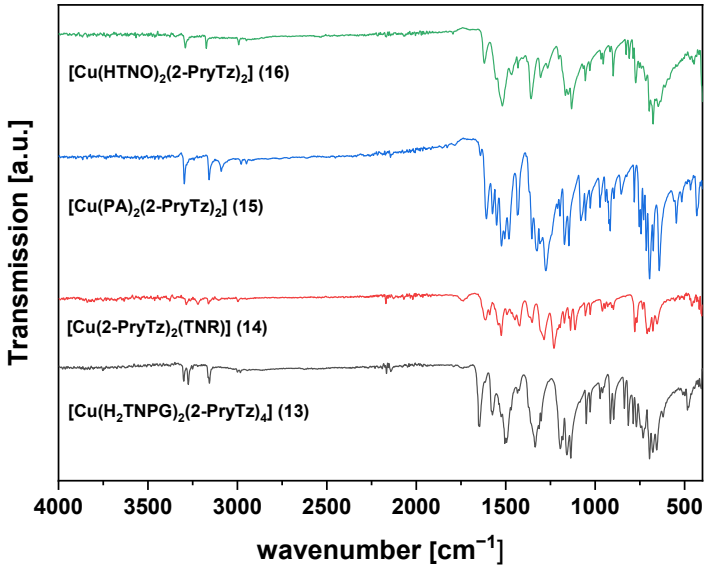

Figure S23. IR spectra of compounds **13**–**16**.

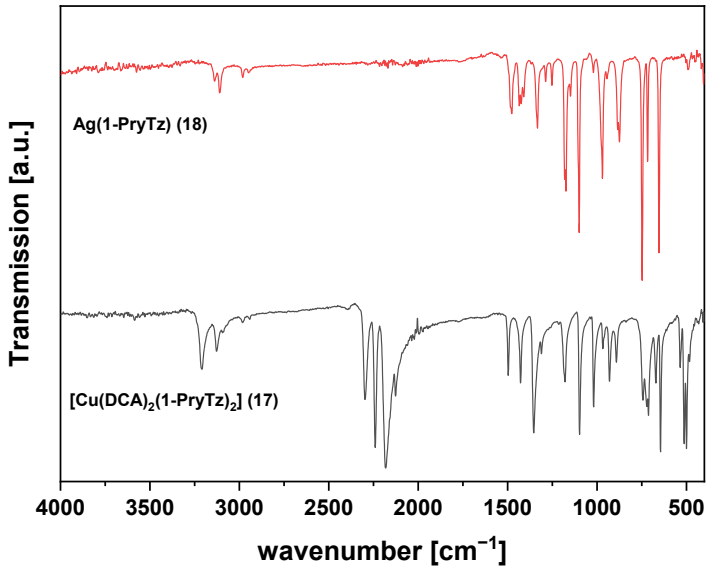

Figure S24. IR spectra of compounds **17** and **18**.

5.6.6 Thermal Analysis of 1–18

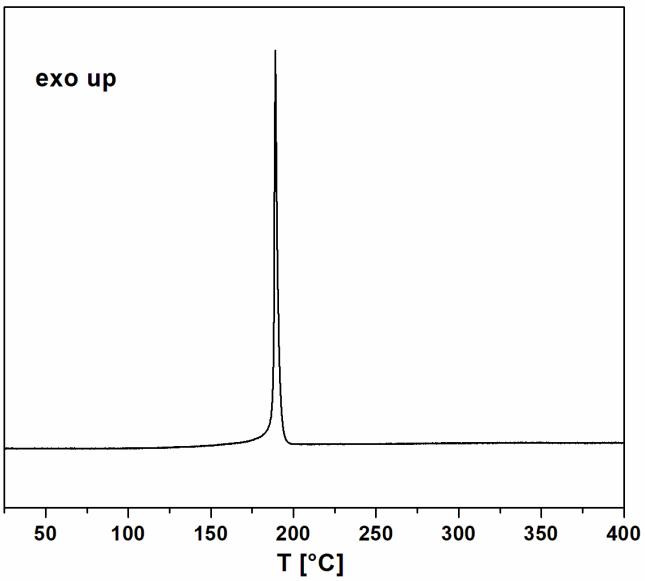

Figure S25. DTA plot of 1-PryTz in the range of 25–400 °C.

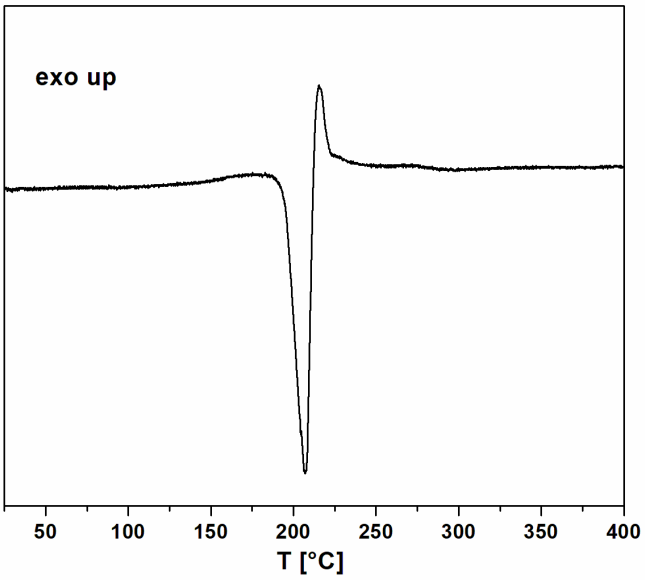

Figure S26. DTA plot of 2-PryTz in the range of 25–400 °C.

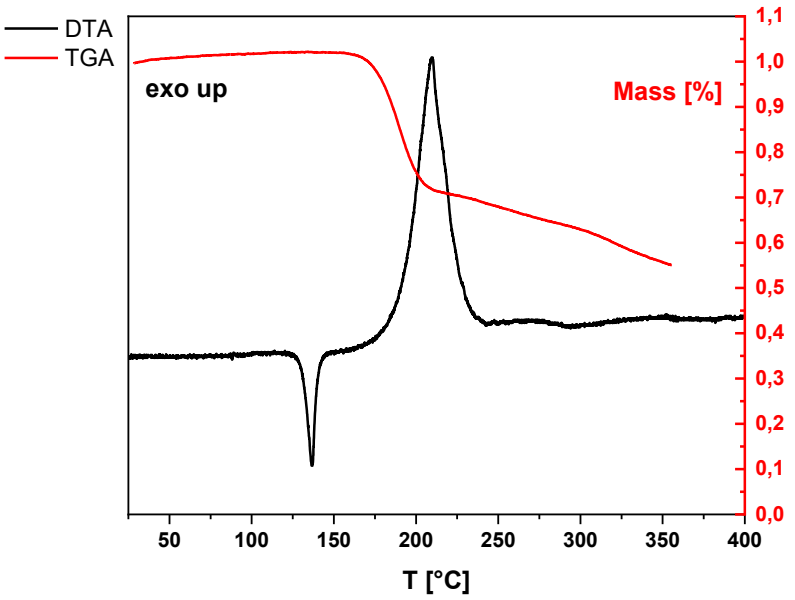

Figure S27. DTA (black) and TGA (red) plot of 1-((1*H*-1,2,3-triazol-4-yl)methyl)-1*H*-tetrazole in the range of 25–400 °C.

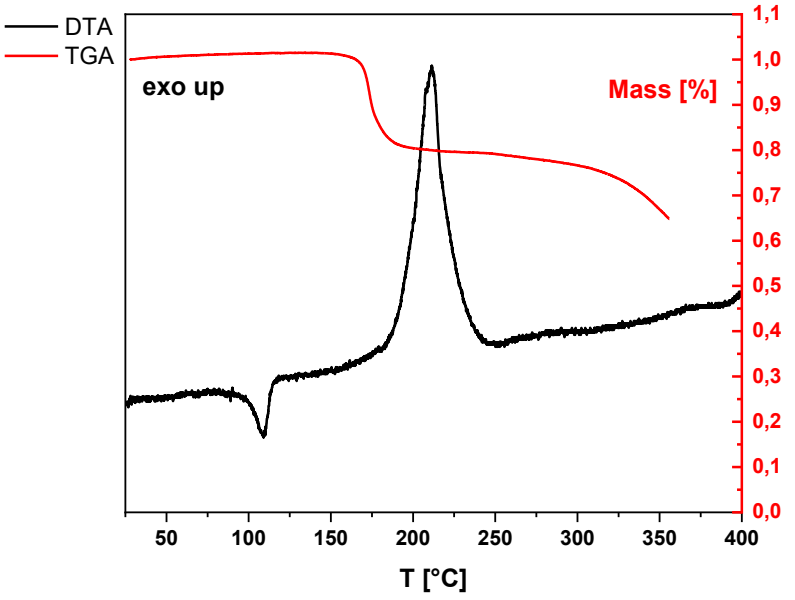

Figure S28. DTA (black) and TGA (red) plot of 1-((1-(2-(1*H*-tetrazol-1-yl)ethyl)-1*H*-1,2,3-triazol-4-yl)methyl)-1*H*-tetrazole in the range of 25–400 °C.

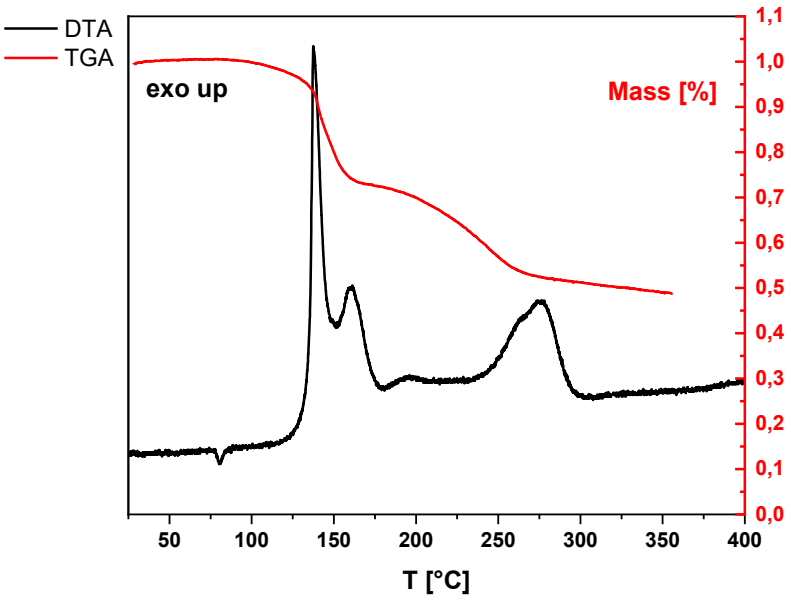

Figure S29. DTA (black) and TGA (red) plot of $[Cu(1\text{-}PryTz)_6](ClO_4)_2$ in the range of 25–400 °C.

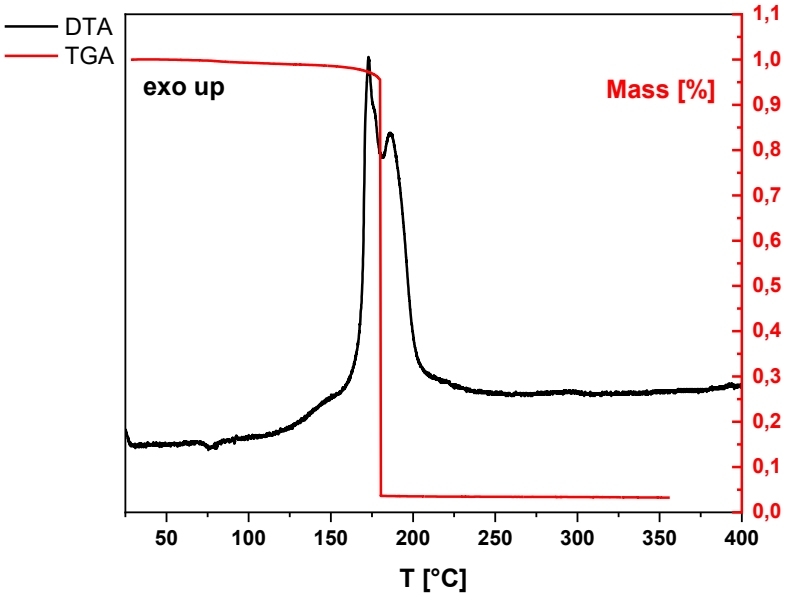

Figure S30. DTA (black) and TGA (red) plot of $[Fe(1\text{-}PryTz)_6](ClO_4)_2 \cdot H_2O$ in the range of 25–400 °C.

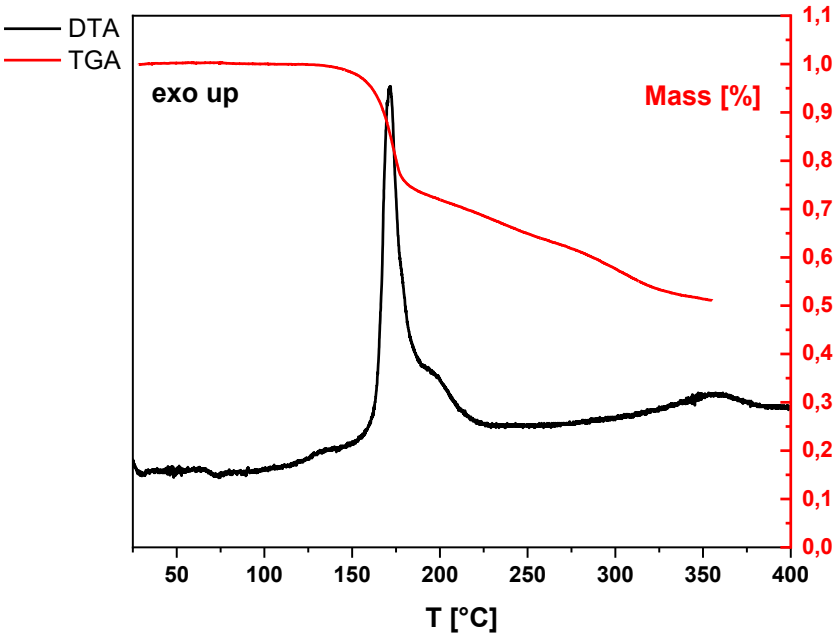

Figure S31. DTA plot of $[Zn(1\text{-PryTz})_6](ClO_4)_2 \cdot H_2O$ in the range of 25–400 °C.

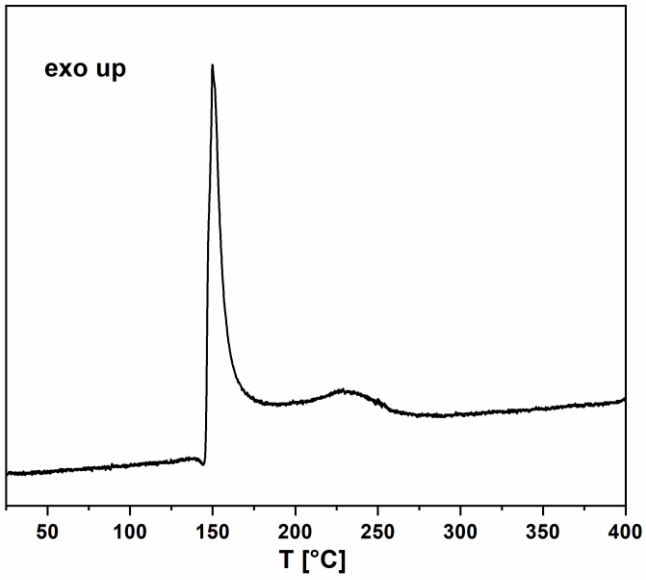

Figure S32. DTA plot of $[Cu(H_2TNPG)_2(1\text{-PryTz})_4] \cdot ½\ H_2O$ in the range of 25–400 °C.

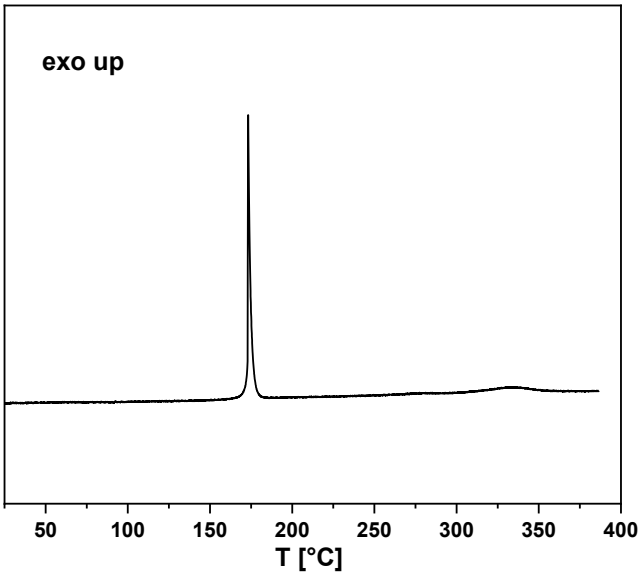

Figure S33. DTA plot of $[Cu(HTNR)_2(1\text{-}PryTz)_2]$ in the range of 25–400 °C.

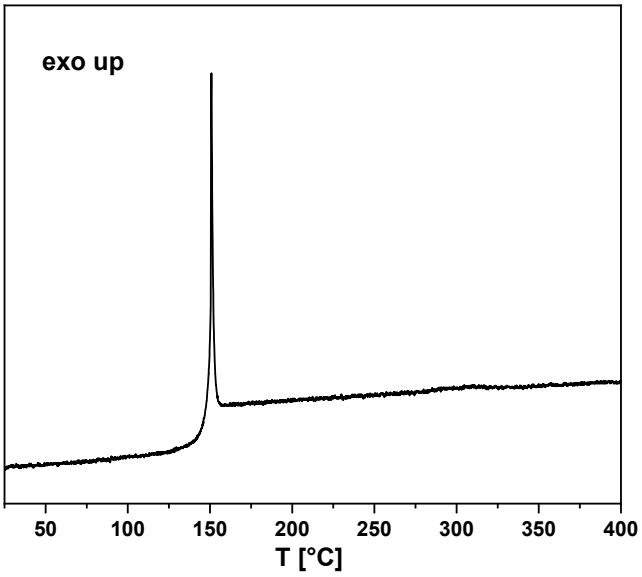

Figure S34. DTA plot of $[Cu(1\text{-}PryTz)_2(TNR)]$ in the range of 25–400 °C.

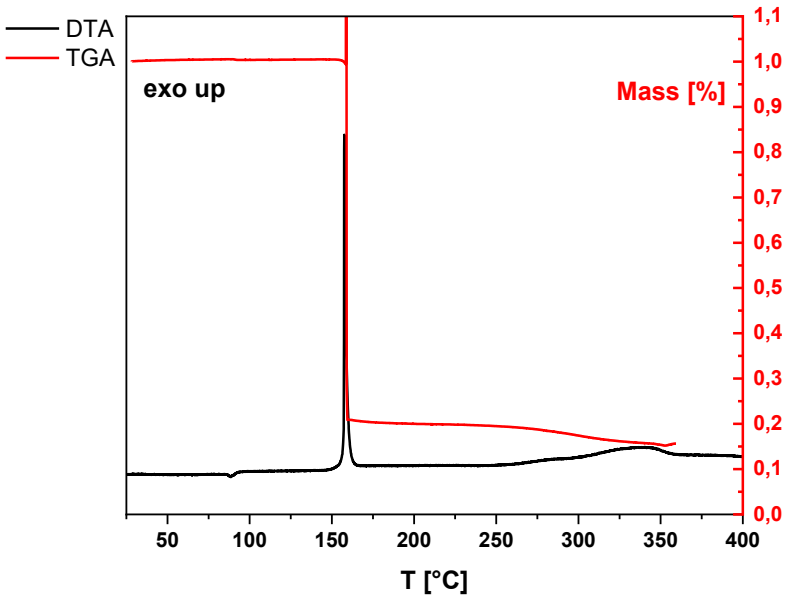

Figure S35. DTA plot of $[Cu(PA)_2(1\text{-}PryTz)_2]$ in the range of 25–400 °C.

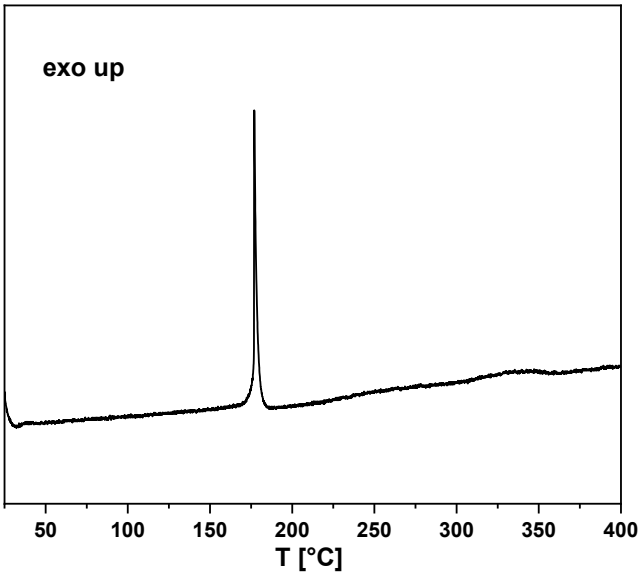

Figure S36. DTA plot of $[Cu(HTNO)_2(1\text{-}PryTz)_2]$ in the range of 25–400 °C.

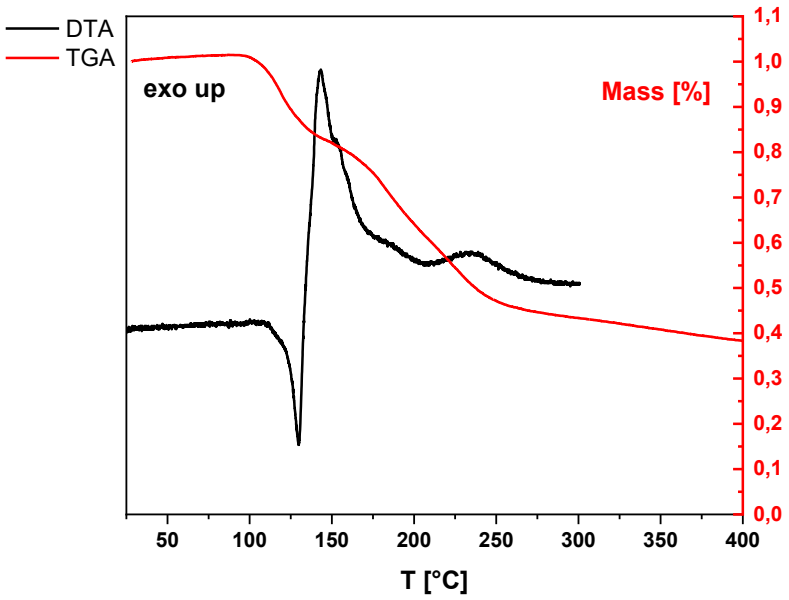

Figure S37. DTA plot of $[Cu(H_2TNPG)_2(2\text{-}PryTz)_4]$ in the range of 25–300 °C.

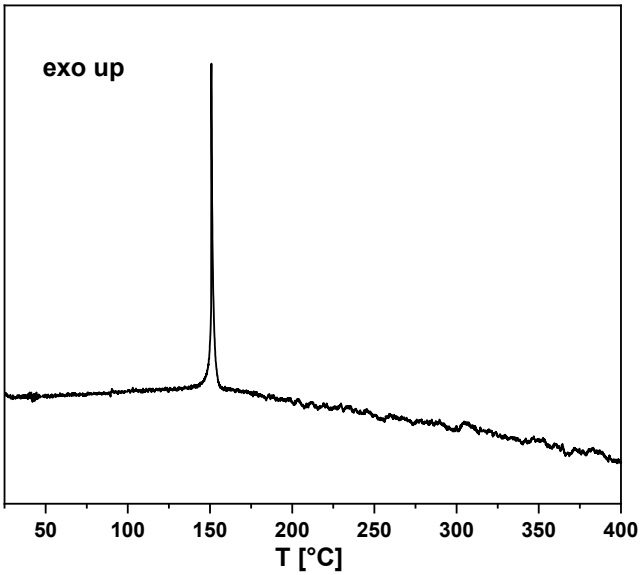

Figure S38. DTA plot of $[Cu(2\text{-}PryTz)_2(TNR)]$ in the range of 25–400 °C.

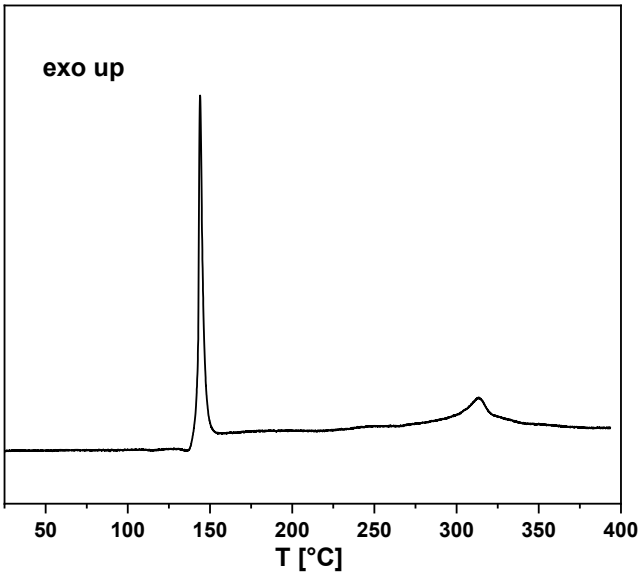

Figure S39. DTA plot of $[Cu(PA)_2(2\text{-}PryTz)_2]$ in the range of 25–400 °C.

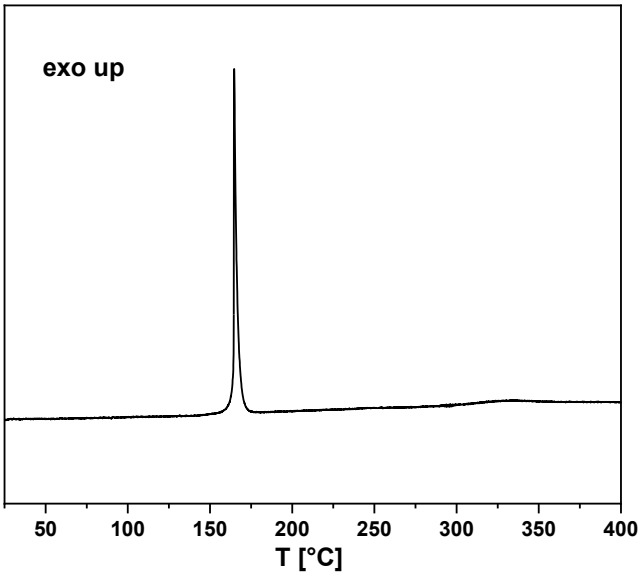

Figure S40. DTA plot of $[Cu(HTNO)_2(2\text{-}PryTz)_2]$ in the range of 25–400 °C.

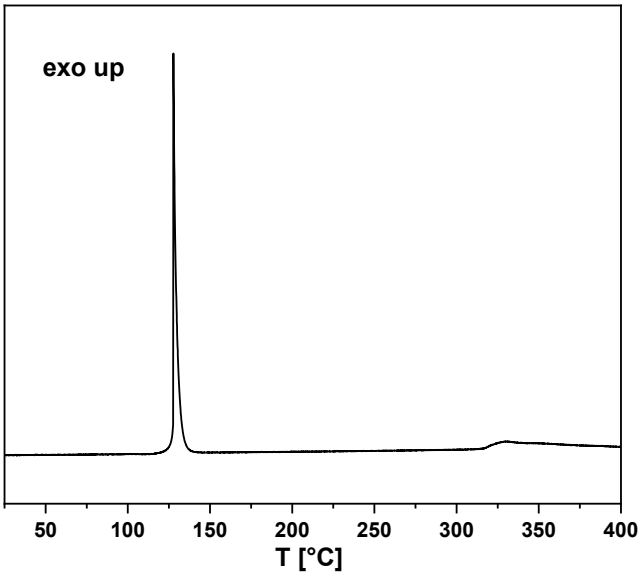

Figure S41. DTA plot of $[Cu(DCA)_2(1\text{-PryTz})_2]$ in the range of 25–400 °C.

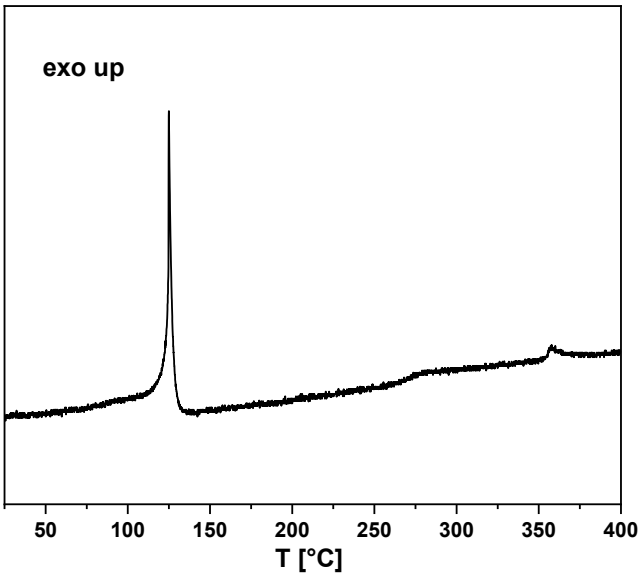

Figure S42. DTA plot of Ag(1-PryTz) in the range of 25–400 °C.

5.6.7 Hot Plate and Hot Needle Testing

Figure S43. Reaction of $[Cu(1\text{-PryTz})_6](ClO_4)_2$ during hot plate (left) and hot needle test (right).

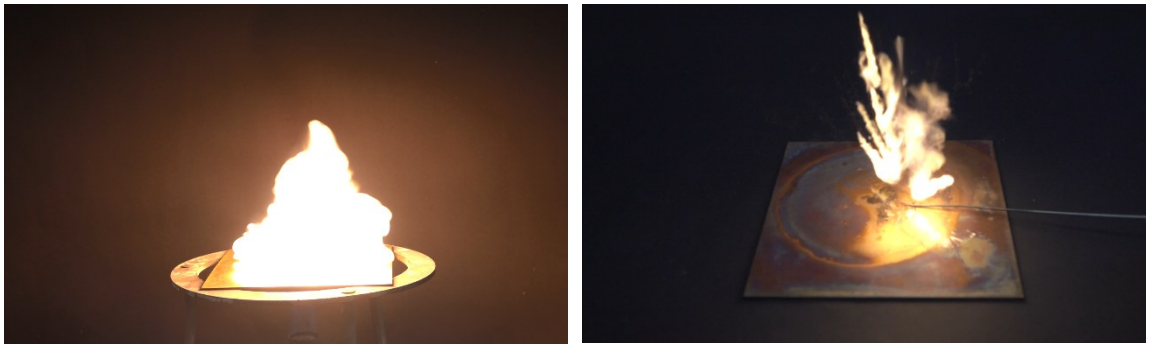

Figure S44. Deflagration of $[Fe(1\text{-PryTz})_6](ClO_4)_2 \cdot H_2O$ during hot plate (left) and hot needle test (right).

Figure S45. Reaction of $[Zn(1\text{-PryTz})_6](ClO_4)_2 \cdot H_2O$ during hot plate (left) and hot needle test (right).

Figure S46. Reaction of $[Cu(H_2TNPG)_2(1\text{-}PryTz)_4] \cdot ½\ H_2O$ during hot plate (left) and hot needle test (right).

Figure S47. Reaction of $[Cu(HTNR)_2(1\text{-}PryTz)_2]$ during hot plate (left) and hot needle test (right).

Figure S48. Reaction of $[Cu(1\text{-}PryTz)_2(TNR)]$ during hot plate (left) and hot needle test (right).

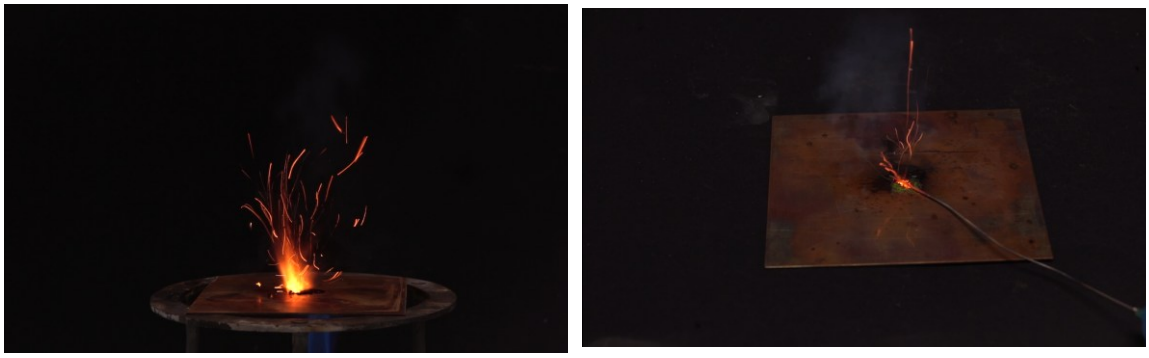

Figure S49. Reaction of $[Cu(PA)_2(1\text{-PryTz})_2]$ during hot plate (left) and hot needle test (right).

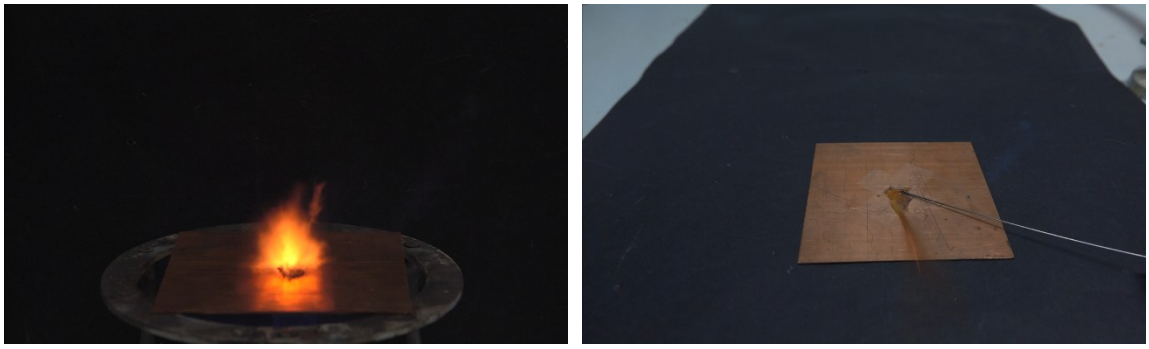

Figure S50. Decomposition of $[Cu(HTNO)_2(1\text{-PryTz})_2]$ during hot plate (left) and hot needle test (right).

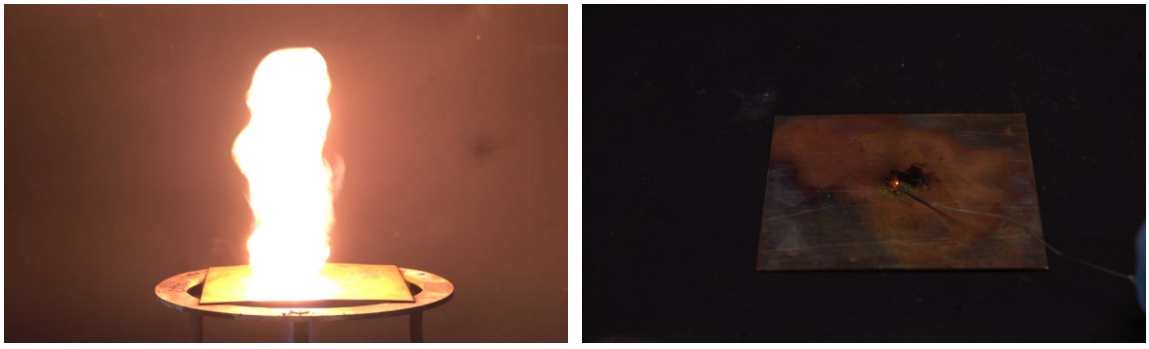

Figure S51. Reaction of $[Cu(H_2TNPG)_2(2\text{-PryTz})_4]$ during hot plate (left) and hot needle test (right).

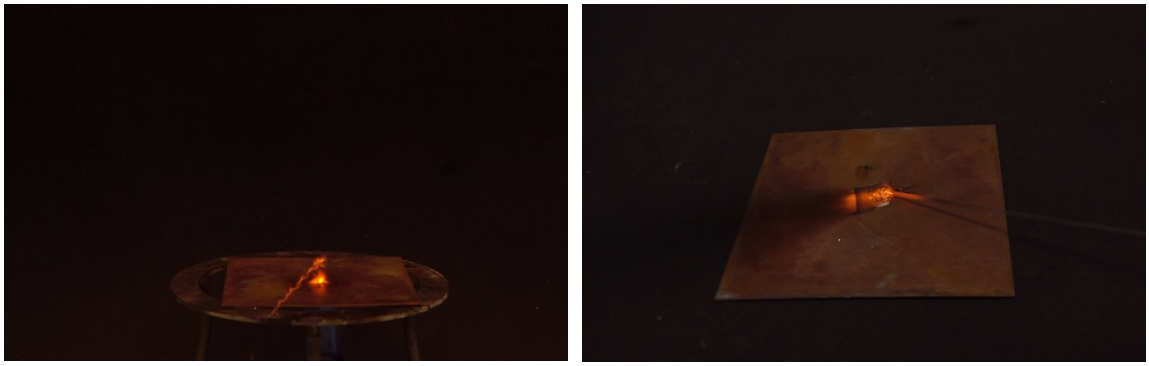

Figure S52. Reaction of [Cu(2-PryTz)$_2$(TNR)] during hot plate (left) and hot needle test (right).

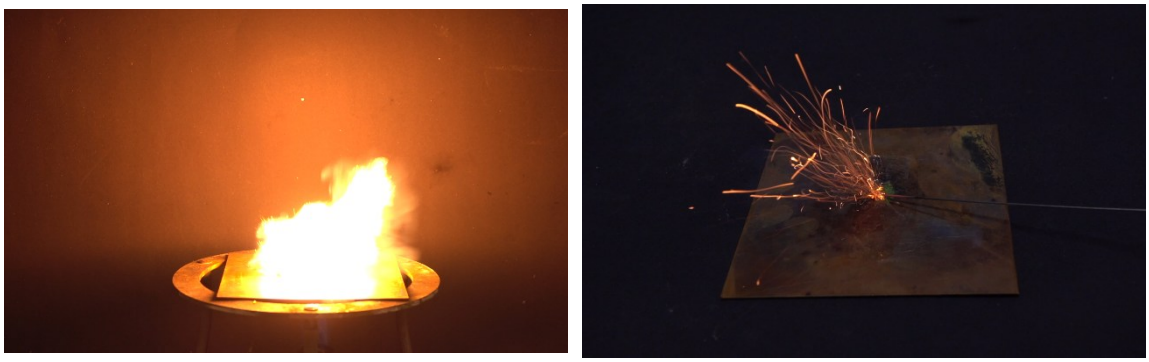

Figure S53. Reaction of [Cu(PA)$_2$(2-PryTz)$_2$] during hot plate (left) and hot needle test (right).

Figure S54. Reaction of [Cu(HTNO)$_2$(2-PryTz)$_2$] during hot plate (left) and hot needle test (right).

Figure S55. Detonation of $[Cu(DCA)_2(1\text{-PryTz})_2]$ during hot plate (left) and hot needle test (right).

5.6.8 Laser Initiation Experiments

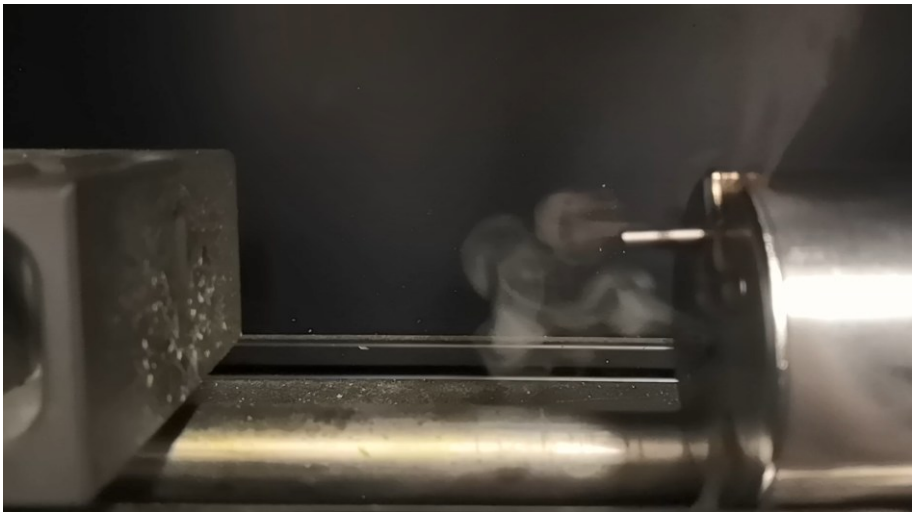

Figure S56. Decomposition of $[Cu(H_2TNPG)_2(1\text{-PryTz})_4] \cdot ½\ H_2O$ during laser irradiation (10 A, 30 ms, 4 V).

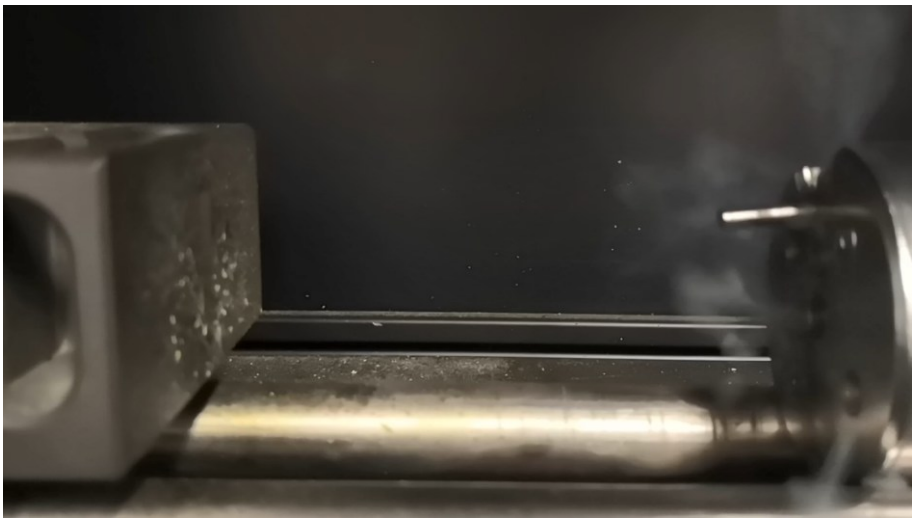

Figure S57. Decomposition of $[Cu(HTNR)_2(1\text{-PryTz})_2]$ during laser irradiation (10 A, 30 ms, 4 V).

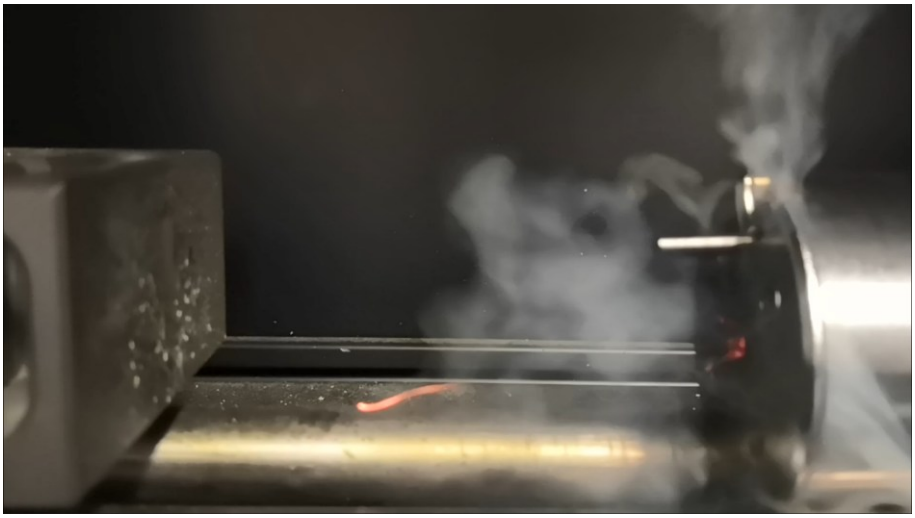

Figure S58. Decomposition of $[Cu(HTNO)_2(1\text{-}PryTz)_2]$ during laser irradiation (10 A, 30 ms, 4 V).

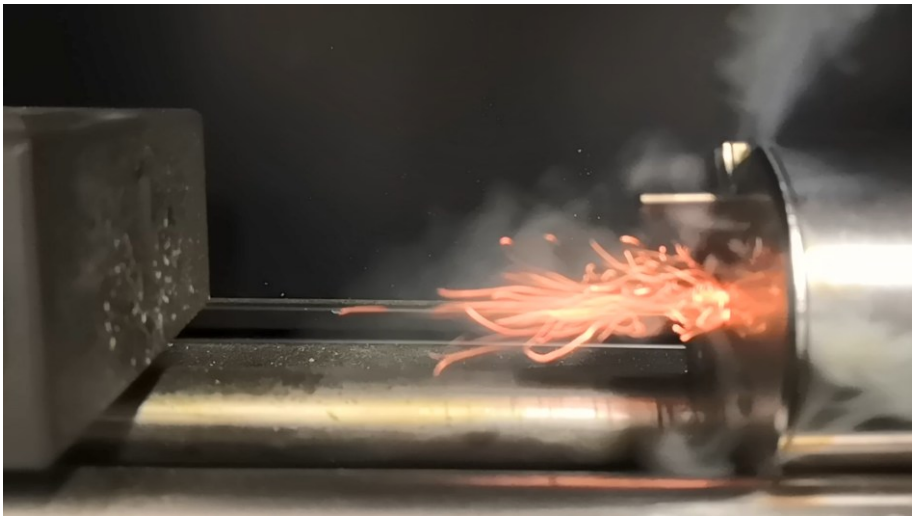

Figure S59. Decomposition of $[Cu(TNR)(2\text{-}PryTz)_2]$ during laser irradiation (10 A, 30 ms, 4 V).

Figure S60. Decomposition of $[Cu(DCA)_2(1\text{-PryTz})_2]$ during laser irradiation (10 A, 30 ms, 4 V).

5.6.9 General Methods

All chemicals and solvents were employed as received (Sigma-Aldrich, Fluka, Acros, ABCR). ^{1}H, ^{13}C{^{1}H}, and ^{15}N spectra were recorded at ambient temperature using a JEOL Bruker 27400, Eclipse 270, JEOL EX 400 or a JEOL Eclipse 400 instrument. The chemical shifts quoted in ppm in the text refer to typical standards such as tetramethylsilane (^{1}H, ^{13}C) nitromethane (^{14}N,^{15}N) in acetonitrile-d_3 or acetone-d_6 as the solvent. Endothermic and exothermic events of the described compounds, which indicate melting, loss of crystal water or decomposition, are given as the extrapolated onset temperatures. The samples were measured in a range of 25–400 °C at a heating rate of 5 °C min^{-1} through differential thermal analysis (DTA) with an OZM Research DTA 552-Ex instrument. Infrared spectra were measured with pure samples on a Perkin-Elmer BXII FT-IR system with a Smith DuraSampler IR II diamond ATR. Determination of the carbon, hydrogen, and nitrogen contents was carried out by combustion analysis using an Elementar Vario El (nitrogen values determined are often lower than the calculated ones' due to their explosive behavior). Impact sensitivity tests were carried out according to STANAG 4489[S23] with a modified instruction[S24] using a BAM (Bundesanstalt für Materialforschung) drophammer.[S25] Friction sensitivity tests were carried out according to STANAG 4487[S28] with a modified instruction[S29] using the BAM friction tester. [S25,S26] The classification of the tested compounds results from the "UN Recommendations on the Transport of Dangerous Goods". [S30,S31] Additionally, all compounds were tested upon the sensitivity toward electrical discharge using the OZM Electric Spark XSpark10 device. [S26] Energetic properties have been calculated with the EXPLO5 6.05.04 computer code[S32] using the, to RT converted, X-ray density and calculated solid state heats of formation. These were computed by the atomization method as described in recently published papers. Electronic enthalpies were calculated with the Gaussian09 software[S13] suite using the CBS-4M method.

5.6.10 Experimental Section

Caution! All investigated compounds are energetic materials and some of them show sensitivities towards various stimuli (e.g. elevated temperatures, impact, friction or electronic discharge). Although no hazards occurred, proper security precautions (safety glasses, face shield, earthed equipment and shoes, leather jacket, Kevlar sleeves, and earplugs) have to be worn while synthesizing and handling the described compounds.

Propargyltetrazole

1- and 2-Propargyltetrazole were synthesized in a modified procedure from Popova *et al.* by adding a 80 % solution of propargyl bromide (12.0 mL, 108 mmol, 1.00 eq.) to a solution of tetrazole (11.4 g, 162 mmol, 1.50 eq.) and sodium hydroxide (6.49 mL, 162 mmol, 1.50 eq.) in acetonitrile (200 mL) and water (20 mL).[S33] The solution was heated to 60 °C for 24 h. After cooling down the solvent was evaporated under reduced pressure followed by purification via column chromatography (SiO_2, iHex/EtOAc, 9:1, gradient: 5 %/L) to obtain 1-PryTz (5.03 g, 46.5 mmol, 43 %) and 2-PryTz (1.11 g, 10.3 mmol, 10 %) in form of yellow oils.

1-PryTz (1)

^{1}H NMR (d_3-MeCN, 25 °C) δ 9.18 (s, 1H, *H*CN_4), 5.40–5.39 (d, 2H, C*H*$_2$), 2.97–2.96 (t, 1H, C*H*) ppm. **^{13}C NMR** (d_3-MeCN, 25 °C) δ 143.9 (*C*N_4), 76.9 (*C*H), 75.2 (CH_2-*C*-CH), 38.5 (*C*H_2) ppm. **^{15}N NMR** (d_3-MeCN, 25 °C) δ 10.4 (d, *N3*, J = 3.2 Hz), −14.6 (s, *N2*), −53.2 (d, *N4*, J = 12.2 Hz), −148.8 (d, *N1*, J = 9.3 Hz) ppm. **DTA** (5 °C min^{-1}) onset: 187 °C (exothermic). **IR** (ATR, cm^{-1}): $\tilde{\upsilon}$ = 3285 (m), 3276 (m), 3137 (w), 2980 (w), 2954 (vw), 2135 (w), 1752 (vw), 1717 (w), 1678 (w), 1630 (vw), 1482 (m), 1428 (m), 1349 (w), 1340 (m), 1293 (w), 1255 (w), 1168 (s), 1101 (vs), 1024 (w), 968 (m), 954 (m), 874 (m), 750 (vs), 719 (s), 650 (vs), 459 (w). **EA** ($C_4H_4N_4$, 108.10 g mol^{-1}) calc.: C 44.44 H 3.73 N 51.83 %, found C 43.46 H 4.13 N 48.76 %. R_f = 0.17 (iHex/EtOAc, 8:2, $KMnO_4$). **BAM drop hammer**: 20 J. **Friction tester**: >360 N.

2-PryTz (2)

^{1}H NMR (d_3-MeCN, 25 °C) δ 8.65 (s, 1H, *H*CN_4), 5.55–5.54 (d, 2H, C*H*$_2$), 2.91–2.90 (t, 1H, C*H*) ppm. **^{13}C NMR** (d_3-MeCN, 25 °C) δ 154.1 (*C*N_4), 76.9 (*C*H), 75.3 (CH_2-*C*-CH), 43.3 (*C*H_2) ppm. **^{15}N NMR** (d_3-MeCN, 25 °C) δ −2.2 (s, *N3*), −47.4 (d, *N4*, J = 12.6 Hz),

−76.6 (d, *N1*, *J* = 15.0 Hz), −101.9 (s, *N2*) ppm. **DTA** (5 °C min^{-1}) onset: 195 °C (endothermic). **IR** (ATR, cm^{-1}): $\tilde{\nu}$ = 3288(w), 3281(w), 3146(vw), 2988(w), 2952(vw), 2138(w), 1736(vw), 1624(vw), 1453(w), 1428(w), 1355(s), 1283(s), 1193(m), 1143(w), 1129(m), 1027(s), 1008(m), 955(m), 884(m), 766(vs), 706(s), 675(vs), 653(s), 459(m). **EA** ($C_4H_4N_4$, 108.10 g mol^{-1}) calc.: C 44.44 H 3.73 N 51.83 %, found C 44.13 H 3.47 N 51.33 %. R_f = 0.51 (iHex/EtOAc, 8:2, $KMnO_4$). **BAM drop hammer**: <1 J. **Friction tester**: >360 N.

1-((1*H*-1,2,3-triazol-4-yl)methyl)-1*H*-tetrazole (3)

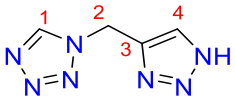

Figure S61. Assignment of numbers to the carbon atoms of compound **3** for clarification of the NMR spectra.

Compound **3** was produced by application of the Banert cascade. [S34, S35] A 80 % propargylbromide solution (12.4 mL, 112 mmol, 1.12 eq.) was added to a solution of sodium azide (6.50 g, 100 mmol, 1.00 eq.) in 90 mL of water and 220 mL of 1,4-dioxane. The resulting solution was stirred at room temperature for 24 h. Concentrated ammonia (1.00 L) was added and the solution was heated to 70 °C for three days. The resulting solution was evaporated *in vacuo*. Sodium azide (6.50 g, 100 mmol, 1.00 eq.) and triethyl orthoformate (50.0 mL, 300 mmol, 3.00 eq.) were added to the residue. Under vigorous stirring, glacial acetic acid (23.0 mL, 400 mmol, 4.00 eq.) was added dropwise. The resulting suspension was heated to 80 °C overnight. Evaporation under reduced pressure resulted in a yellow oil, to which little ethylacetate was added. The solution was allowed to slowly evaporate at room temperature which left a yellow solid. The solid was dissolved in water and left at 4 °C, yielding compound **3** (0.91 g, 6.02 mmol, 6 %) as light yellow needles, suitable for X-Ray diffraction analysis. **^{1}H NMR** (d_6-Acetone, 25 °C) δ 14.34 (br, 1H, N*H*), 9.22 (s, 1H, C1*H*), 7.97 (s, C4*H*), 5.94 (s, 2H, C2H_2) ppm. **^{13}C NMR** (d_6-Acetone, 25 °C) δ 144.3 (*C1*), 142.0 (*C3*) 133.9 (*C4*), 43.6 (*C2*) ppm. **DTA** (5 °C min^{-1}) onset: 131 °C (endothermic), 192 °C (exothermic). **IR** (ATR, cm^{-1}): $\tilde{\nu}$ = 3279 (m), 3267 (m), 3254 (m), 3240 (m), 3235 (m), 3203 (m), 3143 (m), 3129 (m), 3093 (m), 3005 (m), 2005 (m), 1557 (m), 1486 (m), 1463 (m), 1438 (m), 1423 (m), 1371 (m), 1360 (m), 1340 (m), 1301 (m), 1283 (m), 1251 (m), 1225 (s), 1174 (s), 1143 (m), 1097 (s), 1061 (s), 1028 (m), 979 (m), 970 (m), 921 (m), 869 (m), 819 (m), 785 (vs), 725 (s), 684 (vs), 657 (s), 650 (s),

632 (m), 492 (w), 471 (w), 429 (w), 408 (w), 725 (s), 684 (vs), 657 (s), 650 (s), 632 (m), 492 (w), 471 (w), 429 (w), 408 (w). **EA** ($C_4H_5N_7$, 151.13 g mol^{-1}) calc.: C 31.79 H 3.33 N 64.88 %, found C 31.89 H 3.46 N 64.71 %. **HRMS** (ESI) m/z: $[M-H]^-$ calc. for $C_4H_4N_7$: 150.05337; found: 150.05341. **BAM drop hammer**: >40 J. **Friction tester**: >360 N. **ESD**: >1.5 J.

1-((1-(2-(1*H*-tetrazol-1-yl)ethyl)-1*H*-1,2,3-triazol-4-yl)methyl)-1*H*-tetrazole (4)

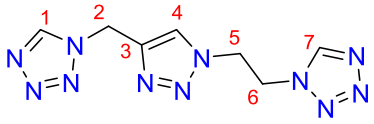

Figure S62. Assignment of numbers to the carbon atoms of compound **4** for clarification of the NMR spectra.

1-Azidoethyltetrazole (1.39 g, 10.0 mmol, 1.00 eq.) was produced according to the literature[S36] and dissolved in 100 mL of deionized water. 1-Propargyltetrazole (1.08 g, 10.0 mmol, 1.00 eq.), copper(II) sulfate pentahydrate (0.10 g, 0.40 mmol, 0.04 eq.) and (+)-sodium-L-ascorbate (0.50 g, 2.50 mmol, 0.25 eq.) were added and the solution was stirred overnight at room temperature. Half of the solvent was evaporated *in vacuo*. The solution was extracted with EtOAc (3×200 mL) and the combined organic phases were dried over sodium sulfate. After evaporation of the solvent, the obtained solid was suspended in EtOH, filtered off and washed with EtOH and Et_2O to yield compound **4** (1.34 g, 5.42 mmol, 54 %) as a colorless solid. Single crystals suitable for X-Ray diffraction analysis could be obtained by recrystallizing little substance from water. **^{1}H NMR** (d_6-Acetone, 25 °C) δ 9.12 (s, 1H, C1*H*), 8.96 (s, 1H, C7*H*), 8.08 (s, 1H, C4*H*), 5.84 (s, 2H, C2H_2), 5.193–5.05 (m, 4H, C5H_AH_A'-C6H_BH_B') ppm. **^{13}C NMR** (d_6-Acetone, 25 °C) δ 144.7 (*C7*), 144.3 (*C1*), 142.0 (*C3*), 125.6 (*C4*), 50.18 (*C5*), 48.7 (*C6*), 43.9 (*C2*) ppm. **DTA** (5 °C min^{-1}) onset: 101 °C (endothermic), 194 °C (exothermic). **IR** (ATR, cm^{-1}): $\tilde{\upsilon}$ = 3162 (w), 3134 (m), 3121 (w), 3102 (w), 3084 (w), 3022 (w), 1766 (w), 1741 (w), 1733 (w), 1636 (w), 1560 (w), 1535 (w), 1479 (m), 1466 (m), 1444 (m), 1433 (m), 1378 (w), 1354 (w), 1339 (w), 1314 (w), 1291 (w), 1277 (w), 1253 (m), 1237 (m), 1230 (m), 1206 (w), 1170 (s), 1129 (m), 1101 (vs), 1058 (s), 1039 (m), 1019 (m), 968 (m), 934 (m), 922 (m), 906 (w), 884 (m), 866 (m), 844 (m), 788 (s), 748 (s), 722 (m), 700 (m), 922 (m), 906 (w), 884 (m), 866 (m), 844 (m), 788 (s), 748 (s), 722 (m), 700 (m), 688 (m), 678 (m), 667 (m), 656 (s), 629 (m), 617 (m), 500 (m), 490 (m), 453 (w), 439 (w), 426 (w), 405 (m). **EA** ($C_7H_9N_{11}$, 247.23 g mol^{-1}) calc.: C 34.01 H 3.67 N 62.32 %, found C 34.05 H 3.57

N 60.14 %. **HRMS** (EI) m/z: $[M]^+$ calc. for $C_7H_9N_{11}$: 247.1042; found: 247.1036. **BAM drop hammer**: >40 J. **Friction tester**: >360 N. **ESD**: 1.0 J.

General procedure A for perchlorate complexes

1-or 2-Propargyltetrazole (162 mg, 1.50 mmol, 6.00 eq.) was dissolved in 1 mL of water and added to a solution of the respective perchlorate salt ($Cu(ClO_4)_2 \cdot 6\ H_2O$: 92.6 mg, 0.25 mmol, 1.00 eq., $Fe(ClO_4)_2 \cdot 6\ H_2O$: 90.7 mg, 0.25 mmol, 1.00 eq., $Zn(ClO_4)_2 \cdot 6\ H_2O$: 93.1 mg, 0.25 mmol, 1.00 eq.) in 1 mL of water. After evaporation at rt over 2 weeks, the obtained solids were filtered off via suction filtration and washed with small amounts of cold EtOAc.

General procedure B for complexes with nitroaromatic anions

A suspension of $CuCO_3 \times Cu(OH)_2$ (55.3 mg, 0.25 mmol, 0.50 eq.) and the respective nitroaromatic species (279 mg, 1.00 mmol of H_3TNPG, 245 mg, 1.00 mmol or 123mg, 0.50 mmol of H_2TNR, 229 mg, 1.00 mmol of HPA, 259 mg, 1.00 mmol of H_2TNO) in 5 mL of water was heated to 80 °C until a clear solution was obtained. To this solution, the ligand (1- or 2-PryTz, 108 mg, 1.00 mmol, 2.00 eq.) was added. The solution was kept at 80 °C for 5 min. and then left at room temperature to crystallize for 3 weeks. The resulting suspension was filtered off and washed with little cold water, ethanol and diethyl ether.

General procedure C for complexes with nitroaromatic anions

A suspension of $CuCO_3 \times Cu(OH)_2$ (55.3 mg, 0.25 mmol, 0.50 eq.) and the respective nitroaromatic species (1.00 mmol or 123mg, 0.50 mmol of H_2TNR, 229 mg, 1.00 mmol of HPA, 259 mg, 1.00 mmol of H_2TNO) in 3 mL of water was heated to 80 °C until a clear solution was obtained. To this solution, a solution of the ligand (2-PryTz, 108 mg, 1.00 mmol, 2.00 eq.) in 2 mL of EtOH was added. The solution was kept at 80 °C for 5 min. and then left at room temperature to crystallize for 2 weeks. The resulting suspension was filtered off and washed with little cold water, ethanol and diethyl ether.

$[Cu(1\text{-}PryTz)_6](ClO_4)_2$ (5)

Compound **3** was obtained according to general procedure **A** as a blue solid (0.21 mg, 0.23 mmol, 92 %). **DTA** (5 °C min^{-1}) onset: 79 °C (endothermic), 135 °C (exothermic). **IR** (ATR, cm^{-1}): $\tilde{\upsilon}$ = 3302 (m), 3293 (m), 3286 (m), 3276 (m), 3136 (m), 2025 (m), 1502 (m), 1439 (m), 1426 (m), 1349 (m), 1316 (m), 1302 (w), 1266 (w), 1178 (m), 1156 (m), 1098

(vs), 1079 (vs), 1022 (m), 1007 (m), 985 (m), 979 (m), 966 (m), 956 (m), 945 (m), 892 (m), 750 (s), 713 (m), 683 (s), 649 (s), 622 (vs), 404 (m). **EA** ($C_{24}H_{24}Cl_2CuN_{24}O_8$, 911.06 g mol^{-1}) calc.: C 31.64 H 2.66 N 36.90 %, found C 31.89 H 2.95 N 37.73 %. **BAM drop hammer**: 2 J. **Friction tester**: 5 N (at grain size: 100–500 µm). **ESD**: 25 mJ.

[Fe(1-PryTz)$_6$](ClO$_4$)$_2$ · H$_2$O (6)

Compound **4** was obtained according to general procedure **A** as a brown solid (0.13 g, 0.14 mmol, 56 %). **DTA** (5 °C min^{-1}) onset: 74 °C (endothermic), 168 °C (exothermic). **IR** (ATR, cm^{-1}): $\tilde{\nu}$ = 3499 (vw), 3299 (w), 3280 (w), 3133 (w), 2994 (vw), 2960 (vw), 2140 (vw), 1621 (vw), 1500 (w), 1428 (w), 1349 (w), 1308 (w), 1273 (vw), 1180 (m), 1155 (w), 1098 (s), 1079 (vs), 1024 (w), 992 (m), 956 (w), 944 (w), 897 (w), 754 (m), 716 (m), 684 (m), 649 (s), 622 (vs), 477 (w), 470 (w), 459 (w), 435 (w).**EA** ($C_{24}H_{26}Cl_2FeN_{24}O_9$, 921.38 g mol^{-1}) calc.: C 31.29 H 2.84 N 36.49 %, found C 31.54 H 2.54 N 36.76 %. **BAM drop hammer**: 2 J. **Friction tester**: 6 N (at grain size: 100–500 µm). **ESD**: 50 mJ.

[Zn(1-PryTz)$_6$](ClO$_4$)$_2$ · H$_2$O (7)

Compound **5** was obtained according to general procedure **A** as a colorless solid (0.12 g, 0.13 mmol, 52 %). **DTA** (5 °C min^{-1}) onset: 70 °C (endothermic), 164 °C (exothermic). **IR** (ATR, cm^{-1}): $\tilde{\nu}$ = 3518 (w), 3302 (w), 3291 (w), 3139 (vw), 2991 (vw), 1724 (w), 1629 (vw), 1509 (w), 1500 (vw), 1445 (vw), 1433 (w), 1374 (vw), 1352 (w), 1314 (vw), 1299 (vw), 1250 (vw), 1216 (vw), 1179 (w), 1159 (w), 1100 (s), 1080 (vs), 1026 (w), 994 (m), 951 (w), 933 (w), 895 (w), 848 (vw), 752 (m), 731 (w), 716 (m), 703 (w), 676 (w), 649 (s), 623 (vs), 469 (w).**EA** ($C_{24}H_{26}Cl_2N_{24}O_9Zn$, 930.91 g mol^{-1}) calc.: C 30.97 H 2.82 N 36.11 %, found C 30.78 H 2.70 N 36.52%. **BAM drop hammer**: 2 J. **Friction tester**: 15 N (at grain size: 100–500 µm). **ESD**: 50 mJ.

[Cu(H$_2$TNPG)$_2$(1-PryTz)$_4$] · ½ H$_2$O (8)

Compound **6** was obtained according to general procedure **B** as a green solid (0.30 g, 0.29 mmol, 59 %). **DTA** (5 °C min^{-1}) onset: 145 °C (exothermic). **IR** (ATR, cm^{-1}): $\tilde{\nu}$ = 3283 (w), 3141 (w), 1645 (s), 1569 (m), 1515 (s), 1506 (s), 1496 (s), 1454 (w), 1446 (m), 1436 (w), 1420 (m), 1335 (vs), 1284 (m), 1179 (vs), 1158 (vs), 1136 (s), 1094 (s), 1024 (w), 1005 (m), 969 (w), 958 (w), 945 (w), 917 (m), 904 (m), 888 (w), 834 (m), 817 (m), 784 (m), 760 (m), 748 (s), 736 (s), 712 (s), 694 (s), 671 (s), 667 (s), 651 (vs), 632 (s), 590

(m), 578 (w). **EA** ($C_{28}H_{20.5}CuN_{22}O_{18.25}$, 1020.65 g mol^{-1}) calc.: C 33.10 H 1.98 N 30.33 %, found C 33.04 H 1.79 N 30.47 %. **BAM drop hammer**: <1 J. **Friction tester**: 80 N (at grain size: 100–500 µm). **ESD**: 160 mJ.

[Cu(HTNR)$_2$(1-PryTz)$_2$] (9)

Compound **7** was obtained according to general procedure **B** as a green solid (0.31 g, 0.40 mmol, 80 %). **DTA** (5 °C min^{-1}) onset: 172 °C (exothermic). **IR** (ATR, cm^{-1}): $\tilde{\upsilon}$ = 3283 (m), 3149 (w), 3060 (w), 2981 (w), 2942 (w), 2142 (w), 1633 (m), 1561 (s), 1536 (vs), 1511 (s), 1482 (m), 1453 (m), 1426 (m), 1359 (s), 1341 (s), 1334 (s), 1311 (s), 1281 (s), 1211 (m), 1170 (s), 1095 (vs), 1030 (m), 1012 (m), 973 (m), 945 (m), 927 (m), 898 (m), 830 (w), 782 (m), 765 (m), 744 (s), 715 (s), 697 (vs), 681 (s), 651 (s), 577 (w), 563 (w), 538 (w), 514 (w), 497 (w), 468 (w), 458 (w), 440 (m), 651 (s), 577 (w), 563 (w), 538 (w), 514 (w), 497 (w), 468 (w), 458 (w), 440 (m), 431 (m), 421 (w), 406 (w). **EA** ($C_{20}H_{12}CuN_{14}O_{16}$, 766.99 g mol^{-1}) calc.: C 31,28 H 1.58 N 25.54 %, found C 31.05 H 1.55 N 25.60 %. **BAM drop hammer**: <1 J. **Friction tester**: 96 N (at grain size: 100–500 µm). **ESD**: 160 mJ.

[Cu(1-PryTz)$_2$(TNR)] (10)

Compound **8** was prepared according to general procedure **B** and precipitated out of the solution within one day as a green solid (0.17 g, 0.33 mmol, 65 %). **DTA** (5 °C min^{-1}) onset: 150 °C (exothermic). **IR** (ATR, cm^{-1}): $\tilde{\upsilon}$ = 3310 (w), 3247 (w), 3156 (w), 3139 (w), 2137 (w), 1582 (s), 1553 (s), 1524 (s), 1481 (m), 1445 (s), 1423 (s), 1368 (m), 1342 (m), 1294 (vs), 1241 (s), 1171 (s), 1109 (s), 1095 (vs), 1031 (w), 1012 (s), 972 (m), 935 (m), 917 (w), 898 (m), 881 (m), 792 (m), 774 (m), 749 (s), 735 (m), 708 (vs), 674 (s), 650 (s), 584 (m), 556 (w), 445 (m), 418 (s), 409 (m). **EA** ($C_{14}H_9CuN_{11}O_8$, 522.84 g mol^{-1}) calc.: C 32.16 H 1.74 N 29.47 %, found C 32.12 H 1.71 N 29.37 %. **BAM drop hammer**: <1 J. **Friction tester**: 40 N (at grain size: 100–500 µm). **ESD**: 250 mJ.

[Cu(PA)$_2$(1-PryTz)$_2$] (11)

Compound **9** was prepared according to general procedure **B** as a green solid (0.30 g, 0.41 mmol, 81 %). **DTA** (5 °C min^{-1}) onset: 86 °C (endothermic), 157 °C (exothermic). **IR** (ATR, cm^{-1}): $\tilde{\upsilon}$ = 3296 (w), 3145 (w), 3105 (w), 3083 (vw), 3001 (w), 1636 (w), 1606 (s), 1577 (s), 1540 (s), 1509 (s), 1470 (m), 1448 (m), 1429 (m), 1418 (m), 1338 (vs), 1279 (s),

1275 (vs), 1178 (m), 1167 (s), 1157 (m), 1095 (s), 1018 (s), 948 (m), 918 (s), 898 (m), 841 (m), 826 (w), 790 (s), 754 (m), 744 (s), 715 (vs), 688 (s), 663 (s), 655 (vs), 604 (w), 590 (w), 576 (w), 551 (m), 535 (m), 521 (w), 504 (m), 492 (w), 467 (m), 604 (w), 590 (w), 576 (w), 551 (m), 535 (m), 521 (w), 504 (m), 492 (w), 467 (m), 452 (w), 445 (w), 439 (w), 416 (m).**EA** ($C_{20}H_{12}CuN_{14}O_{14}$, 735.00 g mol^{-1}) calc.: C 32.64 H 1.64 N 26.65 %, found C 32.36 H 1.72 N 26.98 %. **BAM drop hammer**: 2 J. **Friction tester**: 160 N (at grain size: 100–500 µm). **ESD**: 250 mJ.

[Cu(HTNO)$_2$(1-PryTz)$_2$] (12)

Compound **10** was prepared according to general procedure **B** as a brown solid (0.27 g, 0.34 mmol, 68 %). **DTA** (5 °C min^{-1}) onset: 177 °C (exothermic). **IR** (ATR, cm^{-1}): $\tilde{\nu}$ = 3306 (w), 3254 (w), 3157 (w), 3141 (w), 1617 (m), 1551 (s), 1528 (vs), 1524 (vs), 1509 (s), 1502 (s), 1467 (m), 1455 (m), 1416 (m), 1364 (s), 1311 (s), 1280 (m), 1180 (s), 1164 (vs), 1144 (s), 1094 (s), 1083 (m), 1060 (m), 1041 (m), 1019 (m), 972 (w), 952 (w), 906 (m), 887 (w), 828 (m), 809 (m), 787 (m), 745 (m), 711 (m), 696 (vs), 683 (s), 647 (vs), 613 (m), 605 (m), 599 (m), 531 (w), 502 (w), 493 (w), 474 (w), 683 (s), 647 (vs), 613 (m), 605 (m), 599 (m), 531 (w), 502 (w), 493 (w), 474 (w), 459 (w), 431 (w), 419 (m), 403 (m). **EA** ($C_{22}H_{16}CuN_{14}O_{16}$, 796.00 g mol^{-1}) calc.: C 33.20 H 2.03 N 24.62 %, found C 32.95 H 1.82 N 25.16 %. **BAM drop hammer**: <1 J. **Friction tester**: 120 N (at grain size: 100–500 µm). **ESD**: 90 mJ.

[Cu(H$_2$TNPG)$_2$(2-PryTz)$_4$] (13)

Compound **11** was prepared according to general procedure **B** as a green solid (0.18 g, 0.18 mmol, 35 %) and crystallized within 7 days. **DTA** (5 °C min^{-1}) onset: 123 °C (endothermic to exothermic). **IR** (ATR, cm^{-1}): $\tilde{\nu}$ = 3300 (w), 3275 (w), 3250 (vw), 3163 (w), 3156 (w), 3000 (w), 2983 (w), 2167 (w), 2142 (vw), 1744 (vw), 1651 (s), 1646 (s), 1618 (w), 1574 (m), 1538 (m), 1525 (m), 1505 (s), 1495 (s), 1470 (m), 1434 (m), 1429 (w), 1372 (m), 1335 (s), 1313 (s), 1302 (s), 1195 (s), 1181 (s), 1158 (vs), 1136 (vs), 1085 (m), 1050 (s), 1028 (m), 972 (m), 959 (m), 952 (w), 915 (s), 896 (m), 837 (m), 815 (s), 787 (s), 770 (s), 745 (s), 732 (s), 952 (w), 915 (s), 896 (m), 837 (m), 815 (s), 787 (s), 770 (s), 745 (s), 732 (s), 721 (s), 696 (vs), 678 (vs), 656 (vs), 620 (m), 602 (m), 574 (m), 557 (m), 543 (w), 534 (w), 510 (m), 498 (m), 484 (m), 477 (m), 461 (m), 430 (w), 420 (w), 407 (w). **EA** ($C_{28}H_{20}CuN_{22}O_{18}$, 1016.15 g mol^{-1}) calc.: C 33.10 H 1.98 N 30.33 %, found C 32.97 H

2.13 N 30.05 %. **BAM drop hammer**: <1 J. **Friction tester**: 40 N (at grain size: 100–500 µm). **ESD**: 250 mJ.

[Cu(2-PryTz)$_2$(TNR)] (14)

Compound **12** was prepared according to general procedure **C** as a green solid (0.19 g, 0.36 mmol, 72 %), which precipitated out of the solution within one day. Single crystals suitable for X-ray diffraction analysis were obtained from further evaporation of the mother liquor. **DTA** (5 °C min^{-1}) onset: 150 °C (exothermic). **IR** (ATR, cm^{-1}): $\tilde{\nu}$ = 3285 (w), 3221 (w), 3162 (w), 2997 (w), 1736 (w), 1612 (m), 1589 (m), 1560 (w), 1542 (m), 1525 (s), 1493 (m), 1468 (m), 1448 (m), 1422 (m), 1366 (m), 1353 (m), 1286 (s), 1230 (vs), 1208 (s), 1196 (s), 1172 (m), 1146 (m), 1138 (s), 1113 (s), 1055 (m), 1028 (m), 960 (m), 945 (w), 930 (w), 907 (w), 898 (w), 779 (s), 767 (m), 735 (w), 709 (s), 698 (s), 677 (s), 654 (m), 582 (w), 555 (w), 532 (vw), 503 (w), 470 (w), 709 (s), 698 (s), 677 (s), 654 (m), 582 (w), 555 (w), 532 (vw), 503 (w), 470 (w), 457 (w), 419 (w), 404 (m). **EA** ($C_{14}H_9CuN_{11}O_8$, 522.84 g mol^{-1}) calc.: C 32.16 H 1.74 N 29.47 %, found C 32.20 H 1.75 N 29.52 %. **BAM drop hammer**: <1 J. **Friction tester**: 48 N (at grain size: 100–500 µm). **ESD**: 200 mJ.

[Cu(PA)$_2$(2-PryTz)$_2$] (15)

Compound **13** was prepared according to general procedure **C** as a green solid (0.24 g, 0.33 mmol, 65 %). **DTA** (5 °C min^{-1}) onset: 142 °C (exothermic). **IR** (ATR, cm^{-1}): $\tilde{\nu}$ = 3297 (m), 3158 (w), 3090 (w), 2979 (w), 2950 (w), 1641 (w), 1608 (m), 1574 (m), 1551 (s), 1524 (s), 1506 (s), 1482 (s), 1435 (m), 1431 (m), 1368 (m), 1354 (s), 1325 (s), 1309 (s), 1276 (vs), 1210 (m), 1197 (m), 1172 (s), 1147 (s), 1080 (m), 1054 (m), 1027 (m), 973 (m), 942 (m), 930 (m), 922 (s), 916 (s), 895 (m), 854 (m), 824 (w), 781 (m), 753 (s), 743 (s), 729 (m), 714 (s), 696 (vs), 675 (s), 642 (vs), 559 (m), 781 (m), 753 (s), 743 (s), 729 (m), 714 (s), 696 (vs), 675 (s), 642 (vs), 559 (m), 546 (s), 516 (m), 486 (m), 475 (m), 467 (m), 447 (w), 432 (m), 409 (m). **EA** ($C_{20}H_{12}CuN_{14}O_{14}$, 735.95 g mol^{-1}) calc.: C 32.64 H 1.64 N 26.65 %, found C 32.40 H 1.68 N 26.36 %. **BAM drop hammer**: 2 J. **Friction tester**: 120 N (at grain size: 100–500 µm). **ESD**: 160 mJ.

[Cu(HTNO)$_2$(2-PryTz)$_2$] (16)

Compound **14** was prepared according to general procedure **C** as a brown solid (0.32 g, 0.40 mmol, 80 %). **DTA** (5 °C min^{-1}) onset: 164 °C (exothermic). **IR** (ATR, cm^{-1}): $\tilde{\nu}$ =

3291 (w), 3174 (w), 2993 (w), 1795 (vw), 1619 (m), 1552 (m), 1519 (s), 1467 (m), 1431 (m), 1403 (m), 1378 (m), 1359 (s), 1305 (m), 1266 (m), 1204 (m), 1159 (s), 1151 (s), 1132 (s), 1066 (m), 1055 (m), 1030 (m), 967 (m), 955 (m), 917 (w), 899 (m), 827 (w), 810 (m), 788 (m), 774 (m), 753 (m), 741 (m), 717 (m), 698 (s), 676 (vs), 662 (s), 647 (s), 634 (s), 609 (s), 587 (m), 555 (m), 542 (m), 469 (m), 455 (m), 662 (s), 647 (s), 634 (s), 609 (s), 587 (m), 555 (m), 542 (m), 469 (m), 455 (m), 447 (m), 433 (m), 420 (w). **EA** ($C_{22}H_{16}CuN_{14}O_{16}$, 796.00 g mol^{-1}) calc.: C 33.20 H 2.03 N 24.62 %, found C 33.11 H 2.18 N 24.54 %. **BAM drop hammer**: <1 J. **Friction tester**: 72 N (at grain size: 100–500 µm). **ESD**: 200 mJ.

[Cu(DCA)$_2$(1-PryTz)$_2$] (17)

Copper(II) nitrate trihydrate (0.24 g, 1.00 mmol, 1.00 eq.) was dissolved in 4 mL of water. 1-Propargyltetrazole (0.43 g, 4.00 mmol, 4.00 eq.) was added and the solution was stirred for 5 minutes at 60 °C. A solution of sodium dicyanamide (0.18 g, 2.00 mmol, 2.00 eq.) in 1 mL of water was added dropwise. The resulting solution was stirred for 30 minutes at 60 °C which led to precipitation of light blue [Cu(DCA)$_2$(1-PryTz)$_2$] (0.33 g, 0.80 mmol, 80 %), which was filtered off, washed with water and dried on air. Single crystals suitable for X-Ray diffraction analysis were obtained by further evaporation of the mother liquor. **DTA** (5 °C min^{-1}) onset: 120 °C (exothermic). **IR** (ATR, cm^{-1}): $\tilde{\upsilon}$ = 3209 (m), 3128 (w), 3094 (w), 2982 (w), 2942 (vw), 2297 (m), 2240 (s), 2182 (vs), 2127 (m), 1497 (m), 1428 (m), 1354 (s), 1311 (m), 1214 (w), 1179 (m), 1098 (s), 1019 (s), 968 (w), 930 (m), 892 (m), 743 (m), 722 (s), 713 (s), 671 (m), 645 (vs), 535 (m), 513 (s), 500 (s), 483 (m), 432 (w), 411 (vw). **EA** ($C_{12}H_8CuN_{14}$, 411.84 g mol^{-1}) calc.: C 35.00 H 1.96 N 47.62 %, found C 34.59 H 2.31 N 47.77 %. **BAM drop hammer**: 4 J. **Friction tester**: >360 N (at grain size: 100–500 µm). **ESD**: 90 mJ.

Ag(1-PryTz) (18)

Compound **18** was produced in a modified literature procedure.[S37] 1-PryTz (0.51 g, 4.73 mmol, 1.00 eq.) was dissolved in a mixture of 5 mL of deionized water and 5 mL concentrated ammonia. Silvernitrate (0.80 g, 4.73 mmol, 1.00 eq.) was then added in portions, which led to the precipitation of a colorless solid. After stirring for 5 minutes at room temperature, the suspension filtered off and washed with water, ethanol and diethyl ether to yield **18** (0.85 g, 3.95 mmol, 84 %) as a colorless solid. **DTA** (5 °C min^{-1}) onset: 124 °C (exothermic). **IR** (ATR, cm^{-1}): $\tilde{\upsilon}$ = 3139 (w), 3110 (w), 2981 (w), 2949 (vw), 1477 (w), 1435 (w), 1424 (w), 1410 (w), 1333 (m), 1287 (w), 1252 (w), 1181 (m), 1174 (s), 1149

(w), 1100 (s), 1060 (vw), 1021 (vw), 970 (m), 945 (w), 885 (m), 875 (m), 748 (vs), 717 (m), 654 (s), 502 (vw), 492 (vw), 450 (vw), 417 (vw), 404 (w). **EA** ($C_4H_3AgN_4$, 214.96 g mol^{-1}) calc.: C 22.35 H 1.41 N 26.06 %, found C 22.31 H 1.70 N 25.87 %.

5.6.11 References

[S1] CrysAlisPRO (Version 171.33.41), Oxford Diffraction Ltd., **2009**.

[S2] A. Altomare, G. Cascarano, C. Giacovazzo, and A. Guagliardi, *J. Appl. Crystallogr.*, **1992**, *26*, 343.

[S3] A. Altomare, G. Cascarano, C. Giacovazzo, A. Guagliardi, A. G. G. Moliterni, M. C. Burla, G. Polidori, M. Camalli and R. Spagna, SIR97, **2003**.

[S4] A. Altomare, M. C. Burla, M. Camalli, G. L. Cascarano, C. Giacovazzo, A. Guagliardi, A. G. G. Moliterni, G. Polidori and R. Spagna, *J. Appl. Crystallogr.*, **1999**, *32*, 115.

[S5] G. M. Sheldrick, SHELXL-97, University of Göttingen, Germany, **1997**.

[S6] G. M. Sheldrick, *Acta Crystallogr. Sect. A*, **2008**, *64*, 112.

[S7] G. M. Sheldrick, *Acta Crystallogr. Sect. A*, **2015**, *71*, 3–8.

[S8] A. L. Spek, PLATON, Utrecht University, The Netherlands, **1999**.

[S9] L.J. Farrugia, *J. Appl. Cryst.*, **2012**, *45*, 849.

[S10] O. V. Dolomanov, L. J. Bourhis, R. J. Gildea, J. A. K. Howard and H. Puschmann, J. *Appl. Cryst.*, **2009**, *42*, 339–341.

[S11] Empirical absorption correction using spherical harmonics, implemented in SCALE3 ABSPACK scaling algorithm (CrysAlisPro Oxford Diffraction Ltd., Version 171.33.41, **2009**).

[S12] APEX3, Bruker AXS Inc., Madison, Wisconsin, USA.

[S13] M. J. Frisch, G. W. Trucks, H. B. Schlegel, G. E. Scuseria, M. A. Robb, J. R. Cheeseman, G. Scalmani, V.Barone, B. Mennucci, G. A. Petersson, H. Nakatsuji, M. Caricato, X. Li, H.P. Hratchian, A. F. Izmaylov, J. Bloino, G. Zheng, J. L. Sonnenberg, M. Hada, M. Ehara, K. Toyota, R. Fukuda, J. Hasegawa, M. Ishida, T. Nakajima, Y. Honda, O. Kitao, H. Nakai, T. Vreven, J. A. Montgomery, Jr., J. E. Peralta, F. Ogliaro, M. Bearpark, J. J. Heyd, E. Brothers, K. N. Kudin, V. N. Staroverov, R. Kobayashi, J. Normand, K. Raghavachari, A. Rendell, J. C. Burant, S. S. Iyengar, J. Tomasi, M. Cossi, N. Rega, J. M. Millam, M.Klene, J. E. Knox, J. B. Cross, V. Bakken, C. Adamo, J.

Jaramillo, R. Gomperts, R. E. Stratmann, O. Yazyev, A. J. Austin, R. Cammi, C. Pomelli, J. W. Ochterski, R. L. Martin, K. Morokuma, V. G. Zakrzewski, G. A. Voth, P. Salvador, J. J. Dannenberg, S. Dapprich, A. D. Daniels, O. Farkas, J.B. Foresman, J. V. Ortiz, J. Cioslowski and D. J. Fox, Gaussian 09 A.02, Gaussian, Inc., Wallingford, CT, USA, **2009**.

[S14] J. W. Ochterski, G. A. Petersson and J. A. Montgomery Jr., *J. Chem. Phys.*, **1996**, *104*, 2598–2619.

[S15] J. A. Montgomery Jr., M. J. Frisch, J. W. Ochterski and G. A. Petersson, *J. Chem. Phys.*, **2000**, *112*, 6532–6542.

[S16] L. A. Curtiss, K. Raghavachari, P. C. Redfern and J. A. Pople, *J. Chem. Phys.*, **1997**, *106*, 1063–1079.

[S17] E. F. C. Byrd and B. M. Rice, *J. Phys. Chem. A*, **2006**, *110*, 1005–1013.

[S18] B. M. Rice, S. V. Pai and J. Hare, *Comb. Flame*, **1999**, *118*, 445–458.

[S19] P. J. Lindstrom and W. G. Mallard, NIST Standard Reference Database Number 69, http://webbook.nist.gov/chemistry/, (accessed Mai 2022).

[S20] M. S. Westwell, M. S. Searle, D. J. Wales and D. H. Williams, *J. Am. Chem. Soc*. **1995**, *117*, 5013–5015.

[S21] F. Trouton, *Philos. Mag.* **1884**, *18*, 54–57.

[S22] Spackman, P. R.; Turner, M. J.; McKinnon, J. J.; Wolff, S. K.; Grimwood, D. J.; Jayatilaka, D.; Spackman, M. A., *J. Appl. Cryst.* **2021**, *54* (3), 1006–1011.

[S23] NATO standardization agreement (STANAG) on explosives, impact sensitivity tests, no. 4489, 1st ed., Sept. 17, 1999.

[S24] WIWEB-Standardarbeitsanweisung 4-5.1.02, Ermittlung der Explosionsgefährlichkeit, hier der Schlagempfindlichkeit mit dem Fallhammer, Nov. 8, 2002.

[S25] BAM, http://www.bam.de, (accessed Mai 2022).

[S26] OZM, http://www.ozm.cz, (accessed Mai 2022).

[S27] Military Standard 1751A (MIL-STD-1751A): safety and performance tests for qualification of explosives (high explosives, propellants and pyrotechnics), method 1016, Dec. 11, 2001.

[S28] NATO standardization agreement (STANAG) on explosive, friction sensitivity tests, no. 4487, 1st ed., Aug. 22, 2002.

[S29] WIWEB-Standardarbeitsanweisung 4-5.1.03, Ermittlung der Explosionsgefährlichkeit oder der Reibeempfindlichkeit mit dem Reibeapparat, Nov. 8, 2002.

[S30] UN Model Regulation: Recommendations on the Transport of Dangerous Goods – Manual of Tests and Criteria, section 13.4.2.3.3, 2015.

[S31] Impact: insensitive > 40 J, less sensitive ≥ 35 J, sensitive ≥ 4 J, very sensitive ≤ 3 J; Friction: insensitive > 360 N, less sensitive = 360 N, sensitive < 360 N and > 80 N, very sensitive ≤ 80 N, extremely sensitive ≤ 10 N. According to the UN Recommendations on the Transport of Dangerous Goods, 5th ed., **2009**.

[S32] M. Sućeska, EXPLO5 Version 6.05 User's Guide. Zagreb, Croatia: OZM; **2018**.

[S33] E. A. Popova, G. K. Ovsepyan, A. V. Protas, E. B. Erkhitueva, M. K. Kukhanova, Y. L. Yesaulkova, V. V. Zarubaev, G. L. Starova, R. V. Suezov, A. V. Eremin, V. A. Ostrovskii, R. E. Trifonov, *Nucleosides, Nucleotides & Nucleic Acids* **2019**, *38*, 713–731.

[S34] K. Banert, *Chem. Ber.* **1989**, *122*, 911–918.

[S35] K. Banert, M. Hagedorn, C. Hemeltjen, A. Ihle, K. Weigand, H. Priebe, *ARKIVOC* **2016**, *2016*, 338–361.

[S36] M. H. H. Wurzenberger, M. S. Gruhne, M. Lommel, N. Szimhardt, T. M. Klapötke, J. Stierstorfer, *Chem. Asian J.* **2019**, *14*, 2018–2028.

[S37] R. Matyáš, J. Šelešovský, T. Musil, *J. Hazard. Mat.* **2012**, *213–214*, 236–241.

6 1- and 2-Tetrazolylacetonitrile as Versatile Ligands for Laser Ignitable Energetic Coordination Compounds

Simon M. J. Endraß, Thomas M. Klapötke, Marcus Lommel, Jörg Stierstorfer, Martin L. Weidemann, and Melanie Werner

published in *ChemPlusChem,* **2024**

DOI: 10.1002/cplu.202400031

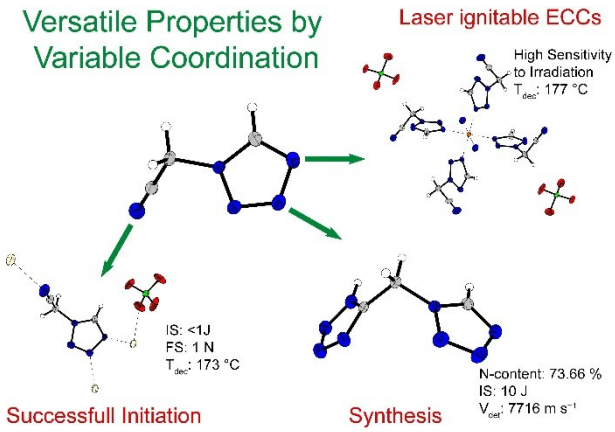

Abstract: 1- and 2-Tetrazolylacetonitrile (1- and 2-TAN) have been produced by the reaction of chloroacetonitrile with 1*H*-Tetrazole under basic conditions. They further were reacted with sodium azide in the presence of zinc(II) chloride to form 5-((1*H*-tetrazol-1-yl)methyl)-1*H*-tetrazole (1-HTMT) and 5-((2*H*-tetrazol-2-yl)methyl)-1*H*-tetrazole (2-HTMT). The nitrogen-rich compounds have been applied as ligands for Energetic Coordination Compounds (ECCs) and show interesting coordinative behavior due to different bridging modes. The structural variability of the compounds has been proved by low temperature X-Ray analysis. The ECCs were analyzed for their sensitivities to provide information about the safety of handling and their capability to serve as primary explosives in detonator setups to replace the commonly used lead styphnate and azide. All colored ECCs were evaluated for their ignitability by laser initiation in translucent polycarbonate primer caps. In addition the spin-crossover characteristics of $[Fe(1\text{-}TAN)_6](ClO_4)_2$ were highlighted by the measurement of the temperature-dependent susceptibility curve.

6.1 Introduction

Nitrile functionalities are versatile and relatively stable groups, which are therefore very interesting for synthetic chemists. They allow the preparation of amines and aldehydes by reduction [1, 2], the formation of amides or carboxylic acids [3], ketones and tertiary amines by reaction with metal-organic Grignard reagents [4], as well as tetrazole moieties by 1,3-dipolar cycloadditions. [5, 6] In addition, the nitrile function allows the formation of coordination compounds with a broad range of transition metals. [7, 8] By combining this easily available side chain functionality with the coordinative behavior and high enthalpy of formation of the tetrazole ring, 2-(1*H*-tetrazol-1-yl)acetonitrile and 2-(2*H*-tetrazol-2-yl)acetonitrile (1- and 2-TAN) can be formed and used for complexation of transition metals. [9, 10] This allows for the formation of high-nitrogen Energetic Coordination Compounds (ECCs) with high positive heats of formation. Due to their slightly different donor sites, they might be characterized as *Janus Head* ligands. [11] This allows the adjustability of the composition of the ECC, due to increase of coordination of the less favored site upon the reduction of equivalents used. While in other cases the goal of the *Janus Head* ligand is to combine functional groups that allow coordination to different cations on the two sites and hereby achieve e.g. catalytic activity, the idea of the TAN ligands was to improve and study the ligand to anion ratio in the ECCs. [12, 13] By adding

the possibility to coordinate to the tetrazole ring as well as the nitrile function, different stoichiometric relations of ligand and oxidizer in the ECCs, and therefore beneficial properties, might be obtained. [14, 15] Figure 1 shows examples of CHN-based tetrazole ligands, which have been previously applied in ECCs. For these cases, only ligand-to-perchlorate ratios of 3:1 were obtained by complexation of Cu(II)-, Fe(II)- and Zn(II)-perchlorate.

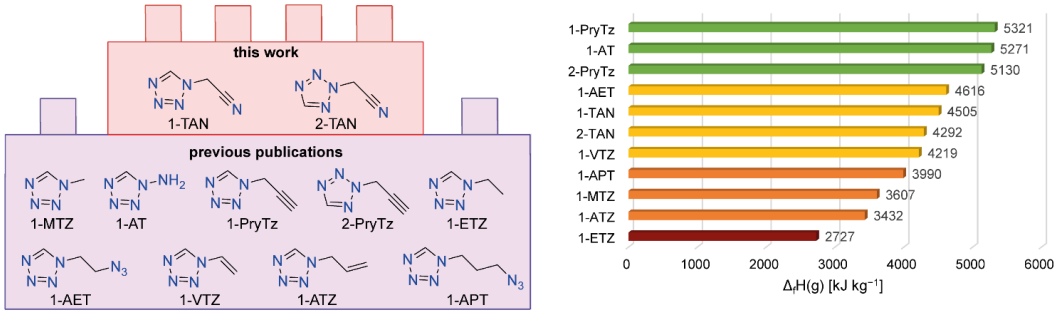

Figure 1. Examples of previously published mono-tetrazole ligands as building blocks for energetic coordination compounds which are based on CHN including their gas-phase enthalpies of formation. [16-21]

This work seeks to introduce 1- and 2-TAN as building blocks for ECCs with the possibility to alter the coordination mode and observe the desired impact on the energetic properties. In addition, previous publications have shown the possibility of creating acidic *C*-linked tetrazoles, which are derived from nitrile functionalities and can be used for the formation of energetic salts. [9, 22-25] Therefore, ring-closure of respectively 1- and 2-TAN was performed to obtain 5-((1*H*-tetrazol-1-yl)methyl)-1*H*-tetrazole (1-HTMT) and 5-((2*H*-tetrazol-2-yl)methyl)-1*H*-tetrazole (2-HTMT). Those two molecules possess high nitrogen contents of above 70 %. Furthermore, they allow for different bridging modes between metal centers and the ratio of ligand to additional anion compared to the *N,N*-ditetrazolylmethane ligands, which have successfully been applied in primary explosives and for laser initiation. [26]

6.2 Results and Discussion

6.2.1 Synthesis

The two ligands of interest (1- and 2-TAN) were obtained by a chloride-tetrazolate exchange reaction. As seen in Scheme 1, the reaction was performed in a mixture of

acetonitrile and acetone (5:1) to exploit the solvent dependent stabilization, and therefore obtain equal amounts of both isomers. [27] After the reaction, purification was conducted by column chromatography in EtOAc/iHex (1:1) to obtain a moderate overall yield of 68 %. Both compounds were obtained as yellow liquids, however samples of **1** crystallized after several weeks of storage at 4 °C. Therefore, the crystal structure and melting point could be obtained.

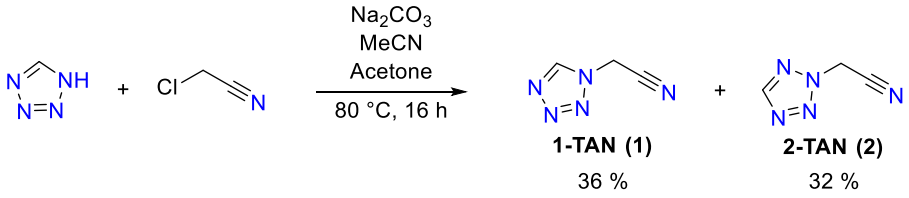

Scheme 1. Synthesis of 1- and 2-tetrazolylacetonitrile.

One important goal of the research on ECCs is their potential to serve as replacements for lead azide and lead styphnate in detonators and primer caps. The main reason for this is the toxicity of lead. [28] The need for replacements was further manifested in the restrictions on the use of both substances, which were enacted by the European Union. [29, 30] Promising candidates as successors of lead azide and lead styphnate, that are known to literature, are ECCs based on copper(II) azide. [31-34] Attempts of preparing copper(II) azide complexes with **1** and **2** lead to impure products according to elemental analysis. Therefore, layering experiments were conducted to investigate the possible species. A solution of sodium azide and ligand in water was separated from an ethanolic solution of copper(II) chloride by a 1:1 mixture of ethanol and water. The slow mixing of the layers lead to formations of a single crystal in the case of the 1-TAN ligand. Single crystal analysis revealed the formation of 5-((1*H*-tetrazol-1-yl)methyl)tetrazol-1-ide as one of the products, most likely in a copper-catalyzed manner. To investigate the behavior of this anion further, the neutral compounds were prepared by zinc-catalyzed click chemistry as proposed by *Demko* and *Sharpless* (Scheme 2). [35] The obtained 5-((1*H*-tetrazol-1-yl)methyl)-1*H*-tetrazole (1-HTMT) and 5-((2*H*-tetrazol-2-yl)methyl)-1*H*-tetrazole (2-HTMT) were analyzed concerning their energetic properties and applicability of their anions for the formation of ECCs.

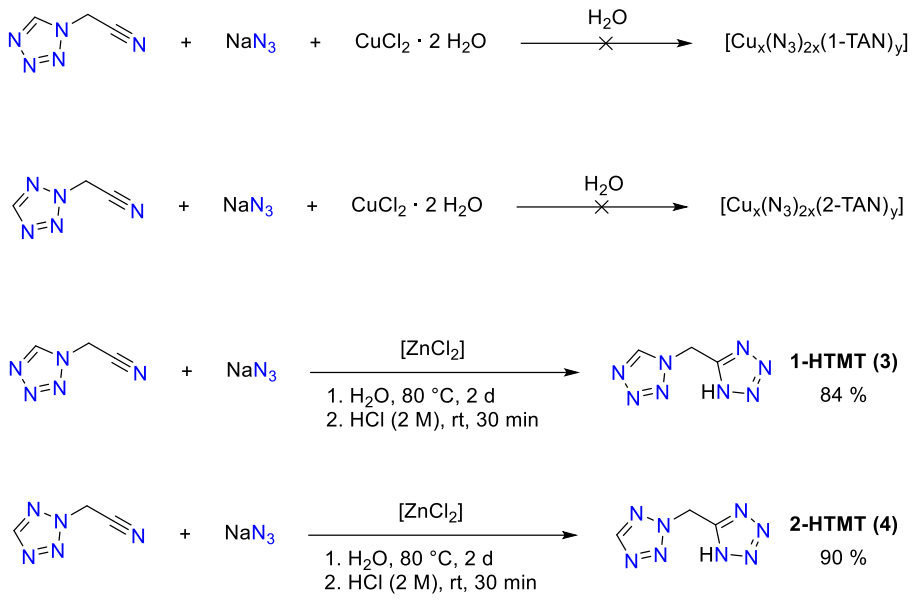

Scheme 2. Formation of 1- and 2-HTMT by zinc-catalyzed tetrazole-ring closure to the nitrile groups of 1- and 2-TAN.

1- and 2-TAN were applied in coordination compounds of different transition metal perchlorates and copper(II) nitrate. Transition metals which are known for their high toxicity levels like chromium, cobalt and nickel were excluded. [36-38] An overview of successful complexation attempts is given in Scheme 3. Attempts of complexation with $Mn(ClO_4)_2 \cdot 6\,H_2O$ were discarded due to the formation of MnO_2 within one day. Complexation of most perchlorates with **2** did not lead to a solid product and were therefore of no interest for this work.

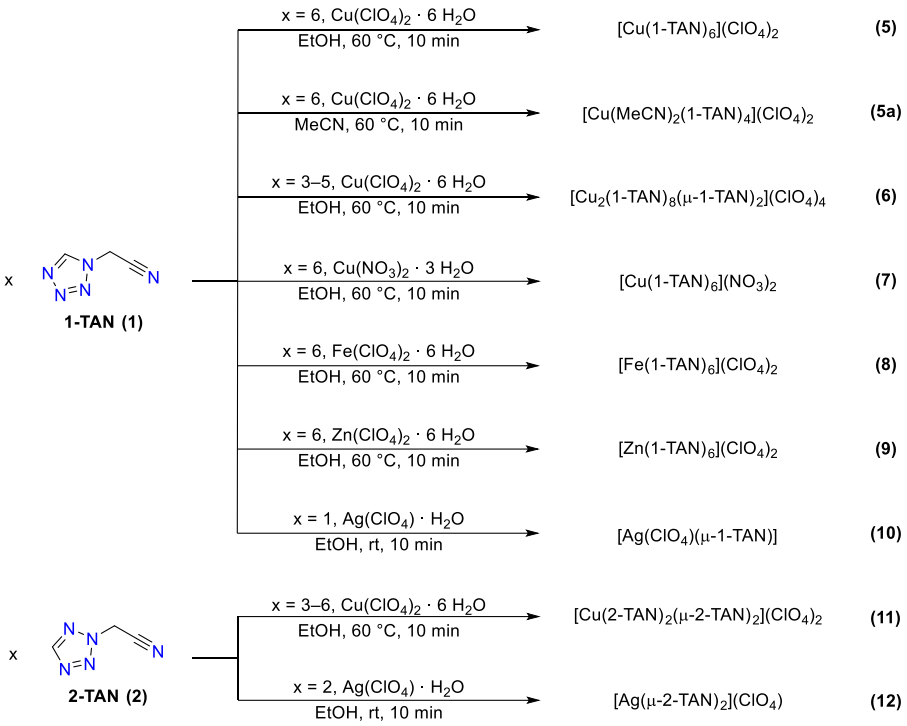

Scheme 3. Complexation of transition metal perchlorates and nitrates with 1- and 2-TAN.

Scheme 4 shows the ECCs of 1-TAN with copper salts of nitroaromatic anions. To obtain those, the respective nitrophenol (H_3TNPG: trinitrophloroglucinol, H_2TNR: styphnic acid, HPA: picric acid, H_2TNO: trinitro-orcinol) was combined with basic copper carbonate and water and heated to 80 °C until a clear solution was obtained. To these solutions, ligand was added under stirring. After stirring for 10 minutes at 80 °C, the solution was allowed to cool to room temperature. Since the usual coordination pattern of the copper(II) trinitrophloroglucinate complexes involves four ligands and coordination by the nitroaromatics hydroxides, there might be possible side species along the structure that was observed by single crystal X-Ray diffraction. Unlike expected, 1-TAN functions as a bridging ligand in **16**, allowing for a ratio of copper, anion and ligand of 1:1:1.

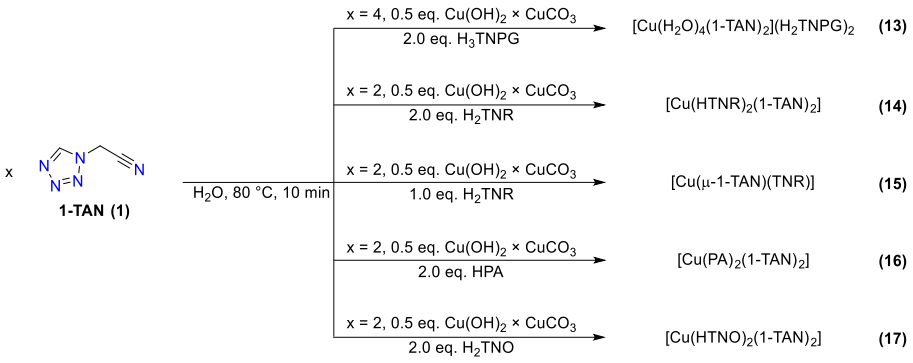

Scheme 4. ECCs with nitroaromatic anions that contain the 1-TAN ligand.

As seen in Scheme 5, the copper(II) trinitrophloroglucinate complex that was produced from 2-TAN showed some irregularities as well. The nitrile functionality of the ligand was hydrolyzed, and 2-(2*H*-tetrazol-2-yl)acetamide (2-TAA) was incorporated instead, which lead to impurity according to elemental analysis.

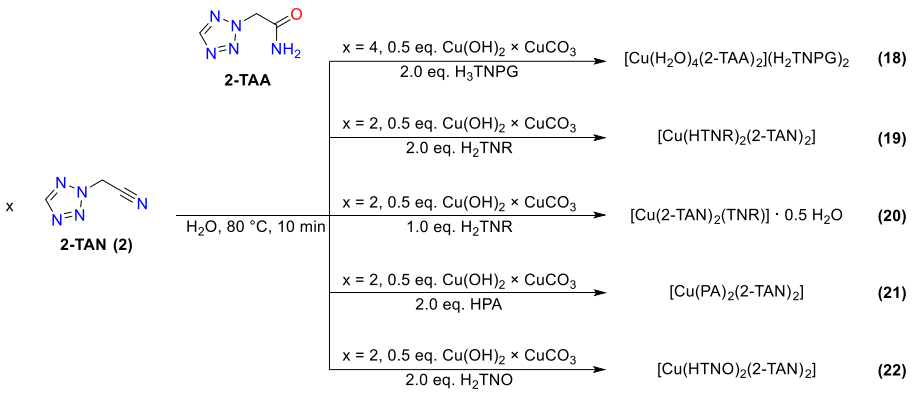

Scheme 5. ECCs derived from the 2-TAN ligand with nitroaromatic anions.

Scheme 6 shows that copper(II) azides with both, azide and tetrazolate anion were formed by deprotonation of **3** or **4** in the presence of sodium azide, followed by subsequent addition of copper(II) sulfate pentahydrate in aqueous solution. Species **23** was also obtained from 1-TAN by attempting the formation of $[Cu_x(N_3)_{2x}(1\text{-TAN})_y]$, as mentioned in Scheme 2. Copper(II) azides with additional negative anions that have recently been published, proved their thermal stability and were tested as sensitive in levels which appear to be interesting tradeoffs between performance and handling. [39, 40]

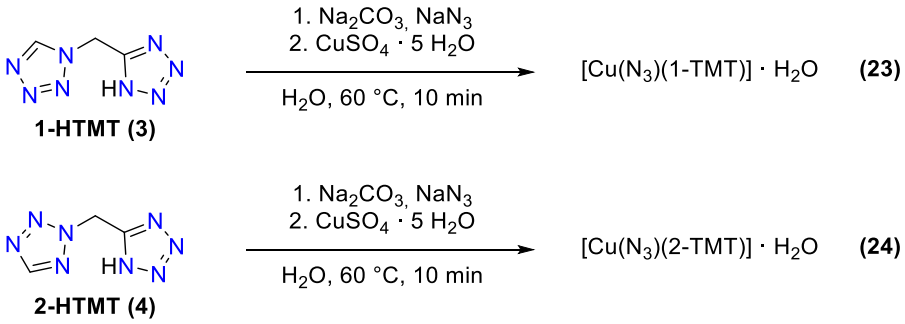

Scheme 6. Copper(II) azides **23** and **24**, with the tetrazolate anions 1-TMT and 2-TMT.

6.2.2 Crystal Structures

All compounds, except for **2**, which was only obtained as a liquid, **15**, **21** (low crystal quality) and **24**, which precipitated as an amorphous solid, were analyzed by low-temperature X-Ray diffraction analysis. Structures were solved using the Olex2 software suite [41] using SHELXT [42] and refined using full-matrix least squares method on *F2* by SHELXL. [43, 44] Graphical illustration of the solved structures was performed using DIAMOND4 [45], showing non-hydrogen atoms as thermal ellipsoids at 50 % probability level and hydrogen atoms as small spheres of arbitrary radius. Crystal structures, that are not shown in this section can be found in the Supporting Information. Figure 2 shows the crystal structures of the nitrogen-rich ligands a) 1-TAN, b) 1-HTMT and c) 2-HTMT. While **1** ($P2_12_12_1$) and **3** (*Pbca*) crystallized in orthorhombic space groups, **4** was obtained in the monoclinic space group *Cc*. Recalculation of the X-Ray densities to room temperature results in densities of 1.50 g cm^{-3} for 1-TAN and close to 1.60 g cm^{-3} for both 1-HTMT and 2-HTMT. These densities were used for the calculation of the detonation parameters by EXPLO5. [46, 47]

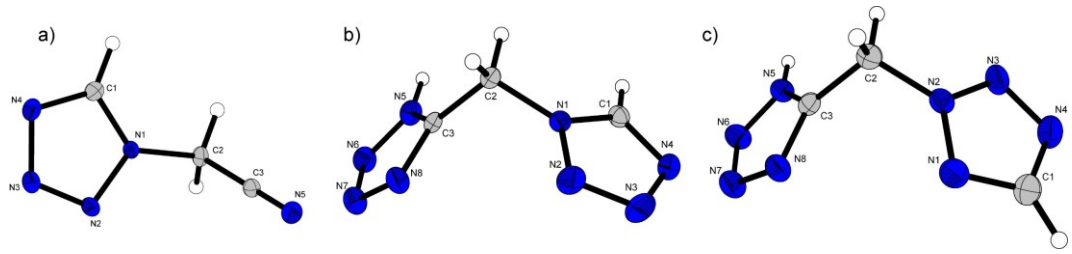

Figure 2. Crystal structures of a) 1-TAN, Selected bond lengths [Å]: N1–N2 1.3477(16), N5–C3 1.1398(16), N1–C1 1.3356(18), C2–C3 1.4710(16), N1–C2 1.4559(16), N2–N3 1.2972(17), N3–N4 1.3654(16), N4–C1 1.3136(19); Selected bond angles [°]: N2–N1–C1 108.71(11), N5–C3–C2 179.03(14), N2–N1–C2 121.85(10), C1–N1–C2 129.26(11), N1–N2–N3 105.90(10), N2–N3–N4 111.02(11), N3–N4–C1 105.42(12), N1–C1–N4 108.96(13), N1–C2–C3 110.80(10); b) 1-HTMT, Selected bond lengths [Å]: N1–N2 1.3405(17), N1–C1 1.3353(18), N1–C2 1.4713(17), N5–N6 1.3413(19), N5–C3 1.3378(17), N8–N7 1.3531(18), N8–C3 1.3229(18), N2–N3 1.303(2), N6–N7 1.306(2), N4–N3 1.345(2), N4–C1 1.3235(19), C3–C2 1.4850(19); Selected bond angles [°]: N2–N1–C2 121.86(12), C1–N1–N2 108.52(12), C1–N1–C2 129.61(13), C3–N5–N6 108.70(13), C3–N8–N7 105.64(12), N3–N2–N1 106.09(12), N7–N6–N5 106.10(12), N6–N7–N8 110.93(12), C1–N4–N3 105.60(13), N5–C3–C2 126.69(13), N8–C3–N5 108.63(12), N8–C3–C2 124.68(12), N2–N3–N4 111.13(12), N4–C1–N1 108.65(14), N1–C2–C3 110.81(11); c) 2-HTMT, Selected bond lengths [Å]: N5–N6 1.342(3), N5–C3 1.328(3), N2–N3 1.312(3), N2–N1 1.330(3), N2–C2 1.456(3), N8–N7 1.359(3), N8–C3 1.318(3), N6–N7 1.298(3), N3–N4 1.321(3), N1–C1 1.325(3), N4–C1 1.341(3), C3–C2 1.494(3); Selected bond angles [°]: C3–N5–N6 109.04(19), N3–N2–N1 114.40(19), N3–N2–C2 122.50(19), N1–N2–C2 123.08(18), C3–N8–N7 105.96(18), N7–N6–N5 106.19(18), N6–N7–N8 110.41(18), N2–N3–N4 105.92(19), C1–N1–N2 100.77(18), N3–N4–C1 105.79(19), N5–C3–C2 126.92(19), N8–C3–N5 108.39(18), N8–C3–C2 124.67(19), N2–C2–C3 110.77(17), N1–C1–N4 113.1(2).

The copper(II), iron(II) and zinc(II) coordination compounds showed coordination patterns in form of distorted octahedrons. In the cases of $[Fe(1\text{-}TAN)_6](ClO_4)_2$ and $[Zn(1\text{-}TAN)_6](ClO_4)_2$ the deviation from a perfect octahedron can be found in the angles between the coordination bonds, which slightly differ from 90°, while all coordination bonds show similar length due to the high symmetry of the trigonal $R\bar{3}$ space group in which both crystallized. Figure 3 shows the difference in the structure of $[Fe(1\text{-}TAN)_6](ClO_4)_2$ a) below and b) above the temperature at which the spin-crossover (SCO) was observed. Since both structures were obtained by measurement of the same single crystal, the structural changes, such as the shortened coordination bond, can be seen as a result of the SCO.

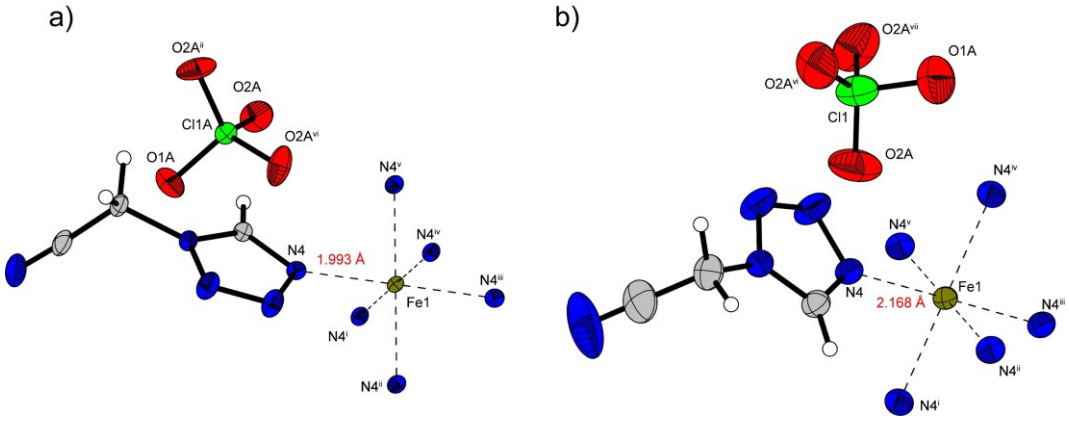

Figure 3. Crystal structures of $[Fe(1\text{-}TAN)_6](ClO_4)_2$ at a) 93 K; Selected bond lengths [Å]: Fe1–N4 1.9925(17); Symmetry codes: (i): −y, x−y, z; (ii): −x+y, −x, z; (iii): −x, −y, 1−z; (iv): y, −x+y, 1−z; (v): x−y, x, 1−z; (vi): 1−y, x−y, z; (vii): 1−x+y, 1−x, z; and b) 193 K; Selected bond lengths [Å]: Fe1–N4 2.1680(16); Symmetry codes: (i): 2−x, 1+x−y, z; (ii): 1+x−y, x, 1−z; (iii): 2−x, 2−y, 1−z; (iv): y, 1−x+y, 1−z; (v): 1−x+y, 2−x, z; (vi): −x+y, 1−x, z; (vii): 1−y, 1+x−y, z.

The structural variety increases in the case of the three differently coordinated copper(II) perchlorates $[Cu(1\text{-}TAN)_6](ClO_4)_2$ (**5**), $[Cu_2(1\text{-}TAN)_8(\mu\text{-}1\text{-}TAN)_2](ClO_4)_4$ (**6**) and $[Cu(2\text{-}TAN)_2(\mu\text{-}2\text{-}TAN)_2](ClO_4)_2$ (**11**). Crystallization of **5** occurs in the triclinic space group *P*−1 with three formula units per unit cell. The coordination sphere (Figure 4) shows the typical *Jahn-Teller* elongation distortion, that is expected for the d^9-case.

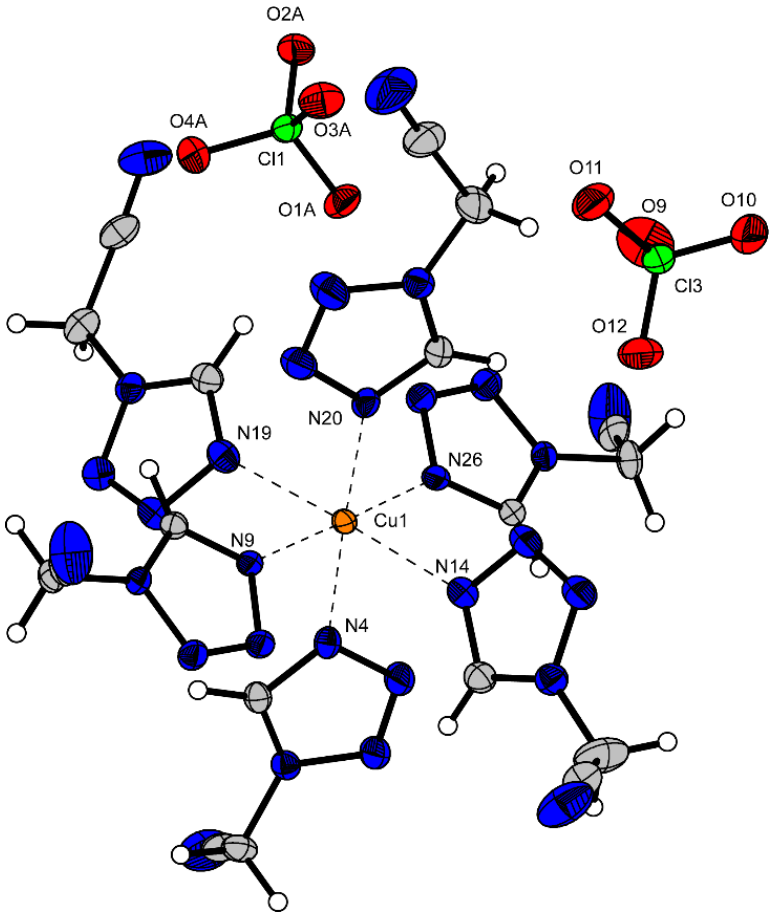

Figure 4. Coordination sphere of $[Cu(1\text{-TAN})_6](ClO_4)_2$. Selected bond lengths [Å]: Cu1–N4 2.058(2), Cu1–N9 2.028(2), Cu1–N14 2.366(2), Cu1–N19 2.321(2), Cu1–N20 2.054(2), Cu1–N26 2.027(2); Selected bond angles [°]: N4–Cu1–N9 89.34(8), N4–Cu1–N14 87.89(8), N4–Cu1–N19 91.12(8), N4–Cu1–N20 177.70(8), N4–Cu1–N26 91.00(8), N9–Cu1–N14 91.24(8), N9–Cu1–N19 86.56(8), N9–Cu1–N20 91.35(8), N9–Cu1–N26 178.56(8), N14–Cu1–N19 177.59(8), N14–Cu1–N20 89.90(8), N14–Cu1–N26 90.18(8), N19–Cu1–N20 91.12(8), N19–Cu1–N26 92.04(8), N20–Cu1–N26 88.37(8).

By reducing the amount of ligand that is used to five equivalents, $[Cu_2(1\text{-TAN})_8(\mu\text{-}1\text{-TAN})_2](ClO_4)_4$ is formed. The structure of the coordination sphere is displayed in Figure 5. For reason of clarity the non-coordinating perchlorate anions are not shown. The compound crystallized in the triclinic space group $P\bar{1}$ with one formula unit per unit cell. Both, the angles and the coordination bond lengths describe two highly distorted octahedra which are bridged by two 1-TAN ligands *via* the nitrogen atoms in 3- and 4-position of the tetrazole ring. The $N8^{i}$-Cu bond of these bridging ligands shows an especially increased bond length of 2.831 Å, clarifying the occupation of the z^2-axis together with a terminal tetrazole ligand (2.260 Å). The ligand's substituents take up positions in which they avoid steric interaction by stacking like saw teeth.

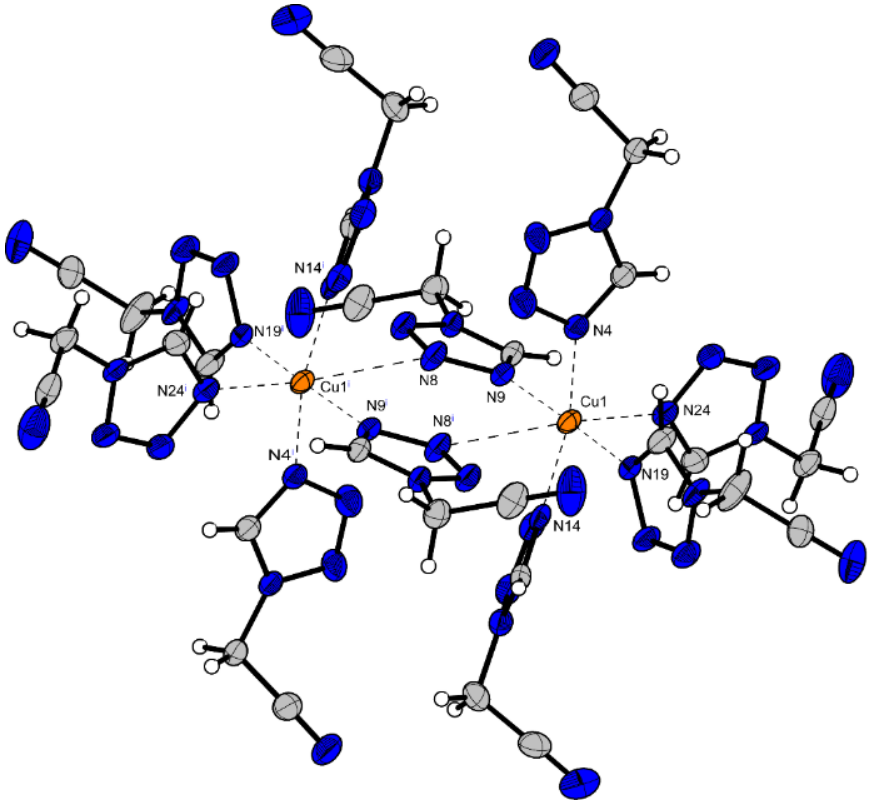

Figure 5. Coordination sphere of $[Cu_2(1\text{-TAN})_8(\mu\text{-}1\text{-TAN})_2](ClO_4)_4$. Selected bond lengths [Å]: Cu1–N4 2.015(3), Cu1–N9 2.022(3), Cu1–N14 2.011(3), Cu1–N19 2.034(3), Cu1–N24 2.260(3), Cu1–N8^{i} 2.831(3); Selected bond angles [°]: N4–Cu1–N9 87.75(12), N4–Cu1–N14 167.12(13), N4–Cu1–N19 90.01(12), N4–Cu1–N24 99.80(13), N4–Cu1–N8^{i} 89.33(12), N9–Cu1–N14 89.08(12), N9–Cu1–N19 175.06(13), N9–Cu1–N24 93.72(12); Symmetry codes: (i): 1−x, 1−y, 1−z.

$[Cu(2\text{-TAN})_2(\mu\text{-}2\text{-TAN})_2](ClO_4)_2$ (Figure 6) demonstrates yet another coordination mode of the tetrazolylacetonitrile ligands. Since the bridging capabilities of the tetrazole ring are majorly influenced by the steric demand of the side-chain, the 3-position of the tetrazole ring is blocked in 2-TAN. This allows for the nitrile's coordination to the copper center in the elongated z^2-axis, while the tetrazole rings occupy the *xy*-plane. Ultimately, a two-dimensional coordination polymer is formed. As expected, the densities of the three copper perchlorates $[Cu(1\text{-TAN})_6](ClO_4)_2$, $[Cu_2(1\text{-TAN})_8(\mu\text{-}1\text{-TAN})_2](ClO_4)_4$, and the polymeric ECC $[Cu(2\text{-TAN})_2(\mu\text{-}2\text{-TAN})_2](ClO_4)_2$ increase with increasing connectivity between the copper(II) centers from 1.654 (**5**), over 1.719 (**6**) to 1.777 g cm^{-3} (**11**) recalculated to room temperature.

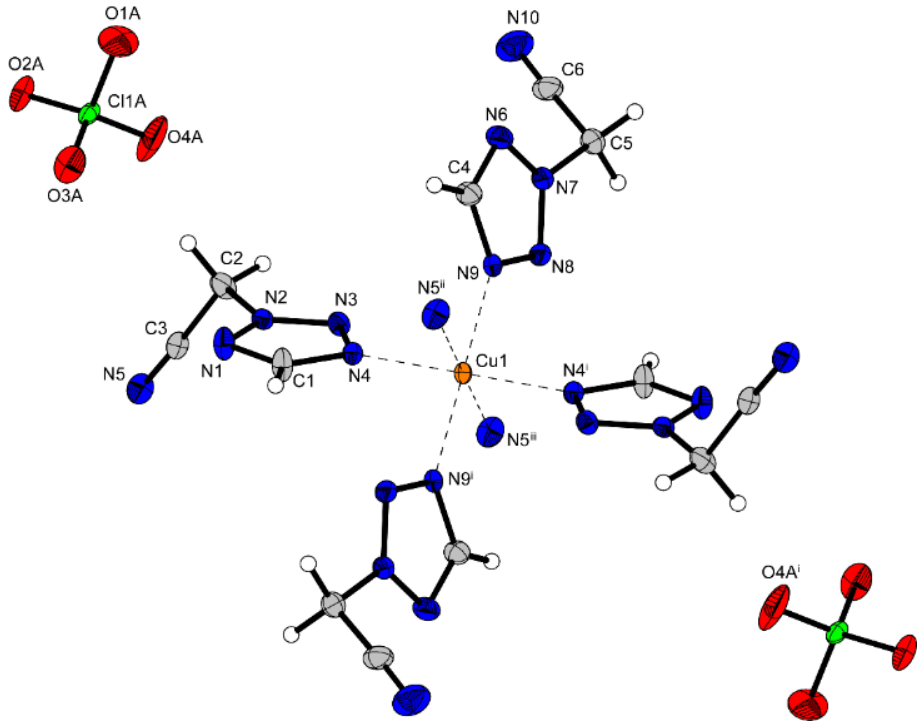

Figure 6. Coordination sphere of $[Cu(2\text{-TAN})_2(\mu\text{-}2\text{-TAN})_2](ClO_4)_2$. Selected bond lengths [Å]: Cu1–N4 1.9976(17), Cu1–N9 2.0341(17), Cu1–N5^{ii} 2.3442(19); Selected bond angles [°]: N4–Cu1–N9 89.11(7), N4–Cu1–N5^{ii} 89.49(7), N5^{ii}–Cu1–N9 88.01(7); Symmetry codes: (i): 2−x, 1−y, 1−z; (ii): 3/2−x, −1/2+y, 1/2−z; (iii): 1/2+x, 3/2−y, 1/2+z.

Figure 7 shows the coordination structure of $[Ag(ClO_4)(\mu\text{-}1\text{-TAN})]$ (**10**) in which each molecule of 1-TAN coordinates to three silver(I) centers. The polymeric structure is completed by coordination of the perchlorate anions. In combination, a 3D-polymeric network is formed. **10** crystallizes in the monoclinic space group *C*2/*c* with a high density of 2.539 g cm^{-3} at the measurement temperature of 123 K. The high density of the polymeric network, in combination with the heavy silver(I) cations and the ideal ratio of ligand to perchlorate, that, in theory, allows for the formation of gaseous N_2, CO, H_2O and HCl next to elemental silver as the only solid product, are a good prerequisite for a high-performing primary explosive.

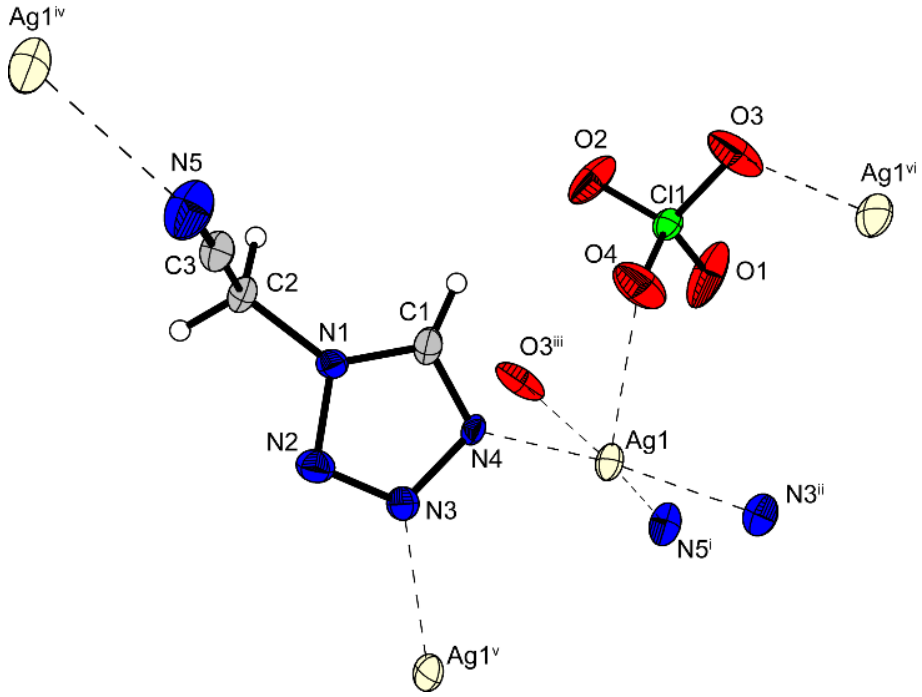

Figure 7. Coordination sphere of [Ag(ClO$_4$)(μ-1-TAN)]. Selected bond lengths [Å]: Ag1–N4 2.244(4), Ag1–N5^{i} 2.356(5), Ag1–N3^{ii} 2.348(4); Selected bond angles [°]: N4–Ag1–N5 146.09(14), N4–Ag1–N3 121.50(15), N3–Ag1–N5 85.60(15); Symmetry codes: (i): 1/2+x, 1/2+y, z; (ii): 1/2−x, −1/2+y, 1/2−z; (iii): x, 1+y, z; (iv): −1/2+x, −1/2+y, z; (v): 1/2−x, 1/2+y, 1/2−z.

In contrast, [Ag(μ-2-TAN)$_2$](ClO$_4$) (**12**) crystallizes in the monoclinic space group *P*2/*c* with a significantly lower density compared to **10**. The density of 2.159 g cm^{-3} at 123 K can again be explained by the polymeric network. Unlike 1-TAN, 2-TAN can only bridge between two silver(I) centers. This leads to the formation of a 1D-polymeric chains, which are intercalated by disordered perchlorate anions (Figure 8). This reduces the space filling of the structure compared to [Ag(ClO$_4$)(μ-1-TAN)]. In addition, the ratio of ligand to perchlorate and therefore fuel to oxidizer is increased compared to **10**.

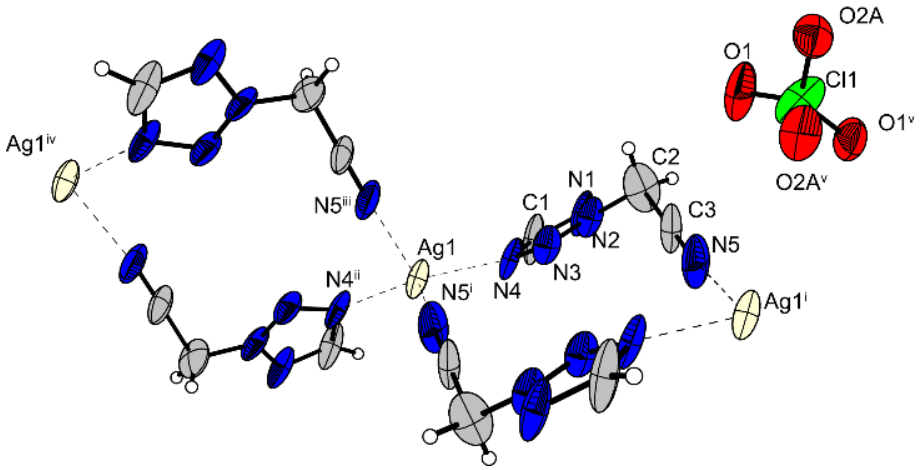

Figure 8. Coordination sphere of $[Ag(\mu\text{-2-TAN})_2](ClO_4)$. Selected bond lengths [Å]: Ag1–N4 2.239(4), Ag1–N5 2.446(4); Selected bond angles [°]: N4–Ag1–N4^{ii} 145.17(19), N4–Ag1–N5^{i} 95.19(13), N4–Ag1–N5^{iii} 111.29(16); Symmetry codes: (i): 2−x, 1−y, 1−z; (ii): 2−x, y, 1/2−z; (iii): x, 1−y, −1/2+z; (iv): 2−x, 1−y, −z; (v): 1−x, y, 3/2−z.

In summary, the 1- and 2-TAN ligands show coordinative behavior as described in Figure 9. While 1-TAN can act as a bridging ligand at two positions of the tetrazole ring and the nitrile, 2-TAN only shows coordination at the 4-position of the ring, in addition to the nitrile. This behavior was observed in the cases of copper(II) and silver(I) perchlorates by low temperature X-Ray diffraction. For compound **15** a similar behavior is estimated to lead to the composition [Cu(TNR)(μ-1-TAN)].

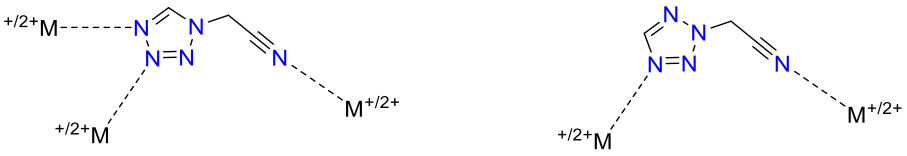

Figure 9. Schematic overview of the coordinative behaviour of 1- and 2-TAN.

The structure of $[Cu(N_3)(1\text{-TMT})] \cdot H_2O$ (**23**), as seen in Figure 10, was obtained by dissolving sodium azide and 1-TAN in water. On top, a mixture of water and ethanol (1:1) was poured, followed by an ethanolic solution of copper(II) nitrate trihydrate. Slow diffusion of the separate phases lead to formation of **23** as a green single crystal. The cyclization of which formed the 1-TMT anion might have taken place by copper catalysis. Both, the tetrazolate and the azide anion bridge between two copper(II) centers each in coordination modes which have been previously described by the groups of Li and Sañudo.[48] Hereby, two dimensional porous networks are formed in which water was incorporated.

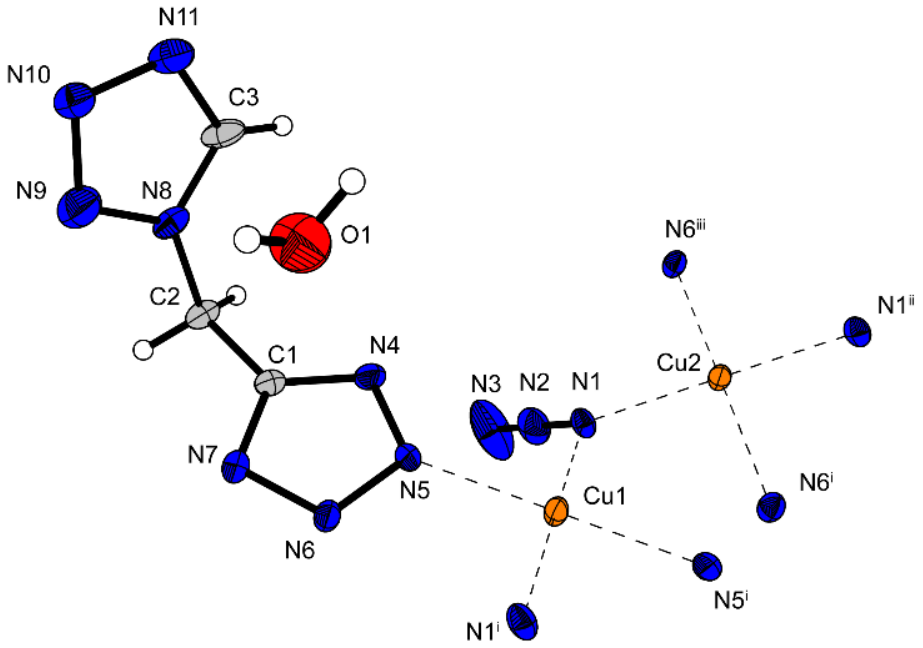

Figure 10. Crystal structure of $[Cu(N_3)(1\text{-TMT})] \cdot H_2O$. Selected bond lengths [Å]: Cu1–N1 1.990(3), Cu1–N5 1.993(3), Cu2–N6^{iii} 1.997(3), Cu2–N1 1.992(3); Selected bond angles [°]: N1–Cu2–N6^{iii} 93.60(11), N1–Cu1–N5 93.54(11), Cu1–N1–Cu2 114.32(13); Symmetry codes: (i): 1−x, −y, 1−z; (ii): −x, −y, 1−z; (iii): −1+x, y, z.

6.2.3 Energetic Properties

The properties of the nitrogen-rich compounds **1**–**4** are listed in Table 1. The enthalpies of formation of the condensed phases were calculated using the atomization method of each room temperature CBS-4M enthalpy. Further details about the calculation are given in the Supporting Information. The enthalpies of formation of each compound were used for determination of the detonation parameters at the Chapman-Jouguet point by EXPLO5 (V7.01.01.). [47] In addition, using CrystalExplorer, Hirshfeld calculations of compounds **1**, **3** and **4** were performed to get an insight into the interactions with neighboring molecules. [49] As expected, mainly stabilizing interactions were observed. The results are shown in the Supporting Information. To get an insight in the sensitivity of the ECCs, thermal analysis was conducted by DTA (OZM DTA 551-EX) or DSC (Mettler-Toledo DSC822e). Endothermic signals were further investigated by TGA (Perkin Elmer TGA4000) and for melting points with a Büchi B-540 device. A thermal stability of above 150 °C is often considered as a necessity for primary explosives. [50] This benchmark is reached for most of the compounds, except for $[Cu(1\text{-TAN})_6](NO_3)_2$ (**7**), $[Ag(\mu\text{-}2\text{-TAN})_2](ClO_4)$ (**12**), $[Cu(\mu\text{-}1\text{-TAN})(TNR)]$ (**15**), and $[Cu(N_3)(2\text{-TMT})] \cdot H_2O$ (**24**). The impact and friction sensitivities were obtained by applying the 1 of 6 method with BAM

standard devices. Electrostatic discharge values were measured with the OZM XSpark10 device. These values clarify, that the ECCs should be handled with extreme caution, as most of them are categorized as very sensitive or sensitive to impact as well as sensitive to friction according to the "UN Recommendations on the Transport of Dangerous Goods". [51] An overview of the values is given in Table 2. By performing hot plate and hot needle tests, an insight in the behavior to rapid heating in open and confined environment is gained. While detonations and sharp deflagrations indicate potential use as replacement of lead azide in detonator setups, which can be further tested by priming tests, combustion or decomposition of the material excludes the substance from potential use.

Table 1. Physicochemical properties of compounds **1–4**.

	1-TAN	**2-TAN**	**1-HTMT**	**2-HTMT**
Formula	$C_3H_3N_5$	$C_3H_3N_5$	$C_3H_4N_8$	$C_3H_4N_8$
M [g mol^{-1}]	109.09	109.09	152.12	152.12
IS [J] [a]	>40	>40	10	15
FS [N] [b]	>360	>360	360	360
ESD [J] [c]	1.5	-	1.0	0.5
T_{endo}/T_{exo} [°C]	42/164	-/195	136/165	97/176
ρ [g cm^{-3}]	1.50 [d]	1.30[e]	1.62[d]	1.61[d]
N [%] [f]	64.20	64.20	73.66	73.66
$\Delta_f H°$ [kJ mol^{-1}] [g]	432.1	426.0	578.6	564.9
EXPLO5 V7.01.01				
$-\Delta_{Ex}U$ [kJ kg^{-1}] [h]	3767	3844	3778	3691
$T_{det.}$ [K] [i]	2703	2737	2715	2677
V_0 [L kg^{-1}] [j]	646	661	707	708
P_{CJ} [kbar] [k]	159	114	208	203
$V_{det.}$ [m s^{-1}] [l]	6759	6202	7716	7636

[a] Impact sensitivity (BAM drophammer (1 of 6)). [b] Friction sensitivity (BAM friction tester (1 of 6)). [c] Electrostatic discharge devise (OZM XSpark10). [d] From X-Ray diffraction analysis recalculated to 298 K. [e] Pycnometrically determined. [f] Nitrogen content. [g] Enthalpy of formation. [h] Energy of explosion. [i] Detonation temperature. [j] Volume of detonation products (assuming only gaseous products). [k] Detonation pressure at the Chapman − Jouguet point. [l] Detonation velocity.

The capability of the promising substances to initiate PETN was tested in detonator setups. Therefore, 200 mg of PETN with a grain size below 100 µm was filled into a copper shell and pressed by lowering a weight of 8 kg onto. The shell was then placed on a copper witness plate. The substance of question (50 mg) was filled loosely on top, and a type A igniter was crimped to the top of the shell. Initiation was considered successful if a hole in the witness plate was observed. Incomplete initiation of PETN was observed in most tests, leading to deformation of the shell, which was then stuck on the witness plate. Only in the case of [Ag(ClO_4)(μ-1-TAN)] successful propagation of the detonation was feasible as seen in Figure 11. This is especially interesting because of the facile preparation. 1-TAN can be

obtained without cost- and time-consuming column chromatography by tetrazole ring closure on the commercially available 2-aminoacetonitrile hydrochloride. [52] Since TGA revealed the loss of water of compound **23** at temperatures below 50 °C, it was dried at 80 °C until no OH stretch was visible in the IR. It's capability to initiate PETN was tested in this setup in its hydrated and dried form. In both cases the result was negative.

Figure 11. PETN initiation setup. Left: negative attempt with no damage to shell or plate, right: positive initiation by **10**.

Additionally, all colored ECCs were tested for laser initiation. Therefore, approximately 25 mg of substance were pressed into translucent polycarbonate primer caps with a force of 1.5 kN. The primer caps were then sealed by UV-curable adhesive and tested for their reaction to irradiation with a single pulsed laser. The InGaAs laser diode operates with a theoretical maximum power output of 45 W at a wavelength of 915 nm. The sample was placed in the focal distance of the optical lens and irradiated according to the parameters seen in Table 3. The irradiation of $[Cu_2(1\text{-}TAN)_8(\mu\text{-}1\text{-}TAN)_2](ClO_4)_4$ (**6**) and $[Cu(2\text{-}TAN)_2(\mu\text{-}2\text{-}TAN)_2](ClO_4)_2$ (**11**), with their improved ligand to perchlorate ratio due to bridging, showed violent detonations. Especially the comparison between $[Cu(1\text{-}TAN)_6](ClO_4)_2$ (**5**), which decomposes, and **6** is interesting, since the minor stoichiometric change leads to such a major difference in performance. This discrepancy cannot be explained by differences of the thermal stabilities as both **6** and **11** show higher decomposition temperatures than **5**. Both, $[Cu(N_3)(1\text{-}TMT)] \cdot H_2O$ (**23**) and $[Cu(N_3)(2\text{-}TMT)] \cdot H_2O$ (**24**) were used in only 10 mg scale for the laser initiation to prevent damage to the setup by their strong detonation that was observed during hot plate and hot needle tests. The output, especially of **23**, qualifies it as a potent compound for laser ignitable primer caps with moderate sensitivities and high thermal stability.

Table 2. Thermal stability and sensitivities to mechanical and electrical stimuli of compounds **5–24**. Compounds **5a**, **13** and **18** are excluded for purity reasons.

Compound	No.	T_{endo}[a] [°C]	T_{exo}[b] [°C]	IS[c] [J]	FS[d] [N]	ESD[e] [mJ]	HP[f]	HN[g]
$[Cu(1\text{-}TAN)_6](ClO_4)_2$	**5**	-	173	<1	108	33	Def.	Def.
$[Cu_2(1\text{-}TAN)_8(\mu\text{-}1\text{-}TAN)_2](ClO_4)_4$	**6**	-	177	<1	60	160	Def.	Det.
$[Cu(1\text{-}TAN)_6](NO_3)_2$	**7**	75	117	>40	>360	106	Dec.	Dec.
$[Fe(1\text{-}TAN)_6](ClO_4)_2$	**8**	-	188	2	60	33	Def.	Def.
$[Zn(1\text{-}TAN)_6](ClO_4)_2$	**9**	-	180	10	240	1080	Dec.	Dec.
$[Ag(ClO_4)(\mu\text{-}1\text{-}TAN)]$	**10**	-	173	<1	1	5	Def.	Def.
$[Cu(2\text{-}TAN)_2(\mu\text{-}2\text{-}TAN)_2](ClO_4)_2$	**11**	-	190	<1	1.5	13	Def.	Det.
$[Ag(\mu\text{-}2\text{-}TAN)_2](ClO_4)$	**12**	-	67	<1	6	5	Def.	Det.
$[Cu(HTNR)_2(1\text{-}TAN)_2]$	**14**	-	205	3	240	63	Def.	Dec.
$[Cu(\mu\text{-}1\text{-}TAN)(TNR)]$	**15**	-	143	2	160	63	Dec.	Dec.
$[Cu(PA)_2(1\text{-}TAN)_2]$	**16**	-	170	2	>360	106	Comb.	Dec.
$[Cu(HTNO)_2(1\text{-}TAN)_2]$	**17**	-	181	2	360	63	Dec.	Dec.
$[Cu(HTNR)_2(2\text{-}TAN)_2]$	**19**	-	192	3	160	250	Comb.	Dec.
$[Cu(2\text{-}TAN)_2(TNR)] \cdot 0.5\ H_2O$	**20**	-	170	2	>360	250	Def.	Dec.
$[Cu(PA)_2(2\text{-}TAN)_2]$	**21**	-	194	3	>360	480	Comb.	Comb.
$[Cu(HTNO)_2(2\text{-}TAN)_2]$	**22**	-	174	2	288	480	Comb.	Dec.
$[Cu(N_3)(1\text{-}TMT)] \cdot H_2O$	**23**	-	208	<1	50	6	Det.	Det.
$[Cu(N_3)(2\text{-}TMT)] \cdot H_2O$	**24**	-	128	<1	7.5	13	Det.	Det.

[a] Onset temperature of endothermic event in the DTA or DSC (heating rate of 5 °C min^{-1}), indicating a melting point of the compound. [b] Onset of exothermic event in the DTA or DSC. [c] Impact sensitivity (BAM drophammer (1 of 6)). [d] Friction sensitivity (BAM friction tester (1 of 6)). [e] Electrostatic discharge devise (OZM XSpark10). [f] Hot plate test (det.: detonation, def.: deflagration, dec.: decomposition, comb.: combustion). [g] Hot needle test (det.: detonation, def.: deflagration, dec.: decomposition, comb.: combustion). [h] Endo-to-exo-transition.

Table 3. Priming capability and laser ignitability results of the relevant ECCs.

Compound	No.	PETN initiation	Laser parameters[a]			
			6 A, 1 ms, 4 V	7 A, 1 ms, 4 V	7 A, 15 ms, 4 V	10 A, 30 ms, 4 V
$[Cu(1\text{-}TAN)_6](ClO_4)_2$	**5**	Neg.	-	-	Dec.	Dec.
$[Cu_2(1\text{-}TAN)_8(\mu\text{-}1\text{-}TAN)_2](ClO_4)_4$	**6**	Neg.	Det.	Det.	Det.	-
$[Cu(1\text{-}TAN)_6](NO_3)_2$	**7**	-	-	-	Dec.	Dec.
$[Fe(1\text{-}TAN)_6](ClO_4)_2$	**8**	-	-	-	Comb.	Def.
$[Ag(ClO_4)(\mu\text{-}1\text{-}TAN)]$	**10**	Pos.	-	-	-	-
$[Cu(2\text{-}TAN)_2(\mu\text{-}2\text{-}TAN)_2](ClO_4)_2$	**11**	Neg.	Det.	Det-	Det.	-
$[Ag(\mu\text{-}2\text{-}TAN)_2](ClO_4)$	**12**	Neg.	-	-	-	-
$[Cu(HTNR)_2(1\text{-}TAN)_2]$	**14**	-	-	-	-	Dec.
$[Cu(\mu\text{-}1\text{-}TAN)(TNR)]$	**15**	-	-	-	-	Dec.
$[Cu(PA)_2(1\text{-}TAN)_2]$	**16**	-	-	-	-	Dec.
$[Cu(HTNO)_2(1\text{-}TAN)_2]$	**17**	-	-	-	-	Dec.
$[Cu(HTNR)_2(2\text{-}TAN)_2]$	**19**	-	-	-	-	Dec.
$[Cu(2\text{-}TAN)_2(TNR)] \cdot 0.5\ H_2O$	**20**	-	-	-	-	Dec.
$[Cu(PA)_2(2\text{-}TAN)_2]$	**21**	-	-	-	-	Dec.
$[Cu(HTNO)_2(2\text{-}TAN)_2]$	**22**	-	-	-	-	Dec.
$[Cu(N_3)(1\text{-}TMT)] \cdot H_2O$	**23**	Neg.	Det.	Det.	-	-
$[Cu(N_3)(2\text{-}TMT)] \cdot H_2O$	**24**	Neg.	Det.	Det.	-	-

[a] Operating parameters: voltage U = 4 V, current I = 6–10 A, pulse length τ = 1–30 ms, theoretical maximal output power P_{max} = 45 W, wavelength λ = 915 nm (Det.: detonation, Def.: deflagration, Dec.: decomposition, Comb.: combustion, Neg.: negative).

6.2.4 Magnetic Properties

Since a thermochromic effect of $[Fe(1\text{-}TAN)_6](ClO_4)_2$ was observed during the low temperature X-Ray diffraction analysis, the magnetic properties of the coordination compound were further investigated. Magnetization measurements were performed with a Quantum Design Inc. physical property measurement system, which is equipped with a vibrating sample magnetometer. The sample was measured in a temperature range of 2–300 K at a field of ±30 kOe with the PPMS *MultiVu* software package. [53] Figure 12 shows the temperature dependent spin-crossover behavior of the compound, which explains the change of color from colorless at room temperature to purple while cooling in the nitrogen stream. The difference between the effective momentum μ_{eff} and the theoretical value might be explained by aging of the iron(II) perchlorate hexahydrate and subsequent oxidation to iron(III). [54] Similar observations have been reported for other thermally induced switches from the high spin $^5T_2$ to low spin $^1A_1$ population in octahedral iron(II) coordination compounds with different types of ligands. [55-58] The bond lengths, that can be observed

for the Fe(II)-N coordination bond, show a clear reaction to the spin crossover by shortening from 2.1680(14) Å at 193 K to 1.9925(15) Å at 93 K. Such changes of close to 0.2 Å have been previously described for other examples in literature. [59]

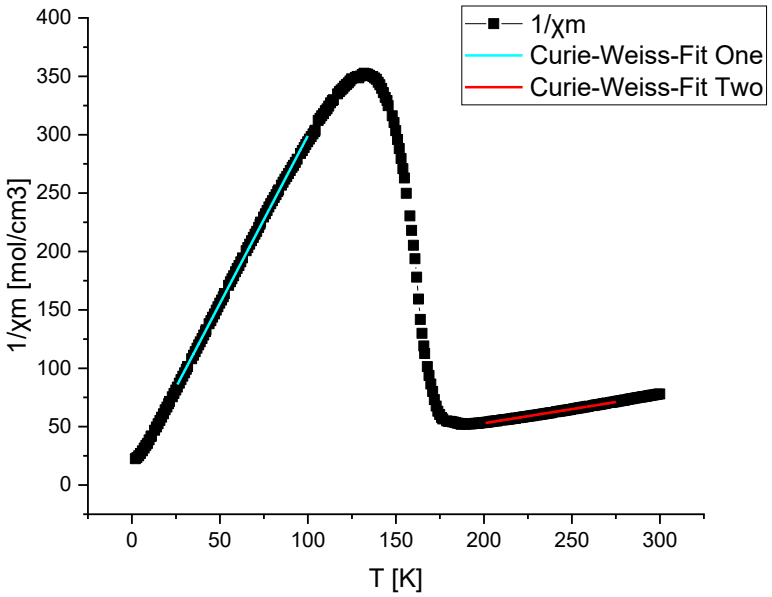

Figure 12. Inverted plot of the molar magnetic susceptibility of $[Fe(1\text{-}TAN)_6](ClO_4)_2$ at a field strength of $B = 3\,T$. The two Curie-Weiss-Fits (cyan for $T < 125\,K$ and red for $T > 170\,K$) indicate effective magnetic moments of $\mu_{eff} = 1.6676 \pm 0.00303\,\mu_B$ below 125 K and $\mu_{eff} = 5.74723 \pm 0.01407\,\mu_B$ above 170 K.

The authors have cited additional references within the Supporting Information. [41-45, 47, 49, 51, 60-79]

6.3 Conclusion

The four nitrogen-rich ligands 1-TAN, 2-TAN, 1-HTMT and 2-HTMT were successfully synthesized and applied to energetic coordination compounds. A total of 21 ECCs was produced of which 18 were analyzed by X-Ray diffraction analysis, supporting the structural variety of the coordination modes, which were expected from the ligands. Hereby, it was possible to alter the ratio of ligand to anion for the copper(II) perchlorates in a way which allowed laser initiation at low energies. The case of $[Ag(ClO_4)(\mu\text{-}1\text{-}TAN)]$, which was used as a primary explosive to initiate a charge of PETN, supports the idea, that structural optimization of the ligand allows for an improvement of the ratio of fuel to oxidizer and therefore the performance of an energetic material. This is of special interest,

since the ligand can be produced relatively cost efficient from commercially available chemicals. As a second, highly interesting ECC, $[Cu(N_3)(1\text{-TMT})] \cdot H_2O$ was characterized as an option for thermally and mechanically stable laser priming caps. Additionally, the magnetic properties of $[Fe(1\text{-TAN})_6](ClO_4)_2$ were studied, revealing a high-spin to low-spin transition below 170 K.

6.4 Acknowledgements

We gratefully acknowledge the financial support of this work by the Ludwig-Maximilians-Universität München. The authors also thank Dr. Peter Mayer for his contributions to the crystallographic data and Mr. Stefan Huber for sensitivity measurements.

6.5 References

[1] K. Soai, A. Ookawa, *J. Org. Chem.* **1986**, *51*, 4000–4005.

[2] C. M. Suter, E. W. Moffett, *J. Am. Chem. Soc.* **1934**, *56*, 487–487.

[3] V. Y. Kukushkin, A. J. L. Pombeiro, *Inorg. Chim. Acta* **2005**, *358*, 1–21.

[4] M. S. M. Pearson-Long, F. Boeda, P. Bertus, *Adv. Synth. Catal.* **2017**, *359*, 179–201.

[5] P. R. Sruthi, S. Anas, *J. Polym. Sci.* **2020**, *58*, 1039–1061.

[6] R. J. H. Gregory, *Chem. Rev.* **1999**, *99*, 3649–3682.

[7] B. N. Storhoff, H. C. Lewis Jr, *Coord. Chem. Rev.* **1977**, *23*, 1–29.

[8] S. F. Rach, F. E. Kühn, *Chem. Rev.* **2009**, *109*, 2061–2080.

[9] S. R. Buzilova, Y. V. Brekhov, A. V. Afonin, G. A. Gareev, L. I. Vereshchagin, *Zh. Obshch. Khim.* **1989**, *25*, 1524–1528.

[10] T. M. Klapötke, J. Stierstorfer, in *Green Energetic Materials*, **2014**, pp. 133–178.

[11] C. Kling, D. Leusser, T. Stey, D. Stalke, *Organometallics* **2011**, *30*, 2461–2463.

[12] L. Mahalakshmi, D. Stalke, in *Structure and Bonding*, Springer Berlin Heidelberg, **2002**, pp. 85–115.

[13] F. Baier, Z. Fei, H. Gornitzka, A. Murso, S. Neufeld, M. Pfeiffer, I. Rüdenauer, A. Steiner, T. Stey, D. Stalke, *J. Organomet. Chem.* **2002**, *661*, 111–127.

[14] C. Zhang, T.-W. Wang, Z.-J. Lu, Z.-X. Yi, B.-L. Kuang, S. Bu, Z.-M. Xie, Y. Li, K. Wang, J.-G. Zhang, *J. Phys. Chem. C* **2023**, *127*, 12923–12930.

[15] T.-W. Wang, Z.-J. Lu, Z.-X. Yi, Z.-M. Xie, L. Zhang, B.-L. Kuang, Y. Li, J.-G. Zhang, *Cryst. Growth Des.* **2023**, *23*, 5528–5534

[16] N. Szimhardt, M. H. H. Wurzenberger, A. Beringer, L. J. Daumann, J. Stierstorfer, *J. Mater. Chem. A* **2017**, *5*, 23753–23765.

[17] N. Szimhardt, M. H. H. Wurzenberger, L. Zeisel, M. S. Gruhne, M. Lommel, J. Stierstorfer, *J. Mater. Chem. A* **2018**, *6*, 16257–16272.

[18] M. H. H. Wurzenberger, M. S. Gruhne, M. Lommel, N. Szimhardt, T. M. Klapötke, J. Stierstorfer, *Chem. Asian J.* **2019**, *14*, 2018–2028.

[19] M. H. H. Wurzenberger, S. M. J. Endraß, M. Lommel, T. M. Klapötke, J. Stierstorfer, *ACS Appl. Energy Mater.* **2020**, *3*, 3798–3806.

[20] M. Rösch, M. S. Gruhne, M. Lommel, S. M. J. Endraß, J. Stierstorfer, *Inorg. Chem.* **2023**, *62*, 1488–1507.

[21] S. M. J. Endraß, T. M. Klapötke, J. T. Lechner, J. Stierstorfer, *FirePhysChem* **2023**, *3*, 330–338.

[22] H. Tourani, M. R. Naimi-Jamal, M. G. Dekamin, *ChemistrySelect* **2018**, *3*, 8332–8337.

[23] D. Kumar, G. H. Imler, D. A. Parrish, J. n. M. Shreeve, *J. Mater. Chem. A* **2017**, *5*, 16767–16775.

[24] T. M. Klapötke, C. M. Sabaté, M. Rasp, *Dalton Trans.* **2009**, 1825–1834.

[25] T. Wu, R. Zhou, D. Li, *Inorg. Chem. Commun.* **2006**, *9*, 341–345.

[26] M. H. H. Wurzenberger, V. Braun, M. Lommel, T. M. Klapötke, J. Stierstorfer, *Inorg. Chem.* **2020**, *59*, 10938–10952.

[27] R. E. Trifonov, V. A. Ostrovskii, *Russ. J. Org. Chem.* **2006**, *42*, 1585–1605.

[28] A. L. Wani, A. Ara, J. A. Usmani, *Interdiscip. Toxicol.* **2015**, *8*, 55–64.

[29] DIRECTIVE 2011/65/EU OF THE EUROPEAN PARLIAMENT AND OF THE COUNCIL of 8 June 2011 on the restriction of the use of certain hazardous substances in electrical and electronic equipment, *European Union*, **2011**.

[30] COMMISSION DELEGATED DIRECTIVE (EU) 2021/647 of 15 January 2021 amending, for the purposes of adapting to scientific and technical progress, Annex III to Directive 2011/65/EU of the European Parliament and of the Council as regards an exemption for the use of certain lead and hexavalent chromium compounds in electric and electronic initiators of explosives for civil (professional) use, *European Union*, **2021**.

[31] M. M. Puszynski, N. Mehta, G. Cheng, K. D. Oyler, D. Fischer, T. M. Klapötke, J. Stierstorfer, *J. J. Inorg. Chem.* **2016**, *1*, 003.

[32] M. H. H. Wurzenberger, M. Lommel, M. S. Gruhne, N. Szimhardt, J. Stierstorfer, *Angew. Chem. Int. Ed.* **2020**, *59*, 12367–12370.

[33] M. H. H. Wurzenberger, M. S. Gruhne, M. Lommel, N. Szimhardt, J. Stierstorfer, *Materials Advances* **2022**, *3*, 579–591.

[34] H. Li, Y. Wang, Z. Wei, X. Yang, L. Liang, L. Xia, M. Long, Z. Li, T. Zhang, *Chem. Eng. J.* **2022**, *430*, 132739.

[35] Z. P. Demko, K. B. Sharpless, *J. Org. Chem.* **2001**, *66*, 7945–7950.

[36] T. L. Desmarias, M. Costa, *Curr. Opin. Toxicol.* **2019**, *14*, 1–7.

[37] L. Leyssens, B. Vinck, C. Van Der Straeten, F. Wuyts, L. Maes, *Toxicology* **2017**, *387*, 43–56.

[38] K. K. Das, R. C. Reddy, I. B. Bagoji, S. Das, S. Bagali, L. Mullur, J. P. Khodnapur, M. S. Biradar, **2019**, *30*, 141–152.

[39] Y.-F. Yan, J.-G. Xu, F. Wen, Y. Zhang, H.-Y. Bian, B.-Y. Li, N.-N. Zhang, F.-K. Zheng, G.-C. Guo, *Inorg. Chem. Front.* **2022**, *9*, 5884–5892.

[40] Y.-F. Yan, Q.-Y. Wang, M. Cui, H.-Y. Bian, Y.-F. Han, J.-G. Xu, F.-K. Zheng, G.-C. Guo, *Chem. Eng. J.* **2023**, *472*, 144982.

[41] O. V. Dolomanov, L. J. Bourhis, R. J. Gildea, J. A. K. Howard, H. Puschmann, *J. Appl. Cryst.* **2009**, *42*, 339–341.

[42] G. M. Sheldrick, *Acta Crystallogr. Sect. A* **2015**, *71*, 3–8.

[43] *SHELXL-97* G. M. Sheldrick, University of Göttingen, Germany, **1997**.

[44] G. M. Sheldrick, *Acta Crystallogr. Sect. A* **2008**, *64*, 112–122.

[45] *Diamond - Crystal and Molecular Structure Visualization* H. Putz, K. Brandenburg, Crystal Impact, Bonn, Germany,

[46] M. Sućeska, *Propellants, Explos. Pyrotech.* **1991**, *16*, 197–202.

[47] *EXPLO5* V7.01.01, M. Sućeska, Zagreb, **2023**.

[48] Y.-B. Xie, L. Gan, E. Carolina Sañudo, H. Zheng, J. Zhao, M. Zhao, B. Wang, J.-R. Li, *CrystEngComm* **2015**, *17*, 4136–4142.

[49] P. R. Spackman, M. J. Turner, J. J. McKinnon, S. K. Wolff, D. J. Grimwood, D. Jayatilaka, M. A. Spackman, *J. Appl. Cryst.* **2021**, *54*, 1006–1011.

[50] N. Mehta, K. Oyler, G. Cheng, A. Shah, J. Marin, K. Yee, *Z. Anorg. Allg. Chem.* **2014**, *640*, 1309–1313.

[51] Impact: insensitive > 40 J, less sensitive ≥ 35 J, sensitive ≥ 4 J, very sensitive ≤ 3 J; Friction: insensitive > 360 N, less sensitive = 360 N, sensitive < 360 N and > 80 N, very sensitive ≤ 80 N, extremely sensitive ≤ 10 N, **1999**.

[52] P. N. Gaponik, V. P. Karavai, Y. V. Grigor'ev, *Chem. Heterocycl. Compd.* **1985**, *21*, 1255–1258.

[53] *MultiVu* Version 1.5.11, Quantum Design Inc., San Diego, USA, **2013**.

[54] S. Mugiraneza, A. M. Hallas, *Commun. Phys.* **2022**, *5*, 95.

[55] P. Gütlich, A. B. Gaspar, Y. Garcia, *Beilstein J. Org. Chem.* **2013**, *9*, 342–391.

[56] B. N. Figgis, J. Lewis, in *Progress in Inorganic Chemistry*, **1964**, pp. 37–239.

[57] V. Braun, M. H. H. Wurzenberger, V. Weippert, J. Stierstorfer, *New J. Chem.* **2021**, *45*, 11042–11050.

[58] D. Plaza‐Lozano, A. Conde‐Gallardo, J. Olguín, *Eur. J. Inorg. Chem.* **2021**, *2021*, 2846‐2856.

[59] E. Collet, P. Guionneau, *C. R. Chim.* **2018**, *21*, 1133–1151.

[60] *CrysAlisPRO* Version 171.33.41, Oxford Diffraction Ltd, **2009**.

[61] *PLATON* A. L. Spek, Utrecht University, The Netherlands, **1999**.

[62] L. J. Farrugia, *J. Appl. Cryst.* **2012**, *45*, 849.

[63] *Empirical absorption correction using spherical harmonics, implemented in SCALE3 ABSPACK scaling algorithm* Version 171.33.41, CrysAlisPro Oxford Diffraction Ltd., **2009**.

[64] *APEX3* Bruker AXS Inc., Madison, Wisconsin, USA,

[65] *Gaussian 09 A.02* M. J. Frisch, G. W. Trucks, H. B. Schlegel, G. E. Scuseria, M. A. Robb, J. R. Cheeseman, G. Scalmani, V.Barone, B. Mennucci, G. A. Petersson, H. Nakatsuji, M. Caricato, X. Li, H.P. Hratchian, A. F. Izmaylov, J. Bloino, G. Zheng, J. L. Sonnenberg, M. Hada, M. Ehara, K. Toyota, R. Fukuda, J. Hasegawa, M. Ishida, T. Nakajima, Y. Honda, O. Kitao, H. Nakai, T. Vreven, J. A. Montgomery Jr., J. E. Peralta, F. Ogliaro, M. Bearpark, J. J. Heyd, E. Brothers, K. N. Kudin, V. N. Staroverov, R. Kobayashi, J. Normand, K. Raghavachari, J. C. B. A. Rendell, S. S. Iyengar, J. Tomasi, M. Cossi, N. Rega, J. M. Millam, M.Klene, J. E. Knox, J. B. Cross, V. Bakken, C. Adamo, J. Jaramillo, R. Gomperts, R. E. Stratmann, O. Yazyev, A. J. Austin, R. Cammi, C. Pomelli, J. W. Ochterski, R. L. Martin, K. Morokuma, V. G. Zakrzewski, G. A. Voth, P. Salvador, J. J. Dannenberg, S.

Dapprich, A. D. Daniels, O. Farkas, J.B. Foresman, J. V. Ortiz, J. Cioslowski, D. J. Fox, Gaussian Inc, Wallingford, CT, USA, **2009**.

[66] J. W. Ochterski, G. A. Petersson, J. A. M. Jr., *J. Chem. Phys.* **1996**, *104*, 2598–2619.

[67] J. A. Montgomery Jr., M. J. Frisch, J. W. Ochterski, G. A. Petersson, *J. Chem. Phys.* **2000**, *112*, 6532–6542.

[68] L. A. Curtiss, K. Raghavachari, P. C. Redfern, J. A. Pople, *J. Chem. Phys.* **1997**, *106*, 1063–1079.

[69] E. F. C. Byrd, B. M. Rice, *J. Phys. Chem. A* **2006**, *110*, 1005–1013.

[70] B. M. Rice, S. V. Pai, J. Hare, *Comb. Flame* **1999**, *118*, 445–458.

[71] http://webbook.nist.gov/chemistry/, accessed Mai **2022.**

[72] M. S. Westwell, M. S. Searle, D. J. Wales, D. H. Williams, *J. Am. Chem. Soc.* **1995**, *117*, 5013–5015.

[73] F. Trouton, *Philos. Mag.* **1884**, *18*, 54–57.

[74] NATO standardization agreement (STANAG) on explosives, impact sensitivity tests, no. 4489, **1999**.

[75] WIWEB-Standardarbeitsanweisung 4–5.1.02, Ermittlung der Explosionsgefährlichkeit, hier der Schlagempfindlichkeit mit dem Fallhammer, **2002**.

[76] NATO standardization agreement (STANAG) on explosive, friction sensitivity tests, no. 4487, **2002**.

[77] WIWEB-Standardarbeitsanweisung 4–5.1.03, Ermittlung der Explosionsgefährlichkeit oder der Reibeempfindlichkeit mit dem Reibeapparat, **2002**.

[78] https://www.ozm.cz/, accessed December **2021.**

[79] *UN Model Regulation: Recommendations on the Transport of Dangerous Goods – Manual of Tests and Criteria, section 13.4.2.3.3* **2015**.

6.6 Supporting Information

6.6.1 Compound Overview

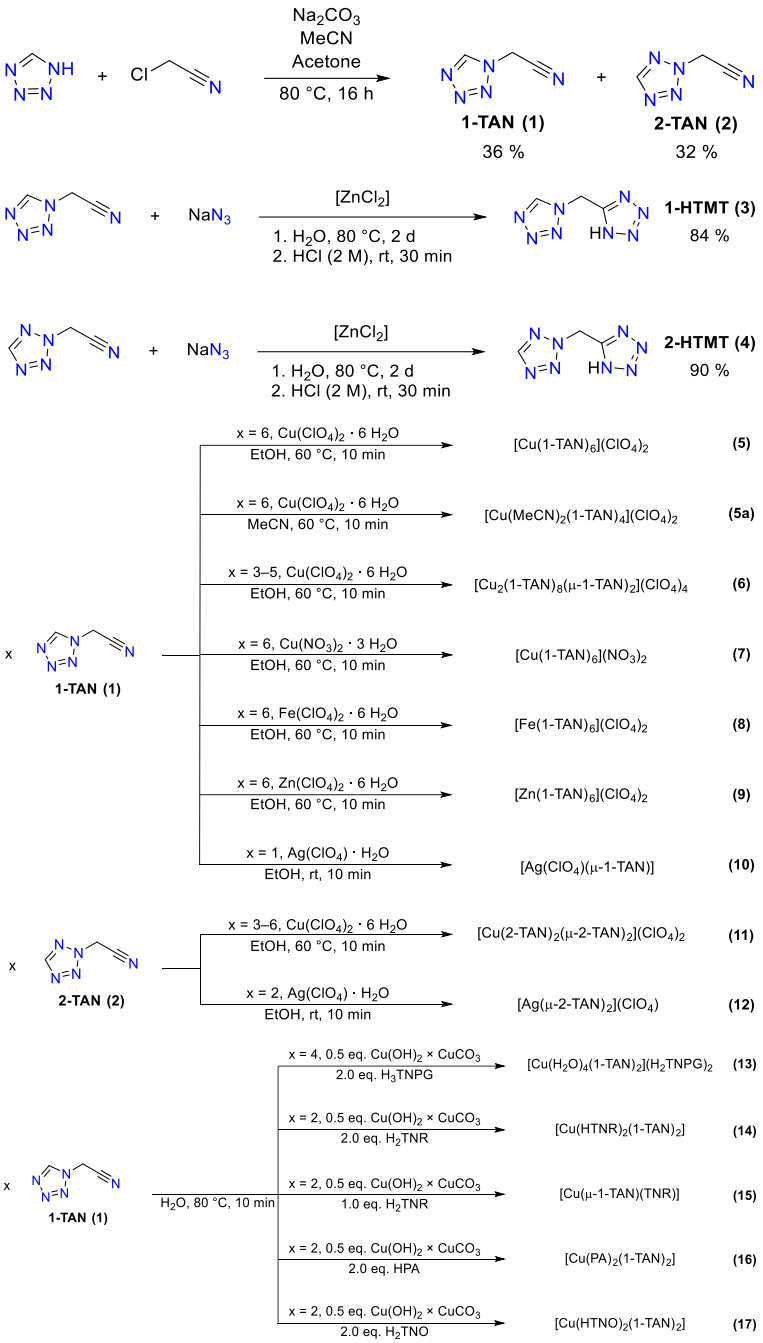

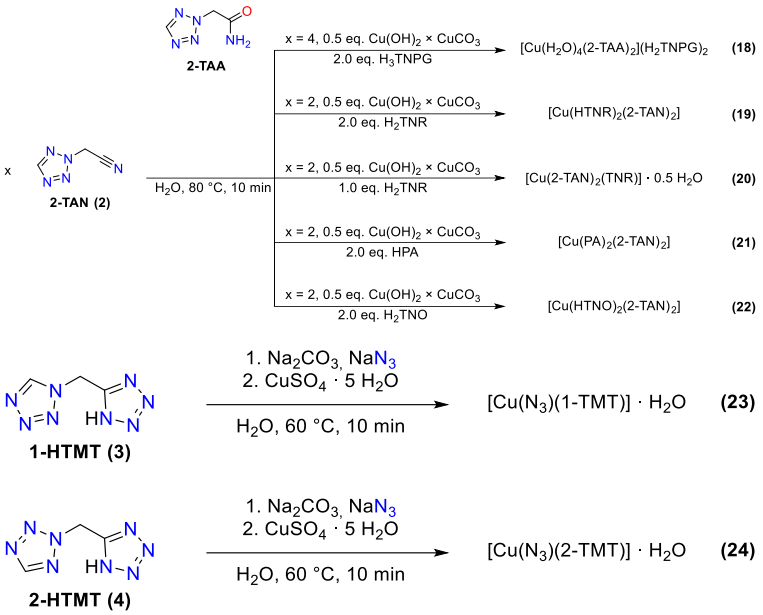

6.6.2 Single Crystal X-Ray Diffraction

For all crystalline compounds an Oxford Xcalibur3 diffractometer with a CCD area detector or Bruker D8 Venture TXS diffractometer equipped with a multilayer monochromator, a Photon 2 detector, and a rotating-anode generator were employed for data collection using Mo-Kα radiation (λ = 0.7107 Å). On the Oxford device, data collection and reduction were carried out using the CrysAlisPRO software.[S1] On the Bruker diffractometer, the data were collected with the Bruker Instrument Service v3.0.21, the data reduction was performed using the SAINT V8.18C software (Bruker AXS Inc., 2011). The structures were solved by direct methods (SHELXT[S2]), refined by full-matrix least-squares on *F2* (SHELXL[S3, S4]) and finally checked using the PLATON software[S5] integrated in the WinGX[S2, S6] or Olex2[S7] software suite. The non-hydrogen atoms were refined anisotropically and the hydrogen atoms were located and freely refined. The absorptions were corrected by a SCALE3 ABSPACK or SADABS Bruker APEX3 multi-scan method.[S8, S9] All DIAMOND4[S10] plots are shown with thermal ellipsoids at the 50 % probability level and hydrogen atoms are shown as small spheres of arbitrary radius.

Table S1. Crystallographic data and crystal structure refinement details of compounds **1**, **3** and **4**.

	1-TAN	***1-HTMT***	***2-HTMT***
Formula	$C_3H_3N_5$	$C_3H_4N_8$	$C_3H_4N_8$
FW [g mol^{-1}]	109.1	152.14	152.14
Crystal system	orthorhombic	orthorhombic	monoclinic
Space group	$P2_12_12_1$ (No. 19)	*Pbca* (No. 61)	*Cc* (No. 9)
Color / Habit	colorless plate	colorless plate	colorless plate
Size [mm]	0.10 x 0.50 x 0.50	0.05 x 0.20 x 0.50	0.02 x 0.08 x 0.10
a [Å]	5.5888(4)	6.7759(7)	5.0605(2)
b [Å]	6.4211(4)	9.3640(12)	19.3801(8)
c [Å]	13.0839(8)	19.178(3)	6.7695(3)
α [°]	90	90	90
β [°]	90	90	111.656(1)
γ [°]	90	90	90
V [Å^3]	469.53(5)	1216.8(3)	617.04(4)
Z	4	8	4
$\rho_{calc.}$ [g cm^{-3}]	1.543	1.661	1.638
μ [mm^{-1}]	0.114	0.127	0.126
F(000)	224	624	312
$\lambda_{MoK\alpha}$ [Å]	0.71073	0.71073	0.71073
T [K]	90	123	173
θ Min-Max [°]	3.1, 32.5	2.1, 32.6	3.9, 26.4
Dataset	−8:8; −9:9; −19:19	−9:9; −11:13; −28:27	−6:6; −24:24; −8:8
Reflections collected	9556	13228	5167
Independent refl.	1622	2096	1236
R_{int}	0.05	0.047	0.023
Observed reflections	1501	1516	1212
Parameters	86	116	117
R_1 (obs)[a]	0.0324	0.0495	0.0242
wR_2 (all data)[b]	0.0797	0.135	0.0635
S [c]	1.05	1.03	1.14
Resd. dens [e Å^{-3}]	−0.23, 0.25	−0.26, 0.39	−0.19, 0.12
Absorption correction	multi-scan	multi-scan	multi-scan
CCDC	2320800	2320810	2320794

[a] $R_1 = \Sigma||F_0|-|F_c||/\Sigma|F_0|$; [b] $wR_2 = [\Sigma[w(F_0^2-F_c^2)^2]/\Sigma[w(F_0)^2]]^{1/2}$; $w = [\sigma c^2(F_0^2)+(xP)^2+yP]^{-1}$ and $P=(F_0^2+2F_c^2)/3$; [c] $S = \{\Sigma[w(F_o^2-F_c^2)^2]/(n-p)\}^{1/2}$ (n = number of reflections; p = total number of parameters).

Table S2. Crystallographic data and crystal structure refinement details of compounds **5**, **5a**, **6** and **7**.

	[Cu(1-TAN)$_6$](ClO$_4$)$_2$	*[Cu(MeCN)$_2$(1-TAN)$_4$](ClO$_4$)$_2$*	*[Cu$_2$(1-TAN)$_8$(μ-1-TAN)$_2$](ClO$_4$)$_2$*	*[Cu(1-TAN)$_6$](NO$_3$)$_2$*
Formula	$C_{18}H_{18}CuN_{30}$, 2(ClO_4)	$C_{16}H_{18}CuN_{22}$, 2(ClO_4)	$C_{30}H_{30}Cu_2N_{50}$, 4(ClO_4)	$C_{18}H_{18}CuN_{30}$, 2(NO_3)
FW [g mol^{-1}]	917.05	780.96	1615.94	842.18
Crystal system	triclinic	triclinic	triclinic	monoclinic
Space group	*P*−1 (No. 2)	*P*−1 (No. 2)	*P*−1 (No. 2)	*P*2$_1$/*c* (No. 14)
Color / Habit	blue plate	blue plate	blue block	blue block
Size [mm]	0.10 x 0.30 x 0.40	0.02 x 0.10 x 0.10	0.20 x 0.35 x 0.50	0.35 x 0.50 x 0.50
a [Å]	11.5173(4)	9.9200(7)	10.6479(12)	9.5557(5)
b [Å]	15.1969(4)	10.1001(7)	11.2538(12)	18.3485(6)
c [Å]	17.8511(4)	10.1984(8)	14.4011(13)	10.2908(5)
α [°]	111.607(2)	99.078(3)	68.934(9)	90
β [°]	105.828(3)	110.623(2)	70.575(9)	101.314(5)
γ [°]	98.008(3)	117.928(2)	86.445(9)	90
V [Å^3]	2692.48(16)	777.94(10)	1515.4(3)	1769.25(14)
Z	3	1	1	2
$\rho_{calc.}$ [g cm^{-3}]	1.697	1.667	1.771	1.581
μ [mm^{-1}]	0.847	0.954	0.986	0.703
F(000)	1389	395	814	854
$\lambda_{MoK\alpha}$ [Å]	0.71073	0.71073	0.71073	0.71073
T [K]	123	173	96	96
θ Min-Max [°]	1.9, 26.4	3.1, 30.5	1.9, 26.4	2.4, 26.4
Dataset	−14:14; −18:18; −21:22	−14:14; −14:14; −14:14	−12:13; −14:14; −17:17	−11:10; −22:22; −12:12
Reflections collected	23906	19882	12198	15533
Independent refl.	10986	4750	6197	3494
R_{int}	0.028	0.037	0.044	0.039
Observed reflections	8822	4272	4750	2935
Parameters	930	224	500	287
R_1 (obs)[a]	0.0392	0.0307	0.0503	0.0526
wR_2 (all data)[b]	0.1045	0.0797	0.1415	0.1417
S [c]	1.04	1.04	1.06	1.04
Resd. dens [e Å^{-3}]	−0.54, 1.01	−0.43, 0.50	−0.87, 0.89	−0.48, 1.77
Absorption correction	multi-scan	multi-scan	multi-scan	multi-scan
CCDC	2320807	2320809	2320808	2320797

[a] $R_1 = \Sigma||F_0|-|F_c||/\Sigma|F_0|$; [b] $wR_2 = [\Sigma[w(F_0^2-F_c^2)^2]/\Sigma[w(F_0)^2]]^{1/2}$; $w = [\sigma c^2(F_0^2)+(xP)^2+yP]^{-1}$ and $P=(F_0^2+2F_c^2)/3$; [c] $S = \{\Sigma[w(F_o^2-F_c^2)^2]/(n-p)\}^{1/2}$ (n = number of reflections; p = total number of parameters).

Table S3. Crystallographic data and crystal structure refinement details of compounds **8** and **9**.

	[Fe(1-TAN)$_6$](ClO$_4$)$_2$	*[Fe(1-TAN)$_6$](ClO$_4$)$_2$*	*[Zn(1-TAN)$_6$](ClO$_4$)$_2$*
Formula	$C_{18}H_{18}FeN_{30}$, 2(ClO_4)	$C_{18}H_{18}FeN_{30}$, 2(ClO_4)	$C_{18}H_{18}N_{30}Zn$, 2(ClO_4)
FW [g mol^{-1}]	909.37	909.37	918.89
Crystal system	trigonal	trigonal	trigonal
Space group	*R*−3 (No.148)	*R*−3 (No.148)	*R*−3 (No.148)
Color / Habit	violet block	colorless block	colorless plate
Size [mm]	0.04 x 0.08 x 0.08	0.04 x 0.08 x 0.08	0.05 x 0.15 x 0.30
a [Å]	10.4824(7)	10.6024(3)	10.5839(7)
b [Å]	10.4824(7)	10.6024(3)	10.5839(7)
c [Å]	27.9859(18)	28.8545(10)	28.553(2)
α [°]	90	90	90
β [°]	90	90	90
γ [°]	120	120	120
V [Å^3]	2663.1(5)	2809.0(2)	2770.0(4)
Z	3	3	3
$\rho_{calc.}$ [g cm^{-3}]	1.701	1.613	1.653
μ [mm^{-1}]	0.666	0.631	0.897
F(000)	1380	1380	1392
$\lambda_{MoK\alpha}$ [Å]	0.71073	0.71073	0.71073
T [K]	93	193	91
θ Min-Max [°]	3.7, 28.4	3.6, 28.3	2.1, 26.4
Dataset	−13:13; −14:13; −37:35	−14:13; −14:14; −38:37	−13:13; −13:13; −32:35
Reflections collected	17114	19384	7903
Independent refl.	1483	1551	1260
R_{int}	0.078	0.04	0.051
Observed reflections	1357	1387	1171
Parameters	123	121	120
R_1 (obs)[a]	0.0403	0.0369	0.035
wR_2 (all data)[b]	0.0885	0.0982	0.0782
S [c]	1.09	1.1	1.13
Resd. dens [e Å^{-3}]	−0.41, 0.35	−0.92, 0.48	−0.88, 0.33
Absorption correction	multi-scan	multi-scan	multi-scan
CCDC	2320799	2320804	2320796

[a] $R_1 = \Sigma||F_0|-|F_c||/\Sigma|F_0|$; [b] $wR_2 = [\Sigma[w(F_0^2-F_c^2)^2]/\Sigma[w(F_0)^2]]^{1/2}$; $w = [\sigma c^2(F_0^2)+(xP)^2+yP]^{-1}$ and $P=(F_0^2+2F_c^2)/3$; [c] $S = \{\Sigma[w(F_o^2-F_c^2)^2]/(n-p)\}^{1/2}$ (n = number of reflections; p = total number of parameters).

Table S4. Crystallographic data and crystal structure refinement details of compounds **10**, **11** and **12**.

	[Ag(ClO$_4$)(μ-1-TAN)]	*[Cu(2-TAN)$_2$(μ-2-TAN)$_2$](ClO$_4$)$_2$*	*[Ag(μ-2-TAN)$_2$](ClO$_4$)*
Formula	$C_3H_3AgN_5$, ClO_4	$C_{12}H_{12}CuN_{20}$, 2(ClO_4)	$C_6H_6AgN_{10}$, ClO_4
FW [g mol^{-1}]	316.42	698.86	425.53
Crystal system	monoclinic	monoclinic	monoclinic
Space group	*C*2/*c* (No. 15)	*P*2$_1$/*n* (No. 14)	*P*2/*c* (No. 13)
Color / Habit	colorless needle	blue plate	colorless plate
Size [mm]	0.01 x 0.05 x 0.50	0.10 x 0.30 x 0.50	0.10 x 0.30 x 0.50
a [Å]	18.5516(16)	8.9790(5)	8.898(2)
b [Å]	5.1916(4)	13.7764(8)	5.2372(6)
c [Å]	18.152(2)	10.6914(6)	14.0760(16)
α [°]	90	90	90
β [°]	108.775(11)	106.539(6)	93.814(14)
γ [°]	90	90	90
V [Å^3]	1655.2(3)	1267.79(13)	654.50(18)
Z	8	2	2
$\rho_{calc.}$ [g cm^{-3}]	2.54	1.831	2.159
μ [mm^{-1}]	2.756	1.157	1.784
F(000)	1216	702	416
$\lambda_{MoK\alpha}$ [Å]	0.71073	0.71073	0.71073
T [K]	123	95	123
θ Min-Max [°]	3.8, 26.4	2.5, 32.7	2.9, 32.2
Dataset	−22:17; −6:6; −22:22	−13:13; −20:19; −16:15	−12:12; −5:7; −20:19
Reflections collected	5736	15045	6673
Independent refl.	1692	4310	2149
R_{int}	0.048	0.043	0.043
Observed reflections	1240	3140	1483
Parameters	127	242	111
R_1 (obs)[a]	0.034	0.0417	0.0471
wR_2 (all data)[b]	0.0848	0.0983	0.111
S [c]	1.03	1.05	1.04
Resd. dens [e Å^{-3}]	−0.82, 1.01	−0.62, 0.91	−1.78, 0.81
Absorption correction	multi-scan	multi-scan	multi-scan
CCDC	2320814	2320802	2320812

[a] $R_1 = \Sigma||F_0|-|F_c||/\Sigma|F_0|$; [b] $wR_2 = [\Sigma[w(F_0^2-F_c^2)^2]/\Sigma[w(F_0)^2]]^{1/2}$; $w = [\sigma c^2(F_0^2)+(xP)^2+yP]^{-1}$ and $P=(F_0^2+2F_c^2)/3$; [c] $S = \{\Sigma[w(F_o^2-F_c^2)^2]/(n-p)\}^{1/2}$ (n = number of reflections; p = total number of parameters).

Table S5. Crystallographic data and crystal structure refinement details of compounds **13**, **14** and **16**.

	[Cu(H$_2$O)$_4$(1-TAN)$_2$](H$_2$TNPG)$_2$]	*[Cu(HTNR)$_2$(1-TAN)$_2$]*	*[Cu(PA)$_2$(1-TAN)$_2$]*
Formula	$C_6H_{14}CuN_{10}O_4$, 2($C_6H_2N_3O_9$)	$C_{18}H_{10}CuN_{16}O_{16}$	$C_{18}H_{10}CuN_{16}O_{14}$
FW [g mol^{-1}]	874.02	769.96	737.96
Crystal system	triclinic	triclinic	triclinic
Space group	*P*−1 (No. 2)	*P*−1 (No. 2)	*P*−1 (No. 2)
Color / Habit	green block	green plate	green block
Size [mm]	0.09 x 0.10 x 0.17	0.05 x 0.10 x 0.45	0.10 x 0.15 x 0.20
a [Å]	5.3321(2)	6.0794(3)	5.9532(5)
b [Å]	9.7354(3)	10.6466(15)	10.5971(12)
c [Å]	15.6308(6)	11.0141(11)	10.9313(13)
α [°]	105.467(1)	89.056(10)	92.665(9)
β [°]	91.287(1)	85.282(7)	102.371(9)
γ [°]	96.350(1)	73.878(9)	91.191(8)
V [Å^3]	776.07(5)	682.52(13)	672.54(13)
Z	1	1	1
$\rho_{calc.}$ [g cm^{-3}]	1.87	1.873	1.822
μ [mm^{-1}]	0.828	0.912	0.916
F(000)	443	387	371
$\lambda_{MoK\alpha}$ [Å]	0.71073	0.71073	0.71073
T [K]	173	90	97
θ Min-Max [°]	3.0, 27.5	2.7, 26.4	2.6, 32.6
Dataset	−6:6; −12:12; −20:20	−7:7; −13:13; −13:13	−8:7; −12:15; −12:16
Reflections collected	13848	5619	7827
Independent refl.	3555	2792	4426
R_{int}	0.031	0.029	0.035
Observed reflections	3307	2318	3367
Parameters	295	233	223
R_1 (obs)[a]	0.0271	0.0463	0.0478
wR_2 (all data)[b]	0.0688	0.1057	0.1047
S [c]	1.06	1.04	1.07
Resd. dens [e Å^{-3}]	−0.36, 0.35	−0.47, 1.82	−0.52, 0.51
Absorption correction	multi-scan	multi-scan	multi-scan
CCDC	2320815	2320801	2320813

[a]$R_1 = \Sigma||F_0|-|F_c||/\Sigma|F_0|$; [b]$wR_2 = [\Sigma[w(F_0^2-F_c^2)^2]/\Sigma[w(F_0)^2]]^{1/2}$; $w = [\sigma c^2(F_0^2)+(xP)^2+yP]^{-1}$ and $P=(F_0^2+2F_c^2)/3$; [c]$S = \{\Sigma[w(F_o^2-F_c^2)^2]/(n-p)\}^{1/2}$ (n = number of reflections; p = total number of parameters).

Table S6. Crystallographic data and crystal structure refinement details of compounds **17**, **18** and **19**.

	[Cu(HTNO)$_2$(1-TAN)$_2$]	*[Cu(H$_2$O)$_4$(2-TAA)$_2$](H$_2$TNPG)$_2$]*	*[Cu(HTNR)$_2$(2-TAN)$_2$]*
Formula	$C_{20}H_{14}CuN_{16}O_{16}$	$C_6H_{18}CuN_{10}O_6$, 2($C_6H_2N_3O_7$), 4(O)	$C_{18}H_{10}CuN_{16}O_{16}$
FW [g mol^{-1}]	798.01	909.87	769.96
Crystal system	triclinic	triclinic	triclinic
Space group	*P*−1 (No. 2)	*P*−1 (No. 2)	*P*−1 (No. 2)
Color / Habit	green plate	green block	green block
Size [mm]	0.05 x 0.20 x 0.25	0.10 x 0.25 x 0.30	0.15 x 0.30 x 0.40
a [Å]	6.3646(6)	5.2478(3)	6.5167(3)
b [Å]	9.3110(9)	11.5528(7)	8.4993(6)
c [Å]	12.0270(9)	13.3699(7)	13.3044(7)
α [°]	89.406(7)	89.633(4)	97.777(5)
β [°]	83.687(7)	87.166(5)	95.188(4)
γ [°]	88.749(8)	82.027(5)	104.903(5)
V [Å^3]	708.22(11)	801.76(8)	699.50(7)
Z	1	1	1
$\rho_{calc.}$ [g cm^{-3}]	1.871	1.885	1.828
μ [mm^{-1}]	0.883	0.81	0.89
F(000)	403	463	387
$\lambda_{MoK\alpha}$ [Å]	0.71073	0.71073	0.71073
T [K]	91	123	123
θ Min-Max [°]	2.8, 29.4	2.3, 32.7	2.5, 32.7
Dataset	−8:8; −10:12; −15:16	−7:7; −16:16; −19:19	−8:9; −12:10; −20:15
Reflections collected	5566	9419	7608
Independent refl.	3224	5262	4587
R_{int}	0.032	0.023	0.033
Observed reflections	2513	4465	3676
Parameters	246	332	271
R_1 (obs)[a]	0.0491	0.0382	0.0525
wR_2 (all data)[b]	0.1079	0.0887	0.1372
S [c]	1.07	1.04	1.05
Resd. dens [e Å^{-3}]	−0.44, 0.46	−0.46, 0.52	−0.79, 0.96
Absorption correction	multi-scan	multi-scan	multi-scan
CCDC	2320803	2320805	2320811

[a]$R_1 = \Sigma||F_0|-|F_c||/\Sigma|F_0|$; [b]$wR_2 = [\Sigma[w(F_0^2-F_c^2)^2]/\Sigma[w(F_0)^2]]^{1/2}$; $w = [\sigma c^2(F_0^2)+(xP)^2+yP]^{-1}$ and $P=(F_0^2+2F_c^2)/3$; [c]$S = \{\Sigma[w(F_o^2-F_c^2)^2]/(n-p)\}^{1/2}$ (n = number of reflections; p = total number of parameters).

Table S7. Crystallographic data and crystal structure refinement details of compounds **20**, **22** and **23**.

	[Cu(2-TAN)$_2$(TNR)] · 0.5 H$_2$O	*[Cu(HTNO)$_2$(2-TAN)$_2$]*	*[Cu(N$_3$)(1-TMT)] · H$_2$O*
Formula	$2(C_{12}H_7CuN_{13}O_8)$, H_2O	$C_{20}H_{14}CuN_{16}O_{16}$	$C_3H_3CuN_{11}$, H_2O
FW [g mol^{-1}]	1067.73	798.01	274.72
Crystal system	triclinic	triclinic	triclinic
Space group	*P*−1 (No. 2)	*P*−1 (No. 2)	*P*−1 (No. 2)
Color / Habit	green block	brown plate	green block
Size [mm]	0.15 x 0.20 x 0.30	0.10 x 0.20 x 0.40	0.02 x 0.04 x 0.16
a [Å]	7.8807(3)	6.3587(4)	6.691(6)
b [Å]	9.4482(3)	9.2123(5)	8.804(8)
c [Å]	14.2151(6)	12.5616(7)	9.461(8)
α [°]	73.995(3)	98.027(4)	117.699(18)
β [°]	88.852(4)	92.402(5)	110.675(13)
γ [°]	78.634(3)	95.354(5)	90.05(2)
V [Å^3]	996.79(7)	724.32(7)	452.4(7)
Z	1	1	2
$\rho_{calc.}$ [g cm^{-3}]	1.779	1.829	2.017
μ [mm^{-1}]	1.175	0.863	2.416
F(000)	536	403	274
$\lambda_{MoK\alpha}$ [Å]	0.71073	0.71073	0.71073
T [K]	123	123	173
θ Min-Max [°]	2.3, 26.4	2.2, 32.7	3.8, 26.4
Dataset	−9:9; −11:9; −17:17	−9:9; −13:13; −18:18	−8:8; −10:10; −11:11
Reflections collected	9544	8729	9633
Independent refl.	4073	4760	1838
R_{int}	0.04	0.03	0.062
Observed reflections	3145	3834	1711
Parameters	319	269	152
R_1 (obs)[a]	0.048	0.0426	0.0283
wR_2 (all data)[b]	0.1284	0.0991	0.0755
S [c]	1.05	1.03	1.07
Resd. dens [e Å^{-3}]	−0.66, 0.50	−0.45, 0.51	−0.35, 0.35
Absorption correction	multi-scan	multi-scan	multi-scan
CCDC	2320806	2320816	2320795

[a] $R_1 = \Sigma||F_0|-|F_c||/\Sigma|F_0|$; [b] $wR_2 = [\Sigma[w(F_0^2-F_c^2)^2]/\Sigma[w(F_0)^2]]^{1/2}$; $w = [\sigma c^2(F_0^2)+(xP)^2+yP]^{-1}$ and $P=(F_0^2+2F_c^2)/3$; [c] $S = \{\Sigma[w(F_o^2-F_c^2)^2]/(n-p)\}^{1/2}$ (n = number of reflections; p = total number of parameters).

Figure S1 shows the crystal structure of $[Cu(MeCN)_2(1\text{-}TAN)_4](ClO_4)_2$. The compound crystallized in the triclinic space group $P\bar{1}$ with one formula unit per unit cell and a density of 1.667 g cm^{-3} at 173 K. This compound was obtained, by attempting the formation of **5** in acetonitrile. By doing so, the acetonitrile was incorporated to the coordination sphere, occupying the elongated z^2-axis.

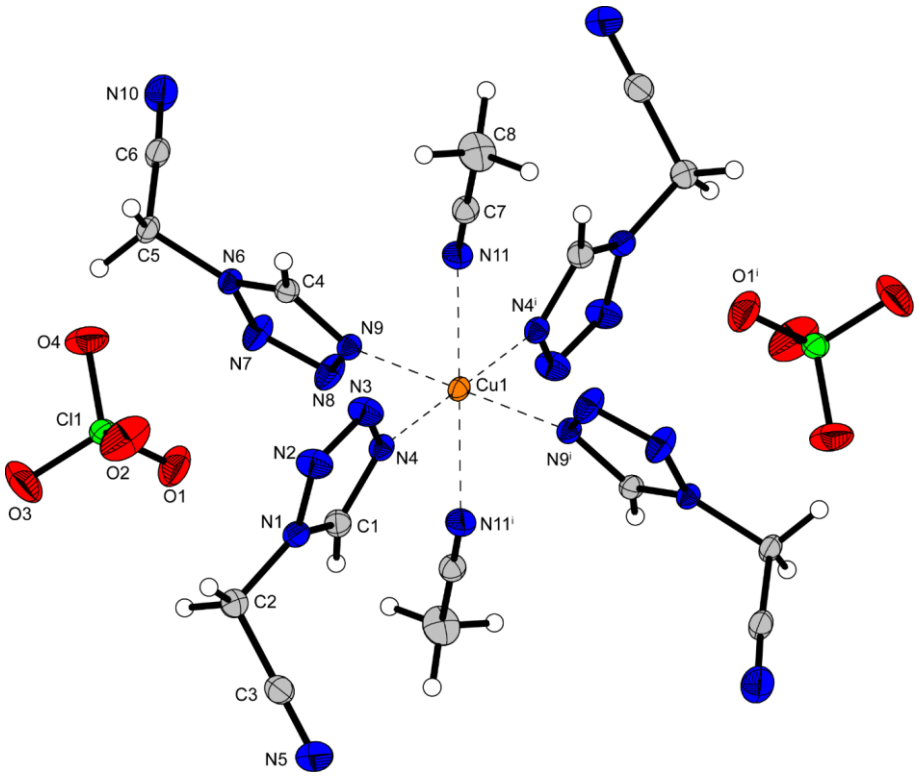

Figure S1. Crystal structure of $[Cu(MeCN)_2(1\text{-}TAN)_4](ClO_4)_2$. Selected bond lengths [Å]: Cu1–N4 2.0236(14), Cu1–N9 2.0401(15), Cu1–N11 2.3216(17); Selected bond angles [°]: N4–Cu1–N9 90.89(6), N4–Cu1–N11 91.48(6), N9–Cu1–N11 88.59(6); Symmetry codes: (i): 2−x, 1−y, 1−z.

Figure S2 shows the crystal structure of $[Cu(1\text{-}TAN)_6](NO_3)_2$. The coordination sphere shows the typical *Jahn-Teller* elongation distortion of copper(II). It crystallizes in the monoclinic space group $P2_1/c$ with a density of 1.581 g cm^{-3} at 96 K and two formula units per unit cell.

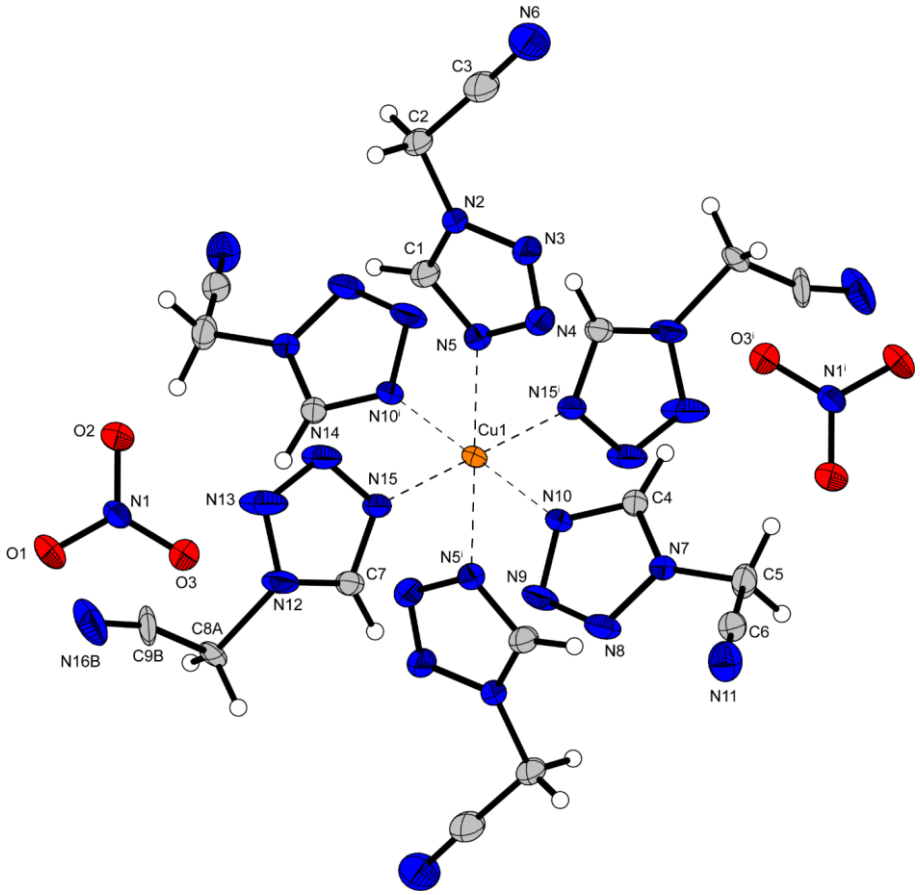

Figure S2. Crystal structure of $[Cu(1\text{-}TAN)_6](NO_3)_2$. Selected bond lengths [Å]: Cu1–N5 2.375(2), Cu1–N10 2.043(2), Cu1–N15 2.018(2); Selected bond angles [°]: N5–Cu1–N10 92.94(9), N5–Cu1–N15 91.56(9), N10–Cu1–N15 91.51(10); Symmetry codes: (i): 1−x, 1−y, 1−z.

Figure S3 shows the crystal structure of $[Zn(1\text{-}TAN)_6](ClO_4)_2$. The compound crystallized in the trigonal space group *R*−3 with three formula units per unit cell and a density of 1.653 g cm^{-3} at 91 K.

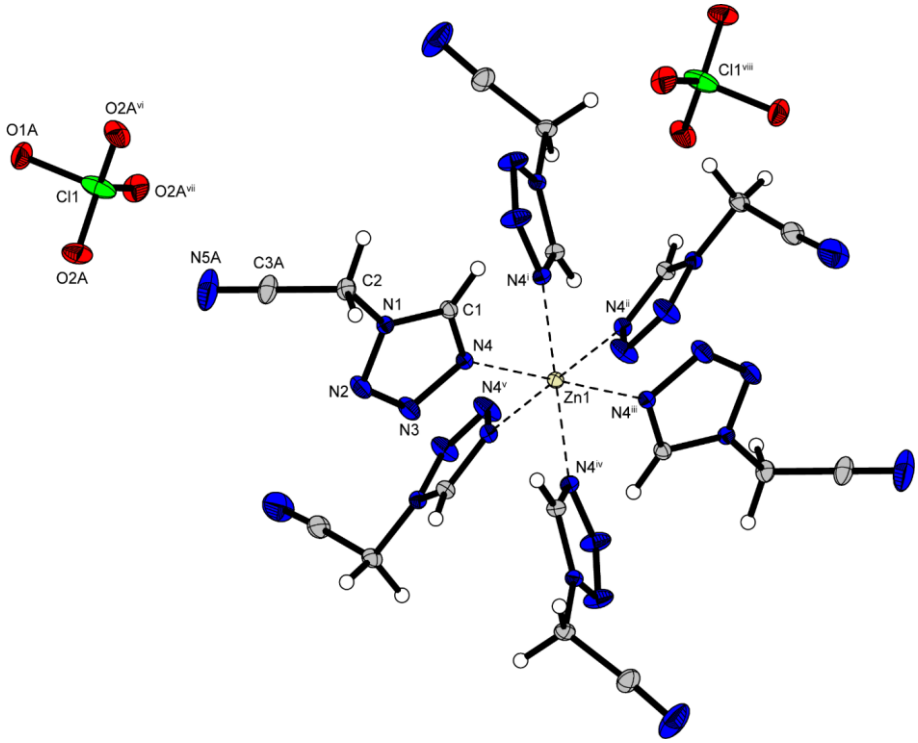

Figure S3. Crystal structure of $[Zn(1\text{-}TAN)_6](ClO_4)_2$. Selected bond lengths [Å]: Zn1–N4 2.1583(18); Selected bond angles [°]: N4–Zn1–N4^{i} 91.55(8); Symmetry codes: (i): −x+y, 1−x, z; (ii): −1/3+y, 1/3−x+y, 4/3−z; (iii): 2/3−x, 4/3−y, 4/3−z; (iv): 2/3+x−y, 1/3+x, 4/3−z; (v): 1−y, 1+x−y, z; (vi): −x+y, 1−x, z; (vii): 1−y, 1+x−y, z; (viii): −x, 1−y, 1−z.

Figure S4 shows the crystal structure of $[Cu(H_2O)_4(1\text{-}TAN)_2](H_2TNPG)_2$. The compound crystallized in the triclinic space group *P*−1 with one formula unit per unit cell and a density of 1.870 g cm^{-3} at 173 K.

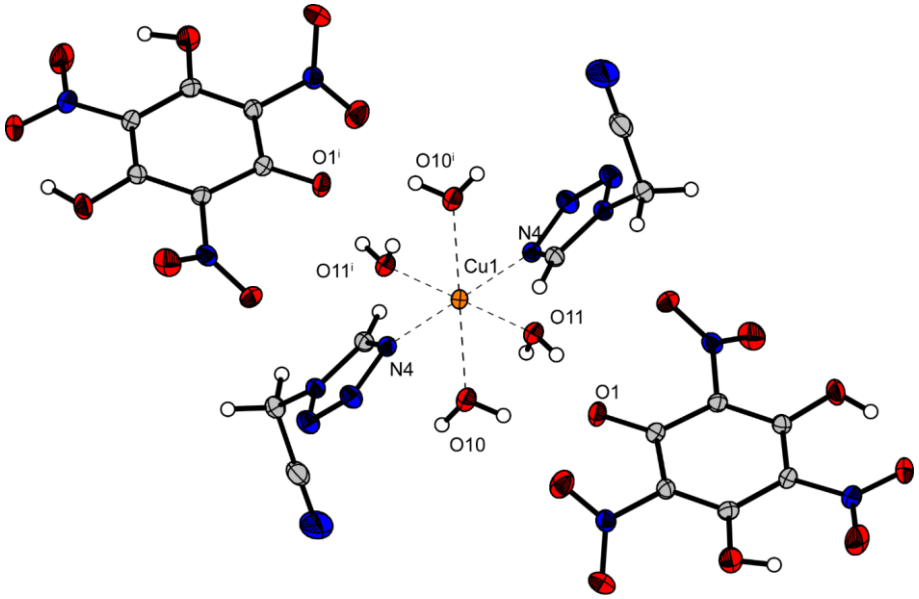

Figure S4. Crystal structure of $[Cu(H_2O)_4(1\text{-}TAN)_2](H_2TNPG)_2$. Selected bond lengths [Å]: Cu1–O10 2.3913(13), Cu1–O11 1.9754(11), Cu1–N4 2.0164(13); Selected bond angles [°]: O10–Cu1–O11 89.98(5), O10–Cu1–N4 92.70(5), O11–Cu1–N4 86.73(5); Symmetry codes: (i): 1−x, 1−y, 2−z.

Figure S5 shows the crystal structure of $[Cu(HTNR)_2(1\text{-}TAN)_2]$. The compound crystallized in the triclinic space group $P\bar{1}$ with one formula unit per unit cell and a density of 1.873 g cm^{-3} at 90 K.

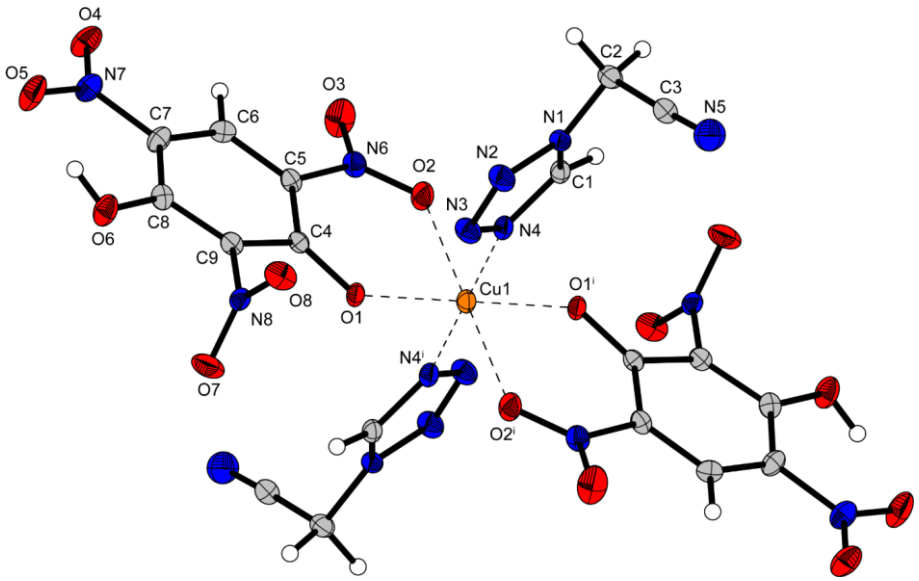

Figure S5. Crystal structure of $[Cu(HTNR)_2(1\text{-}TAN)_2]$. Selected bond lengths [Å]: Cu1–O1 1.9333(19), Cu1–O2 2.315(2), Cu1–N4 2.001(2); Selected bond angles [°]: O1–Cu1–O2 82.12(8), O1–Cu1–N4 90.38(9), O2–Cu1–N4 94.24(9); Symmetry codes: (i): 1−x, 1−y, 1−z.

Figure S6 shows the crystal structure of $[Cu(PA)_2(1\text{-}TAN)_2]$. The compound crystallized in the triclinic space group $P\bar{1}$ with one formula unit per unit cell and a density of 1.822 g cm^{-3} at 97 K.

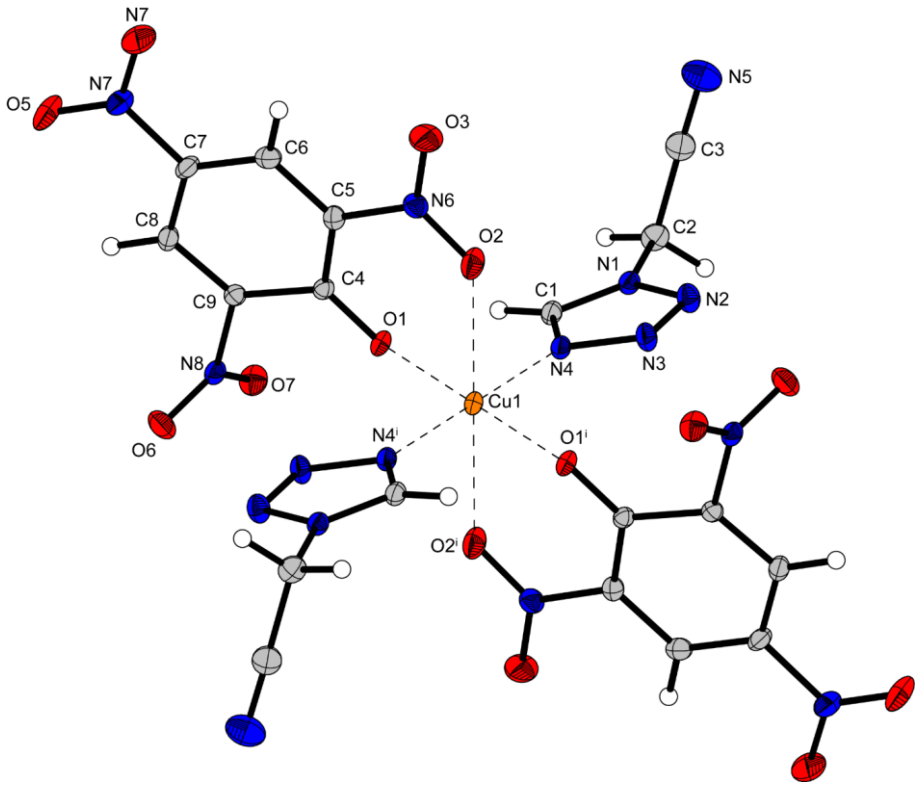

Figure S6. Crystal structure of $[Cu(PA)_2(1\text{-}TAN)_2]$. Selected bond lengths [Å]: Cu1–O1 1.9401(15), Cu1–O2 2.3865(18), Cu1–N4 1.9825(17); Selected bond angles [°]: O1–Cu1–O2 78.18(6), O1–Cu1–N4 89.29(7), O2–Cu1–N4 83.64(7); Symmetry codes: (i): 1−x, 1−y, 1−z.

Fehler! Verweisquelle konnte nicht gefunden werden. Figure S7 shows the crystal s tructure of $[Cu(HTNO)_2(1\text{-}TAN)_2]$. The compound crystallized in the triclinic space group *P*−1 with one formula unit per unit cell and a density of 1.871 g cm^{-3} at 91 K.

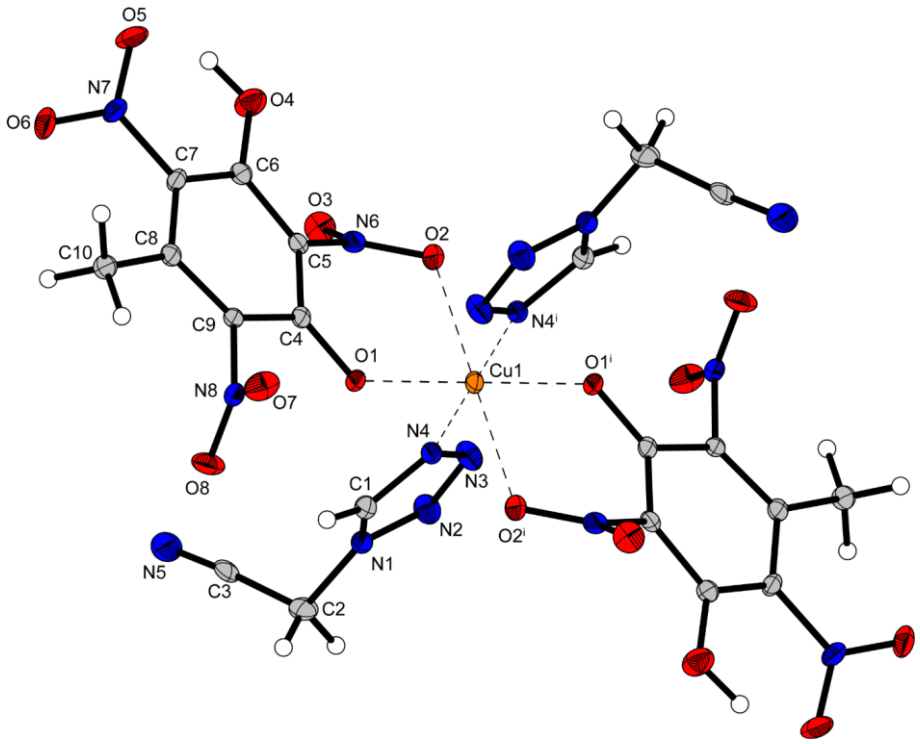

Figure S7. Crystal structure of $[Cu(HTNO)_2(1\text{-}TAN)_2]$. Selected bond lengths [Å]: Cu1–O1 1.9515(19), Cu1–O2 2.3207(19), Cu1–N4 1.991(3); Selected bond angles [°]: O1–Cu1–O2 84.87(7), O1–Cu1–N4 88.70(9), O2–Cu1–N4 88.99(9); Symmetry codes: (i): 1−x, 2−y, 1−z.

Figure S8 shows the crystal structure of $[Cu(H_2O)_4(2\text{-}TAA)_2](H_2TNPG)_2$. For reasons of clarity, only one anion is shown. The compound crystallized in the triclinic space group *P*−1 with one formula unit per unit cell and a density of 1.885 g cm^{-3} at 123 K.

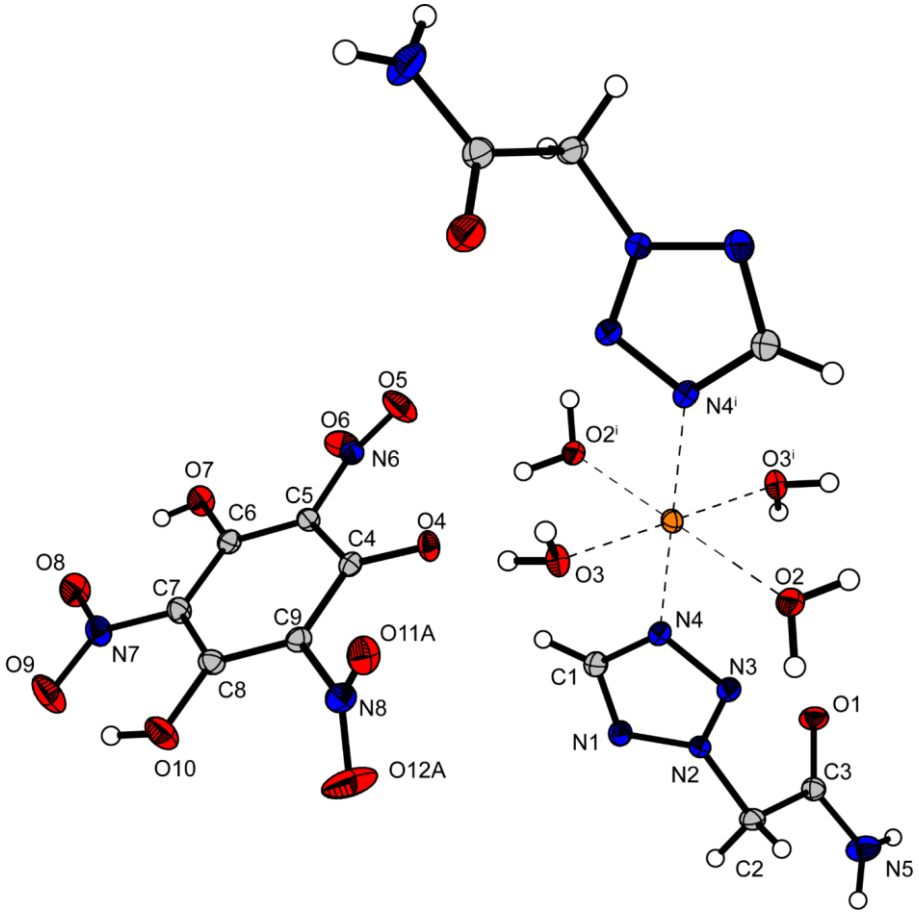

Figure S8. Crystal structure of $[Cu(H_2O)_4(2\text{-}TAA)_2](H_2TNPG)_2$. Selected bond lengths [Å]: Cu1–O3 1.9587(11), Cu1–O2 2.4460(12), Cu1–N4 2.0074(13); Selected bond angles [°]: O3–Cu1–O2 90.42(5), O3–Cu1–O2 89.58(5), O3–Cu1–N4 90.03(5); Symmetry codes: (i): 1−x, 1−y, 2−z.

Figure S9 shows the crystal structure of $[Cu(HTNR)_2(2\text{-}TAN)_2]$. The compound crystallized in the triclinic space group *P*−1 with one formula unit per unit cell and a density of 1.828 g cm^{-3} at 123 K.

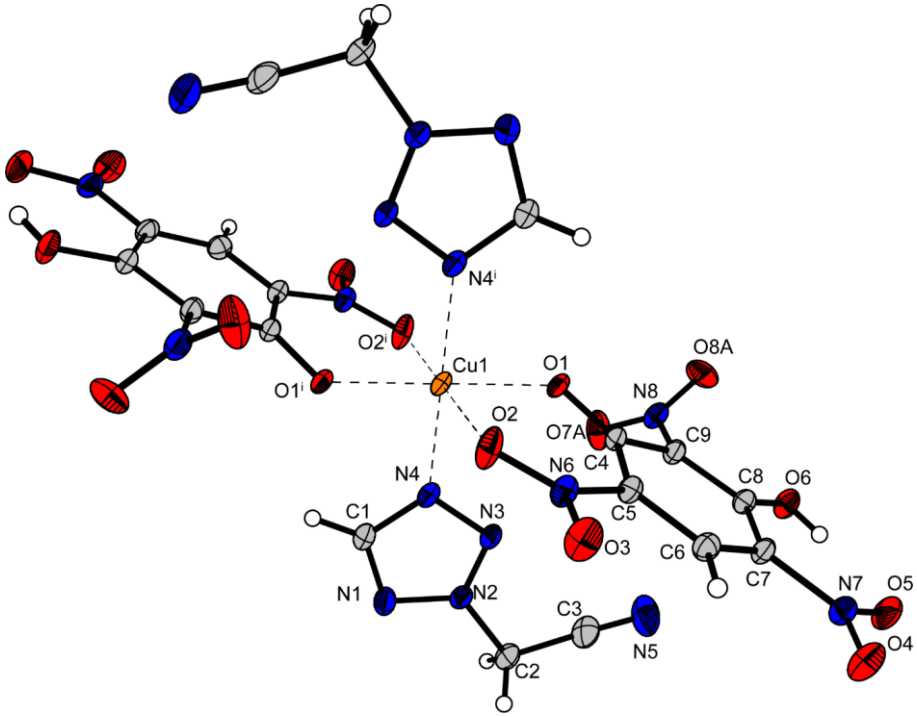

Figure S9. Crystal structure of $[Cu(HTNR)_2(2\text{-}TAN)_2]$. Selected bond lengths [Å]: Cu1–O1 1.9160(15), Cu1–O2 2.4103(18), Cu1–N4 2.0138(19); Selected bond angles [°]: O1–Cu1–O2 78.01(6), O1–Cu1–N4 93.11(7), N4–Cu1–O2 89.48(7); Symmetry codes: (i): 1−x, −y, 1−z.

Figure S10 shows the crystal structure of $[Cu(2\text{-}TAN)_2(TNR)] \cdot 0.5\ H_2O$. The compound crystallizes in the triclinic space group P−1 with a density of 1.779 g cm^{-3} at 123 K.

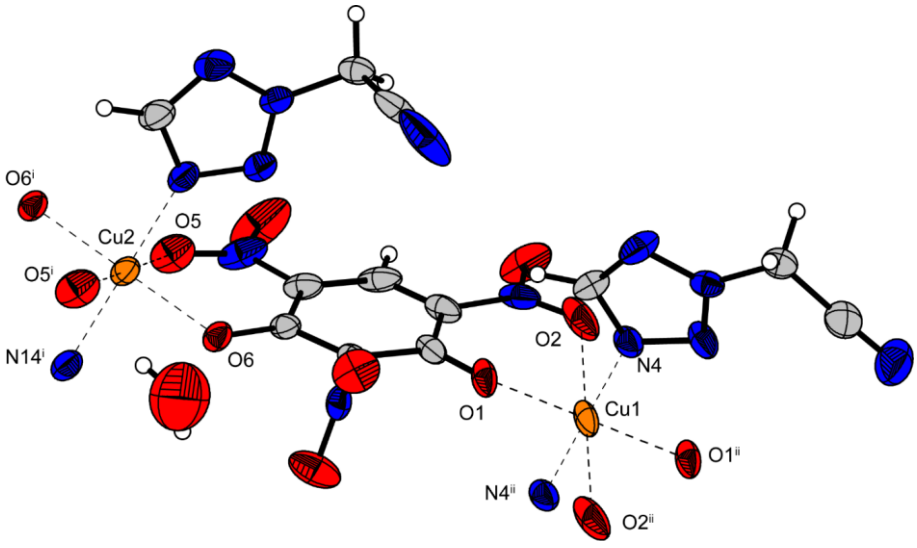

Figure S10. Crystal structure of $[Cu(2\text{-}TAN)_2(TNR)] \cdot 0.5\ H_2O$. Selected bond lengths [Å]: Cu1–O1 1.892(2), Cu1–O2 2.350(3), Cu1–N4 2.037(3), Cu2–O5 2.359(3), Cu2–O6 1.916(2), Cu2–N14 2.021(3); Selected bond angles [°]: O1–Cu1–O2 80.62(10), O1–Cu1–N4 87.37(11), O2–Cu1–N4 91.85(11), O5–Cu2–O6 79.22(10), O5–Cu2–N14 94.36(10), O6–Cu2–N14 93.03(10); Symmetry codes: (i): −x, 1−y, −z; (ii): 1−x, 1−y, 1−z.

Fehler! Verweisquelle konnte nicht gefunden werden. Figure S11 shows the crystal s tructure of $[Cu(HTNO)_2(2\text{-}TAN)_2]$. The compound crystallized in the triclinic space group *P*−1 with one formula unit per unit cell and a density of 1.829 g cm^{-3} at 123 K.

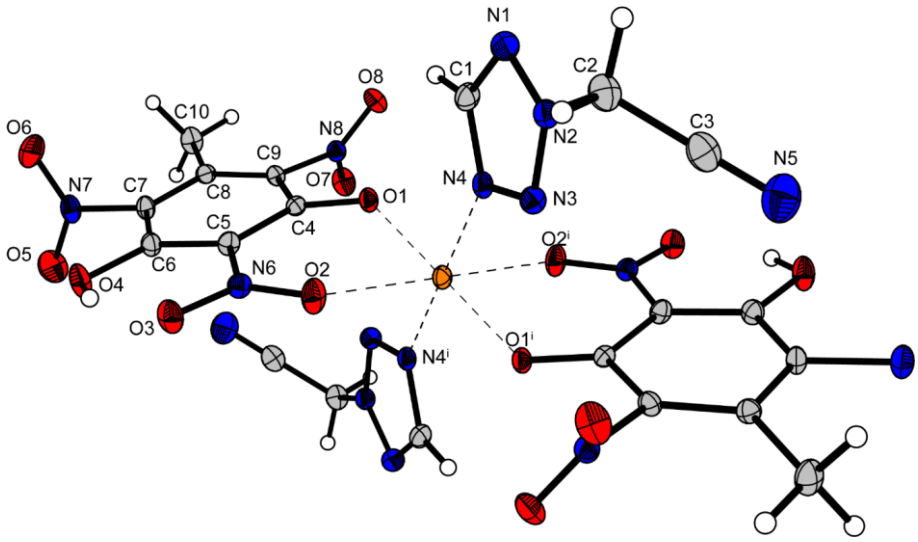

Figure S11. Crystal structure of $[Cu(HTNO)_2(2\text{-}TAN)_2]$. Selected bond lengths [Å]: Cu1–O1 1.9341(13), Cu1–O2 2.3718(13), Cu1–N4 1.9926(15); Selected bond angles [°]: O1–Cu1–O2 76.34(5), O1–Cu1–N4 88.30(6), N4–Cu1–O2 91.06(5); Symmetry codes: (i): 1−x, −y, 1−z.

6.6.3 Computations

All calculations were carried out using the Gaussian G09 program package.[S11] The enthalpies (H) and free energies (G) were calculated using the complete basis set (CBS) method of Petersson and coworkers in order to obtain very accurate energies. The CBS models use the known asymptotic convergence of pair natural orbital expressions to extrapolate from calculations using a finite basis set to the estimated complete basis set limit. CBS-4 begins with a HF/3-21G(d) geometry optimization; the zero-point energy is computed at the same level. It then uses a large basis set SCF calculation as a base energy, and a MP2/6-31+G calculation with a CBS extrapolation to correct the energy through second order. A MP4(SDQ)/6-31+(d,p) calculation is used to approximate higher order contributions. In this study we applied the modified CBS-4M method (M referring to the use of minimal population localization) which is a re-parametrized version of the original CBS-4 method and also includes some additional empirical corrections. The enthalpies of the gas-phase species M were computed according to the atomization energy method (E1) (Table S8 & Table S9).[S11-16]

$$\Delta_f \mathrm{H}^\circ_{(g,M,298)} = H_{(Molecule,298)} - \sum H^\circ_{(Atoms,298)} + \sum \Delta_f H^\circ_{(Atoms,298)} \qquad \text{(E1)}$$

Table S8. Literature values for atomic $\Delta \boldsymbol{H^\circ_f}^{\mathbf{298}}$ / kcal mol^{-1}

	$-H^{298}$ [a.u.]	NIST[S17]
H	0.50091	52.1
C	37.786156	171.3
N	54.522462	113.0
O	74.991202	59.6

The gas-phase heat of formations were converted to the solid/liquid state ones for neutrals: by subtracting the vaporization/sublimation enthalpies (calculated using the Trouton rule).[S18, 19] The calculation results are summarized in Table S9.

$$\Delta U_m = \Delta H_m - \Delta n\, R\, T \qquad \text{(E2)}$$

Table S9. CBS-4M results

Compound	$-H^{298}$[a] [a.u.]	$\Delta_f H^\circ(g,M)$[b] [kJ mol^{-1}]	$\Delta_f H^\circ(s/l)$[c] [kJ mol^{-1}]	Δn[d]	$\Delta_f U(s/l)$[e] [kJ mol^{-1}]
1-TAN	−389.254773	491.4	432.1	−4.0	442.0
2-TAN	−389.26361	468.2	426.0	−4.0	435.9
1-HTMT	−553.88376	655.5	578.6	−6.0	593.5
2-HTMT	−553.891776	634.5	564.9	−6.0	579.8

[a] CBS-4M electronic enthalpy; [b] gas phase enthalpy of formation; [c] standard condensed state enthalpy of formation; [d] Δn being the change of moles of gaseous components when formed; [e] solid state energy of formation.

Hirshfeld analysis was carried out with the CRYSTAL EXPLORER code.[S20] **Figure S** shows, that 13.5 % of 1-TAN, 20.1 % of 1-HTMT and 17.8 % of 2-HTMT are destabilizing N···N interactions, while the majority (65.1 % for 1-TAN, 63.2 % for 1-HTMT and 67.3 % for 2-HTMT) are stabilizing N···H interactions.

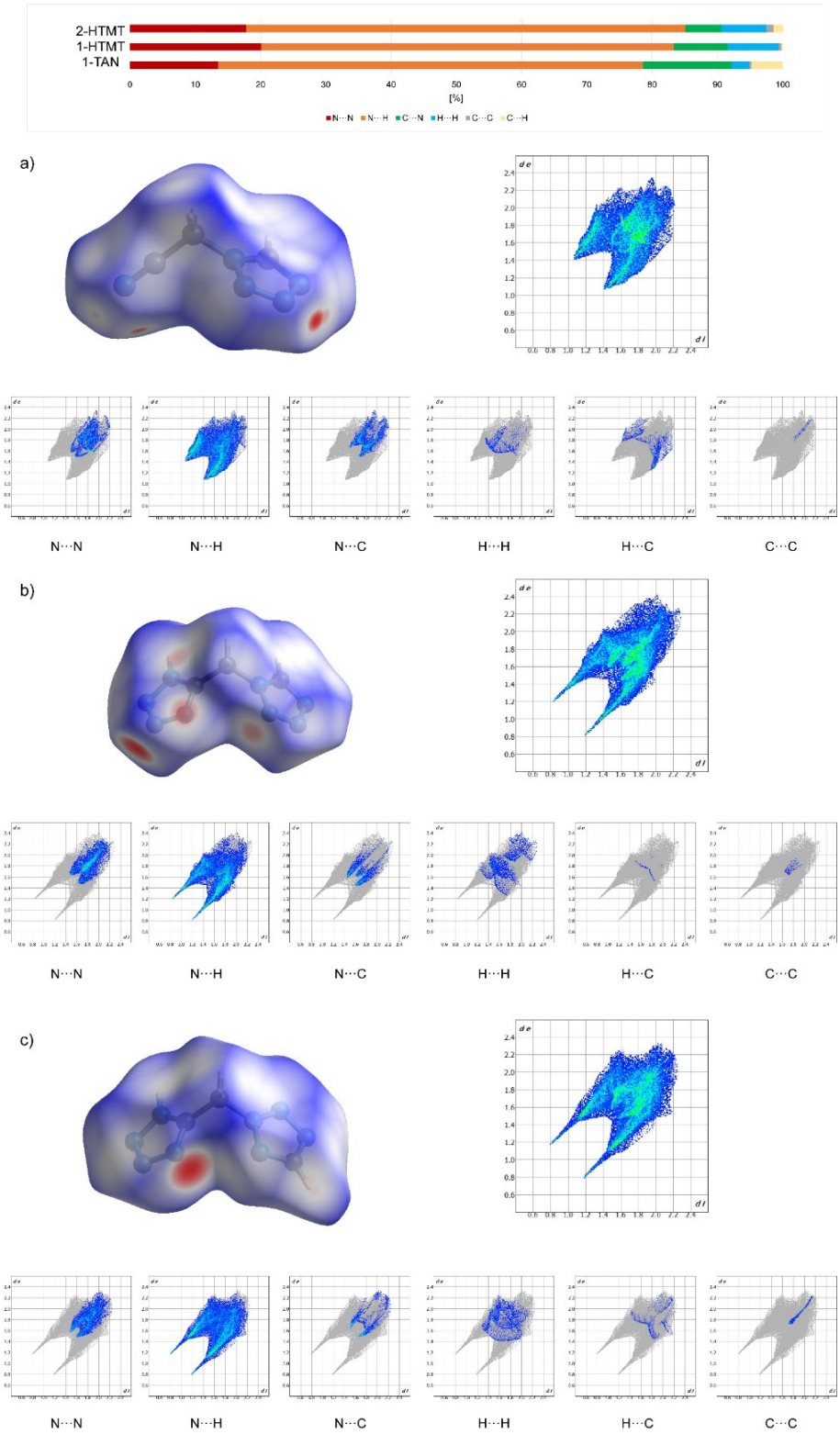

Figure S12. Hirshfeld analysis of compounds a) **1**, b) **3** and c) **4**.

6.6.4 NMR Spectroscopy of 1–4

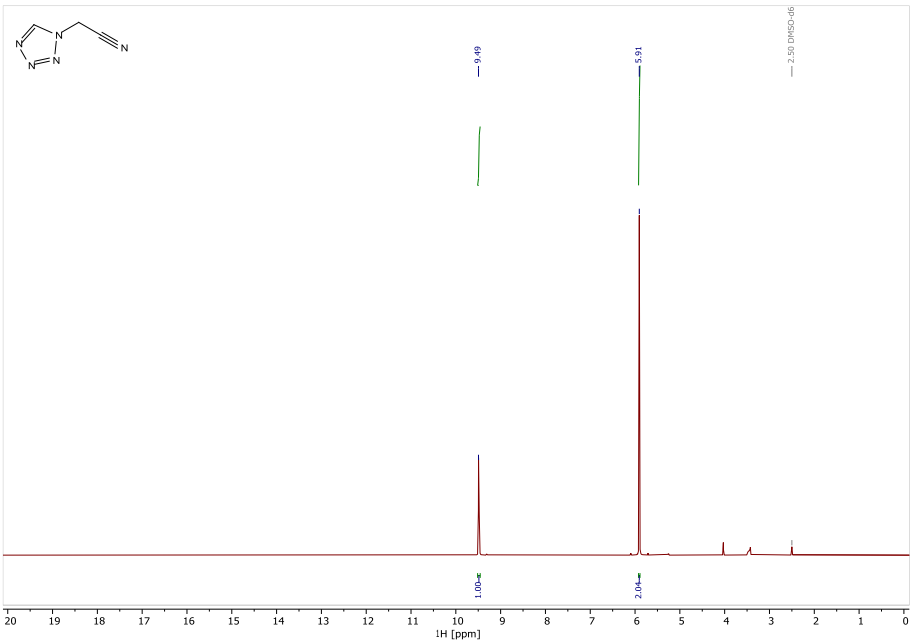

Figure S13. ^{1}H-NMR of 1-TAN.

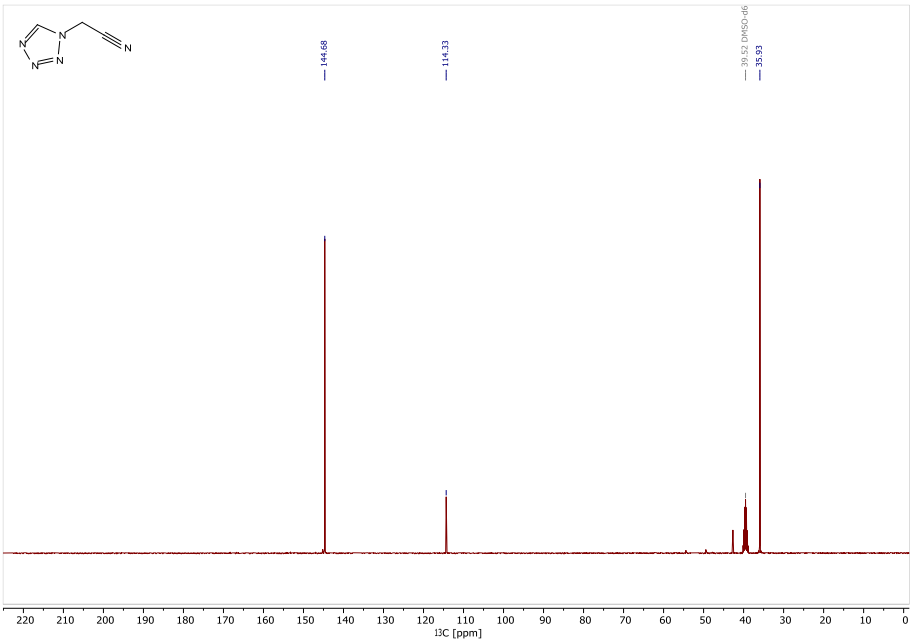

Figure S14. ^{13}C-NMR of 1-TAN.

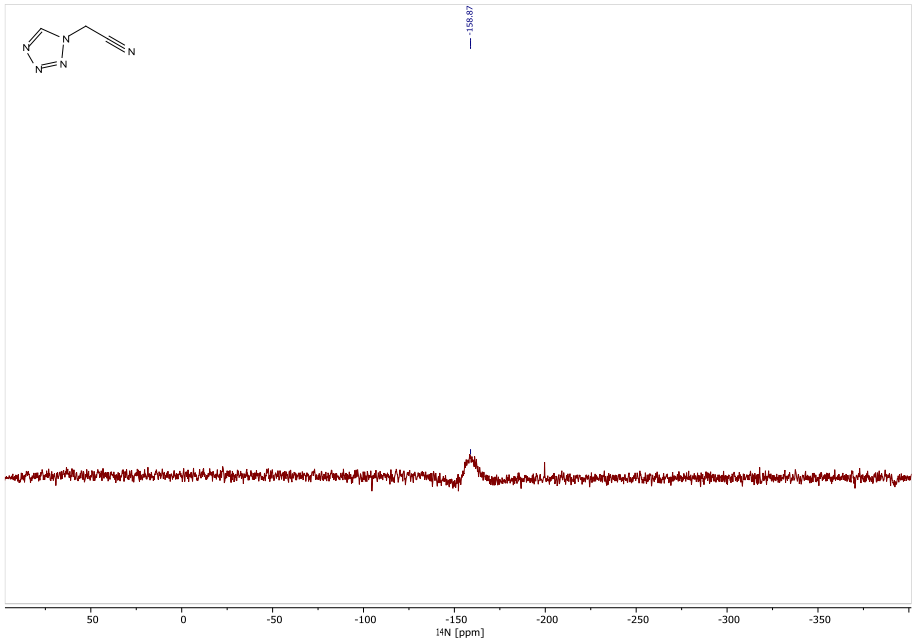

Figure S15. ^{14}N-NMR of 1-TAN.

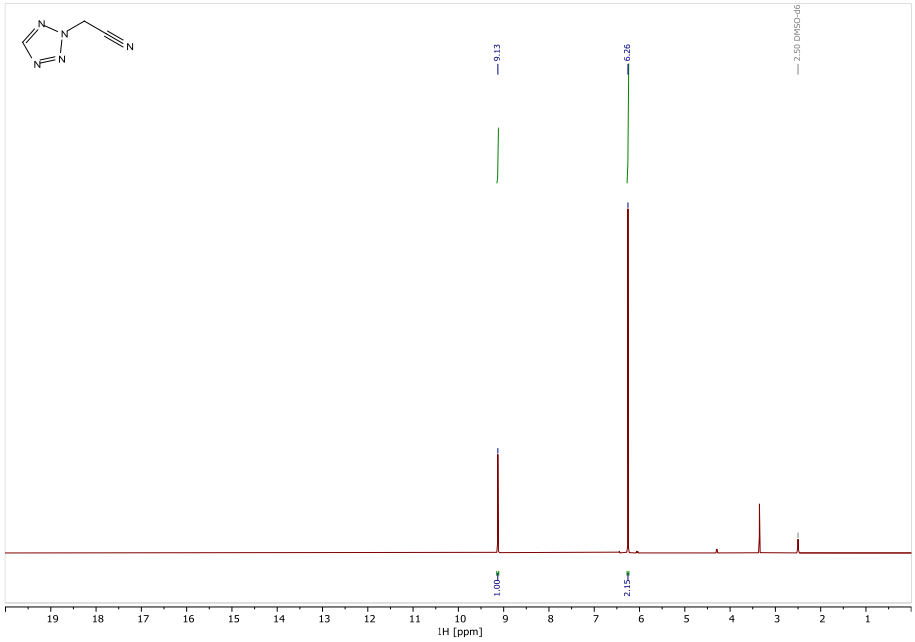

Figure S16. ^{1}H-NMR of 2-TAN.

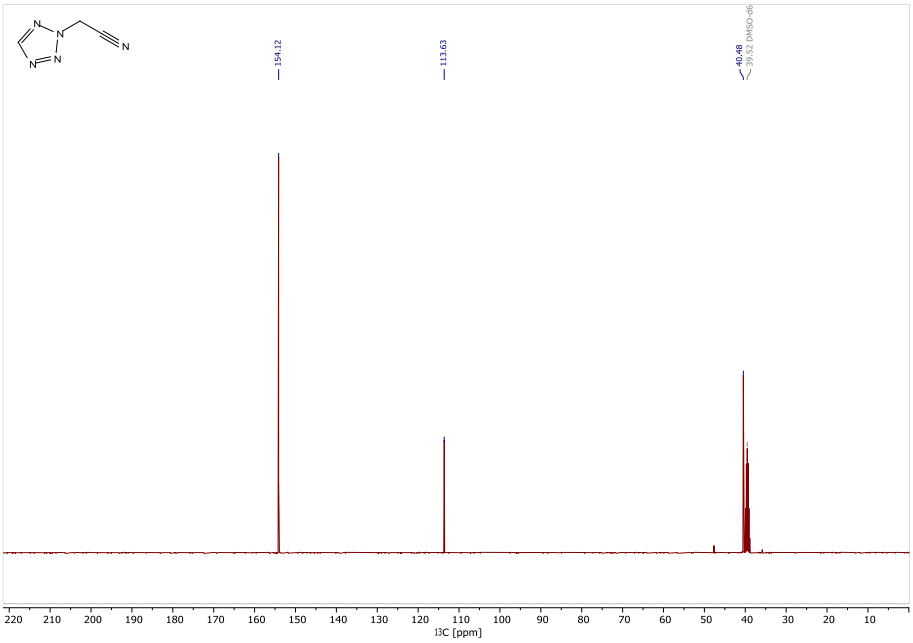

Figure S17. ^{13}C-NMR of 2-TAN.

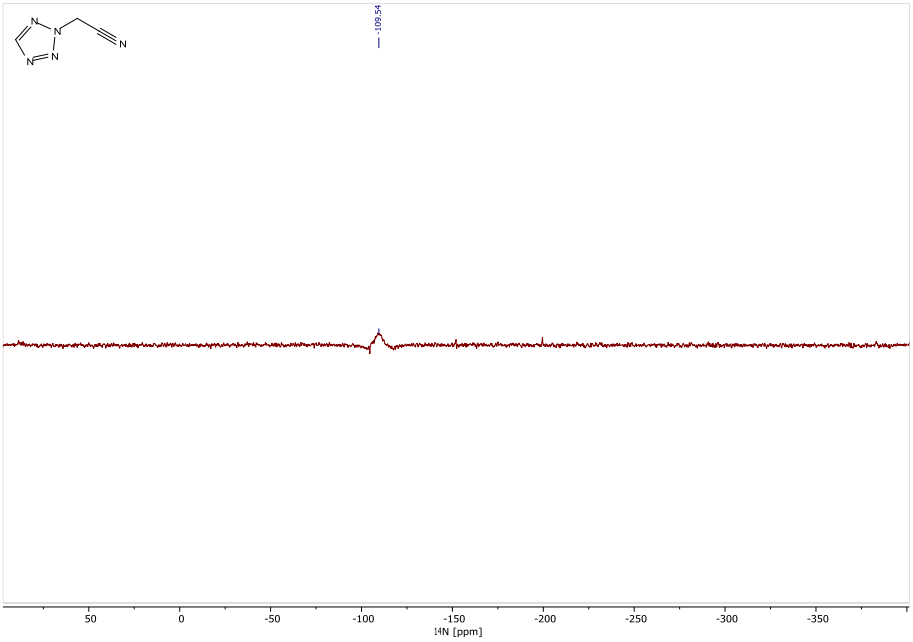

Figure S18. ^{14}N-NMR of 2-TAN.

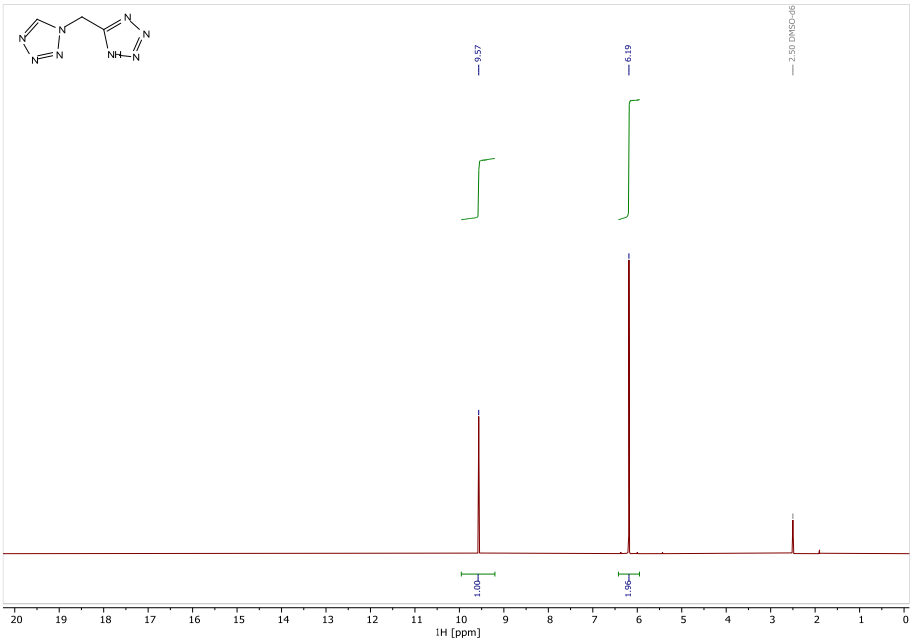

Figure S19. [1]H-NMR of 1-HTMT.

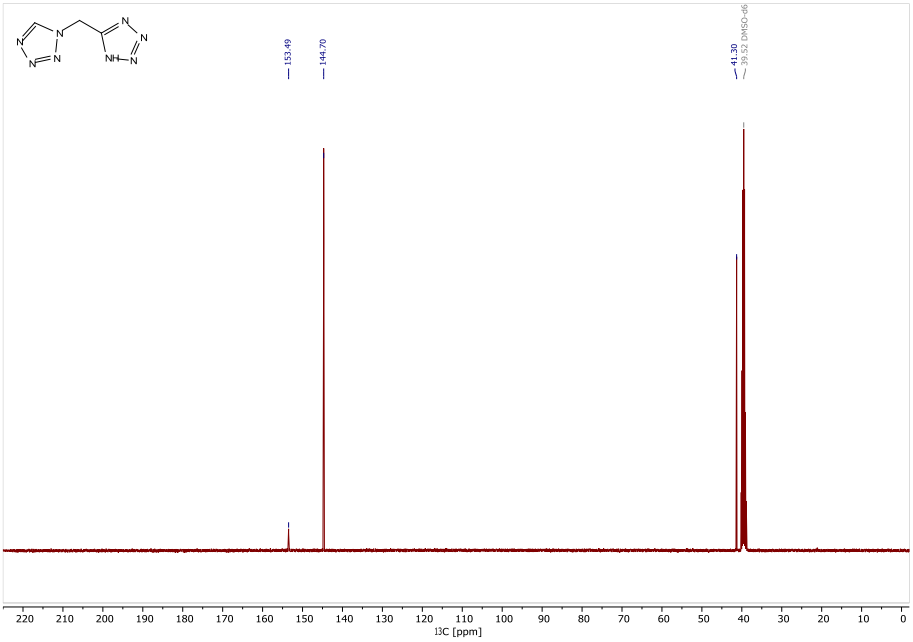

Figure S20. [13]C-NMR of 1-HTMT.

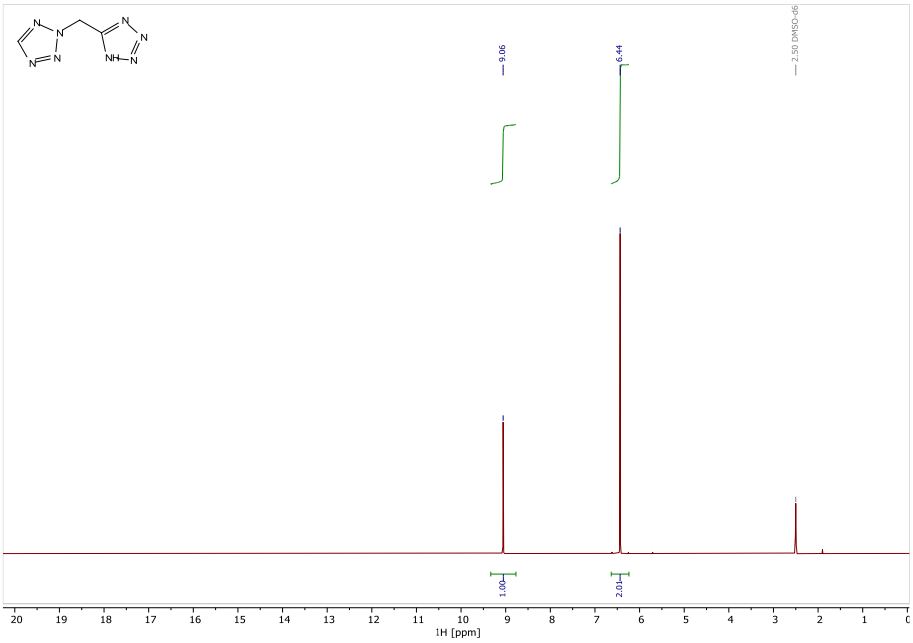

Figure S21. [1]H-NMR of 2-HTMT.

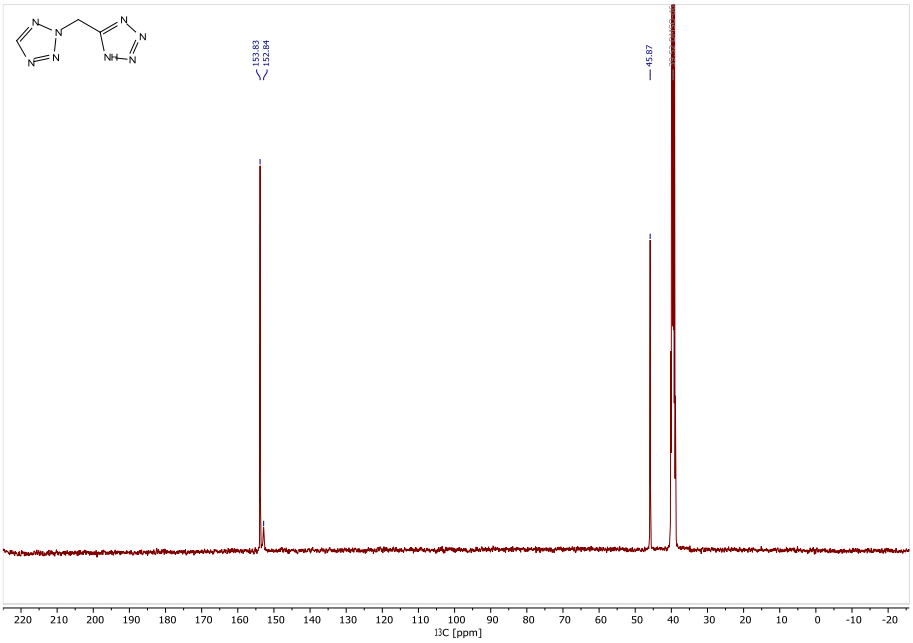

Figure S22. [13]C-NMR of 2-HTMT.

6.6.5 IR Spectroscopy of 1–24

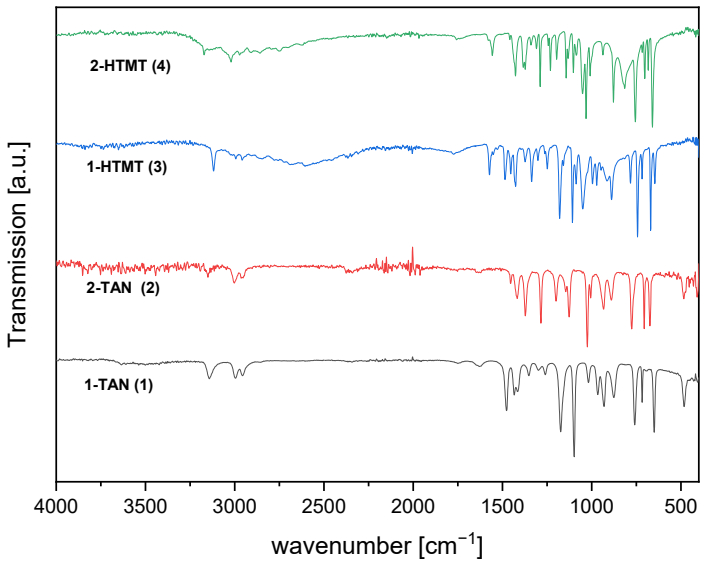

Figure S23. IR Spectroscopy of compounds **1**–**4**.

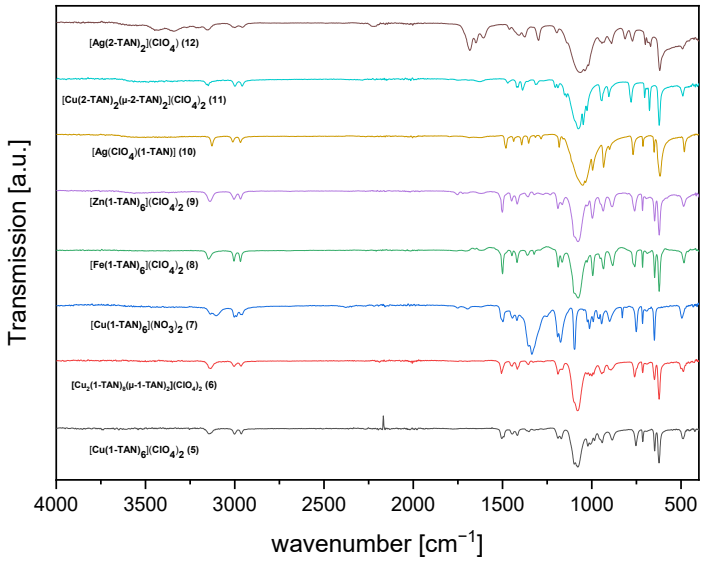

Figure S24. IR Spectroscopy of compounds **5**–**12**.

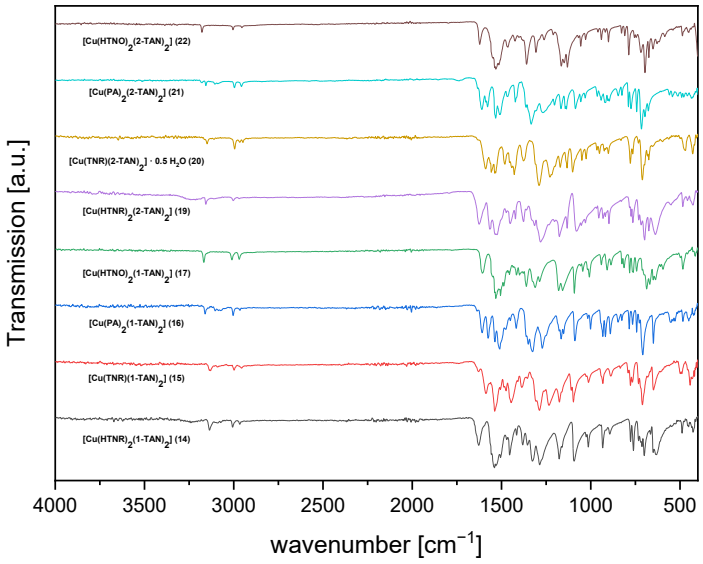

Figure S25. IR Spectroscopy of compounds **14**–**17** and **19**–**22**.

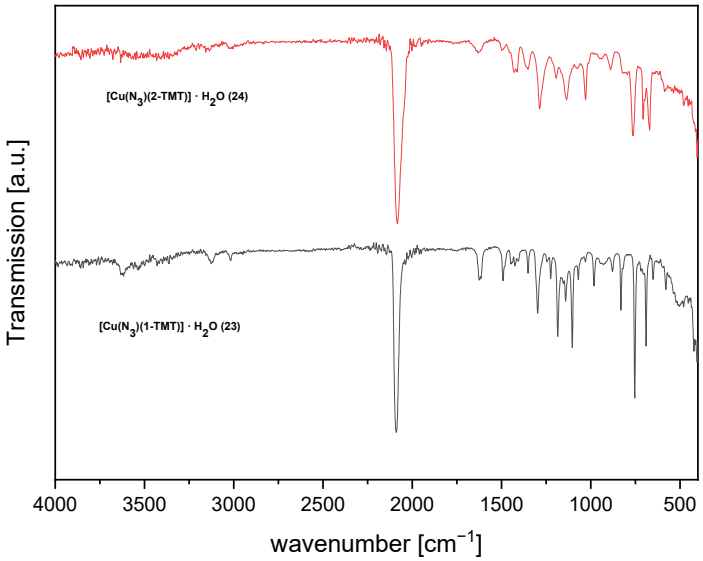

Figure S26. IR Spectroscopy of compounds **23** and **24**.

6.6.6 Thermal analysis of 1–24

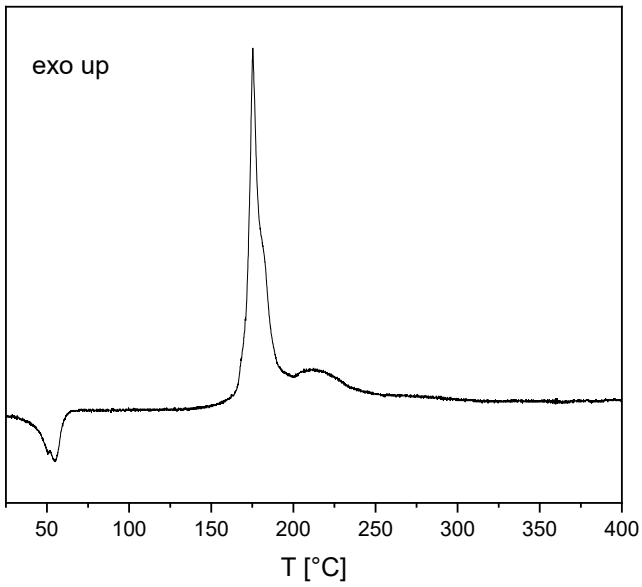

Figure S27. DTA plot of 1-TAN in the range of 25–400 °C.

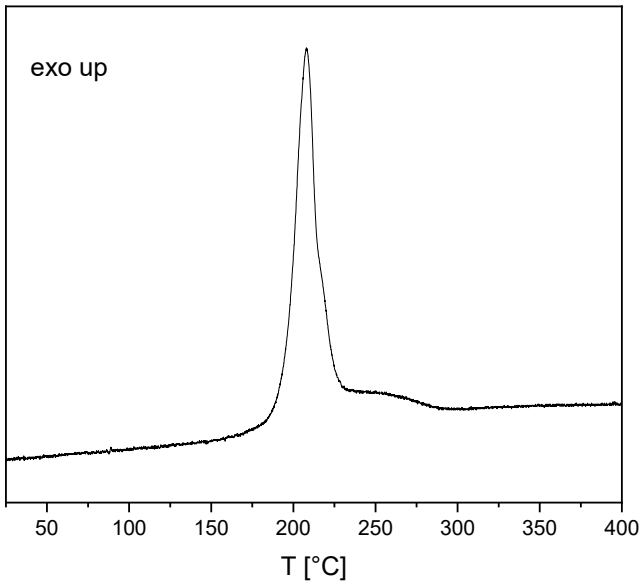

Figure S28. DTA plot of 2-TAN in the range of 25–400 °C.

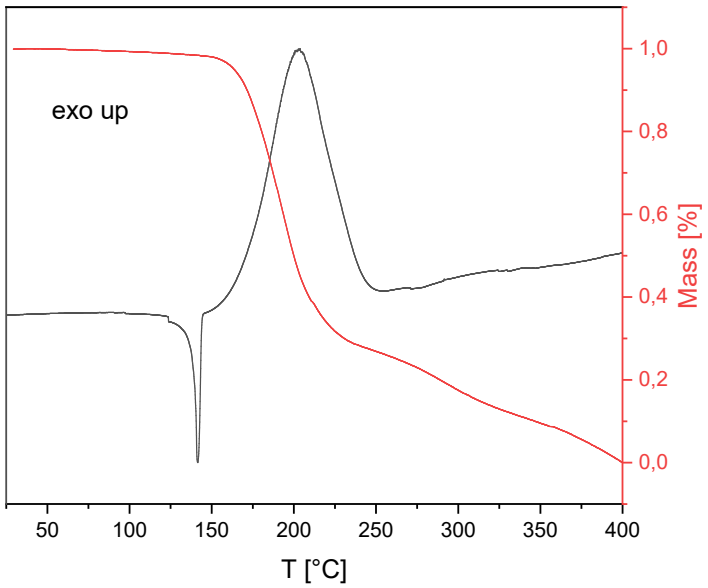

Figure S29. DSC (black) and TGA (red) plot of 1-HTMT in the range of 25–400 °C.

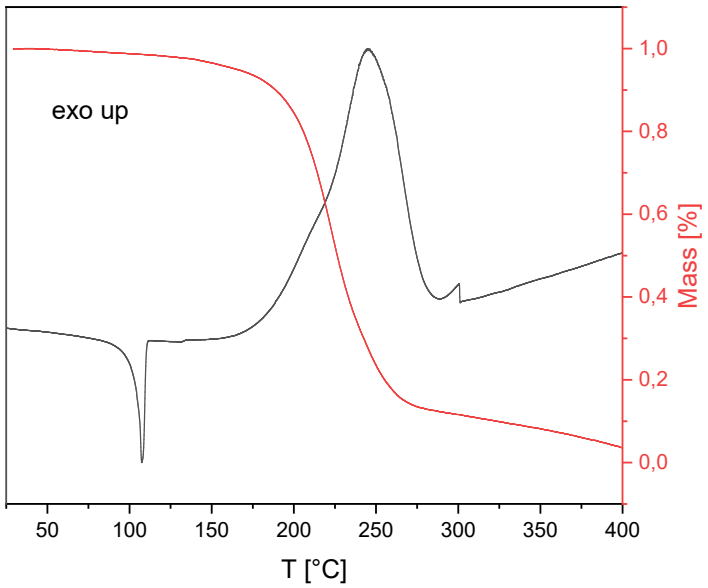

Figure S30. DSC (black) and TGA (red) plot of 2-HTMT in the range of 25–400 °C.

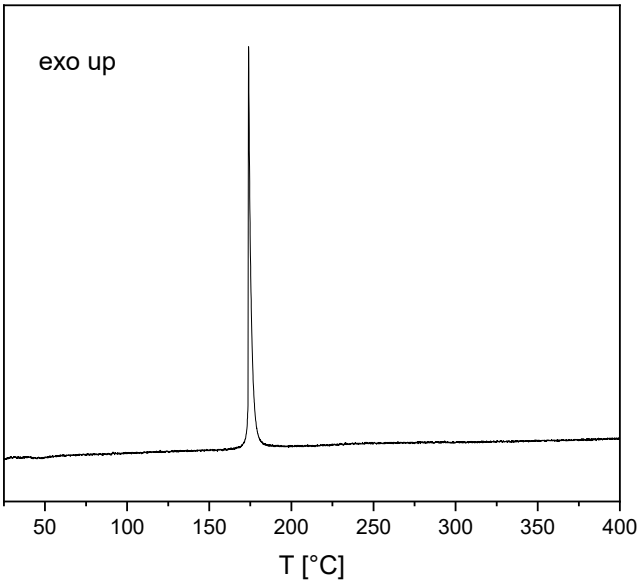

Figure S31. DTA plot of $[Cu(1\text{-}TAN)_6](ClO_4)_2$ in the range of 25–400 °C.

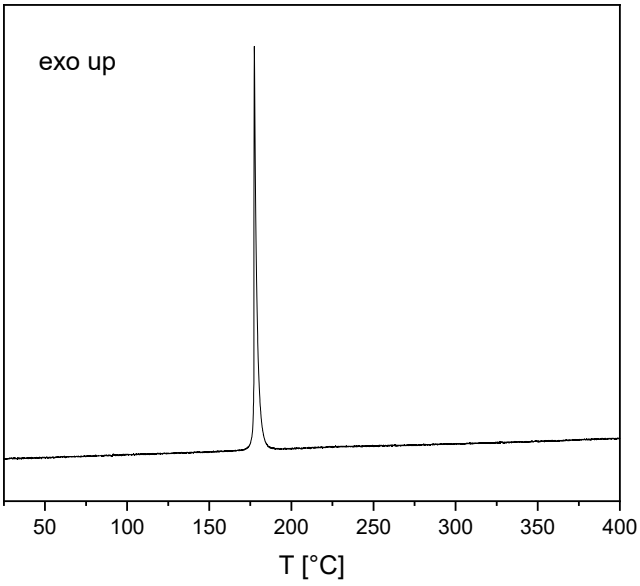

Figure S32. DTA plot of $[Cu_2(1\text{-}TAN)_8(\mu\text{-}1\text{-}TAN)_2](ClO_4)_2$ in the range of 25–400 °C.

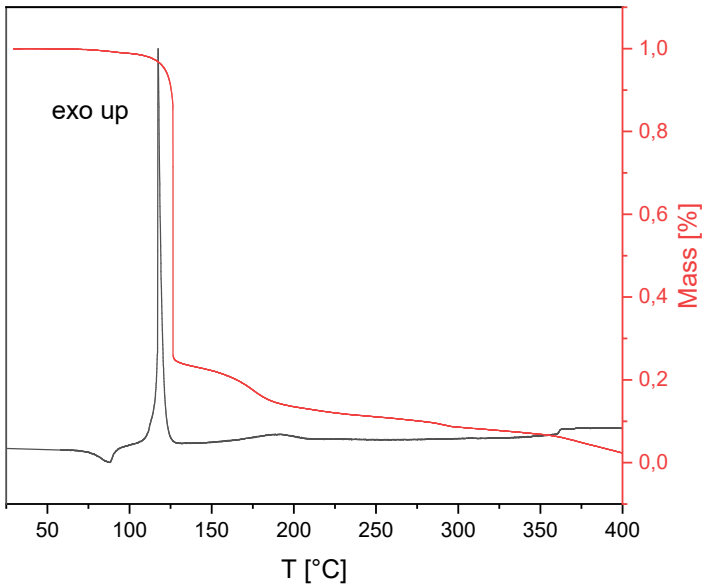

Figure S33. DTA (black) and TGA (red) plot of $[Cu(1\text{-}TAN)_6](NO_3)_2$ in the range of 25–400 °C.

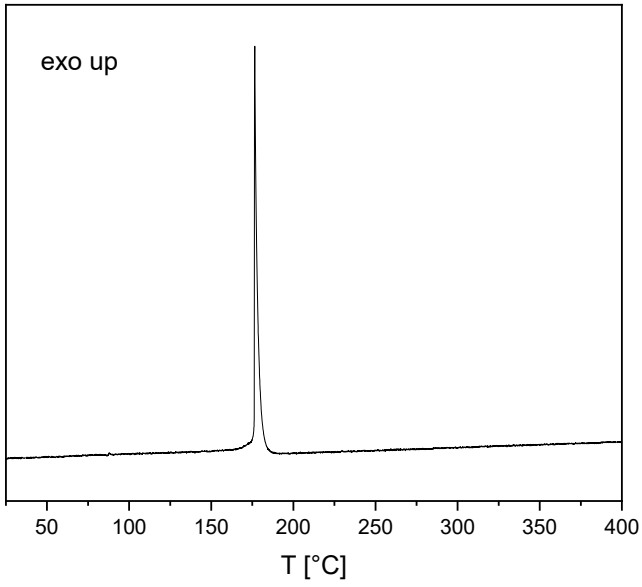

Figure S34. DTA plot of $[Fe(1\text{-}TAN)_6](ClO_4)_2$ in the range of 25–400 °C.

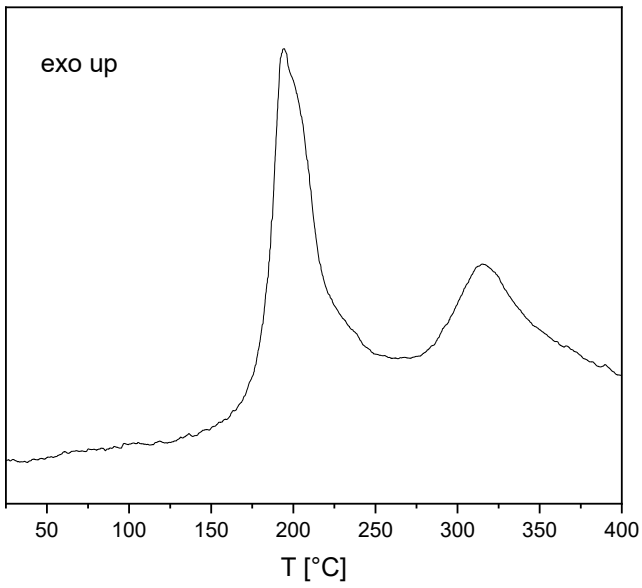

Figure S35. DTA plot of $[Zn(1\text{-TAN})_6](ClO_4)_2$ in the range of 25–400 °C.

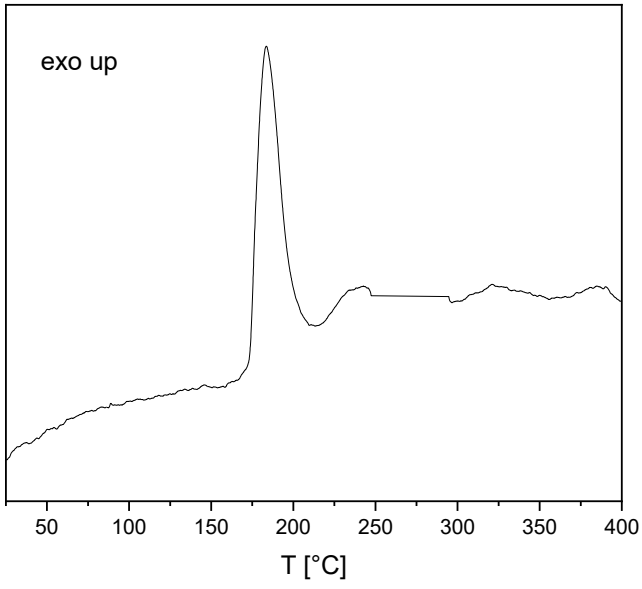

Figure S36. DTA plot of $[Ag(ClO_4)(\mu\text{-1-TAN})]$ in the range of 25–400 °C.

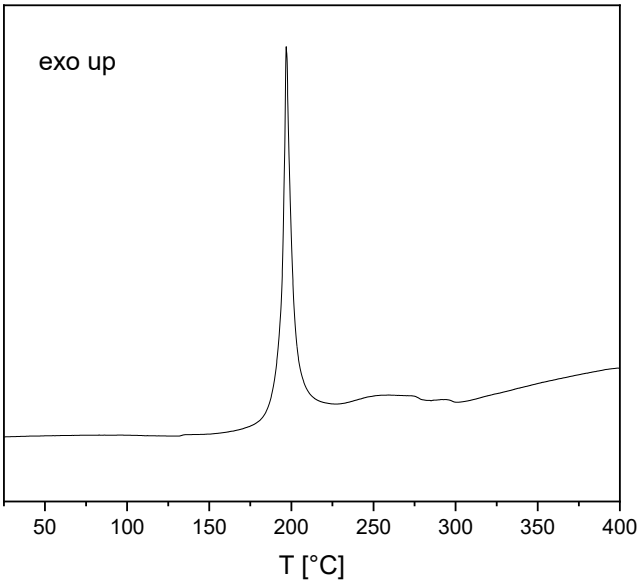

Figure S37. DSC plot of $[Cu(2\text{-}TAN)_2(\mu\text{-}2\text{-}TAN)_2](ClO_4)_2$ in the range of 25–400 °C.

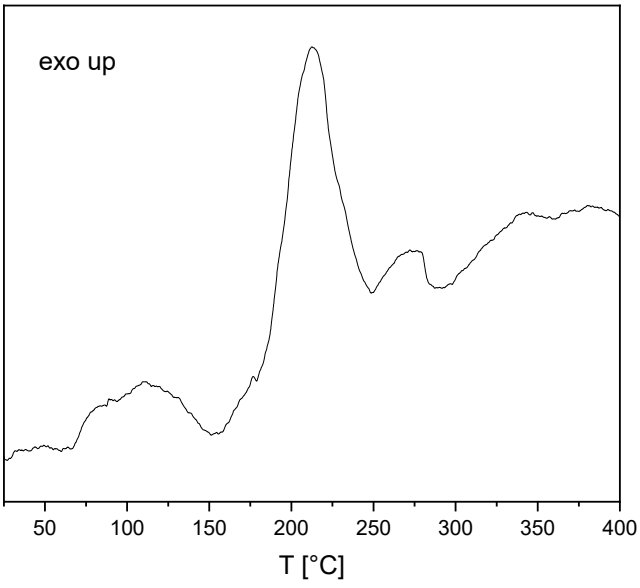

Figure S38. DTA plot of $[Ag(\mu\text{-}2\text{-}TAN)_2](ClO_4)$ in the range of 25–400 °C.

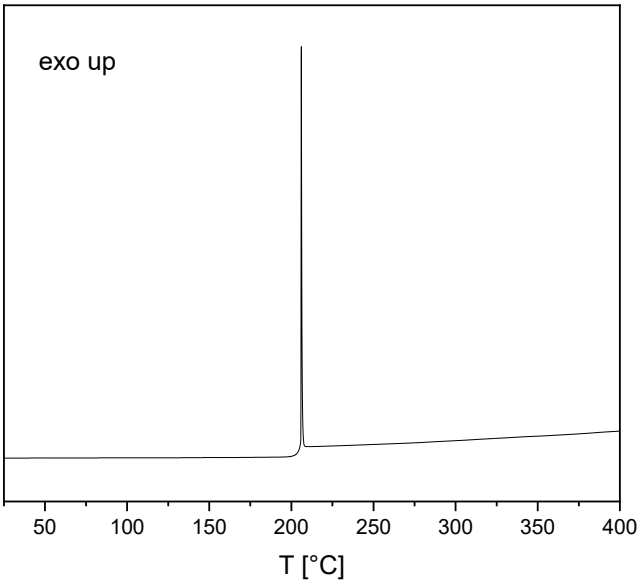

Figure S39. DSC plot of $[Cu(HTNR)_2(1\text{-}TAN)_2]$ in the range of 25–400 °C.

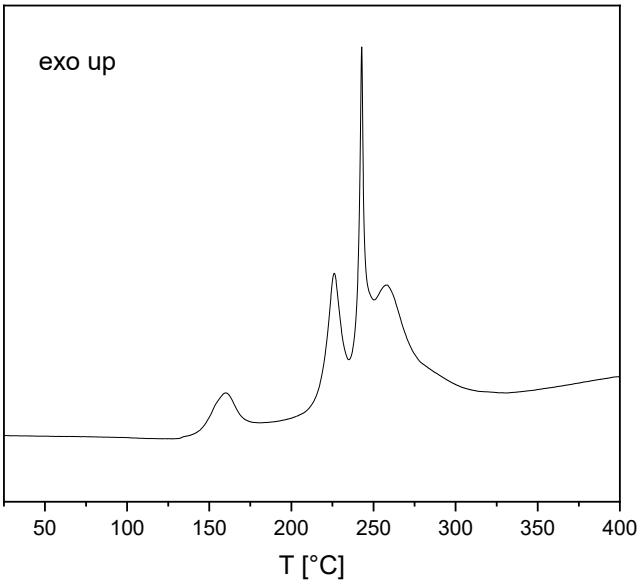

Figure S40. DSC plot of $[Cu(\mu\text{-}1\text{-}TAN)_2(TNR)]$ in the range of 25–400 °C.

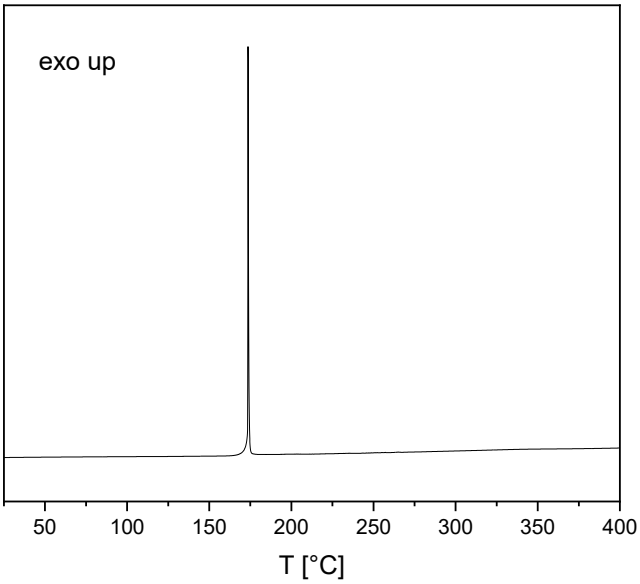

Figure S41. DSC plot of $[Cu(PA)_2(1\text{-}TAN)_2]$ in the range of 25–400 °C.

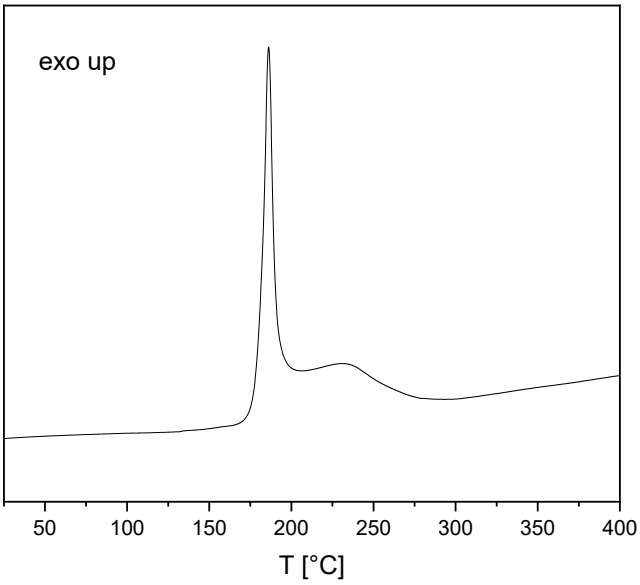

Figure S42. DSC plot of $[Cu(HTNO)_2(1\text{-}TAN)_2]$ in the range of 25–400 °C.

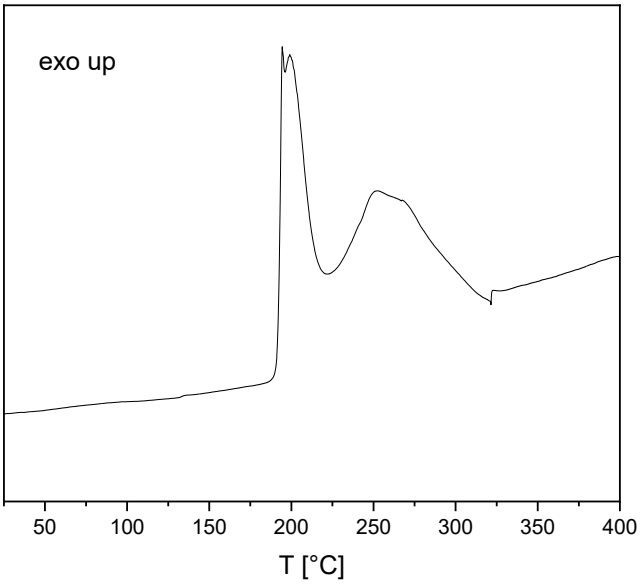

Figure S43. DSC plot of $[Cu(HTNR)_2(2\text{-}TAN)_2]$ in the range of 25–400 °C.

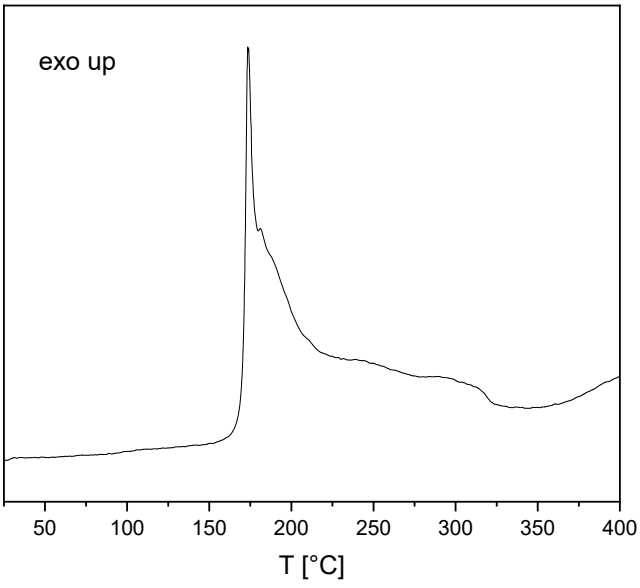

Figure S44. DTA plot of $[Cu(2\text{-}TAN)_2(TNR)]$ in the range of 25–400 °C.

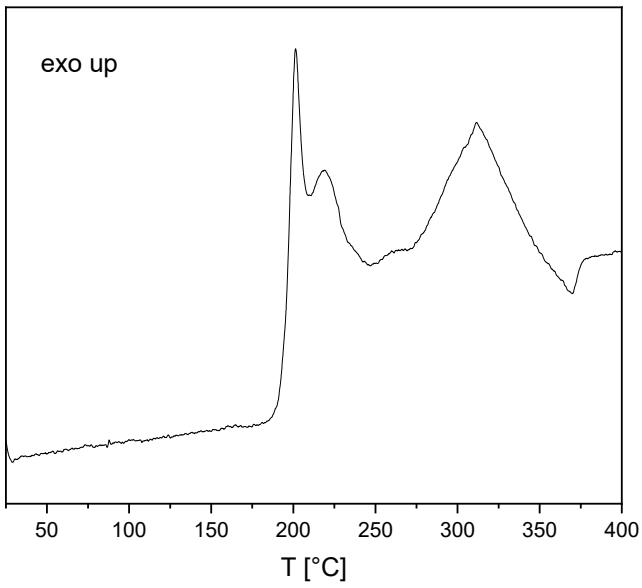

Figure S45. DTA plot of $[Cu(PA)_2(2\text{-}TAN)_2]$ in the range of 25–400 °C.

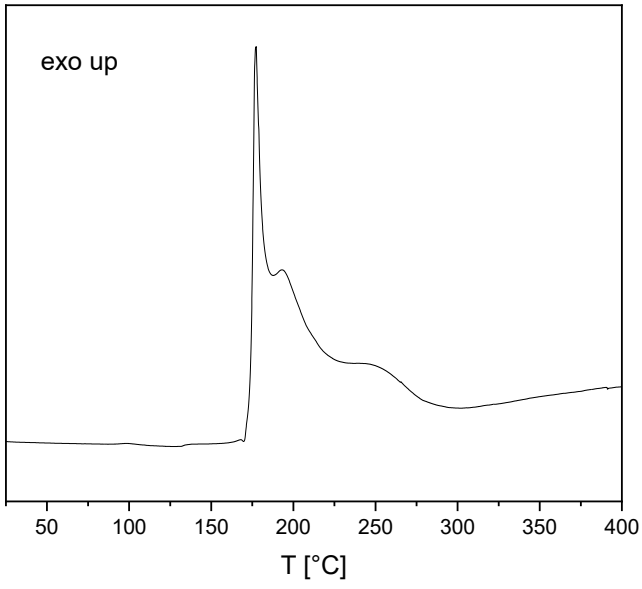

Figure S46. DSC plot of $[Cu(HTNO)_2(2\text{-}TAN)_2]$ in the range of 25–400 °C.

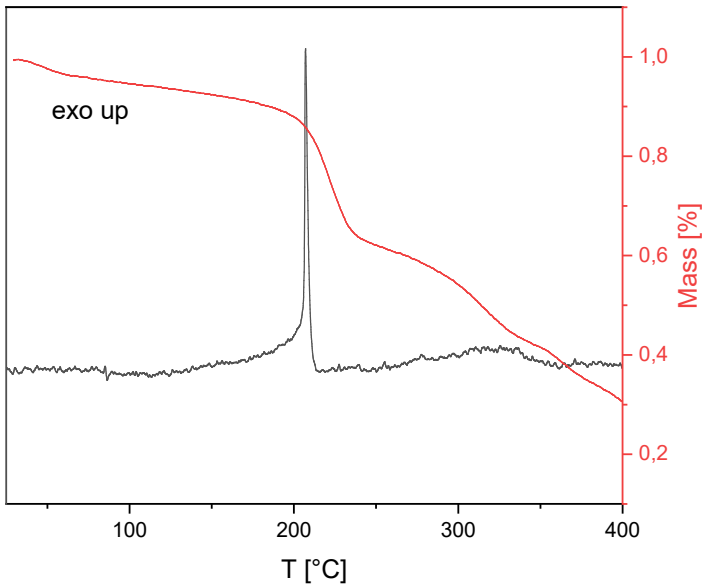

Figure S47. DTA (black) and TGA (red) plot of $[Cu(N_3)(1\text{-TMT})] \cdot H_2O$ in the range of 25–400 °C.

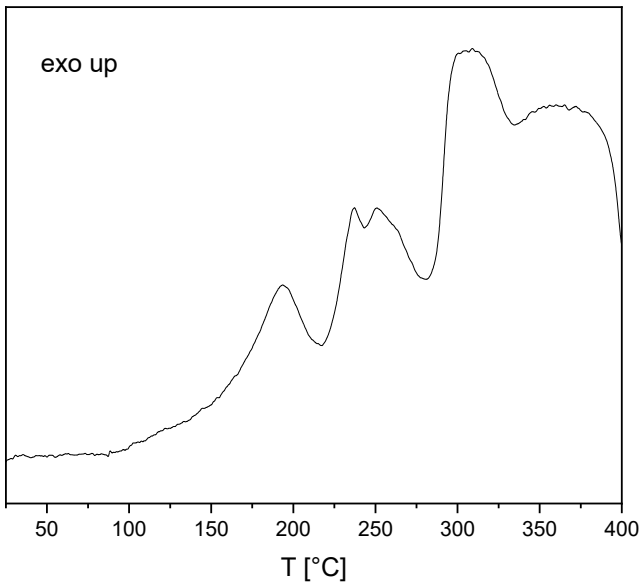

Figure S48. DTA plot of $[Cu(N_3)(2\text{-TMT})] \cdot H_2O$ in the range of 25–400 °C.

6.6.7 Hot Plate and Hot Needle Testing

Figure S49. Hot plate (left) and hot needle test of **5**.

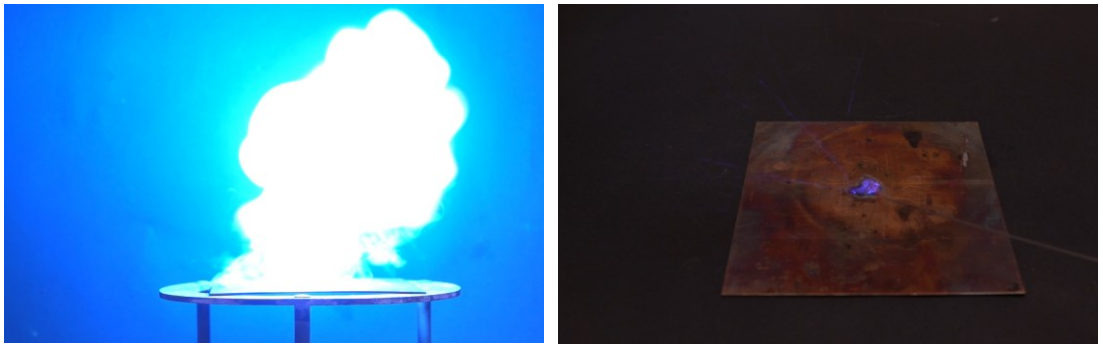

Figure S50. Hot plate (left) and hot needle test of **6**.

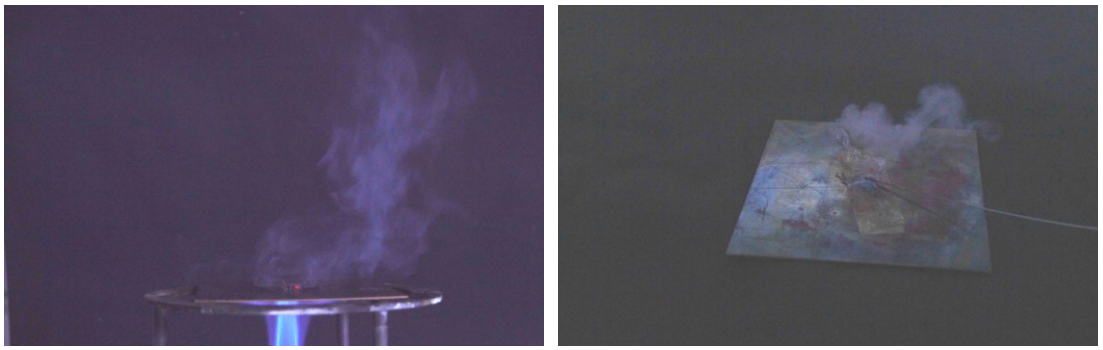

Figure S51. Hot plate (left) and hot needle test of **7**.

Figure S52. Hot plate (left) and hot needle test of **8**.

Figure S53. Hot plate (left) and hot needle test of **9**.

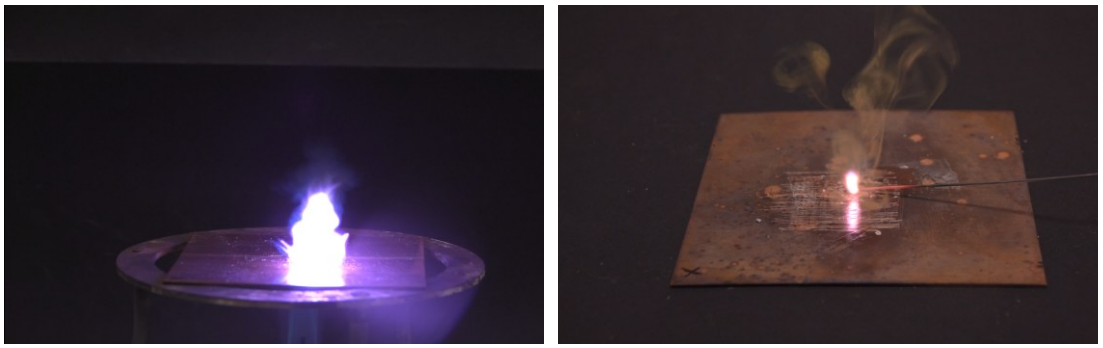

Figure S54. Hot plate (left) and hot needle test of **10**.

Figure S55. Hot plate (left) and hot needle test of **11**.

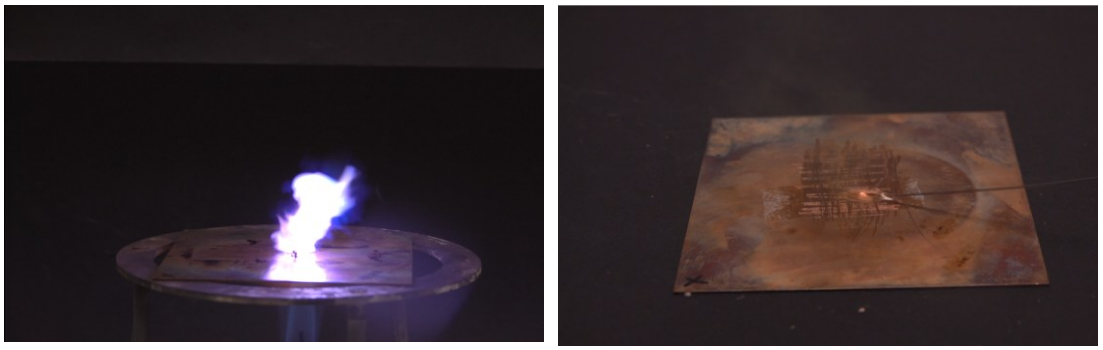

Figure S56. Hot plate (left) and hot needle test of **12**.

Figure S57. Hot plate (left) and hot needle test of **14**.

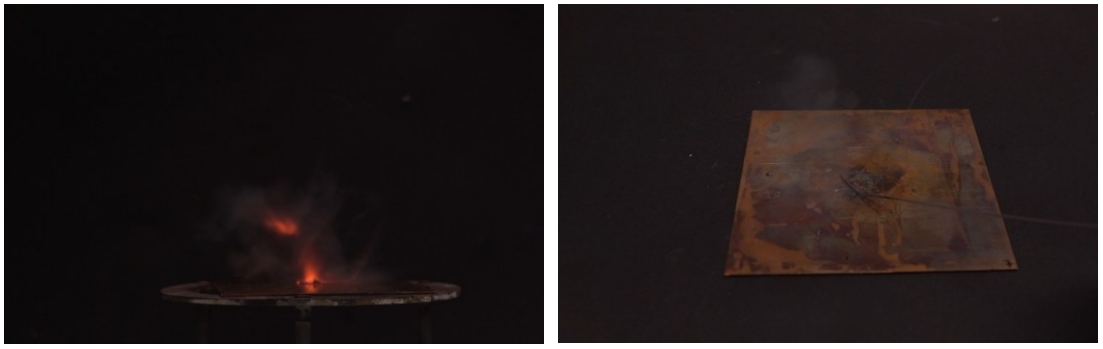

Figure S58. Hot plate (left) and hot needle test of **15**.

Figure S59. Hot plate (left) and hot needle test of **16**.

Figure S60. Hot plate (left) and hot needle test of **17**.

Figure S61. Hot plate (left) and hot needle test of **19**.

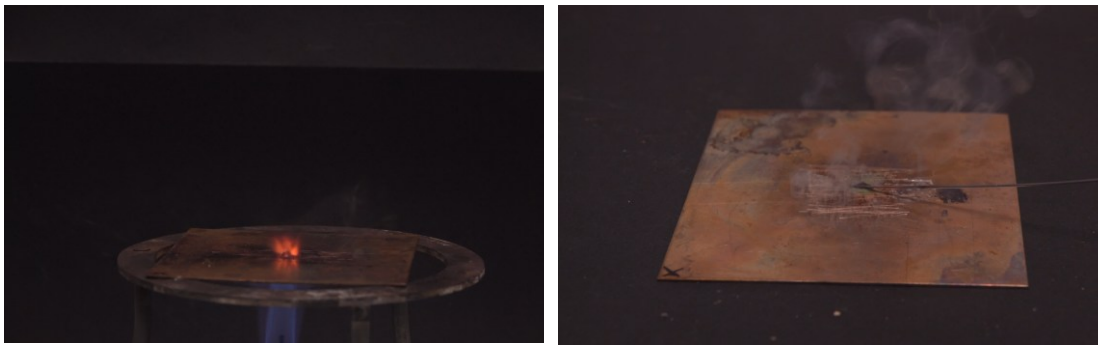

Figure S62. Hot plate (left) and hot needle test of **20**.

Figure S63. Hot plate (left) and hot needle test of **21**.

Figure S64. Hot plate (left) and hot needle test of **22**.

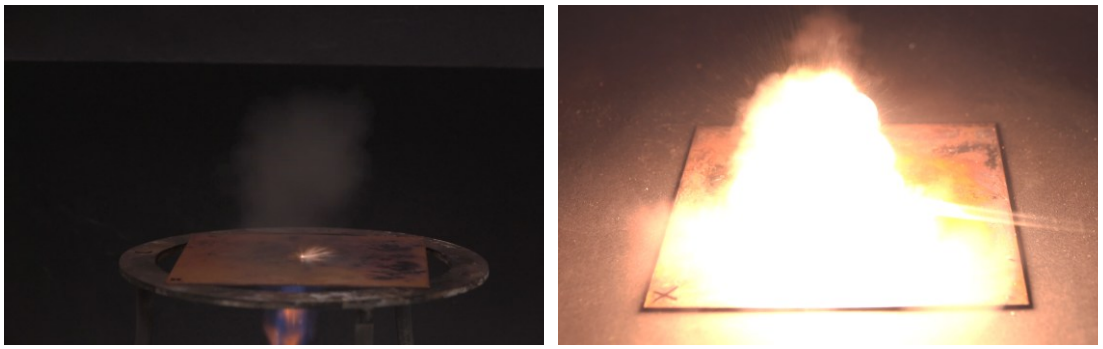

Figure S65. Hot plate (left) and hot needle test of **23**.

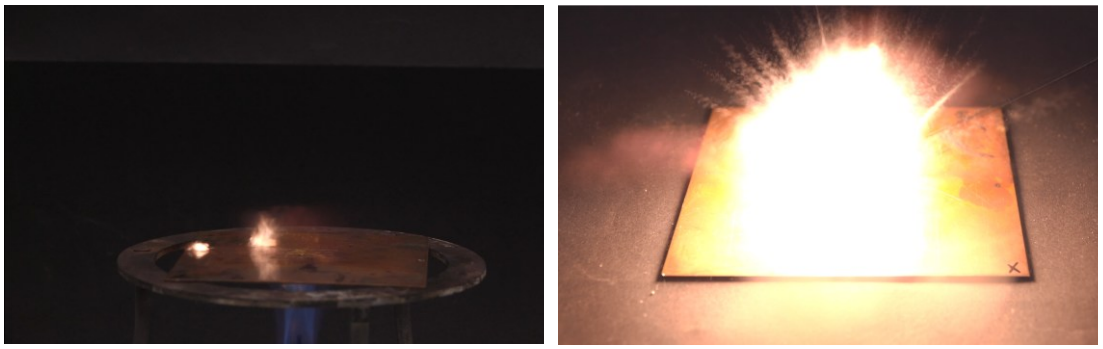

Figure S66. Hot plate (left) and hot needle test of **24**.

6.6.8 Laser Initiation Experiments

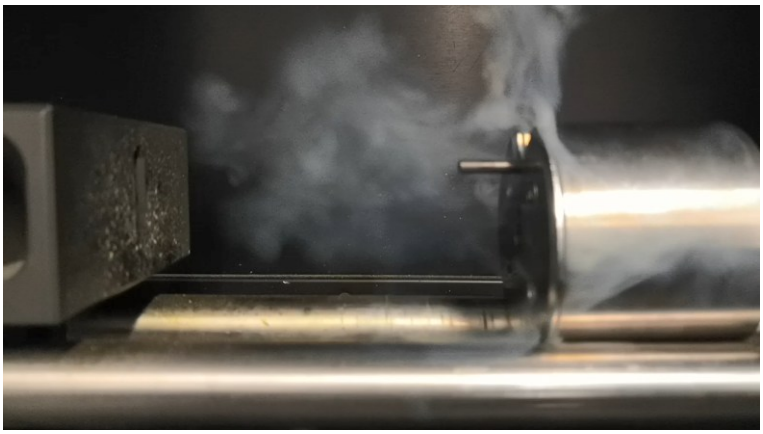

Figure S67. Decomposition of $[Cu(1\text{-}TAN)_6](ClO_4)_2$ during laser irradiation (10 A, 30 ms, 4 V).

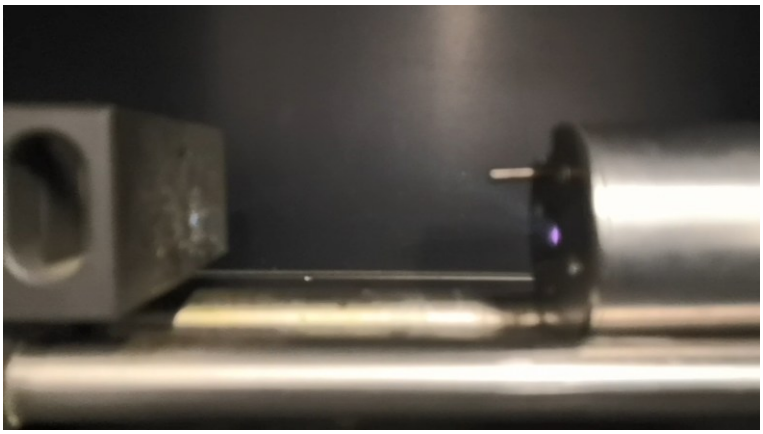

Figure S68. Detonation of $[Cu_2(1\text{-}TAN)_8(\mu\text{-}1\text{-}TAN)_2](ClO_4)_2$ during laser irradiation (6 A, 1 ms, 4 V).

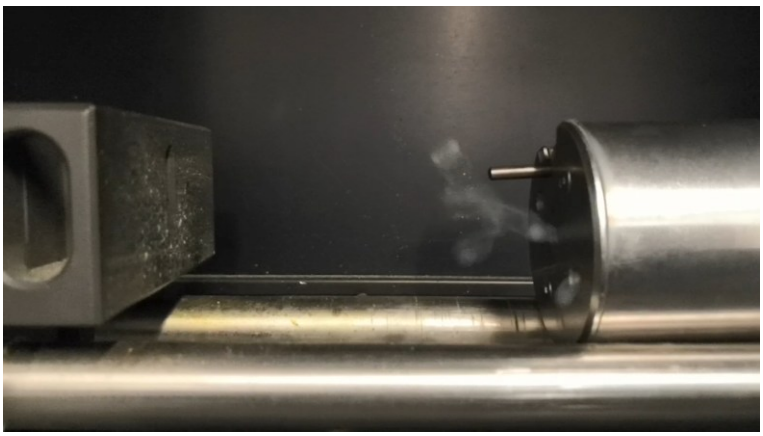

Figure S69. Decomposition of $[Cu(1\text{-}TAN)_6](NO_3)_2$ during laser irradiation (10 A, 30 ms, 4 V).

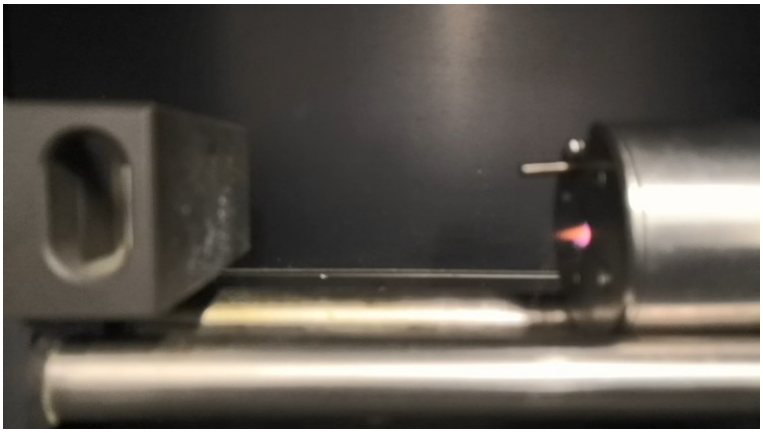

Figure S70. Deflagration of $[Fe(1\text{-}TAN)_6](ClO_4)_2$ during laser irradiation (10 A, 30 ms, 4 V).

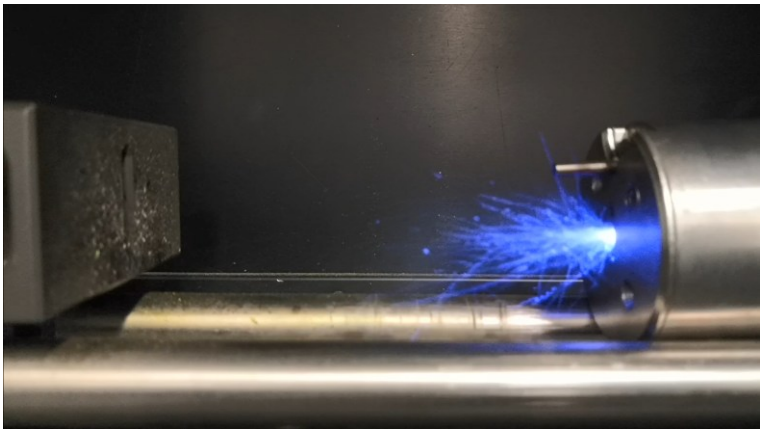

Figure S71. Detonation of $[Cu(2\text{-}TAN)_2(\mu\text{-}2\text{-}TAN)_2](ClO_4)_2$ during laser irradiation (6 A, 1 ms, 4 V).

Figure S72. Decomposition of $[Cu(HTNR)_2(1\text{-}TAN)_2]$ during laser irradiation (10 A, 30 ms, 4 V).

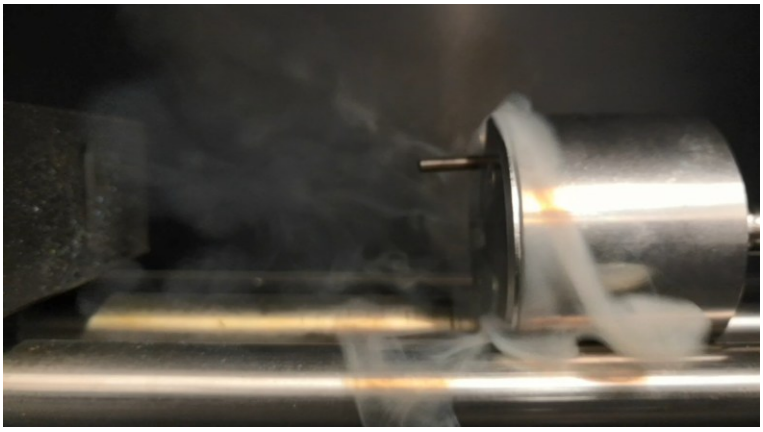

Figure S73. Decomposition of [Cu(TNR)(μ-1-TAN)] during laser irradiation (10 A, 30 ms, 4 V).

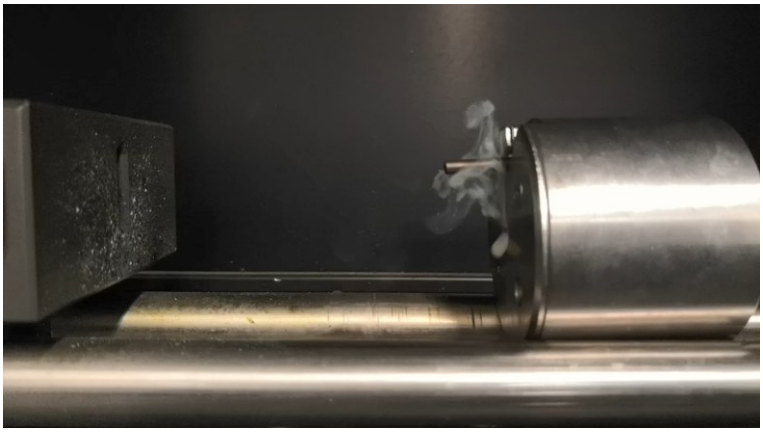

Figure S74. Decomposition of $[Cu(PA)_2(1\text{-}TAN)_2]$ during laser irradiation (10 A, 30 ms, 4 V).

Figure S75. Decomposition of $[Cu(HTNO)_2(1\text{-}TAN)_2]$during laser irradiation (10 A, 30 ms, 4 V).

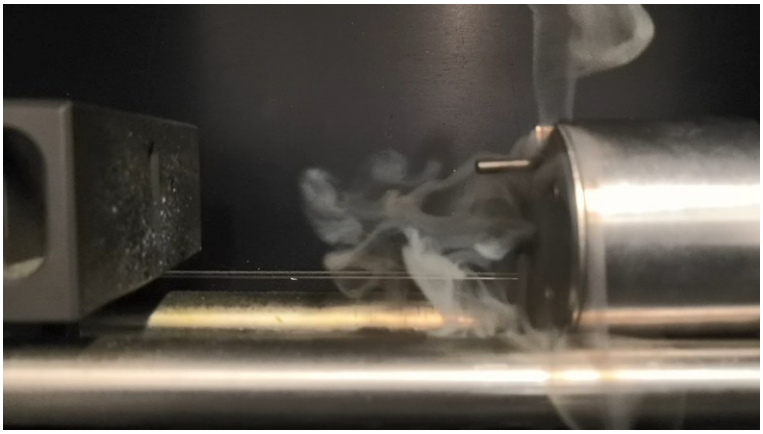

Figure S76. Decomposition of $[Cu(HTNR)_2(2\text{-}TAN)_2]$during laser irradiation (10 A, 30 ms, 4 V).

Figure S77. Decomposition of $[Cu(TNR)(2\text{-}TAN)_2] \cdot H_2O$ during laser irradiation (10 A, 30 ms, 4 V).

Figure S78. Decomposition of $[Cu(PA)_2(2\text{-}TAN)_2]$ during laser irradiation (10 A, 30 ms, 4 V).

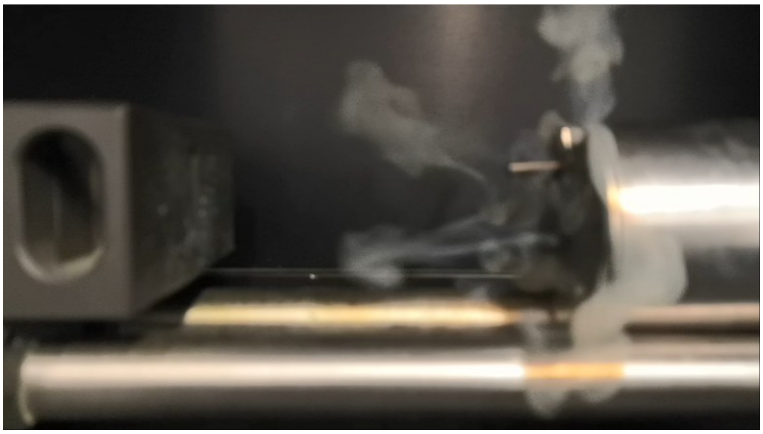

Figure S79. Decomposition of $[Cu(HTNO)_2(2\text{-}TAN)_2]$ during laser irradiation (10 A, 30 ms, 4 V).

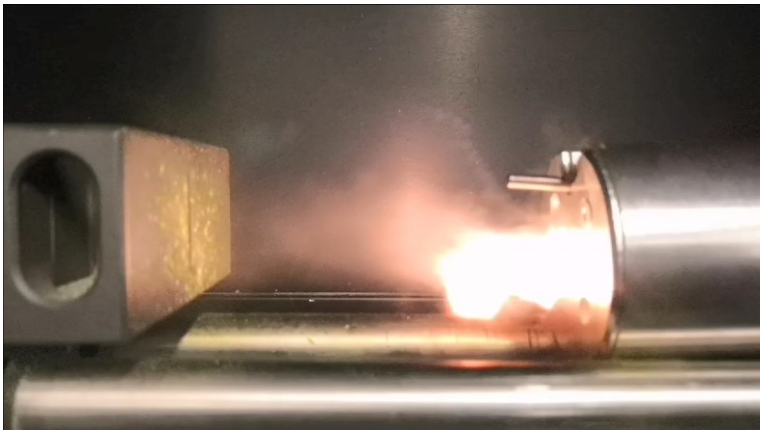

Figure S80. Detonation of $[Cu(N_3)(1\text{-}TMT)] \cdot H_2O$ during laser irradiation (6 A, 1 ms, 4 V).

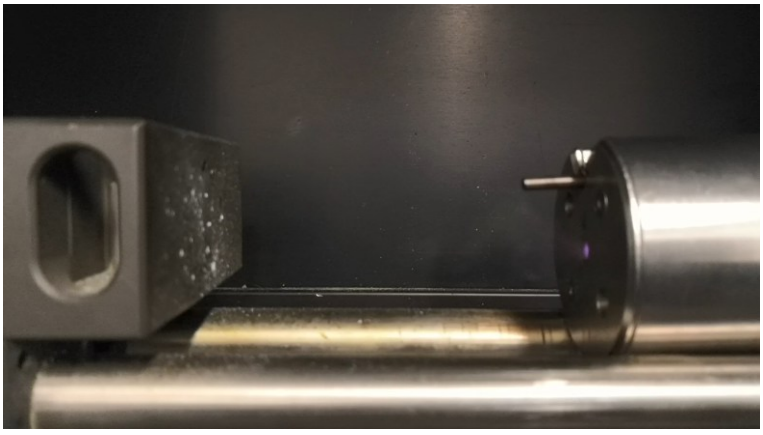

Figure S81. Detonation of $[Cu(N_3)(2\text{-}TMT)] \cdot H_2O$ during laser irradiation (6 A, 1 ms, 4 V).

6.6.9 General Methods

All chemicals and solvents were employed as received (Sigma-Aldrich, Fluka, Acros, ABCR). ^{1}H, ^{13}C{^{1}H}, and ^{14}N spectra were recorded at ambient temperature using a JEOL Bruker 27400, Eclipse 270, JEOL EX 400 or a JEOL Eclipse 400 instrument. The chemical shifts quoted in ppm in the text refer to typical standards such as tetramethylsilane (^{1}H, ^{13}C) nitromethane (^{14}N,^{15}N) in DMSO-d_6 as the solvent. Endothermic and exothermic events of the described compounds, which indicate melting, loss of crystal water or decomposition, are given as the extrapolated onset temperatures. The samples were measured in a range of 25–400 °C at a heating rate of 5 °C min^{-1} through differential thermal analysis (DTA) with an OZM Research DTA 552-Ex instrument. Infrared spectra were measured with pure samples on a Perkin-Elmer BXII FT-IR system with a Smith DuraSampler IR II diamond ATR. Determination of the carbon, hydrogen, and nitrogen contents was carried out by combustion analysis using an Elementar Vario El (nitrogen values determined are often lower than the calculated ones' due to their explosive behavior). Impact sensitivity tests were carried out according to STANAG 4489[S21] with a modified instruction[S22] using a BAM (Bundesanstalt für Materialforschung) drophammer.[S23] Friction sensitivity tests were carried out according to STANAG 4487[S24] with a modified instruction[S25] using the BAM friction tester.[S23, 26] The classification of the tested compounds results from the "UN Recommendations on the Transport of Dangerous Goods".[S27, 28] Additionally, all compounds were tested upon the sensitivity toward electrical discharge using the OZM Electric Spark XSpark10 device.[S26] Energetic properties have been calculated with the EXPLO5 7.01.01 computer code[S29] using the, to RT converted, X-ray density and calculated solid state heats of formation. These were computed by the atomization method as described in recently published papers. Electronic enthalpies were calculated with the Gaussian09 software[S11] suite using the CBS-4M method. The laser initiation experiments were performed with a 45 W InGaAs laser diode operating in the single-pulsed mode. The diode is attached to an optical fiber with a core diameter of 400 µm and a cladding diameter of 480 µm. The optical fiber is connected via a SMA type connecter directly to the laser and to a collimator. This collimator is coupled to an optical lens, which was positioned in its focal distance (f = 29.9 mm) to the sample. The lens is shielded from the explosive by a sapphire glass. Approximately 25 mg of the ECC was pressed into a transparent polycarbonate cap with a pressure force of 1.5 kN and sealed by a UV-curing adhesive. The

confined samples were irradiated at a wavelength of 915 nm, a voltage of 4 V, currents of 6–10 A and varying pulse lengths.

6.6.10 Experimental Section

Caution! All investigated compounds are energetic materials and some of them show sensitivities towards various stimuli (e.g. elevated temperatures, impact, friction or electronic discharge). Although no hazards occurred, proper security precautions (safety glasses, face shield, earthed equipment and shoes, leather jacket, Kevlar sleeves, and earplugs) have to be worn while synthesizing and handling the described compounds.

2-(1*H*-tetrazol-1-yl)acetonitrile (1-TAN, 1) and 2-(2*H*-tetrazol-2-yl)acetonitrile (2-TAN, 2)

1*H*-Tetrazole (10.0 g, 0.14 mol, 1.0 eq.) was dissolved in MeCN (200 mL) and acetone (50 mL). Na_2CO_3 (18.2 g, 0.17 mmol, 1.2 eq.) and Chloroacetonitrile (10.8 mL, 0.17 mmol, 1.2 eq.) were added and the resulting suspension was stirred at 80 °C for 16 h leading to brown discoloration. The reaction mixture was then filtered off and the filtrate was evaporated under reduced pressure, followed by separation of the isomers by column chromatography (SiO_2, EtOAc/iHex 1:1). The two isomers 1-TAN (5.50 g, 50.4 mmol, 36 %) and 2-TAN (4.89 g, 44.8 mmol, 32 %) were obtained as yellow oils. When stored in the refrigerator, 1-TAN crystallized within several weeks.

1-TAN (1)

^{1}H NMR (400 MHz, DMSO-d_6, 25 °C, ppm) δ: 9.49 (s, 1H, -C*H*), 5.91 (s, 2H, -CH_2). **^{13}C NMR** (100 MHz, DMSO-d_6, 25 °C, ppm) δ: 144.7 (-*C*HN_4), 114.3 (-*C*N), 35.9 (-*C*H_2). **^{14}N NMR** (29 MHz, DMSO-d_6, 25 °C, ppm) δ −159. **DTA** (5 °C min^{-1}) onset: 42 °C (endothermic), 164 °C (exothermic). **IR** (ATR, cm^{-1}): $\tilde{\nu}$ = 3143 (w), 2995 (w), 2956 (w), 1749 (vw), 1628 (vw), 1477 (m), 1434 (m), 1416 (m), 1352 (w), 1298 (w), 1260 (w), 1174 (s), 1098 (vs), 1018 (w), 966 (m), 931 (m), 876 (m), 759 (s), 718 (m), 696 (w), 671 (w), 650 (s), 539 (w), 525 (w), 507 (w), 482 (m), 453 (w), 448 (w), 429 (w), 422 (w), 406 (w). **EA** ($C_3H_3N_5$, 109.09) calcd.: C 33.03, H 2.77, N 64.20 %; found: C 33.24, H 2.70, N 64.17 %. **HRMS** (EI): calcd. for $(C_3H_4N_5)^+$ $[M+H]^+$: 110.0461, found: 110.0461. ***R*$_f$**: 0.23

(EtOAc/iHex, 1:1, $KMnO_4$). **BAM drophammer**: >40 J. Friction tester: >360 N. **ESD**: 1.5 J (at grain size 100–500 μm).

2-TAN (2)

^{1}H NMR (400 MHz, DMSO-d_6, 25 °C, ppm) δ: 9.13 (s, 1H, -C*H*), 6.26 (s, 2H, -CH_2). **^{13}C NMR** (100 MHz, DMSO-d_6, 25 °C, ppm) δ: 154.1 (-*C*HN_4), 113.6 (-*C*N), 40.5 (-*C*H_2). **^{14}N NMR** (29 MHz, DMSO-d_6, 25 °C, ppm) δ: −110. **DTA** (5 °C min^{-1}) onset: 195 °C (exothermic). **IR** (ATR, cm^{-1}): $\tilde{\nu}$ = 3002 (m), 2960 (m), 1454 (m), 1418 (m), 1372 (s), 1284 (s), 1200 (m), 1145 (m), 1127 (s), 1025 (vs), 1006 (m), 933 (s), 890 (m), 776 (s), 706 (s), 674 (s), 484 (m), 474 (m), 454 (m), 448 (m), 430 (m), 410 (m). **EA** ($C_3H_3N_5$, 109.09) calcd.: C 33.03, H 2.77, N 64.20 %; found: C 33.48, H 2.93, N 61.99 %. **HRMS** (EI): calcd. for $(C_3H_4N_5)^+$ $[M+H]^+$: 110.0461, found: 110.0462. ***R*$_f$**: 0.70 (EtOAc/iHex, 1:1, $KMnO_4$). **BAM drophammer:** > 40 J; **Friction tester:** >360 N.

Procedure for the preparation of 5-((1*H*-tetrazol-1-yl)methyl)-1*H*-tetrazole (1-HTMT, 3) and 5-((2*H*-tetrazol-2-yl)methyl)-1*H*-tetrazole (2-HTMT, 4)

1- or 2-TAN (1.67 g, 15.3 mmol, 1.0 eq.) was dissolved in 50 mL of deionized water. Sodium azide (1.05 g, 16.1 mmol, 1.05 eq.) and zinc(II) chloride (1.04 g, 7.66 mmol, 0.5 eq.) was added and the solution was stirred at 80 °C for 2 d under reflux, which led to precipitation of a colorless solid. After cooling down, the pH was adjusted to 1 by addition of 2 M aqueous HCl, resulting in a clear solution, which was stirred for another 30 min at ambient temperature. The aqueous phase was extracted with EtOAc (3 × 200 mL). The combined organic phases were dried over $MgSO_4$, filtered off. Approximately 90 % of the solvent was evaporated *in vacuo*. The leftover solution was poured in a crystallization dish to allow for slow evaporation of the solvent at ambient temperature, which led to formation of colorless crystals in both cases. 1-HTMT was obtained in a yield of 84 % (1.96 g, 12.9 mmol). 2-HTMT was obtained in a yield of 90 % (2.10 g, 13.8 mmol).

1-HTMT (3)

^{1}H NMR (400 MHz, DMSO-d_6, 25 °C, ppm) δ: 9.57 (s, 1H, -C*H*), 6.19 (s, 2H, -CH_2). **^{13}C NMR** (100 MHz, DMSO-d_6, 25 °C, ppm) δ: 153.5 (-*C*), 144.7 (-*C*H), 41.30 (-*C*H_2-). **DSC** (5 °C min^{-1}) onset: 136 °C (endothermic) 165 °C (exothermic). **IR** (ATR, cm^{-1}): $\tilde{\nu}$ = 3118 (m), 2994 (w), 2959 (w), 2606 (w), 1773 (w), 1573 (m), 1551 (w), 1528 (w), 1486 (m), 1453 (m), 1426 (m), 1336 (m), 1249 (m), 1179 (s), 1108 (s), 1087 (m), 1050 (s), 996 (m),

972 (m), 948 (m), 915 (m), 889 (s), 783 (m), 743 (vs), 718 (m), 670 (vs), 646 (m). **EA** ($C_3H_4N_8$, 152.12) calcd.: C 23.69, H 2.65, N 73.66 %; found: C 23.45, H 2.82, N 72.41 %. **HRMS** (ESI): calcd. For $(C_3H_3N_8)^-$ [M−H]: 151.04862, found: 151.04842. **BAM drophammer**: 10 J. Friction tester: >360 N. **ESD**: 1.0 J (at grain size 100–500 μm).

2-HTMT (4)

^{1}H NMR (400 MHz, DMSO-d_6, 25 °C, ppm) δ: 9.06 (s, 1H, -C*H*), 6.44 (s, 2H, -CH_2). **^{13}C NMR** (100 MHz, DMSO-d_6, 25 °C, ppm) δ: 155.8 (-*C*), 152.8 (*C*H), 37.6 (-*C*H_2-). **DSC** (5 °C min^{-1}) onset: 97 °C (endothermic) 176 °C (exothermic). **IR** (ATR, cm^{-1}): $\tilde{\nu}$ = 3172 (w), 3054 (w), 3021 (m), 2973 (w), 2906 (w), 2859 (w), 2745 (w), 1757 (w), 1579 (w), 1557 (w), 1459 (w), 1427 (m), 1383 (m), 1373 (m), 1340 (w), 1310 (w), 1289 (m), 1243 (w), 1231 (m), 1196 (m), 1143 (m), 1132 (m), 1103 (m), 1086 (w), 1051 (s), 1032 (vs), 1009 (m), 937 (w), 878 (s), 815 (s), 756 (vs), 717 (w), 703 (m), 683 (m), 660 (vs). **EA** ($C_3H_4N_8$, 152.12) calcd.: C 23.69, H 2.65, N 73.66 %; found: C 23.79, H 2.69, N 74.04 %. **HRMS** (ESI): calcd. For $(C_3H_3N_8)^-$ [M−H]: 151.04862, found: 151.04842. **BAM drophammer**: 15 J. Friction tester: >360 N. **ESD**: 0.5 J (at grain size 100–500 μm).

General Procedure A for the formation of perchlorate and nitrate containing ECCs 5–12:

A solution of one equivalent of the respective perchlorate or nitrate ($Cu(ClO_4)_2 \cdot 6\ H_2O$: 0.25 mmol, 92.6 mg; $Fe(ClO_4)_2 \cdot 6\ H_2O$: 0.25 mmol, 90.7 mg; $Zn(ClO_4)_2 \cdot 6\ H_2O$: 0.25 mmol, 93.1 mg; $Cu(NO_3)_2 \cdot 3\ H_2O$: 0.25 mmol, 60.4 mg; $Ag(ClO_4) \cdot H_2O$: 1.0 mmol, 225.3 mg) in 5 mL of EtOH was stirred at 60 °C or rt in the case of silver perchlorate. A solution of 1- or 2-TAN in 5 mL of EtOH was manually added. The resulting solution was stirred at reaction temperature for 10 min. and then allowed to crystallize at room temperature. Within 3 days crystalline products of all compounds were obtained. Structure **5a** was obtained after using MeCN instead of EtOH in a similar manner.

General Procedure B for the formation of ECCs 13–22 with nitroaromatic anions:

A suspension of $CuCO_3 \times Cu(OH)_2$ (55.3 mg, 0.25 mmol, 0.5 eq.) and the respective nitroaromatic species (279 mg, 1.00 mmol of H_3TNPG, 245 mg, 1.00 mmol or 123mg, 0.50 mmol of H_2TNR, 229 mg, 1.00 mmol of HPA, 259 mg, 1.00 mmol of H_2TNO) in 5 mL of water was heated to 80 °C until a clear solution was obtained. To this solution, the ligand (1- or 2-TAN, 109 mg, 1.00 mmol, 2.0 eq.) was added. The solution was kept at

80 °C for 5 min. and then left at room temperature to crystallize for 3 weeks. The resulting suspension was filtered off and washed with little cold water, ethanol and diethyl ether.

General Procedure C for the formation of copper azides 22 and 23:

1-HTMT or 2-HTMT (152 mg, 1.00 mmol, 1.0 eq.), sodium carbonate (53.0 mg, 0.50 mmol, 0.5 eq) and sodium azide (65.0 mg, 1.00 mmol, 1.0 eq.) were suspended in 20 mL of water at 60 °C and stirred until a clear solution was obtained. To this solution, a preheated solution of $CuSO_4 \cdot 5\ H_2O$ (250 mg, 1.00 mmol, 1.0 eq.) in 5 mL of water was added dropwise, leading to precipitation of a green solid. The suspension was stirred for 10 min at 60 °C, filtered off hot and washed with water and EtOH, followed by drying on air.

$[Cu(1\text{-}TAN)_6](ClO_4)_2$ (5)

5 was obtained as blue solid in a yield of 88 % (201 mg, 0.22 mmol) according to General Procedure A with 6.0 eq. of 1-TAN.

DTA (5 °C min^{-1}) onset: 173 °C (exothermic). **IR** (ATR, cm^{-1}): $\tilde{\nu}$ = 3137 (w), 3003 (w), 2966 (w), 1505 (m), 1449 (w), 1416 (w), 1357 (w), 1329 (vw), 1274 (vw), 1191 (w), 1167 (w), 1099 (vs), 1076 (vs), 1020 (w), 1007 (m), 986 (w), 936 (m), 888 (w), 761 (m), 715 (m), 688 (w), 648 (m), 622 (s), 576 (vw), 570 (vw), 509 (vw), 489 (w), 461 (vw), 437 (vw), 424 (vw). **EA** ($C_{18}H_{18}Cl_2CuN_{30}O_8$, 916.99) calcd.: C 23.58, H 1.98, N 45.82 %; found: C 23.57, H 1.98, N 45.15 %. **BAM drophammer**: < 1 J. Friction tester: 108 N. **ESD**: 33 mJ (at grain size 100–500 µm).

$[Cu_2(1\text{-}TAN)_8(\mu\text{-}1\text{-}TAN)_2](ClO_4)_2$ (6)

6 was obtained as blue solid in a yield of 44 % (88.9 mg, 0.11mmol) according to General Procedure A with 3.0, 4.0 or 5.0 eq. of 1-TAN.

DTA (5 °C min^{-1}) onset: 177 °C (exothermic). **IR** (ATR, cm^{-1}): $\tilde{\nu}$ = 3143 (w), 3135 (w), 3004 (w), 2965 (w), 1506 (w), 1447 (w), 1417 (w), 1355 (vw), 1189 (w), 1165 (w), 1079 (vs), 1026 (w), 1012 (m), 999 (m), 989 (w), 944 (w), 934 (w), 892 (w), 760 (m), 715 (w), 690 (vw), 649 (m), 623 (s), 500 (w), 487 (w). **EA** ($C_{30}H_{30}Cl_4Cu_2N_{50}O_{16}$, 1615.80) calcd.: C 22.30, H 1.87, N 43.34 %; found: C 22.02, H 1.85, N 43.25 %. **BAM drophammer**: <1 J. Friction tester: 60 N. **ESD**: 160 mJ (at grain size 100–500 µm).

[Cu(1-TAN)$_6$](NO$_3$)$_2$ (7)

7 was obtained as blue powder in a yield of 72 % (148 mg, 0.18 mmol) according to General Procedure A with 6.0 eq. of 1-TAN.

DTA (5 °C min^{-1}) onset: 75 °C (endothermic), 117 °C (exothermic). **IR** (ATR, cm^{-1}): $\tilde{\nu}$ = 3136 (w), 3105 (w), 3003 (w), 2990 (w), 2959 (w), 1749 (vw), 1694 (w), 1498 (m), 1444 (w), 1419 (m), 1355 (s), 1335 (vs), 1251 (w), 1191 (s), 1175 (s), 1097 (vs), 1045 (w), 1025 (m), 1013 (m), 992 (m), 965 (w), 959 (m), 945 (m), 900 (m), 829 (w), 751 (m), 716 (m), 693 (w), 649 (s), 495 (w). **EA** ($C_{18}H_{18}CuN_{32}O_6$, 842.11) calcd.: C 25.67, H 2.15, N 53.23 %; found: C 25.74, H 2.35, N 52.08 %. **BAM drophammer**: >40 J. Friction tester: >360 N. **ESD**: 106 mJ (at grain size 100–500 µm).

[Fe(1-TAN)$_6$](ClO$_4$)$_2$ (8)

8 was obtained as yellow-brownish solid in a yield of 40 % (87.5 mg, 0.10 mmol) according to General Procedure A with 6.0 eq. of 1-TAN.

DTA (5 °C min^{-1}) onset: 188 °C (exothermic). **IR** (ATR, cm^{-1}): $\tilde{\nu}$ = 3147 (w), 3004 (w), 2968 (w), 1700 (vw), 1654 (vw), 1627 (vw), 1500 (m), 1447 (w), 1419 (m), 1361 (w), 1323 (w), 1291 (vw), 1188 (m), 1166 (m), 1076 (vs), 1027 (m), 994 (m), 953 (w), 934 (m), 882 (m), 759 (m), 716 (m), 688 (w), 648 (s), 623 (s), 483 (m). **EA** ($C_{18}H_{18}Cl_2FeN_{30}O_8$, 909.289) calcd.: C 23.78, H 2.00, N 46.21 %; found: C 23.74, H 1.78, N 45.77 %. **BAM drophammer**: 2 J. Friction tester: 60 N. **ESD**: 33 mJ (at grain size 100–500 µm).

[Zn(1-TAN)$_6$](ClO$_4$)$_2$ (9)

9 was obtained as a silver-grey solid in a yield of 83 % (92.3 mg, 0.10 mmol) according to General Procedure A with 6.0 eq. of 1-TAN.

DTA (5 °C min^{-1}) onset: 173 °C (exothermic). **IR** (ATR, cm^{-1}): $\tilde{\nu}$ = 3139 (w), 3004 (w), 2968 (w), 1752 (vw), 1723 (vw), 1700 (vw), 1617 (vw), 1501 (m), 1449 (w), 1418 (w), 1357 (w), 1322 (vw), 1273 (vw), 1232 (vw), 1189 (m), 1166 (w), 1078 (vs), 1028 (m), 997 (m), 936 (m), 886 (m), 800 (vw), 760 (m), 716 (m), 694 (w), 648 (s), 622 (s), 557 (w), 520 (w), 485 (m), 451 (w), 445 (w), 429 (vw), 415 (w). **EA** ($C_{18}H_{18}Cl_2ZnN_{30}O_8$, 916.059) calcd.: C 23.53, H 1.97, N 45.73 %; found: C 23.46, H 1.84, N 44.69 %. **BAM drophammer**: 10 J. Friction tester: 240 N. **ESD**: 1080 mJ (at grain size 100–500 µm).

[Ag(ClO$_4$)(μ-1-TAN)] (10)

10 was obtained as a colorless solid in a yield of 83 % (263 mg, 0.83 mmol) according to General Procedure A with 1.0 eq. of 1-TAN. **DTA** (5 °C min^{-1}) onset: 173 °C (exothermic). **IR** (ATR, cm^{-1}): $\tilde{\nu}$ = 3128 (w), 3011 (w), 2968 (w), 1792 (vw), 1697 (vw), 1623 (vw), 1481 (w), 1437 (w), 1393 (w), 1354 (w), 1284 (vw), 1183 (w), 1161 (vw), 1051 (vs), 1035 (vs), 995 (s), 934 (s), 900 (m), 769 (m), 713 (w), 651 (m), 618 (s), 548 (vw), 482 (m). **EA** ($C_3H_3AgClN_5O_4$, 316.41) calcd.: C 11.39, H 0.96, N 22.13 %; found: C 11.29, H 1.21, N 21.74 %. **BAM drophammer**: <1 J. Friction tester: 1 N. **ESD**: 5 mJ (at grain size 100–500 µm).

[Cu(2-TAN)$_2$(μ-2-TAN)$_2$](ClO$_4$)$_2$ (11)

11 was obtained as a dark blue solid in a yield of 80 % (139 mg, 0.20 mmol) according to General Procedure A with 3.0, 4.0, 5.0 or 6.0 eq. of 2-TAN.

DSC (5 °C min^{-1}) onset: 190 °C (exothermic). **IR** (ATR, cm^{-1}): $\tilde{\nu}$ = 3148 (w), 2999 (w), 2958 (w), 1471 (w), 1421 (m), 1412 (m), 1387 (m), 1315 (w), 1286 (w), 1204 (w), 1190 (w), 1153 (m), 1141 (m), 1072 (vs), 1047 (vs), 1025 (s), 942 (m), 904 (m), 780 (s), 703 (m), 694 (w), 677 (s), 622 (vs), 593 (w), 583 (w), 575 (w), 569 (w), 489 (m), 451 (w). **EA** ($C_{12}H_{12}Cl_2CuN_{20}O_8$, 698.81) calcd.: C 20.63, H 1.73, N 40.09 %; found: C 20.22, H 2.19, N 38.00 %. **BAM drophammer**: <1 J. Friction tester: 1.5 N. **ESD**: 13 mJ (at grain size <100 µm).

[Ag(μ-2-TAN)$_2$](ClO$_4$) (12)

10 was obtained as a colorless solid in a yield of 57 % (243 mg, 0.57 mmol) according to General Procedure A with 2.0 eq. of 2-TAN.

DTA (5 °C min^{-1}) onset: 67 °C (exothermic). **IR** (ATR, cm^{-1}): $\tilde{\nu}$ = 3443 (w), 3345 (w), 3269 (w), 3216 (w), 3150 (w), 3006 (w), 2957 (w), 2221 (w), 1683 (m), 1648 (m), 1607 (m), 1461 (w), 1408 (w), 1375 (m), 1298 (m), 1195 (w), 1064 (vs), 1039 (vs), 1019 (s), 943 (m), 932 (m), 889 (m), 814 (m), 772 (m), 700 (m), 685 (m), 671 (m), 619 (vs), 491 (m). **EA** ($C_6H_6AgClN_{10}O_4$, 425.50) calcd.: C 16.94, H 1.42, N 32.92 %; found: C 16.92, H 1.51, N 32.87 %. **BAM drophammer**: <1 J. Friction tester: 6 N. **ESD**: 5 mJ (at grain size 100–500 µm).

[Cu(H$_2$O)$_4$(1-TAN)$_2$](H$_2$TNPG)$_2$ (13)

Within two weeks crystals of compound **13** were obtained. No further analysis was conducted due to impurity of the sample according to elemental analysis.

[Cu(HTNR)$_2$(1-TAN)$_2$] (14)

Within two weeks green crystals of complex **14** suitable for X-ray diffraction were obtained (271 mg, 0.35 mmol, 70 %).

DSC (5 °C min^{-1}) onset: 205 °C (exothermic). **IR** (ATR, cm^{-1}): $\tilde{\nu}$ = 3136 (w), 3006 (w), 2966 (w), 1627 (m), 1557 (s), 1540 (vs), 1532 (vs), 1506 (s), 1471 (m), 1455 (s), 1415 (m), 1381 (m), 1355 (m), 1327 (s), 1286 (vs), 1177 (s), 1161 (s), 1093 (s), 1026 (m), 1014 (m), 933 (s), 893 (m), 777 (m), 761 (s), 732 (m), 720 (m), 713 (m), 701 (s), 665 (m), 650 (s), 632 (s), 488 (m), 452 (w), 427 (m). **EA** ($C_{18}H_{10}CuN_{16}O_{16}$, 769.92) calcd.: C 28.08, H 1.31, N 29.11 %; found: C 28.09, H 1.45, N 29.25 %. **BAM drophammer**: 3 J. Friction tester: 240 N. **ESD**: 63 mJ (at grain size 100–500 μm).

[Cu(μ-1-TAN)(TNR)] (15)

Compound **15** was obtained as a green solid after two weeks (196 mg, 0.47 mmol, 94 %).

DSC (5 °C min^{-1}) onset: 143 °C (exothermic). **IR** (ATR, cm^{-1}): $\tilde{\nu}$ = 3136 (w), 2998 (w), 1628 (w), 1587 (s), 1564 (m), 1538 (vs), 1507 (m), 1486 (m), 1475 (s), 1446 (s), 1408 (m), 1387 (m), 1355 (m), 1307 (s), 1287 (vs), 1260 (s), 1234 (s), 1176 (s), 1109 (m), 1097 (s), 1026 (m), 1013 (m), 932 (m), 888 (m), 835 (w), 791 (w), 778 (m), 767 (m), 732 (m), 711 (s), 681 (m), 667 (w), 649 (m), 609 (w), 499 (w), 490 (w), 443 (m), 433 (m), 419 (m). **EA** ($C_9H_4CuN_8O_8$, 415.73) calcd.: C 26.00, H 0.97, N 26.95 %; found: C 26.23, H 1.18, N 27.46 %. **BAM drophammer**: 2 J. Friction tester: 160 N. **ESD**: 63 mJ (at grain size <100 μm).

[Cu(PA)$_2$(1-TAN)$_2$] (16)

Coordination compound **16** was obtained within 16 days as green crystals (271 mg, 0.37 mmol, 74 %).

DSC (5 °C min^{-1}) onset: 170 °C (exothermic). **IR** (ATR, cm^{-1}): $\tilde{\nu}$ = 3161 (w), 3104 (w), 3003 (w), 1637 (w), 1609 (m), 1575 (s), 1537 (s), 1510 (s), 1476 (m), 1450 (m), 1418 (m), 1361 (s), 1350 (s), 1326 (vs), 1272 (s), 1177 (m), 1166 (s), 1152 (m), 1089 (s), 1017 (w), 1001 (m), 932 (s), 918 (s), 891 (m), 847 (m), 826 (m), 785 (m), 766 (m), 743 (m), 728 (m),

709 (vs), 649 (s), 550 (m), 540 (m), 528 (m), 484 (m), 451 (m), 423 (w). **EA** ($C_{18}H_{10}CuN_{16}O_{14}$, 737.92) calcd.: C 29.30, H 1.37, N 30.37 %; found: C 29.26, H 1.50, N 30.36 %. **BAM drophammer**: 2 J. Friction tester: >360 N. **ESD**: 106 mJ (at grain size 100–500 µm).

[Cu(HTNO)$_2$(1-TAN)$_2$] (17)

After 15 days green crystals of the copper(II) complex **17** were isolated (307 mg, 0.39 mmol, 78 %).

DSC (5 °C min^{-1}) onset: 181 °C (exothermic). **IR** (ATR, cm^{-1}): $\tilde{\nu}$ = 3168 (w), 3010 (w), 2969 (w), 1607 (m), 1549 (m), 1538 (s), 1532 (vs), 1515 (s), 1511 (s), 1506 (vs), 1487 (s), 1463 (m), 1456 (m), 1435 (m), 1417 (m), 1399 (m), 1378 (m), 1361 (s), 1312 (s), 1286 (s), 1180 (s), 1158 (s), 1092 (s), 1057 (m), 1045 (m), 1018 (m), 1008 (m), 941 (m), 908 (m), 887 (m), 825 (m), 814 (m), 782 (m), 766 (m), 762 (m), 743 (m), 712 (m), 701 (m), 687 (s), 669 (s), 650 (s), 637 (s), 609 (m), 595 (m), 566 (w), 541 (w), 533 (w), 523 (w), 515 (w), 498 (w), 484 (m), 415 (w). **EA** ($C_{20}H_{14}CuN_{16}O_{16}$, 797.01) calcd.: C 30.10, H 1.77, N 28.09 %; found: C 30.05, H 1.95, N 27.93 %. **BAM drophammer**: 2 J. Friction tester: 360 N. **ESD**: 63 mJ (at grain size 100–500 µm).

[Cu(H$_2$O)$_4$(2-TAA)$_2$](H$_2$TNPG)$_2$ (18)

Within two weeks green crystals of coordination compound **18** were isolated. No further analysis was conducted due to impurity of the sample according to elemental analysis.

[Cu(HTNR)$_2$(2-TAN)$_2$] (19)

After 16 days green crystals of coordination compound **19** were isolated (274 mg, 0.36 mmol, 72 %).

DSC (5 °C min^{-1}) onset: 192 °C (exothermic). **IR** (ATR, cm^{-1}): $\tilde{\nu}$ = 3156 (w), 3003 (w), 1626 (s), 1565 (s), 1535 (s), 1525 (s), 1474 (m), 1451 (s), 1422 (m), 1377 (s), 1360 (m), 1315 (s), 1281 (vs), 1234 (s), 1203 (s), 1176 (s), 1132 (s), 1080 (s), 1053 (s), 1030 (s), 968 (m), 955 (m), 931 (m), 918 (m), 898 (s), 829 (w), 782 (m), 774 (m), 764 (s), 732 (m), 718 (s), 698 (vs), 675 (s), 638 (s), 550 (w), 484 (m), 459 (w), 427 (w). **EA** ($C_{18}H_{10}CuN_{16}O_{16}$, 769.92) calcd.: C 28.08, H 1.31, N 29.11 %; found: C 28.08, H 1.40, N 29.24 %. **BAM drophammer**: 3 J. Friction tester: 160 N. **ESD**: 250 mJ (at grain size 100–500 µm).

[Cu(2-TAN)$_2$(TNR)] · 0.5 H$_2$O (20)

Compound **20** was obtained after 13 days as a green solid (238 mg, 0.22 mmol, 45 %). **DTA** (5 °C min^{-1}) onset: 170 °C (exothermic). **IR** (ATR, cm^{-1}): $\tilde{\nu}$ = 3149 (w), 2995 (w), 2966 (w), 2949 (w), 1589 (s), 1563 (m), 1557 (s), 1538 (s), 1533 (s), 1506 (w), 1481 (m), 1455 (m), 1442 (s), 1429 (s), 1377 (m), 1290 (vs), 1228 (s), 1218 (s), 1200 (s), 1171 (s), 1133 (s), 1102 (s), 1050 (m), 1026 (m), 1003 (w), 966 (m), 951 (m), 925 (m), 916 (w), 902 (m), 831 (w), 778 (m), 765 (m), 733 (w), 711 (s), 698 (m), 682 (m), 675 (m), 653 (w), 599 (w), 470 (m), 429 (m), 419 (w). **EA** ($C_{24}H_{16}Cu_2N_{26}O_{17}$, 1067.65) calcd.: C 27.00, H 1.51, N 34.11 %; found: C 26.86, H 1.78, N 34.25 %. **BAM drophammer**: 2 J. Friction tester: >360 N. **ESD**: 250 mJ (at grain size 100–500 µm).

[Cu(PA)$_2$(2-TAN)$_2$] (21)

Green crystals of compound **21** were obtained within 15 days (219 mg, 0.30 mmol, 60 %). **DSC** (5 °C min^{-1}) onset: 194 °C (exothermic). **IR** (ATR, cm^{-1}): $\tilde{\nu}$ = 3178 (vw), 3156 (w), 3106 (w), 3090 (w), 2996 (w), 2957 (w), 1736 (vw), 1634 (w), 1610 (s), 1588 (m), 1578 (m), 1533 (s), 1510 (s), 1465 (m), 1423 (m), 1362 (m), 1334 (vs), 1309 (s), 1268 (s), 1203 (m), 1167 (s), 1143 (s), 1136 (s), 1086 (s), 1056 (m), 1031 (m), 964 (m), 942 (m), 921 (m), 917 (m), 904 (m), 897 (m), 846 (m), 825 (m), 789 (m), 775 (s), 743 (s), 716 (vs), 696 (s), 677 (s), 606 (w), 560 (m), 543 (m), 512 (m), 502 (w), 491 (m), 479 (m), 459 (m), 434 (m), 428 (m), 418 (m), 409 (w). **EA** ($C_{18}H_{10}CuN_{16}O_{14}$, 737.92) calcd.: C 29.30, H 1.37, N 30.37 %; found: C 29.12, H 1.61, N 30.33 %. **BAM drophammer**: 3 J. Friction tester:>360 N. **ESD**: 480 mJ (at grain size 100–500 µm).

[Cu(HTNO)$_2$(2-TAN)$_2$] (22)

After two weeks brown crystals suitable for X-ray diffraction were obtained (330 mg, 0.41 mmol, 82 %).

DSC (5 °C min^{-1}) onset: 174 °C (exothermic). **IR** (ATR, cm^{-1}): $\tilde{\nu}$ = 3178 (w), 3004 (w), 2954 (w), 1622 (m), 1549 (s), 1538 (vs), 1532 (vs), 1515 (s), 1464 (m), 1424 (m), 1403 (m), 1379 (m), 1360 (s), 1307 (s), 1262 (m), 1210 (w), 1165 (s), 1149 (s), 1131 (s), 1069 (m), 1056 (m), 1029 (m), 960 (w), 941 (m), 919 (w), 901 (m), 828 (w), 809 (w), 787 (s), 755 (m), 745 (m), 719 (s), 696 (vs), 675 (s), 651 (m), 629 (m), 618 (m), 585 (w), 550 (w), 539 (w), 530 (w), 523 (w), 513 (w), 486 (w), 451 (w), 438 (w). **EA** ($C_{20}H_{14}CuN_{16}O_{16}$,

797.01) calcd.: C 30.10, H 1.77, N 28.09 %; found: C 30.06, H 1.81, N 28.30 %. **BAM drophammer**: 2 J. Friction tester: 288 N. **ESD**: 480 mJ (at grain size 100–500 µm).

[Cu(N$_3$)(1-TMT)] · H$_2$O (23)

Compound **23** was obtained as a light green powder according to General Procedure C (213 mg, 0.77 mmol, 77 %).

DTA (5 °C min^{-1}) onset: 208 °C (exothermic). **IR** (ATR, cm^{-1}): $\tilde{\nu}$ = 3624 (w), 3126 (w), 3017 (vw), 2089 (vs), 1625 (w), 1619 (w), 1491 (w), 1483 (w), 1447 (w), 1438 (w), 1425 (w), 1405 (vw), 1351 (w), 1297 (m), 1246 (w), 1225 (w), 1185 (m), 1161 (w), 1141 (m), 1104 (m), 1070 (w), 1030 (w), 982 (w), 922 (w), 878 (w), 831 (m), 820 (w), 754 (s), 720 (w), 690 (m), 651 (w), 579 (w), 510 (m), 422 (m), 415 (m), 404 (s). **EA** ($C_3H_5CuN_{11}O$, 274.70) calcd.: C 13.12, H 1.83, N 56.09 %; found: C 13.42, H 2.12, N 53.54 %. **BAM drophammer**: <1 J. Friction tester: 50 N. **ESD**: 6 mJ (at grain size <100 µm).

[Cu(N$_3$)(2-TMT)] · H$_2$O (24)

Compound **24** was obtained as a light green powder according to General Procedure C (195.3 mg, 0.71 mmol, 71 %).

DTA (5 °C min^{-1}) onset: 128 °C (exothermic). **IR** (ATR, cm^{-1}): $\tilde{\nu}$ = 3394 (vw), 2084 (vs), 1632 (vw), 1498 (vw), 1429 (w), 1413 (w), 1352 (w), 1286 (m), 1194 (w), 1136 (m), 1075 (w), 1029 (m), 1014 (w), 949 (w), 889 (w), 822 (w), 764 (m), 707 (m), 700 (m), 670 (m), 583 (w), 479 (m), 404 (s). **EA** ($C_3H_5CuN_{11}O$, 274.70) calcd.: C 13.12, H 1.83, N 56.09 %; found: C 13.09, H 2.00, N 52.45 %. **BAM drophammer**: <1 J. Friction tester: 7.5 N. **ESD**: 0.5 mJ (at grain size <100 µm).

6.6.11 References

[S1] *CrysAlisPRO* Version 171.33.41, Oxford Diffraction Ltd, **2009**.

[S2] G. M. Sheldrick, *Acta Crystallogr. Sect. A* **2015**, *71*, 3–8.

[S3] *SHELXL-97* G. M. Sheldrick, University of Göttingen, Germany, **1997**.

[S4] G. M. Sheldrick, *Acta Crystallogr. Sect. A* **2008**, *64*, 112–122.

[S5] *PLATON* A. L. Spek, Utrecht University, The Netherlands, **1999**.

[S6] L. J. Farrugia, *J. Appl. Cryst.* **2012**, *45*, 849.

[S7] O. V. Dolomanov, L. J. Bourhis, R. J. Gildea, J. A. K. Howard, H. Puschmann, *J. Appl. Cryst.* **2009**, *42*, 339–341.

[S8] *Empirical absorption correction using spherical harmonics, implemented in SCALE3 ABSPACK scaling algorithm* Version 171.33.41, CrysAlisPro Oxford Diffraction Ltd., **2009**.

[S9] *APEX3* Bruker AXS Inc., Madison, Wisconsin, USA,

[S10] *Diamond - Crystal and Molecular Structure Visualization* H. Putz, K. Brandenburg, Crystal Impact, Bonn, Germany,

[S11] *Gaussian 09 A.02* M. J. Frisch, G. W. Trucks, H. B. Schlegel, G. E. Scuseria, M. A. Robb, J. R. Cheeseman, G. Scalmani, V.Barone, B. Mennucci, G. A. Petersson, H. Nakatsuji, M. Caricato, X. Li, H.P. Hratchian, A. F. Izmaylov, J. Bloino, G. Zheng, J. L. Sonnenberg, M. Hada, M. Ehara, K. Toyota, R. Fukuda, J. Hasegawa, M. Ishida, T. Nakajima, Y. Honda, O. Kitao, H. Nakai, T. Vreven, J. A. Montgomery Jr., J. E. Peralta, F. Ogliaro, M. Bearpark, J. J. Heyd, E. Brothers, K. N. Kudin, V. N. Staroverov, R. Kobayashi, J. Normand, K. Raghavachari, J. C. B. A. Rendell, S. S. Iyengar, J. Tomasi, M. Cossi, N. Rega, J. M. Millam, M.Klene, J. E. Knox, J. B. Cross, V. Bakken, C. Adamo, J. Jaramillo, R. Gomperts, R. E. Stratmann, O. Yazyev, A. J. Austin, R. Cammi, C. Pomelli, J. W. Ochterski, R. L. Martin, K. Morokuma, V. G. Zakrzewski, G. A. Voth, P. Salvador, J. J. Dannenberg, S. Dapprich, A. D. Daniels, O. Farkas, J.B. Foresman, J. V. Ortiz, J. Cioslowski, D. J. Fox, Gaussian Inc, Wallingford, CT, USA, **2009**.

[S12] J. W. Ochterski, G. A. Petersson, J. A. M. Jr., *J. Chem. Phys.* **1996**, *104*, 2598–2619.

[S13] J. A. Montgomery Jr., M. J. Frisch, J. W. Ochterski, G. A. Petersson, *J. Chem. Phys.* **2000**, *112*, 6532–6542.

[S14] L. A. Curtiss, K. Raghavachari, P. C. Redfern, J. A. Pople, *J. Chem. Phys.* **1997**, *106*, 1063–1079.

[S15] E. F. C. Byrd, B. M. Rice, *J. Phys. Chem. A* **2006**, *110*, 1005–1013.

[S16] B. M. Rice, S. V. Pai, J. Hare, *Comb. Flame* **1999**, *118*, 445–458.

[S17] http://webbook.nist.gov/chemistry/, accessed Mai **2022.**

[S18] M. S. Westwell, M. S. Searle, D. J. Wales, D. H. Williams, *J. Am. Chem. Soc.* **1995**, *117*, 5013–5015.

[S19] F. Trouton, *Philos. Mag.* **1884**, *18*, 54–57.

[S20] P. R. Spackman, M. J. Turner, J. J. McKinnon, S. K. Wolff, D. J. Grimwood, D. Jayatilaka, M. A. Spackman, *J. Appl. Cryst.* **2021**, *54*, 1006–1011.

[S21] NATO standardization agreement (STANAG) on explosives, impact sensitivity tests, no. 4489, **1999**.

[S22] WIWEB-Standardarbeitsanweisung 4–5.1.02, Ermittlung der Explosionsgefährlichkeit, hier der Schlagempfindlichkeit mit dem Fallhammer, **2002**.

[S23] http://www.bam.de, accessed December **2021.**

[S24] NATO standardization agreement (STANAG) on explosive, friction sensitivity tests, no. 4487, **2002**.

[S25] WIWEB-Standardarbeitsanweisung 4–5.1.03, Ermittlung der Explosionsgefährlichkeit oder der Reibeempfindlichkeit mit dem Reibeapparat, **2002**.

[S26] https://www.ozm.cz/, accessed December **2021.**

[S27] *UN Model Regulation: Recommendations on the Transport of Dangerous Goods – Manual of Tests and Criteria, section 13.4.2.3.3* **2015**.

[S28] Impact: insensitive > 40 J, less sensitive ≥ 35 J, sensitive ≥ 4 J, very sensitive ≤ 3 J; Friction: insensitive > 360 N, less sensitive = 360 N, sensitive < 360 N and > 80 N, very sensitive ≤ 80 N, extremely sensitive ≤ 10 N, **1999**.

[S29] *EXPLO5* V7.01.01, M. Sućeska, Zagreb, **2023**.

7 *N*-Azidoethyl azoles through *N*-alkylation under highly harmonized reaction conditions: synthesis, characterization and complexation as energetic coordination compounds

Lukas Bauer, Simon M. J. Endraß, Thomas M. Klapötke, Jörg Stierstorfer, and Nicole Zeitlmeir

published in *Journal of Heterocyclic Chemistry,* **2024**

DOI: 10.1002/jhet.4803

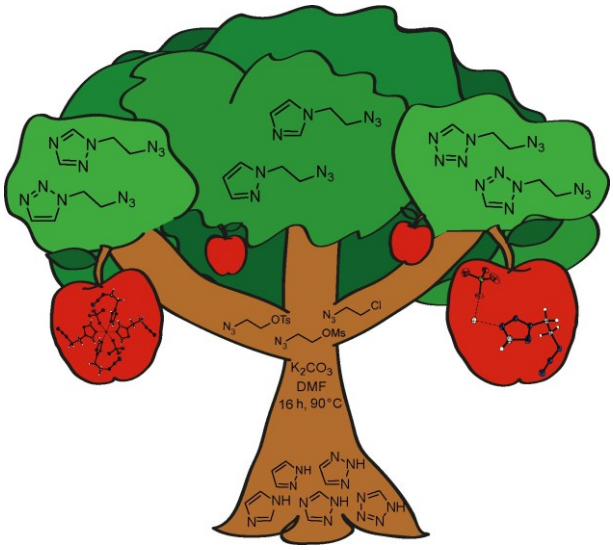

Abstract: Organic azides are universally important in many areas of chemistry, particularly in organic synthesis. The availability of these azides often depends on specific transfer reagents and reaction conditions, or only work with certain substrates. Customizable transfer reagents offer a safe and direct pathway to desired compounds, thereby increasing the availability of *N*-alkyl-azides. In an effort to streamline the synthesis and broaden the scope of *N*-azidoethyl-containing molecules, three different versatile azidoethyl transfer reagents were synthesized and a uniform reaction protocol with azoles as substrates, including imidazole, pyrazole, 1,2,3-triazole, 1,2,4-triazole, and tetrazole was established. The resulting azidoethyl-azoles were further used as ligands for energetic coordination compounds in an effort to create new lead-free primary explosives. A comprehensive characterization of the transfer reagents, the azidoethyl containing products and energetic coordination compounds was conducted using multinuclear NMR, elemental analysis, mass spectrometry and IR spectroscopy. Furthermore, their thermal stability and sensitivity toward friction and impact were determined as well as the detonation properties were calculated by using the EXPLO5 code.

7.1 Introduction

Azides have been shown to be indispensable since the discovery of organic azides by Grieß [1] and the first isolation of the azide anion by Curtius [2]. A large amount of applications have been found for azide containing molecules, which are now essential in a wide range of applications, including biology [3], chemistry [4], medicine [5-6] and materials science [7]. Azides can be used in substitution- and addition-reactions as well as for functional group transformations as either targets or starting materials. From these compounds, a variety of functional groups can be obtained including otherwise difficult to access reactive species such as nitrenes and nitrenium ions, as shown in Figure 1 [4, 8-11]. Possible azide reactions can be seen in Figure 1 and include the Azido-Mannich reaction [12], Staudinger ligation [13] as well as the Staudinger reaction [14], direct oxidation to nitro derivatives [15], the Schmidt reaction [16] and starting from acyl azides the Curtius rearrangement [17]. In recent years, the use as building blocks in traditional organic chemistry for cycloadditions of nitrogen rich azoles such as tetrazole or triazole has gained a lot of attraction. The concept of click chemistry, introduced by Sharpless, refers to a set of reactions characterized by their reliability, ease of use, low production of by-products,

and ability to generate high yields of often nitrogen-rich products under mild conditions [18-19].

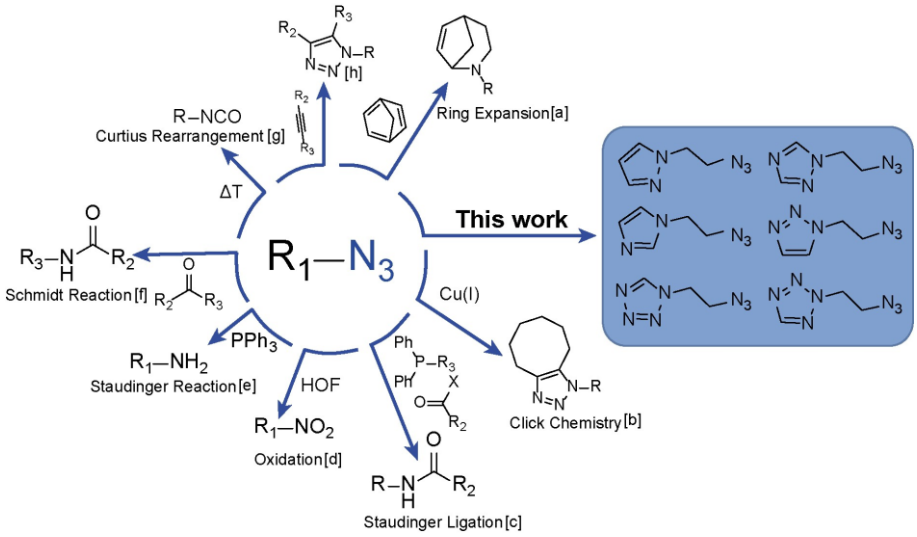

Figure 1. The versatility of organic azides in synthesis [4, 8-17].

In the field of applied energetic materials, azides also have a well-established history (Figure 2). Sodium azide, the most common representative, has the advantage of being a cheap and easy to handle source of the azide anion for synthesis but is also used itself as a gas generating agent airbags [20]. Lead azide is still widely used as primary explosive, cyanuric triazide is easily prepared from cyanuric chloride and acts as initiator, and glycidyl azide polymer (GAP) is an energetic polymer that sees use as an energetic binder [21-23].

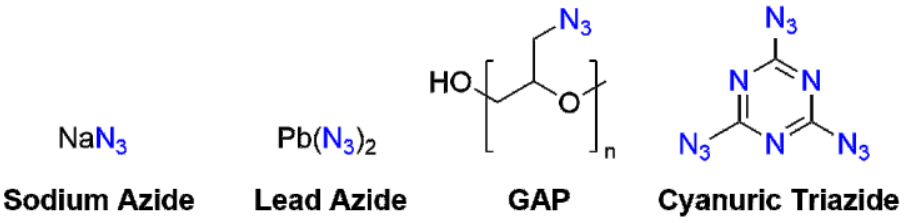

Figure 2. Examples for azides with use as energetic materials [21, 23].

Other compounds containing the azidomethyl functionality, like in GAP, have already been of research interest in recent years as possible energetic plasticizers [24], primary explosives [25-26] and melt-castable alternatives to TNT [27]. However, the presence of the azidomethyl group can induce heightened sensitivity to mechanical stimuli, posing challenges for practical applications in certain scenarios. Lengthening the alkyl chain from methyl to ethyl can help to make the compounds more insensitive, while still profiting from

the high heat of formation, that an azido group contributes [10]. Also, when comparing 1-azidomethyl-tetrazole with 1-azidoethyl-tetrazole (1-AET) a decrease in melting temperature can be observed, as the ethyl derivative is a liquid at room temperature compared to the *N*-azidomethyl derivative which melts at 54 °C [28-29]. Extending the alkyl chain length in the right system can result in achieving a melting point within the suitable range for melt castable energetic materials [24]. Given the significance of the azido functionality in organic synthesis in general and more specifically in the field of energetic materials, a reliable method of introducing the functional group is essential. The most important way of introducing azides is *via* nucleophilic substitution from halides, sulfonates, sulfites or groups of similar properties [30]. A straightforward introduction of the azide functionality along with an alkyl chain can be accomplished with the use of an azidoalkyl transfer. [31] This effectively reduces the number of reaction steps required to obtain new compounds, while providing the safety benefit of adding the explosophoric group at the end of the synthesis route. *N*-Alkylation has been performed under many different reaction conditions and with many different bases, but the lack of uniform reaction conditions hinders the development of new compounds. In some cases, alkylation is also preferred because of the accessibility of desired products. The aforementioned 1-AET can be selectively obtained from 2-azidoethylamine, however 2-(2-azidoethyl)-tetrazole (2-AET) is not available through this reaction route [28]. Alkyl transfer offers a practical method of obtaining previously uncharacterized but promising compounds such as 2-AET. Transfer reactions in general are of considerable importance in chemical synthesis due to the ability to efficiently introduce alkyl groups onto diverse substrates [32-33]. During the development of these unified conditions, the goal of extending the reaction protocol to higher substituted azoles was set and already achieved for several nitropyrazole derivatives [34]. This facile route allows access to a multitude of new *N*-azidoethyl azoles, which can then be used as neat compounds or further used as ligands for energetic coordination compounds (ECCs). This opens the possibility to slightly alter their coordination sphere, leading to homologous ECCs with different mechanical properties [35-36]. Recent publications have underlined their potential to serve as non-toxic alternatives for lead azide, yet an ideal alternative is still to be found [37-38].

In this paper, we present a simple synthetic strategy to obtain the *N*-azidoethyl moiety *via* a standardized reaction protocol that is applicable to all common *N*-unsubstituted azoles and can be extended to higher substituted heterocycles as required. The primary objective

of this work was to establish a versatile reaction protocol, thereby improving the feasibility of screening for novel compounds. In addition, some of the promising new compounds were tested as ligands in ECCs with different metal cations and anions as well as co-ligands, in an effort to create non-toxic, lead-free energetic materials as new primary explosives.

7.2 Results and Discussion

7.2.1 Synthesis

The azidoethyl transfer reagents 2-azidoethyl-4-methylbenzenesulfonate (**2**), 2-azidoethyl-methylsulfonate (**3**) and 1-azido-2-chloroethane (**4**) were prepared according to modified literature and reacted with several unsubstituted azoles to yield the corresponding azidoethyl derivatives. [39-40] The synthesis can be divided into three separate parts: First, the synthesis of the transfer reagents **2**–**4** (Scheme 1). Second, the application of the transfer reagents on unsubstituted azoles to obtain compounds **5**–**10** (Scheme 2). Third, the synthesis of energetic coordination compounds using compounds **8**–**10** as ligands (Schemes 3, 4, 5).

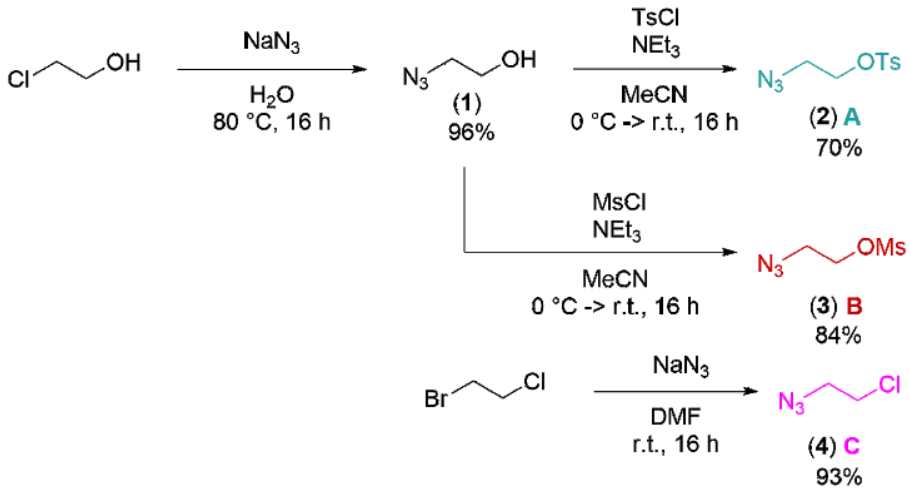

Scheme 1. Synthesis of the azidoethyl transfer reagents **2**–**4**.

The starting material for transfer reagents **2** and **3**, 2-azidoethan-1-ol (**1**), was synthesized based on a modified literature procedure [40]. Commercially available 2-chloroethanol was treated with sodium azide in water at 80 °C to perform a chloride-azide exchange reaction and yield the corresponding azidoethanol **1** in excellent yields. The transfer reagents **2** and **3** were prepared according to the literature. [39-40] The alcohol functionality was reacted with

p-toluenesulfonyl chloride or methanesulfonyl chloride, resulting in the tosylation or mesylation of the respective hydroxy group, yielding compounds **2** and **3** as transfer reagents. Compound **4** was obtained similarly to azidoethanol by bromide to azide exchange reaction of 1-bromo-2-chloroethane in DMF at room temperature. The following azidoethyl transfer reactions were carried out in a standardized reaction protocol. The unsubstituted azoles were dissolved in DMF and reacted with the respective transfer reagents **2**–**4** with 1.5 eq potassium carbonate as base at 90 °C for 16 h.

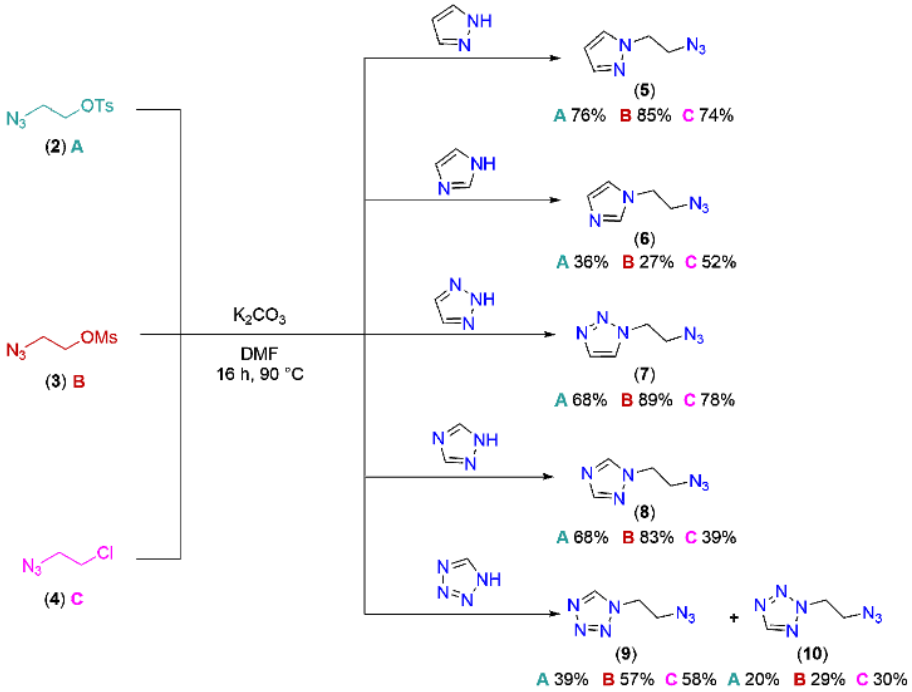

Scheme 2. Synthesis of the azideoethyl containing azoles **5**–**10** under universal reaction conditions using the transfer reagents **2**–**4**.

Through this reaction, the products 1-(2-azidoethyl)-pyrazole (**5**) (AEPy), 1-(2-azidoethyl)-imidazole (**6**) (AEIm), 1-(2-azidoethyl)-1,2,3-triazole (**7**) (AE123Tri), 1-(2-azidoethyl)-1,2,4-triazole (**8**) (AE124Tri), and 1-(2-azidoethyl)-tetrazole (**9**) (1-AET) as well as 2-(2-azidoethyl)-tetrazole (2-AET) (**10**) were obtained with the use of three different transfer reagents as depicted in Scheme 2. No other isomer for both triazole derivatives **7** and **8** were observed. One factor at a time optimization reactions were carried out to test different bases, solvent systems, and reaction temperatures and times. In order to ensure the viability of this reaction for a wide range of substrates, the goal of the optimization was identifying reaction conditions that can ensure successful reaction with any commonly used azole. For optimization of yield and efficiency of single reactions of interest, a more detailed approach

like using design of experiment is recommended [41]. The results can be seen in Table 1. Pyrazole and tetrazole were chosen as substrates for base and solvent optimization, the temperatures were tested individually for each heterocycle. K_2CO_3, $KHCO_3$, Cs_2CO_3, NEt_3, and LiOH were tested as bases with K_2CO_3 giving the best results. DMF and a water-DMF mixture as well as acetonitrile were investigated as solvent systems, but DMF resulted less side product formation and less failed reactions. Reaction temperatures were ranged from 70–100 °C. For optimized yields 90 °C was confirmed as the best temperature, but it is worth noting that different temperatures gave better yields for certain heterocycles, such as 70 °C for imidazole.

Table 1. Reaction conditions investigated for the transfer reaction.

Azole	T [°C]	t [h]	Base	Solvent	Yield [%]
Pyrazole	90	16	K_2CO_3	DMF	85[a]
Pyrazole	100	16	K_2CO_3	DMF	88[a]
Pyrazole	90	16	$KHCO_3$	DMF	79[a]
Pyrazole	90	16	Cs_2CO_3	DMF	np.[a]
Pyrazole	90	4	K_2CO_3	DMF	11[a]
Pyrazole	90	16	K_2CO_3	MeCN	np.[a]
Pyrazole	90	16	K_2CO_3	DMF/H_2O	np. [a]
Imidazole	90	16	K_2CO_3	DMF	52[b]
Imidazole	70	16	K_2CO_3	DMF	63[b]
1,2,3-Triazole	90	16	K_2CO_3	DMF	89[a]
1,2,3-Triazole	70	16	K_2CO_3	DMF	58[a]
1,2,4-Triazole	90	16	K_2CO_3	DMF	83[a]
1,2,4-Triazole	70	16	K_2CO_3	DMF	64[a]
Tetrazole[c]	90	16	K_2CO_3	DMF	62[b]
Tetrazole[c]	90	16	NEt_3	DMF	53[b]
Tetrazole[c]	90	16	LiOH	DMF	52[b]
Tetrazole[c]	80	16	K_2CO_3	DMF	np.[b]

[a] 2-Azidoethyl-methylsulfonate (**3**) as transfer reagent. [b] 2-Azidoethyl-4-methylbenzenesulfonate (**2**) as transfer reagent. [c] Overall yield of both isomers before column chromatography determined through NMR spectroscopy.

It has been previously reported that 1-AET can act as a ligand in ECCs with copper, silver, zinc, and iron as central metal ions and with common anions like nitrate or perchlorate. [25] This allows that the energetic properties of the ligand itself, as well as its complexation behavior, to be studied and compared with 1-AET. As seen in Scheme 3, 2-AET coordinated to silver(I) perchlorate and the nitroaromatic copper(II) salts in the expected stoichiometry, similar to 1-AET [42]. While [Ag(μ-2-AET)(ClO_4)] was obtained by combining ethanolic solutions of the ligand and silver perchlorate, the nitroaromatic ECCs were prepared by stirring a suspension of the respective neutral nitrophenol derivative with basic copper carbonate in water until a clear solution was obtained. The addition of 2-AET,

followed by stirring at elevated temperatures allowed the formation of the ECCs, which precipitated upon cooling to room temperature until the yield stagnated within few days.

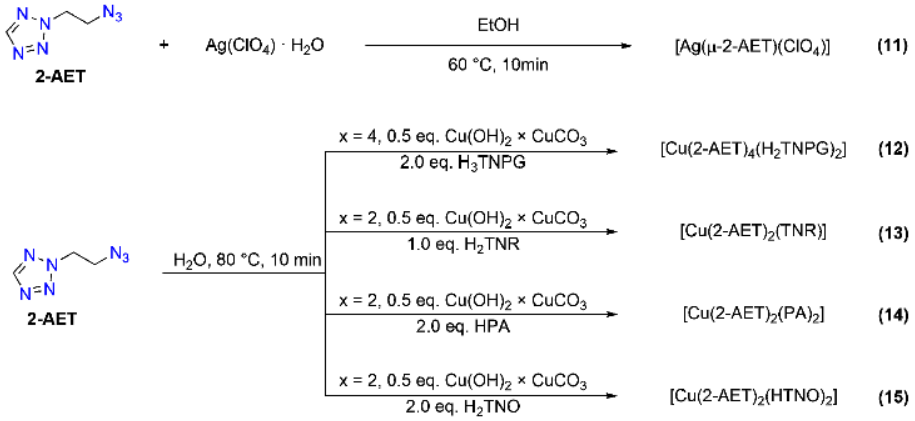

Scheme 3. Synthesis of ECCs **11**–**15** with 2-AET as ligand.

The reaction scheme for the formation of the ECCs with the AE124Tri ligand can be seen in Scheme 4. This ligand allows the formation of ECCs with an improved ratio of ligand to anion, and therefore a better trade-off between fuel and oxidizing agent, like in the cases of $[Cu(AE124Tri)_4(ClO_4)_2]$ and $[Cu(AE124Tri)_4(NO_3)_2]$.

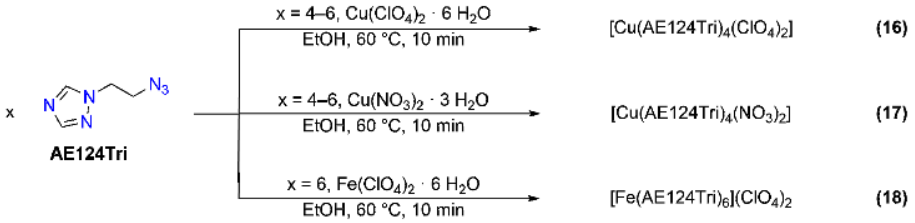

Scheme 4. ECCs **16**–**18** obtained by combination of the AE124Tri ligand with copper(II) perchlorate or nitrate and iron(II) perchlorate.

A potential use for ECCs is their application as successors of lead azide and lead styphnate, which are to be banned in the EU for civil application in detonators [43-44]. If the exemption, which expires in April 2026, is not extended, this could lead to a serious demand for alternatives. ECCs based on copper azide might be one possible alternative for such an application, as existing plants could most likely be used with only minor adjustments. Therefore, $[Cu_2(2\text{-}AET)(N_3)_4]$ (**19**) and $[Cu_3(AE124Tri)_2(N_3)_6]$ (**20**) were synthesized and evaluated as potential candidates, as seen in Scheme 5. Their synthesis was conducted by straightforward precipitation from aqueous solutions of copper(II) nitrate trihydrate and ligand by addition of sodium azide. In the case of **19**, a small amount of ethanol had to be added to improve the solubility of the ligand. Attempts without the addition of EtOH lead

to the precipitation of neat $Cu(N_3)_2$, which represents an even more serious safety thread than **19** [45]

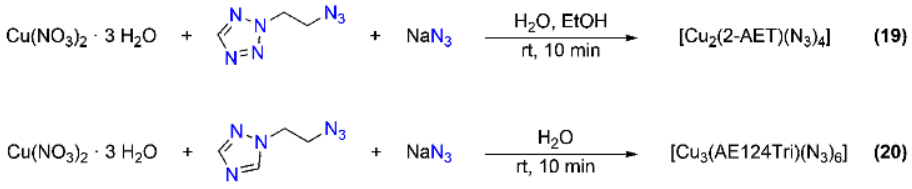

Scheme 5. Synthesis of the copper(II) azides **19** and **20**.

7.2.2 Characterization

DTA analysis of the compounds was determined with an OZM Research DTA 552-Ex instrument with a heating rate of 5 °C min^{-1} in open test tubes. All compounds show thermal stability in the expected range of ~200 °C with the lowest thermally stable being the 1-AET (**9**) with an onset of decomposition of 193 °C and the highest thermal stability for 1-(2-azidoethyl)-1,2,3-triazole (**7**) 214 °C. An exception is AEPy (**5**) that evaporates at 216 °C. Increasing the heating rate to 10 °C min^{-1} allows to indentify the decomposition temperature at 225 °C. The thermal behaviour can be seen in Figure 3.

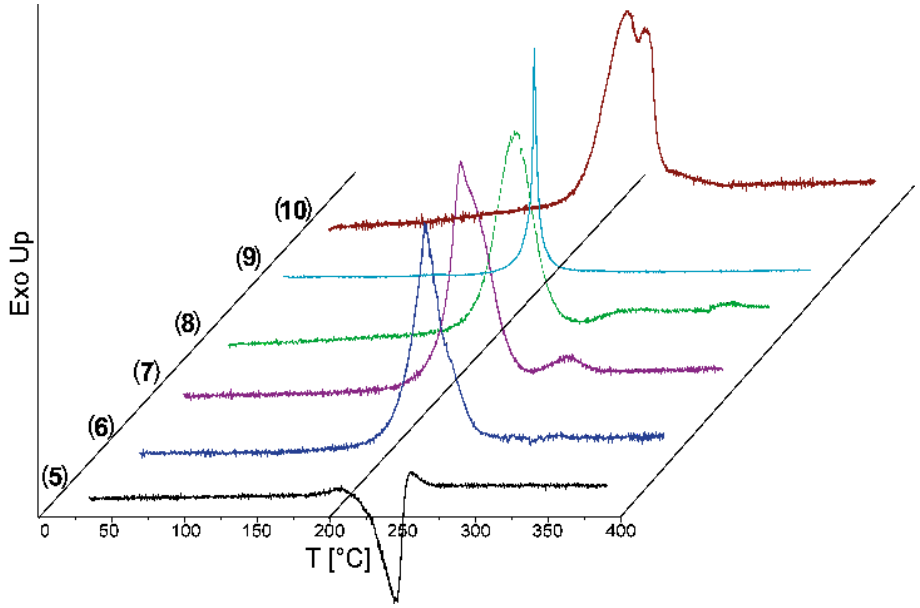

Figure 3. DTA plots of compounds **5**–**10** with a heating rate of 5 °C min^{-1}.

To screen new molecules efficiently, highly specific characterisation methods are required. Azides show a strong asymmetric vibration resulting in a vibrational band in the region of 2100 cm^{-1}, which can be used to confirm a newly introduced azide group [46].

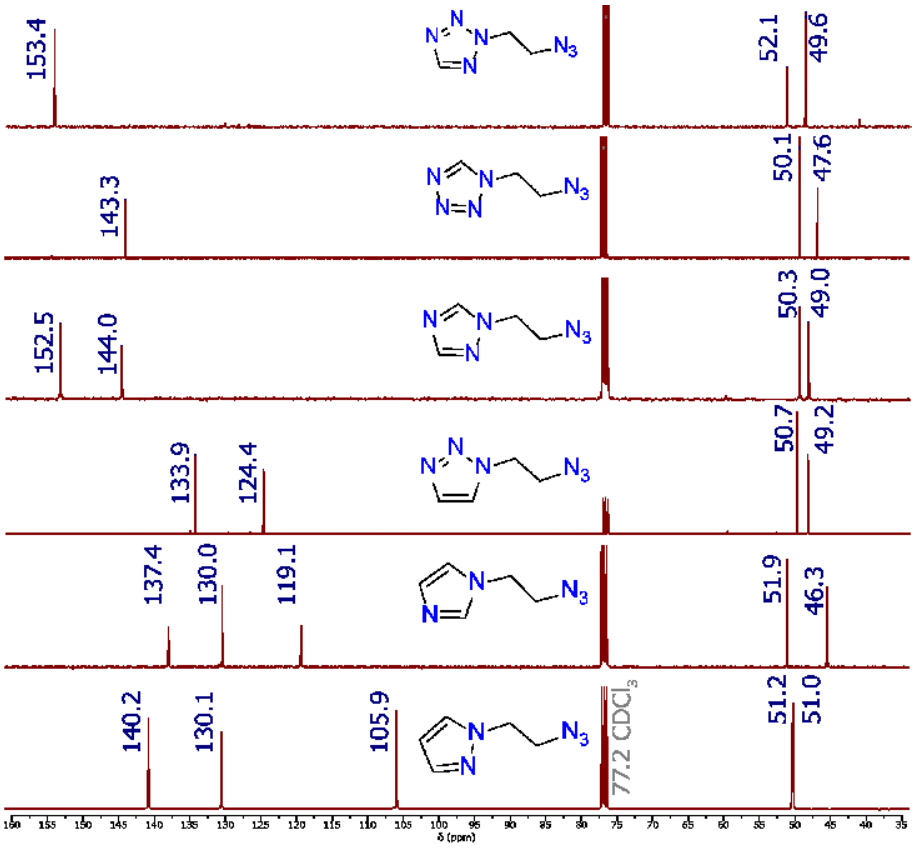

Figure 4. ^{13}C NMR spectra of compounds **5**–**10** measured in $CDCl_3$.

Additionally, ^{1}H and ^{13}C NMR spectroscopy are particularly useful to see if the reaction was successful (Figure 4). The resonances can be divided into two groups. The newly introduced ethyl groups were assigned upfield and the ring positions shifted downfield. The shifts of the CH_2 groups belonging to the ethyl functionality range from 3.63 ppm to 4.93 ppm for ^{1}H NMR and from 46.3 ppm to 51.9 ppm in the ^{13}C NMR. The second set of resonances, shifted downfield, range from 6.22 ppm to 9.44 ppm for the ^{1}H-NMR and 105.9 ppm to 153.4 ppm for the carbon atoms in the ^{13}C-NMR. This allows easy evaluation as the CH_2-resonances are clearly distinguishable from the starting materials and a slight shift in the aromatic positions indicates a successful alkylation for the ring signals.

7.2.3 Physicochemical Properties

The presented azidoethyl azoles **5**–**10** can be classified as potential energetic materials and were therefore investigated for their energetic properties. As expected, products with adjacent nitrogens as in pyrazole and 1,2,3-triazole have a higher heat of formation than their respective isomers imidazole and 1,2,4-triazole [47-48]. Due to the high influence of the

density on the detonation parameters, 1-(2-azidoethyl)-imidazole (**6**) outperformes 1-(2-azidoethyl)-pyrazole (**5**) although the heat of formation is lower. Among the synthesized azoles, the tetrazole derivatives **9** and **10** show the highest values for detonation velocity, which can be attributed to their high heat of formation, density, and high nitrogen content. According to the "Recommendations on the Transport of Dangerous Goods" [49], all compounds are insensitive toward friction and only 1-AET (**9**) and 2-AET (**10**) show sensitivity toward impact. While 2-AET is more thermally stable (201 °C to 193 °C), 1-AET shows a lower sensitivity toward impact (9 J to 3 J). This trend has previously been observed for other 1-tetrazole and 2-tetrazole isomers, reinforcing the idea that tetrazole isomers have different advantages that can be used based on the needs for application [50].

Table 2. Physicochemical properties and EXPLO5 V7.01.01 calculation results of compounds **5**–**10**.

Compound	**5**	**6**	**7**	**8**	**9**	**10**
Formula	$C_5H_7N_5$	$C_5H_7N_5$	$C_4H_6N_6$	$C_4H_6N_6$	$C_3H_5N_7$	$C_3H_5N_7$
M [g mol^{-1}]	137.15	137.15	138.13	138.13	139.12	139.12
IS [J][a]	>40	>40	>40	>40	9	3
FS [N][b]	>360	>360	>360	>360	>360	>360
ρ [g cm^{-3}][c]	1.08	1.18	1.21	1.22	1.25	1.26
N [%][d]	51.07	51.07	60.8	60.8	70.5	70.5
T_{dec} [°C][e]	216	210	214	197	193	201
$\Delta_f H^\circ$ [kJ mol^{-1}][f]	420.9	383.7	510.8	442.9	592.8	568.6
EXPLO5 V7.01.01[g]						
$-\Delta_{Ex} U^0$ [kJ kg^{-1}][h]	3380	3141	3948	3495	4452	4292
T_{det} [K][i]	2889	2070	2560	2359	2974	2889
P_{CJ} [GPa][j]	7.1	8.5	10.8	10.4	13.2	13.1
V_{det} [m s^{-1}][k]	5311	5706	6217	6110	6677	6670

[a] Impact sensitivity (BAM drophammer (1 of 6)). [b] Friction sensitivity (BAM friction tester (1 of 6)). [c] Determined pycnometrically [d] Nitrogen content. [e] Decomposition temperature; Melting point (DTA; β = 5 °C min^{-1}). [f] Calculated enthalpy of formation.[g] EXPLO5 Version V7.01.01 [51]. [h] Energy of explosion. [i] Detonation temperature. [j] Detonation pressure at Chapman-Jouguet point. [k] Detonation velocity.

Table 3 shows that all ECCs that carry the 2-AET ligand can be characterized as very sensitive toward impact. Except for compound **11** they are more sensitive toward friction compared to the respective ECC that contains the 1-AET ligand. It is of no surprise, that ECCs, that carry the AE124Tri ligand instead of 1-AET, are significantly less sensitive to mechanical stimuli due to the lower enthalpy of formation of the ligand, and therefore in sum, of the ECC [48]. Compounds **11** and **13** proved to undergo detonative behavior under the confined conditions of the hot needle test. Therefore, those two ECCs were selected for initiation experiments with pentaerythritol tetranitrate as main charge within self-assembled detonators that contain net explosive quantities of 250 mg.

Table 3. Sensitivities of compounds **11**–**20** against external stimuli in comparison with literature-known analogs which carry the 1-AET ligand.

Compound	No.	T_{endo}[a] [°C]	T_{exo}[b] [°C]	IS[c] [J]	FS[d] [N]	ESD[e] [mJ]	HP[f]	HN[g]
[Ag(μ-2-AET)(ClO_4)]	**11**	151[h]	151[h]	<1	0.6	13	det.	det.
[Ag(1-AET)](ClO_4) [42]		-	165	<1	0.6	65	det.	det.
[Cu(2-AET)$_4$(H_2TNPG)$_2$]	**12**	-	145	<1	54	250	def.	def.
[Cu(1-AET)$_4$(H_2TNPG)$_2$] [42]		-	121	1.5	84	84	def.	def.
[Cu(2-AET)$_2$(TNR)]	**13**	151[h]	151[h]	<1	30	200	def.	det.
[Cu(1-AET)$_2$(TNR)] [42]		-	177	<1	240	123	def.	def.
[Cu(2-AET)$_2$(PA)$_2$]	**14**	-	169	2	192	160	def.	dec.
[Cu(1-AET)$_2$(PA)$_2$] [42]		-	183	3	252	226	def.	def.
[Cu(2-AET)$_2$(HTNO)$_2$]	**15**	-	141	<1	80	160	def.	def.
[Cu(1-AET)$_2$(HTNO)$_2$] [52]		-	191	<1	>360	90	def.	dec.
[Cu(AE124Tri)$_4$(ClO_4)$_2$]	**16**	-	171	<1	108	50	def.	dec.
[Cu(1-AET)$_6$](ClO_4)$_2$ [42]		135	158	<1	15	368	def.	det.
[Cu(AE124Tri)$_4$(NO_3)$_2$]	**17**	117, 153	179	35	>360	42	dec.	dec.
[Cu(1-AET)$_2$(H_2O)(NO_3)$_2$] [42]		94, 121	152	10	108	840	def.	def.
[Fe(AE124Tri)$_6$](ClO_4)$_2$	**18**	128[h]	128[h]	7.5	120	160	def.	dec.
[Fe(1-AET)$_6$](ClO_4)$_2$ [42]		-	151	3	3.75	65	det.	det.
[Cu_2(2-AET)(N_3)$_4$]	**19**	-	143	<1	<0.1	2.5	det.	det.
[Cu_3(AE124Tri)$_2$(N_3)$_6$]	**20**	-	112	<1	0.2	2.5	det.	det.
[Cu(1-AET)(N_3)$_2$] [45]		-	131	<1	<0.1	1.1	det.	det.

[a] Onset temperature of endothermic event in the DTA (heating rate of 5 °C min^{-1}), indicating a melting point of the compound; [b] Onset of exothermic event in the DTA; [c] Impact sensitivity (BAM drophammer (1 of 6)); [d] Friction sensitivity (BAM friction tester (1 of 6)); [e] Electrostatic discharge devise (OZM XSpark10); [f] Hot plate test (det.: detonation, def.: deflagration, dec.: decomposition); [g] Hot needle test (det.: detonation, def.: deflagration, dec.: decomposition); [h] Endo-to-exo-transition.

The outcomes of the performance tests of compounds **11**–**20** can be found in Table 4. To test the performance of the ECCs as primary explosives in detonator setups, 200 mg of PETN (< 100 µm) were pressed in a copper shell (diameter: 7 mm, length: 88 mm), by lowering a weight of 8 kg on top. The shell was then placed on a copper witness plate with a thickness of 1 mm. Then 50 mg of the respective ECC was loosely filled on top of the PETN and a type A electric igniter was crimped to the shell. In the case of compound **11**, **19** and **20**, positive initiation of the PETN, indicated by penetration of the witness plate (Figure 5), was feasible.

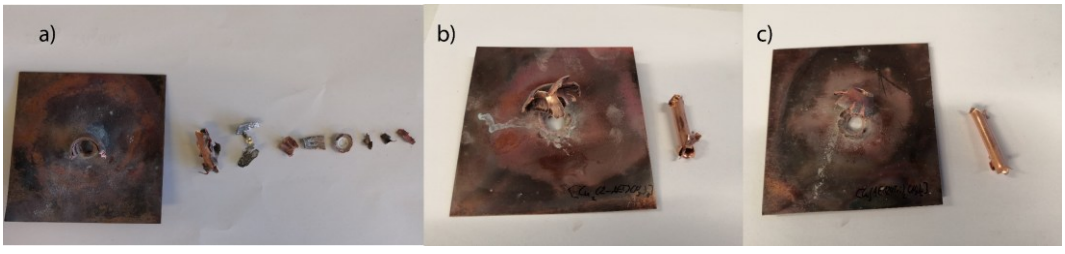

Figure 5. Outcomes of the initiation by **a)** [Ag(μ-2-AET)(ClO_4)], **b)** [Cu_2(2-AET)(N_3)$_4$] and **c)** [Cu_3(AE124Tri)$_2$(N_3)$_6$].

The ignitability of colored compounds by laser was tested by pressing 25 mg of sample into a polycarbonate primer cap with a force of 1.5 kN. The surface was then sealed with UV-curable adhesive. The samples were irradiated by a 45 W InGaAs laser (λ = 915 nm) operating in single-pulse mode. Additional information on the setup can be found in the Supporting Information. Compounds **13**, **14** and **16** showed detonative behavior during irradiation under certain specification. The detailed settings can be seen in the supporting information. For safety reasons, **19** and **20** were not tested in this setup. Their high sensitivities against mechanical manipulation do not allow manual compression of any kind. Such handling, if necessary, should only be done under increased safety standards and by trained professionals only.

Table 4. Outcomes of the PETN and laser initiation experiments.

Compound	No.	PETN initiation[a]	Laser parameter[b]			
			7 A, 15 ms	7 A, 30 ms	8 A, 30 ms	10 A, 30 ms
[Ag(μ-2-AET)(ClO_4)]	**11**	pos.	-	-	-	-
[Cu(2-AET)$_4$(H_2TNPG)$_2$]	**12**	-	-	-	neg.	det.
[Cu(2-AET)$_2$(TNR)]	**13**	neg.	-	-	neg.	det.
[Cu(2-AET)$_2$(PA)$_2$]	**14**	-	-	-	-	def.
[Cu(2-AET)$_2$(HTNO)$_2$]	**15**	-	-	-	-	neg.
[Cu(AE124Tri)$_4$(ClO_4)$_2$]	**16**	-	det.	det.	-	-
[Cu(AE124Tri)$_4$(NO_3)$_2$]	**17**	-	-	-	-	neg.
[Fe(AE124Tri)$_6$](ClO_4)$_2$	**18**	-	dec.	-	-	dec.
[Cu_2(2-AET)(N_3)$_4$]	**19**	pos.	-	-	-	-
[Cu_3(AE124Tri)$_2$(N_3)$_6$]	**20**	pos.	-	-	-	-

[a] pos.: positive, neg.: negative, -: not performed [b] Operating parameters: voltage U = 4 V, current I = 7–10 A, pulse length τ = 15–30 ms, theoretical maximal output power P_{max} = 45 W, wavelength λ = 915 nm (det.: detonation, def.: deflagration, dec.: decomposition, neg.: negative).

7.2.4 Crystal Structures

Figure 6 shows the crystal structure of [Ag(μ-2-AET)(ClO_4)] including some bond distances of interest. Unlike [Ag(1-AET)](ClO_4), which crystallized in the triclinic space group $P\bar{1}$ with a calculated density of 2.470 g cm^{-3} (173 K) [42], the ECC produced from the 2-isomer crystallized in the monoclinic space group $P2_1/c$ with a slightly lower density of 2.412 g cm^{-3} (173 K). A direct comparison shows, that [Ag(1-AET)](ClO_4) forms a one-dimensional polymeric network in which the 1-azidoethyl ligand is the linking unit. In the case of [Ag(μ-2-AET)(ClO_4)], the bond distances to the silver(I) atom are shortened in comparison and the perchlorate ion takes a major role in building a three-dimensional coordination network. The slightly lower theoretical maximum density can be explained by the formation of pores within the three-dimensional structure.

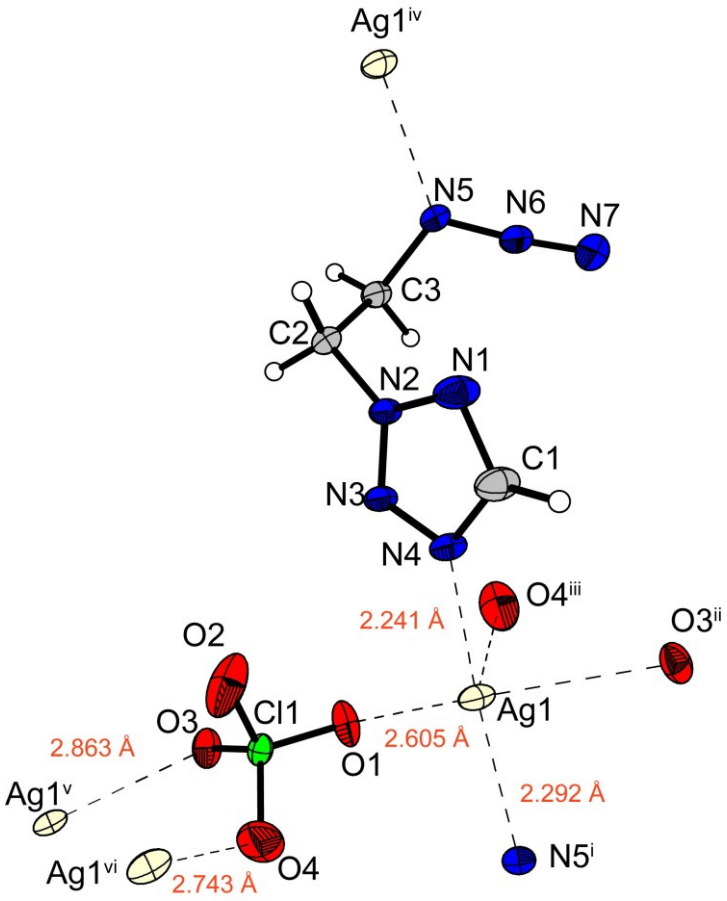

Figure 6. Coordination polymer of [Ag(μ-2-AET)(ClO_4)]. Selected bond lengths [Å]: Ag1–O1 2.6049(16), Ag1–N4 2.2405(17), Ag1–N5^{i} 2.2917(17); Selected bond angles [°]: O1–Ag1–N4 103.17(6), O1–Ag1–N5^{i} 93.17(5), N4–Ag1–N5^{i} 156.94(6); Symmetry codes: (i) −x, −1/2+y, 3/2−z, (ii) −1+x, 1/2−y, 1/2+z, (iii) x, 1/2−y, 1/2+z, (iv) −x, 1/2+y, 3/2−z, (v) 1+x, 1/2−y, −1/2+z, (vi) x, 1/2−y, −1/2+z.

The coordination spheres of a) [Cu(2-AET)$_4$(H_2TNPG)$_2$], b) [Cu(2-AET)$_2$(TNR)], c) [Cu(2-AET)$_2$(PA)$_2$] and d) [Cu(2-AET)$_2$(HTNO)$_2$] are shown in Figure 7. While all four compounds crystallized in the triclinic space group *P*−1, only three of them showed densities close to 1.8 g cm^{-3} at the respective temperature. It was not possible to perform a low-temperature X-ray measurement of [Cu(2-AET)$_2$(HTNO)$_2$], due to cracking of the single crystals at reduced temperatures. The crystal structure was therefore determined at room temperature, leading to increased sizes of the thermal ellipsoids. In all cases, coordination was observed as expected for Cu(II) compounds. The crystal structures all feature *Jahn-Teller*-like distorted octahedral coordination spheres

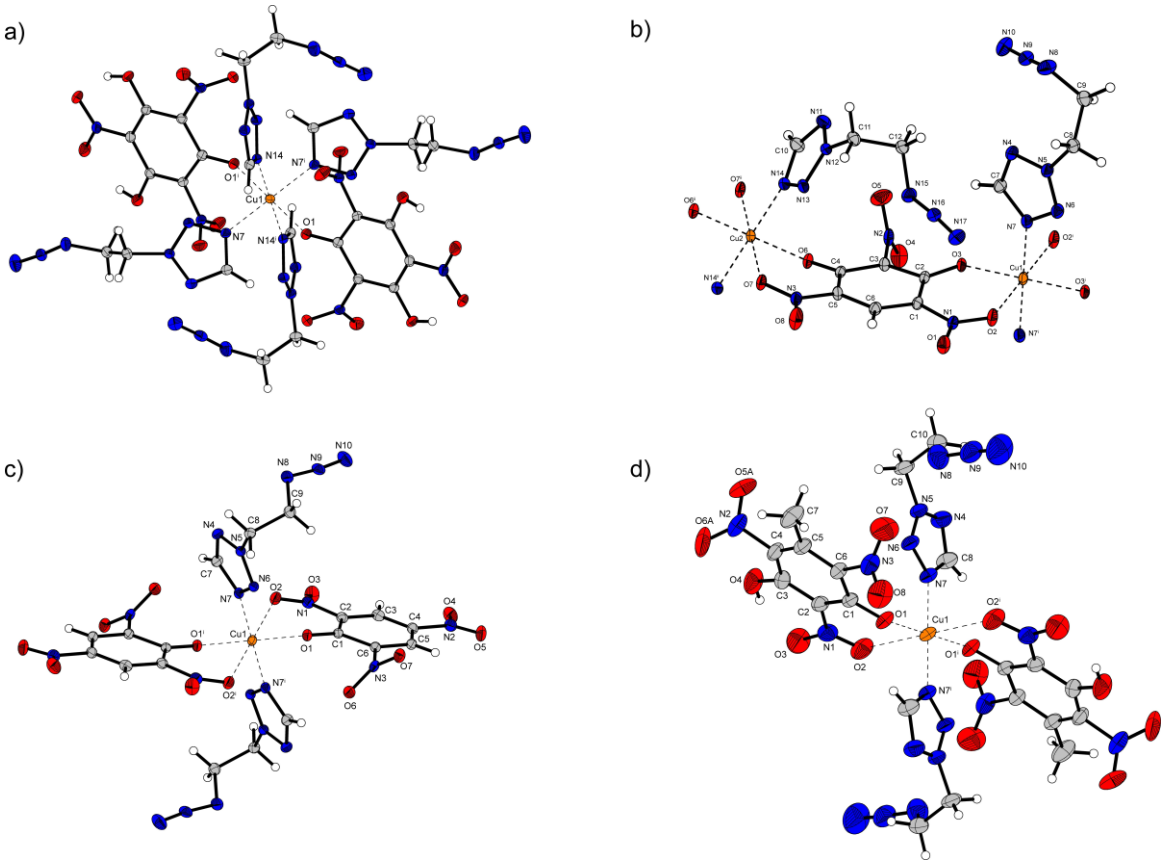

Figure 7. a) Crystal structure of $[Cu(2\text{-}AET)_4(H_2TNPG)_2]$. Selected bond lengths [Å]: Cu1–O1 2.3345(15), Cu1–N7 2.0227(18), Cu1–N14 2.0156(18); Selected bond angles [°]: O1–Cu1–N7 84.23(6), O1–Cu1–N14 89.16(7); Symmetry codes: (i) 1−x, 1−y, 1−z. **b)** Crystal structure of $[Cu(2\text{-}AET)_2(TNR)]$. Selected bond lengths [Å]: Cu1–O2 2.3077(17), Cu1–O3 1.9341(15), Cu1–N7 2.0202(18), Cu2–O6 1.9396(16), Cu2–O7 2.3094(17), Cu2–N14 2.0164(18); Selected bond angles [°]: O2–Cu1–O3 82.88(6), O2–Cu1–N7 92.59(6), O3–Cu1–N7 89.00(7), O6–Cu2–O7 81.14(6), O6–Cu2–N14 87.56(7); Symmetry codes: (i) 1−x, 1−y, −z, (ii) 2−x, 1−y, 1−z. **c)** Crystal structure of $[Cu(2\text{-}AET)_2(PA)_2]$. Selected bond lengths [Å]: Cu1–O1 1.9220(16), Cu1–O2 2.3728(19), Cu1–N7 1.9951(18); Selected bond angles [°]: O1–Cu1–O2 78.71(7), O1–Cu1–N7 90.22(7), O2–Cu1–N7 90.32(7); Symmetry codes: (i) −x, −y, 1−z. **d)** Crystal structure of $[Cu(2\text{-}AET)_2(HTNO)_2]$. Cu1–O1 1.9272(13), Cu1–O2 2.423(2), Cu1–N7 2.0007(19); Selected bond angles [°]: O1–Cu1–O2 75.24(6), O1–Cu1–N7 92.41(7), O2–Cu1–N7 90.75(7); Symmetry codes: (i) 1−x, 1−y, −z.

The crystal structure of $[Cu(AE124Tri)_4(ClO_4)_2]$ is shown in Figure 8. The compound crystallized in the triclinic space group *P*−1 with a density of 1.717 g cm^{-3} at 100 K. Unlike its structural relative 1-AET, the copper(II) perchlorate ECC of 1-(2-azidoethyl)-1,2,4-triazole (AE124Tri), does not show a ratio of 1:6 between copper and ligand [42]. Instead, the ligands occupy the *xy*-plane, leaving the elongated z^2-axis open for coordination by two perchlorate anions.

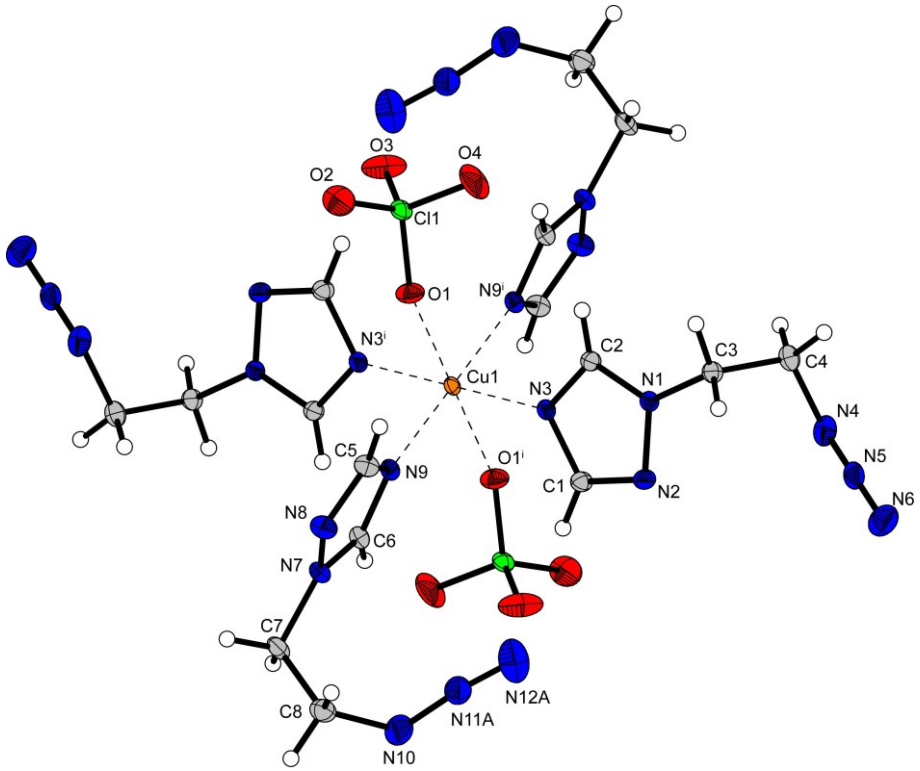

Figure 8. Crystal structure of $[Cu(2\text{-}AE124Tri)_4(ClO_4)_2]$. Selected bond lengths [Å]: Cu1–O1 2.4406(12), Cu1–N3 2.0027(12), Cu1–N9 2.0251(14); Selected bond angles [°]: O1–Cu1–N3 87.40(5), O1–Cu1–N9 87.11(5), N3–Cu1–N9 89.26(5); Symmetry codes: (i) 1−x, 1−y, 1−z.

7.3 Conclusion

This work documents the successful synthesis and characterization of 1-(2-azidoethyl)-pyrazole (**5**), -imidazole (**6**), -1,2,3-triazole (**7**), -1,2,4-triazole (**8**), and -tetrazole (**9**) as well as 2-(2-azidoethyl)-tetrazole (**10**) through a uniform reaction protocol using the transfer reagents 2-azidoethyl-4-methylbenzenesulfonate (**2**), 2-azidoethyl-methanesulfonate (**3**) and 1-azido-2-chloroethane (**4**), in moderate to very good yields. A reaction protocol was established that can be applied to any azole and that will result in a successful alkylation. For this, the reaction parameters were screened and it was concluded that the use of DMF as solvent, potassium carbonate as base, and 90 °C as reaction temperature showed the best overall results. Triazole and tetrazole derivatives were further used as ligands in ECCs, where they showed promising properties as potential primary explosives. Three of the ECCs, which were put to test, initiated PETN in the setup used. Another set of three ECCs was successfully used in laser initiation experiments and brought to detonation by single-pulse irradiation. Furthermore, the established reaction protocol can be extended to various

functionalized heterocycles as substrates, to obtain more previously uncharacterized azidoethyl-containing compounds in a fast, safe and reliable way.

7.4 Experimental Section

Caution! *Some of the described compounds may be energetic with sensitivities towards impact, friction, heat or electrostatic discharge. No major hazards occurred during the preparation. Wearing additional safety equipment (Kevlar® gloves, earplugs, face shield, leather coat, as well as earthed shoes and equipment) is recommended.*

Solvents for the reaction were bought from different suppliers and were used without further purification. As far as not specifically explained, all reactions were performed under standard conditions. NMR spectra were recorded using a Bruker 400, JEOL Eclipse 400, at ambient temperature. The chemical shifts were determined to external standards: Me_4Si (^1H 399.8/400.2 MHz; ^{13}C 100.5/100.6 MHz). Infrared spectra were measured using a PerkinElmer Spectrum One spectrometer equipped with a Smiths DuraSamplIR ATR device. All spectra were recorded at ambient temperature under standard atmosphere. Analysis of C/H/N/S/Cl contents were performed using an Elementar vario El or Elementar vario micro.

2-Azidoethan-1-ol (1)

2-Chloroethanol (36.3 g, 30.0 mL, 0.451 mol, 1.0 eq.) was dissolved in H_2O (160 mL) and the mixture was cooled down to 0 ºC. NaN_3 (29.4 g, 0.452 mol, 1.0 eq.) was added in portions and the solution was allowed to warm up to ambient temperature and was stirred for 10 min. More NaN_3 (19.6 g, 0.301 mol, 0.67 eq.) was added and the solution was heated up to 80 ºC and left stirring for 16 h. The solution was extracted with Et_2O (3 × 100 mL) and the organic phase was washed with brine (50 mL), dried over $MgSO_4$ and the solvent was removed under reduced pressure to yield 2-azidoethan-1-ol (**1**) (37.7 g, 0.433 mol, 96%) as a colorless liquid.**^{1}H NMR (400.2 MHz, DMSO-*d*$_6$)**: δ (ppm) = 5.00 (t, 1H), 3.57 (m, 2H), 3.26 (m, 2H). **^{13}C NMR (100.6 MHz, DMSO-*d*$_6$)**: δ (ppm) = 60.2, 52.9. **IR (rel. int.)**: $\tilde{\nu}$ (cm^{-1}) = 2979 (m), 2097 (vs), 1736 (m), 1598 (m), 1443 (m), 1366 (s), 1350 (m), 1293 (m), 1241 (s), 1190 (s), 1176 (vs), 1097 (s), 1047 (s), 1020 (m), 915 (s), 816 (m), 771 (m). **MS** (ESI+) m/z: [$C_2H_6N_3O_3$] calc.: 88.0511 $[M+H]^+$; found: 88.0506.

2-Azidoethyl-4-methylbenzenesulfonate (2)

2-Azidoethan-1-ol (**1**) (20.0 g, 0.230 mol, 1.0 eq.) was dissolved in MeCN (200 mL) and the solution was cooled down to 0 ºC. NEt_3 (34.8 g, 48.0 mL, 0.345 mol, 1.5 eq.) was added dropwise and the reaction mixture was left stirring for 15 min at −10 ºC. Tosyl chloride (44.1 g, 0.230 mol, 1.0 eq.) dissolved in MeCN (200 mL) was added dropwise and the solution was allowed to warm up to ambient temperature. The resulting white precipitate was filtered off and the clear colorless solution was left stirring for 16 h at ambient temperature. The solvent was removed under reduced pressure and H_2O (100 mL) was added. The aqueous phase was extracted with EtOAc (3 × 100 mL) and the combined organic layers were washed with HCl (2 M, 100 mL), $NaHCO_3$ (saturated, 100 mL) and brine (100 mL). After drying the organic layer over anhydrous $MgSO_4$, the solvent was removed under reduced pressure to yield 2-azidoethyl-4-methylbenzene-sulfonate (**2**) (41.0 g, 0.170 mol, 73%) as a slightly orange liquid that was used without further purification. **^{1}H NMR (400.1 MHz, DMSO-*d*$_6$)**: δ (ppm) = 7.80 (d, 2H), 7.50 (d, 2H) 4.16 (t, 2H), 3.54 (t, 2H), 2.43 (s, 2H). **^{13}C NMR (100.6 MHz, DMSO-*d*$_6$)**: δ (ppm) = 145.7, 132.5, 130.7, 128.1, 69.8, 49.5, 21.6. **IR (rel. int.)**: $\tilde{\nu}$ (cm^{-1}) = 2109 (m), 1597 (w), 1441 (w), 1361 (s), 1305 (m), 1295 (m), 1189 (s), 1172 (vs), 1096 (m), 1018 (m), 911 (s), 814 (s), 767 (s), 661 (s), 655 (s), 571 (s), 552 (vs), 529 (s), 487 (m), 447 (m).

2-Azidoethyl-methylsulfonate (3)

2-Azidoethan-1-ol (**1**) (20.3 g, 0.233 mol, 1.0 eq.) was dissolved in MeCN (200 mL) and the solution was cooled down to 0 ºC. NEt_3 (35.4 g, 48.7 mL, 0.350 mol, 1.5 eq.) was added dropwise and the reaction mixture was left stirring for 15 min at −10 ºC. Methanesulfonyl chloride (26.7 g, 0.233 mol, 1.0 eq.) dissolved in MeCN (200 mL) was added dropwise and the solution was allowed to warm up to ambient temperature. The resulting white precipitate was filtered off and the clear colorless solution was left stirring for 16 h at ambient temperature. The solvent was removed under reduced pressure and H_2O (100 mL) was added. The aqueous phase was extracted with EtOAc (3 × 100 mL) and the combined organic layers were washed with HCl (2 M, 100 mL), $NaHCO_3$ (saturated, 100 mL) and brine (100 mL). After drying the organic layer over anhydrous $MgSO_4$, the solvent was removed under reduced pressure to yield 2-azidoethyl-methylsulfonate (**3**) (32.4 g, 0.170 mol, 84%) as a slightly yellow liquid, that was used without further purification.**^{1}H NMR (400.1 MHz, $CDCl_3$)**: δ (ppm) = 4.34 (t, 2H), 3.59 (t, 2H), 3.08 (s, 3H). **^{13}C NMR**

(100.6 MHz, $CDCl_3$): δ (ppm) = 67.6, 50.0, 37.9. **IR (rel. int.)**: $\tilde{\nu}$ (cm^{-1}) = 3031 (vw), 2941 (vw), 2109 (vs), 2099 (s), 1442 (w), 1347 (s), 1301 (m), 1226 (w), 1169 (vs), 1016 (m), 967 (s), 911 (vs), 845 (w), 798 (s), 749 (w), 732 (m), 638 (w), 554 (w), 524 (vs), 492 (m), 441 (s), 420 (w). **Elem. Anal. Calcd**. for $C_3H_7N_3O_3S$: C, 21.82; N, 25.44; H, 4.27; S, 19.41. Found: C, 21.69; N, 25.26; H, 4.18, S, 19.73. **HR-MS** (ESI+) m/z: [$C_3H_7N_3O_3S$] calc.: 166.0286 $[M+H]^+$; found: 165.9928.

1-Azido-2-chloroethane (4)

1-Bromo-2-chloroethane (40.0 g, 0.279 mol, 1.0 eq) was dissolved in DMF (100 mL) and sodium azide (18.1 g, 0.279 mol, 1.0 eq) was added in portions over two hours. The solution was stirred for 16 h at ambient temperature. Water (500 mL) was added and the reaction mixture was extracted with Et_2O (3 × 300 mL) and washed with LiCl solution (1 × 100 mL) and brine (1 × 100 mL). The combined organic phases were dried over anhydrous $MgSO_4$ and the solvent was removed under reduced pressure to yield 1-azido-2-chloroethane (**4**) (27.43 g, 260.0 mmol, 93%) as yellow liquid that was used without further purification. **^{1}H NMR (400.1 MHz, DMSO-*d*$_6$)**: δ (ppm) = 3.58 (m, 2H), 3.41 (m, 2H). **^{13}C NMR (100.6 MHz, DMSO-*d*$_6$)**: δ (ppm) = 52.6, 42.7. **IR (rel. int.)**: $\tilde{\nu}$ (cm^{-1}) = 2929 (w), 2168 (w), 2102 (vs), 2045 (w), 1672 (vs), 1594 (w), 1571 (w), 1503 (w), 1441 (m), 1407 (w), 1387 (m), 1345 (m), 1313 (s), 1285 (s), 1260 (s), 1186 (w), 1091 (m), 1063 (w), 1022 (w), 994 (w), 972 (w), 918 (w), 828 (w), 758 (w), 749 (w), 660 (s), 637 (m), 553 (m), 481 (w), 450 (s).

General Procedure for the Azidoethyl Transfer:

The azole (2 g, 1.0 eq) was dissolved in DMF (10 mL) and potassium carbonate (1.5 eq) and the azidoethyl transfer reagent (1.0 eq) were added under stirring and the mixture was heated to 90 °C for 16 h. After cooling down to room temperature, water (100 mL) was added and the aqueous phase was extracted with EtOAc (3 × 100 mL). The combined organic layers were washed with LiCl (aq. 10%, 3 × 50 ml) and brine (50 ml), dried over anhydrous $MgSO_4$ and the solvent was removed under reduced pressure. The crude product was subjected to flash column chromatography (*i*-hexane:ethyl acetate). The azidoethyl azoles **3**–**8** were obtained as liquids.

1-(2-Azidoethyl)-pyrazole (**5**) was purified by column chromatography (*i*-hexane:ethyl acetate 30:70, R_f = 0.62) to yield a yellowish liquid (76%). **^{1}H NMR (400.2 MHz, $CDCl_3$)**: δ (ppm) = 7.56 (s, 1H), 7. 45 (s, 1H), 6.29 (t, 1H), 4.27 (t, 2H), 3.71 (t, 2H). **^{13}C NMR (100.6 MHz, $CDCl_3$)**: δ (ppm) = 140.4, 130.2, 106.1, 51.3, 51.2. **IR (rel. int.)**: $\tilde{\nu}$ (cm^{-1}) = 2930 (w), 2858 (w), 2098 (vs), 1727 (w), 1515 (m), 1441 (m), 1397 (m), 1352 (m), 1283 (s), 1215 (m), 1172 (w), 1091 (m), 1066 (w), 1042 (m), 966 (m). **Elem. Anal. Calcd**. for $C_5H_7N_5$: C, 43.79; N, 51.07; H, 5.14. Found: C, 43.43; N, 49.08; H, 5.22, **HR-MS** (ESI+) m/z: [$C_5H_8N_5$] calc.: 138.0780 $[M+H]^+$; found: 138.0773.

1-(2-Azidoethyl)-imidazole (**6**) was purified by column chromatography (methanol:ethyl acetate 5:95, R_f = 0.11) to yield a yellowish liquid (36%). **^{1}H NMR (400.2 MHz, $CDCl_3$)**: δ (ppm) = 7.56 (dd, 1H), 7.09 (dd, 1H), 6.97 (dd, 1H), 4.09 (t, 2H), 3.62 (t, 2H). **^{13}C NMR (100.6 MHz, $CDCl_3$)**: δ (ppm) = 137.4, 130.0, 119.1, 51.9, 46.3. **IR (rel. int.)**: $\tilde{\nu}$ (cm^{-1}) = 2984 (w), 2936 (w), 2102 (m), 1733 (s), 1510 (w), 1445 (m), 1373 (m), 1239 (vs), 1190 (m), 1178 (m), 1120 (w), 1108 (m), 1095 (m), 1084 (m), 1044 (s), 1011 (m). **Elem. Anal. Calcd.** for $C_5H_7N_5$: C, 43.79; N, 48.05; H, 5.14. Found: C, 43.89; N, 48.05; H, 5.22, **HR-MS** (ESI+) m/z: [$C_5H_8N_5$] calc.: 138.0780 $[M+H]^+$; found: 138.0775.

1-(2-Azidoethyl)-1,2,3-triazole (**7**) was purified by column chromatography (*i*-hexane:ethyl acetate 30:70, R_f = 0.30) to yield a yellowish liquid (68%). **^{1}H NMR (400.2 MHz, $CDCl_3$)**: δ (ppm) = 7.66 (s, 1H), 7.65 (s, 1H), 4.53 (t, 2H), 3.82 (t, 2H). **^{13}C NMR (100.6 MHz, $CDCl_3$)**: δ (ppm) = 133.9, 124.4, 50.7, 49.1. **IR (rel. int.)**: $\tilde{\nu}$ (cm^{-1}) = 3146 (w), 3127 (w), 2959 (vw), 2941 (vw), 2098 (vs), 1438 (w), 1352 (m), 1283 (s), 1217 (s), 1076 (m), 1032 (m), 788 (s). **Elem. Anal. Calcd.** for $C_4H_6N_6$: C, 34.78; N, 60.84; H, 4.38. Found: C, 35.12; N, 59.87; H, 4.29, **HR-MS** (ESI+) m/z: [$C_4H_7N_6$] calc.: 139.0732 $[M+H]^+$; found: 139.0726.

1-(2-Azidoethyl)-1,2,4-triazole (**8**) was purified by column chromatography (*i*-hexane:ethyl acetate 10:90, R_f = 0.33) to yield a yellowish liquid (69%). **^{1}H NMR (400.2 MHz, $CDCl_3$)**: δ (ppm) = 8.11 (s, 1H), 7.94 (s, 1H), 4.26 (t, 2H), 3.72 (t, 2H). **^{13}C NMR (100.6 MHz, $CDCl_3$)**: δ (ppm) = 152.4, 144.0, 50.1, 48.9. **IR (rel. int.)**: $\tilde{\nu}$ (cm^{-1}) = 3121 (w), 2946 (w), 2098 (vs), 1508 (s), 1439 (m), 1351 (m), 1274 (vs), 1208 (m), 1179 (w), 1138 (s), 1067 (w), 1010 (m), 958 (m). **Elem. Anal. Calcd.** for $C_4H_6N_6$: C, 34.78; N, 60.84;

H, 4.38. Found: C, 34.74; N, 58.98; H, 4.14, **HR-MS** (ESI+) m/z: [$C_4H_7N_6$] calc.: 139.0732 $[M+H]^+$; found: 139.0725.

1-(2-Azidoethyl)-tetrazole (**9**) was purified by column chromatography (*i*-hexane:ethyl acetate 40:60, R_f = 0.46) to yield a yellowish liquid (39%). **^{1}H NMR (400.1 MHz, CDCl$_3$)**: δ (ppm) = 8.74 (s, 1H), 4.59 (t, 2H), 3.88 (t, 2H). **^{13}C NMR (100 MHz, CDCl$_3$)**: δ (ppm) = 143.3, 50.1, 47.6. **IR (rel. int.)**: $\tilde{\nu}$ (cm^{-1}) = 3262 (m), 3145 (m), 3137 (m), 2956 (m), 2924 (m), 2853 (m), 2102 (vs), 1741 (w), 1484 (m), 1439 (m), 1352 (m), 1287 (s), 1258 (m), 1227 (m), 1171 (s), 1103 (vs), 965 (m), 874 (w), 677 (m), 657 (m), 554 (m), 486 (m). **Elem. Anal. Calcd**. for $C_3H_5N_7$: C, 25.90; N, 70.48; H, 3.62. Found: C, 26.13; N, 69.40; H, 4.01. **HR-MS** (ESI+) m/z: [$C_3H_5N_7$] calc.: 140.0685 $[M+H]^+$; found: not found.

2-(2-Azidoethyl)-tetrazole (**10**) was purified by column chromatography (*i*-hexane:ethyl acetate 40:60, R_f = 0.70) to yield a yellowish liquid (20%). **^{1}H NMR (400.1 MHz, CDCl$_3$)**: δ (ppm) = 8.56 (s, 1H), 4.81 (t, 2H), 3.93 (t, 2H). **^{13}C NMR (100 MHz, CDCl$_3$)**: δ (ppm) = 153.4, 52.1, 49.6. **IR (rel. int.)**: $\tilde{\nu}$ (cm^{-1}) = 3145 (m), 2100 (vs), 1443 (m), 1367 (m), 1350 (m), 1282 (s), 1234 (m), 1189 (m), 1152 (m), 1132 (m), 1027 (s), 1008 (m), 884 (w), 710 (m), 697 (m), 666 (m), 552 (m), 489 (m). **Elem. Anal. Calcd.** for $C_3H_5N_7$: C, 25.90; N, 70.48; H, 3.62. Found: C, 26.03; N, 69.10; H, 3.97. **HR-MS** (ESI+) m/z: [$C_3H_6N_7$] calc.: 140.0685 $[M+H]^+$; found: 140.0680.

7.5 Acknowledgement

For financial support of this work the Ludwig Maximilian University (LMU), EMTO GmbH, the Office of Naval Research (ONR) under grant no. ONR N00014-19-1-2078 and the Strategic Environmental Research and Development Program (SERDP) under contract no. W912HQ19 C0033 are gratefully acknowledged. For graphical and computational assistance, we would like to thank Dr. Jasmin Lechner and Dr. Christian Riedelsheimer. The synthetic work of Lennart Kirchhoff, Aleyna Memet Oglou and Victoria Hauptmann is gratefully acknowledged.

7.6 Notes

Parts of this work were published on the NTREM 2023 conference. [53,54]

7.7 References

[1] P. Griess, *J. Chem. Soc.* **1867**, *20*, 36–102.

[2] T. Curtius, *Ber. Dtsch. Chem. Ges.* **1890**, *23*, 3023–3033.

[3] A. G. Habeeb, P. N. Praveen Rao, E. E. Knaus, *J. Med. Chem.* **2001**, *44*, 3039–3042.

[4] S. Bräse, C. Gil, K. Knepper, V. Zimmermann, *Angew. Chem. Int. Ed.* **2005**, *44*, 5188–5240.

[5] K. A. H. Chehade, K. Kiegiel, R. J. Isaacs, J. S. Pickett, K. E. Bowers, C. A. Fierke, D. A. Andres, H. P. Spielmann, *J. Am. Chem. Soc.* **2002**, *124*, 8206–8219.

[6] F. Mésange, M. Sebbar, J. Capdevielle, J.-C. Guillemot, P. Ferrara, F. Bayard, M. Poirot, J.-C. Faye, *Bioconjugate Chem.* **2002**, *13*, 766–772.

[7] M. H. V. Huynh, M. A. Hiskey, J. G. Archuleta, E. L. Roemer, *Angew. Chem. Int. Ed.* **2005**, *44*, 737–739.

[8] C. Doebelin, M. Schmitt, C. Antheaume, J.-J. Bourguignon, F. Bihel, *J. Org. Chem* **2013**, *78*, 11335–11341.

[9] P. P. Goswami, V. P. Suding, A. S. Carlson, J. J. Topczewski, *Eur. J. Org. Chem.* **2016**, *2016*, 4805–4809.

[10] T. Keicher, S. Löbbecke, in *Organic Azides*, **2009**, pp. 1–27.

[11] F. Himo, T. Lovell, R. Hilgraf, V. V. Rostovtsev, L. Noodleman, K. B. Sharpless, V. V. Fokin, *J. Am. Chem. Soc.* **2005**, *127*, 210–216.

[12] P. Desai, K. Schildknegt, K. A. Agrios, C. Mossman, G. L. Milligan, J. Aubé, *J. Am. Chem. Soc.* **2000**, *122*, 7226–7232.

[13] S. S. van Berkel, M. B. van Eldijk, J. C. M. van Hest, *Angew. Chem. Int. Ed.* **2011**, *50*, 8806–8827.

[14] R. Zhang, S. Liu, K. J. Edgar, *Carbohydr. Polym.* **2017**, *171*, 1–8.

[15] S. Rozen, M. Carmeli, *J. Am. Chem. Soc.* **2003**, *125*, 8118–8119.

[16] X.-J. Li, J.-B. Qiao, J. Sun, X.-Q. Li, P. Gu, *Org. Lett.* **2014**, *16*, 2865–2867.

[17] H. Ishikawa, B. P. Bondzic, Y. Hayashi, *Eur. J. Org. Chem.* **2011**, *2011*, 6020–6031.

[18] V. V. Rostovtsev, L. G. Green, V. V. Fokin, K. B. Sharpless, *Angew. Chem. Int. Ed.* **2002**, *41*, 2596–2599.

[19] H. C. Kolb, M. G. Finn, K. B. Sharpless, *Angew. Chem. Int. Ed.* **2001**, *40*, 2004–2021.

[20] E. A. Betterton, *Crit. Rev. Environ. Sci. Technol.* **2003**, *33*, 423–458.

[21] M. B. Frankel, L. R. Grant, J. E. Flanagan, *J. Propuls. Power* **1992**, *8*, 560–563.

[22] J. P. Agrawal, Hodgson, Robert, *Organic Chemistry of Explosives*, J. Wiley & Sons, Chichester, **2008**.

[23] T. M. Klapötke, *Chemistry of High-Energy Materials*, 6th. ed., De Gruyter, Berlin/Boston, **2022**.

[24] Y. Tang, J. M. Shreeve, *Chem. Eur. J.* **2015**, *21*, 7285–7291.

[25] M. Kofen, M. Lommel, M. H. H. Wurzenberger, T. M. Klapötke, J. Stierstorfer, *Chem.: Asian J.* **2022**, *28*, e202200492.

[26] T. Lenz, T. M. Klapötke, M. Mühlemann, J. Stierstorfer, *Propellants Explos. Pyrotech.* **2021**, *46*, 723–731.

[27] L. Bauer, M. Benz, T. M. Klapötke, T. Lenz, J. Stierstorfer, *J. Org. Chem* **2021**, *86*, 6371–6380.

[28] M. H. H. Wurzenberger, M. S. Gruhne, M. Lommel, N. Szimhardt, T. M. Klapötke, J. Stierstorfer, *Chem.: Asian J.* **2019**, *14*, 2018–2028.

[29] M. Kofen, M. Lommel, M. H. H. Wurzenberger, T. M. Klapötke, J. Stierstorfer, *Chem. Eur. J.* **2022**, *28*, e202200492.

[30] J. Haase, in *Organic Azides*, **2009**, pp. 29–51.

[31] H. Xue, B. Twamley, J. M. Shreeve, *J. Mater. Chem.* **2005**, *15*, 3459–3465.

[32] S. P. Desai, M. T. Zambri, M. S. Taylor, *J. Org. Chem* **2022**, *87*, 5385–5394.

[33] S. Cao, Y. Liu, C. Hu, C. Wen, J.-P. Wan, *ChemCatChem* **2018**, *10*, 5007–5011.

[34] E. Reinhardt, T. Lenz, L. Bauer, J. Stierstorfer, T. M. Klapötke, *Molecules* **2023**, *28*, 6489.

[35] K. A. McDonald, S. Seth, A. J. Matzger, *Cryst. Growth Des.* **2015**, *15*, 5963–5972.

[36] Q. Zhang, J. M. Shreeve, *Angew. Chem. Int. Ed.* **2014**, *53*, 2540–2542.

[37] K. Pawlus, T. Jarosz, A. Stolarczyk, in *Applied Sciences, Vol. 12*, **2022**.

[38] Y.-F. Yan, J.-G. Xu, F. Wen, Y. Zhang, H.-Y. Bian, B.-Y. Li, N.-N. Zhang, F.-K. Zheng, G.-C. Guo, *Inorg. Chem. Front.* **2022**, *9*, 5884–5892.

[39] Q. Zhou, W. Wu, K. Jia, G. Qi, X. S. Sun, P. Li, *Eur. J. Med. Chem.* **2022**, *244*, 114830.

[40] H. Choi, H. J. Shirley, P. A. Hume, M. A. Brimble, D. P. Furkert, *Angew. Chem. Int. Ed.* **2017**, *56*, 7420–7424.

[41] C. J. Taylor, A. Pomberger, K. C. Felton, R. Grainger, M. Barecka, T. W. Chamberlain, R. A. Bourne, C. N. Johnson, A. A. Lapkin, *Chem. Rev.* **2023**, *123*, 3089–3126.

[42] M. H. H. Wurzenberger, M. S. Gruhne, M. Lommel, N. Szimhardt, T. M. Klapötke, J. Stierstorfer, *Chem. Asian J.* **2019**, *14*, 2018–2028.

[43] DIRECTIVE 2011/65/EU OF THE EUROPEAN PARLIAMENT AND OF THE COUNCIL of 8 June 2011 on the restriction of the use of certain hazardous substances in electrical and electronic equipment, European Union, **2011**.

[44] COMMISSION DELEGATED DIRECTIVE (EU) 2021/647 of 15 January 2021 amending, for the purposes of adapting to scientific and technical progress, Annex III to Directive 2011/65/EU of the European Parliament and of the Council as regards an exemption for the use of certain lead and hexavalent chromium compounds in electric and electronic initiators of explosives for civil (professional) use, European Union, **2021**.

[45] M. H. H. Wurzenberger, M. S. Gruhne, M. Lommel, N. Szimhardt, J. Stierstorfer, *Mater. Adv.* **2022**, *3*, 579–591.

[46] E. Lieber, C. N. R. Rao, T. S. Chao, C. W. W. Hoffman, *Anal. Chem.* **1957**, *29*, 916–918.

[47] M. A. M. Rashid, S. G. Cho, C. H. Choi, *Comput. Theor. Chem.* **2018**, *1130*, 148–159.

[48] T. M. Klapötke, J. Stierstorfer, in *Green Energetic Materials*, **2014**, pp. 133–178.

[49] Impact: insensitive > 40 J, less sensitive ≥ 35 J, sensitive ≥ 4 J, very sensitive ≤ 3 J; Friction: insensitive > 360 N, less sensitive = 360 N, sensitive < 360 N and > 80 N, very sensitive ≤ 80 N, extremely sensitive ≤ 10 N, According to: Recommendations on the Transport of Dangerous Goods, Manual of Tests and Criteria, 4$^{th.}$ Edition, New York-Geneva, **1999**.

[50] J. Bauer, M. Benz, T. M. Klapötke, J. Stierstorfer, *Dalton Trans.* **2022**, *51*, 11806–11813.

[51] *EXPLO5 V7.01.01*, M. Sućeska, Zagreb, Croatia, **2023**.

[52] S. M. J. Endraß, A. Neuer, T. M. Klapötke, J. Stierstorfer, *ChemistrySelect* **2022**, *7*, e202203140.

[53] L. Bauer, L. Kirchhoff, T. M. Klapötke, J. Stierstorfer, *New Trends in Research of Energetic Materials* Pardubice, Czech Republic, 19–21 April, **2023**, 263–270.

[54] L. Bauer, S. M. J. Endraß, T. M. Klapötke, J. Stierstorfer, *New Trends in Research of Energetic Materials* Pardubice, Czech Republic, 19–21 April, **2023**, 256–262.

7.8 Supporting Information

7.8.1 Experimental Information

General Methods

All chemicals and solvents were employed as received (Sigma-Aldrich, Fluka, Acros, ABCR). ^{1}H, ^{13}C [S1] spectra were recorded at ambient temperature using a Bruker 400, JEOL Eclipse 400. The chemical shifts quoted in ppm in the text refer to typical standards such as tetramethylsilane (^{1}H, ^{13}C) nitromethane (^{14}N,^{15}N). Endothermic and exothermic events of the described compounds, which indicate melting, loss of crystal water or decomposition, are given as the extrapolated onset temperatures. The samples were measured in a range of 25–400 °C at a heating rate of 5 °C min^{-1} through differential thermal analysis (DTA) with an OZM Research DTA 552-Ex instrument. Infrared spectra were measured with pure samples on a Perkin-Elmer BXII FT-IR system with a Smith DuraSampler IR II diamond ATR. Determination of the carbon, hydrogen, and nitrogen contents was carried out by combustion analysis using an Elementar Vario El and Elementar Vario Micro (nitrogen values determined are often lower than the calculated ones' due to their explosive behavior). Impact sensitivity tests were carried out according to STANAG 4489 [S2] with a modified instruction [S3] using a BAM (Bundesanstalt für Materialforschung) drophammer. [S4] Friction sensitivity tests were carried out according to STANAG 4487 [S5] with a modified instruction [S6] using the BAM friction tester. [S4, S7] The classification of the tested compounds results from the "UN Recommendations on the Transport of Dangerous Goods". [S8, S9] Additionally, all ECCs were tested upon the sensitivity toward electrical discharge using the OZM Electric Spark XSpark10 device. [S7] Hot plate and hot needle tests were performed in order to classify the initiation capability of selected complexes. The samples were fixed on a copper plate underneath adhesive tape and initiated by a red-hot needle. Strong deflagration or detonation of the compound usually indicates a valuable primary explosive. The safe and straightforward hot plate test only shows the behavior of the unconfined sample toward fast heating on a copper plate. It does not necessarily allow any conclusions on a compound´s capability as a suitable primary explosive. Initiation capability tests of the newly investigated complexes toward pentaerythritol tetranitrate (PETN) were carried out in a cooper shell with a diameter of 7 mm and a length of 88 mm filled with 200 mg of sieved PETN (grain size < 100 µm).

First, PETN was pressed with a weight of 8 kg, then the primary explosive to be investigated was subsequently filled on top of the main charge. The shell was sealed by an insulator, placed in a retaining ring, which was soldered to a copper witness plate with a thickness of 1 mm and finally initiated by a type A electric igniter. A positive test is indicated by a hole in the copper plate and fragmentation of the shell caused by a deflagration-to-detonation transition (DDT) of PETN. The laser initiation experiments were performed with a 45 W InGaAs laser diode operating in the single-pulsed mode. The diode is attached to an optical fiber with a core diameter of 400 μm and a cladding diameter of 480 μm. The optical fiber is connected via a SMA type connecter directly to the laser and to a collimator. This collimator is coupled to an optical lens, which was positioned in its focal distance (f = 29.9 mm) to the sample. The lens is shielded from the explosive by a sapphire glass. Approximately 25 mg of the carefully pestled compound to be investigated was filled into a transparent polycarbonate cap, pressed with a pressure force of 1.5 kN and sealed by a UV-curing adhesive. The confined samples were irradiated at a wavelength of 915 nm, a voltage of 4 V, a current of 7–10 A and pulse lengths of 0.1–30 ms. Energetic properties have been calculated with the EXPLO5 7.01.01 computer code [S10] using the, to RT converted, X-ray density and calculated solid state heats of formation. These were computed by the atomization method as described in recently published papers. Electronic enthalpies were calculated with the Gaussian09 software [S11] suite using the CBS-4M method.

CAUTION! *All investigated compounds are energetic materials (some of the compounds are primary explosives!), which show partly increased sensitivities toward various stimuli (e.g. elevated temperatures, impact, friction or electrostatic discharge). Therefore, proper security precautions (safety glasses, face shield, earthed equipment and shoes, leather jacket, Kevlar gloves, Kevlar sleeves and ear plugs) have to be worn while synthesizing and handling the described compounds.*

General Procedure A for the formation of perchlorate and nitrate containing ECCs:
A solution of one equivalent of the respective perchlorate or nitrate ($Cu(ClO_4)_2 \cdot 6\ H_2O$: 0.25 mmol, 92.6 mg; $Fe(ClO_4)_2 \cdot 6\ H_2O$: 0.25 mmol, 90.7 mg; $Cu(NO_3)_2 \cdot 3\ H_2O$: 0.25 mmol, 60.4 mg; $Ag(ClO_4) \cdot H_2O$: 1.0 mmol, 225.3 mg) in 5 mL of EtOH was stirred at 60 °C or rt in the case of silver perchlorate. A solution of 2-AET or AE124Tri in 1 mL

of EtOH was manually added. The resulting mixture was stirred at reaction temperature for 10 min. and then allowed to crystallize at room temperature. The compounds precipitated during addition or within one day, were filtered off and washed with cold EtOH.

General Procedure B for the formation of ECCs with nitroaromatic anions:

A suspension of $CuCO_3{\times}Cu(OH)_2$ (55.3 mg, 0.25 mmol, 0.5 eq.) and the respective nitroaromatic species (279 mg, 1.00 mmol of H_3TNPG, 123mg, 0.50 mmol of H_2TNR, 229 mg, 1.00 mmol of HPA, 259 mg, 1.00 mmol of H_2TNO) in 5 mL of water was heated to 80 °C until a clear solution was obtained. To this solution, the ligand (2-AET or AE124Tri) was added. The solution was kept at 80 °C for 5 min. and then left at room temperature to crystallize. Single crystalline precipitate was obtained in all cases within two days.

[Ag(μ-2-AET)(ClO_4)] (11)

[Ag(μ-2-AET)(ClO_4)] was obtained as a colorless solid in a yield of 77 % (267 mg, 0.77 mmol).

DTA (5 °C min^{-1}) onset: 151 °C (endothermic to exothermic). **IR** (ATR, cm^{-1}): $\tilde{\nu}$ = 3156 (w), 3019 (w), 2142 (s), 2098 (w), 1464 (w), 1433 (w), 1371 (w), 1343 (w), 1305 (w), 1254 (m), 1241 (w), 1224 (m), 1191 (w), 1168 (w), 1152 (m), 1121 (m), 1095 (s), 1080 (s), 1056 (s), 1039 (vs), 1012 (s), 960 (m), 929 (m), 888 (m), 848 (m), 824 (w), 818 (w), 692 (m), 662 (m), 616 (vs), 580 (w), 559 (w), 549 (m), 535 (w), 520 (w), 484 (s), 469 (w), 457 (w), 449 (w), 436 (w), 426 (w), 419 (m), 411 (w). **EA** ($C_3H_5AgClN_7O_4$, 346.44) calcd.: C 10.40, H 1.45, N 28.30 %; found: C 10.78, H 1.65, N 27.10 %. **BAM drophammer**: <1 J. **Friction tester**: 0.6 N. **ESD**: 13 mJ (at grain size 100–500 µm).

[Cu(2-AET)$_4$(H_2TNPG)$_2$] (12)

[Cu(2-AET)$_4$(H_2TNPG)$_2$] was obtained in a yield of 62 % as a green crystalline solid (353 mg, 0.31 mmol)

DTA (5 °C min^{-1}) onset: 145 °C (exothermic). **IR** (ATR, cm^{-1}): $\tilde{\nu}$ = 3149 (m), 3032 (vw), 2992 (vw), 2231 (vw), 2108 (s), 2098 (s), 2057 (w), 1809 (vw), 1652 (s), 1598 (w), 1558 (s), 1530 (s), 1515 (vs), 1506 (vs), 1471 (m), 1461 (m), 1444 (m), 1424 (w), 1373 (m), 1360 (s), 1344 (s), 1304 (s), 1274 (m), 1207 (s), 1195 (s), 1165 (s), 1158 (s), 1147 (vs), 1137 (s), 1091 (m), 1068 (m), 1051 (m), 1042 (m), 1021 (s), 967 (w), 953 (w), 938 (w), 916 (m), 906

(s), 842 (s), 814 (m), 780 (s), 762 (m), 746 (m), 714 (s), 707 (s), 690 (vs), 676 (s), 667 (s), 642 (s), 627 (s), 550 (m), 500 (m), 487 (m), 468 (m), 450 (w), 439 (w), 424 (w), 414 (w), 404 (m). **EA** ($C_{24}H_{24}CuN_{34}O_{18}$, 1140.22) calcd.: C 25.28, H 2.12, N 41.77 %; found: C 25.69, H 2.29, N 40.46 %. **BAM drophammer**: <1 J. **Friction tester**: 54 N. **ESD**: 200 mJ (at grain size 100–500 µm).

[Cu(2-AET)$_2$(TNR)$_2$] (13)

[Cu(2-AET)$_2$(TNR)$_2$] was obtained in a yield of 66 % as a green solid with intergrown single crystals (193 mg, 0.33 mmol).

DTA (5 °C min^{-1}) onset: 177 °C (exothermic). **IR** (ATR, cm^{-1}): $\tilde{\nu}$ = 3163 (w), 3153 (w), 3119 (w), 3027 (vw), 2138 (m), 2123 (m), 2102 (s), 2004 (w), 1585 (s), 1548 (s), 1526 (s), 1475 (s), 1470 (s), 1440 (s), 1373 (m), 1353 (m), 1332 (m), 1311 (s), 1287 (vs), 1232 (vs), 1220 (s), 1201 (s), 1170 (s), 1142 (s), 1103 (s), 1066 (m), 1050 (m), 1025 (s), 990 (m), 969 (m), 948 (m), 924 (m), 906 (m), 895 (m), 830 (m), 821 (m), 787 (m), 772 (m), 732 (m), 709 (s), 696 (s), 679 (s), 658 (m), 640 (m), 624 (m), 551 (m), 491 (s), 458 (m), 435 (s), 418 (s), 408 (s). **EA** ($C_{12}H_{11}CuN_{17}O_8$, 584.88) calcd.: C 24.64, H 1.90, N 40.71 %; found: C 24.93, H 1.99, N 40.82 %. **BAM drophammer**: <1 J. **Friction tester**: 30 N. **ESD**: 200 mJ (at grain size 100–500 µm).

[Cu(2-AET)$_2$(PA)$_2$] (14)

[Cu(2-AET)$_2$(PA)$_2$] was obtained as green crystals in a yield of 62 % (249 mg, 0.31 mmol).

DTA (5 °C min^{-1}) onset: 169 °C (exothermic). **IR** (ATR, cm^{-1}): $\tilde{\nu}$ = 3143 (w), 3070 (w), 3032 (w), 2142 (m), 2105 (m), 2102 (m), 2004 (w), 1609 (s), 1575 (s), 1539 (s), 1522 (s), 1510 (s), 1480 (m), 1446 (m), 1416 (m), 1366 (m), 1347 (s), 1327 (vs), 1307 (s), 1279 (s), 1264 (vs), 1235 (s), 1208 (s), 1169 (s), 1149 (s), 1081 (m), 1050 (m), 1033 (m), 1004 (m), 942 (m), 934 (m), 922 (s), 886 (m), 849 (m), 839 (m), 825 (w), 788 (m), 755 (w), 741 (m), 725 (m), 709 (vs), 694 (s), 666 (s), 629 (m), 604 (m), 554 (m), 536 (m), 522 (m), 483 (m), 452 (m), 440 (w), 424 (w), 406 (m). **EA** ($C_{18}H_{14}CuN_{20}O_{14}$, 797.98) calcd.: C 27.09, H 1.77, N 35.11 %; found: C 27.14, H 1.87, N 35.19 %. **BAM drophammer**: 2 J. **Friction tester**: 192 N. **ESD**: 160 mJ (at grain size 100–500 µm).

[Cu(2-AET)$_2$(HTNO)$_2$] (15)

[Cu(2-AET)$_2$(HTNO)$_2$] was obtained as greenish-brown crystals in a yield of 70 % (298 mg, 0.35 mmol,

DTA (5 °C min^{-1}) onset: 141 °C (exothermic). **IR** (ATR, cm^{-1}): $\tilde{\nu}$ = 3162 (w), 3139 (w), 2132 (m), 2100 (m), 2059 (w), 2004 (w), 1615 (m), 1557 (s), 1538 (s), 1532 (vs), 1525 (vs), 1521 (vs), 1488 (s), 1471 (m), 1456 (m), 1441 (m), 1413 (m), 1381 (m), 1361 (s), 1344 (s), 1305 (s), 1283 (s), 1182 (s), 1167 (vs), 1155 (vs), 1143 (vs), 1069 (m), 1061 (m), 1046 (s), 1029 (m), 1003 (m), 955 (m), 913 (m), 907 (m), 882 (m), 828 (m), 811 (m), 789 (s), 767 (w), 742 (m), 712 (m), 691 (vs), 671 (s), 656 (s), 631 (s), 606 (m), 559 (m), 525 (w), 516 (w), 507 (w), 485 (s), 454 (m), 449 (m), 446 (m), 405 (s). **EA** ($C_{20}H_{18}CuN_{20}O_{16}$, 858.03) calcd.: C 28.00, H 2.11, N 32.65 %; found: C 27.91, H 2.17, N 32.50 %. **BAM drophammer**: <1 J. **Friction tester**: 80 N. **ESD**: 160 mJ (at grain size 100–500 µm).

[Cu(AE124Tri)$_4$(ClO$_4$)$_2$] (16)

[Cu(AE124Tri)$_4$(ClO$_4$)$_2$] was obtained as a light purple powder (188 mg, 0.23 mmol, 92 %), which could be recrystallized from methanol to obtain crystals, suitable for single crystal X-Ray diffraction analysis.

DTA (5 °C min^{-1}) onset: 171 °C (exothermic). **IR** (ATR, cm^{-1}): $\tilde{\nu}$ = 3143 (w), 3014 (vw), 2948 (vw), 2140 (w), 2100 (s), 2065 (w), 1532 (m), 1484 (vw), 1447 (w), 1435 (w), 1375 (w), 1355 (w), 1298 (m), 1284 (m), 1271 (m), 1232 (m), 1222 (w), 1186 (w), 1120 (s), 1098 (s), 1060 (vs), 1016 (s), 998 (s), 973 (m), 936 (m), 908 (m), 900 (m), 883 (m), 828 (m), 693 (w), 682 (m), 670 (s), 656 (m), 649 (m), 620 (vs), 560 (w), 553 (w), 487 (m), 461 (w), 458 (w). **EA** ($C_{16}H_{24}Cl_2CuN_{24}O_8$, 814.97) calcd.: C 23.58, H 2.97, N 41.25 %; found: C 23.88, H 3.03, N 39.55 %. **BAM drophammer**: <1 J. **Friction tester**: 108 N. **ESD**: 15 mJ (at grain size <100 µm).

[Cu(AE124Tri)$_4$(NO$_3$)$_2$] (17)

[Cu(AE124Tri)$_4$(NO$_3$)$_2$] was obtained as a light blue powder in a yield of 92 % (171 mg, 0.23 mmol,).

DTA (5 °C min^{-1}) onset: 117, 153 °C (endothermic), 179 °C (exothermic). **IR** (ATR, cm^{-1}): $\tilde{\nu}$ = 3135 (w), 3052 (vw), 3008 (vw), 2951 (vw), 2121 (m), 2095 (s), 2065 (m), 1749 (vw), 1531 (s), 1481 (vw), 1439 (m), 1394 (s), 1371 (m), 1350 (m), 1321 (s), 1299 (s), 1273 (vs), 1231 (s), 1219 (s), 1183 (m), 1127 (vs), 1080 (w), 1067 (w), 1046 (m), 1016 (m), 997

(s), 953 (w), 941 (w), 904 (m), 883 (m), 837 (w), 827 (m), 683 (m), 671 (vs), 654 (m), 648 (s), 639 (m), 559 (w), 508 (w), 487 (m). **EA** ($C_{16}H_{24}CuN_{26}O_6$, 740.09) calcd.: C 25.97, H 3.27, N 49.21 %; found: C 26.22, H 3.27, N 48.86 %. **BAM drophammer**: 35 J. **Friction tester**: >360 N. **ESD**: 42 mJ (at grain size <100).

[Fe(AE124Tri)$_6$](ClO$_4$)$_2$ (18)

[Fe(AE124Tri)$_6$](ClO$_4$)$_2$ was obtained as a beige solid in a yield of 68 % (180 mg, 0.17 mmol).

DTA (5 °C min^{-1}) onset: 128 °C (endothermic to exothermic). **IR** (ATR, cm^{-1}): $\tilde{\nu}$ = 3132 (w), 2935 (vw), 2874 (vw), 2100 (s), 1748 (vw), 1522 (m), 1443 (w), 1372 (w), 1349 (m), 1279 (s), 1213 (m), 1185 (w), 1127 (s), 1079 (vs), 1016 (m), 1010 (m), 989 (m), 967 (w), 876 (m), 833 (w), 759 (vw), 749 (vw), 683 (m), 669 (s), 652 (s), 621 (s), 556 (w), 495 (m). **EA** ($C_{24}H_{36}Cl_2FeN_{36}O_8$, 1083.54) calcd.: C 26.60, H 3.35, N 46.54 %; found: C 26.54, H 3.37, N 46.19 %. **BAM drophammer**: 7.5 J. **Friction tester**: 120 N. **ESD**: 160 mJ (at grain size 100–500 µm).

[Cu$_2$(2-AET)(N$_3$)$_4$] (19)

[Cu$_2$(2-AET)(N$_3$)$_4$] was obtained by first dissolving Cu(NO$_3$)$_2$ · 3 H$_2$O (242 mg, 1.00 mmol, 1.0 eq.) in water (10 mL). 2-AET (139 mg, 1.00 mmol, 1.0 eq.) was added together with 0.5 mL of EtOH to improve the solubility. Under stirring, a solution of NaN$_3$ (130 mg, 2.00 mmol, 2.0 eq.) in 10 mL of water was added dropwise at a speed at which the immediately formed precipitate dissolves again. After complete addition, the resulting suspension was stirred for 10 min. at room temperature. The precipitate was then filtered off, washed with water, EtOH and Et$_2$O, followed by drying on air. The compound was obtained as a dark-brown powder in a yield of 76 % (165 mg, 0.38 mmol) relative to copper(II).

DTA (5 °C min^{-1}) onset: 143 °C (exothermic). **IR** (ATR, cm^{-1}): $\tilde{\nu}$ = 2098 (vs), 2055 (s), 1468 (w), 1444 (w), 1387 (w), 1370 (w), 1348 (m), 1308 (w), 1279 (s), 1254 (m), 1201 (w), 1168 (w), 1139 (m), 1052 (w), 1021 (w), 970 (w), 883 (w), 860 (vw), 834 (w), 691 (m), 670 (m), 650 (w), 626 (w), 591 (w), 579 (m), 552 (w), 498 (m), 409 (m). **EA** ($C_3H_5Cu_2N_{19}$, 434.30) calcd.: C 8.30, H 1.16, N 61.28 %; found: C 8.20, H 1.27, N 60.05 %. **BAM drophammer**: <1 J. **Friction tester**: <0.1 N. **ESD**: 2.5 mJ (at grain size <100).

$[Cu_3(AE124Tri)_2(N_3)_6]$ (20)

$[Cu_3(AE124Tri)_2(N_3)_6]$ was obtained by first dissolving $Cu(NO_3)_2 \cdot 3\ H_2O$ (242 mg, 1.00 mmol, 1.0 eq.) in water (10 mL). AE124Tri (138 mg, 1.00 mmol, 1.0 eq.) was added to the solution. Under stirring, a solution of NaN_3 (130 mg, 2.00 mmol, 2.0 eq.) in 10 mL of water was added dropwise at a speed at which the immediately formed precipitate dissolves again. After complete addition, the resulting suspension was stirred for 10 min. at room temperature. The precipitate was then filtered off, washed with water, EtOH and Et_2O, followed by drying on air. The compound was obtained as a dark-brown powder in a yield of 77 % (183 mg, 0.25 mmol) relative to copper(II).

DTA (5 °C min^{-1}) onset: 112 °C (exothermic). **IR** (ATR, cm^{-1}): $\tilde{\nu}$ = 3116 (w), 2140 (w), 2096 (s), 2080 (vs), 2051 (s), 2034 (m), 2007 (w), 1962 (w), 1537 (w), 1445 (w), 1427 (w), 1380 (vw), 1366 (vw), 1348 (w), 1292 (m), 1284 (m), 1266 (w), 1227 (w), 1214 (w), 1180 (vw), 1127 (m), 1072 (vw), 1019 (w), 1004 (w), 992 (vw), 939 (w), 893 (w), 877 (vw), 838 (vw), 678 (w), 665 (m), 650 (m), 627 (w), 594 (w), 575 (w), 552 (vw), 478 (w), 416 (w). **EA** ($C_8H_{12}Cu_3N_{30}$, 719.03) calcd.: C 13.36, H 1.68, N 58.44 %; found: C 13.01, H 1.65, N 58.44 %. **BAM drophammer**: <1 J. **Friction tester**: 0.2 N. **ESD**: 2.5 mJ (at grain size <100).

7.8.2 NMR Spectroscopy

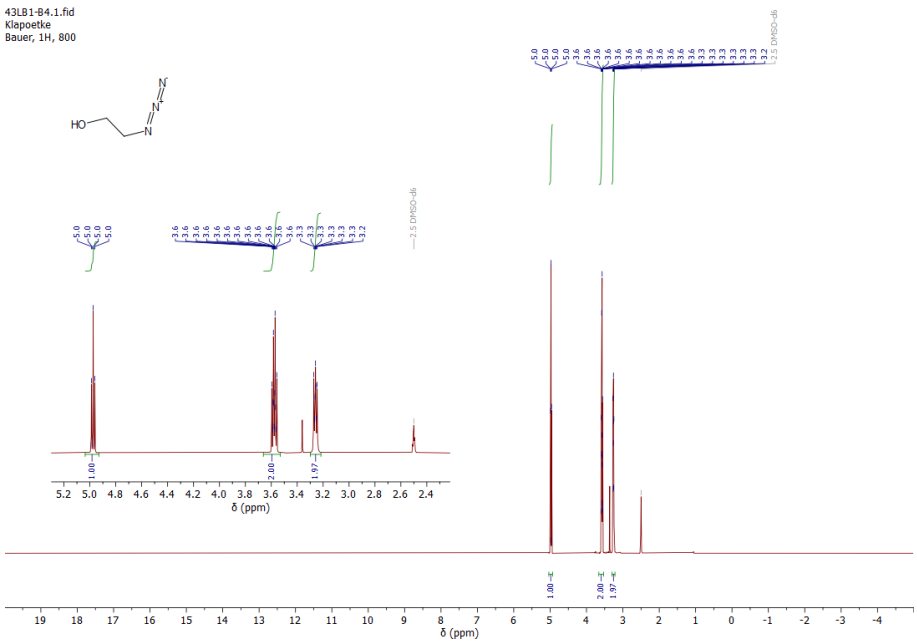

Figure S1. ^1H NMR spectrum of 2-azidoethan-1-ol (**1**).

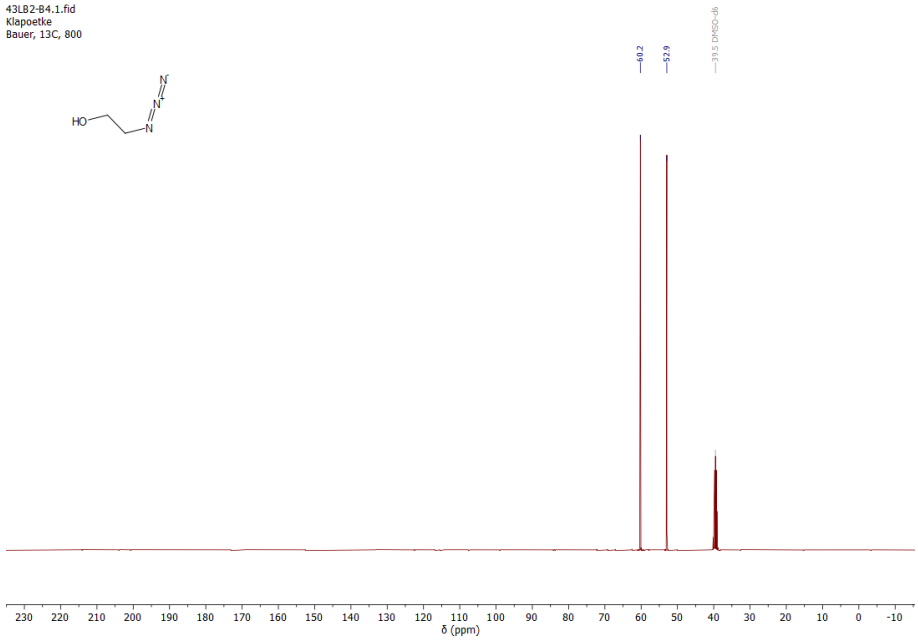

Figure S2. ^{13}C NMR spectrum of 2-azidoethan-1-ol (**1**).

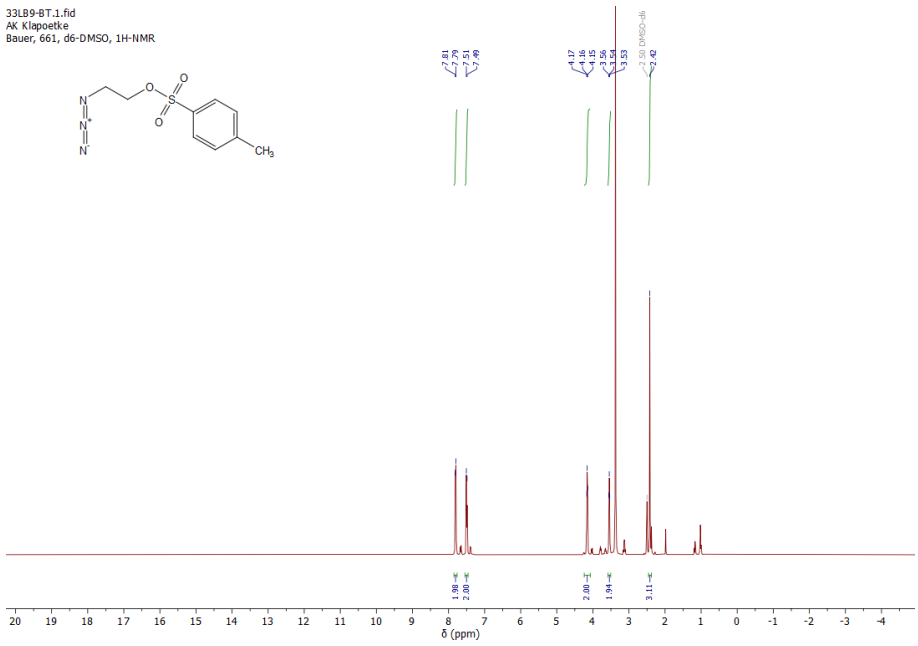

Figure S3. ^{1}H NMR spectrum of 2-azidoethyl-4-methylbenzenesulfonate (**2**).

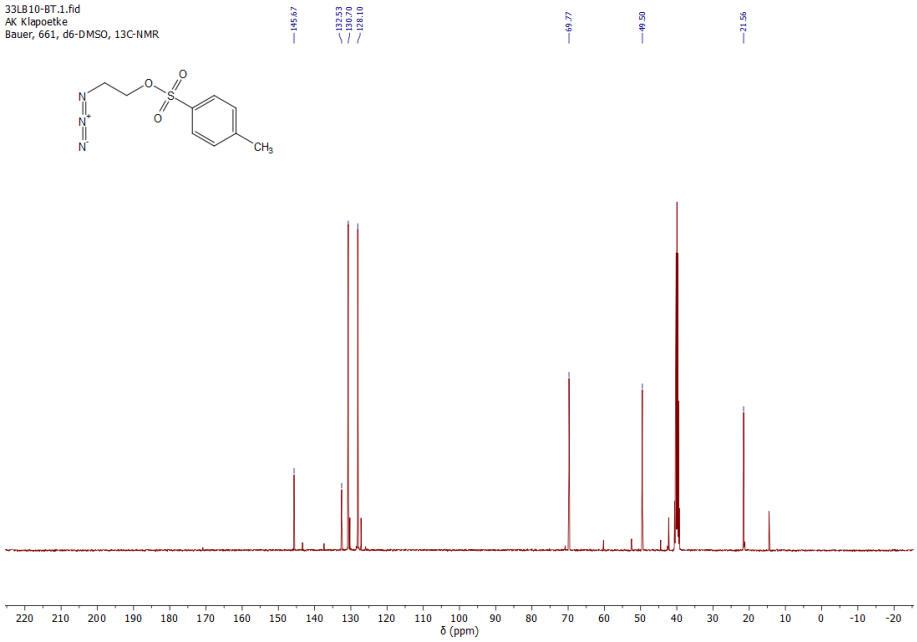

Figure S4. ^{13}C NMR spectrum of 2-azidoethyl-4-methylbenzenesulfonate (**2**).

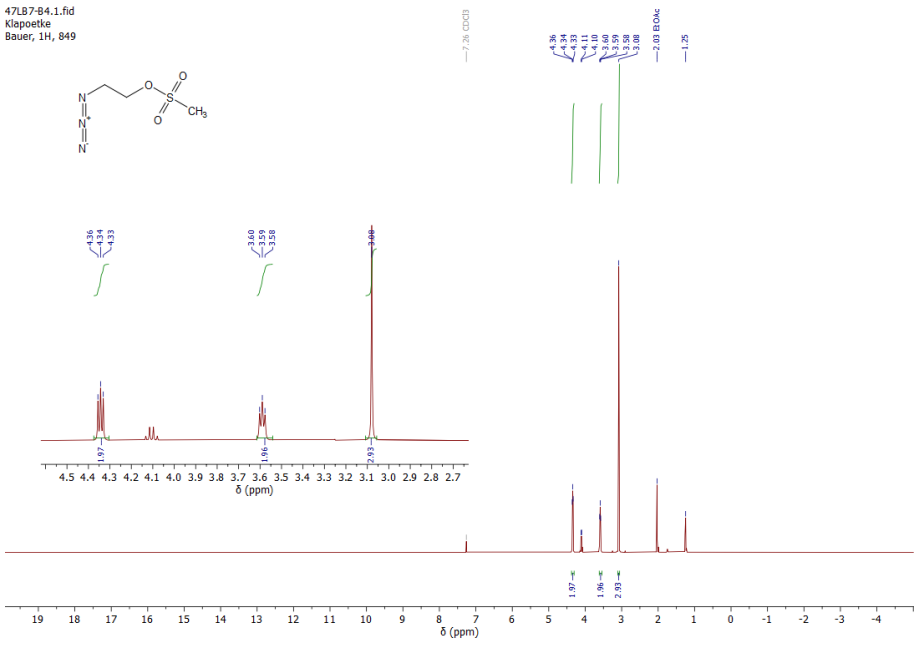

Figure S5. ^{1}H NMR spectrum of 2-azidoethyl-methylsulfonate (**3**).

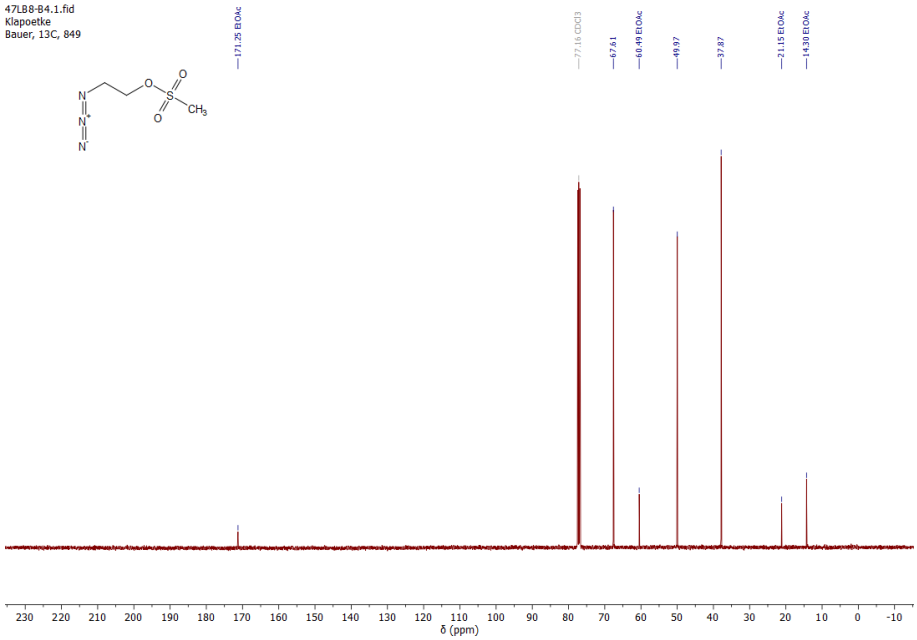

Figure S6. ^{13}C NMR spectrum of 2-azidoethyl-methylsulfonate (**3**).

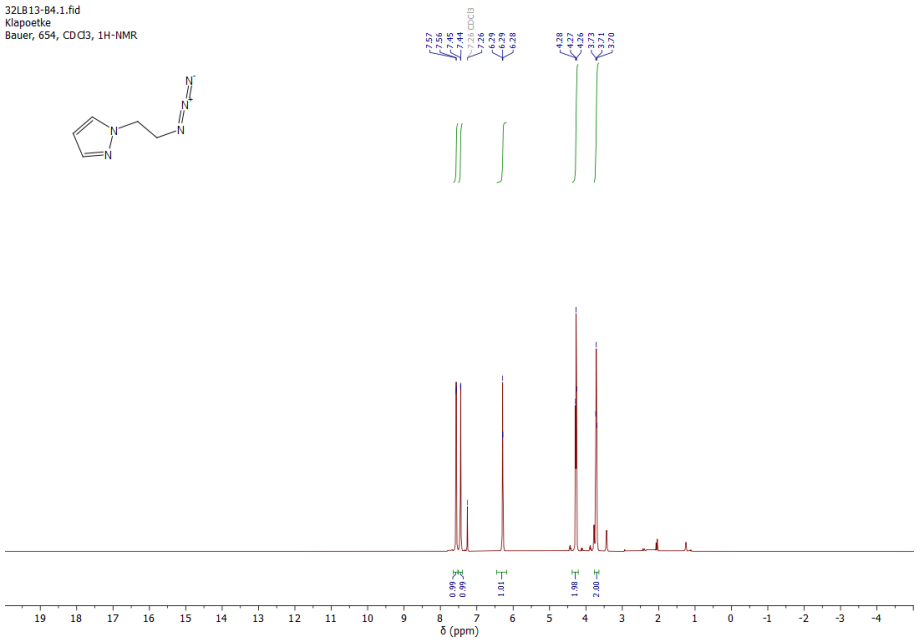

Figure S7. ^{1}H NMR spectrum of 1-(2-azidoethyl)-pyrazole (**5**).

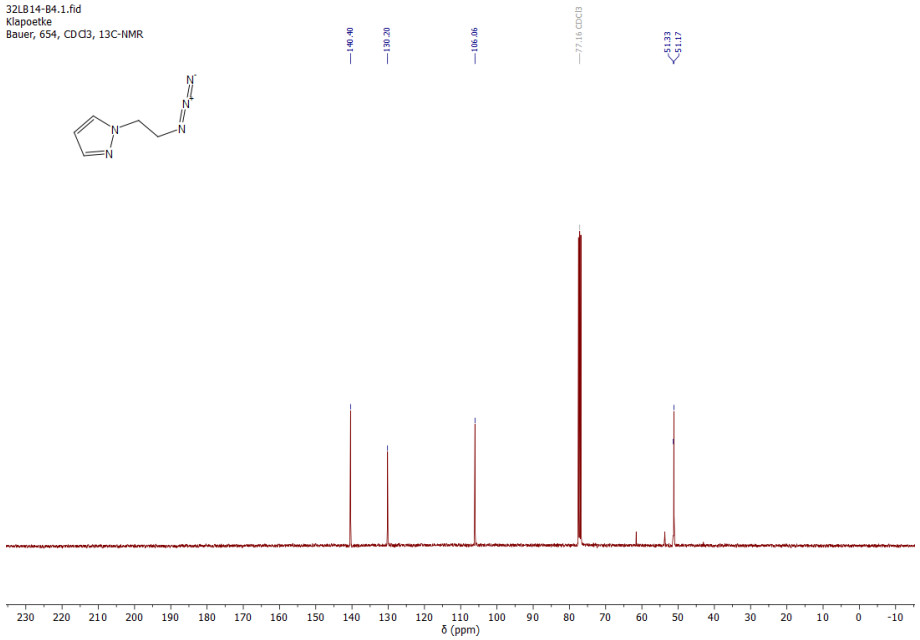

Figure S8. ^{13}C NMR spectrum of 1-(2-azidoethyl)-pyrazole (**5**).

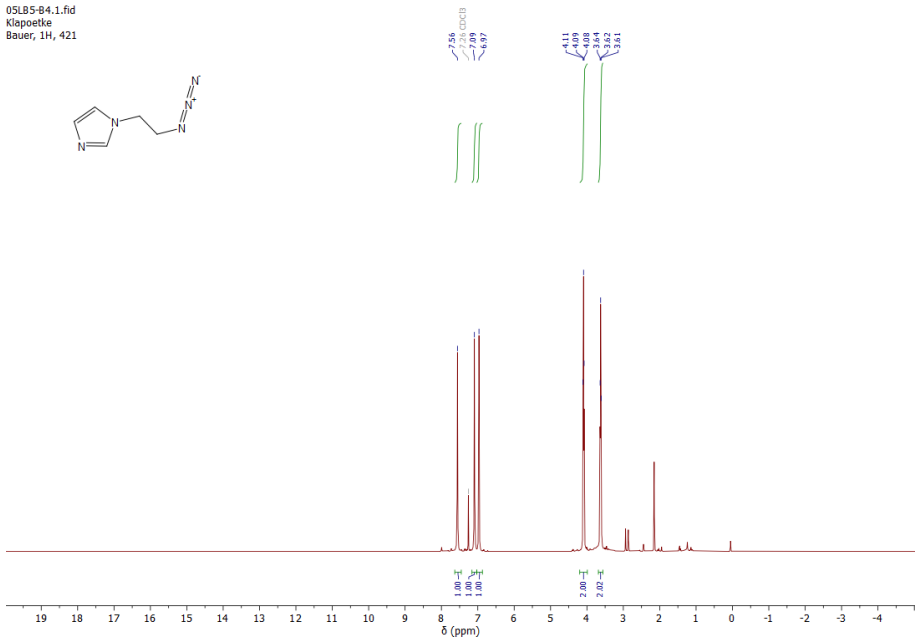

Figure S9. ^{1}H NMR spectrum of 1-(2-azidoethyl)-imidazole (**6**).

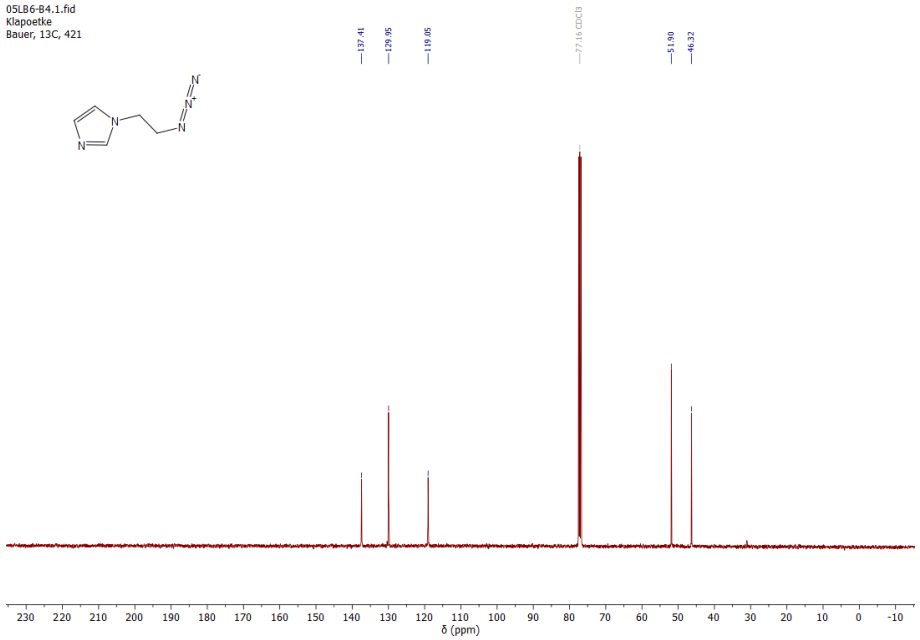

Figure S10. ^{13}C NMR spectrum of 1-(2-azidoethyl)-imidazole (**6**).

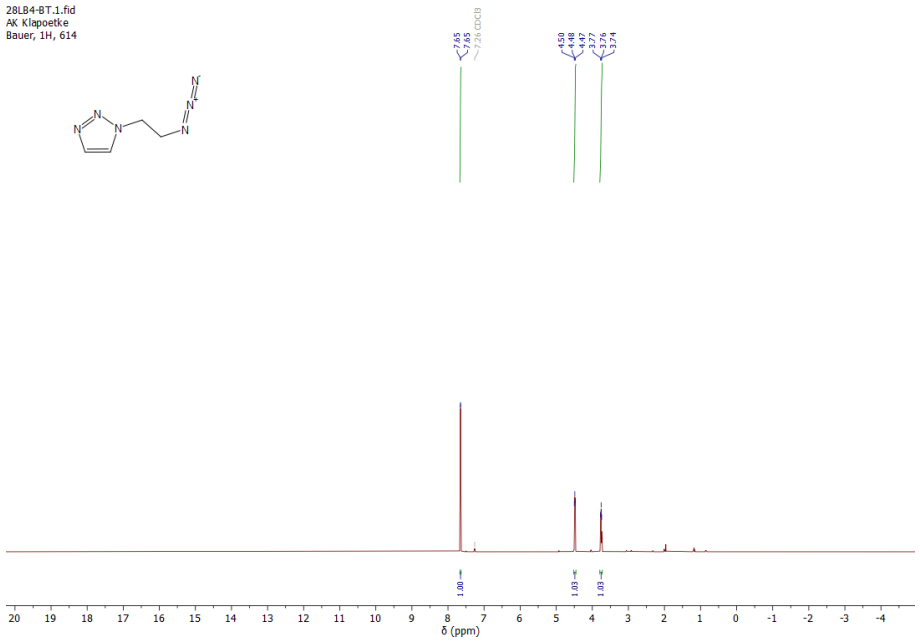

Figure S11. ^{1}H NMR spectrum of 1-(2-azidoethyl)-1,2,3-triazole (**7**).

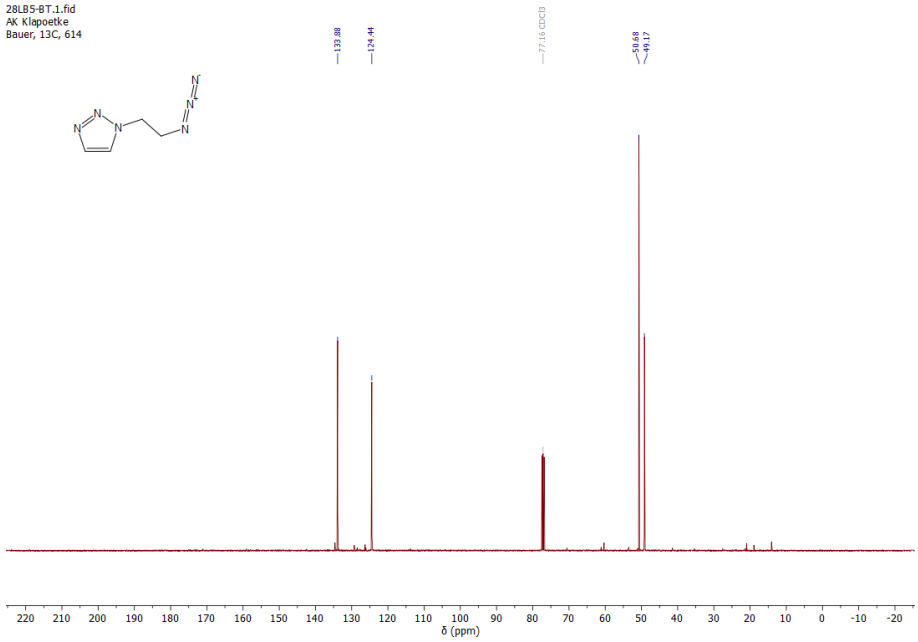

Figure S12. ^{13}C NMR spectrum of 1-(2-azidoethyl)-1,2,3-triazole (**7**).

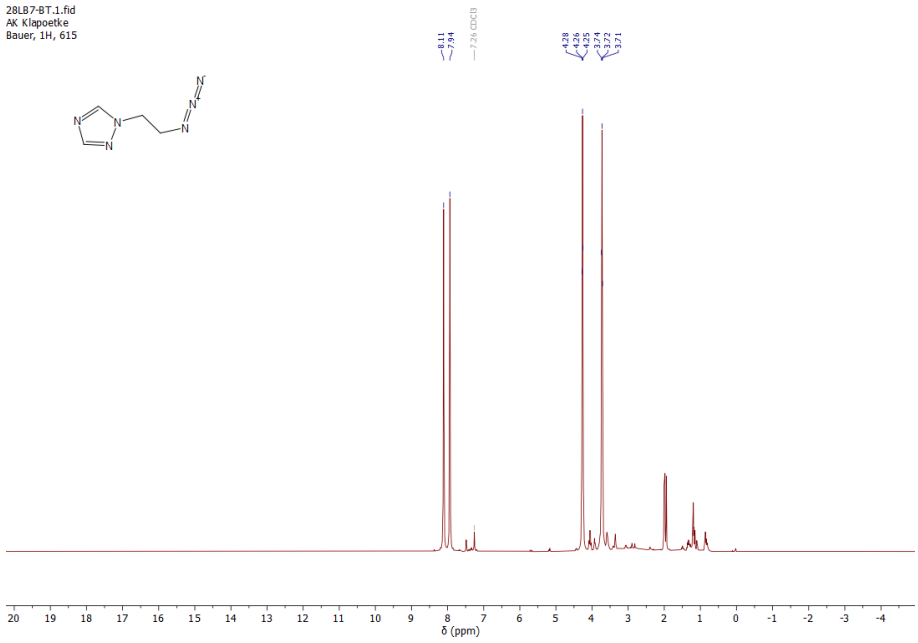

Figure S13. ^{1}H NMR spectrum of 1-(2-azidoethyl)-1,2,4-triazole (**7**).

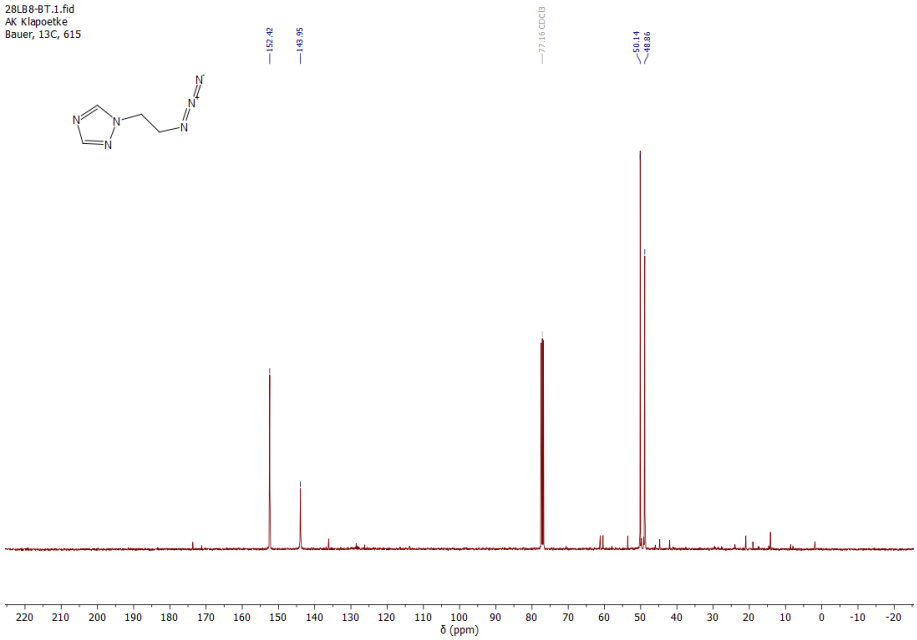

Figure S14. ^{13}C NMR spectrum of 1-(2-azidoethyl)-1,2,4-triazole (**7**).

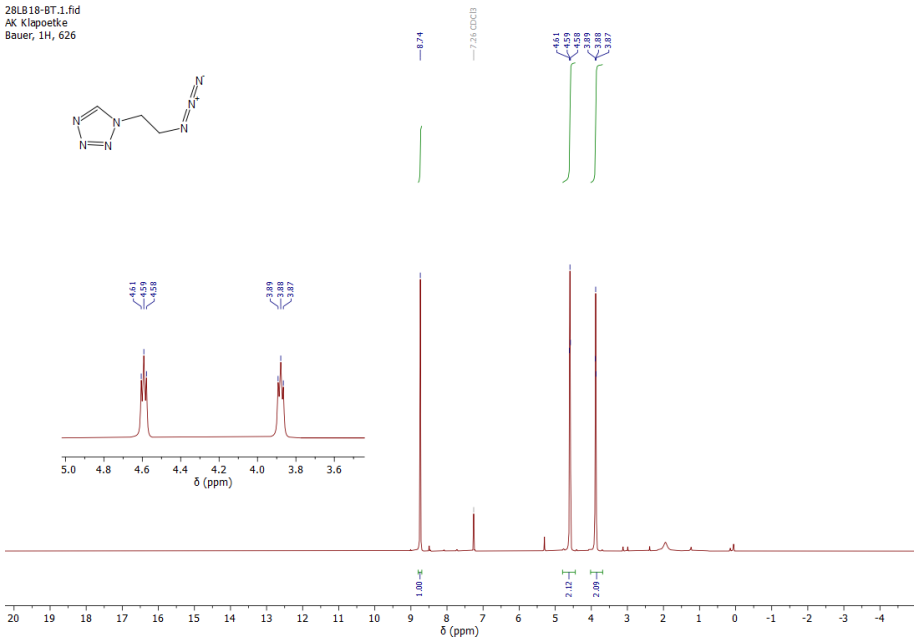

Figure S15. ^{1}H NMR spectrum of 1-(2-azidoethyl)-tetrazole (**9**).

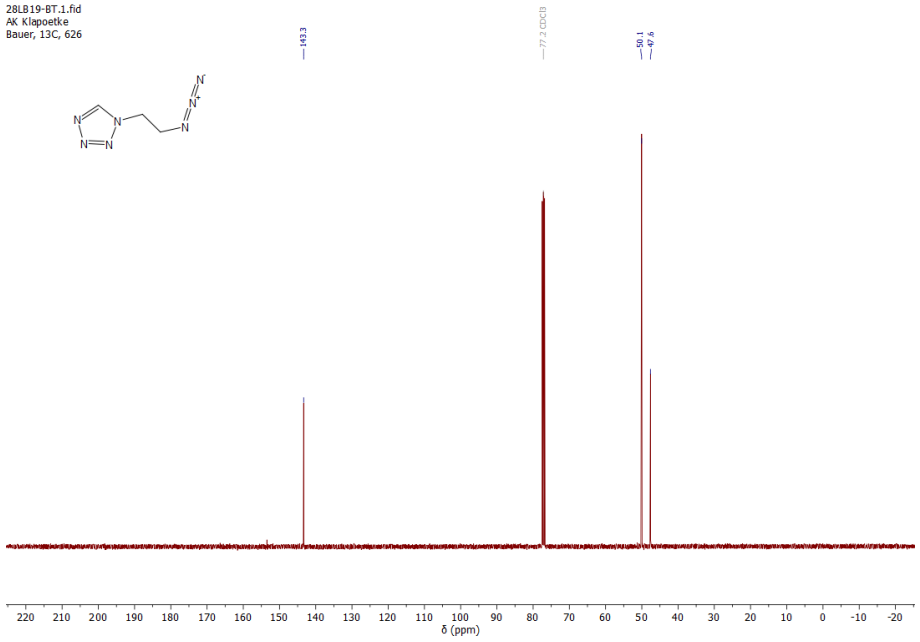

Figure S16. ^{13}C NMR spectrum of 1-(2-azidoethyl)-tetrazole (**9**).

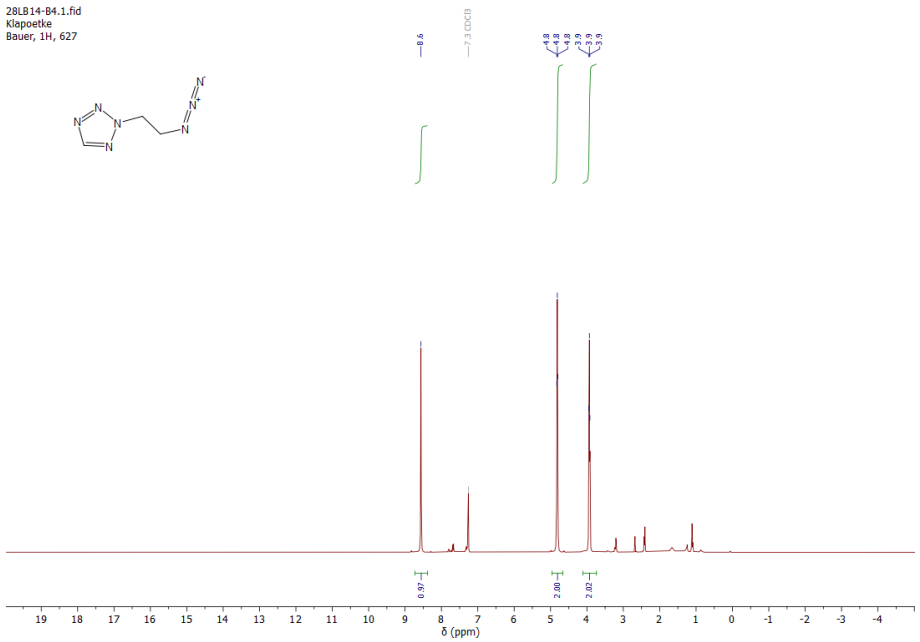

Figure S17. ^{1}H NMR spectrum of 2-(2-azidoethyl)-tetrazole (**10**).

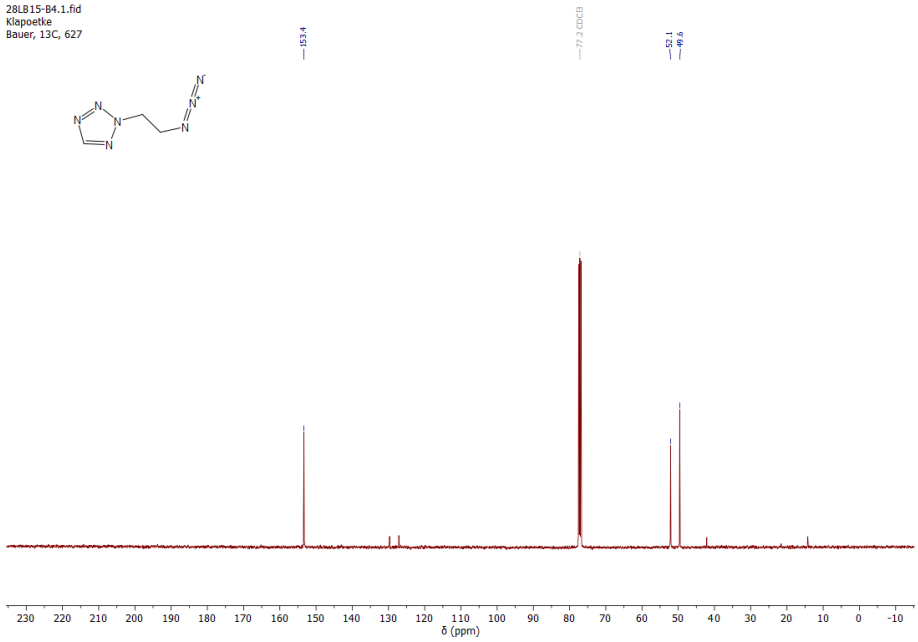

Figure S18. ^{13}C NMR spectrum 2-(2-azidoethyl)-tetrazole (**10**).

7.8.3 IR Spectroscopy

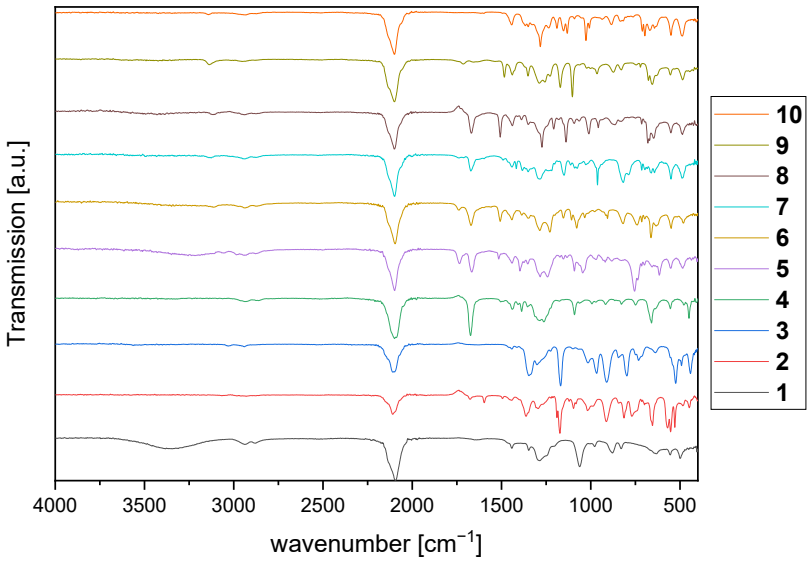

Figure S19. IR spectra of compunds **1**–**10**.

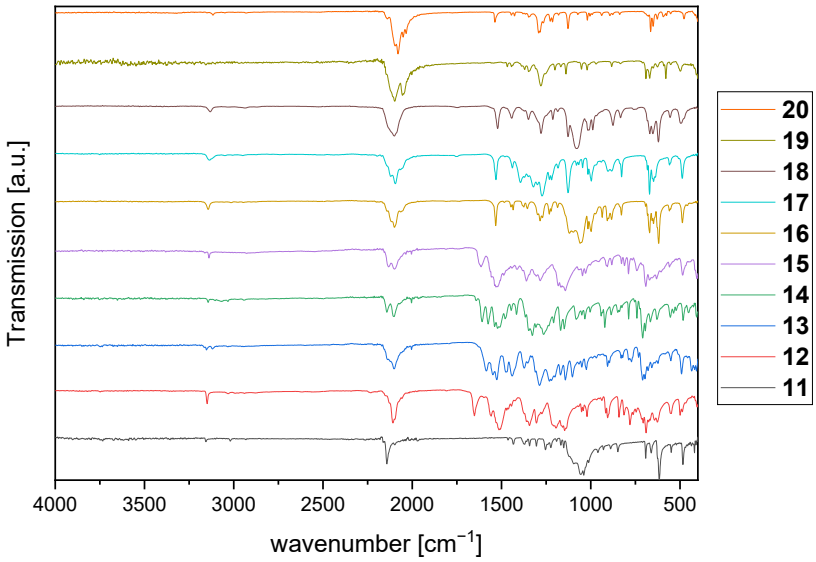

Figure S20. IR spectra of compunds **11**–**20**.

7.8.4 X-Ray Diffraction

For all crystalline compounds an Oxford Xcalibur3 diffractometer with a CCD area detector or Bruker D8 Venture TXS diffractometer equipped with a multilayer monochromator, a Photon 2 detector, and a rotating-anode generator were employed for data collection using Mo-Kα radiation (λ = 0.7107 Å). On the Oxford device, data collection and reduction were carried out using the CrysAlisPRO software. [S12] On the Bruker diffractometer, the data were collected with the Bruker Instrument Service v3.0.21, the data reduction was performed using the SAINT V8.18C software (Bruker AXS Inc., 2011). The structures were solved by direct methods (SHELXT [S13]), refined by full-matrix least-squares on *F2* (SHELXL [S14, S15]) and finally checked using the PLATON software [S16] integrated in the WinGX [S13, S17] or Olex2 [S18] software suite. The non-hydrogen atoms were refined anisotropically and the hydrogen atoms were located and freely refined. The absorptions were corrected by a SCALE3 ABSPACK or SADABS Bruker APEX3 multi-scan method. [S19, S20] All DIAMOND4 [S21] plots are shown with thermal ellipsoids at the 50 % probability level and hydrogen atoms are shown as small spheres of arbitrary radius.

Table S1. Crystallographic data and crystal structure refinement details of compounds **11**, **12** and **13**.

	[Ag(μ-2-AET)(ClO_4)]	***[Cu(2-AET)$_4$(H_2TNPG)$_2$]***	***[Cu(2-AET)$_2$(TNR)]***
Formula	$C_3H_5AgClN_7O_4$	$C_{24}H_{24}CuN_{34}O_{18}$	$C_{12}H_{11}CuN_{17}O_8$
FW [g mol^{-1}]	346.46	1140.31	584.92
Crystal system	monoclinic	triclinic	triclinic
Space group	$P2_1/c$ (No. 14)	$P\bar{1}$ (No. 2)	$P\bar{1}$ (No. 2)
Color / Habit	colorless block	green plate	green prism
Size [mm]	0.05 x 0.07 x 0.12	0.10 x 0.50 x 0.50	0.30 x 0.40 x 0.40
a [Å]	5.2236(2)	8.6008(3)	8.3194(3)
b [Å]	18.1019(7)	11.6961(4)	8.6566(3)
c [Å]	10.1128(4)	22.8864(9)	15.2761(6)
α [°]	90	76.690(3)	104.973(3)
β [°]	93.739(1)	81.696(3)	96.255(3)
γ [°]	90	70.086(3)	91.949(3)
V [Å^3]	954.20(6)	2100.98(14)	1054.26(7)
Z	4	2	2
$\rho_{calc.}$ [g cm^{-3}]	2.412	1.803	1.843
μ [mm^{-1}]	2.407	0.64	1.123
F(000)	672	1158	590
$\lambda_{MoK\alpha}$ [Å]	0.71073	0.71073	0.71073
T [K]	173	94	97
θ Min-Max [°]	3.0, 27.5	2.3, 30.9	2.4, 32.6
Dataset	−6:6; −23:23; −13:13	−12:12; −16:16; −31:32	−9:12; −12:12; −21:23
Reflections collected	16454	24932	12629
Independent refl.	2188	11552	6898
R_{int}	0.024	0.032	0.031
Observed reflections	2071	8858	5113
Parameters	145	713	346
R_1 (obs)[a]	0.0194	0.0466	0.0458
wR_2 (all data)[b]	0.0478	0.1125	0.1148
S [c]	1.1	1.04	1.04
Resd. dens [e Å^{-3}]	−0.62, 0.77	−0.51, 0.57	−0.41, 0.73
Absorption correction	multi-scan	multi-scan	multi-scan
CCDC	2320783	2320784	2320781

[a]$R_1 = \Sigma||F_0|-|F_c||/\Sigma|F_0|$; [b]$wR_2 = [\Sigma[w(F_0^2-F_c^2)^2]/\Sigma[w(F_0)^2]]^{1/2}$; $w = [\sigma c^2(F_0^2)+(xP)^2+yP]^{-1}$ and $P=(F_0^2+2F_c^2)/3$; [c]$S = \{\Sigma[w(F_o^2-F_c^2)^2]/(n-p)\}^{1/2}$ (n = number of reflections; p = total number of parameters).

Table S2. Crystallographic data and crystal structure refinement details of compounds **14**, **15** and **16**.

	[Cu(2-AET)$_2$(PA)$_2$]	***[Cu(2-AET)$_2$(HTNO)$_2$]***	***[Cu(AE124Tri)$_4$(ClO$_4$)$_2$]***
Formula	$C_{18}H_{14}CuN_{20}O_{14}$	$C_{20}H_{18}CuN_{20}O_{16}$	$C_{16}H_{24}Cl_2CuN_{24}O_8$
FW [g mol^{-1}]	798.03	858.08	815.03
Crystal system	triclinic	triclinic	triclinic
Space group	*P*−1 (No. 2)	*P*−1 (No. 2)	*P*−1 (No. 2)
Color / Habit	green prism	brown block	blue block
Size [mm]	0.10 x 0.30 x 0.30	0.06 x 0.07 x 0.13	0.10 x 0.40 x 0.50
a [Å]	8.8651(5)	6.5887(3)	8.5271(4)
b [Å]	9.3831(5)	11.0936(5)	9.1609(5)
c [Å]	9.7735(5)	12.3674(5)	12.0598(7)
α [°]	101.763(4)	75.031(2)	68.548(5)
β [°]	100.345(5)	89.954(2)	82.238(4)
γ [°]	105.452(4)	79.242(2)	64.105(6)
V [Å^3]	743.20(8)	856.87(7)	788.42(9)
Z	1	1	1
$\rho_{calc.}$ [g cm^{-3}]	1.783	1.663	1.717
μ [mm^{-1}]	0.84	0.739	0.947
F(000)	403	435	415
$\lambda_{MoK\alpha}$ [Å]	0.71073	0.71073	0.71073
T [K]	100	297	100
θ Min-Max [°]	2.2, 29.3	3.4, 26.4	2.6, 30.7
Dataset	−12:11; −12:12; −13:13	−8:7; −13:13; −15:15	−11:11; −10:13; −17:16
Reflections collected	10795	10569	8217
Independent refl.	3548	3488	4323
R_{int}	0.038	0.028	0.02
Observed reflections	2923	3223	3835
Parameters	241	280	299
R_1 (obs)[a]	0.0414	0.0352	0.0277
wR_2 (all data)[b]	0.0979	0.0995	0.0719
S [c]	1.05	1.07	1.04
Resd. dens [e Å^{-3}]	−0.35, 0.51	−0.31, 0.38	−0.38, 0.39
Absorption correction	multi-scan	multi-scan	multi-scan
CCDC	2320780	2320782	2320779

[a]$R_1 = \Sigma||F_0|-|F_c||/\Sigma|F_0|$; [b]$wR_2 = [\Sigma[w(F_0^2-F_c^2)^2]/\Sigma[w(F_0)^2]]^{1/2}$; $w = [\sigma c^2(F_0^2)+(xP)^2+yP]^{-1}$ and $P=(F_0^2+2F_c^2)/3$; [c]$S = \{\Sigma[w(F_o^2-F_c^2)^2]/(n-p)\}^{1/2}$ (n = number of reflections; p = total number of parameters).

7.8.5 Hot Plate and Hot Needle Testing

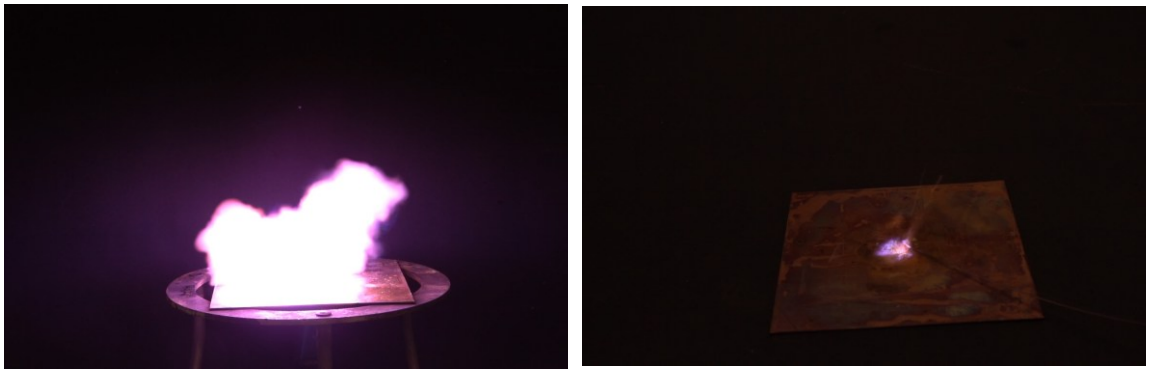

Figure S21. Reaction of [Ag(μ-2-AET)(ClO_4)] during hot plate (left) and hot needle test (right).

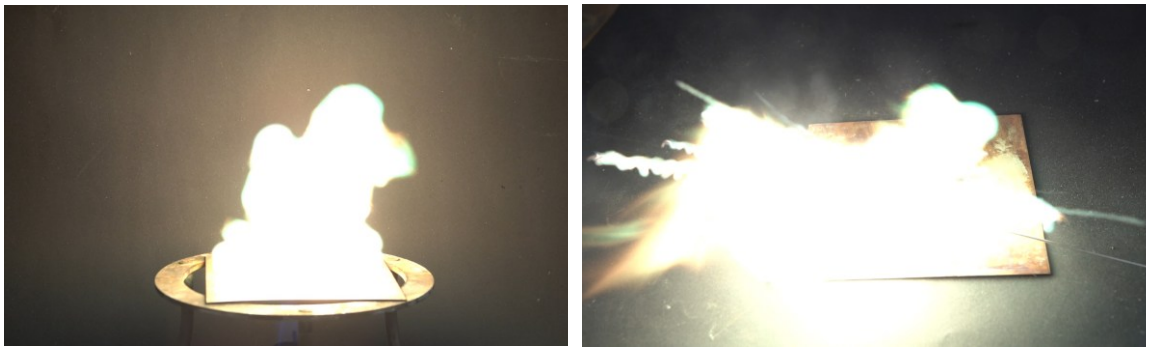

Figure S22. Reaction of [Cu(2-AET)$_4$(H_2TNPG)$_2$] during hot plate (left) and hot needle test (right).

Figure S23. Reaction of [Cu(2-AET)$_2$(TNR)] during hot plate (left) and hot needle test (right).

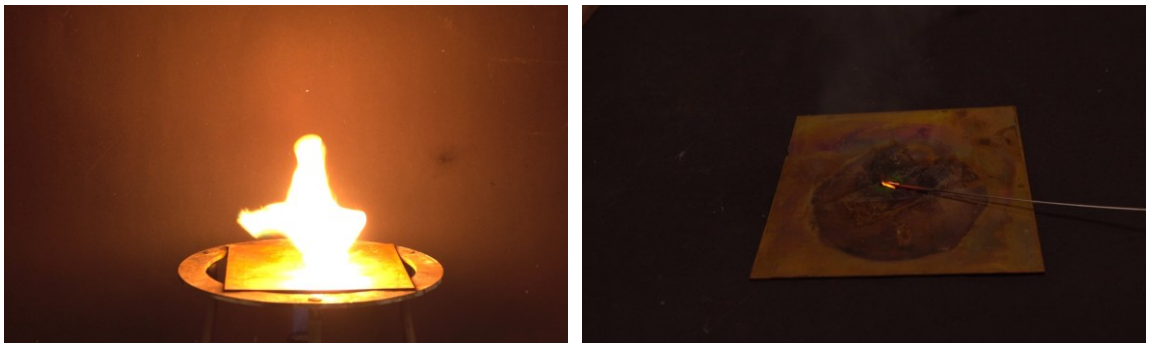

Figure S24. Reaction of $[Cu(2\text{-}AET)_2(PA)_2]$ during hot plate (left) and hot needle test (right).

Figure S25. Reaction of $[Cu(2\text{-}AET)_2(HTNO)_2]$ during hot plate (left) and hot needle test (right).

Figure S26. Reaction of $[Cu(AE124Tri)_4(ClO_4)_2]$ during hot plate (left) and hot needle test (right).

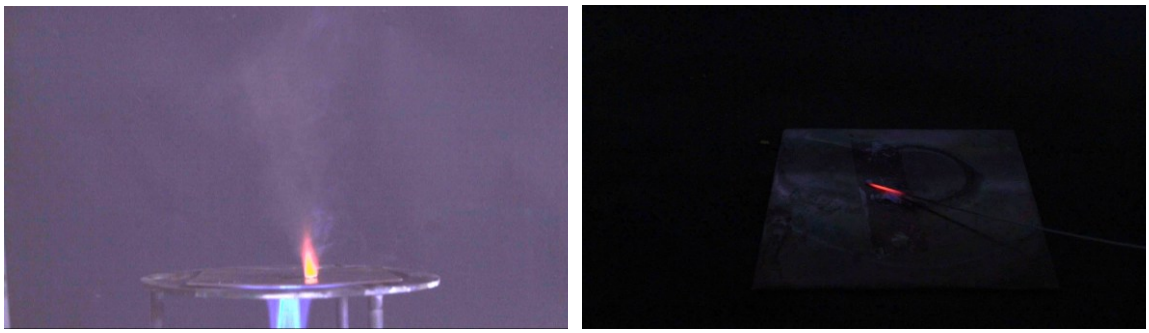

Figure S27. Reaction of $[Cu(AE124Tri)_4(NO_3)_2]$ during hot plate (left) and hot needle test (right).

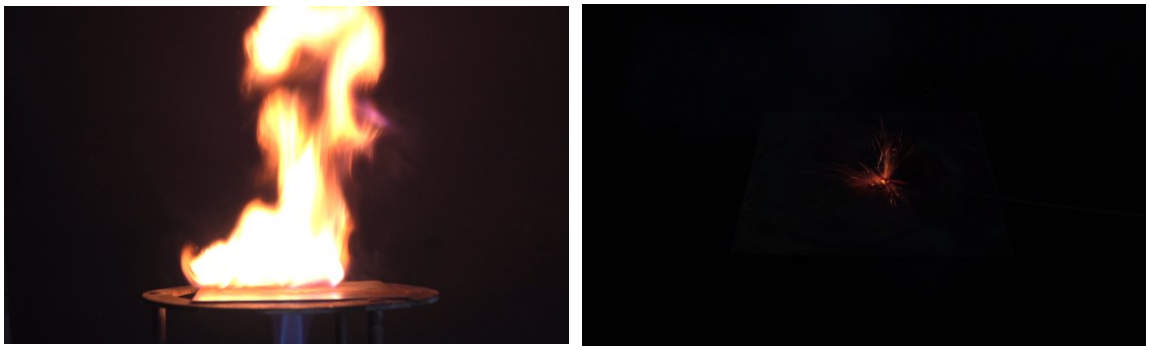

Figure S28. Reaction of $[Fe(AE124Tri)_6](ClO_4)_2$ during hot plate (left) and hot needle test (right).

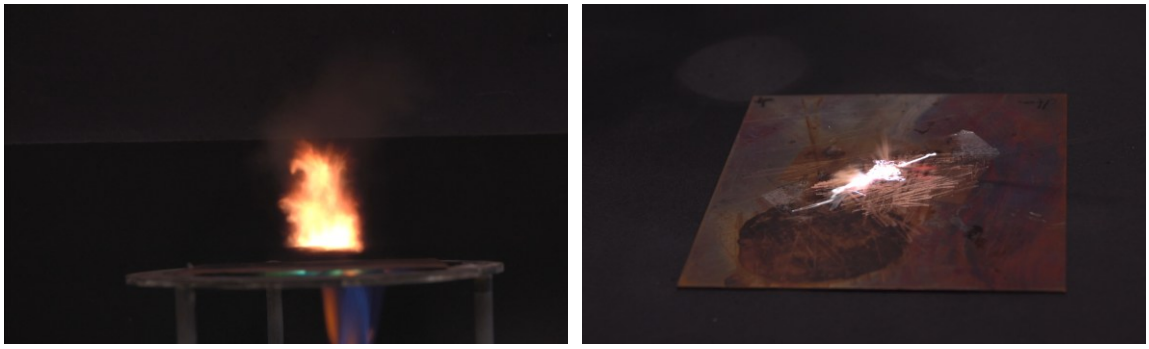

Figure S29. Detonation of $[Cu_2(2\text{-}AET)(N_3)_4]$ during hot plate (left) and hot needle test (right).

Figure S30. Detonation of $[Cu_3(AE124Tri)(N_3)_6]$ during hot plate (left) and hot needle test (right).

7.8.6 Computations

All calculations were carried out using the Gaussian G09 program package. [S11] The enthalpies (H) and free energies (G) were calculated using the complete basis set (CBS) method of Petersson and coworkers in order to obtain very accurate energies. The CBS models use the known asymptotic convergence of pair natural orbital expressions to extrapolate from calculations using a finite basis set to the estimated complete basis set limit. CBS-4 begins with a HF/3-21G(d) geometry optimization; the zero-point energy is computed at the same level. It then uses a large basis set SCF calculation as a base energy, and a MP2/6-31+G calculation with a CBS extrapolation to correct the energy through second order. A MP4(SDQ)/6-31+(d,p) calculation is used to approximate higher order contributions. In this study we applied the modified CBS-4M method (M referring to the use of minimal population localization) which is a re-parametrized version of the original CBS-4 method and also includes some additional empirical corrections. The enthalpies of the gas-phase species M were computed according to the atomization energy method (E1) (Table S3 & Table S4). [S11, 22-26]

$$\Delta_f \mathrm{H}^\circ_{(g,M,298)} = H_{(Molecule,298)} - \sum H^\circ_{(Atoms,298)} + \sum \Delta_f H^\circ_{(Atoms,298)} \qquad \text{(E1)}$$

Table S3. Literature values for atomic $\Delta \boldsymbol{H^\circ_f}^{\mathbf{298}}$ / kcal mol^{-1}

	$-H^{298}$ [a.u.]	NIST [S27]
H	0.50091	52.1
C	37.786156	171.3
N	54.522462	113.0
O	74.991202	59.6

The gas-phase heat of formations were converted to the solid/liquid state ones for neutrals: by subtracting the vaporization/sublimation enthalpies (calculated using the Trouton rule). [S28-29] The calculation results are summarized in Table S.

$$\Delta U_m = \Delta H_m - \Delta n\, R\, T \qquad \text{(E2)}$$

Table S4. CBS-4M results

Compound	$-H^{298}$[a] [a.u.]	$\Delta_f H°(g,M)$[b] [kJ mol^{-1}]	$\Delta_f H°(s/l)$[c] [kJ mol^{-1}]	Δn[d]	$\Delta_f U(l)$[e] [kJ mol^{-1}]
AEPy (5)	−467.719370	464.4	420.9	−6.0	435.8
AEIm(6)	−467.733549	427.2	383.7	−6.0	398.6
AE123Tri(7)	−483.744376	554.6	510.8	−6.0	525.6
AE124Tri(8)	−483.770792	485.2	442.9	−6.0	457.8
1-AET(**9**)	−499.773188	634.8	592.8	−6.0	607.7
2-AET(**10**)	−499.782134	611.3	568.6	−6.0	583.5

[a] CBS-4M electronic enthalpy; [b] gas phase enthalpy of formation; [c] standard condensed state enthalpy of formation; [d] Δn being the change of moles of gaseous components when formed; [e] solid state energy of formation.

7.8.7 References

[S1] Y. Dong, X. Liang, H. Yuan, S. Qi, F. Chen, D. Wang, *Green Chemistry* **2008**, *10*, 990–994.

[S2] NATO standardization agreement (STANAG) on explosives, impact sensitivity tests, no. 4489, According to: 1st ed., **1999**.

[S3] WIWEB-Standardarbeitsanweisung 4–5.1.02, Ermittlung der Explosionsgefährlichkeit, hier der Schlagempfindlichkeit mit dem Fallhammer, According to: **2002**.

[S4] BAM, http://www.bam.de, accessed December 2021.

[S5] NATO standardization agreement (STANAG) on explosive, friction sensitivity tests, no. 4487, According to: 1st. Edition, **2002**.

[S6] WIWEB-Standardarbeitsanweisung 4–5.1.03, Ermittlung der Explosionsgefährlichkeit oder der Reibeempfindlichkeit mit dem Reibeapparat, According to: **2002**.

[S7] OZM, https://www.ozm.cz/, accessed December **2021**.

[S8] Impact: insensitive > 40 J, less sensitive ≥ 35 J, sensitive ≥ 4 J, very sensitive ≤ 3 J; Friction: insensitive > 360 N, less sensitive = 360 N, sensitive < 360 N and > 80 N, very sensitive ≤ 80 N, extremely sensitive ≤ 10 N, According to: Recommendations on the Transport of Dangerous Goods, Manual of Tests and Criteria, 4th edition, New York-Geneva, **1999**.

[S9] *UN Model Regulation: Recommendations on the Transport of Dangerous Goods – Manual of Tests and Criteria, section 13.4.2.3.3*, **2015**.

[S10] M. Sućeska, *EXPLO5* V7.01.01, Zagreb, **2023**.

[S11] M. J. Frisch, G. W. Trucks, H. B. Schlegel, G. E. Scuseria, M. A. Robb, J. R. Cheeseman, G. Scalmani, V.Barone, B. Mennucci, G. A. Petersson, H. Nakatsuji, M. Caricato, X. Li, H.P. Hratchian, A. F. Izmaylov, J. Bloino, G. Zheng, J. L. Sonnenberg, M. Hada, M. Ehara, K. Toyota, R. Fukuda, J. Hasegawa, M. Ishida, T. Nakajima, Y. Honda, O. Kitao, H. Nakai, T. Vreven, J. A. Montgomery Jr., J. E. Peralta, F. Ogliaro, M. Bearpark, J. J. Heyd, E. Brothers, K. N. Kudin, V. N. Staroverov, R. Kobayashi, J. Normand, K. Raghavachari, J. C. B. A. Rendell, S. S. Iyengar, J. Tomasi, M. Cossi, N. Rega, J. M. Millam, M.Klene, J. E. Knox, J. B. Cross, V. Bakken, C. Adamo, J. Jaramillo, R. Gomperts, R. E. Stratmann, O. Yazyev, A. J. Austin, R. Cammi, C. Pomelli, J. W. Ochterski, R. L. Martin, K. Morokuma, V. G. Zakrzewski, G. A. Voth, P. Salvador, J. J. Dannenberg, S. Dapprich, A. D. Daniels, O. Farkas, J.B. Foresman, J. V. Ortiz, J. Cioslowski, D. J. Fox, *Gaussian 09 A.02*, Gaussian Inc, Wallingford, CT, USA, **2009**.

[S12] *CrysAlisPRO*, Version 171.33.41, Oxford Diffraction Ltd, **2009**.

[S13] G. M. Sheldrick, *Acta Crystallogr. Sect. A* **2015**, *71*, 3–8.

[S14] G. M. Sheldrick, *SHELXL-97*, University of Göttingen, Germany, **1997**.

[S15] G. M. Sheldrick, *Acta Crystallogr. Sect. A* **2008**, *64*, 112–122.

[S16] A. L. Spek, *PLATON*, Utrecht University, The Netherlands, **1999**.

[S17] L. J. Farrugia, *J. Appl. Cryst.* **2012**, *45*, 849.

[S18] O. V. Dolomanov, L. J. Bourhis, R. J. Gildea, J. A. K. Howard, H. Puschmann, *J. Appl. Cryst.* **2009**, *42*, 339–341.

[S19] *Empirical absorption correction using spherical harmonics, implemented in SCALE3 ABSPACK scaling algorithm*, Version 171.33.41, CrysAlisPro Oxford Diffraction Ltd., **2009**.

[S20] *APEX3*, Bruker AXS Inc., Madison, Wisconsin, USA,

[S21] H. Putz, K. Brandenburg, *Diamond - Crystal and Molecular Structure Visualization*, Crystal Impact, Bonn, Germany,

[S22] J. W. Ochterski, G. A. Petersson, J. A. M. Jr., *J. Chem. Phys.* **1996**, *104*, 2598–2619.

[S23] J. A. Montgomery Jr., M. J. Frisch, J. W. Ochterski, G. A. Petersson, *J. Chem. Phys.* **2000**, *112*, 6532–6542.

[S24] L. A. Curtiss, K. Raghavachari, P. C. Redfern, J. A. Pople, *J. Chem. Phys.* **1997**, *106*, 1063–1079.

[S25] E. F. C. Byrd, B. M. Rice, *J. Phys. Chem. A* **2006**, *110*, 1005–1013.

[S26] B. M. Rice, S. V. Pai, J. Hare, *Comb. Flame* **1999**, *118*, 445–458.

[S27] P. J. Lindstrom, W. G. Mallard, NIST Standard Reference Database Number 69, http://webbook.nist.gov/chemistry/, accessed Mai 2022.

[S28] M. S. Westwell, M. S. Searle, D. J. Wales, D. H. Williams, *J. Am. Chem. Soc.* **1995**, *117*, 5013–5015.

[S29] F. Trouton, *Philos. Mag.* **1884**, *18*, 54–57.

8 1-Amino-5-nitriminotetrazolate as a Promising Anion in Safe yet Powerful Energetic Coordination Compounds

Maximilian Benz, Simon M. J. Endraß, Thomas M. Klapötke, Jörg Stierstorfer, and Sadiq Strey

published in *Dalton Transactions,* **2025**

DOI: 10.1039/D4DT03086A

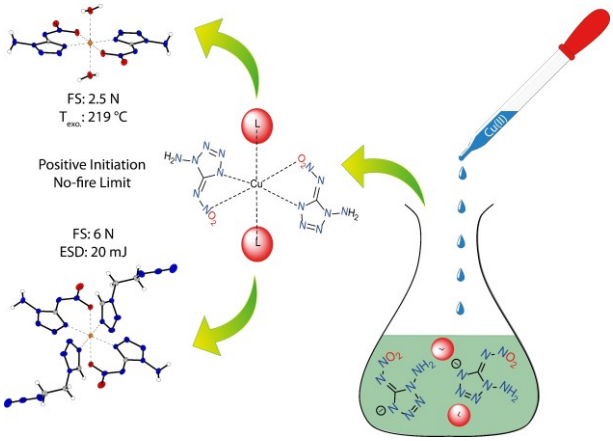

Abstract: Ammonium 1-amino-5-nitriminotetrazolate (NH_4ANIT) was used as a precursor for Energetic Coordination Compounds (ECCs). The highly energetic copper salt $[Cu(ANIT)_2(H_2O)_2]$ was selectively prepared. Reaction of NH_4ANIT with copper(II) nitrate trihydrate followed by the addition of neutral ligands (L) such as 1,2-di(1*H*-tetrazol-1-yl)ethane (1,1-dte), 1,3-di(1*H*-tetrazol-1-yl)propane (1,1-dtp), 1-(2-azidoethyl)-1*H*-tetrazole (1-AET), produced energetic coomplexes of the types $[Cu(ANIT)_2(L)_2]$ and $[Cu(ANIT)_2(\mu\text{-}L)]$. The structural characteristica of these ECCs were analyzed by low temperautre single crystal X-ray diffraction analysis. Their energetic parameters, such as impact and friction sensitivities according to BAM, were evaluated to give an insight in the value of the ANIT anion for replacements of the commercially used lead azide (LA) and lead styphnate (LS) as a primary explosive. The two most promising candidates $[Cu(ANIT)_2(H_2O)_2]$ and $[Cu(ANIT)_2(1\text{-}AET)_2]$ were analyzed concerning their particle distribution and sphericity by laser diffraction particle size analysis and scanning electron microscopy to allow an insight in the processability of these substances.

8.1 Introduction

The ecological effects of the use of blasting is gaining significant importance in the field of energetic materials. For a long time, the intention of developing new energetic materials was mainly driven by academic interests combined with the military demand for improving its performances. [1] Nowadays the industrial demand is also increasing due to legislation, as well as the awareness of the negative effects, which released compounds have. [2-4] Especially the effects of lead, distributed in soil and water through the use of lead azide (LA) and lead styphnate (LS) as primary explosives have to be mentioned. [5,6] Alongside the reliability and ecological impact, personal safety of the operating staff plays a crucial role in producing, transporting and handling of explosives. [7] One way of reducing the amount of toxic waste released upon blasting, is to replace LA and LS with compounds that do not share the heavy metal toxicity of lead. One approach to accomplish this goal is the use of energetic coordination compounds (ECCs). These ECCs benefit from the use of less toxic metals such as copper and iron, while compensating for the loss of density by incorporating highly energetic ligands and anions. To be considered green alternatives,

their central metal should exhibit as little toxicity as possible. Furthermore, the anions and ligands should ideally be non-toxic and have a straightforward synthesis.

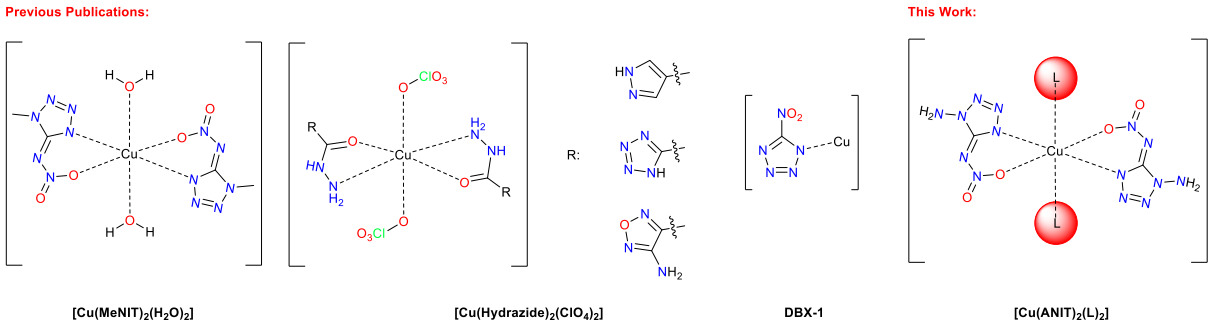

Figure 1. Schematic drawing of $[Cu(ANIT)_2(L)_2]$ compared to DBX-1 and previously published ECCs with chelating ligands.[8-12]

By applying the nitrogen-rich ammonium 1-amino-5-nitriminotetrazolate (NH_4ANIT) as a precursor substance for the synthesis, the ANIT anion can be introduced to the world of ECCs. This creates the option to produce ECCs of the types $[Cu(ANIT)_2(L)_2]$ and $[Cu(ANIT)_2(\mu\text{-}L)]$ (Figure 1).

By using the chelating ANIT anion, ECCs with lower solubility in water should be obtained. Similar approaches have recently been shown in several publications, which rely on the chelating effect of aromatic hydrazides as ligands. [10-12] Compared to recently studied ECCs, the compounds presented in this work do not rely on typical oxidizing anions like chlorate, perchlorate, bromate or nitroaromatic anions, which are known for their toxicity. [12-17] Furthermore, existing 5-nitriminotetrazolates with different substituents apart from the amino group could be used in a similar manner. [18,19] This would further increase the variability of the ECC concept, as previous publications focused more on the acidic character of the 5-nitriminotetrazolates creating the resulting salts and ECCs with aqua-ligands. [8,19-21]

As a comparable compound, which also aims for a reduction of environmental damage, copper(I) 5-nitrotetrazolate (DBX-1) was selected. While the simple composition of DBX-1 looks very promising, the need for very clean sodium nitrotetrazolate as a precursor can be considered as a drawback in terms of processing safety, as it requires the intermediate formation of diazoniumtetrazolate. [9,13,22,23] This intermediate species can reportedly undergo microdetonations within solution. [24,25]

This work seeks to introduce copper(II) and iron(II) 1-amino-5-nitriminotetrazolate based coordination compounds as primary explosives with mechanical stability that exceeds commercially used LA and LS.

8.2 Results and Discussion

8.2.1 Synthesis

NH_4ANIT was chosen as a bench-stable precursor substance. Its higher thermal stability ($T_{dec.}$: 185 °C) and resistance to friction (20 N) compared to the neutral HANIT ($T_{dec.}$: 145 °C, FS: 5 N) allow for safer handling. [26] Its synthesis, starting from 1,5-DAT, is shown in Scheme 1. Protection of the sp^3-hybridized amino group is necessary due to higher reactivity. After nitration with N_2O_5, the protection group is cleaved during quenching on iced water. As reported in the literature, nitration under protic conditions is not feasible due to the lability of the protection group. [26] The formation of NH_4ANIT is then performed with ethanolic ammonia.

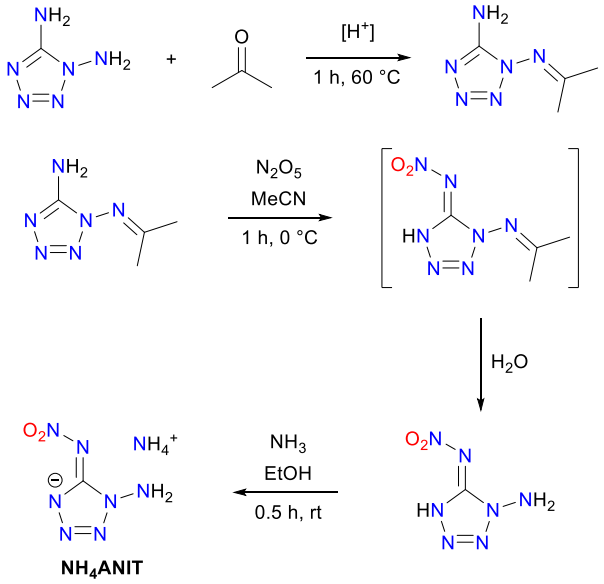

Scheme 1. Synthesis of NH_4ANIT as a precursor for ECCs.

The complexation was then conducted as shown in Scheme 2. Ammonium 1-amino-5-nitriminotetrazolate (NH_4ANIT), was synthesized according to Benz *et al.*. [26] By dissolving NH_4ANIT in water at 60 °C and adding $Cu(NO_3)_2 \cdot 3\ H_2O$, an aqueous solution of $[Cu(ANIT)_2(H_2O)_2]$ (**1**) can be obtained. Using only small amounts of water as a solvent

hereby leads to precipitation of **1** in a yield of 52 %. By addition of another aqueous solution of the respective ligand to a solution of **1**, the aqua-ligands can be exchanged for high heat of formation, nitrogen-rich ligands. Crystallization at room temperature then allowed for the formation of the ECCs **2**–**8**, except for **5a**. To evaluate the value of the ANIT anion for ECCs, complexation attempts were carried out with several neutral ligands. In some cases of more polar ligands such as ammonia, 1-methyl-tetrazole, 1- and 2-amino-tetrazole, as well as 1-nitratomethyl-tetrazole, either no solid compounds were obtained or the elemental analyses were differing from the values of the expected products. One possible contamination observed in these cases was $[Cu(ANIT)_2(H_2O)_2]$ (**1**), which was confirmed by single crystal X-ray diffraction analysis. Successful complexation was obtained in the cases of the ligands shown in Figure 2. While ethylenediamine (en) was purchased by Sigma Aldrich, 1,2-di(1*H*-tetrazol-1-yl)ethane (1,1-dte), 1,3-di(1*H*-tetrazol-1-yl)propane (1,1-dtp), 1,4-di(1*H*-tetrazol-1-yl)butane (1,1-dtb), 2-(1*H*-tetrazol-1-yl)ethyl nitrate (1-NET), 1-(2-azidoethyl)-1*H*-tetrazole (1-AET) and 1-(3-azidopropyl)-1*H*-tetrazole (1-APT) were synthesized according to the literature. [27-32]

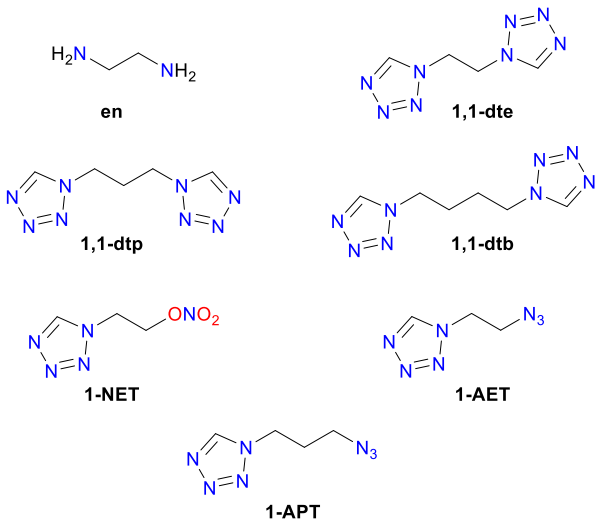

Figure 2. Ligands used to create ECCs with the ANIT anion.

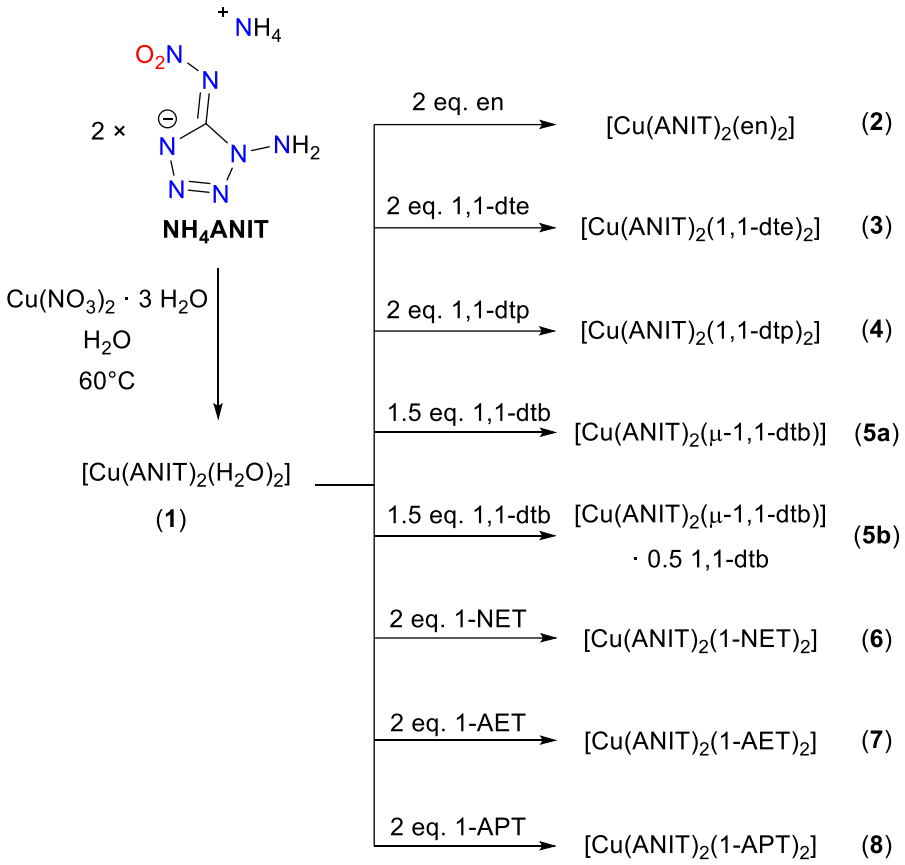

Scheme 2. Successful complexation attempts with NH_4ANIT as a starting material.

By changing the procedure to general procedure B, precipitation of **3**–**8**, excluding **5b**, was successfully achieved. Therefore, NH_4ANIT and the respective ligand were dissolved together at 60 °C in less solvent. In these cases, a solution of $CuSO_4 \cdot 5\ H_2O$ was added dropwise. Precipitation occurred during addition or upon stirring for a few minutes, resulting in product with increased flowability.

By applying the procedure for precipitation to $FeSO_4 \cdot 1.5\ H_2O$, $[Fe(ANIT)_2(H_2O)_2] \cdot 2\ H_2O$ was obtained (Scheme 3) in a yield of 68 % within 10 minutes. The exact procedure is given in the experimental section. Similar attempts with $Fe(NO_3)_3 \cdot 9\ H_2O$, $MnSO_4 \cdot 4\ H_2O$ and $Zn(NO_3)_2 \cdot 6\ H_2O$ did not result in solid products or impure compounds according to elemental analysis in attempts with the abovementioned ligands.

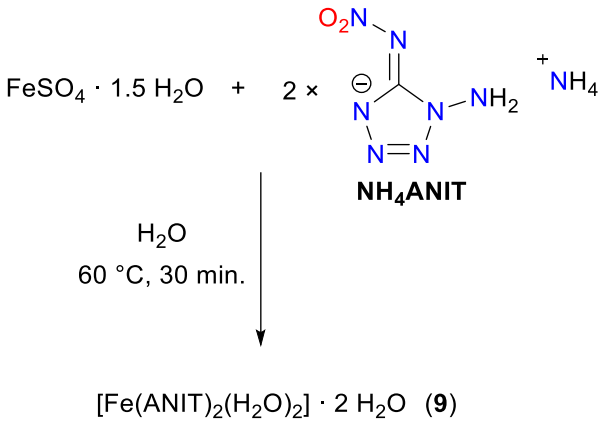

Scheme 3. Precipitation of $[Fe(ANIT)_2(H_2O)_2] \cdot 2\ H_2O$ (**9**).

8.2.2 Crystal Structures

All crystalline products were analyzed by low-temperature X-ray diffraction analysis. The structures were solved in the Olex2 software suite [33] using SHELXT [34] and refined using full-matrix least squares method on *F2* by SHELXL. [35,36] Figures of the crystal structures were created in DIAMOND4 [37] displaying non-hydrogen atoms as thermal ellipsoids at 50 % probability level. Hydrogen atoms are shown as small spheres of arbitrary radius. Deposition Numbers 2394591 (for **1**), 2394593 (for **3**), 2394588 (for **4**), 2394623 (for **5a**), 2394590 (for **5b**), 2394592 (for **7**), 2394589 (for **8**), 2394622 (for **9**) contain the supplementary crystallographic data for this paper. These data are provided free of charge by the joint Cambridge Crystallographic Data Center and Fachinformationszentrum Karlsruhe Access Structures service www.ccdc.cam.ac.uk/structures.

Single crystals suitable for X-ray diffraction analysis of $[Cu(ANIT)_2(H_2O)_2]$ (**1**) can be obtained from evaporation of the aqueous solution at room temperature. The structure, as seen in Figure 3 consists of two almost planar units of ANIT, coordinating to the copper(II) center. The torsion angle between the tetrazole and the nitrimine (N7–N6–C1–N4) can be determined to be 4.27(17)°. The elongated z^2-axis is occupied by two molecules of water. Hydrogen bonding between the ANIT anion and the water ligands results in alternating zigzag stacked layers of **1** as seen in Figure 3b).

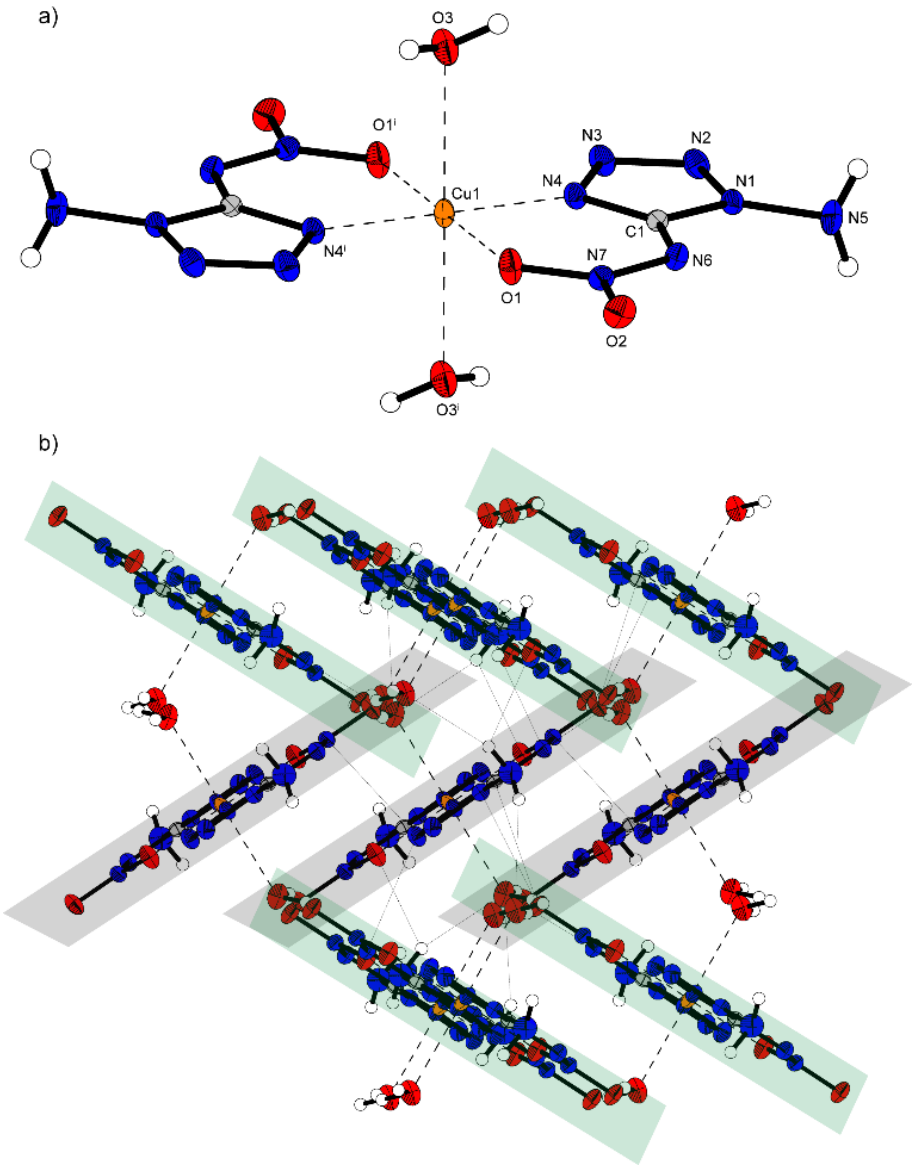

Figure 3. Crystal structure of **a)** the coordination sphere of $[Cu(ANIT)_2(H_2O)_2]$ (**1**) and **b)** as a representation of its zigzag layers. Selected bond lengths [Å]: Cu1–O1 2.0206(16), Cu1–O3 2.3996(19), Cu1–N4 1.9200(16); Selected bond angles [°]: O1–Cu1–O3 93.25(4), O1–Cu1–N4 85.57(4), O3–Cu1–N4 90.02(4); Symmetry codes: (i): 1−x, 1−y, 1−z.

By replacing the water units of **1** by ligands, with stronger coordination to the metal center, the nitro group of the ANIT anion is pushed out of the plane of the ring. The *xy* plane in $[Cu(ANIT)_2(1,1\text{-dte})_2]$ (**3**) is therefore fully occupied by tetrazole rings, leaving only the z^2-orbital for coordination of the nitrimine. This results in an increased torsion angle of −13.4(2)° between the tetrazole ring and the nitrimine (N7–N6–C1–N4). Surprisingly, the typical crosslinking characteristics, known for di(1*H*-tetrazol-1-yl)alkane-ligands did not lead to bridging between the copper(II) centers and therefore the desired decrease of water-

solubility. Instead, using one equivalent of ligand resulted in impure samples, which can be explained by the crystallization of **1** alongside with the desired ECCs.

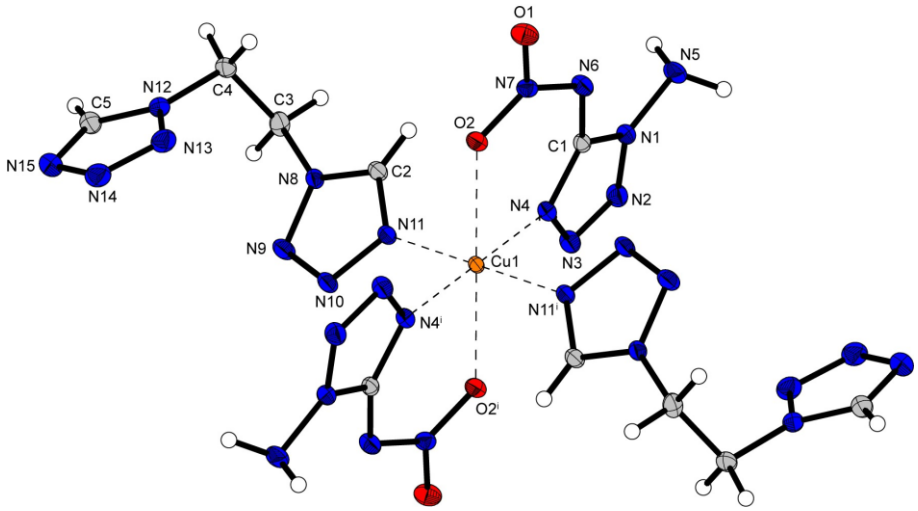

Figure 4. Crystal structure of $[Cu(ANIT)_2(1,1\text{-dte})_2]$ (**3**). Selected bond lengths [Å]: Cu1–O2 2.2842(11), Cu1–N4 1.9754(12), Cu1–N11 2.0390(12); Selected bond angles [°]: O2–Cu1–N4 77.21(4), O2–Cu1–N11 88.76(4), N4–Cu1–N11 88.76(5); Symmetry codes: (i): −x, 1−y, 1−z.

The incorporation of a ligand with higher steric demand, such as 1,1-dtp leads to yet another increase of the torsion angle N7–N6–C1–N4 to 20.6(5)° in $[Cu(ANIT)_2(1,1\text{-dtp})_2]$ (**4**). This results in a significantly longer Cu1–O1 bond of 2.408(2) Å compared to 2.2842(11) Å in **3**.

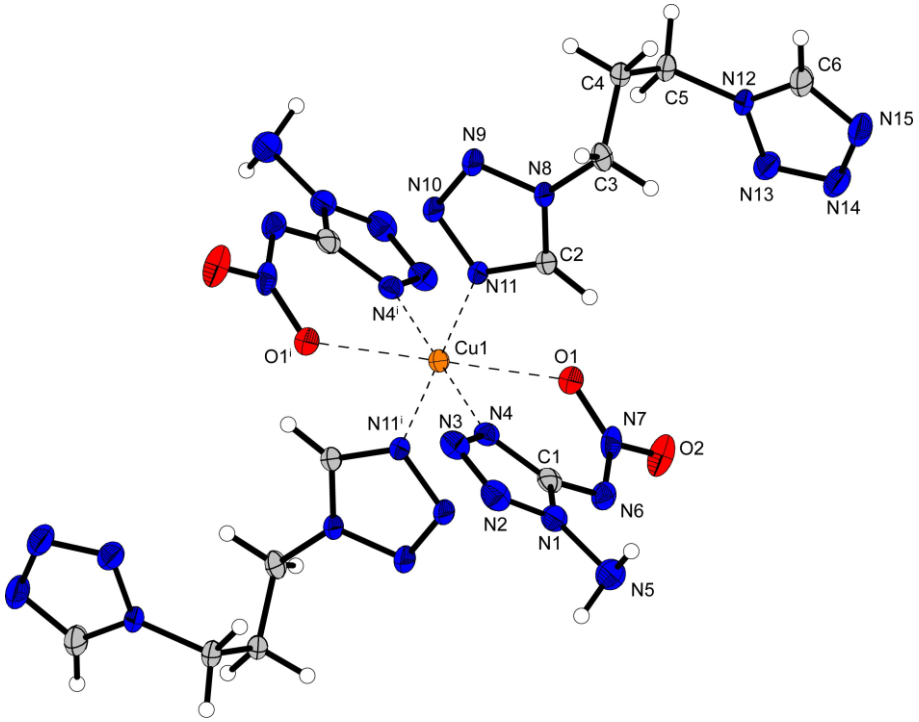

Figure 5. Crystal structure of $[Cu(ANIT)_2(1,1\text{-dtp})_2]$ (**4**). Selected bond lengths [Å]: Cu1–O1 2.408(2), Cu1–N4 1.998(2), Cu1–N11 2.001(2); Selected bond angles [°]: N11–Cu1–O1 87.66(9), N4–Cu1–O1 73.99(9), N4–Cu1–N11 88.25(9); Symmetry codes: (i): 1−x, −y, 2−z.

Unlike 1,1-dte and 1,1-dtp, 1,1-dtb manages to bridge between two copper(II) centers, forming 1D-polymeric chains (Figure 6, Figure 7). While precipitation results in **5a**, which does not incorporate additional ligand, the slow evaporation allows for the formation of **5b**. By recrystallization of **5a** from small amounts of water, single crystals suitable for X-ray diffraction analysis were obtained. The crystal structure shows that in **5a** 1,1-dtb does not only coordinate *via* the N4 position of the tetrazole ring, but also *via* N3. This leads to a zigzag of alternatively coordinated copper(II) centers as demonstrated in Figure 6 b).

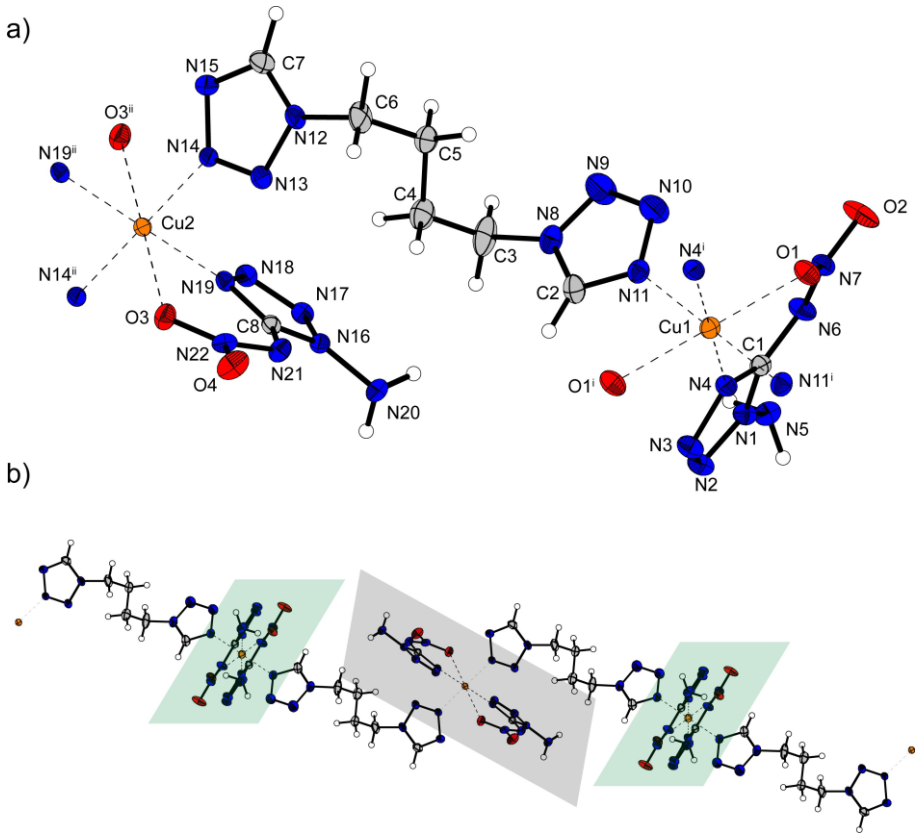

Figure 6. Asymmetric unit of [Cu(ANIT)$_2$(μ-1,1-dtb)] (**5a**) **(a)** and polymeric representation **(b)**. Selected bond lengths [Å]: Cu2–O3 2.3803(16), Cu2–N19 1.9857(18), Cu2–N14 2.0226(18), Cu1–O1 2.2906(15), Cu1–N11 2.0140(19), Cu1–N4 1.988(2); Selected bond angles [°]: N19–Cu2–O3 74.79(7), N19–Cu2–N14 91.01(7), N14–Cu2–O3 92.55(7), N11–Cu1–O1 94.35(7), N4–Cu1–O1 78.06(7), N4–Cu1–N11 87.37(8); Symmetry codes: (i): 1−x, 2−y, −z; (ii): −1−x, 1−y, 1−z.

Unlike in **5a**, the polymeric chains of **5b** are solely formed by coordination of the N4 of 1,1-dtb. When slowly crystallized with excess of 1,1-dtb, these chains are connected with each other by hydrogen bonds between the ANIT amino group and N25, which belongs to a non-coordinating co-crystallized 1,1-dtb molecule. The distances between N25 and the two hydrogen atoms of the amino group are 2.5775 Å (H5A) and 2.5936 Å (H5B) respectively, allowing for interaction. The tetrazole rings of the non-coordinating 1,1-dtb furthermore show perfect coplanar stacking with the tetrazole rings of the ANIT anions.

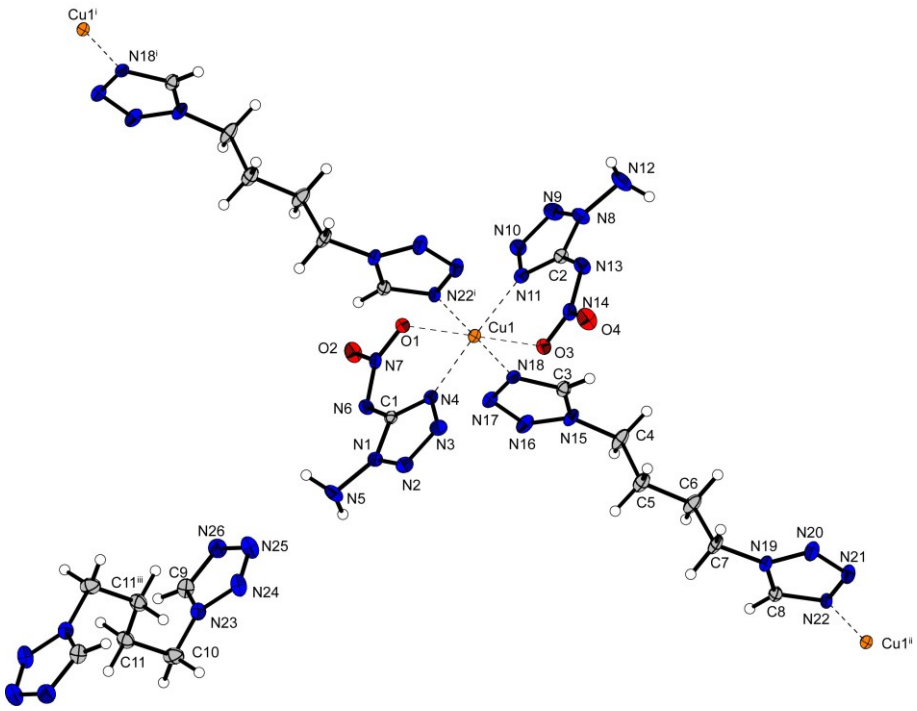

Figure 7. Crystal structure of [Cu(ANIT)$_2$(μ-1,1-dtb)] · 0.5 1,1-dtb (**5b**). Selected bond lengths [Å]: Cu1–O1 2.3457(17), Cu1–O3 2.3592(18), Cu1–N22^i 2.0081(18), Cu1–N18 2.0038(18), Cu1–N4 1.9709(19), Cu1–N11 1.9876(19); Selected bond angles [°]: O1–Cu1–O3 177.01(6), N22^i–Cu1–O1 87.70(7), N22^i–Cu1–O3 89.84(7), N18–Cu1–O1 91.52(7), N18–Cu1–O3 90.94(7), N18–Cu1–N22^i 179.22(9), N4–Cu1–O1 77.14(7), N4–Cu1–O3 101.15(7), N4–Cu1–N22^i 89.23(8), N4–Cu1–N18 90.54(7), N4–Cu1–N11 177.05(9), N11–Cu1–O1 105.71(7), N11–Cu1–O3 76.03(7), N11–Cu1–N22^i 91.64(7), N11–Cu1–N18 88.64(8); Symmetry codes: (i): 1−x, 1−y, z; (ii): 1+x, 1+y, z; (iii): −x, −y, 2−z.

The structural motif remains the same in the cases of [Cu(ANIT)$_2$(1-AET)$_2$] (**7**) (Figure 8) and [Cu(ANIT)$_2$(1-APT)$_2$] (**8**) (Figure 9). Similar to the di(1*H*-tetrazol-1-yl)alkane-ligands, the torsion angle N7–N6–C1–N4 increases in the case of the more sterically demanding ligand 1-APT (14.3(3)°) compared to 1-AET (12.7(3)°). Similarly, the z^2-axis is hereby elongated.

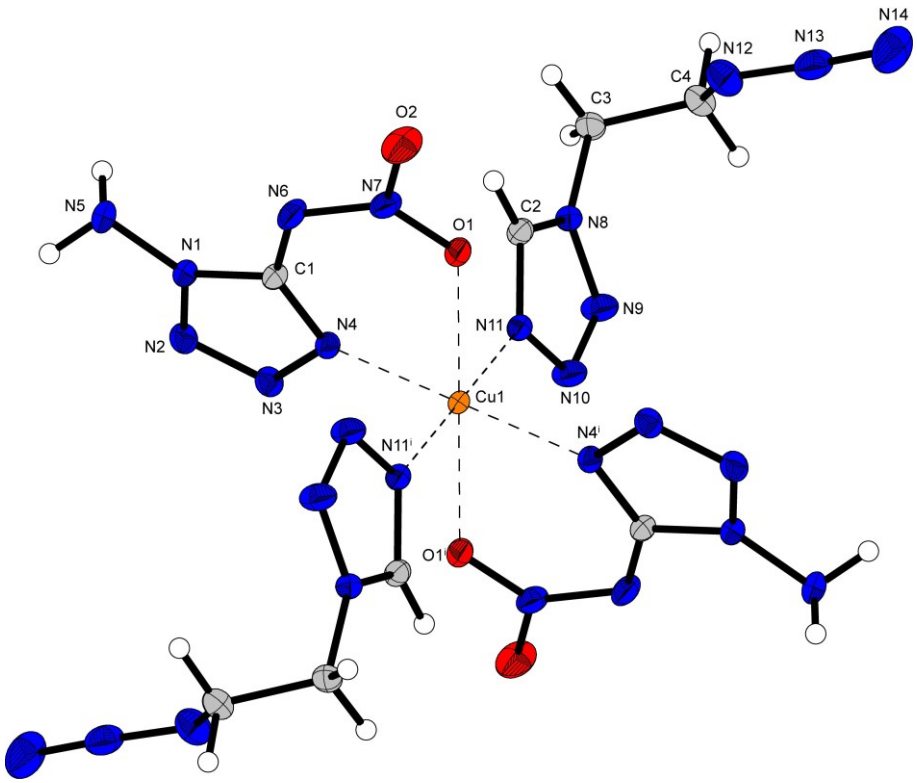

Figure 8. Crystal structure of $[Cu(ANIT)_2(1\text{-}AET)_2]$ (**7**). Selected bond lengths [Å]: Cu1–O1 2.3119(11), Cu1–N4 1.9823(12), Cu1–N11 2.0147(13); Selected bond angles [°]: O1–Cu1–N4 76.75(5), O1–Cu1–N11 86.36(5), N4–Cu1–N11 89.24(5); Symmetry codes: (i): 1−x, 1−y, 1−z.

While **7** crystallized in the triclinic space group $P\bar{1}$, crystallization of **8** occurs in the monoclinic space group $P2_1/n$. The direct comparison shows, that the recalculated room temperature density decreases from 1.864 to 1.731 g cm^{-3} by increasing the chain length of the ligand from 1-AET to 1-APT.

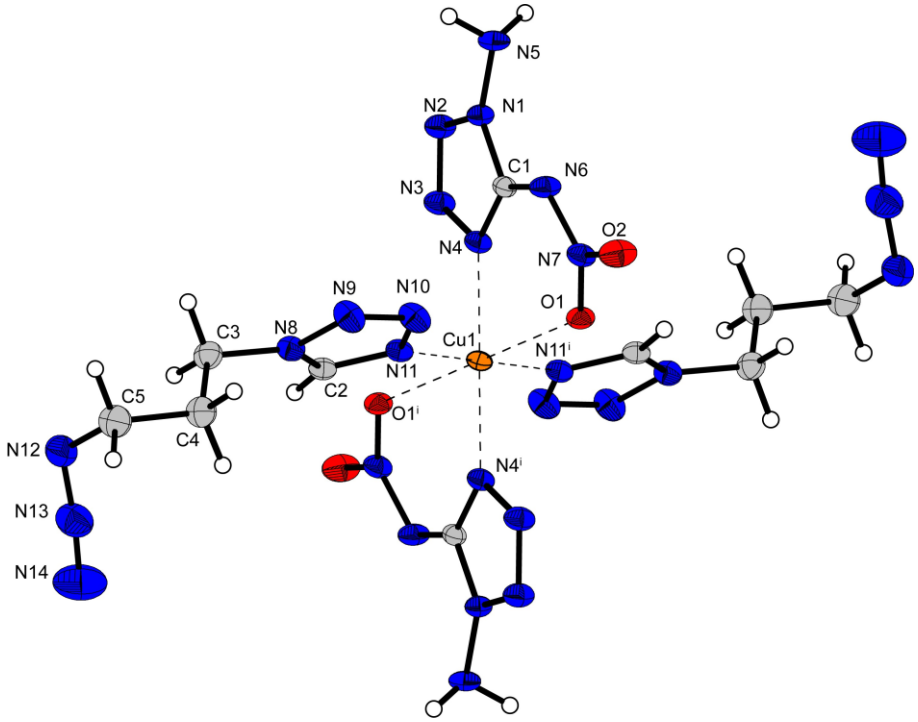

Figure 9. Crystal structure of $[Cu(ANIT)_2(APT)_2]$ (**8**). Selected bond lengths [Å]: Cu1–O1 2.3308(14), Cu1–N11 2.0034(17), Cu1–N4 1.9969(15); Selected bond angles [°]: N11–Cu1–O1 89.95(6), N4–Cu1–O1 77.17(6), N4–Cu1–N11 89.89(7); Symmetry codes: (i): 1−x, 1−y, 1−z.

Single crystals of $[Fe(ANIT)_2(H_2O)_2] \cdot 2\ H_2O$ (**9**) were obtained by letting the filtrate of the precipitation evaporate at room temperature. Interestingly, **9** did not crystallize in the usual pattern, which was observed for the $[Cu(ANIT)_2(L)_2]$-type. Cu(II) seems to favor coordination over the *N*4-position of the tetrazole ring, forming a six-membered ring with the nitro group. In **9** however, coordination occurs via the amino group and the nitrimine's nitrogen to form five-membered rings. The crystal structure (Figure 10) reveals, that this is accompanied with significantly longer distances between the Fe(II)-center and its ligands compared to the distances observed for **1**.

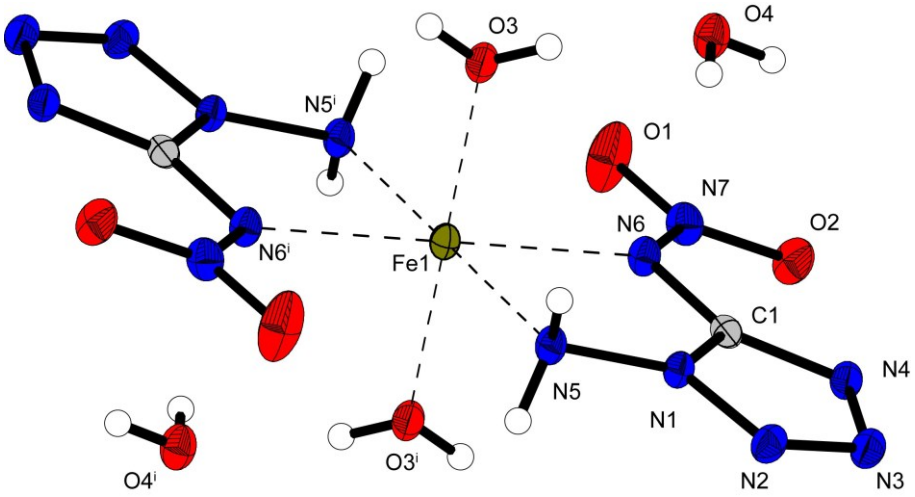

Figure 10. Crystal structure of $[Fe(ANIT)_2(H_2O)_2] \cdot 2\,H_2O$ (**9**). Selected bond lengths [Å]: Fe1–O3 2.0649(10), Fe1–N5 2.2642(11), Fe1–N6 2.1674(11); Selected bond angles [°]: O3–Fe1–N5 90.31(4), O3–Fe1–N6 91.95(4), N6–Fe1–N5 76.63(4); Symmetry codes: (i): 2−x, 1−y, −z.

8.2.3 Energetic Properties

Evaluations of the neutral compound HANIT and the precursor substance NH_4ANIT have been previously reported. [26] The potential of ANIT as a highly energetic anion is therefore of no doubt. Therefore, the substances produced in this work, were characterized for their potential to serve as primary explosives. The thermal stabilities were measured by differential thermal analyses with an OZM DTA 551-ex. Endothermic signals were further investigated for mass loss with a Perkin Elmer TGA4000 and melting points with a Büchi B-540 device. The onset of the endothermic peak of $[Cu(ANIT)_2(H_2O)_2]$, which was observed at 87 °C in the DTA was confirmed to be the loss of the two aqua ligands by TGA. Interestingly, the differential thermal analysis of $[Cu(ANIT)_2(\mu\text{-}1,1\text{-dtb})]$ (**5a**) and $[Cu(ANIT)_2(\mu\text{-}1,1\text{-dtb})] \cdot 0.5$ 1,1-dtb (**5b**) suggests, that the incorporation of the additional 1,1-dtb leads to a decrease of thermal stability. Impact and Friction sensitivities were determined on BAM standard devices using the 1 of 6 method. The sensitivities against electrostatic discharge (ESD) were obtained with an OZM XSpark10 device. The mechanical sensitivities, which were observed, result in classification of all compounds as very sensitive to impact and very sensitive or even extremely sensitive (**1**, **6** and **7**) to friction according to the UN Recommendations on the Transport of Dangerous Goods. [38] The surprisingly high sensitivity of **1** and **5a** (compared to **3**,

4 and **5b**) can be explained by their zigzag oriented coordination spheres. All other structures obtained show no signs of alternation of plane orientation. The respective values can be found in Table 1. As first insights in the performances of the ECCs, hot plate (HP) and hot needle (HN) tests were performed as shown in Figure 11. These tests give an information of the reaction the substances show towards rapid heating in open and confined environment. Obtaining a detonation or sharp deflagration in these tests can indicate the potential to initiate PETN in detonator setups.

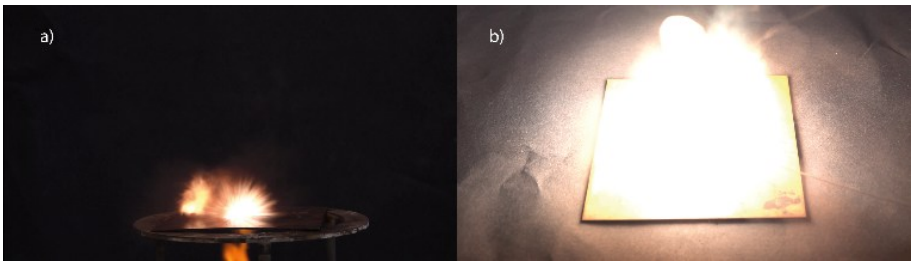

Figure 11. a) Hot plate and **b)** hot needle test of $[Cu(ANIT)_2(H_2O)_2]$ (**1**).

For this reason, compounds **1** ($[Cu(ANIT)_2(H_2O)_2]$), **3** ($[Cu(ANIT)_2(1,1\text{-dte})_2]$), **5a** ($[Cu(ANIT)_2(\mu\text{-}1,1\text{-dtb})]$), **7** ($[Cu(ANIT)_2(1\text{-AET})_2]$), **8** ($[Cu(ANIT)_2(1\text{-APT})_2]$) and **9** ($[Fe(ANIT)_2(H_2O)_2] \cdot 2\ H_2O$) were tested for their initiation capability. Therefore, 200 mg of PETN (< 100 μm) was compressed into a copper detonator shell by lowering an 8 kg weight onto. The shell was then placed on a copper witness plate, filled with the substance of interest (50/150 mg) and ignited by a type A electrical igniter. A schematic cross-section of the setup can be seen in Figure 12. The test is considered positive in cases of penetration of the witness plate.

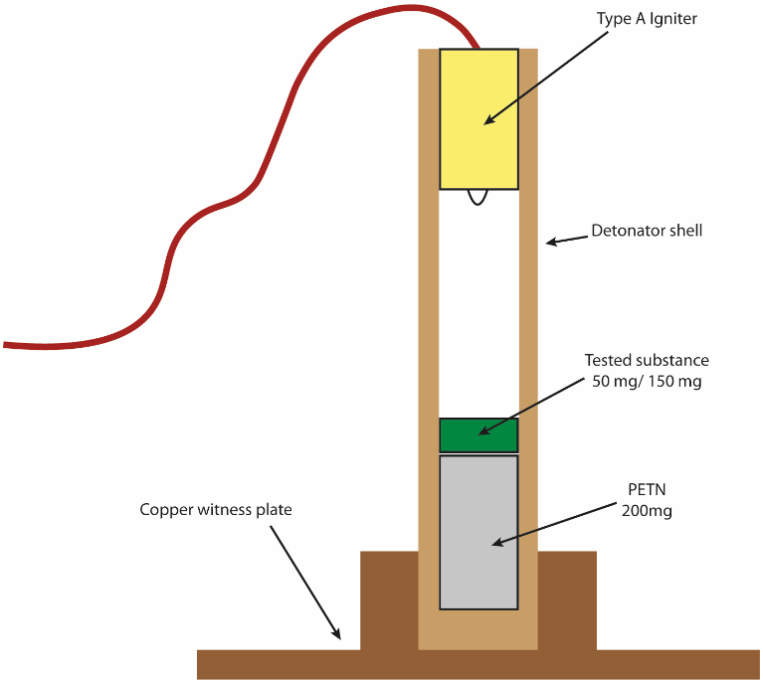

Figure 12. Schematic structure of the initiation test setup.

As **3**, **5a**, **7**, **8** and **9** did not manage to initiate the PETN charge successfully with 50 mg of substance, the amounts were increased to 150 mg. This led to an increased fragmentation and deformation of the shell in the cases of **3**, **5a** and **8**, without successful initiation. The outcome of the initiation test with **9** is not included in Figure 13, as no change to the setup was visible. Only 150 mg of **7** managed to undergo a deflagration to detonation transition (DDT) and transmit this detonation to the PETN completely. This might be a result of the increased carbon content in $[Cu(ANIT)_2(1\text{-}AET)_2]$ compared to $[Cu(ANIT)_2(H_2O)_2]$. While the sum formula of $[Cu(ANIT)_2(H_2O)_2]$ theoretically allows for full conversion of the compound into Cu, N_2, H_2O, and CO, $[Cu(ANIT)_2(1\text{-}AET)_2]$ shows a significant change of the fuel to oxidizer ratio. This balance of fuel to oxidizer has previously been shown to influence the potential of ECCs. [39-41]

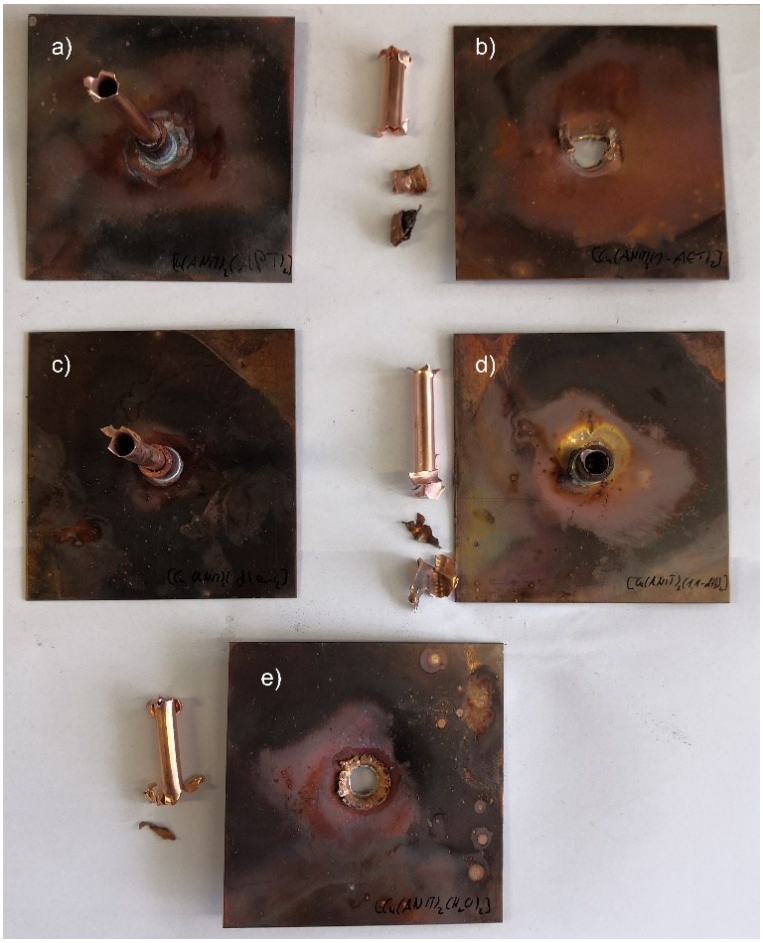

Figure 13. Outcomes of the PETN initiation tests: **a)** $[Cu(ANIT)_2(1\text{-}APT)_2]$ (**8**), **b)** $[Cu(ANIT)_2(1\text{-}AET)_2]$ (**7**), **c)** $[Cu(ANIT)_2(1,1\text{-}dte)_2]$ (**3**), **d)** $[Cu(ANIT)_2(\mu\text{-}1,1\text{-}dtb)_2]$ (**5a**), **e)** $[Cu(ANIT)_2(H_2O)_2]$ (**1**).

Table 1. Thermal stability and sensitivities to external stimuli of compounds **1–9**.

Compound	No.	T_{endo}[a] [°C]	T_{exo}[b] [°C]	IS[c] [J]	FS[d] [N]	ESD[e] [mJ]	HP[f]	HN[g]	Initiation
$[Cu(ANIT)_2(H_2O)_2]$	**1**	87	219	<1	2.5	13	Det.	Def.	Pos.
$[Cu(ANIT)_2(en)_2]$	**2**	117	178	3	360	120	Def.	Dec.	-
$[Cu(ANIT)_2(1,1\text{-dte})_2]$	**3**	-	177	<1	30	200	Def.	Det.	Neg.[k]
$[Cu(ANIT)_2(1,1\text{-dtp})_2]$	**4**	-	167	<1	54	200	Def.	Def.	-
$[Cu(ANIT)_2(\mu\text{-}1,1\text{-dtb})]$	**5a**	-	169	<1	20	50	Det.	Det.	Neg.[k]
$[Cu(ANIT)_2(\mu\text{-}1,1\text{-dtb})] \cdot 0.5$ 1,1-dtb	**5b**	-	156	<1	54	50	Def.	Dec.	-
$[Cu(ANIT)_2(1\text{-NET})_2]$	**6**	-	151	<1	8	160	Def.	Def.	-
$[Cu(ANIT)_2(1\text{-AET})_2]$	**7**	-	159	<1	6	20	Def.	Det.	Pos.[k]
$[Cu(ANIT)_2(1\text{-APT})_2]$	**8**	-	167	<1	20	120	Def.	Det.	Neg.[k]
$[Fe(ANIT)_2(H_2O)_2] \cdot 2\ H_2O$	**9**	118[h]	118[h]	15	288	60	Det.	Dec.	Neg.[k]
DBX-1 [7,9]		-	330[i]	<1	<0.1	0.012[j]	Det.	Det.	Pos.
LA (RD-1333) [7,13,42]		-	320-350	4	≤0.1	0.007–5	Det.	Det.	Pos.

[a] Onset temperature of endothermic event in the DTA (heating rate $\beta = 5$ °C min^{-1}), indicating a melting point of the compound. [b] Onset of exothermic event in the DTA. [c] Impact sensitivity (BAM drophammer (1 of 6)). [d] Friction sensitivity (BAM friction tester (1 of 6)). [e] Electrostatic discharge devise (OZM XSpark10). [f] Hot plate test (det.: detonation, def.: deflagration, dec.: decomposition, comb.: combustion). [g] Hot needle test (det.: detonation, def.: deflagration, dec.: decomposition, comb.: combustion). [h] endo to exo transition. [i] $\beta = 20$ K min^{-1}. [j] Minimum Fire Level. [k] 150 mg of substance, 200 mg of PETN.

Apart from the initiation capability and sensitivity of a substance, a major factor for its value is processability. The common technique of loading primary explosives volumetrically calls for a certain flowability of the substance. [43] A narrow particle size distribution, with low amounts of very fine particles and high sphericity contribute to this flowability. [44] Typically, very fine particles are removed during production by filtration of the product through grounded metal sieves of a certain mesh. This ensures the removal of very fine dust, which can negatively influence the powder properties, such as the sensitivity to electrostatic discharge, which is influenced by the particle size. [45] Furthermore, the particle sizes and shapes should be as reproducible as possible. With a strategy for the precipitation of the compounds **1** and **7** from aqueous medium a first advantage for the production is the use of non-toxic, non-flammable solvent. To investigate other impact factors of processability, the products of the precipitation attempts were analyzed in *i*-PrOH using a Microtrac SYNC particle size analyzer. Figure 14 shows the particle size distribution of both compounds, which reveal an even distribution of particles with a majority between 10–100 µm. These particles furthermore were detected to be mostly spherical, allowing a good flowability of the powder.

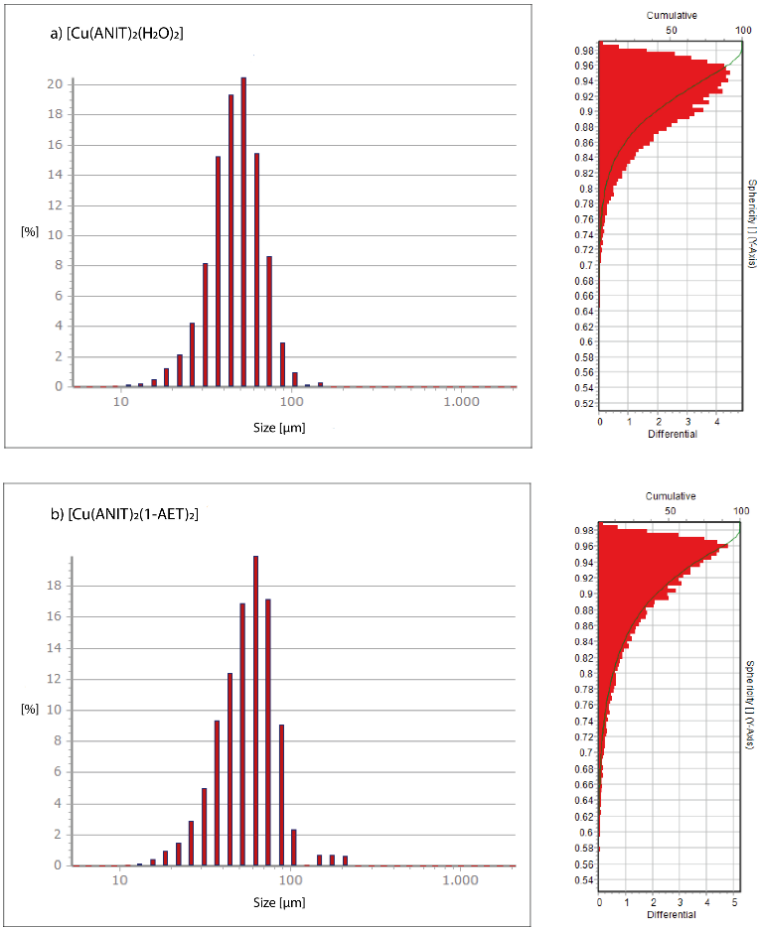

Figure 14. Particle size measurement data obtained by Microtrac SYNC of **a)** $[Cu(ANIT)_2(H_2O)_2]$ (**1**) (d_{10}: 24.63 µm, d_{50}: 52.98 µm, d_{90}: 94.72 µm) and **b)** $[Cu(ANIT)_2(1\text{-}AET)_2]$ (**7**) (d_{10}: 23.36 µm, d_{50}: 46.37 µm, d_{90}: 79.07 µm).

Figure 15 shows scanning electron microscope images of $[Cu(ANIT)_2(H_2O)_2]$ (**1**) at 120× (left), 700× (middle), and 3300× (right) magnification as well as $[Cu(ANIT)_2(1\text{-}AET)_2]$ (**7**) at 70× (left), 550× (middle), and 1200× (right) magnification. The images reveal the nature of the primary particles during crystallization. Compound **1**, when precipitated according to the modified general procedure B consists of intergrown needles, which form spherical secondary particles, that were observed in the particle size measurements. Compound **7** on the other hand can be precipitated according to general procedure B to form intergrown platelets. These again did form secondary particles of spherical nature. The full-sized images can be found in the supporting information.

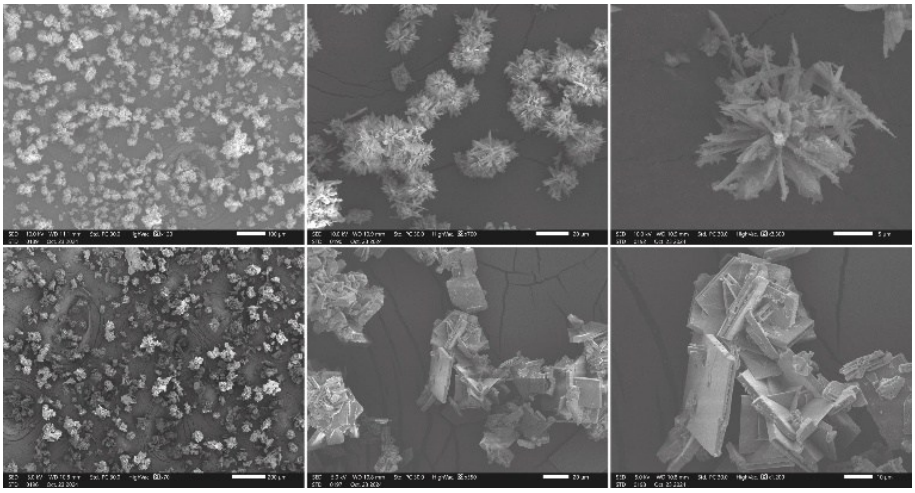

Figure 15. Scanning electron microscope images of top: $[Cu(ANIT)_2(H_2O)_2]$ (**1**) and bottom: $[Cu(ANIT)_2(1\text{-}AET)_2]$ (**7**).

8.3 Conclusion

In summary, nine new Energetic Coordination Compounds, including the easily available and highly energetic anion 1-amino-5-nitriminotetrazolate were introduced and investigated concerning their physicochemical properties. Hereby, an important insight on the safety of handling of compounds of the type $[Cu(ANIT)_2(L)_2]$ is generated. Direct comparison with the commercially used lead azide, as well as the green alternative copper(I) nitrotetrazolate (DBX-1) shows, that this type of ECCs is mechanically more stable, yet of lower thermal stability. Similar to DBX-1, most ECCs presented in this work, can be precipitated from aqueous solution. Performance tests revealed, that initiation of PETN is feasible with 150 mg of $[Cu(ANIT)_2(1\text{-}AET)_2]$ and 50 mg of $[Cu(ANIT)_2(H_2O)_2]$. The observed high sphericity and even particle size distribution are good perquisites for the processing of both compounds, as they allow even filling of the detonator shells.

8.4 Experimental Section

Caution! All investigated compounds are energetic materials and some of them show sensitivities towards various stimuli (e.g. elevated temperatures, impact, friction or electronic discharge). Although no hazards occurred, proper security precautions (safety glasses, face shield, earthed equipment and shoes, leather jacket, Kevlar sleeves, and earplugs) have to be worn while synthesizing and handling the described compounds.

General Procedure A for the formation of $[Cu(ANIT)_2(H_2O)_2]$ (1) and the ECCs 2–8:
NH_4ANIT was prepared according to the literature. [26] 81.1 mg (0.50 mmol. 2.0 eq.) of NH_4ANIT was then dissolved in water (10 mL) at 60 °C. $Cu(NO_3)_2 \cdot 3\ H_2O$ (60.4 mg, 0.25 mmol, 1.0 eq.) was then added to the solution, resulting in a change of color from yellow to green. By addition of a second aqueous solution (5 mL) of the respective ligand, the ECCs **2**–**8** can be formed. After stirring at 60 °C for 10 min, the solutions can be transferred to a crystallization dish. After 4–7 days, the compounds of interest crystallized, could be filtered off and washed with little cold H_2O and EtOH.
By allowing the solvent to evaporate at room temperature, instead of the addition of ligands, single crystals of **1** can be obtained. Crystals of **1** were also obtained by using small polar tetrazoles as ligands.

General Procedure B for the precipitation of the ECCs 3–9:
To obtain the ECCs in a more homogeneous form, precipitation can be performed by first dissolving 81.1 mg (0.50 mmol. 2.0 eq.) of NH_4ANIT and the respective ligand in water (4 mL) at 60 °C. A solution of $CuSO_4 \cdot 5\ H_2O$ (62.4 mg, 0.25 mmol, 1.0 eq.) in 1 mL of water is then added dropwise upon stirring for 10 minutes. Cooling to rt, while stirring for 20 minutes, leads to precipitation of the ECC from aqueous solution. The ECC can then be filtered off, washed with small amounts of cold water, followed by EtOH and drying on air.

$[Cu(ANIT)_2(H_2O)_2]$ (1):
NH_4ANIT (81.1 mg, 0.50 mmol, 2.0 eq.) is dissolved in 3 mL of deionized water and stirred at 60 °C. A solution of $CuSO_4 \cdot 5\ H_2O$ (62.4 mg, 0.25 mmol, 1.0 eq.) in 1 mL of water is then added dropwise upon stirring for 10 minutes. The solution is allowed to cool to room temperature and stirred for 30 min, during which precipitation of a luminous green solid occurs. The suspension is then filtered off, washed with little water and EtOH before drying on air. This procedure yields 50.3 mg of **1** (0.13 mmol, 52 %). **DTA** (5 °C min^{-1}) onset: 87 °C (endothermic), 219 °C (exothermic). **IR** (ATR, cm^{-1}): $\tilde{\nu}$ = 3452 (m), 3338 (w), 3287 (w), 3192 (w), 1622 (m), 1533 (m), 1491 (m), 1475 (m), 1394 (vs), 1336 (s), 1313 (vs), 1258 (vs), 1149 (m), 1116 (m), 1042 (m), 1014 (s), 898 (m), 881 (m), 776 (m), 756 (m), 730 (s), 707 (m), 685 (m), 549 (s), 529 (s), 484 (s), 425 (s), 411 (s), 404 (s). **EA** ($C_2H_8CuN_{14}O_6$, 387.72) calcd.: C 6.20, H 2.08, N 50.58 %; found: C 6.46, H 2.41, N

49.92 %. **BAM drophammer**: < 1 J. **Friction tester:** 2.5 N. **ESD**: 13 mJ (at grain size <100 μm).

[Cu(ANIT)$_2$(en)$_2$] (2):

Addition of ethylenediamine (30.1 mg, 0.50 mmol, 2.0 eq.), dissolved in 5 mL of water to the aqueous solution of **1** (10 mL), led to intense purple discoloration. Compound **2** (36.6 mg, 0.08 mmol) was obtained in a yield of 32 %. **DTA** (5 °C min^{-1}) onset: 117 °C (endothermic), 178 °C (exothermic). **IR** (ATR, cm^{-1}): $\tilde{\nu}$ = 3320 (m), 3290 (m), 3278 (m), 3244 (m), 3220 (m), 3198 (m), 3156 (m), 2952 (w), 2901 (w), 1656 (w), 1626 (m), 1588 (m), 1508 (m), 1457 (m), 1436 (w), 1428 (w), 1411 (m), 1401 (m), 1383 (m), 1370 (s), 1307 (vs), 1287 (s), 1265 (vs), 1160 (m), 1107 (m), 1090 (m), 1042 (s), 1016 (s), 1005 (s), 983 (m), 960 (m), 883 (m), 823 (m), 778 (m), 729 (s), 706 (m), 701 (m), 679 (m), 544 (m), 531 (m), 521 (m), 475 (m), 461 (m), 418 (w). **EA** ($C_6H_{20}CuN_{18}O_4$, 471.89) calcd.: C 15.27, H 4.27, N 53.43 %; found: C 15.14, H 4.46, N 49.51 %. **BAM drophammer**: 3 J. **Friction tester:** 360 N. **ESD**: 120 mJ (at grain size 100–500 μm).

[Cu(ANIT)$_2$(1,1-dte)$_2$] (3):

Addition of 1,2-di(1*H*-tetrazol-1-yl)ethane (83.1 mg, 0.50 mmol, 2.0 eq.), dissolved in 5 mL of water to the aqueous solution of **1** (10 mL), yielded **3** (133.6 mg, 0.20 mmol), which was obtained in a yield of 80 %. **DTA** (5 °C min^{-1}) onset: 177 °C (exothermic). **IR** (ATR, cm^{-1}): $\tilde{\nu}$ = 3364 (w), 3095 (m), 1737 (m), 1627 (w), 1535 (w), 1508 (m), 1474 (m), 1458 (m), 1431 (m), 1421 (s), 1402 (s), 1380 (m), 1364 (m), 1334 (m), 1287 (s), 1236 (vs), 1192 (vs), 1174 (s), 1148 (s), 1106 (s), 1094 (vs), 1048 (m), 1012 (m), 999 (m), 970 (m), 947 (m), 926 (m), 910 (m), 891 (s), 843 (m), 797 (m), 769 (m), 763 (m), 726 (m), 705 (m), 688 (m), 670 (m), 657 (s), 640 (s), 529 (m), 491 (m), 473 (m). **EA** ($C_{10}H_{16}CuN_{30}O_4$, 683.99) calcd.: C 17.56, H 2.36, N 61.44 %; found: C 17.64, H 2.53, N 60.68 %. **BAM drophammer**: < 1 J. **Friction tester:** 30 N. **ESD**: 200 mJ (at grain size < 100 μm).

[Cu(ANIT)$_2$(1,1-dtp)$_2$] (4):

Addition of 1,3-di(1*H*-tetrazol-1-yl)propane (90.1 mg, 0.50 mmol, 2.0 eq.), dissolved in 5 mL of water to the aqueous solution of **1** (10 mL), yielded **4** (122 mg, 0.17 mmol). **4** was obtained in a yield of 68 %. **DTA** (5 °C min^{-1}) onset: 167 °C (exothermic). **IR** (ATR, cm^{-1}): $\tilde{\nu}$ = 3327 (w), 3214 (w), 3088 (w), 2987 (w), 1650 (vw), 1509 (m), 1465 (m), 1456 (m), 1445 (m), 1434 (m), 1414 (s), 1396 (m), 1350 (m), 1324 (m), 1284 (s), 1237 (s), 1190

(m), 1171 (s), 1162 (m), 1140 (m), 1104 (vs), 1044 (m), 1035 (m), 1019 (m), 1005 (m), 967 (m), 912 (m), 896 (m), 876 (m), 851 (m), 832 (m), 774 (m), 758 (m), 736 (m), 723 (w), 701 (m), 679 (w), 667 (m), 655 (m), 632 (m), 618 (m), 610 (m), 525 (w), 468 (m), 430 (m), 422 (w). **EA** ($C_{12}H_{20}CuN_{30}O_4$, 712.04) calcd.: C 20.24, H 2.83, N 59.01 %; found: C 20.30, H 3.01, N 58.77 %. **BAM drophammer**: < 1 J. **Friction tester:** 54 N. **ESD**: 200 mJ (at grain size < 100 µm).

[Cu(ANIT)$_2$(*µ*-1,1-dtb)] (5a):

With 1,4-di(1*H*-tetrazol-1-yl)butane (73.8 mg, 0.38 mmol, 1.5 eq.), precipitation according to General Procedure B yielded **5a** (102.5 mg, 0.19 mmol, 76 %). **DTA** (5 °C min^{-1}) onset: 169 °C (exothermic). **IR** (ATR, cm^{-1}): $\tilde{\nu}$ = 3313 (w), 3216 (w), 3188 (w), 3126 (w), 1640 (w), 1520 (m), 1512 (m), 1472 (m), 1460 (m), 1441 (m), 1418 (s), 1404 (s), 1367 (m), 1327 (s), 1290 (vs), 1254 (s), 1201 (m), 1191 (m), 1180 (m), 1148 (m), 1108 (s), 1083 (m), 1073 (m), 1016 (m), 1004 (m), 969 (m), 937 (m), 889 (m), 875 (m), 823 (w), 796 (m), 773 (m), 759 (m), 733 (m), 721 (w), 707 (w), 675 (m), 668 (m), 648 (m), 524 (w), 473 (m), 459 (m). **EA** ($C_8H_{14}CuN_{22}O_4$, 545.90) calcd.: C 17.60, H 2.59, N 56.45 %; found: C 17.74, H 2.92, N 55.62 %. **BAM drophammer**: < 1 J. **Friction tester:** 20 N. **ESD**: 50 mJ (at grain size < 100 µm).

[Cu(ANIT)$_2$(*µ*-1,1-dtb)] · 0.5 1,1-dtb (5b):

Addition of 1,4-di(1*H*-tetrazol-1-yl)butane (73.8 mg, 0.38 mmol, 1.5 eq.), dissolved in 5 mL of water to the aqueous solution of **1** (10 mL), yielded **5b** (104.0 mg, 0.16 mmol, 64 %). **DTA** (5 °C min^{-1}) onset: 156 °C (exothermic). **IR** (ATR, cm^{-1}): $\tilde{\nu}$ = 3318 (m), 3312 (m), 3306 (m), 3280 (m), 3194 (w), 3128 (m), 1673 (w), 1641 (w), 1520 (m), 1513 (m), 1472 (m), 1460 (m), 1439 (m), 1417 (s), 1404 (s), 1367 (m), 1326 (s), 1289 (vs), 1254 (s), 1201 (m), 1190 (m), 1182 (m), 1148 (m), 1108 (s), 1082 (w), 1071 (w), 1043 (m), 1016 (m), 1004 (m), 939 (m), 888 (m), 828 (w), 797 (m), 773 (m), 760 (m), 733 (m), 721 (w), 707 (m), 675 (m), 668 (m), 647 (m), 526 (w), 472 (m), 462 (m), 456 (m), 439 (m), 428 (m), 424 (m), 419 (m). **EA** ($C_{22}H_{19}CuN_{26}O_4$, 642.99) calcd.: C 20.55, H 2.98, N 56.64 %; found: C 20.81, H 2.87, N 56.79 %. **BAM drophammer**: < 1 J. **Friction tester:** 54 N. **ESD**: 50 mJ (at grain size 100–500 µm).

[Cu(ANIT)$_2$(1-NET)$_2$] (6):

Addition of 2-(1*H*-tetrazol-1-yl)ethyl nitrate (79.6 mg, 0.50 mmol, 2.0 eq.), dissolved in 5 mL of water to the aqueous solution of **1** (10 mL), yielded **6** (123.0 mg, 0.18 mmol), which was obtained in a yield of 72 %. **DTA** (5 °C min^{-1}) onset: 151 °C (exothermic). **IR** (ATR, cm^{-1}): $\tilde{\nu}$ = 3367 (w), 3217 (w), 3138 (w), 1634 (s), 1520 (m), 1506 (m), 1463 (m), 1450 (m), 1434 (m), 1397 (s), 1366 (m), 1337 (m), 1287 (vs), 1242 (vs), 1180 (s), 1171 (s), 1102 (s), 1073 (w), 1064 (w), 1026 (m), 1013 (m), 981 (m), 883 (s), 849 (s), 770 (m), 755 (m), 735 (s), 718 (m), 703 (m), 674 (m), 660 (m), 650 (s), 593 (w), 565 (m), 540 (m), 527 (w), 492 (w), 471 (m), 404 (m). **EA** ($C_8H_{14}CuN_{24}O_{10}$, 669.90) calcd.: C 14.34, H 2.11, N 50.18 %; found: C 14.27, H 2.36, N 49.87 %. **BAM drophammer**: < 1 J. **Friction tester:** 8 N. **ESD**: 160 mJ (at grain size 100–500 µm).

[Cu(ANIT)$_2$(1-AET)$_2$] (7):

Addition of 1-(2-azidoethyl)-1*H*-tetrazole (69.6 mg, 0.50 mmol, 2.0 eq.), dissolved in 5 mL of water to the aqueous solution of **1** (10 mL), yielded **7** (69.5 mg, 0.11 mmol, 44 %). Precipitation according to general procedure B increased the yield to 71 % (112.4 mg, 0.18 mmol). **DTA** (5 °C min^{-1}) onset: 159 °C (exothermic). **IR** (ATR, cm^{-1}): $\tilde{\nu}$ = 3326 (w), 3215 (w), 3143 (m), 2139 (m), 2114 (m), 2099 (m), 1640 (w), 1541 (vw), 1510 (m), 1473 (m), 1458 (m), 1437 (m), 1414 (s), 1397 (s), 1377 (m), 1348 (s), 1338 (s), 1309 (s), 1286 (vs), 1249 (vs), 1176 (s), 1159 (s), 1101 (vs), 1065 (w), 1022 (s), 1011 (s), 953 (w), 920 (m), 897 (s), 835 (m), 800 (w), 769 (m), 761 (m), 734 (m), 721 (w), 706 (m), 677 (s), 652 (s), 625 (m), 579 (w), 558 (m), 526 (m), 496 (m), 468 (m), 414 (w). **EA** ($C_8H_{14}CuN_{28}O_4$, 629.94) calcd.: C 15.25, H 2.24, N 62.26 %; found: C 15.04, H 2.41, N 61.77 %. **BAM drophammer**: < 1 J. **Friction tester:** 6 N. **ESD**: 20 mJ (at grain size <100 µm).

[Cu(ANIT)$_2$(1-APT)$_2$] (8):

Addition of 1-(3-azidopropyl)-1*H*-tetrazole (76.6 mg, 0.50 mmol, 2.0 eq.), dissolved in 5 mL of water to the aqueous solution of **1** (10 mL), yielded **8** (111.9mg, 0.17 mmol). Therefore, it was obtained in a yield of 68 %. **DTA** (5 °C min^{-1}) onset: 167 °C (exothermic). **IR** (ATR, cm^{-1}): $\tilde{\nu}$ = 3328 (w), 3250 (w), 3238 (w), 3197 (w), 3129 (w), 2116 (m), 2091 (m), 2069 (w), 2057 (w), 2048 (w), 2039 (w), 2032 (w), 2025 (w), 1609 (w), 1523 (m), 1511 (w), 1478 (m), 1462 (m), 1446 (w), 1423 (s), 1409 (s), 1385 (m), 1364 (w), 1329 (s), 1285 (s), 1249 (vs), 1217 (s), 1190 (m), 1157 (m), 1108 (m), 1092 (m), 1066

(w), 1024 (m), 994 (w), 969 (m), 915 (m), 885 (w), 849 (m), 829 (w), 819 (w), 783 (w), 776 (m), 762 (w), 743 (w), 734 (m), 714 (m), 680 (w), 665 (m), 655 (m), 613 (w), 600 (w), 563 (w), 536 (w), 488 (w), 484 (w), 466 (m), 412 (w). **EA** ($C_{10}H_{18}CuN_{28}O_4$, 657.99) calcd.: C 18.25, H 2.76, N 59.60 %; found: C 18.51, H 2.71, N 58.97 %. **BAM drophammer**: < 1 J. **Friction tester:** 20 N. **ESD**: 120 mJ (at grain size < 100 µm).

$[Fe(ANIT)_2(H_2O)_2] \cdot 2\ H_2O$ (9):

NH_4ANIT (81.1 mg, 0.50 mmol, 2.0 eq.) is dissolved in 3 mL of deionized water and stirred at 60 °C. A solution of $FeSO_4 \cdot 1.5\ H_2O$ (38.0 mg, 0.25 mmol) in 1 mL of water is then added dropwise upon stirring for 10 minutes. The solution is allowed to cool to room temperature and stirred for 30 min, during which precipitation of a beige solid occurs. The suspension is then filtered off, washed with little water and EtOH before drying on air. Compound **9** is obtained in a yield of 68 % (71.6 mg, 0.17 mmol). **DTA** (5 °C min^{-1}) onset: 118 °C (endothermic to exothermic transition). **IR** (ATR, cm^{-1}): $\tilde{\nu}$ = 3533 (m), 3353 (m), 3281 (m), 3069 (m), 1667 (w), 1644 (w), 1616 (w), 1521 (s), 1476 (s), 1435 (s), 1418 (m), 1367 (w), 1323 (s), 1279 (s), 1269 (s), 1175 (m), 1110 (m), 1078 (s), 1031 (w), 972 (w), 911 (w), 775 (m), 734 (s), 716 (s), 697 (s), 590 (vs), 530 (s), 509 (m), 457 (m), 419 (m), 405 (m). **EA** ($C_2H_{12}FeN_{14}O_8$, 416.05) calcd.: C 5.77, H 2.91, N 47.13 %; found: C 5.80, H 3.05, N 45.80 %. **BAM drophammer**: 15 J. **Friction tester:** 288 N. **ESD**: 60 mJ (at grain size <100 µm).

8.5 Author Contributions

Dr. Maximilian Benz: writing – review & editing; Simon M. J. Endraß: writing – original draft, conceptualization, investigation; Prof. Dr. Dr. h.c. Thomas M. Klapötke: resources, funding acquisition; Dr. Jörg Stierstorfer: supervision, writing – review & editing; Sadiq Strey: investigation.

8.6 Acknowledgements

We gratefully acknowledge the financial support of this work by the Ludwig-Maximilians-Universität München. The authors would like to thank Marcus Lommel and Jan Cremers for their contribution to this work.

8.7 Notes and References

[1] M. A. Ilyushin, I. V. Tselinsky and I. V. Shugalei, *Cent. Eur. J. Energ. Mater.*, **2012**, 9, 293–327.

[2] DIRECTIVE 2011/65/EU OF THE EUROPEAN PARLIAMENT AND OF THE COUNCIL of 8 June 2011 on the restriction of the use of certain hazardous substances in electrical and electronic equipment, European Union, **2011**.

[3] COMMISSION DELEGATED DIRECTIVE (EU) 2021/647 of 15 January 2021 amending, for the purposes of adapting to scientific and technical progress, Annex III to Directive 2011/65/EU of the European Parliament and of the Council as regards an exemption for the use of certain lead and hexavalent chromium compounds in electric and electronic initiators of explosives for civil (professional) use, European Union, **2021**.

[4] M. H. V. Huynh, M. A. Hiskey, T. J. Meyer and M. Wetzler, *Proc. Natl. Acad. Sci. U.S.A.*, **2006**, 103, 5409–5412.

[5] P. J. Landrigan, A. S. McKinney, L. C. Hopkins, W. W. Rhodes, Jr, W. A. Price and D. H. Cox, *JAMA*, **1975**, 234, 394–397.

[6] D. R. S. Lima, M. L. S. Bezerra, E. B. Neves and F. R. Moreira, *Rev. Environ. Health*, **2011**, 26, 101–110.

[7] M. S. Gruhne, M. Lommel, M. H. H. Wurzenberger, N. Szimhardt, T. M. Klapötke and J. Stierstorfer, *Propellants, Explos. Pyrotech.*, **2020**, 45, 147–153.

[8] G. Geisberger, T. M. Klapötke and J. Stierstorfer, *Eur. J. Inorg. Chem.*, **2007**, 2007, 4743–4750.

[9] J. W. Fronabarger, M. D. Williams, W. B. Sanborn, J. G. Bragg, D. A. Parrish and M. Bichay, *Propellants, Explos. Pyrotech.*, **2011**, 36, 541–550.

[10] T. Wang, S. Bu, Z. Lu, B. Kuang, Z. Yi, Z. Xie, C. Zhang, Y. Li and J. Zhang, *Chem. Eng. J.*, **2023**, 457, 141267.

[11] T. Wang, S. Bu, K. Wang, L. Zhang, Z. Yi, C. Zhang, W. Cao, S. Zhu and J. Zhang, *Chem. Eng. J.*, **2023**, 452, 139472.

[12] T. Wang, Z. Lu, S. Bu, B. Kuang, L. Zhang, Z. Yi, K. Wang, S. Zhu and J. Zhang, *Def. Technol.*, **2024**, 31, 271–277.

[13] K. D. Oyler, in *Green Energetic Materials*, **2014**, pp. 103–132.

[14] N. Szimhardt, M. H. H. Wurzenberger, A. Beringer, L. J. Daumann and J. Stierstorfer, *J. Mater. Chem. A*, **2017**, 5, 23753–23765.

[15] M. H. H. Wurzenberger, N. Szimhardt and J. Stierstorfer, *Inorg. Chem.*, **2018**, 57, 7940–7949.

[16] G. Lei, W. Cheng, Z.-J. Lu, T. Zhang, Z. Li and J. Zhang, *Mater. Horiz.*, **2023**, 10, 5775–5781.

[17] O. Isayev, B. Rasulev, L. Gorb and J. Leszczynski, *Mol. Divers.*, **2006**, 10, 233–245.

[18] J. A. Garrison and R. M. Herbst, *J. Org. Chem.*, **1957**, 22, 278–283.

[19] N. Fischer, T. M. Klapötke, D. G. Piercey and J. Stierstorfer, *Z. Anorg. Allg. Chem.*, **2012**, 638, 302–310.

[20] N. Fischer, T. M. Klapötke and J. Stierstorfer, *Z. Anorg. Allg. Chem.*, **2011**, 637, 1273–1276.

[21] D. Fischer, T. M. Klapötke and J. Stierstorfer, *Eur. J. Inorg. Chem.*, **2015**, 2015, 4628–4632.

[22] T. M. Klapötke, D. G. Piercey, N. Mehta, K. D. Oyler, M. Jorgensen, S. Lenahan, J. S. Salan, J. W. Fronabarger and M. D. Williams, *Z. Anorg. Allg. Chem.*, **2013**, 639, 681–688.

[23] R. H. Muir, J. Bragg, A. Pearsall, M. Jorgensen, B. Sims, K. Yonoski, N. Mehta and J. S. Salan, *Org. Process Res. Dev.*, **2021**, 25, 1882–1888.

[24] W. H. Gilligan and M. J. Kamlet, US Department of Navy, US4093623A, **1977**.

[25] D. D. Ford, S. Lenahan, M. Jörgensen, P. Dubé, M. Delude, P. E. Concannon, S. R. Anderson, K. D. Oyler, G. Cheng, N. Mehta and J. S. Salan, *Org. Process Res. Dev.*, **2015**, 19, 673–680.

[26] M. Benz, T. M. Klapötke, J. Stierstorfer and M. Voggenreiter, *ACS Appl. Energy Mater.*, **2023**, 1, 3–6.

[27] J. Schweifer, P. Weinberger, K. Mereiter, M. Boca, C. Reichl, G. Wiesinger, G. Hilscher, P. J. van Koningsbruggen, H. Kooijman, M. Grunert and W. Linert, *Inorg. Chim. Acta*, **2002**, 339, 297–306.

[28] N. Szimhardt, M. H. H. Wurzenberger, T. M. Klapötke, J. T. Lechner, H. Reichherzer, C. C. Unger and J. Stierstorfer, *J. Mater. Chem. A*, **2018**, 6, 6565–6577.

[29] P. J. Van Koningsbruggen, Y. Garcia, H. Kooijman, A. L. Spek, J. G. Haasnoot, O. Kahn, J. Linares, E. Codjovi and F. Varret, *J. Chem. Soc., Dalton Trans.*, **2001**, 466–471.

[30] M. S. Gruhne, T. Lenz, M. Rösch, M. Lommel, M. H. H. Wurzenberger, T. M. Klapötke and J. Stierstorfer, *Dalton Trans.*, **2021**, 50, 10811–10825.

[31] M. H. H. Wurzenberger, M. S. Gruhne, M. Lommel, N. Szimhardt, T. M. Klapötke and J. Stierstorfer, *Chem. Asian J.*, **2019**, 14, 2018–2028.

[32] M. H. H. Wurzenberger, S. M. J. Endraß, M. Lommel, T. M. Klapötke and J. Stierstorfer, *ACS Appl. Energy Mater.*, **2020**, 3, 3798–3806.

[33] O. V. Dolomanov, L. J. Bourhis, R. J. Gildea, J. A. K. Howard and H. Puschmann, *J. Appl. Cryst.*, **2009**, 42, 339–341.

[34] G. M. Sheldrick, *Acta Crystallogr. Sect. A*, **2015**, 71, 3–8.

[35] *SHELXL-97*, University of Göttingen, G. M. Sheldrick, Germany, **1997**.

[36] G. M. Sheldrick, *Acta Crystallogr. Sect. A*, **2008**, 64, 112–122.

[37] *Diamond - Crystal and Molecular Structure Visualization*, Crystal Impact, H. Putz and K. Brandenburg, Bonn, Germany,

[38] Impact: insensitive > 40 J, less sensitive ≥ 35 J, sensitive ≥ 4 J, very sensitive ≤ 3 J; Friction: insensitive > 360 N, less sensitive = 360 N, sensitive < 360 N and > 80 N, very sensitive ≤ 80 N, extremely sensitive ≤ 10 N, According to: Recommendations on the Transport of Dangerous Goods, Manual of Tests and Criteria, 4$^{th.}$ Edition, New York-Geneva, **1999**.

[39] C. Zhang, T.-W. Wang, Z.-J. Lu, Z.-X. Yi, B.-L. Kuang, S. Bu, Z.-M. Xie, Y. Li, K. Wang and J.-G. Zhang, *J. Phys. Chem. C*, **2023**, 127, 12923–12930.

[40] T.-W. Wang, Z.-J. Lu, Z.-X. Yi, Z.-M. Xie, L. Zhang, B.-L. Kuang, Y. Li and J.-G. Zhang, *Cryst. Growth Des.*, **2023**, 23, 5528–5534

[41] S. M. J. Endraß, T. M. Klapötke, M. Lommel, J. Stierstorfer, M. L. Weidemann and M. Werner, *ChemPlusChem*, **2024**, 89, e202400031.

[42] T. M. Klapötke, *Energetic Materials Encyclopedia*, DeGruyter, Berlin/Boston, 2nd edn., **2021**.

[43] R. Matyáš and J. Pachman, in *Primary Explosives*, Springer Berlin Heidelberg, Berlin, Heidelberg, **2013**, pp. 11–36.

[44] A. J. Tulis, *J. Hazard. Mat.*, **1980**, 4, 3–10.

[45] T. M. Klapötke, *Chemistry of High-Energy Materials*, De Gruyter, Berlin, Boston, 6th edn., **2022**.

8.8 Supporting Information

8.8.1 Compound Overview

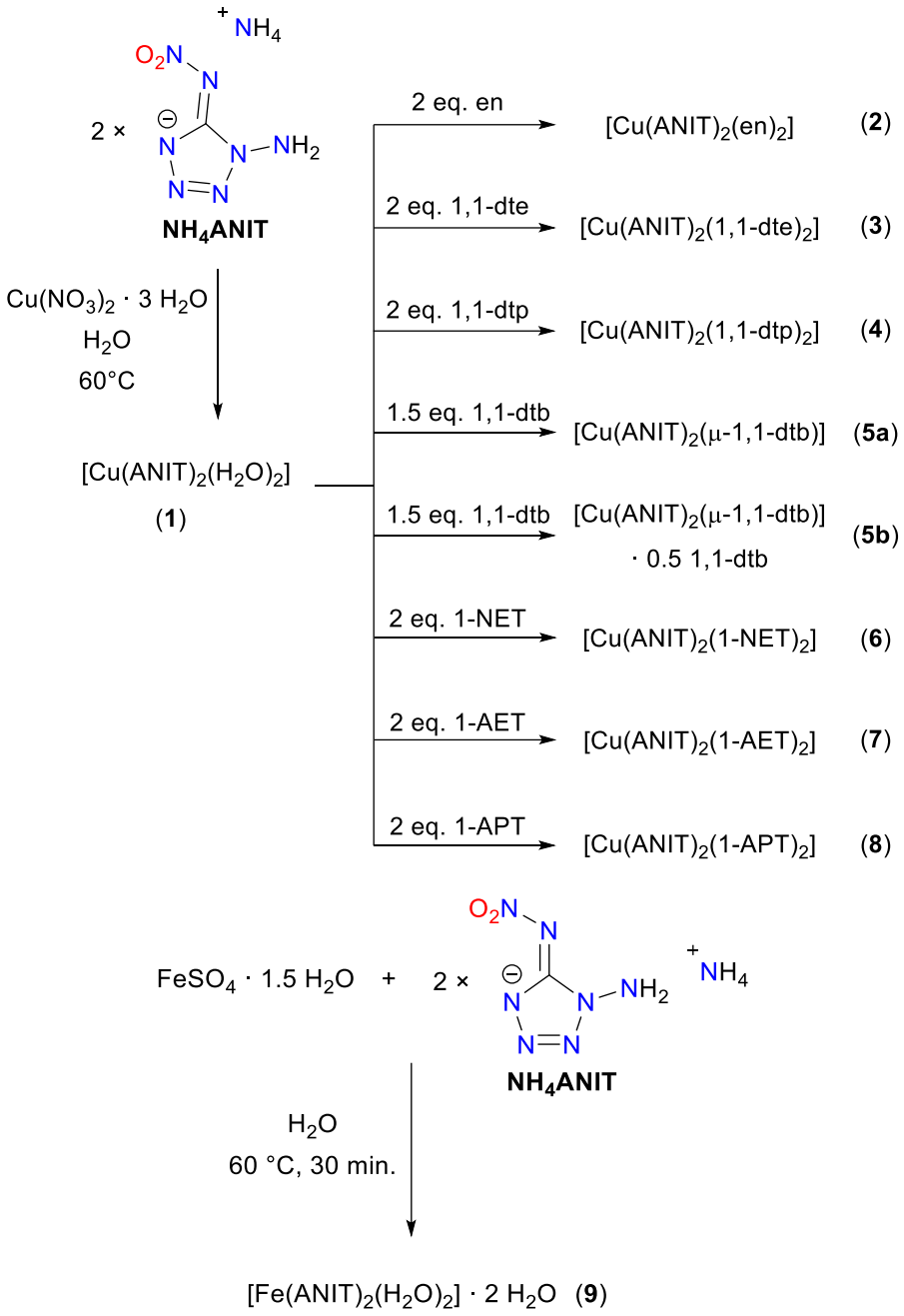

8.8.2 Single Crystal X-Ray Diffraction

For all crystalline compounds an Oxford Xcalibur3 diffractometer with a CCD area detector or Bruker D8 Venture TXS diffractometer equipped with a multilayer monochromator, a Photon 2 detector, and a rotating-anode generator were employed for data collection using Mo-Kα radiation (λ = 0.7107 Å). On the Oxford device, data collection and reduction were carried out using the CrysAlisPRO software. [S1] On the Bruker diffractometer, the data were collected with the Bruker Instrument Service v3.0.21, the data reduction was performed using the SAINT V8.18C software (Bruker AXS Inc., 2011). The structures were solved by direct methods (SHELXT [S2]), refined by full-matrix least-squares on *F2* (SHELXL [S3]) and finally checked using the PLATON software [S4] integrated in the WinGX [S2], [S5] or Olex2 [S6] software suite. The non-hydrogen atoms were refined anisotropically and the hydrogen atoms were located and freely refined. The absorptions were corrected by a SCALE3 ABSPACK or SADABS Bruker APEX3 multi-scan method. [S7], [S8] All DIAMOND4 [S9] plots are shown with thermal ellipsoids at the 50% probability level and hydrogen atoms are shown as small spheres of arbitrary radius.

Table S1. Crystallographic data and crystal structure refinement details of compounds **1**, **3** and **4**.

	$[Cu(ANIT)_2(H_2O)_2]$	$[Cu(ANIT)_2(1,1\text{-dte})_2]$	$[Cu(ANIT)_2(1,1\text{-dtp})_2]$
Formula	$C_2H_8CuN_{14}O_6$	$C_{10}H_{16}CuN_{30}O_4$	$C_{12}H_{20}CuN_{30}O_4$
FW [g mol^{-1}]	387.76	684.07	712.12
Crystal system	monoclinic	monoclinic	triclinic
Space group	$P2_1/n$ (No. 14)	$P2_1/c$ (No. 14)	$P\bar{1}$ (No. 2)
Color / Habit	Green Block	Blue Block	Blue Block
Size [mm]	0.08 x 0.10 x 0.20	0.06 x 0.10 x 0.20	0.10 x 0.40 x 0.50
a [Å]	5.605(3)	8.5508(2)	7.1719(5)
b [Å]	9.087(6)	11.3930(3)	8.6415(6)
c [Å]	11.608(7)	12.2836(3)	10.9893(9)
α [°]	90	90	81.323(6)
β [°]	95.790(12)	93.955(1)	77.233(6)
γ [°]	90	90	86.399(6)
V [Å^3]	588.2(6)	1193.81(5)	656.33(9)
Z	2	2	1
$\rho_{calc.}$ [g cm^{-3}]	2.19	1.903	1.802
μ [mm^{-1}]	1.93	1.009	0.922
F(000)	390	694	363
$\lambda_{MoK\alpha}$ [Å]	0.71073	0.71073	0.71073
T [K]	173	173	123
θ Min-Max [°]	3.5, 36.3	3.0, 33.2	1.9, 26.4
Dataset	−9: 9; −15: 15; −19: 19	−13: 13; −17: 17; −18: 18	−8: 8; −7: 10; −13: 13
Reflections collected	18072	33006	4779
Independent refl.	2861	4565	2631
R_{int}	0.034	0.064	0.049
Observed reflections	2539	3707	2256
Parameters	120	237	222
R_1 (obs)[a]	0.0262	0.034	0.0507
wR_2 (all data)[b]	0.069	0.0826	0.1419
S [c]	1.09	1.05	1.04
Resd. dens [e Å^{-3}]	−0.37, 0.48	−0.52, 0.35	−0.74, 0.94
Absorption correction	multi-scan	multi-scan	multi-scan
CCDC	2394591	2394593	2394588

[a] $R_1 = \Sigma||F_0|-|F_c||/\Sigma|F_0|$; [b] $wR_2 = [\Sigma[w(F_0^2-F_c^2)^2]/\Sigma[w(F_0)^2]]^{1/2}$; $w = [\sigma c^2(F_0^2)+(xP)^2+yP]^{-1}$ and $P=(F_0^2+2F_c^2)/3$; [c] $S = \{\Sigma[w(F_o^2-F_c^2)^2]/(n-p)\}^{1/2}$ (n = number of reflections; p = total number of parameters).

Table S2. Crystallographic data and crystal structure refinement details of compounds **5a**, **5b**, and **7**.

	[Cu(ANIT)$_2$(μ-1,1-dtb)]	[Cu(ANIT)$_2$(μ-1,1-dtb)] · 0.5 1,1-dtb	[Cu(ANIT)$_2$(1-AET)$_2$]
Formula	$C_8H_{14}CuN_{22}O_4$	$C_8H_{14}CuN_{22}O_4$, $C_3H_5N_4$	$C_8H_{14}CuN_{28}O_4$
FW [g mol^{-1}]	545.95	643.06	630.01
Crystal system	triclinic	triclinic	triclinic
Space group	*P*−1 (No. 2)	*P*−1 (No. 2)	*P*−1 (No. 2)
Color / Habit	Blue Block	Blue Needle	Blue Plate
Size [mm]	0.05 x 0.15 x 0.15	0.01 x 0.10 x 0.50	0.02 x 0.06 x 0.12
a [Å]	7.5130(5)	8.5054(5)	7.6635(3)
b [Å]	10.4994(6)	9.3145(6)	8.3252(3)
c [Å]	13.9744(10)	16.4303(10)	8.8503(3)
α [°]	90.076(5)	73.794(5)	94.183(1)
β [°]	104.597(6)	78.909(5)	93.961(1)
γ [°]	110.881(6)	80.601(5)	92.207(1)
V [Å^3]	991.61(12)	1218.27(13)	561.26(4)
Z	2	2	1
$\rho_{calc.}$ [g cm^{-3}]	1.829	1.753	1.864
μ [mm^{-1}]	1.178	0.978	1.062
F(000)	554	656	319
$\lambda_{MoK\alpha}$ [Å]	0.71073	0.71073	0.71073
T [K]	123	123	173
θ Min-Max [°]	2.1, 32.6	2.3, 31.9	3.2, 30.5
Dataset	−10: 10; −14: 15; −21: 15	−12: 12; −11: 13; −23: 22	−10: 10; −11: 11; −12: 12
Reflections collected	11878	13732	16193
Independent refl.	6501	7379	3413
R_{int}	0.033	0.043	0.039
Observed reflections	4682	5249	3053
Parameters	335	395	215
R_1 (obs)[a]	0.0464	0.05	0.0319
wR_2 (all data)[b]	0.1041	0.1016	0.0728
S [c]	1.03	1.04	1.08
Resd. dens [e Å^{-3}]	−0.56, 0.99	−0.53, 0.56	−0.37, 0.40
Absorption correction	multi-scan	multi-scan	multi-scan
CCDC	2394623	2394590	2394592

[a]$R_1 = \Sigma||F_0|-|F_c||/\Sigma|F_0|$; [b]$wR_2 = [\Sigma[w(F_0^2-F_c^2)^2]/\Sigma[w(F_0)^2]]^{1/2}$; $w = [\sigma c^2(F_0^2)+(xP)^2+yP]^{-1}$ and $P=(F_0^2+2F_c^2)/3$; [c]$S = \{\Sigma[w(F_o^2-F_c^2)^2]/(n-p)\}^{1/2}$ (n = number of reflections; p = total number of parameters).

Table S3. Crystallographic data and crystal structure refinement details of compounds **1**, **3** and **4**.

	$[Cu(ANIT)_2(1\text{-}APT)_2]$	$[Fe(ANIT)_2(H_2O)_2] \cdot 2\ H_2O$
Formula	$C_{10}H_{18}CuN_{28}O_4$	$C_2H_8FeN_{14}O_6$, $2(H_2O)$
FW [g mol^{-1}]	658.06	416.11
Crystal system	monoclinic	triclinic
Space group	$P2_1/n$ (No. 14)	$P\bar{1}$ (No. 2)
Color / Habit	Violet Block	Yellow Plate
Size [mm]	0.15 x 0.20 x 0.25	0.02 x 0.10 x 0.12
a [Å]	11.4578(7)	6.4691(4)
b [Å]	5.8393(4)	6.9872(4)
c [Å]	18.8934(13)	8.3330(5)
α [°]	90	74.463(2)
β [°]	92.536(6)	71.796(2)
γ [°]	90	86.373(2)
V [Å^3]	1262.84(14)	344.65(4)
Z	2	1
$\rho_{calc.}$ [g cm^{-3}]	1.731	2.005
μ [mm^{-1}]	0.948	1.177
F(000)	670	212
$\lambda_{MoK\alpha}$ [Å]	0.71073	0.71073
T [K]	123	173
θ Min-Max [°]	2.0, 32.8	2.7, 29.6
Dataset	−16: 16; −8: 8; −28: 28	−8: 8; −9: 9; −11: 11
Reflections collected	14870	8421
Independent refl.	4314	1924
R_{int}	0.045	0.034
Observed reflections	3095	1836
Parameters	204	139
R_1 (obs)[a]	0.0422	0.0245
wR_2 (all data)[b]	0.1076	0.0609
S [c]	1.04	1.13
Resd. dens [e Å^{-3}]	−0.58, 0.50	−0.40, 0.42
Absorption correction	multi-scan	multi-scan
CCDC	2394589	2394622

[a]$R_1 = \Sigma||F_0|-|F_c||/\Sigma|F_0|$; [b]$wR_2 = [\Sigma[w(F_0^2-F_c^2)^2]/\Sigma[w(F_0)^2]]^{1/2}$; $w = [\sigma c^2(F_0^2)+(xP)^2+yP]^{-1}$ and $P=(F_0^2+2F_c^2)/3$; [c]$S = \{\Sigma[w(F_o^2-F_c^2)^2]/(n-p)\}^{1/2}$ (n = number of reflections; p = total number of parameters).

8.8.3 IR Spectroscopy of 1–9

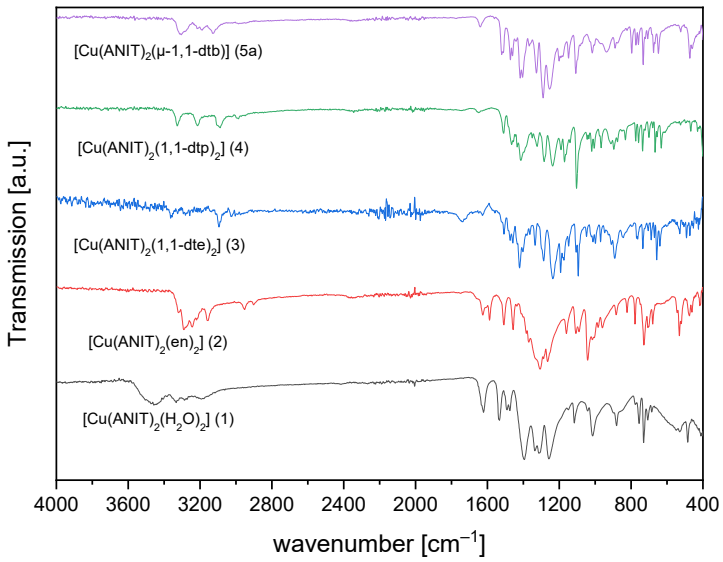

Figure S1. IR spectra of **1**–**5a**.

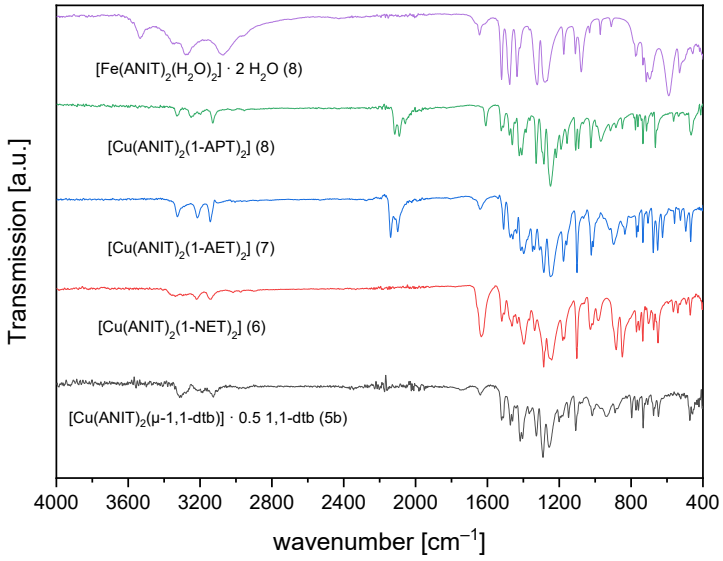

Figure S2. IR spectra of **5b**–**9**.

8.8.4 Thermal Analysis of 1–9

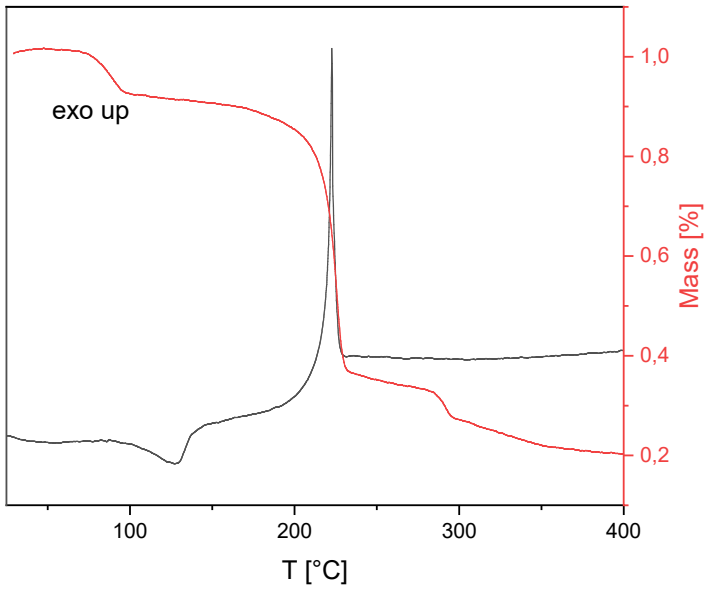

Figure S3. DTA (black) and TGA (red) plot of $[Cu(ANIT)_2(H_2O)_2]$ (**1**) in the range of 25–400 °C.

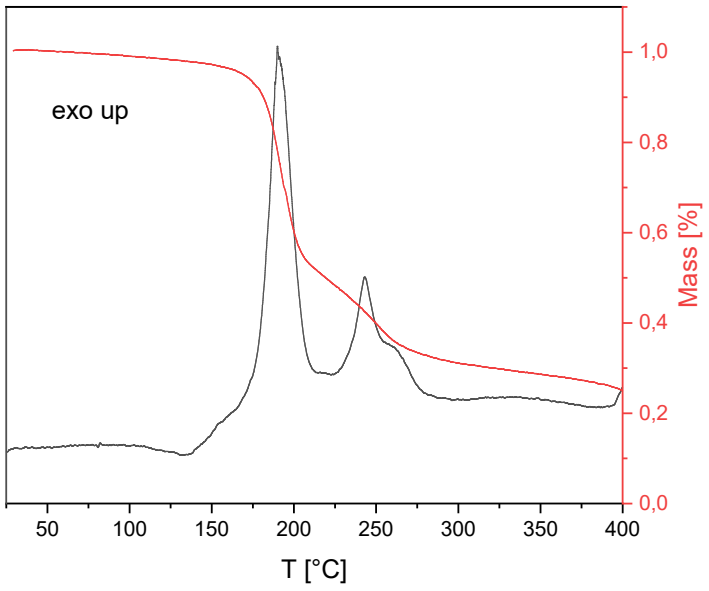

Figure S4. DTA (black) and TGA (red) plot of $[Cu(ANIT)_2(en)_2]$ (**2**) in the range of 25–400 °C.

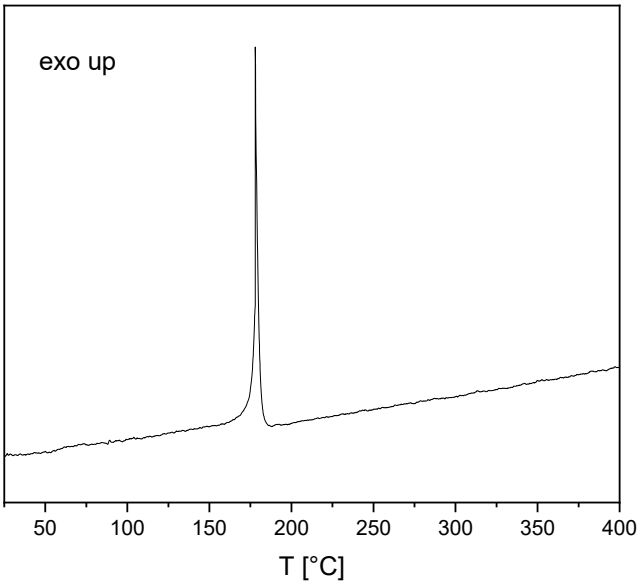

Figure S5. DTA plot of $[Cu(ANIT)_2(1,1\text{-dte})_2]$ (**3**) in the range of 25–400 °C.

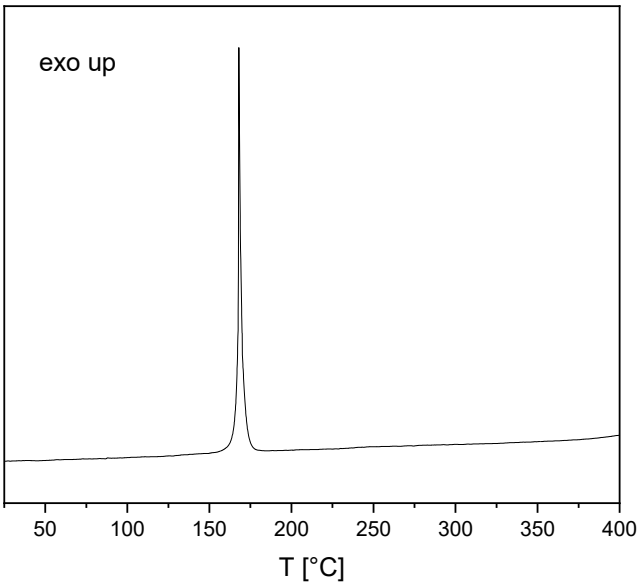

Figure S6. DTA plot of $[Cu(ANIT)_2(1,1\text{-dtp})_2]$ (**4**) in the range of 25–400 °C.

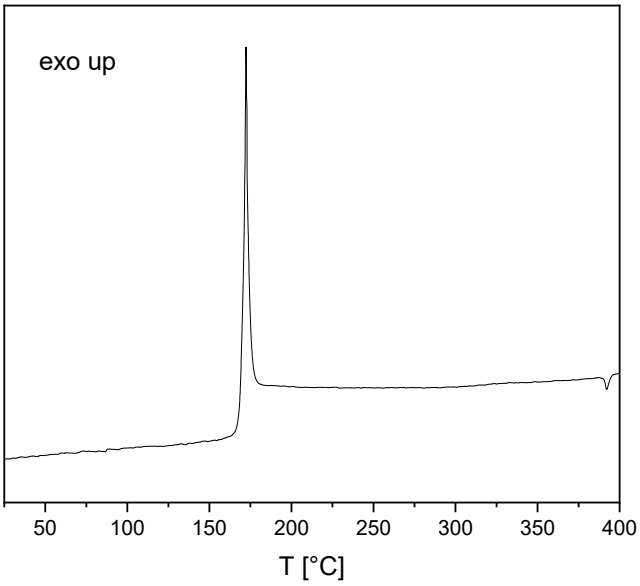

Figure S7. DTA plot of [Cu(ANIT)$_2$(μ-1,1-dtb)] (**5a**) in the range of 25–400 °C.

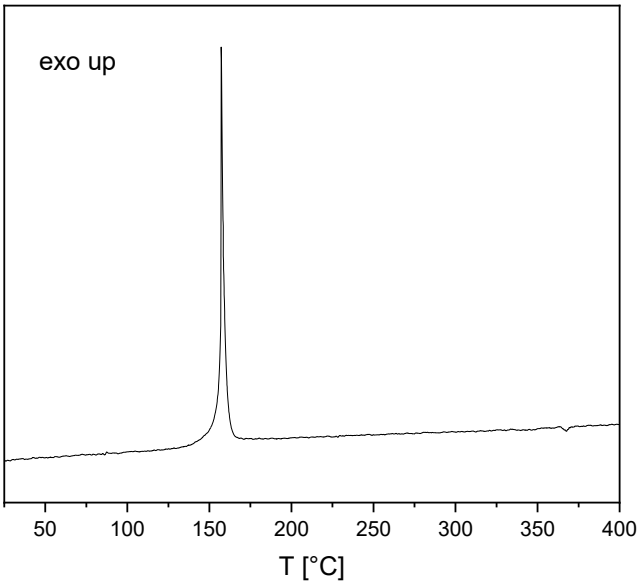

Figure S8. DTA plot of [Cu(ANIT)$_2$(μ-1,1-dtb)] · 0.5 1,1-dtb (**5b**) in the range of 25–400 °C.

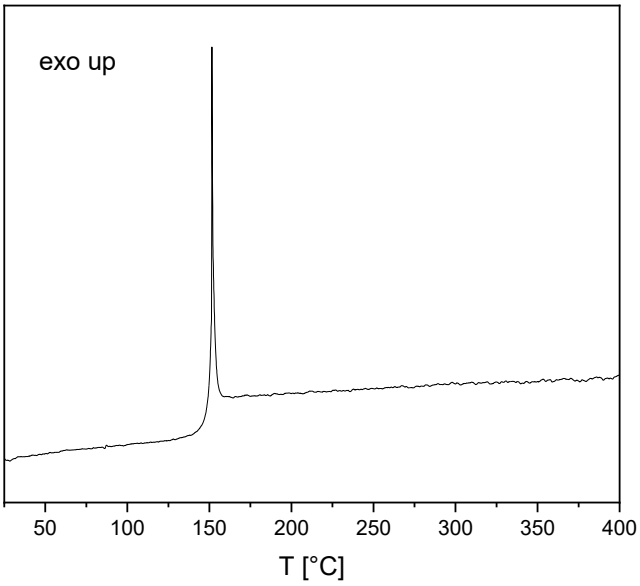

Figure S9. DTA plot of $[Cu(ANIT)_2(1\text{-}NET)_2]$ (**6**) in the range of 25–400 °C.

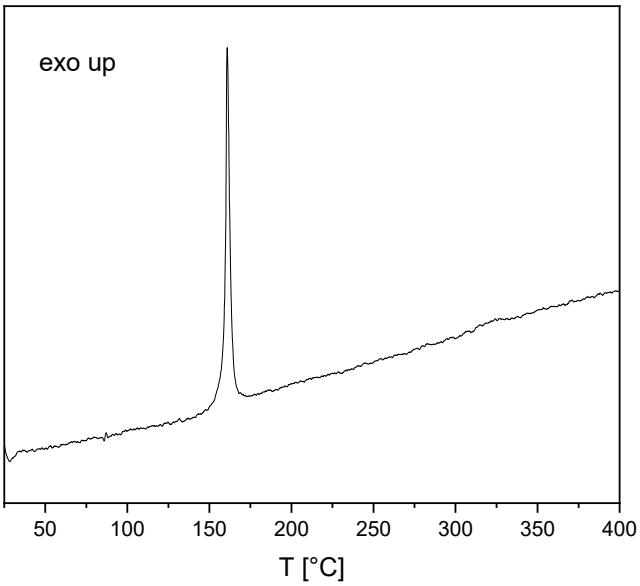

Figure S10. DTA plot of $[Cu(ANIT)_2(1\text{-}AET)_2]$ (**7**) in the range of 25–400 °C.

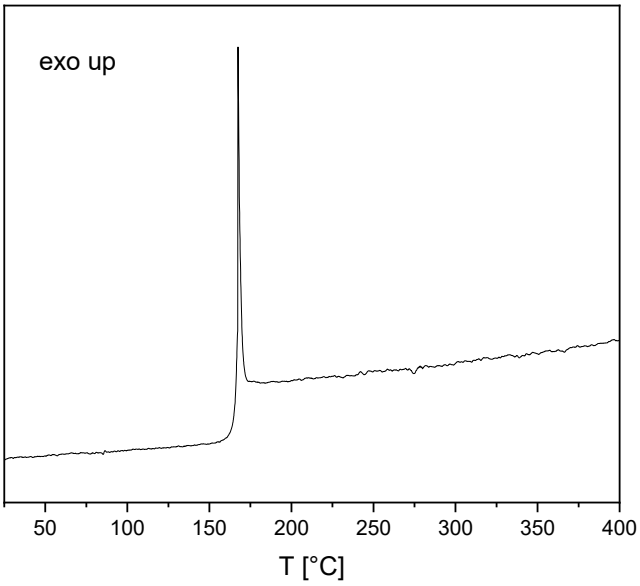

Figure S11. DTA plot of $[Cu(ANIT)_2(1\text{-}APT)_2]$ (**8**) in the range of 25–400 °C.

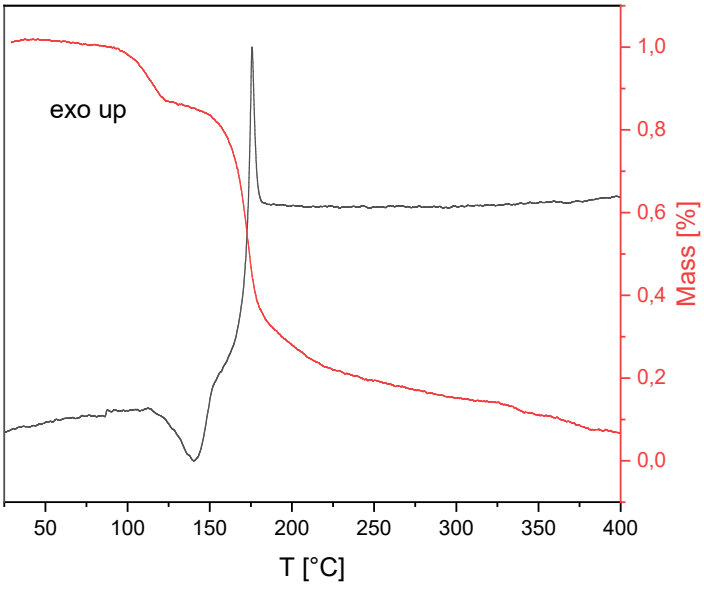

Figure S12. DTA (black) and TGA (red) plot of $[Fe(ANIT)_2(H_2O)_2] \cdot 2\ H_2O$ (**9**) in the range of 25–400 °C.

8.8.5 Hot Plate and Hot Needle Testing

Figure S13. Hot plate (left) and hot needle test of **1**.

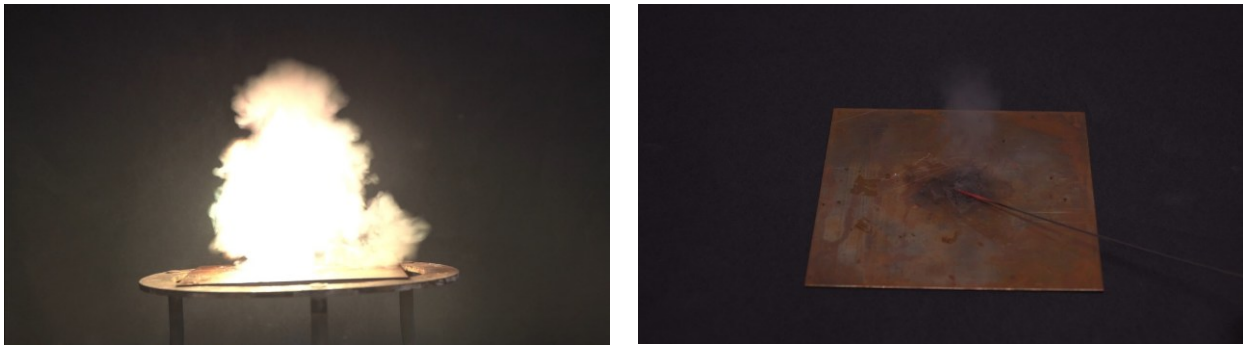

Figure S14. Hot plate (left) and hot needle test of **2**.

Figure S15. Hot plate (left) and hot needle test of **3**.

Figure S16. Hot plate (left) and hot needle test of **4**.

Figure S17. Hot plate (left) and hot needle test of **5a**.

Figure S18. Hot plate (left) and hot needle test of **5b**.

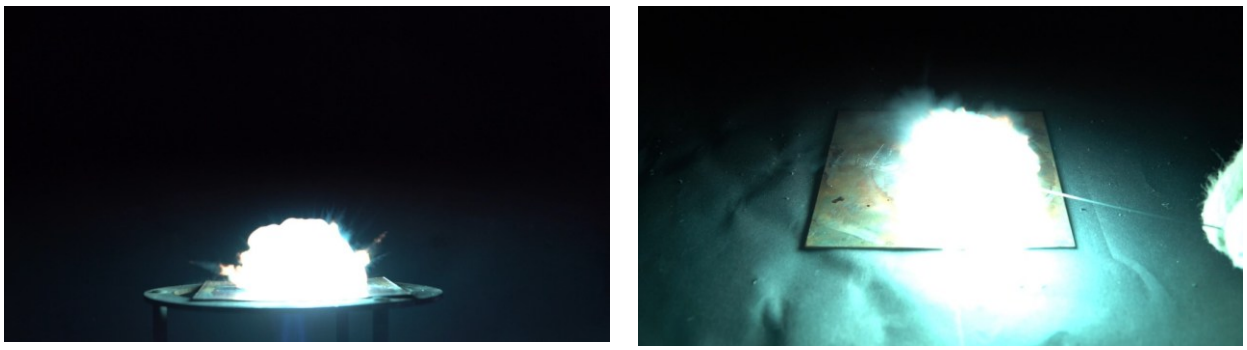

Figure S19. Hot plate (left) and hot needle test of **6**.

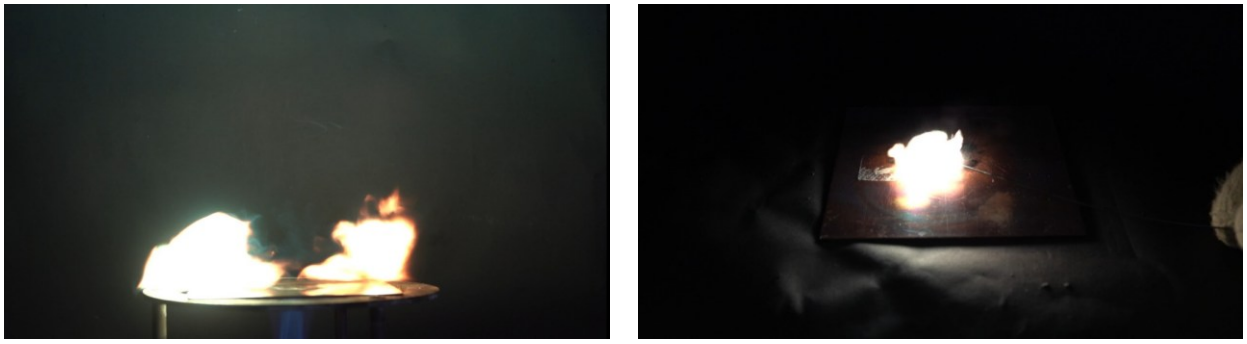

Figure S20. Hot plate (left) and hot needle test of **7**.

Figure S21. Hot plate (left) and hot needle test of **8**.

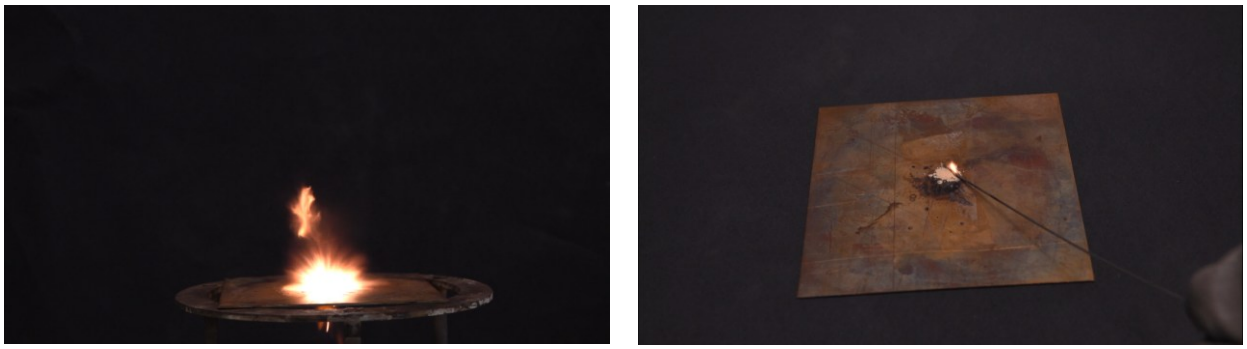

Figure S22. Hot plate (left) and hot needle test of **9**.

8.8.6 Scanning Electron Microscopy

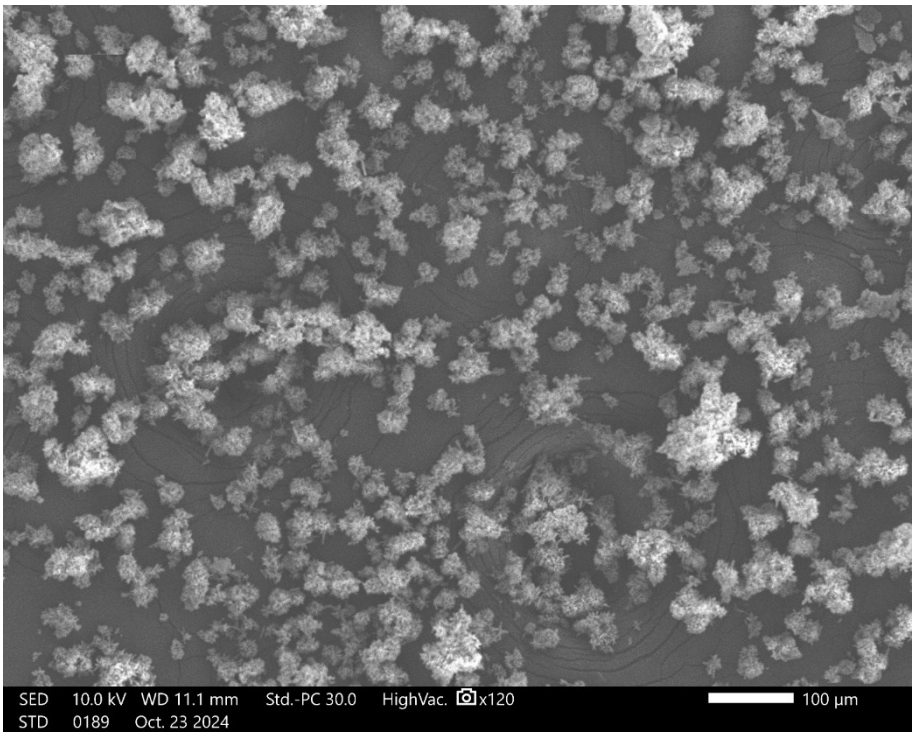

Figure S23. SEM image of **1** at 120× magnification.

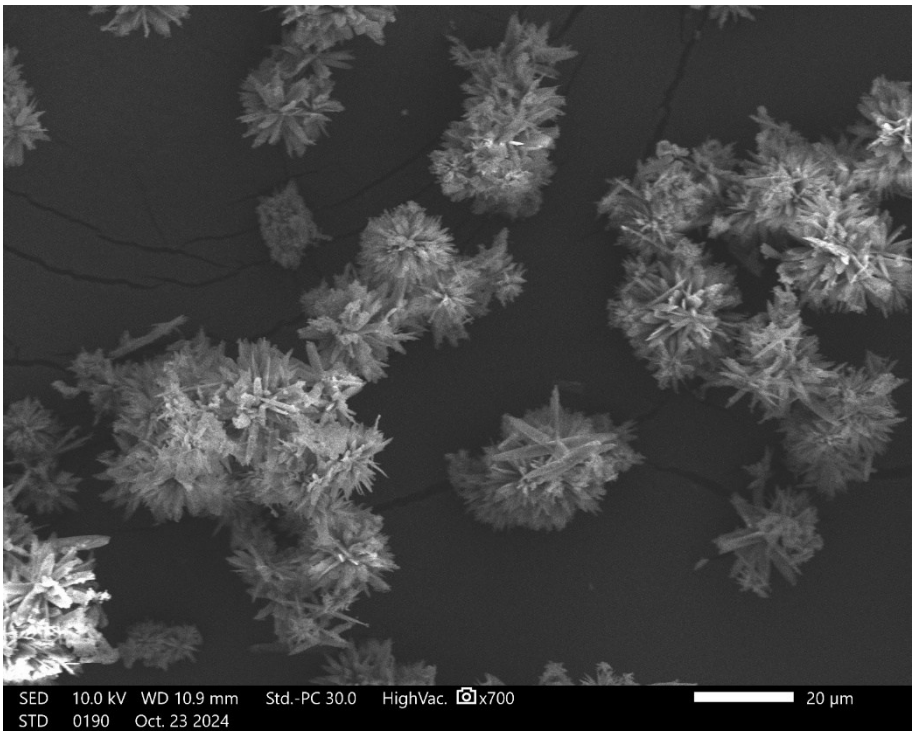

Figure S24. SEM image of **1** at 700× magnification.

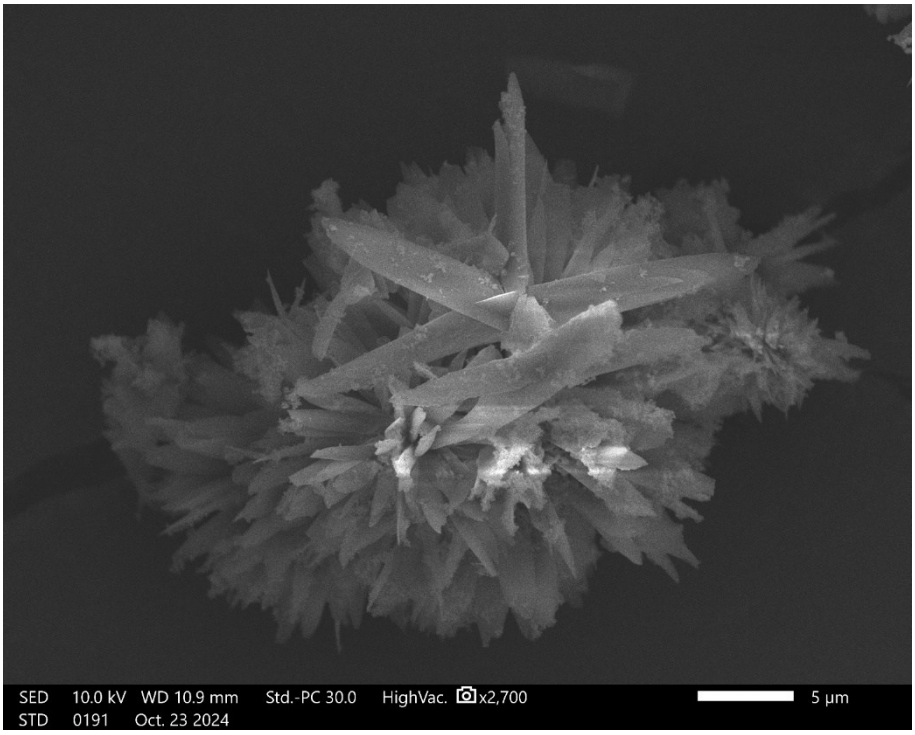

Figure S25. SEM image of **1** at 2700× magnification.

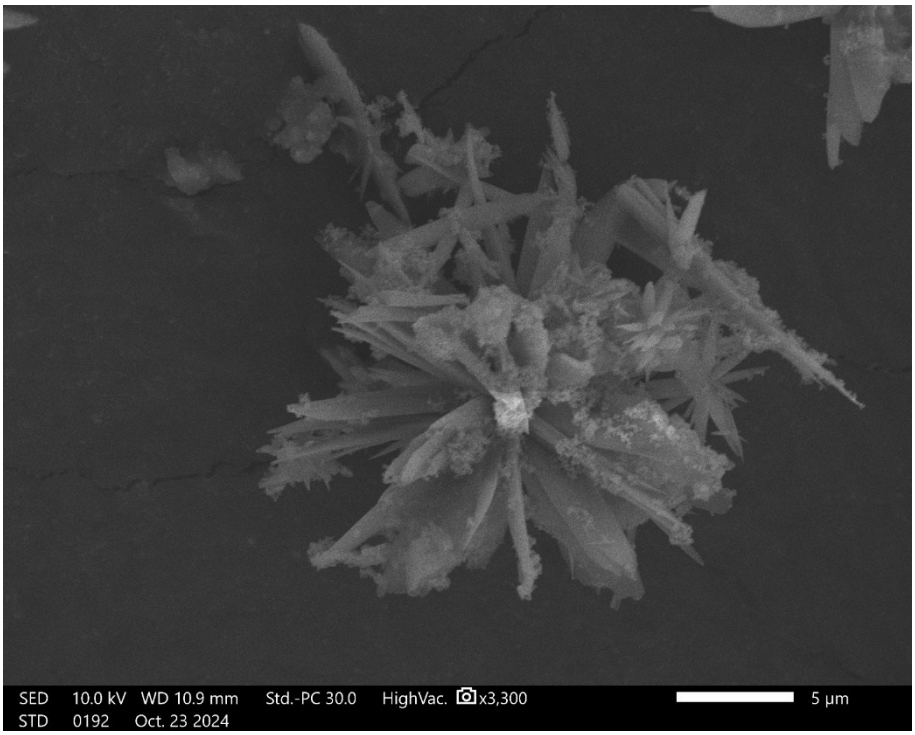

Figure S26. SEM image of **1** at 3300× magnification.

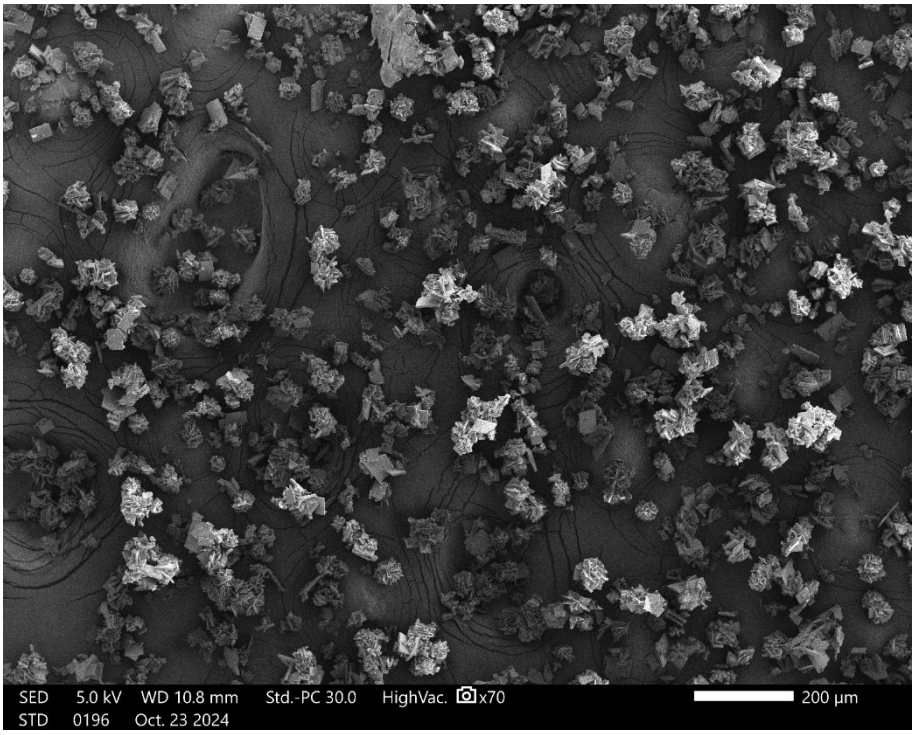

Figure S27. SEM image of **7** at 70× magnification.

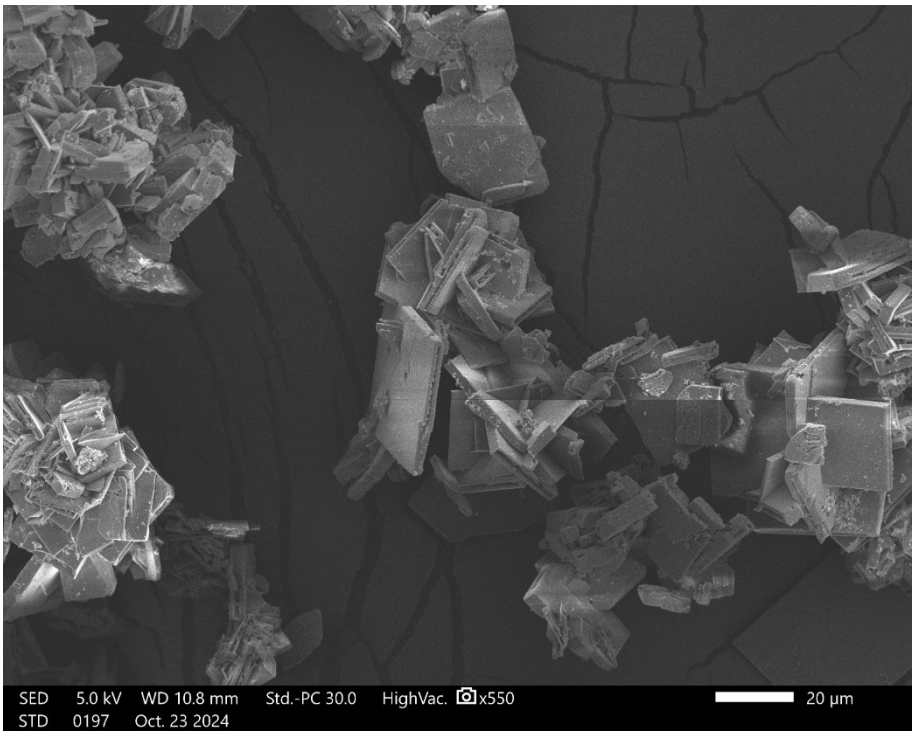

Figure S28. SEM image of **7** at 550× magnification.

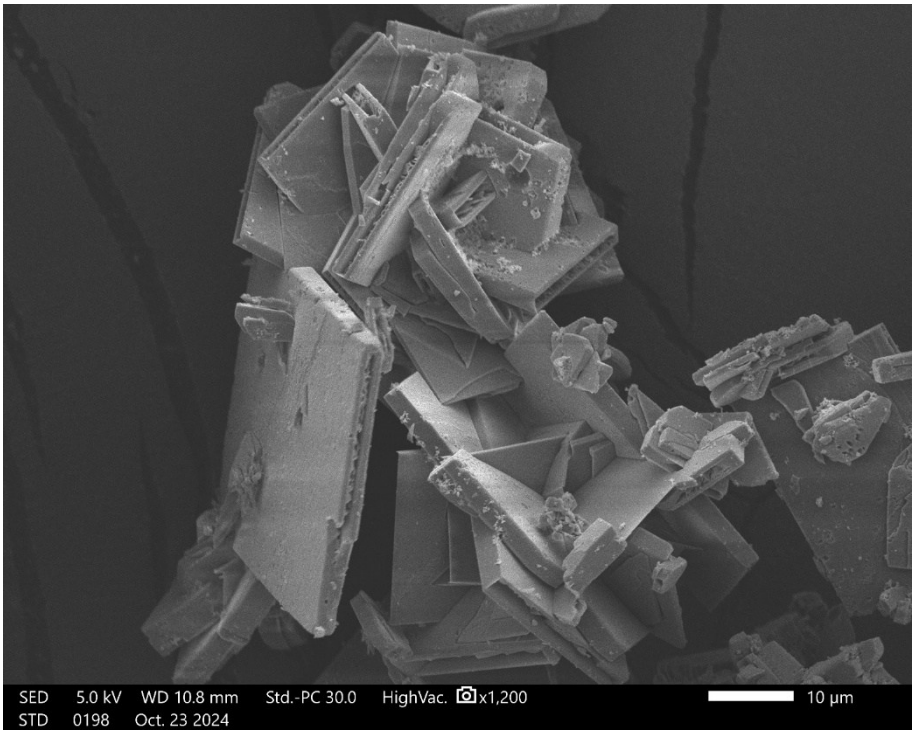

Figure S29. SEM image of **7** at 1200× magnification.

Figure S30. SEM image of **7** at 5500× magnification.

8.8.7 Experimental and Analytical Methods

All chemicals and solvents were employed as received (Sigma-Aldrich, Fluka, Acros, ABCR). Endothermic and exothermic events of the described compounds, which indicate melting, loss of crystal water or decomposition, are given as the extrapolated onset temperatures. The samples were measured in a range of 25–400 °C at a heating rate of 5 °C min^{-1} through differential thermal analysis (DTA) with an OZM Research DTA 552-Ex instrument. Infrared spectra were measured with pure samples on a Perkin-Elmer BXII FT-IR system with a Smith DuraSampler IR II diamond ATR. Determination of the carbon, hydrogen, and nitrogen contents was carried out by combustion analysis using an Elementar Vario El (nitrogen values determined are often lower than the calculated ones' due to their explosive behavior). Impact sensitivity tests were carried out according to STANAG 4489 [S10] with a modified instruction [S11] using a BAM (Bundesanstalt für Materialforschung) drophammer. [S12] Friction sensitivity tests were carried out according to STANAG 4487 [S13] with a modified instruction [S14] using the BAM friction tester. [S12, 15] The classification of the tested compounds results from the "UN Recommendations on the Transport of Dangerous Goods". [S16] Additionally, all compounds were tested upon the sensitivity toward electrical discharge using the OZM Electric Spark XSpark10 device. [S15] The morphology of selected samples was determined by a JEOL JSM-IT210 scanning electron microscope (SEM). The samples were gold-coated (Quorum Q 150R ES plus) to hinder electrostatic charging and to increase the conductivity.

8.8.8 References

[S1] *CrysAlisPRO*, Version 171.33.41, Oxford Diffraction Ltd, **2009**.

[S2] G. M. Sheldrick, *Acta Crystallogr. Sect. A* **2015**, *71*, 3–8.

[S3] a) G. M. Sheldrick, *SHELXL-97*, University of Göttingen, Germany, **1997**; b) G. M. Sheldrick, *Acta Crystallogr. Sect. A* **2008**, *64*, 112–122.

[S4] A. L. Spek, *PLATON*, Utrecht University, The Netherlands, **1999**.

[S5] L. J. Farrugia, *J. Appl. Cryst.* **2012**, *45*, 849.

[S6] O. V. Dolomanov, L. J. Bourhis, R. J. Gildea, J. A. K. Howard, H. Puschmann, *J. Appl. Cryst.* **2009**, *42*, 339–341.

[S7] *Empirical absorption correction using spherical harmonics, implemented in SCALE3 ABSPACK scaling algorithm*, Version 171.33.41, CrysAlisPro Oxford Diffraction Ltd., **2009**.

[S8] *APEX3*, Bruker AXS Inc., Madison, Wisconsin, USA,

[S9] H. Putz, K. Brandenburg, *Diamond - Crystal and Molecular Structure Visualization*, Crystal Impact, Bonn, Germany,

[S10] NATO standardization agreement (STANAG) on explosives, impact sensitivity tests, no. 4489, 1st ed., 1999.

[S11] WIWEB-Standardarbeitsanweisung 4–5.1.02, Ermittlung der Explosionsgefährlichkeit, hier der Schlagempfindlichkeit mit dem Fallhammer, According to: **2002**.

[S12] BAM, http://www.bam.de, accessed December 2021.

[S13] NATO standardization agreement (STANAG) on explosive, friction sensitivity tests, no. 4487, According to: 1st. Edition, **2002**.

[S14] WIWEB-Standardarbeitsanweisung 4–5.1.03, Ermittlung der Explosionsgefährlichkeit oder der Reibeempfindlichkeit mit dem Reibeapparat, According to: **2002**.

[S15] OZM, https://www.ozm.cz/, accessed December 2021.

[S16] a) *UN Model Regulation: Recommendations on the Transport of Dangerous Goods – Manual of Tests and Criteria, section 13.4.2.3.3*, **2015**; b) Impact: insensitive > 40 J, less sensitive ≥ 35 J, sensitive ≥ 4 J, very sensitive ≤ 3 J; Friction: insensitive > 360 N, less sensitive = 360 N, sensitive < 360 N and > 80 N, very sensitive ≤ 80 N, extremely sensitive ≤ 10 N, According to: Recommendations on the Transport of Dangerous Goods, Manual of Tests and Criteria, 4th edition, New York-Geneva, **1999**.

9 Summary and Conclusion

This dissertation summarizes the work on new energetic coordination compounds (ECCs) as primary explosives with several peer-reviewed publications as a first author, shared first author or co-author. Together with the classical academic research, a cooperation with an industrial partner was established in which four literature-known primary explosives were studied and optimized. Additional work on ammeline and its perchlorate salts was published in Angewandte Chemie. This work was excluded from this dissertation, as it does not align with the focus of this thesis. Furthermore, a publication on the synthesis of nitramine- and oxapropane-bridged tetrazoles *via* one-step Finklestein reaction was published in Chemistry–A European Journal. While this work presented 11 new energetic materials, some with very promising properties, it included only two new ECCs, both with very limited potential. The work is therefore also excluded from this thesis. As explained in Chapter 1, the motivation for this thesis was the variation of the three components of ECCs, which are the central metal, the anion and the ligand. The goal hereby was to study the influence of each component and optimize toward usability as primary explosives. As general methods, characterization was conducted by single-crystal X-ray diffraction, multinuclear NMR spectroscopy (^{1}H, ^{13}C, ^{14}N, ^{15}N, ^{207}Pb), infrared spectroscopy, elemental analysis, mass spectrometry, thermal analysis (DTA, DSC, TGA), sensitivity measurements (BAM drophammer, BAM friction tester, OZM XSpark 10 ESD tester), hot plate and hot needle test, laser initiation and PETN initiation. Powder properties of promising candidates were analyzed by scanning electron microscopy and laser diffraction particle size analysis.

9.1 Summary of Chapter 2

Trinitro-orcinol (5-methyl-2,4,6-trinitrobenzene-1,3-diol, H_2TNO) was prepared and characterized. Its energetic properties and vapor pressure were compared to those of styphnic acid (2,4,6-trinitrobenzene-1,3-diol, H_2TNR) and trinitro-toluene (2-methyl-1,3,5-trinitrobenzene, TNT). As expected, due to their characteristic structural motifs, both performance parameters and vapor pressure lie between those of H_2TNR and TNT. H_2TNO was further deprotonated for usage as an anion in ECCs. The main goal hereby was to compare those to ECCs with the anions of styphnic acid. Therefore, 17 new compounds were prepared and studied concerning their physicochemical and structural properties. The

expected result of obtaining mechanically more stable relatives of the styphnate ECCs, was surprisingly not achieved. Instead, the results indicated that the $HTNO^-$ anion coordinates to the metal center *via* the hydroxy and the nitro group in 2-position of the ring, unlike $HTNR^-$, which typically coordinates *via* the hydroxy and the nitro group in 6-position (Figure 1). As a result, the ECCs of $HTNO^-$ were more sensitive to impact and in many cases less sensitive to friction, which might make the trinitro-orcinolates valuable options for primer caps or the first stage of stab detonators.

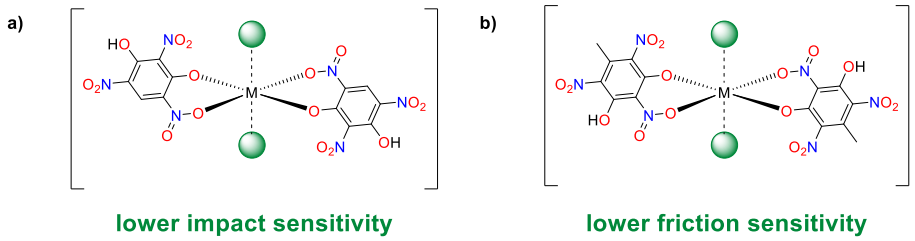

Figure 1. Classical coordination motif of **a)** styphnate containing ECCs compared to that of **b)** trinitro-orcinolates.

9.2 Summary of Chapter 3

The underlying publication of this chapter describes the first-time synthesis of 1-nitroato-methyltetrazole (1-NAMT) in two steps, starting from tetrazole. Reaction of tetrazole with paraformaldehyde under basic catalysis results in an isomeric mixture of 1- and 2-hydroxy-methyltetrazole. Nitration of this mixture with acetyl nitrate then gives 1-NAMT, while 2-NAMT decomposes during the process. As expected for a compound with the sum formula $C_2H_3N_5O_3$, 1-NAMT is very sensitive toward mechanical stimuli and possesses the typical low thermal stability of organic nitrates. When used as a ligand in ECCs, it passes on these properties to the coordination compound and thereby limits the overall stability (Figure 2). While nitroaromatic anions such as picrate (PA^-) may stabilize the friction sensitivity and thermal stability, they drastically reduce the performance compared to $[Cu(1\text{-}NAMT)_6](ClO_3)_2$, which showed promising results in the laser initiation trials.

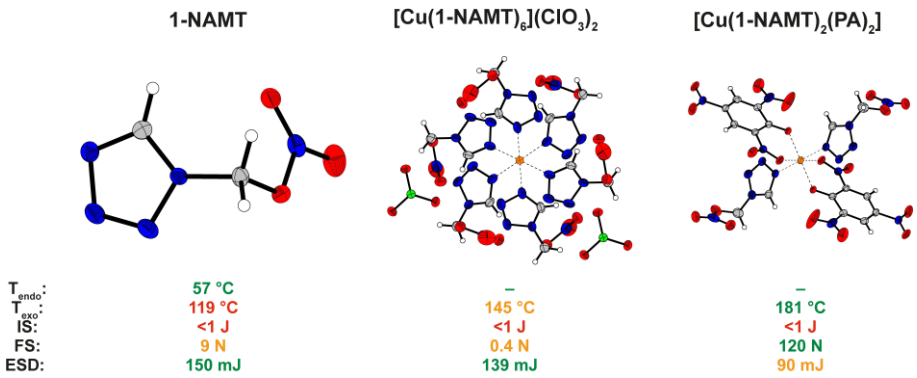

Figure 2. Properties of 1-NAMT, $[Cu(1\text{-}NAMT)_6](ClO_3)_2$ and $[Cu(1\text{-}NAMT)_2(PA)_2]$.

9.3 Summary of Chapters 4–6

As an alternative approach to increase the enthalpy of formation of the ligand, and therefore the energy content of the ECCs, tetrazoles with unsaturated side-chains (Figure 3) were introduced. For comparison, the previously studied 1-ethyltetrazole (1-ETZ) and 1-propyltetrazole (1-PTZ) are shown. While 1-allyltetrazole (1-ATZ), 1-propargyltetrazole (1-PryTz), and 1-tetrazolylazetonitrile (1-TAN) can be produced directly from the respective amines or ammonium salts, 1-vinyltetrazole (1-VTZ) has to be prepared starting from 2-chloroethylamine in two steps. The 2-isomers have to be prepared by alkylation of tetrazole, followed by separation of the isomers.

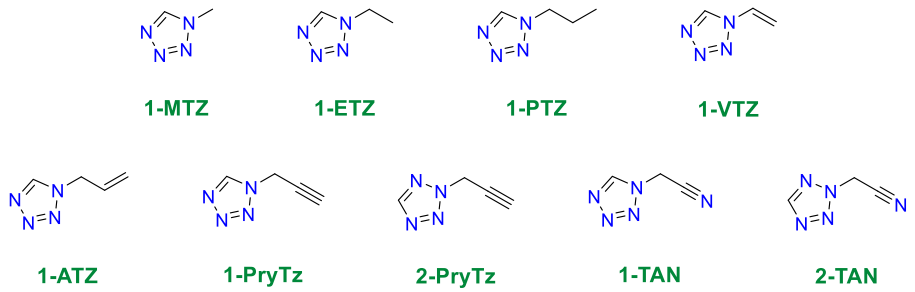

Figure 3. Tetrazole ligands with unsaturated side-chains and their structural relatives 1-MTZ, 1-ETZ and 1-PTZ.

Computation of the gas-phase enthalpies of formation of these compounds at CBS-4M level shows the influence of the oxidation of the side-chains. The gas-phase enthalpies were chosen to reduce the influence of different condensed phases. To improve the comparability, all compounds are shown in kJ kg^{-1}. Figure 4 shows the two trends that can be observed. The first trend, that can be observed is that shorter chains of the same nature result in a higher enthalpy of formation. As a second trend, similar chain lengths with higher

oxidation lead to a higher enthalpy of formation, outweighing the effect of the shorter chain-length.

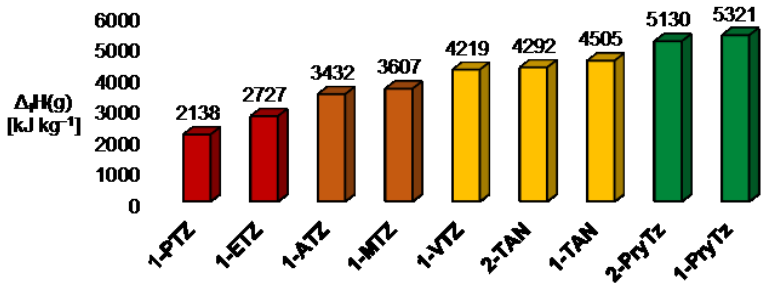

Figure 4. Gas-phase enthalpies of formation of the tetrazole ligands calculated at the CBS-4M level.

The comparison of the gas-phase enthalpies of formation translates directly to the determined sensitivities of ECCs with the type $[Cu(L)_6](ClO_4)_2$ in cases of C_xH_y substituents. Figure 5 shows the relationship between the ligands and the stability of the ECCs. It should be noted, that the oxidation of the side chain has a direct impact on the thermal stability of the ECC.

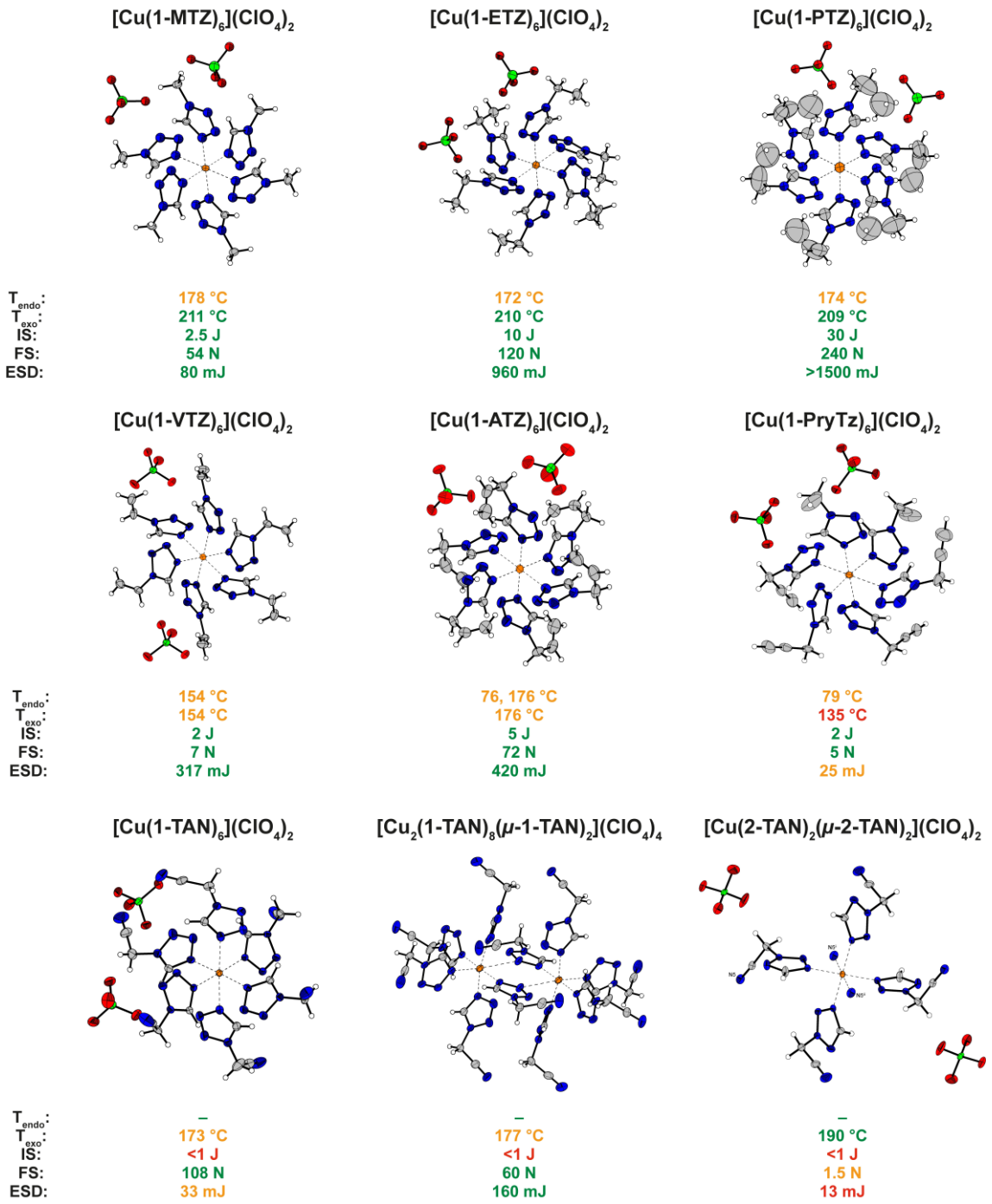

Figure 5. Structural comparison of the copper(II) perchlorates $[Cu(1\text{-}MTZ)_6](ClO_4)_2$, [1] $[Cu(1\text{-}ETZ)_6](ClO_4)_2$, [2] $[Cu(1\text{-}PTZ)_6](ClO_4)_2$, [3-4] $[Cu(1\text{-}VTZ)_6](ClO_4)_2$, $[Cu(1\text{-}ATZ)_6](ClO_4)_2$, $[Cu(1\text{-}PryTz)_6](ClO_4)_2$, $[Cu(1\text{-}TAN)_6](ClO_4)_2$, $[Cu_2(1\text{-}TAN)_8(\mu\text{-}1\text{-}TAN)_2](ClO_4)_4$, and $Cu(2\text{-}TAN)_2(\mu\text{-}2\text{-}TAN)_2](ClO_4)_2$.

By exchanging the alkyne group of 1-PryTz with the isosteric nitrile in 1-TAN, and therefore lowering the overall energy of the ECCs, stability is regained despite the increased nitrogen content. Surprisingly, the impact sensitivity is increased in $[Cu(1\text{-}TAN)_6](ClO_4)_2$. The trend of the friction sensitivity of related tetrazolylacetonitrile systems

(108 > 60 > 1.5 N) can be explained by the ratio between ligand/fuel and anion/oxidizer (3:1 > 5:2 > 2:1). In a similar way the sensitivities of [Ag(ClO_4)(μ-1-TAN)] and [Ag(μ-2-TAN)$_2$](ClO_4) can be explained. Both show increased sensitivities, but only [Ag(ClO_4)(μ-1-TAN)] manages to successfully initiate PETN in the detonator setup. The performance, combined with the fact that the 1-TAN ligand can be produced from the ammonium salt by tetrazole ring closure, acceptable thermal stability and a no-fire limit at the friction tester make this compound a potential lead azide replacement candidate.

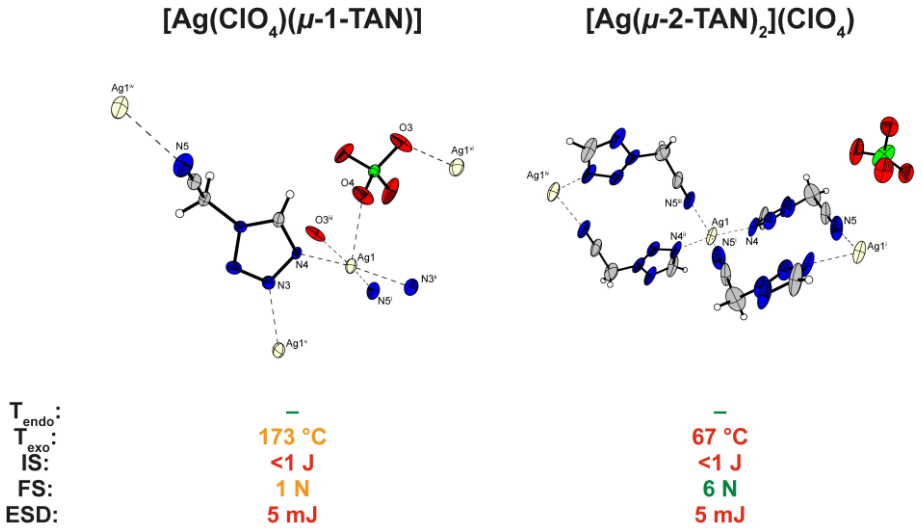

Figure 6. Structures and properties of [Ag(ClO_4)(μ-1-TAN)] and [Ag(μ-2-TAN)$_2$](ClO_4).

9.4 Summary of Chapter 7

Organic azides play an important role in preparative and energetic materials chemistry but in many cases the introduction of azido-alkyl groups lacks uniform conditions. [5-11] Therefore, a straightforward pathway for the introduction of the azidoethyl group to azoles was established for three transfer reagents, which can be produced and handled in a safe manner.

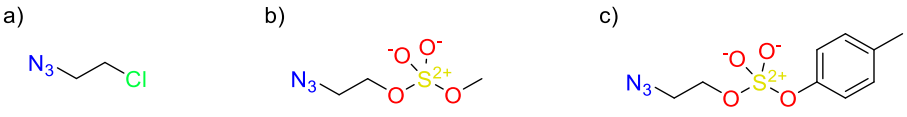

Figure 7. The three azidoethyl transfer reagents used for *N*-alkylation of azoles.

It is of little surprise, that uniform conditions for the alkylation do not lead to maximum yields for all heterocycles, however the accessibility of the reagent and atom economics often play an important role when first synthesizing and evaluating a new compound.

Therefore, 1-azido-2-chloroethane represents a suitable bench-stable reagent, which can be prepared by simple bromide to azide exchange reaction. As a result, the six nitrogen-rich azoles shown in Figure 8 were synthesized and characterized.

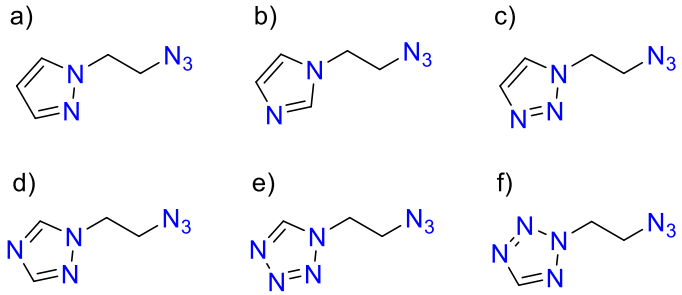

Figure 8. The azido-ethyl azoles obtained by *N*-alkylation **a)** 1-(2-azidoethyl)-pyrazole (AEPy), **b)** 1-(2-azidoethyl)-imidazole (AEIm), **c)** 1-(2-azidoethyl)-1,2,3-triazole (AE123Tri), **d)** 1-(2-azidoethyl)-1,2,4-triazole (AE124Tri), **e)** 1-(2-azidoethyl)-tetrazole (1-AET) as well as **f)** 2-(2-azidoethyl)-tetrazole (2-AET).

1-(2-Azidoethyl)-1,2,4-triazole and 2-2(2-azidoethyl)-tetrazole were then used to create a total of ten ECCs, of which three successfully managed to initate PETN and two were ignitable *via* laser-initiation. While [Ag(μ-2-AET)(ClO_4)], [Cu_2(2-AET)(N_3)$_4$] and [Cu_3(AE124Tri)$_2$(N_3)$_6$] all showed excellent PETN priming capabilities, the two copper(II) azide complexes are extremely sensitive ([Cu_2(2-AET)(N_3)$_4$]: FS <0.1 N, IS <1 J, ESD 2.5 mJ and [Cu_3(AE124Tri)$_2$(N_3)$_6$]: FS 0.2 N, IS <1 J, ESD 2.5 mJ) and lack thermal stability. [Ag(μ-2-AET)(ClO_4)] on the other hand is thermally stable up to 151 °C and shows an acceptable friction sensitivity of 0.6 N.

9.5 Summary of Chapter 8

To replace lead-based primary explosives, ECCs with various combinations of cation, anion and ligand can be used. Overcoming the drawback of the significantly lower density, which is typically observed by the use of 3d-metals, can be challenging. Therefore, as a strategy, anions and ligands with high nitrogen content and high heat of formation can be applied to address this issue. The work presented in this chapter focused on the use of 1-amino-5-nitriminotetrazolate (ANIT) as a highly energetic anion for ECCs. The ANIT anion possesses multiple possible coordination sites, which results in a chelating effect during coordination and therefore reduces the number of additional ligands. Since the typically used ligands consist of mostly carbon, nitrogen and hydrogen, a reduction of the amount of ligand used should result in an improved overall C/O ratio. The literature known

NH_4ANIT was therefore chosen as a relatively safe, bench-stable precursor for the production of ECCs, mostly with the composition $[Cu(ANIT)_2(L)_2]$ and $[Cu(ANIT)_2(\mu\text{-}L)]$, where L represents the ligand. A schematic flow in which NH_4ANIT is first reacted to $[Cu(ANIT)_2(H_2O)_2]$ and then to the respective ECC is given in Figure 9.

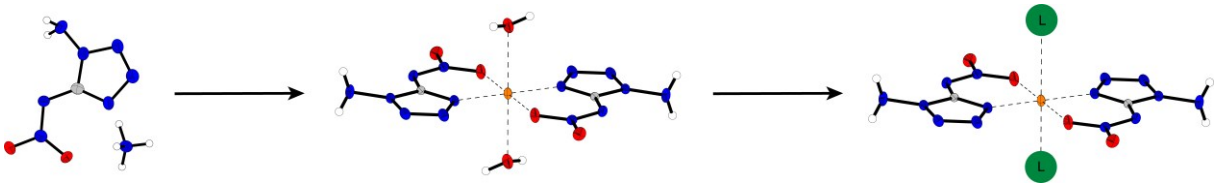

Figure 9. Schematic representation of the use of NH_4ANIT as a precursor for the synthesis of ECCs.

As a result, a total of ten ECCs, which contain the ANIT anion, were established and characterized for the first time. Of these ten, two were able to successfully initiate PETN in the initiation test. An optimized procedure for the precipitation of $[Cu(ANIT)_2(H_2O)_2]$ and $[Cu(ANIT)_2(1\text{-}AET)_2]$ with high sphericity and therefore good flowability was established.

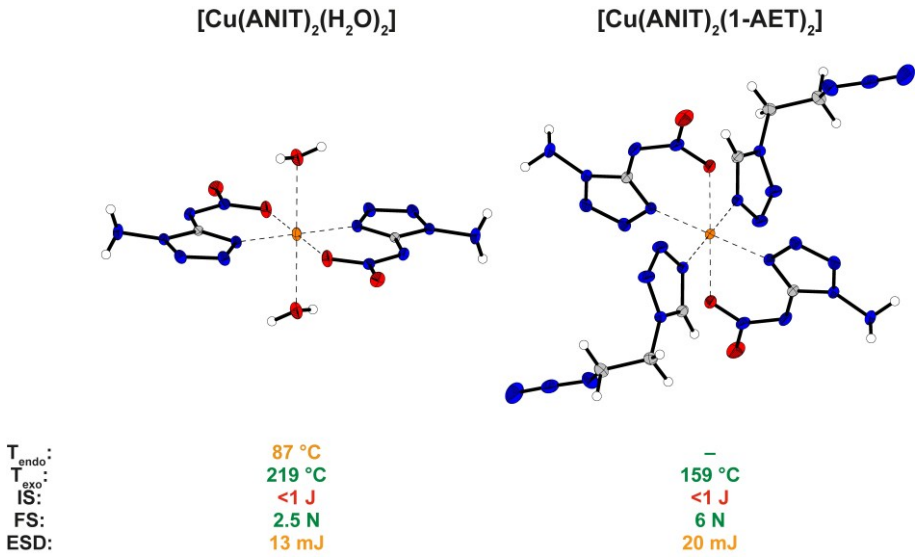

Figure 10. Structures and properties of $[Cu(ANIT)_2(H_2O)_2]$ and $[Cu(ANIT)_2(1\text{-}AET)_2]$.

9.6 Final remarks

In the context of this thesis, a total of nine peer-reviewed articles was published in different journals. Within these, 24 laser-ignitable ECCs and six ECCs with the ability to initiate PETN in detonators were presented. Among the ligands, 1-tetrazolylacetonitrile proved to be of special value, as the incorporation of the triple-bond, paired with the ability to

crosslink metal centers resulted in high overall energies of the ECCs as well as in an adjustable ratio of ligand to anion. The nitrile function further allows the synthesis of other ring-systems, such as tetrazoles or oxadiazoles, which further enhances the synthetic possibilities. 1-Amino-5-nitriminotetrazolate can be identified as the most promising anion presented in this work. Its chelating effect leads to lower aqueous solubility of the coordination compounds and therefore the possibility to produce ECCs with priming ability from aqueous solution. The priming capability of $[Cu(ANIT)_2(H_2O)_2]$, paired with a no-fire limit of 2.5 N of friction force and a high exothermic decomposition temperature of 219 °C make this compound an interesting candidate for the replacement of lead(II) azide. The three most outstanding compounds, which were established during this thesis, are shown in Figure 11. All three compounds show thermal stabilities and sensitivities, which can be considered within acceptable ranges for replacement candidates of commercially used primary explosives.

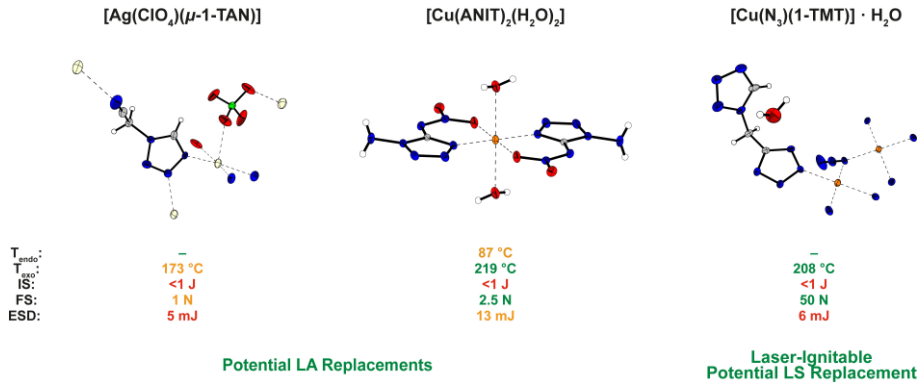

Figure 11. Summary of the three most promising ECCs.

9.7 References

[1] N. Szimhardt, M. H. H. Wurzenberger, A. Beringer, L. J. Daumann, J. Stierstorfer, *J. Mater. Chem. A* **2017**, *5*, 23753–23765.

[2] M. H. H. Wurzenberger, M. S. Gruhne, M. Lommel, N. Szimhardt, T. M. Klapötke, J. Stierstorfer, *Chem. Asian J.* **2019**, *14*, 2018–2028.

[3] A. M. Mills, A. L. Spek, A. F. Stassen, J. G. Haasnoot, J. Reedijk, *CSD Communication* **2007**.

[4] M. H. H. Wurzenberger, S. M. J. Endraß, M. Lommel, T. M. Klapötke, J. Stierstorfer, *ACS Appl. Energy Mater.* **2020**, *3*, 3798–3806.

[5] P. Desai, K. Schildknegt, K. A. Agrios, C. Mossman, G. L. Milligan, J. Aubé, *J. Am. Chem. Soc.* **2000**, *122*, 7226–7232.

[6] S. Bräse, C. Gil, K. Knepper, V. Zimmermann, *Angew. Chem. Int. Ed.* **2005**, *44*, 5188–5240.

[7] F. Himo, T. Lovell, R. Hilgraf, V. V. Rostovtsev, L. Noodleman, K. B. Sharpless, V. V. Fokin, *J. Am. Chem. Soc.* **2005**, *127*, 210–216.

[8] S. S. Van Berkel, M. B. Van Eldijk, J. C. M. Van Hest, *Angew. Chem. Int. Ed.* **2011**, *50*, 8806–8827.

[9] C. Doebelin, M. Schmitt, C. Antheaume, J.-J. Bourguignon, F. Bihel, *J. Org. Chem.* **2013**, *78*, 11335–11341.

[10] H.-H. Xie, J.-L. Weng, J.-X. Song, W.-J. Yang, Q. Wang, M. Cui, F.-K. Zheng, R.-H. Qiu, J.-G. Xu, *Dalton Trans.* **2023**, *52*, 14632–14639.

[11] S. Bräse, K. Banert, *Organic Azides: Syntheses and Applications*, Wiley, **2009**.

10 Appendix

10.1 Additional Publications

10.1.1 On Tautomerism and Amphoterism: An In-Depth Structural and Physicochemical Characterization of Ammeline and Some of Its Salts

Thaddäus J. Koller, Simon M. J. Endraß, Markus Rösch, Kristian Wittaut, Thomas M. Klapötke, and Wolfgang Schnick

published in *Angewandte Chemie* and *Angewandte Chemie International Edition,* **2024**

DOI: 10.1002/ange.202404927 and 10.1002/anie.202404927

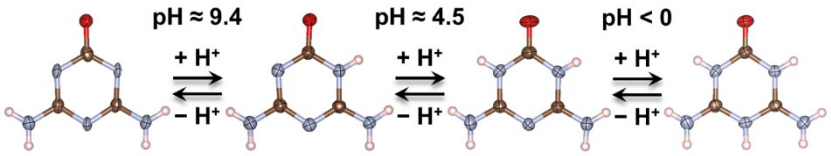

Abstract: Ammeline is a simple, readily available, molecular compound, which has been known for nearly 200 years. Despite that, no proper structural characterization of ammeline has been conducted so far. For this reason, the prevalent tautomeric form of ammeline in the solid remained unknown to this date. In the course of this study, its crystal structure was finally established by single-crystal X-ray diffraction. In this structure, ammeline is exclusively found as its 4,6-diamino-1,3,5triazin-2(1*H*)-one tautomer and adopts layered structure with an exceptionally high hydrogen bond density. Ammeline shows an interesting amphoteric behavior. Therefore, the synthesis and structural characterization of some of its salts were carried out to investigate the influence of the protonation degree on its molecular structure. In particular, the crystal structure of silver ammelinate monohydrate was solved as the first reported structure containing deprotonated ammeline. Moreover, the crystal structures of three different modifications of ammelinium perchlorate were elucidated and the transformation conditions between them were studied. Lastly, the crystal

structure of ammelinediium diperchlorate monohydrate, containing unprecedented doubly protonated ammeline, was determined. The products' thermal behavior was studied by differential thermal analysis and thermogravimetric analysis. The perchlorate salts were additionally examined for their potential as insensitive high-energy-density materials.

10.1.2 Synthesis of Bridged Tetrazoles with Promising Properties and Potential Applications by a One-Step Finkelstein Reaction

Jasmin T. Lechner, Christian Riedelsheimer, Simon M. J. Endraß, Nina M. Gerold, Jennifer Heidrich, Burkhard Krumm, Jörg Stierstorfer, and Thomas M. Klapötke

published in *Chemistry – A European Journal,* **2024**

DOI: 10.1002/chem.202303021

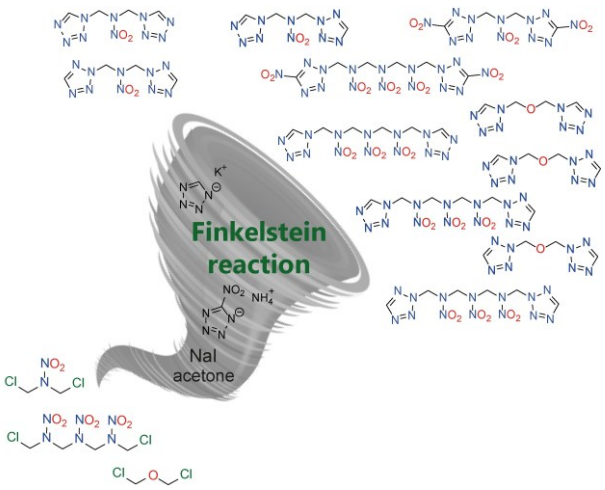

Abstract: Numerous nitramine bridged compounds which show promising combinations of properties have already been identified in the area of energetic materials. In this work, four new nitrazapropane bridged tetrazoles, as well as four new trinitrazaheptane tetrazoles and three oxapropane bridged tetrazoles were synthesized and fully characterized. These new compounds can all be synthesized by a simple, one-step synthesis using Finkelstein conditions. All of these new energetic materials were characterized using NMR spectroscopy, single crystal X-ray diffraction, vibrational analysis and elemental analysis. The thermal behaviour of these compounds was studied by differential thermal analysis (DTA) and partly by thermogravimetric analysis (TGA). The BAM standard method was used to determine the sensitivities towards impact (IS) and friction (FS). The enthalpies of formation were calculated at the CBS-4M level, and the energetic performances were

calculated using the EXPLO5 (V6.06.01) computer code. The properties of the new compounds were compared to each other as well as to the known energetic material RDX. Moreover, the iron(II) and copper(II) perchlorate complexes with 1,3-bis-1,1-tetrazolylnitrazapropane as ligand were prepared and investigated.

10.1.3 Comparison of 1-Propyltetrazole and 1-Azidopropyltetrazole as Ligands for Laser Ignitable Energetic Materials

Maximilian H. H. Wurzenberger, Simon M. J. Endraß, Marcus Lommel, Thomas M. Klapötke, and Jörg Stierstorfter

published in *ACS Applied Energy Materials*, **2020**

DOI: 10.1021/acsaem.0c00229

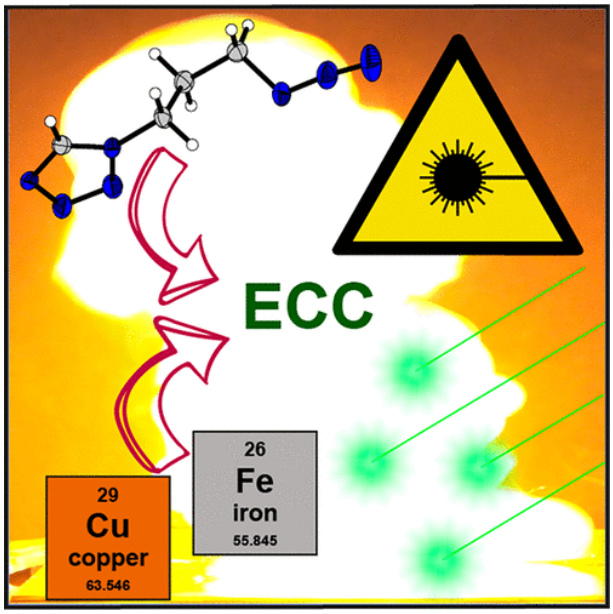

Abstract: Laser ignitable explosives are potential candidates in future applications for replacing toxic and very sensitive primary explosives, which are used in current devices. In this study, the literature unknown ligand 1-azidopropyltetrazole (APT, **1**) was synthesized for the first time and applied in energetic coordination compounds (ECC). The complexes are based on different 3d transition metals (Mn^{2+}, Fe^{2+}, Cu^{2+}, and Zn^{2+}) as well as various oxidizing anions (NO_3^-, ClO_4^-, and ClO_3^-) and were tested toward their capability as laser ignitable explosives. Furthermore, analogous complexes based on the literature known ligand 1-propyltetrazole (PT, **2**) were investigated for comparing the influence of the additional azide group toward the performance of the ECC. Toxicity measurements using *Vibrio fischeri* and the decreased sensitivities prove their usability as safer laser ignitable explosive with lower toxicities compared to currently used explosives.

10.2 List of Conferences

1 24th International Seminar: New Trends in Research of Energetic Materials (NTREM), Pardubice (Czech Republic) 06.04.2022 − 08.04.2022:

Poster presentation:

Trinitro-Orcinol (C7H5N3O8) as anion in energetic metal compounds.

2 25th International Seminar: New Trends in Research of Energetic Materials (NTREM), Pardubice (Czech Republic) 19.04.2022 − 21.04.2022:

Poster presentation:

2-Azidoethyl-tetrazole as a ligand for laser-ignitable energetic materials.

10.3 List of Workshops

1 NEIDEMO – Non-Ideal Detonation Model of Commercial Explosives, Zagreb (Croatia) 11.07.2023 − 12.07.2023:

Oral Presentation:

Primary Explosive Research at LMU Munich and EMTO GmbH.